Measurement of Double Polarization Observables in the Reactions $\gamma p \to p\pi^0$ and $\gamma p \to p\eta$ with the Crystal Barrel/TAPS Experiment at ELSA

von

Jan Hartmann

aus

Dormagen

Bonn, März 2017

Dieser Forschungsbericht wurde als Dissertation von der
Mathematisch-Naturwissenschaftlichen Fakultät der Universität Bonn angenommen und
ist auf dem Hochschulschriftenserver der ULB Bonn
`http://hss.ulb.uni-bonn.de/diss_online` elektronisch publiziert.

1. Gutachterin:	Prof. Dr. Ulrike Thoma
2. Gutachter:	Prof. Dr. Volker Metag
Tag der Promotion:	08.08.2017
Erscheinungsjahr:	2017

II

Abstract

One of the remaining challenges within the standard model of particle physics is to gain a good understanding of QCD in the non-perturbative regime. A key step toward this aim is to obtain further insight into the structure of baryons and their excitation spectrum. To gain access to resonances with small πN partial width, photoproduction experiments provide essential information. However, the measurement of (unpolarized) cross sections is insufficient to unambiguously determine the contributiong amplitudes in a partial wave analysis. The spin degrees of freedom need to be constrained further, approaching the complete experiment requiring single and double polarization measurements with polarized beams, polarized targets and recoil polarimetry.

This work presents such a double polarization measurement performed with the Crystal Barrel/TAPS experiment at the accelerator facility ELSA in Bonn. The photoproduction of single π^0 and η mesons with a linearly polarized photon beam impinging on a transversely polarized proton target was investigated. The reactions were identified nearly background-free by fully reconstructing the $p\gamma\gamma$ final state in an incoming photon energy range from $640\,\mathrm{MeV}$ to $3000\,\mathrm{MeV}$.

A new method was developed to simultaneously extract all accessible polarization observables from the data using an event-based maximum-likelihood fit. Using this method, the target asymmetry T was determined in the full energy range as a function of the beam energy and the scattering angle. In addition, the recoil polarization P and the double polarization observable H were determined in the incoming photon energy range below $975\,\mathrm{MeV}$, where a high degree of linear polarization of the photon beam has been achieved. The results are more precise compared to earlier data from other experiments, and extend the covered range in energy and angle substantially. It is the first measurement of the observable H in the given energy range. Systematic errors were investigated in detail and found to be significantly smaller compared to the statistical uncertainty of the results.

Within the Bonn-Gatchina partial wave analysis, the new results lead to a significant narrowing of the error band for the π^0 photoproduction multipoles, a more precise determination of resonance parameters, in particular $N^* \to N\eta$ branching ratios, further evidence for the poorly known baryon resonance $\Delta(2200)\,7/2^-$, and indications for a new resonance $N(2200)\,5/2^-$.

Main results of this work have already been published in Phys. Rev. Lett. [H+14] and Phys. Lett. B [H+15], and have been submitted for publication in Phys. Lett. B [M+17]. Furthermore, the results of this work are an important basis for the findings reported in [Ani+16] and [Ani+17].

References

[H+14]   J. Hartmann, H. Dutz, A. V. Anisovich, et al. (CBELSA/TAPS Collaboration),
The $N(1520)3/2^-$ helicity amplitudes from an energy-independent multipole analysis based on new polarization data on photoproduction of neutral pions,
Phys. Rev. Lett. **113** (2014) 062001, arXiv: `1407.2163` `[nucl-ex]`.

[H+15]   J. Hartmann, H. Dutz, et al. (CBELSA/TAPS Collaboration),
The polarization observables T, P, and H and their impact on $\gamma p \to p\pi^0$ multipoles, Phys. Lett. B **748** (2015) 212, arXiv: `1506.06226` `[nucl-ex]`.

[M+17]   J. Müller, J. Hartmann, M. Grüner, et al. (CBELSA/TAPS Collaboration),
New data on $\vec{\gamma}\vec{p} \to \eta p$ with polarized photons and protons and their implications for $N^* \to N\eta$ decays, submitted to Phys. Lett. B, 2017.

[Ani+16]   A. V. Anisovich, R. Beck, M. Döring, et al., *The Impact of new polarization data from Bonn, Mainz, and Jefferson Laboratory on $\gamma p \to \pi N$ multipoles*,
Eur. Phys. J. A **52** (2016) 284, arXiv: `1604.05704` `[nucl-th]`.

[Ani+17]   A. V. Anisovich, V. Burkert, J. Hartmann, et al.,
Evidence for $\Delta(2200)7/2^-$ from photoproduction and consequence for chiral-symmetry restoration at high mass, Phys. Lett. B **766** (2017) 357,
arXiv: `1503.05774` `[nucl-ex]`.

Contents

Outline of this Work

This work is structured as follows. The first chapter gives a short introduction to the physics of hadrons as composite systems of strongly interacting constituents in general, and to the spectrum of excited baryons in particular.

The photoproduction of mesons is introduced as a tool for baryon spectroscopy in Chapter 2. The motivation for the measurement of polarization observables in photoproduction experiments is given, and the theoretical principles behind these experiments are presented. The presently available data are discussed, together with state-of-the-art partial wave analyses and models for the interpretation of the data.

In Chapter 3, the Crystal Barrel/TAPS experiment, used to obtain the data for this work, is presented. This includes a discussion of the techniques used to produce a linearly polarized photon beam and to provide spin-polarized protons as target particles. Also, a detailed description of the detector systems used to measure the reaction products is given.

Compared to previous measurements by the Crystal Barrel/TAPS experiment (with unpolarized or longitudinally polarized target), the measurements for this work, with a transversely polarized target, posed an additional challenge in the form of increased background levels. This is addressed in detail in Chapter 4.

Chapter 5 presents the methods used to fully reconstruct the physical events of the reactions that are investigated in this work. This begins with the reconstruction of individual particles and their physical properties like energy and momentum from the electronic signals of the detector. Several cuts are applied to retain only the desired events while rejecting most of the background, thus providing a clean data sample for further analysis.

Chapter 6 covers the determination of the polarization observables. First, the prerequisites like flux normalization and determination of the polarization degrees of beam and target are discussed, before two different methods to extract the polarization observables from the selected data are presented. The systematic uncertainties of these methods are discussed in detail in Chapter 7.

Finally, in Chapter 8, the obtained results are first compared to previous measurements (where available) and to theoretical predictions, before the implications of the results regarding excited baryon states are discussed.

Chapter 1

Introduction

1.1 The Standard Model of Particle Physics

The Standard Model of Particle Physics [Gla61; Sal68; Wei67] can be considered one of the most successful theories in physics. It describes the particles which are the fundamental building blocks of matter, and their interactions. The matter particles are spin-1/2 fermions. They are classified into quarks and leptons, depending on the interactions they participate in. Furthermore, they can be classified into three generations, with corresponding particles in the different generations exhibiting similar physical properties. In each generation there are two leptons and two quarks, for a total of 12 spin-1/2 fermions (see Table 1.1). In addition, each fermion has a corresponding antiparticle.

Table 1.1: The fermions of the Standard Model, and their physical properties [Oli+14].

	generation 1	generation 2	generation 3	electric charge	weak isospin[1]	color charge
quarks	u	c	t	$+2/3$	$+1/2$	r, g, b
	d	s	b	$-1/3$	$-1/2$	r, g, b
leptons	ν_e	ν_μ	ν_τ	0	$+1/2$	
	e	μ	τ	-1	$-1/2$	

The Standard Model is a gauge theory. For each fundamental interaction there is a corresponding symmetry group, which gives rise to the gauge bosons as exchange particles of the interaction (see Table 1.2).

Table 1.2: The interactions of the Standard Model, and their exchange bosons [Oli+14].

interaction	acts on	exchange boson	mass
strong	color charge	g	0
electromagnetic	electric charge	γ	0
weak	weak isospin	$W^\pm$	80.39 GeV
	weak isospin, electric charge	Z^0	91.19 GeV

---

[1] The weak isospin of all left-handed fermions is $T = 1/2$, for right-handed fermions it is $T = 0$. Given in the table is the third component of T for left-handed fermions.

The quantum field theory of the electromagnetic interaction is called quantum electrody-namics (QED). The symmetry group is $U(1)_{em}$, and the corresponding exchange particle is the photon (γ). The coupling strength α of QED is small,[2] allowing precise calculations in perturbation theory with α as the expansion parameter.

The description of the weak interaction is unified with the electromagnetic interaction in the electroweak interaction. It is based on the symmetry group $U(1) \times SU(2)$. To account for the masses of the weak exchange bosons, this symmetry is spontaneously broken to $U(1)_{em}$ by the Higgs mechanism [EB64; Hig64; GHK64], giving rise to an additional scalar particle, the Higgs boson.

The theory of the strong interaction is called quantum chromodynamics (QCD). It incor-porates three charges, called color. It is a non-Abelian gauge theory with the symmetry group SU(3), resulting in 8 gauge bosons which are called gluons (g). Non-Abelian means that the exchange particles themselves carry color charge, allowing for a direct interaction between gluons. This leads to the two peculiar properties of QCD.

1. Asymptotic freedom:
   In QED, the coupling strength α of the interaction increases as a function of the energy scale, or decreases as a function of distance.[3] This effect, called *screening*, can be explained by pairs of virtual particles and antiparticles which screen part of the charge of a particle over distance [Lan55]. In QCD, however, the non-Abelian nature of the interaction leads to *anti-screening*, i.e. the strong coupling constant α_s increases with distance, or decreases as a function of the energy scale, as can be seen in Fig. 1.1. The strong interaction is *asymptotically free* as the energies involved go to infinity [GW73; Wil05]. As a consequence, at higher energies ($\gg 1\,\text{GeV}$), the coupling constant α_s is small enough to allow for a perturbative expansion of the interaction. The Feynman rules of QCD include a quark-antiquark-gluon vertex, analogously to QED, and in addition a 3-gluon and a 4-gluon vertex [BDS13] due to the non-Abelian nature of QCD, leading to the quite different properties of QCD compared to QED.
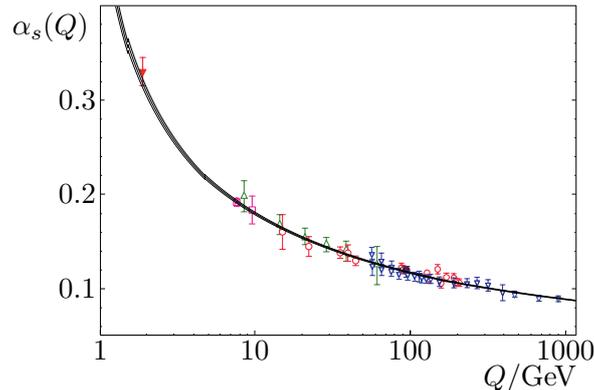
Figure 1.1: Measurements of the strong coupling α_s as a function of the energy scale Q, and the QCD prediction of asymptotic freedom (solid line) [Oli+14].

---

[2] $\alpha \approx 1/137$ for $Q \to 0$ [Oli+14]

[3] Momentum and distance are complementary quantities in quantum mechanics. A larger distance scale thus corresponds to smaller energy scale.

2. Confinement:
   At large distances, or small energy scales, the strength of the strong interaction increases. As a consequence, only objects without color charge can exist in isolation. When two color charges (e.g. a quark and an antiquark) become separated, it is energetically favorable for new quark-antiquark pairs to be created, eventually resulting in color-neutral particles through the process of *hadronization* [BDS13]. Thus, quarks and gluons are *confined* to color-neutral hadrons. However, understanding how QCD gives rise to the physics of hadrons remains—after the discovery of the Higgs boson in 2012 [Aad+12; Cha+12]—one of the most important open questions within the Standard Model.

1.2 Hadrons as Composite Systems of Quarks

Because α_s is too large in the energy regime of hadrons, a perturbative expansion in powers of α_s is not feasible [Gro99]. Other approaches are needed to calculate the properties (e.g. mass, radius, excitation spectrum, decay properties) of hadrons or to describe their interaction.

One such approach are effective field theories, which are not based on quarks and gluons as the relevant degrees of freedom. Instead, mesons and baryons are used as degrees of freedom, while keeping the symmetries imposed by QCD intact. For example, chiral effective field theory [GL84; GL85] is based on the chiral symmetry which is realized in the QCD Lagrangian in the limit of massless quarks. It allows the study of processes like low-energy $\pi\pi$ [BKM91] or πN scattering [BKM95], or near-threshold π^0 photoproduction [Ber+91; BKM96]. While it has been successfully applied to baryon resonances [BMM11], the study of the full baryon spectrum is not possible.

A more phenomenological approach are constituent quark models. Historically, quarks were first introduced by Gell-Mann, Ne'eman, and Zweig as hypothetical constituents of hadrons [Gel62; Nee61; Zwe64]. Gell-Mann realized that all hadrons known at that time could be grouped into multiplets with the same quantum numbers J^P. The three lightest quarks form a representation of SU(3), and the anti-quarks form the conjugate representation. A combination of both yields a nonet which comprises an octet and a singlet.

$$3 \otimes \overline{3} = 8 \oplus 1 \tag{1.1}$$

The lightest mesons as $q\bar{q}$ states are assigned to the $J^{PC} = 0^{-+}$ and $J^{PC} = 1^{--}$ nonets, as is shown in Fig. 1.2. Here, no orbital angular momentum is present between the quarks. For baryons, which are interpreted as qqq states in the quark model, the SU(3) representation yields

$$3 \otimes 3 \otimes 3 = 10 \oplus 8 \oplus 8 \oplus 1. \tag{1.2}$$

For the ground state baryons, only one decuplet and one octet are possible due to symmetry constraints [ADK13]. They are shown in Fig. 1.3. For the excited baryon states, with possible radial excitations or orbital angular momentum between the quarks, all multiplets are—in principle, depending on the symmetry of the wave function—possible.
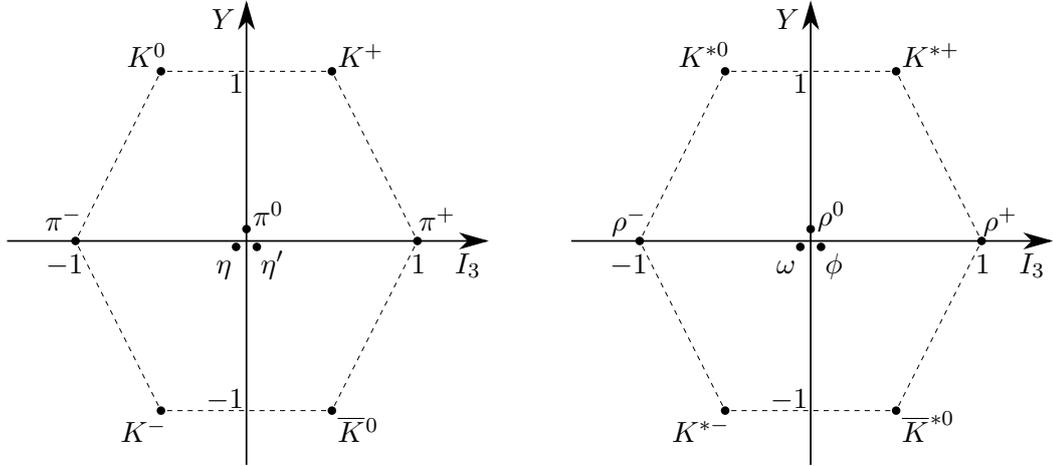
Figure 1.2: The ground state pseudoscalar and vector meson nonets. The mesons are ordered by their third component of the isospin I_3 (horizontal) and their hypercharge $Y = S + B$ (vertical), with strangeness S and baryon number B ($B = 0$ for mesons). Left: $J^{PC} = 0^{-+}$ nonet, right: $J^{PC} = 1^{--}$ nonet.
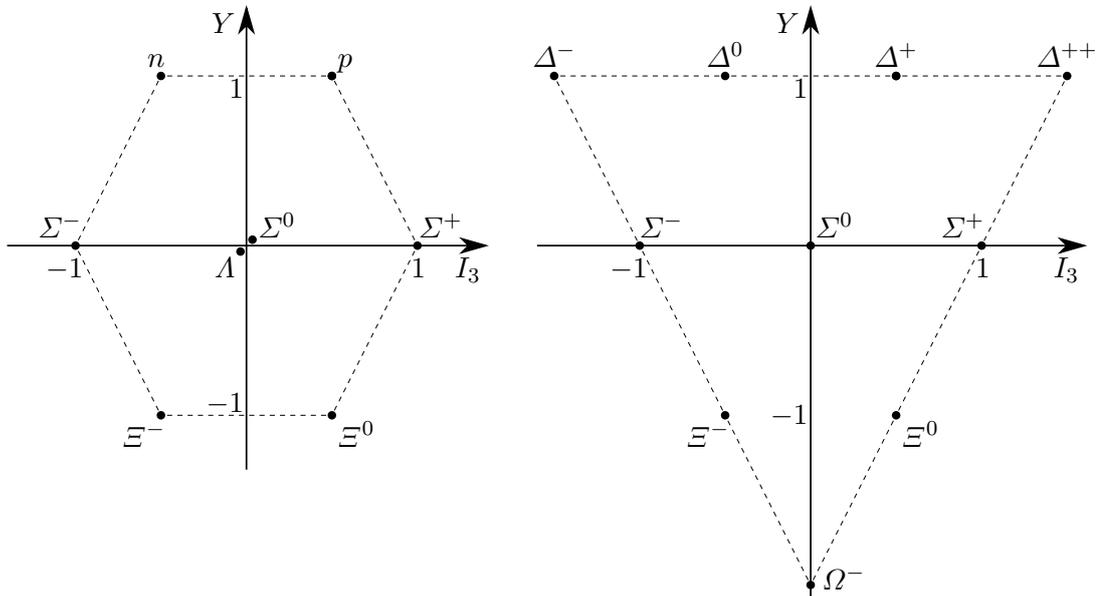
Figure 1.3: The ground state baryon multiplets. The baryons are ordered by their third component of the isospin I_3 (horizontal) and their hypercharge $Y = S + B$ (vertical), with strangeness S and baryon number B ($B = 1$ for baryons). Left: $J^P = 1/2^+$ octet, right: $J^P = 3/2^+$ decuplet.

1.3 The Spectrum of Excited Baryon States

1.3.1 Constituent Quark Models

To calculate the masses of ground state and excited hadrons, quark models try to describe the interaction and the dynamics of constituent quarks in a hadron. The constituent quarks have the same quantum numbers as the current quarks of the Standard Model (cf. Table 1.1), but have significantly higher masses of typically $\approx 300\,\mathrm{MeV}$ for the u and d quark, and $\approx 450\,\mathrm{MeV}$ for the s quark.[4] These constituent quarks are bound by a confining potential, typically increasing linearly with the distance of the quarks. Different models then add different residual interactions to describe the spectrum of possible states.

One of the earlier models predicting the spectrum of excited baryons is the non-relativistic model by Isgur and Karl [IK77; IK79], incorporating hyperfine-like spin-spin interactions. The model was later improved by Capstick and Isgur [CI86] into a relativized quark model based on a one-gluon-exchange potential for the residual interaction, including also spin-orbit interactions. A fully relativistic quark model was developed by Löring, Metsch, and Petry [LMP01], using instanton-induced quark forces instead of one-gluon-exchange [Lör+01]. The general features of the spectrum predicted by quark models are overall similar, but exhibit significant differences in the details. Further discussion is therefore limited to the most recent, fully relativistic model. The predicted spectrum of nucleon and delta resonances, compared to the experimentally known states listed by the Particle Data Group [Oli+14], is shown in Fig. 1.4.

In the low-energy part of the spectrum, the agreement between the model and the experimentally observed spectrum is quite good. For nearly all predicted states below $m \lesssim 1900\,\mathrm{MeV}$, there is also an observed state at similar mass. But nevertheless, there are some discrepancies, e.g. the ordering of positive and negative parity N^* states. The first radial excitation of the proton, the $N(1440)\,1/2^+$, was found experimentally below the orbital excitations $N(1535)\,1/2^-$ and $N(1520)\,3/2^-$. At higher masses, several experimentally observed states appear as nearly mass-degenerate doublets with same J and opposite parity (cf. Fig. 1.4, e.g. $N(1675)\,5/2^-$ & $N(1680)\,5/2^+$, $N(1880)\,1/2^+$ & $N(1895)\,1/2^-$, or $\Delta(1900)\,1/2^-$ & $\Delta(1910)\,1/2^+$, to name just a few). On the other hand, the constituent quark models predict an alternating pattern of states with positive and negative parity.[5]

The most obvious discrepancy between quark model predictions and the experimentally observed states, however, is found at $m \gtrsim 2000\,\mathrm{MeV}$, where the quark models predict many more states than have been found experimentally. There are two possible explanations for this *missing resonance* problem:

---

[4] The mass gap between the nearly massless current quarks and the massive constituent quarks can be explained by spontaneous breaking of the chiral symmetry of QCD, which holds in the limit of massless quarks [Nam60; Gol61].

[5] In Fig. 1.4, this alternating pattern of excitation bands with positive and negative parity is clearly visible only for the Δ resonances, which are not affected by the instanton-induced interaction, since it only acts on flavor-antisymmetric quark pairs, and the Δ states are fully flavor-symmetric. For the N^* spectrum, the excitation bands are less well separated because of the effect of the instanton-induced residual interaction. Therefore, the alternating pattern of positive and negative parity is not very well visible for the N^* states in Fig. 1.4. This is a unique feature of the model [LMP01], the alternating pattern is much more pronounced in the spectrum predicted by other quark models, see e.g. [CI86].
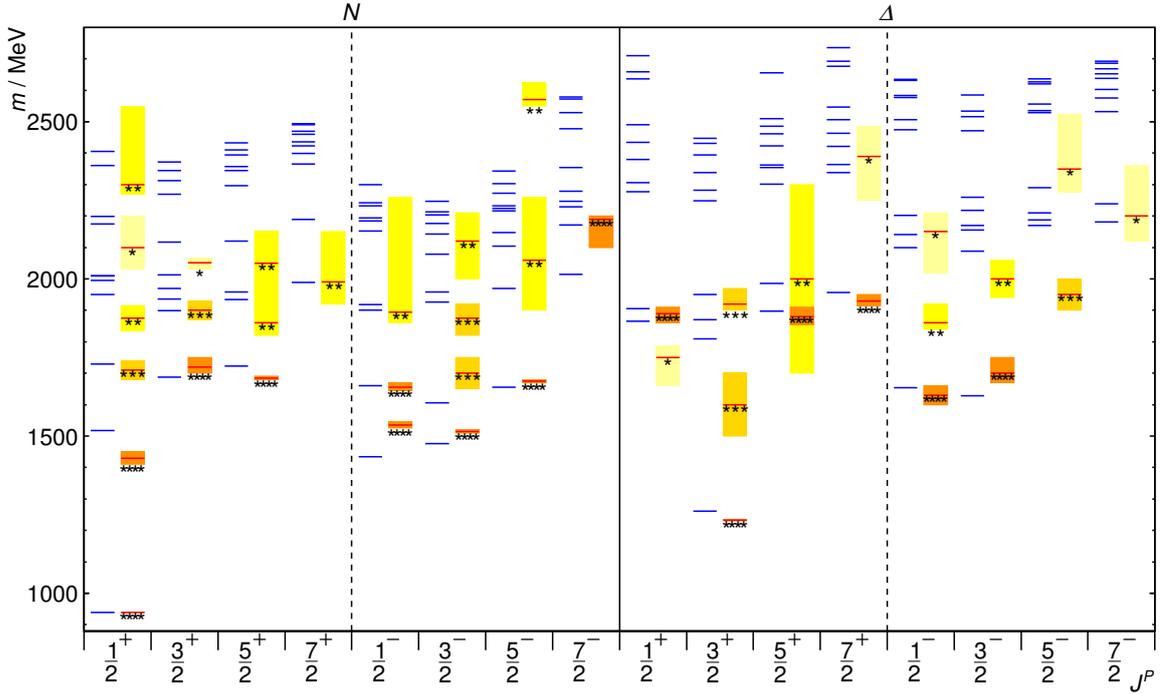
Figure 1.4: The spectrum of N and Δ resonances predicted by Löring, Metsch, and Petry [LMP01] for different J^P (states shown as blue lines on the left of each column), compared to all experimentally observed states listed by the Particle Data Group [Oli+14] (states shown as boxes on the right of each column, the width of the box gives the uncertainty of the state's mass) and their assigned rating (⋆⋆⋆⋆: Existence is certain, and properties are at least fairly well explored. ⋆⋆⋆: Existence is very likely but further confirmation of quantum numbers and branching fractions is required. ⋆⋆: Evidence of existence is only fair. ⋆: Evidence of existence is poor. [Oli+14]).

1. Until 2010, almost all nucleon resonances listed by the Particle Data Group have been discovered in πN scattering [Nak+10]. However, many of the missing resonances are predicted to have nearly vanishing partial decay amplitudes to the πN final state [Met08] and therefore cannot be detected in πN scattering.

2. Alternatively, the missing resonances could be an indication that not all degrees of freedom assumed in the quark model are realized in nature. The degrees of freedom can e.g. be reduced by interpreting baryon resonances as quark-diquark states [Ans+93], where a strongly bound diquark remains in an S-wave state, thus reducing the number of possible excitations. However, recent analyses found evidence of N^* resonances that contradict such a simple quark-diquark model [Nik+08; Thi+15]. A completely different approach, which does not use any quark degrees of freedom, is to generate the resonances dynamically from the interaction between their decay products, as has been proposed e.g. for the $N(1440) \, 1/2^+$ [Kre+00] or $N(1535) \, 1/2^-$ [KSW95; MBM12].

In any case, further measurements—especially in the high-mass region—are needed for a better understanding of the baryon spectrum.

1.3.2 Lattice QCD

In recent years, with ever increasing computing power being available, another approach has become feasible: lattice QCD, i.e. solving QCD numerically in discretized Euclidean space-time [Wil74] in a finite volume. Due to the huge computational cost involved, these calculations are, however, presently not possible at the physical pion mass, but are performed at higher pion masses and need to be extrapolated toward the physical limit. The calculated masses of the ground state mesons and baryons agree very well with the measured masses [Dur+08]. The calculation of excited baryons, on the other hand, is much more involved, because the signal-to-noise ratio of the simulations in Euclidean time decreases with increasing energy of the excited states. The Jefferson Lab group [Edw+11] calculated for the first time the spectrum of nucleon and delta resonances, which is shown in Fig. 1.5. The spectrum bears a large resemblance to the spectrum from the constituent quark model (cf. e.g. [CI86] or the Δ states in Fig. 1.4). The quark model states from different oscillator excitation bands, which appear alternating with positive and negative parity, are clearly visible with the same multiplicity in the lattice QCD calculation, as is indicated in Fig. 1.5 for the two lowest excitation bands. While this resemblance is striking, it does not necessarily mean that the quark model is correct. The states in the lattice QCD calculation cannot decay, and the calculation was done at $m_\pi = 396 \, \text{MeV}$. The pion mass is related to the quark mass by the Gell-Mann-Oakes-Renner relation [GOR68], which states
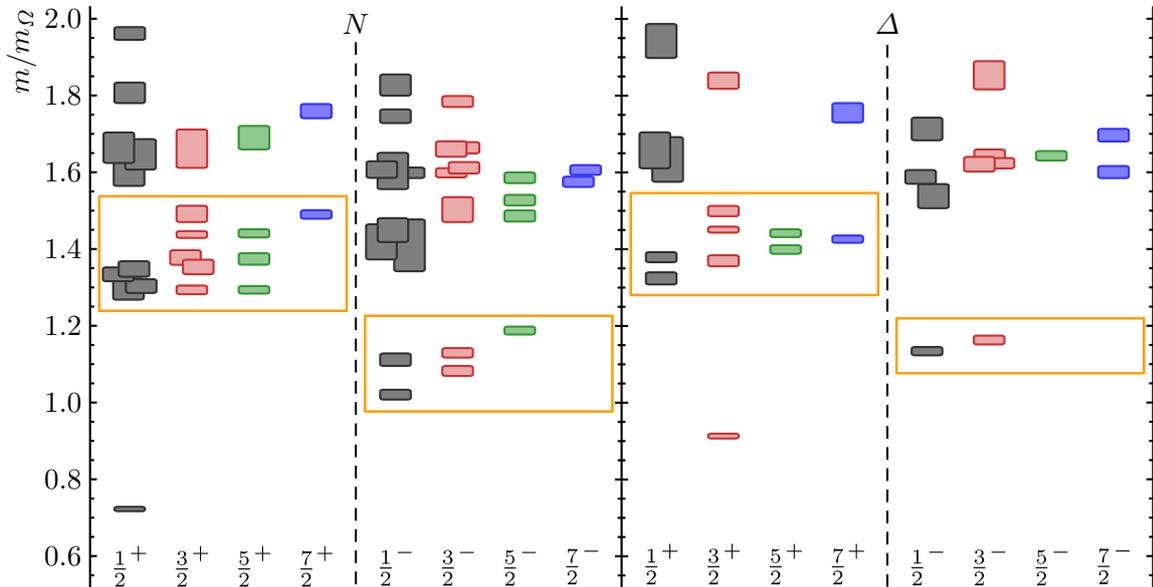
Figure 1.5: The spectrum of N and Δ resonances for different J^P from the lattice at $m_\pi = 396 \, \text{MeV}$, in units of the calculated Ω mass [Edw+11]. States corresponding to the two lowest oscillator excitation bands of the constituent quark model are marked by the orange boxes.

$m_\pi^2 \propto m_u + m_d$. As a consequence, the quark mass in the calculation is approximately one order of magnitude too large, making the quarks significantly heavier than the current quarks of the Standard Model and bringing the quark mass closer to the constituent quarks used in the quark models. If and how the lattice QCD spectrum changes as m_π goes toward the physical pion mass remains an open question.

To summarize, the spectrum of baryon resonances is presently not understood. Open questions regarding the number of states (the missing resonance problem) and also the mass pattern of the existing states need to be answered. From the spectrum of experimentally well-established states it appears that baryons with certain symmetries in their wave function do not appear at all in nature, raising the question: Why, and can this be explained by the inner structure of baryon resonances? The answers to these questions need to be found in theory. But first, one needs to make sure what the spectrum of excited baryons really looks like. Presently, the existence of several states is not well established experimentally and their properties are not precisely determined. Also, there are many potentially undiscovered states, in particular in the mass range above $2\,\mathrm{GeV}$. To greatly improve the experimental data, an extensive experimental program was started in recent years at Jefferson Lab, at MAMI, and at ELSA, establishing photoproduction experiments as the state-of-the-art technique in baryon spectroscopy. Their results will be essential for a deeper theoretical insight to excited hadrons, and hopefully lead to a better understanding of the non-perturbative regime of QCD. The analysis of one such experiment, performed with the Crystal Barrel/TAPS detector at ELSA, is the topic of this work.

Chapter 2

Photoproduction of Mesons

Compared to atomic spectroscopy, where discrete emission and absorption lines are observed, baryon spectroscopy poses an additional challenge. Excited baryon states can decay via the strong interaction, with lifetimes in the order of 10^{-24} s. Thus, the width of the excited states is in the order of $100\,\mathrm{MeV}$ (with $\Gamma = \hbar/\tau$). As a consequence, the excited states are strongly overlapping, and the measurement of the photoabsorption cross section is insufficient to identify excited baryon states, with the exception of the well separated $\Delta(1232)$ resonance. As can be seen in Fig. 2.1, the total photoabsorption cross section of the proton becomes nearly featureless above $E_\gamma \gtrsim 1\,\mathrm{GeV}$. In exclusive reactions, e.g.
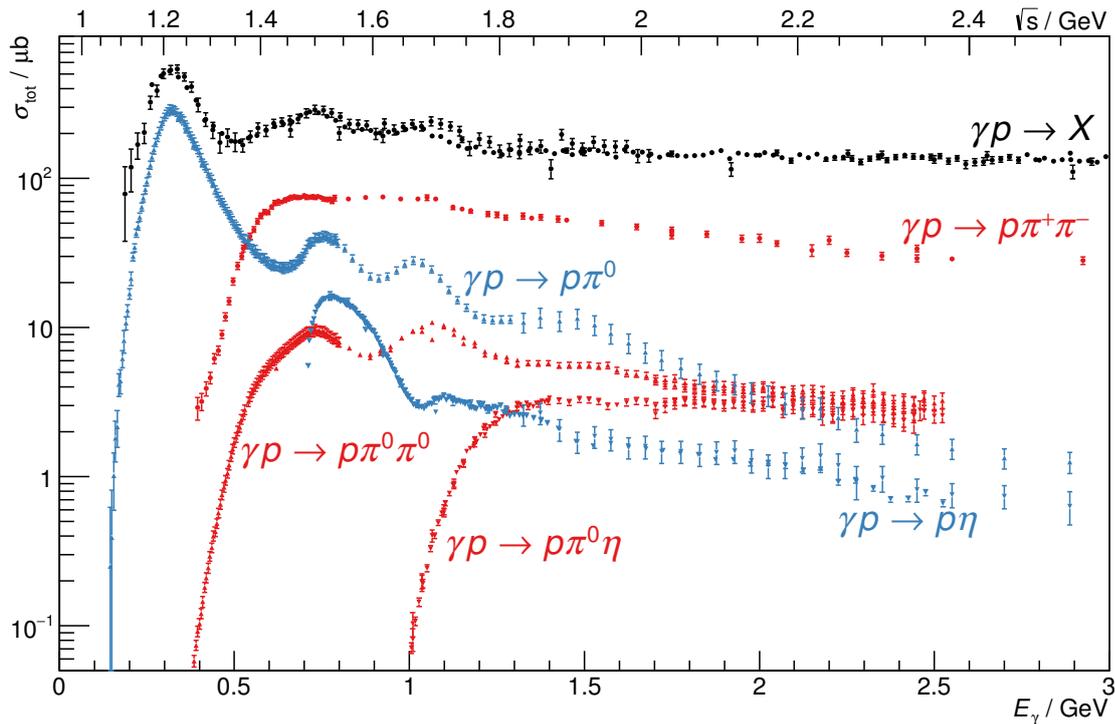
Figure 2.1: The total photoabsorption cross section of the proton (black) [Oli+14], compared to some single (blue) and double (red) meson photoproduction cross sections. Data on $\gamma p \to p\pi^0$ from [Bar+05b; Sch+10], $\gamma p \to p\eta$ from [Cre+05; Cre+09; M+10], $\gamma p \to p\pi^+\pi^-$ from [Str+76; Bra+95; Wu+05], $\gamma p \to p\pi^0\pi^0$ from [T+08; Sch+10; Sok+15b], and $\gamma p \to p\pi^0\eta$ from [Kas+09; Gut+14].

$\gamma p \to p\pi^0$, additional peaks are visible in the cross section. However, these are not caused by single resonances, but are resonance regions with contributions from several resonances (cf. listings in [Oli+14]). Interference between resonances with the same J^P, and with non-resonant background, complicates the situation observed in the total cross section even further. Clearly, additional information is needed to identify the contributing resonances and their quantum numbers. How this can be achieved is discussed in the following.

2.1 Photoproduction of Single Pseudoscalar Mesons

In this section, the theoretical framework for photoproduction of a single pseudoscalar meson M off a nucleon N, i.e. the reaction

$$\gamma N \to BM \tag{2.1}$$

is introduced. For the reactions studied in this work, both the target nucleon N and the recoiling ground state baryon B are protons, and the pseudoscalar meson M is either a π^0 or an η.

2.1.1 Kinematics

The kinematics of each reaction are described by the four-momenta $P = (E, \vec{p})$ of the particles:

$$\gamma(P_\gamma)\, N(P_i) \to B(P_f)\, M(P_M) \tag{2.2}$$

Due to additional constraints from energy and momentum conservation, the masses of the particles, and the arbitrary orientation of the coordinate system used for describing the reaction, there are only two independent parameters describing the reaction. A common choice are the Lorentz-invariant Mandelstam variables s and t,[1] defined as [Man58]

$$s = (P_\gamma + P_i)^2 = (P_f + P_M)^2 \tag{2.3a}$$
$$t = (P_\gamma - P_M)^2 = (P_f - P_i)^2 \tag{2.3b}$$
$$u = (P_\gamma - P_f)^2 = (P_M - P_i)^2. \tag{2.3c}$$

Alternatively, parameters which are more closely related to experimental quantities can be chosen, e.g. the total center-of-mass (CM) energy $W = \sqrt{s}$ and the center-of-mass angle θ of the produced meson with respect to the initial state photon (see Fig. 2.2). For photoproduction experiments with the target proton at rest it is even more convenient to use the energy E_γ of the initial state photon in the lab frame instead of W. The two quantities are directly related:

$$E_\gamma = \frac{W^2 - m_p^2}{2m_p}, \qquad W = \sqrt{m_p\,(m_p + 2E_\gamma)}. \tag{2.4}$$

---

[1] The third Mandelstam variable u is not independent, it can be expressed in terms of s, t, and the masses m of the particles using the relation $s + t + u = m_\gamma^2 + m_i^2 + m_f^2 + m_M^2$.

2.1.2 Scattering Amplitudes and Multipoles

To fully describe the process of single pseudoscalar meson photoproduction off a nucleon, four complex amplitudes are needed [Che+57]. There exist various choices of such amplitudes, depending on the basis used for spin quantization. For example, in the basis of Pauli spinors the differential cross section in the CM frame is given by

$$\frac{\mathrm{d}\sigma}{\mathrm{d}\Omega} = \frac{q}{k}|\langle f \,|\, \mathcal{F} \,|\, i\rangle|^2 \tag{2.5}$$

with initial state $|i\rangle$ and final state $|f\rangle$. The phase-space factor $\frac{q}{k}$ is given by the momentum k of the incoming photon and the momentum q of the produced meson, both in the CM frame. $\mathcal{F}$ can be expressed in terms of the four CGLN[2] amplitudes F_1, F_2, F_4, and F_4 [Che+57],

$$\mathcal{F} = i(\vec{\sigma} \cdot \vec{\delta})F_1 + \frac{(\vec{\sigma} \cdot \vec{q})[\vec{\sigma} \cdot (\vec{k} \times \vec{\delta})]}{q\,k}F_2 + i\frac{(\vec{\sigma} \cdot \vec{k})(\vec{q} \cdot \vec{\delta})}{q\,k}F_3 + i\frac{(\vec{\sigma} \cdot \vec{q})(\vec{q} \cdot \vec{\delta})}{q^2}F_4, \tag{2.6}$$

where $\vec{\sigma}$ is the Pauli spin operator and $\vec{\delta}$ is the photon polarization vector.[3] The amplitudes depend on the kinematic variables, e.g. W and θ. It is, however, possible to separate the energy dependence from the angular dependence by performing an expansion in terms of derivatives of Legendre polynomials P_ℓ [Che+57]:

$$F_1(W,\theta) = \sum_{\ell=0}^{\infty} \big[\ell\, M_{\ell+}(W) + E_{\ell+}(W)\big] P'_{\ell+1}(\cos\theta) \tag{2.7a}$$
$$+ \big[(\ell+1)\, M_{\ell-}(W) + E_{\ell-}(W)\big] P'_{\ell-1}(\cos\theta)$$

$$F_2(W,\theta) = \sum_{\ell=1}^{\infty} \big[(\ell+1)\, M_{\ell+}(W) + \ell\, M_{\ell-}(W)\big] P'_{\ell}(\cos\theta) \tag{2.7b}$$

$$F_3(W,\theta) = \sum_{\ell=1}^{\infty} \big[E_{\ell+}(W) - M_{\ell+}(W)\big] P''_{\ell+1}(\cos\theta) \tag{2.7c}$$
$$+ \big[E_{\ell-}(W) + M_{\ell-}(W)\big] P''_{\ell-1}(\cos\theta)$$

$$F_4(W,\theta) = \sum_{\ell=2}^{\infty} \big[M_{\ell+}(W) - E_{\ell+}(W) - M_{\ell-}(W) - E_{\ell-}(W)\big] P''_{\ell}(\cos\theta) \tag{2.7d}$$

The coefficients, or multipoles, $E_{\ell\pm}$ and $M_{\ell\pm}$ refer to transitions into a final state with orbital angular momentum ℓ between the recoiling baryon and the produced meson, and total angular momentum $J = \ell \pm \frac{1}{2}$. The $E_{\ell\pm}$ refer to transitions initiated by the electrical component of the photon, and the $M_{\ell\pm}$ to transitions initiated by the magnetic component. Thus, each multipole refers to a state with a well defined J^P, with the parity $P = (-1)^{\ell+1}$. In general, each J^P can be reached by two multipoles, one electric and one magnetic,[4] as is also shown in Table 2.1. As a consequence, an *s*-channel resonance with given quantum

---

[2] Named after Chew, Goldberger, Low, and Nambu.

[3] The polarizations of the nucleons in the initial and the final state are not contained in $\mathcal{F}$, but in the spinors $|i\rangle$ and $|f\rangle$.

[4] With the exception of $\frac{1}{2}^-$ and $\frac{1}{2}^+$, for which M_{0+} and E_{1-} are not possible due to parity conservation.

Table 2.1: Quantum numbers J^P of s-channel resonances, the orbital angular momentum ℓ in their decays to a nucleon and a pseudoscalar meson, and the multipoles they can be observed in.

J^P	ℓ	electric multipole	magnetic multipole
$1/2^+$	1	-	M_{1-}
$1/2^-$	0	E_{0+}	-
$3/2^+$	1	E_{1+}	M_{1+}
$3/2^-$	2	E_{2-}	M_{2-}
$5/2^+$	3	E_{3-}	M_{3-}
$5/2^-$	2	E_{2+}	M_{2+}
$7/2^+$	3	E_{3+}	M_{3+}
$7/2^-$	4	E_{4-}	M_{4-}
$\vdots$	$\vdots$	$\vdots$	$\vdots$

numbers J^P contributes to two multipoles. The relative strength of a resonance contribution to the two multipoles depends on the couplings of the resonance to the initial states with helicity $\frac{1}{2}$ and $\frac{3}{2}$.[5] A t- or u-channel process can contribute to *all* multipoles.

2.1.3 Resonances

To calculate the contribution of individual resonances to the scattering amplitude A, a parametrization of the resonance is needed. Two such parameterizations are now briefly introduced.

2.1.3.1 Breit-Wigner Parametrization

For a single resonance with a single decay channel, far away from all relevant thresholds, the amplitude can be described using the Breit-Wigner parametrization [AHK13]

$$A = -\frac{g_a \, g_b}{s - M_{\text{BW}}^2 + i\sqrt{s}\,\Gamma_{\text{BW}}}, \tag{2.8}$$

with Breit-Wigner mass M_{BW} and width Γ_{BW}, and the couplings g_a and g_b to the final and initial state, respectively. If there is more than one resonance with the same quantum numbers contributing to the same channel, the Breit-Wigner parametrization cannot be used, since the sum of two overlapping Breit-Wigner amplitudes violates unitarity [AHK13]. For that reason, the Breit-Wigner parametrization is not well suited to describe broad and in general strongly overlapping nucleon resonances, although it has been widely used in the past.[6] Instead, the K-matrix approach, which will be treated below, can be used to describe more than one resonance in a single partial wave, taking into account also different decay channels.

---

[5] The electric and magnetic multipoles $E_{\ell\pm}$ and $M_{\ell\pm}$ are linearly related to the helicity multipoles $A_{\ell\pm}^{1/2}$ and $A_{\ell\pm}^{3/2}$, from which the helicity couplings of a resonance can be derived. For details see [WTS13].

[6] Cf. e.g. Baryon Listings in the *Review of Particle Physics* from 1998 [Cas+98].

Another shortcoming of the Breit-Wigner parametrization is the fact that the parameters M_{BW} and Γ_{BW} of a single resonance observed in different channels can be different. This happens when the resonance is close to a production threshold [AHK13]. Breit-Wigner parameters should therefore not be used to define resonances [Höh97]. Instead, resonances are defined by poles of the scattering amplitude in the complex energy W plane [DM70]. The real part of the pole position defines the particle mass, and its width is given by twice the imaginary part [KW12]. Only this definition is independent of the used parametrization.

$$W_{\mathrm{pole}} = M_{\mathrm{pole}} - i\frac{\Gamma_{\mathrm{pole}}}{2} \tag{2.9}$$

Only for an isolated resonance, far away from all relevant thresholds, the pole mass and width are identical to the Breit-Wigner parameters. The coupling strength of a resonance to a given channel can be calculated from the residual of the amplitude around the pole [AHK13].

2.1.3.2 K-Matrix Formalism

The probability that an initial state $|b\rangle$ scatters into the final state $|a\rangle$ is, in general, given by

$$S_{ab} = \langle a \,|\, S \,|\, b \rangle, \tag{2.10}$$

where S is called the scattering matrix. Conservation of probability requires S to be unitary [Chu+95], i.e. $S\,S^{\dagger} = S^{\dagger}\,S = \mathbb{1}$, where $\mathbb{1}$ denotes the identity matrix.
It is convenient to eliminate the probability that initial and final states do not interact at all by defining the transition matrix T through

$$S = \mathbb{1} + 2i\sqrt{\rho}\,T\sqrt{\rho}, \tag{2.11}$$

where ρ is a diagonal matrix containing the phase-space of the initial and final states.[7] From the unitarity of S one obtains the relation

$$\left(T^{-1} + i\rho\right)^{\dagger} = T^{-1} + i\rho, \tag{2.12}$$

The K-matrix can now be introduced via

$$K^{-1} = T^{-1} + i\rho. \tag{2.13}$$

resulting in

$$T = K\left(\mathbb{1} - i\rho K\right)^{-1}. \tag{2.14}$$

K is Hermitian, i.e. $K = K^{\dagger}$, symmetric, and therefore also real [Chu+95].

---

[7] For two-particle states, the phase-space is given by $\rho_j(s) = \frac{1}{16\pi}\frac{2q_j}{\sqrt{s}}$, where q is the relative momentum of the two particles [AHK13].

Resonances are introduced in the K-matrix formalism as poles. For n resonances, one obtains

$$K_{ab}(s) = \sum_{k=1}^{n} \frac{g_{ka}(s)\,g_{kb}(s)}{(M_k^2 - s)\cdot\sqrt{\rho_a\rho_b}} + c_{ab}(s) \tag{2.15}$$

where c_{ab} is the non-resonant background and M_k denotes the mass of the kth resonance. The couplings g_{kj} of the kth resonance to channel j are given by

$$g_{kj}^2(s) = M_k \Gamma_{kj}(s), \tag{2.16}$$

with the partial width Γ_{kj} in the channel j. The total width Γ_k for each pole k is given by

$$\Gamma_k(s) = \sum_j \Gamma_{kj}(s). \tag{2.17}$$

More details on the K-matrix formalism can be found e.g. in [Chu+95]. For a single resonance observed in a single channel, the amplitude derived from the K-matrix is identical to the Breit-Wigner amplitude given in Eq. (2.8) [AHK13].

The formalism introduced so far allows, in principle, to calculate the cross section for a given reaction from the parameters of the contributing resonances. What is needed, however, is the inverse: obtaining resonance parameters from measured quantities. How this can be achieved is discussed in the following.

2.1.4 Polarization Observables

The scattering amplitudes introduced in Section 2.1.2, while useful for a theoretical description of meson photoproduction, are not accessible directly in an experiment. Instead, cross sections and asymmetries can be measured. Measuring the unpolarized differential cross section $\left(\frac{d\sigma}{d\Omega}\right)_0$ (i.e. one real function of the kinematic variables) is obviously not sufficient to determine the four complex amplitudes (i.e. eight real functions). The measurement of additional quantities is required. This can be achieved in experiments involving polarization by selecting individual spin states of the initial state, by measuring the polarization in the final state, or both. In that case, the unpolarized cross section is modified by additional terms depending on the polarization [San+11]:

$$
\begin{aligned}
\frac{d\sigma}{d\Omega} = \left(\frac{d\sigma}{d\Omega}\right)_0 \cdot \Big\{ &1\big[1 - \Lambda_y \Lambda'_{y'}\delta_\ell \cos(2\varphi)\big] - \Sigma\big[\delta_\ell\cos(2\varphi) - \Lambda_y\Lambda'_{y'}\big] \\
&+ T\big[\Lambda_y - \Lambda'_{y'}\delta_\ell\cos(2\varphi)\big] + P\big[\Lambda'_{y'} - \Lambda_y\delta_\ell\cos(2\varphi)\big] \\
&- E\big[\Lambda_z\delta_\odot - \Lambda_x\Lambda'_{y'}\delta_\ell\sin(2\varphi)\big] + F\big[\Lambda_x\delta_\odot + \Lambda_z\Lambda'_{y'}\delta_\ell\sin(2\varphi)\big] \\
&+ G\big[\Lambda_z\delta_\ell\sin(2\varphi) + \Lambda_x\Lambda'_{y'}\delta_\odot\big] - H\big[\Lambda_x\delta_\ell\sin(2\varphi) - \Lambda_z\Lambda'_{y'}\delta_\odot\big] \\
&- C_{x'}\big[\Lambda'_{x'}\delta_\odot - \Lambda_y\Lambda'_{z'}\delta_\ell\sin(2\varphi)\big] - C_{z'}\big[\Lambda'_{z'}\delta_\odot + \Lambda_y\Lambda'_{x'}\delta_\ell\sin(2\varphi)\big] \\
&- O_{x'}\big[\Lambda'_{x'}\delta_\ell\sin(2\varphi) + \Lambda_y\Lambda'_{z'}\delta_\odot\big] - O_{z'}\big[\Lambda'_{z'}\delta_\ell\sin(2\varphi) - \Lambda_y\Lambda'_{x'}\delta_\odot\big] \\
&+ L_{x'}\big[\Lambda_z\Lambda'_{x'} + \Lambda_x\Lambda'_{z'}\delta_\ell\cos(2\varphi)\big] + L_{z'}\big[\Lambda_z\Lambda'_{z'} - \Lambda_x\Lambda'_{x'}\delta_\ell\cos(2\varphi)\big] \\
&+ T_{x'}\big[\Lambda_x\Lambda'_{x'} - \Lambda_z\Lambda'_{z'}\delta_\ell\cos(2\varphi)\big] + T_{z'}\big[\Lambda_x\Lambda'_{z'} + \Lambda_z\Lambda'_{x'}\delta_\ell\cos(2\varphi)\big] \Big\}
\end{aligned}
\tag{2.18}
$$

Figure 2.2: Definition of the CM coordinate systems: The reaction is constrained to a plane (yellow) due to momentum conservation. Using this reaction plane, two coordinate systems are defined. For the reaction coordinate system x, y, z (blue) the z-axis points along the direction of the incoming photon and the y-axis is perpendicular to the reaction plane. The recoil coordinate system x', y', z' (red) is rotated around the y-axis, i.e. in the reaction plane, by θ such that the z'-axis points along the direction of produced meson. The angle between the photon polarization (given by the electric field $\vec{E}$) and the reaction plane is given by φ.

where δ_ℓ ($\delta_\odot$) is the degree of linear (circular) photon polarization, φ is the angle of the photon polarization plane w.r.t. the reaction plane, i.e. the x-z-plane, and $\Lambda_{x,y,z}$ ($\Lambda'_{x',y',z'}$) is the polarization of the target (recoil) nucleon along the corresponding axis. For the orientation of the coordinate systems see Fig. 2.2. The blue coefficients, which depend on all independent kinematic variables, are the so-called polarization observables. There exist various conventions for the signs of these observables. In this work the convention as introduced in [BDS75] is used, which is identical to the convention used by the MAID [Dre+99] and SAID [Bri+15] partial wave analysis groups. Other sign conventions used by various theory groups are summarized in [San+12].

The polarization observables can be arranged into four groups, depending on the kind of polarization that contributes to the leading (red) term in Eq. (2.18):

- the single polarization observables Σ (beam asymmetry), T (target asymmetry), and P (recoil polarization),

- the beam-target double polarization observables E, F, G, and H,

- the beam-recoil double polarization observables $C_{x'}$, $C_{z'}$, $O_{x'}$, and $O_{z'}$,

- and the target-recoil double polarization observables $L_{x'}$, $L_{z'}$, $T_{x'}$, and $T_{z'}$.

It should be noted that with each observable there appears an additional (green) term in Eq. (2.18) with different polarization contributions. For the double polarization observables, this is a term depending on all three polarizations. For each single polarization observable, this is a term depending on the other two polarizations. The structure of Eq. (2.18)

has two consequences: First of all, a triple polarization experiment yields no additional information that cannot be obtained by individually performing all three double polarization experiments, and is therefore not needed for single-meson photoproduction. Second, the experimentally challenging measurement of the recoil polarization is only needed to measure the beam-recoil and target-recoil double polarization observables, whereas the single recoil polarization observable P can alternatively be measured in a beam-target double polarization experiment. Such a measurement is part of this work.

Using Eqs. (2.5) and (2.6) it is possible to express the polarization observables in terms of the CGLN amplitudes. To simplify these relations it is useful to introduce for each polarization observable O the corresponding profile function $\check{O}$, which is obtained by multiplying the dimensionless observable with the unpolarized cross section.

$$\check{O} = O \cdot \left(\frac{\mathrm{d}\sigma}{\mathrm{d}\Omega}\right)_0 \tag{2.19}$$

The profile functions can be expressed as real or imaginary parts of linear combinations of bilinear products of the CGLN amplitudes. The explicit expressions for all observables can be found e.g. in [FTS92] or [San+11].

Since there are in total 16 observables, but only four complex amplitudes, a measurement of all observables should over-constrain the amplitudes. It has been shown that the measurement of eight carefully chosen observables is in fact sufficient to determine the CGLN amplitudes (up to one energy and angle dependent phase) in a so-called *complete experiment* [CT97]. However, this is only valid if the measured observables are known with infinite precision. Taking limitations in statistics and accuracy of experimental data into account, a significantly larger number of observables needs to be known [San+11; Tia12]. On the other hand, in order to extract information on excited nucleon states, i.e. *s*-channel resonances, a precise knowledge of the scattering amplitudes is not needed if the multipoles corresponding to the quantum numbers of the contributing resonances are known. Using Eq. (2.7) it is possible to express the profile functions directly in terms of multipoles [Tia12], where in practice the expansion in orbital angular momentum can be truncated at a given maximum angular momentum ℓ_{max}.

$$\check{O}(W, \theta) = \frac{q}{k}\,\sin^{\alpha}(\theta)\sum_{\kappa=0}^{2\ell_{\mathrm{max}}+\beta} a_{\kappa}^{O}(W)\cos^{\kappa}(\theta) \tag{2.20}$$

The parameters α and β are different for the various observables, their values are summarized in Table 2.2. The expansion coefficients $a_{\kappa}^{O}(W)$ are bilinear functions of the multipoles:

$$a_{\kappa}^{O}(W) = \sum_{\ell,\ell'=0}^{\ell_{\mathrm{max}}}\sum_{k,k'=1}^{4} b_{\ell,\ell'}^{k,k'}\,\mathcal{M}_{\ell,k}^{*}(W)\,\mathcal{M}_{\ell',k'}(W) \tag{2.21}$$

where k, k' denote the 4 possible electric and magnetic multipoles for each angular momentum ℓ, namely $\mathcal{M}_{\ell,k} \in \{E_{\ell+}, E_{\ell-}, M_{\ell+}, M_{\ell-}\}$. Explicit expressions for the coupling coefficients $b_{\ell,\ell'}^{k,k'}$ are not given here.[8]

---

[8] In the basis of associated Legendre polynomials the coefficients can be found e.g. in [Wun17].

Table 2.2: The parameters α and β for the truncated multipole expansion of the polarization observables O (see Eq. (2.20)) [Tia12].

O	σ_0	Σ	T	P	E	F	G	H	$C_{x'}$	$C_{z'}$	$O_{x'}$	$O_{z'}$	$L_{x'}$	$L_{z'}$	$T_{x'}$	$T_{z'}$
α	0	2	1	1	0	1	2	1	1	0	1	2	1	0	2	1
β	0	-2	-1	-1	0	-1	-2	-1	0	1	0	-1	0	1	-1	0

2.2 Existing Data

2.2.1 Reaction $\gamma p \rightarrow p\pi^0$

The reaction $\gamma p \rightarrow p\pi^0$ is the best-studied photoproduction reaction. Various measurements of the differential cross section cover the full kinematic region from threshold to $E_\gamma = 2.5\,\text{GeV}$ over the full polar angle. Additionally, some data points at higher energies exist in a limited angular range (see e.g. database at [Bri+15]). In addition, there are several high-precision measurements of the beam asymmetry Σ over a large kinematic range (see e.g. [Spa+10; Bar+05a]). For the other single polarization observables—the target asymmetry T and the recoil polarization P—various measurements have been performed as well (see e.g. database at [Bri+15]); however, the coverage of the polar angle is far from complete at various energies. For the double polarization observables the situation is even worse, with only very few data points available for some observables (see e.g. database at [Bri+15], and Fig. 2.3 for H). Only recently, high-quality results for the observables G [Thi+12; Thi12; Thi+17] and E [Got+14; Got13] have become available. The analysis presented in this work provides information on T, P, and H. The existing data for these observables are shown in Fig. 2.3, as well as the kinematic region accessible in this work.

(a) T (b) P (c) H
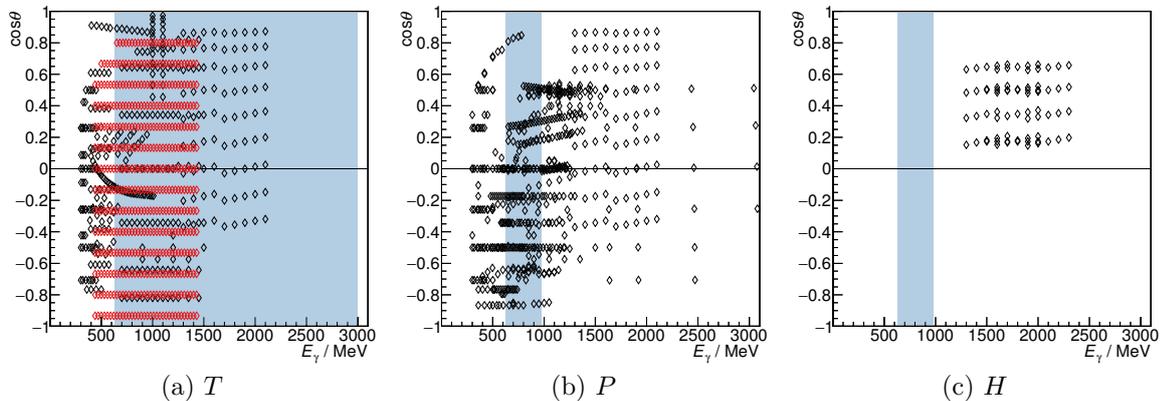
Figure 2.3: The kinematic region covered by previous measurements of the polarization observables T [Gor+74; Gor+75; Gor+78; Boo+77; Fel+76; Her+77; Fuk+78; Bus+79a; Aga+89; Asa+86; Boc+98], P [Gor+74; Bel+83; Kat+80; Bra+80; Bra+86; Mal61], and H [Bus+79b] in the reaction $\gamma p \rightarrow p\pi^0$. The kinematic region accessible in this work is shown as the shaded area. Measurements of T, which were performed at Mainz [Ann+16] in parallel to this work, are shown in red.

2.2.2 Reaction $\gamma p \rightarrow p\eta$

While the available data for the differential cross sections covers nearly the full kinematic region from threshold to $E_\gamma = 3.5\,\text{GeV}$ (see e.g. database at [Bri+15]), and also high-quality data are available for the beam asymmetry Σ up to $E_\gamma = 1.5\,\text{GeV}$ [Els+07; Bar+07], there are only very few measurements of the other polarization observables. The only notable exception is the target asymmetry T, where data covering a significant part of the kinematic region are available [Boc+98]; however, the statistical precision of the measurement is unsatisfactory. Only recently, high-quality data have been published by the A2 collaboration at MAMI [Ako+14] for the observables T and F at energies below $E_\gamma < 1.5\,\text{GeV}$. The existing data points and the kinematic region accessible in this work are summarized in Fig. 2.4 for the observables T, P, and H.

(a) T (b) P (c) H
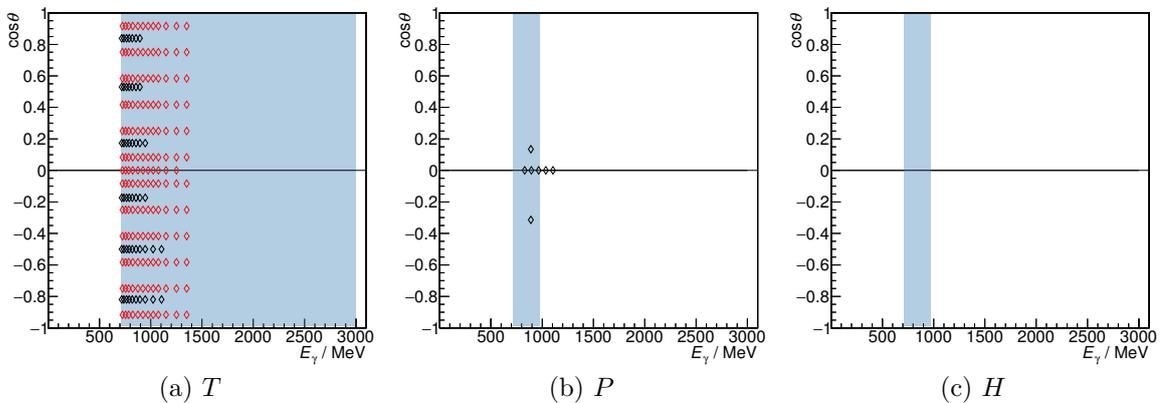
Figure 2.4: The kinematic region covered by previous measurements of the polarization observables T [Boc+98], P [Heu+70; Hon+71], and H in the reaction $\gamma p \rightarrow p\eta$. The kinematic region accessible in this work is shown as the shaded area. Measurements of T, which were performed at Mainz [Ako+14] in parallel to this work, are shown in red.

2.3 Interpretation of the Data

With the currently available data, the complete experiment in pseudoscalar meson photoproduction [CT97] is not yet achieved. It is therefore not possible to extract all contributing partial wave amplitudes from the available data in a model-independent and unambiguous way.[9] Instead, different theoretical frameworks with different model assumptions and different resonance contributions are able to describe the existing data reasonably well. Three of the most prominent models are briefly introduced in the following. Further details on the formalism used by the models can be found in the references given. Other models, which are not discussed here, include the MAID unitary isobar model [Dre+99; DKT07], the JPAC (formerly EBAC) analysis [Jul+08; Kam+09] based on the ANL-Osaka dynamical coupled-channel model [MSL07], and the Gießen coupled-channel model [SLM12; SLM13].

---

[9] And even with a model-independent partial wave analysis based on a complete experiment, the extraction of resonance and background contributions will always retain some model dependence.

2.3.1 George Washington University Partial Wave Analysis

The SAID[10] program developed at George Washington University has a large database of pion-nucleon-scattering and photoproduction data available [Bri+15]. The main focus of the photoproduction analysis is pion photoproduction.[11] The analysis is done in a two-step procedure. First, the underlying multipole contributions are determined by a phenomenological fit to the full database [Arn+02], using additional constraints from πN scattering [Arn+95]. The resonance parameters are determined from fits only to πN elastic scattering and ηN production data. In the past, Born terms and Breit-Wigner amplitudes were used [Arn+95], a more recent analysis uses a K-matrix [Wor+12b] to extract resonance parameters. The photoproduction data are presently only used to determine the γN couplings [Ani+16].

2.3.2 Bonn-Gatchina Partial Wave Analysis

The Bonn-Gatchina partial wave analysis (BnGa PWA) [Ani+15] is, unlike SAID, a multi-channel analysis. It is a simultaneous fit to πN scattering and photoproduction data [Ani+05b; Ani+05a], using a multitude of final states including, among others, $p\pi^0$, $p\eta$, $n\pi^+$, $K^+\Lambda$, $K^+\Sigma^0$, and $K^0\Sigma^+$, as well as multi-meson final states like $p\pi^0\pi^0$ and $p\pi^0\eta$ [Ani+12]. Resonances are mainly included in a K-matrix parametrization or as Breit-Wigner amplitudes in case of some higher-mass resonances. Non-resonant contributions include Born terms, as well as t- and u-channel processes [Ani+10].

The latest BnGa PWA solution prior to this work stems from the year 2011 [Ani+11; Ani+12]. Due to the incompleteness of the existing data, no unique solution was obtained. Instead, 12 different solutions, with different numbers of poles in the various partial waves, describe all the data with similar quality. Several of these solutions yield similar resonance parameters, they are combined into a single class of solutions, with an error derived from their spread [Ani+12]. The 2011 fit resulted in two of these classes of solutions with distinct parameters, called BnGa2011-01 and BnGa2011-02. The most significant difference between the two solutions is found in the $I(J^P) = 1/2(3/2^+)$ partial wave, where the solution BnGa2011-02 finds two close-by resonances around $W = 1900\,\mathrm{MeV}$, whereas the solution BnGa2011-01 finds only one. There are further differences between the two solutions, in particular in the $J^P = 3/2^-$, $5/2^+$, and $7/2^+$ waves. For further details on the differences see [Ani+11]. Obviously, additional data are needed to choose between the two solutions.

2.3.3 Jülich-Bonn Coupled Channel Analysis

The Jülich-Bonn dynamical coupled-channel model aims to provide a tool for the extraction of resonance parameters that obeys theoretical constraints of the S-matrix such as unitarity and analyticity [Rön+13]. The scattering amplitude is constructed based on an effective Lagrangian, with s-channel processes as resonances, and non-resonant contributions given by t- and u-channel exchanges of known mesons and baryons. The effects of

---

[10] Scattering Analysis Interactive Dial-in
[11] There are also other SAID fits available e.g. for η photoproduction [M+10].

important three-body channels like $\pi\pi N$ are included via effective $\pi\Delta$, σN, and ρN channels [Rön+14]. Initially developed for pion-induced reactions, the model was extended to include π and η photoproduction in a semi-phenomenological approach, although additional double polarization data are required for a better determination of the multipoles in η photoproduction [Rön+15].

Chapter 3

Experimental Setup

3.1 The Electron Accelerator ELSA

The Crystal Barrel/TAPS experiment is located at the **EL**ectron **S**tretcher **A**ccelerator ELSA [Hil06] in Bonn. An overview of the accelerator, which provides electrons of an energy up to 3.5 GeV, is shown in Fig. 3.1. As a key feature, it is possible to accelerate polarized electrons. For this, a 50 keV polarized electron source is used [Hil00], providing an electron beam with a polarization degree of more than 80 %. Additionally, a thermal electron gun is available for unpolarized operation.

The electrons from the source are accelerated to 26 MeV in the linear accelerator LINAC 2 and then injected into the booster synchrotron. A second linear accelerator LINAC 1 has recently been undergoing a complete overhaul [Kla11] and cannot presently be used for injection into the synchrotron. It will be available for a planned operation at higher intensity in the future.
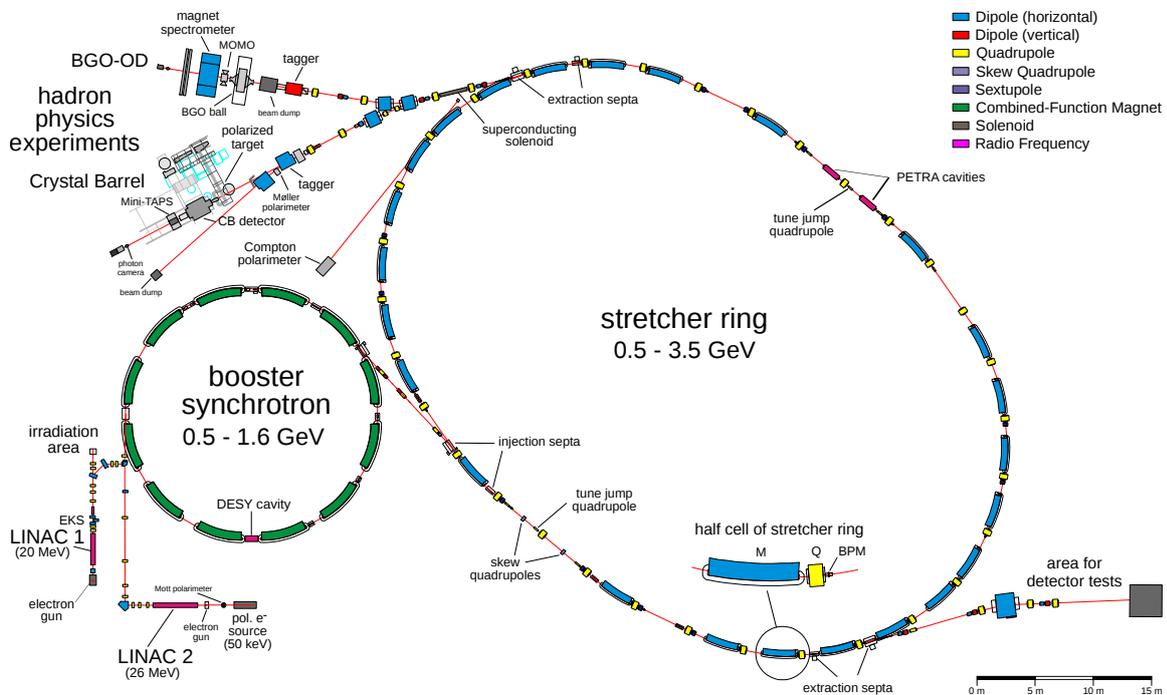
Figure 3.1: Overview of the Electron Stretcher Accelerator ELSA [Fro16].

The booster synchrotron, which operates at a frequency of 50 Hz (as provided by the power grid) can accelerate the electrons up to an energy of 1.6 GeV, although typically the electrons are extracted at 1.2 GeV. The electrons from several synchrotron cycles[1] are accumulated in the stretcher ring and then accelerated to their final energy, with a ramp speed of up to 7 GeV/s. The beam can be stored for a longer period of time, or slowly extracted via resonance extraction [Nec93] to one of the hadron physics experiments. This provides a quasi-continuous[2] beam with an intensity around 1 nA for several seconds, before the stretcher ring has to be filled again. For the experiments related to this thesis, an extraction time of 4 s was used, resulting in a macroscopic duty factor of 70 %. For a stable operation, the intensity and position of the extracted beam can be monitored non-destructively by radio-frequency (RF) cavities [Pus12].

3.2 The Crystal Barrel/TAPS Experiment

An overview of the Crystal Barrel/TAPS experiment is shown in Fig. 3.2. The individual components are described in more detail in the following.

3.2.1 Photon Tagging System

The photon beam for the Crystal Barrel/TAPS experiment is produced from the electron beam in a bremsstrahlung process. Before the components used to produce the photon beam are presented, a short introduction to the bremsstrahlung process is given in the following.

3.2.1.1 Bremsstrahlung

Electrons passing through matter are accelerated by the Coulomb-field of the nuclei or electrons and emit energy in the form of electromagnetic radiation. The first quantum-mechanical description of this bremsstrahlung process was given by Bethe and Heitler [BH34]. Energy and momentum conservation yields

$$E_0 = E + k + T \tag{3.1a}$$
$$\vec{p}_0 = \vec{p} + \vec{k} + \vec{q} \tag{3.1b}$$

with E_0 and $\vec{p}_0$ being the energy and momentum of the incoming electron, E and $\vec{p}$ the energy and momentum of the outgoing electron, k and $\vec{k}$ the energy and momentum of the photon, and T and $\vec{q}$ the kinetic energy and momentum of the recoiling nucleon.
The energy distribution of the produced photons is described by the Bethe-Heitler cross section [BH34]. In the ultra-relativistic case, and neglecting the screening of the target

---

[1] Due to the difference in circumference, seven injections from the synchrotron are needed to completely fill the stretcher ring. A multiple of seven injections can be made to increase the stored beam current. During operation for the Crystal Barrel/TAPS experiment, typically 21 or 28 injections were used, resulting in a beam current around 20 mA in the stretcher ring at a revolution frequency of 1.82 MHz [Hil06].

[2] The beam has a microscopic substructure of < 100 ps wide bunches [Swi13] with a distance of 2 ns. This is a direct result of the 500 MHz electromagnetic fields used for acceleration.
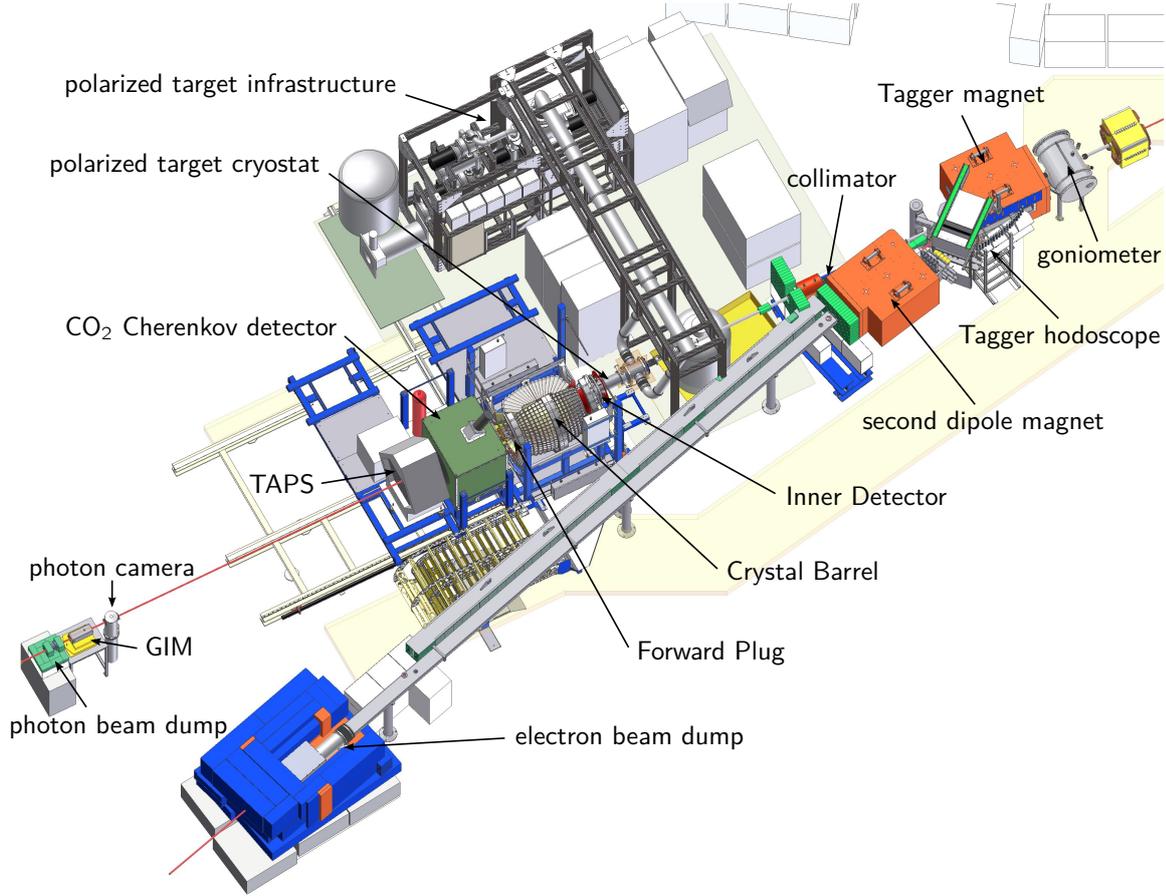
Figure 3.2: Overview of the Crystal Barrel/TAPS experiment at ELSA.

nucleus by its electrons, it is given by

$$\frac{\mathrm{d}\sigma}{\mathrm{d}k} = \frac{4Z^2 r_e^2 \alpha}{k} \left(1 + \left(\frac{E}{E_0}\right)^2 - \frac{2}{3}\frac{E}{E_0}\right)\left(\ln\left(\frac{2E_0 E}{m_e k}\right) - \frac{1}{2}\right). \tag{3.2}$$

with atomic number Z, fine structure constant α, and classical electron radius $r_e = \frac{e^2}{m_e}$, using natural units $\hbar = c = 1$. In first order approximation, the energy spectrum can be described by a $1/k$ distribution. The average opening angle of the photon beam depends on the incoming electron energy:

$$\langle \theta_k \rangle \propto \frac{1}{E_0} \tag{3.3}$$

Since the process is rotationally symmetric around the direction of the incoming electrons, the recoil momentum $\vec{q}$ can be decomposed into a longitudinal component q_l parallel to the incoming electron, and a transverse component q_t perpendicular to q_l. The possible values

for q_l and q_t are constrained by the kinematics of the bremsstrahlung process [Tim69].

$$0 \leq q_t \lesssim m_e \tag{3.4a}$$

$$\delta + \frac{q_t^2}{2E_0} \leq q_l \lesssim \frac{\delta}{x} \tag{3.4b}$$

where $x = \dfrac{k}{E_0}$ is the relative energy of the photon, and with

$$\delta = \frac{m_e^2}{2E_0} \cdot \frac{x}{1-x}. \tag{3.5}$$

While the allowed range for q_t is rather wide, possible values of q_l are limited to a very narrow range. Since q_l and q_t are not independent of each other, the individual limits for q_l and q_t given in Eq. (3.4) are oversimplified and the constraints on $\vec{q}$ need to be investigated two-dimensionally. The kinematically allowed region, called the *pancake*, is shown in Fig. 3.3. The width of the pancake and its position along q_l are given by δ. The upper limit is a consequence of the average opening angle $\langle \theta_k \rangle$ (cf. Eq. (3.3)) and therefore not a sharp constraint.
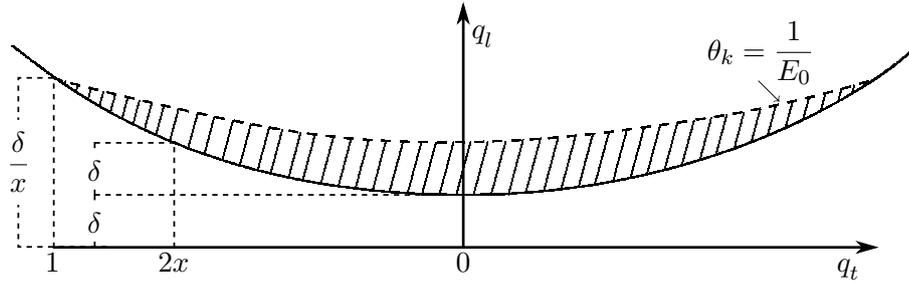
Figure 3.3: Kinematically allowed region for the recoil momentum transfer $\vec{q}$ [Tim69]. The momenta are given in units of m_e.

The bremsstrahlung process can be used to produce a polarized photon beam. A circularly polarized photon beam can be produced using a longitudinally polarized electron beam: in the bremsstrahlung process, the helicity of the electron is transfered—to a certain degree, depending on the relative energy—to the radiated photon. The degree of polarization of the photon beam is given by [OM59]

$$P_\gamma = P_e \cdot \frac{E_\gamma \left(3 + (1 - E_\gamma) \right)}{3 - \left(2 \left(1 - E_\gamma \right) \right) + 3 \left(1 - E_\gamma \right)^2}. \tag{3.6}$$

For the experiments performed for this thesis, however, a linearly polarized photon beam is needed, which can be produced using coherent bremsstrahlung from an unpolarized electron beam. This method, involving the interplay of the kinematic constraints of the bremsstrahlung process and the structure of a periodical crystal lattice, is described in the following.

Coherent Bremsstrahlung

With an amorphous radiator target, the contributions from the individual atoms add incoherently. If a crystal is used as a radiator target, the individual bremsstrahlung amplitudes are added coherently, giving rise to interference effects. The recoil momentum $\vec{q}$ can be absorbed by the crystal lattice if the Laue condition [FKL13]

$$\vec{q} = n \cdot \vec{g} \tag{3.7}$$

is fulfilled, where n is an integer number and $\vec{g}$ is a reciprocal lattice vector of the crystal. The orientation of the scattering plane, which is spanned by $\vec{q} \parallel \vec{g}$ and the momentum of the incoming electron, is fixed for a single $\vec{g}$. Since the orientation of the electric field of the bremsstrahlung photon is determined by this plane, the produced photons for a given $\vec{g}$ are linearly polarized. However, contributions from different $\vec{g}$ can interfere destructively. Since the kinematically allowed region for $\vec{q}$ is limited to the pancake (see Fig. 3.3 and Eq. (3.4)), only a limited number of reciprocal lattice vectors contribute to the process. By properly aligning the crystal, it can be achieved that only a single $\vec{g}$ resides within the allowed pancake region for a given x. Since the position of the pancake depends on x (cf. Eq. (3.5)), the reciprocal lattice vector leaves the pancake at certain values of x. The lower bound of the pancake is a sharp constraint, resulting in a steep drop in the cross section above a certain x. This discontinuity is called the *coherent edge*. Below this discontinuity the cross section slowly decreases with decreasing x, which is a consequence of the diffuse upper edge of the pancake. The position x_d of the discontinuity for a given lattice vector can be influenced by the crystal orientation. But for a given crystal orientation there is always more than one coherent edge visible: Even with only a single reciprocal lattice vector $\vec{g}$ contributing, there are also the coherent edges for $n \cdot \vec{g}$ ($n \in \mathbb{N}$) at higher x. However, the total coherent cross section decreases with increasing x_d [Tim69], making the higher edges less pronounced. The resulting coherent intensity spectrum is shown in Fig. 3.4 for one crystal orientation. The maximum degree of linear polarization for a coherent edge at
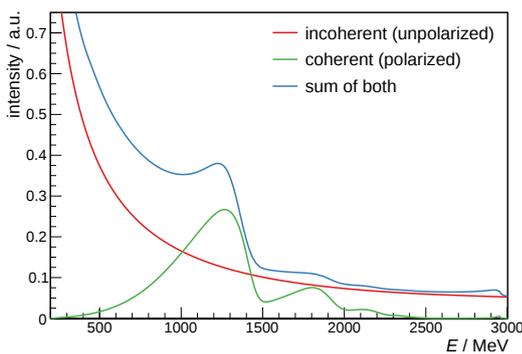
Figure 3.4: Intensity spectrum of coherent bremsstrahlung for a crystal orientation with the coherent edge around $E_\gamma = 1400\,\mathrm{MeV}$ for an incident electron energy of $E_0 = 3.2\,\mathrm{GeV}$.
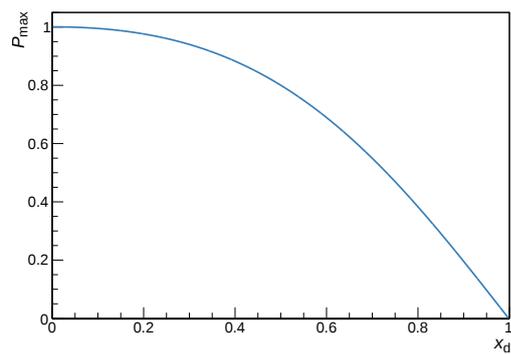
Figure 3.5: The maximum polarization degree of coherent bremsstrahlung with contributions only from a single reciprocal lattice vector g and the coherent edge at the relative energy x_d.

x_d depends on x_d [Tim69]. Higher polarization degrees are achieved at low relative photon energies, as is visualized in Fig. 3.5.

A real crystal is not completely periodical due to thermal motion of the atoms. Hence, the recoil transfer to a single atom is also possible. Consequently, the cross section for bremsstrahlung off a crystal consists of two parts:

$$\sigma_{\text{crystal}} = \sigma_{\text{coherent}} + \sigma_{\text{incoherent}} \tag{3.8}$$

Only the coherent contribution can result in linearly polarized photons, the polarization degree can be calculated from the coherent and incoherent contributions [Nat+03]. Since the intensity of the coherent process decreases for higher coherent edges, the highest achievable polarization decreases even further with x_d than indicated in Fig. 3.5.

3.2.1.2 Goniometer

A 5-axis[3] goniometer is used to precisely position various radiator targets in the electron beam. Copper strips with a thickness of $12\,\mu\text{m}$, $50\,\mu\text{m}$, $150\,\mu\text{m}$, or $300\,\mu\text{m}$ can be used to produce an unpolarized photon beam. In terms of radiation length X_0,[4] this corresponds to a thickness of $8.4 \times 10^{-4}\,X_0$, $3.5 \times 10^{-3}\,X_0$, $1.0 \times 10^{-2}\,X_0$, and $2.1 \times 10^{-2}\,X_0$. Thus, only a small fraction of the electrons emit a bremsstrahlung photon. However, already with the $150\,\mu\text{m}$ copper target, the divergence of the beam increases significantly due to multiple scattering.[5] Additionally, a luminescent screen is available for visual beam diagnostics, and a horizontal or vertical wire can be used to scan the beam profile by recording the rate measured in the tagging spectrometer as a function of the wire position.
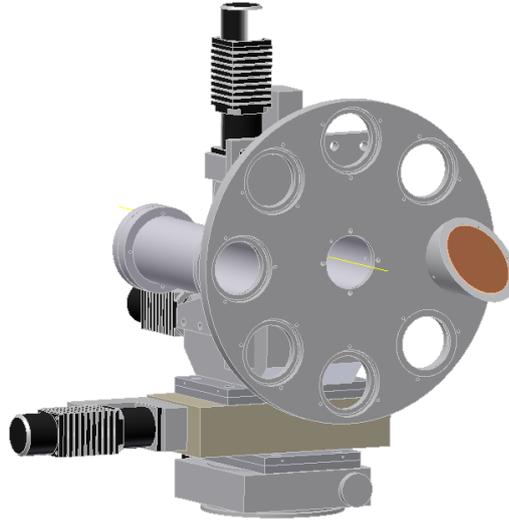
Figure 3.6: Goniometer with various radiator targets [Wal16].

---

[3] Rotation around all three spatial axes, as well as horizontal and vertical movement perpendicular to the beam axis.

[4] The radiation length of copper is $X_0 = 1.435\,\text{cm}$ [Oli+14].

[5] For a radiator thickness of $10^{-2}\,X_0$ ($150\,\mu\text{m}$ Cu) the RMS of the multiple scattering angle is $\theta_0 = 0.4\,\text{mrad}$ [Ber+12], which is comparable to the divergence of the incident electron beam.

Most importantly, a diamond crystal is located at the center of the goniometer, at the crossing point of all three rotational axes. The thickness of the diamond, in terms of X_0, corresponds roughly to the 50 µm copper radiator. By properly aligning the crystal, a linearly polarized photon beam can be produced using coherent bremsstrahlung. The orientation of the polarization plane, as well as the photon energy of the coherent edge, can be freely adjusted. The alignment of the crystal is done using coherent bremsstrahlung itself. The procedure, called the *Stonehenge Technique*, was developed by K. Livingston [Liv09]. Its application at the Crystal Barrel/TAPS experiment is described in detail in [Ebe12; Els07; Els+09].

3.2.1.3 Tagging Spectrometer

For the photoproduction experiments it is crucial to precisely know the initial state. Therefore, the energy of the incident photon needs to be known. It can be determined by measuring the momentum p and thus the energy E of the electrons after the bremsstrahlung process. The energy k of the photon can then be calculated using Eq. (3.1a), with the well known incident electron energy E_0 and neglecting the recoil energy T.[6] This way each photon is energy tagged, hence the name *Photon Tagging System* or just *Tagger*.

The electron momentum p is measured in a dipole spectrometer, which is shown in Fig. 3.7. The electrons are deflected in the field of a dipole magnet and thus separated from the photon beam. For any incident electron energy provided by the accelerator, the magnetic field strength is set such that the electrons that did not emit a bremsstrahlung photon are deflected by 9° [For09]. These electrons, which are the majority, are of no further use. They are deflected by a second dipole magnet and directed to the beam dump. Electrons that did lose part of their energy at the radiator target are deflected by a larger angle compared to the primary electron beam and can be detected by position-sensitive detectors, which are described in the following.

A scintillator bar hodoscope [For09], consisting of 96 individual organic scintillators with photomultiplier (PMT) readout, covers an energy range between $E = 0.021\,E_0$ and $E = 0.825\,E_0$. The bars are positioned such that one electron can be detected in two adjacent bars, in order to suppress background. To increase the energy resolution in the high-energy part of the detector (corresponding to low-energy photons), an additional detector consisting of 480 scintillating fibers [For09] with multi-anode PMT readout is used, covering an energy range from $E = 0.166\,E_0$ to $E = 0.871\,E_0$.

The PMT signals are digitized using leading edge discriminators followed by multi-hit time-to-digital converters (TDCs). The discriminator output signals of two adjacent bars are also combined by a logical AND, and counted by 95 livetime-gated counters for the photon flux measurement. A logical OR of these signals can be used as a trigger signal for the experiment (called `tagger_coinc`). An additional trigger signal is provided by the logical OR of the individual discriminator signals of the bars (called `tagger_or`). Since this signal is more sensitive to background (e.g. from the beam halo), it is not used during normal data-taking operation.

---

[6] The recoil energy T can be neglected since $m_e \ll m_A$.
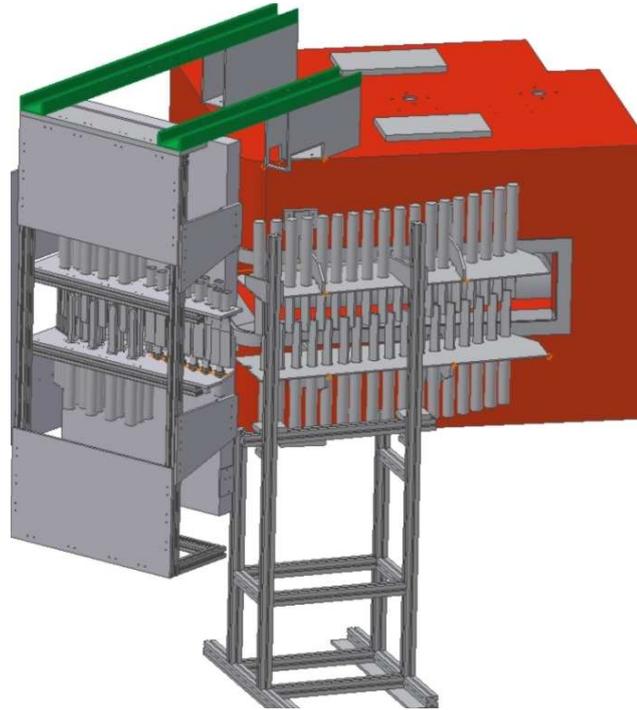
Figure 3.7: Tagging spectrometer comprising dipole magnet, scintillator bars and scintil-
lating fibers [Wal16].

3.2.1.4 Collimator

Before the produced photon beam reaches the target, it is collimated. One reason for
the collimation is to remove the beam halo and to ensure that the transverse profile of
the beam is contained within the target cell. For measurements with a linearly polarized
photon beam, the collimation also increases the polarization degree, due to the different
angular distributions for coherent and incoherent bremsstrahlung [Tim69].
The collimator consists of six individual hollow cylinders made of tungsten with an inner
diameter of $4\,\mathrm{mm}$ and an outer diameter of $20\,\mathrm{mm}$. The length of each cylinder is $4\,\mathrm{cm}$,
resulting in a total length of $24\,\mathrm{cm}$ [For09]. The interactions of the photons with the
collimator produce large quantities of electrons and positrons. These charged particles are
deflected by a dipole magnet behind the collimator and thus removed from the beam.

3.2.2 Gamma Intensity Monitor

For the measurement of cross sections, it is essential to precisely know the photon flux at
the target. It is measured by the Gamma Intensity Monitor (GIM), located at the end of
the photon beam line.
The detector consists of a 4×4 array of PbF_2 crystals with PMT readout (see Fig. 3.8).
Photons impinging on the detector produce an electromagnetic shower and are detected by
the Cherenkov light emitted by the charged particles of the shower. Even though the pulses
have decay times of only a few nanoseconds and the readout electronics has a double pulse
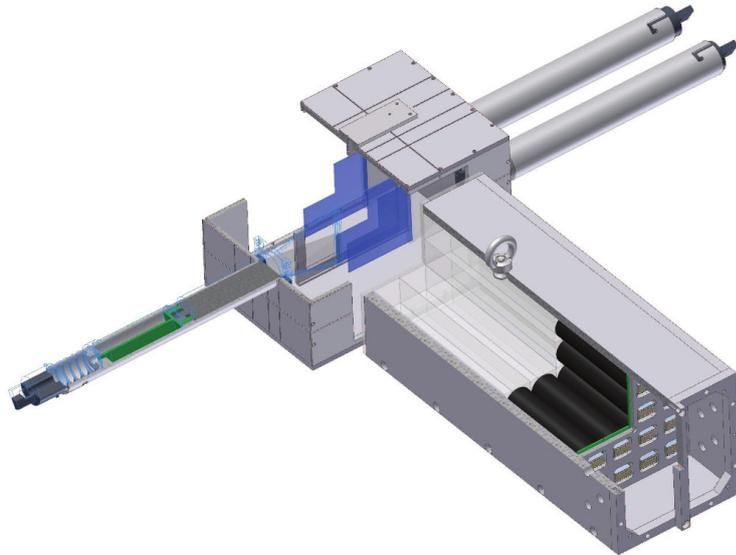
Figure 3.8: Gamma Intensity Monitor consisting of 16 PbF_2 crystals, with the Flux Monitor in front [Wal16].

resolution $\leq 12\,\text{ns}$, the efficiency of the detector decreases significantly for beam photon rates $\gg 1\,\text{MHz}$ due to deadtime effects [Die08; Har08].

To allow the measurement of the photon flux at higher rates a second detector is located in front of the GIM. This Flux Monitor (FluMo) [Die08] consists of a $100\,\mu\text{m}$ thick lead foil as e^+e^- pair production target, followed by two organic scintillators to detect the e^+e^- pairs. A third scintillator is placed in front of the lead foil as a veto detector for charged particles coming along the photon beam. This detector can be calibrated at low beam intensity and can then be used to measure a known fraction of the total flux [Die08]. It can also be used to determine the detection efficiency of the GIM (see Appendix D).

In front of the FluMo, a photon camera is installed to continuously monitor the position of the photon beam during data-taking.

3.2.3 Polarized Target

The polarized target nucleons are provided by the Bonn Frozen Spin Target [Bra+99]. The target is located in a horizontal $^3\text{He}/^4\text{He}$ dilution cryostat. For measurements with polarized protons, butanol (C_4H_9OH) is used as the target material. The free protons in the hydrogen atoms[7] within the butanol are polarized using the method of dynamic nuclear polarization (DNP) [CM97]. At a temperature of about $300\,\text{mK}$ and a magnetic field of $2.5\,\text{T}$, provided by an external superconducting solenoid magnet, free electrons in the target material[8] are nearly completely polarized. The electron polarization is transferred to the protons by microwave irradiation. Depending on the microwave frequency, the proton spin can be aligned parallel or anti-parallel to the magnetic field. A polarization degree of more

---

[7] The carbon and oxygen nuclei are spinless and cannot be polarized.

[8] The target material is doped with paramagnetic radicals to provide the free electrons for the DNP process.

than 85 % can be reached with build-up times around 2 h. Once polarized, the microwaves are switched off and the temperature in the target cell is reduced to $\lesssim 70\,\text{mK}$. At that temperature, a magnetic field around $500\,\text{mT}$,[9] provided by a thin superconducting holding coil inside the target cryostat, is sufficient to achieve relaxation times of several hundred hours. The massive polarizing magnet can then be removed, and the detector system can be placed around the target for a measurement period of several days, before the target needs to be re-polarized again.

For this thesis, a newly developed racetrack coil [Dut16] was used for the first time in the existing cryostat, providing a transversely polarized target. It is significantly thicker than the solenoid coil that was used for previous measurements with a longitudinally polarized target. A detailed investigation of the influence of the new coil on the measurements will be discussed in Chapter 4.

For background measurements, the butanol target material can be replaced with a carbon foam target with identical dimensions and similar density. Further details on the target materials will be given in Section 6.1.1.

3.2.4 Inner Detector

The target is surrounded by a detector for the identification of charged particles, called Inner Detector (see Fig. 3.9). It consists of 513 scintillating fibers with a diameter of 2 mm each, arranged in three layers [Suf+05]. The outer layer has a radius of 6.45 cm and consists of 191 fibers, which are aligned parallel to the beam axis. The fibers in the inner two layers form a helix around the beam axis, as can be seen if Fig. 3.10. The central layer, with a radius of 6.13 cm, consists of 165 fibers with an inclination angle of $+25.7°$. The inner layer, with a radius of 5.81 cm, consists of 157 fibers with an inclination angle of $-24.5°$. This arrangement allows the reconstruction of the interaction point of a charged particle, even if it was only detected in two of the three layers.
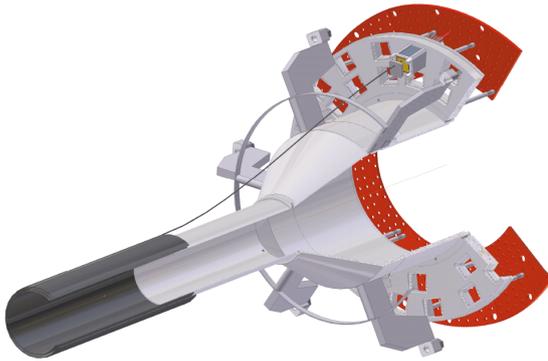
Figure 3.9: Inner Detector with holding structure [Wal16].
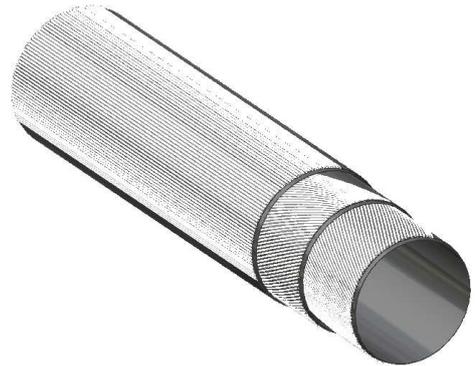
Figure 3.10: Alignment of the scintillating fibers of the Inner Detector [Wal16].

---

[9] The solenoid coil for the longitudinally polarized target provides a field of $600\,\text{mT}$, the racetrack coil for the transversely polarized target used for this work provides a field of $500\,\text{mT}$ [Dut16].

The active area of the detector is 40 cm long. The center of the detector is shifted, compared to the center of the Crystal Barrel calorimeter and the center of the target cell, by 5.1 cm toward the direction of the incoming beam [Grü06]. It covers the polar angle range from $\theta = 21°$ to $\theta = 167°$. The forward end of the fibers is reflective, while the backward end is attached to light guides which lead to multi-anode PMTs. The signals are digitized using leading edge discriminators followed by multi-hit TDCs. Coincident signals in at least two of the three layers can be used as a trigger for the experiment.

3.2.5 Crystal Barrel Calorimeter

The Inner Detector is surrounded by the Crystal Barrel (CB) calorimeter. It consists of 1230 CsI(Tl) crystals with a length of 30 cm each, which corresponds to roughly $16\,X_0$ [Oli+14]. The crystals are mounted in 21 rings in the shape of a barrel around the target, as can be seen in Fig. 3.11. Each ring covers a polar angle range of $\Delta\theta = 6°$, the whole detector covers the polar angle range from $\theta = 30°$ to $\theta = 156°$ and the full azimuthal angle. The last ring ($\theta = 150°$ to $\theta = 156°$) consists of 30 crystal covering an azimuthal angle of $\Delta\phi = 12°$ each, all other rings consist of 60 crystals covering an azimuthal angle of $\Delta\phi = 6°$ each [Ake+92].

Photons impinging on the detector produce an electromagnetic shower. In the longitudinal direction, the shower is (almost) completely contained in the crystals. For a 2 GeV photon, 99 % of its energy is deposited in the calorimeter [Blu+86]. In the transverse direction the energy deposit extends over several crystals. Therefore, an angular resolution better than the granularity of the crystals is achieved for photons by using an energy weighted reconstruction (see Section 5.3.1).

The scintillation light of each crystal is collected by a wavelength shifter at the rear face of the crystal, and then detected by a PIN photo diode (see Fig. 3.12). A charge sensitive preamplifier close to the diode produces an amplified output signal with a rise time of 10 µs to 15 µs and a decay time of more than 100 µs. The amplitude is around 1.5 mV/MeV with a typical noise level around 0.4 mV. This signal is converted by a shaping RC-CR circuit
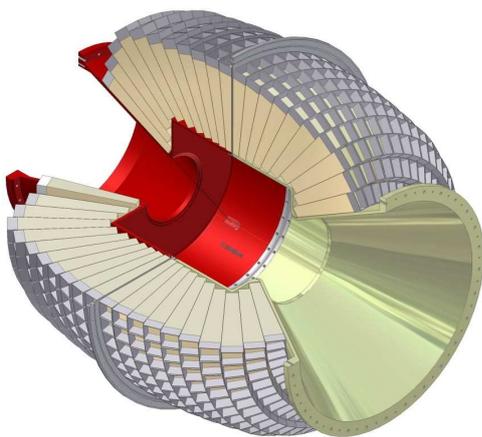
Figure 3.11: The Crystal Barrel calorimeter [Wal16].
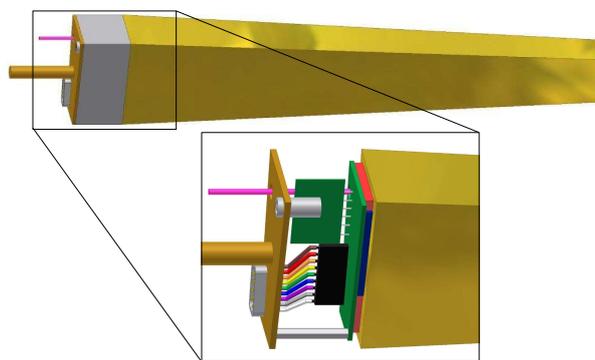
Figure 3.12: One CsI(Tl) crystal with wavelength shifter and front end electronics [Wal16].

into a 6 µs pulse, which is then digitized by a dual-range[10] analog-to-digital converter (ADC) [Ehm00]. For monitoring and calibration purposes, a light-pulser system allows the injection of light with various known relative intensities into the wavelength shifter via optical fibers [Bös06; Bar00].

Due to the slow rise time of the analog signals after the preamplifier, the measurement of the signal time using TDC modules is not useful. Also, no fast trigger signal for the first trigger level (see Section 3.2.9) can be provided. However, the information of the CB calorimeter can be used in the second trigger level. For this purpose, a second output of the shaper modules is connected to discriminators, which provide the digital input signals for the Fast Cluster Encoder (FACE) [Fle01]. FACE determines the number of clusters of crystals with an energy deposit above the discriminator threshold (typically 15 MeV) using cellular logic ASICs.

3.2.6 Forward Plug

The Crystal Barrel calorimeter is extended in forward direction by another detector. This Forward Plug (FP) consists of 90 CsI(Tl) crystals, arranged in three rings (see Fig. 3.13). Due to an additional holding structure between the CB and the FP, the FP crystals are not facing the center of the target, but are shifted by 3 cm along the beam axis, away from the target. The detector covers the polar angle range from $\theta = 11.2°$ to $\theta = 27.5°$ [Fun08]. In contrast to the PIN photo diode readout of the main CB calorimeter, the CsI(Tl) crystals of the FP are read out using PMTs. Their output signal is fast enough to include this detector into the first trigger level (Section 3.2.9). The analog signal is therefore split in a driver module [Hof04]. One branch is used for the energy measurement in a similar way as for the rest of the CB detector, i.e. using shapers and dual-range ADCs. The other branch is fed into rise-time-compensating discriminators [Mar+02] (with a typical threshold around 25 MeV [Fun08]). It is used to provide timing information using TDCs, and two trigger signals provided by a cluster finder module [Fun08]. The first trigger signal is generated when one cluster is identified in the FP, and the second if two or more clusters are identified.

The angular range covered by the FP is not fully covered by the Inner Detector. To allow for the identification of charged particles over the full range, 180 organic scintillators with a thickness of 3 mm are placed in front of the CsI(Tl) crystals [Wen08]. They are arranged in two layers. The scintillators of the rear layer are placed directly in front of the crystals, with each scintillator covering the same solid angle as the corresponding crystal. The front layer is rotated by half the width of a crystal, i.e. by $\Delta\phi = 6°$ around the beam axis. The readout of the scintillators is done using wavelength shifting fibers embedded at both sides of the scintillators, which are then connected to light-guide fibers, as can be seen in Fig. 3.14. The fibers guide the light through the small gap between the FP and the CB calorimeter to the outside and to multi-anode PMTs. Their signals are digitized using leading edge discriminators followed by multi-hit TDCs. Additionally, a logical OR of the discriminator outputs could be used as a trigger signal.

---

[10] Further details on the dual-range ADC are given in Section 5.2.2.1, where the energy calibration is discussed.
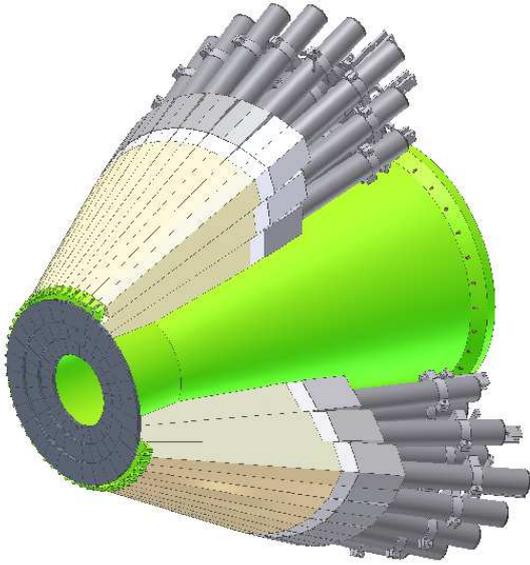
Figure 3.13: Forward Plug for the Crystal Barrel calorimeter [Wal16].
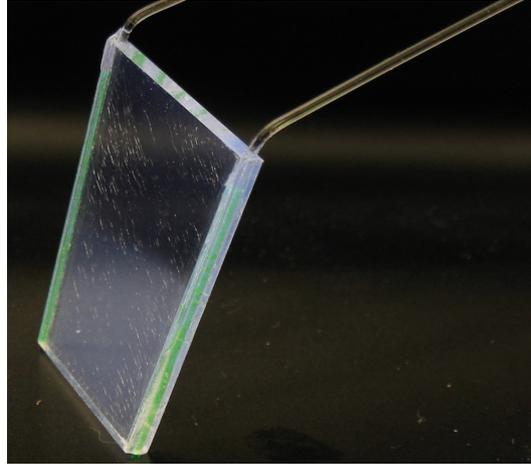
Figure 3.14: One organic scintillator with wavelength shifting fibers [Wen08].

3.2.7 TAPS

In forward direction the detector setup is complemented by the TAPS detector. It is positioned at a distance of $210\,\text{cm}$ from the target center and covers the polar angle range from $\theta = 1°$ to $\theta = 12°$. The calorimeter consists of 216 hexagonal BaF_2 crystals in a forward wall setup, with one crystal missing in the center, around the beam axis (see Fig. 3.15). The crystals have a height of $5.9\,\text{cm}$ and a length of $25\,\text{cm}$ [Nov91], corresponding to roughly $12\,X_0$ [Oli+14]. The rear end of the crystals is cylindrically shaped, with a PMT attached (see Fig. 3.16). Its signals are read out by custom-built readout modules [Dre04], providing energy and timing information for each crystal, using ADC modules as well as constant fraction discriminators followed by TDCs. In addition, two leading edge discriminators with independent thresholds (called `LEDHigh` and `LEDLow`) are used to generate trigger signals. In contrast to the Forward Plug, no cluster finder is used. Instead, the detector is divided into four trigger sectors (see Fig. 3.17), and trigger signals are generated if at least one sector has registered a hit above the `LEDHigh` threshold, or at least two sectors have registered a hit above the `LEDLow` threshold. Both `LEDHigh` and `LEDLow` thresholds are typically set to $80\,\text{MeV}$ for all crystals. The only exception are the two innermost rings of crystals closest to the photon beam, for which the `LEDHigh` discriminator is disabled because of the high rate of background from e^+e^- pairs in these crystals.

For the identification of charged particles and for a $\mathrm{d}E/\mathrm{d}x$ measurement, organic scintillators are placed in front of each BaF_2 crystal (see Fig. 3.16). They have a thickness of $5\,\text{mm}$ and the same dimensions as the crystals. The readout is done by optical fibers connected to multi-anode PMTs [Jan+00]. The signals are digitized by leading edge discriminators and TDCs, as well as ADCs for the $\mathrm{d}E/\mathrm{d}x$ measurement.

Figure 3.16: One TAPS module consisting of BaF_2 crystal and organic scintillator [Dre04].

Figure 3.15: The TAPS detector (without the organic scintillators in front of the crystals).
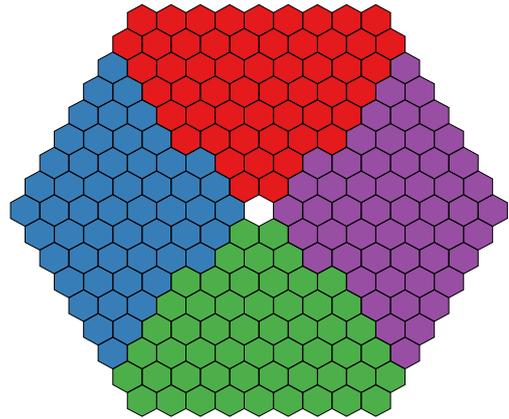
Figure 3.17: Arrangement of the BaF_2 crystals into 4 trigger sectors.

3.2.8 CO$_2$ Cherenkov Detector

In addition to the hadronic reactions that are investigated with the Crystal Barrel/TAPS experiment, there is background from electromagnetic reactions. As the cross section for e^+e^- pair production is proportional to the Z^2 of the target material, this is a big issue for measurements with a butanol target—which contains carbon ($Z = 6$) and oxygen ($Z = 8$) atoms—compared to a pure hydrogen target ($Z = 1$). Also, Compton scattering significantly contributes to the electromagnetic background, in particular at lower energies, as can be seen in Fig. 3.18. The electromagnetic background is produced dominantly in very forward direction at small angles. In order to identify this background at trigger level, a threshold Cherenkov detector [Kai07] is placed in front of the TAPS detector. The detector is a $1.2\,\mathrm{m} \times 1.2\,\mathrm{m} \times 1\,\mathrm{m}$ aluminum box with an entrance and exit window consisting of $50\,\mu\mathrm{m}$ thick Mylar foil at the front and backside. The detector is filled with CO_2 at atmospheric pressure as Cherenkov medium. The produced Cherenkov light is focused by an elliptical mirror to a single PMT located at the top of the detector. The PMT signal is discriminated and can then be used as a (veto) trigger signal. Additionally, the discriminator output is fed into a multi-hit TDC. CO_2 has a refractive index of 1.00045 at atmospheric pressure [Oli+14], this results in a Cherenkov threshold energy of $E_{\min} = 17.4\,\mathrm{MeV}$ for electrons and positrons, which is below the trigger and reconstruction thresholds of TAPS. For all other charged particles, the Cherenkov threshold energy is above the maximum energy of the accelerator.
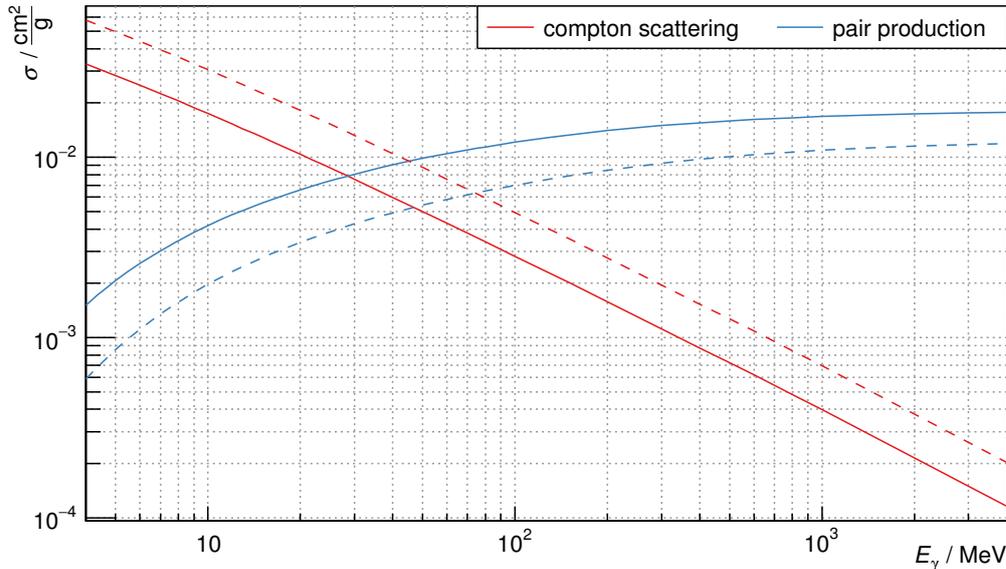
Figure 3.18: Energy dependent total cross section σ for e^+e^- pair production and Compton scattering, for a butanol (solid) or hydrogen (dashed) target (data from [Ber+14]).

3.2.9 Trigger

The digitization and readout of all detector channels for one event takes time in the order of $1\,\mathrm{ms}$.[11] To maximize the livetime[12] of the experiment, it is crucial to avoid the readout of background events. Therefore, the events that are of interest for the analysis have to be identified by the detector electronics, which then triggers the readout of the detectors. This is done in a two-level process: The first level reaches a decision based on all "fast" detector signals, i.e. all signals that are available within $300\,\mathrm{ns}$ [Hof16]. These are the signals from all detectors except the Crystal Barrel calorimeter, as listed in Table 3.1. The first level trigger signal is distributed to all TDC modules as a time reference, it triggers the conversion for all ADC modules, and it starts the Fast Cluster Encoder (FACE) which is used in the second trigger level. Once the FACE information is available to the second level trigger, which takes on average[13] $6\,\mathrm{\mu s}$ [Hof16], the event is either retained and the readout of all detector components is triggered, or a reset signal is distributed to all detector components to discard the event, thus avoiding the long readout time. Both trigger levels are implemented using FPGA modules, described in detail in [Win06]. Different trigger conditions can be selected using different programming of the FPGA modules. For this thesis, two different trigger conditions were used:

---

[11] The actual readout time depends on many variables, including the number of hits in the different sub-detectors, as well as the detectors that are actually read out (CB being the slowest).

[12] The *livetime* is the time in which the experiment is able to detect events. It is smaller than the total time with beam on target because of *deadtime* of the readout electronics.

[13] The actual time depends on the number of clusters found in the Crystal Barrel, it is at most $10\,\mathrm{\mu s}$ [Hof16].

1. Tagger trigger (`new_tagger_coinc_dt`)
   This trigger condition implements a minimum bias trigger. All events with a tagged beam photon, i.e. a coincident hit in two overlapping tagger scintillator bars, are recorded. This trigger is not useful to investigate reactions with small cross sections, such as the photoproduction of mesons. Nevertheless, it is needed as a cross-check for the photon flux determination, and for the determination of the polarization degree in case of measurements with a linearly polarized photon beam.

2. Data trigger (`trig42c`)
   This trigger condition is used to record hadronic reactions. It is designed to record all events with at least two clusters in the calorimeters, and reject electromagnetic background using the CO_2 Cherenkov detector as a veto. It contains several sub-conditions which are combined by a logical OR. The individual sub-conditions are listed in Table 3.2. They cover all possible combinations of two clusters in the calorimeter parts. Only events with no cluster in TAPS or the FP, i.e. only clusters in the CB need an additional first level trigger from the Inner Detector.

Table 3.1: Description of the trigger signals available in the first trigger level.

trigger signal	description
`tagger_or`	a hit in any tagger scintillator bar
`tagger_coinc`	a coincident hit in two adjacent tagger scintillator bars
`gim`	a hit in any of the GIM crystals
`cherenkov`	a hit in the CO_2 Cherenkov detector
`inner`	a coincident hit in at least 2 of the 3 layers of the Inner Detector
`fpv`	a hit in any of the FP organic scintillators[14]
`cf1`	exactly one cluster found by the FP cluster finder
`cf2`	two or more cluster found by the FP cluster finder
`taps1`	a hit in any TAPS sector above `LEDHigh` threshold
`taps2`	two coincident hits in different TAPS sectors above `LEDLow` threshold

Table 3.2: The sub-conditions of the `trig42c` data trigger.

first level	second level (# FACE clusters)
`inner` $\wedge$ `tagger` $\wedge$ NOT `cherenkov`	≥ 2
`cf1` $\wedge$ `tagger` $\wedge$ NOT `cherenkov`	≥ 1
`cf2` $\wedge$ `tagger` $\wedge$ NOT `cherenkov`	bypass
`taps1` $\wedge$ `tagger` $\wedge$ NOT `cherenkov`	≥ 1
`taps2` $\wedge$ `tagger` $\wedge$ NOT `cherenkov`	bypass
`cf1` $\wedge$ `taps1` $\wedge$ `tagger` $\wedge$ NOT `cherenkov`	bypass

---

[14] The `fpv` trigger is only used for detector tests and not during normal data-taking operation.

3.3 Simulation of Crystal Barrel/TAPS Detector System

Due to the complexity of the Crystal Barrel/TAPS detectors, a simulation of the detector system is needed to fully understand the detector performance, and provide additional information that cannot be obtained from the measured data alone. The most important application is the determination of the detector acceptance, but the simulation can also be used for various kinds of cross-checks of the measured data, and for an estimate of the detector performance prior to the actual measurement (cf. Chapter 4).

The principle of the simulation is to track particles and their interactions with the active and passive material of the detector using the Monte Carlo technique [MU49], and calculate the detector response from the simulated energy deposits. This is a standard technique in particle physics, and there exist various simulation packages for this kind of simulation. For the Crystal Barrel/TAPS experiment, the Geant3[15] simulation package [Bru+87] is used within the CBGeant simulation package [Cre01], developed specifically for the Crystal Barrel experiment to provide a complete simulation of the detector setup. In addition, a new simulation package for the Crystal Barrel/TAPS experiment is being developed based on the ROOT framework [BR97] and Virtual Monte Carlo [Kal11]. It produces results compatible with the older CBGeant but allows for a much greater flexibility to implement modifications to the experiment or exchange parts of the simulation by another framework (e.g. using the newer GEANT4 [Ago+03] for particle tracking instead of Geant3).

The simulation packages generate primary particles as requested by the user, and produce output which is compatible with the data produced by the DAQ of the actual experiment, i.e. individual ADC or TDC values for all detector channels. This allows for a detailed investigation of the detector response for individual particles or reactions. It should, however, be noted that the simulation is not an exact replica of the experiment and one expects some minor differences between the simulated data and the actual data. These differences are caused e.g. by the simplifications needed in the simulation to decrease the computational effort, or by minor differences between the detector geometry used for the simulation and the actual detector geometry. With careful fine-tuning of the simulation, these differences can be minimized. This has been done for the detection of photons (which is the main purpose of the detector), but there are remaining discrepancies concerning the exact energy deposits of charged particles and, consequently, their detection thresholds. This introduces a rather large systematic error when a quantitative comparison between data and simulation is done, especially for charged particles. In particular, this is relevant for the determination of the detector acceptance, which is needed for the measurement of cross sections. In principle, this error could be reduced by additional fine-tuning of the simulation for charged particles. However, since this analysis does not require precise knowledge of the detector acceptance (cf. Chapter 6), the simulation is only used for a qualitative comparison to the data. For this purpose, the accuracy of the simulation is more than adequate.

---

[15] **GE**ometry **AN**d **T**racking

Chapter 4

The Transverse Magnetic Field for the Polarized Target

Prior to this work, the Crystal Barrel/TAPS detector setup has never been used with a transversely polarized target. The transverse magnetic field of around 500 mT in the area of the target introduces an additional challenge, because it influences the measurement by deflecting the trajectories of all charged particles.

To get a rough estimate on the size of this effect, the bending radius R of charged particles with a given momentum p is calculated for a homogeneous magnetic field perpendicular to the particle momentum using

$$R = \frac{p}{e \cdot B}. \tag{4.1}$$

For a homogeneous magnetic field of a given length L, the angle of deflection α can then be calculated using

$$\alpha = \arcsin\left(\frac{L \cdot e \cdot B}{p}\right) \qquad \text{(for } \alpha < 90°\text{).} \tag{4.2}$$

The length of the holding coil is approximately 10 cm [Dut16]. As the target cell is at the center of the coil, the average path length through the magnetic field, for particles leaving the target in forward direction,[1] is approximately 5 cm. The angle of deflection as a function of particle momentum is shown in Fig. 4.1, for an expected path length of 5 cm, and for a path length of 10 cm as a worst case scenario assuming the stray field outside the coil has the same integrated strength. To study the influence of this deflection on the detector performance, one has to look at the influence on the hadronic reactions that are to be measured, and at the influence on background reactions.

4.0.1 Influence on Hadronic Reactions

The only charged particle in reactions that are investigated with the current Crystal Barrel/TAPS setup is the recoiling proton. The proton can of course only be detected if it deposits more energy in the calorimeters than the cluster threshold (20 MeV in the Crystal Barrel and 25 MeV in the TAPS detector, see Chapter 5). Due to energy loss in the target

---

[1] The path inside the magnetic field of particles leaving the target at a larger angle to the beam axis is significantly smaller, because the radius of the coil is just 2 cm. For a worst-case estimate it is therefore sufficient to consider only particles in forward direction.
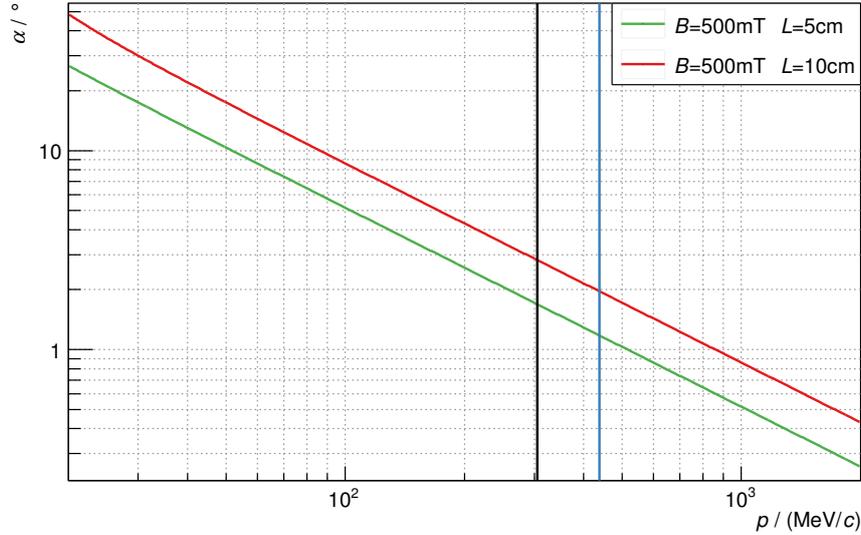
Figure 4.1: The angle of deflection α for charged particles with momentum p in a $L = 5\,\mathrm{cm}$ (green) and $L = 10\,\mathrm{cm}$ (red) long homogeneous magnetic field of $B = 500\,\mathrm{mT}$. The vertical lines correspond to protons with a kinetic energy of $50\,\mathrm{MeV}$ (black) and $100\,\mathrm{MeV}$ (blue), respectively.

and other material in front of the calorimeters no proton with less than 50–60 MeV kinetic energy can be detected. As the trigger threshold is even higher (80 MeV for TAPS) the detector acceptance for reactions with forward protons of less than 100 MeV is very small. The deflection of the detected protons due to the target magnetic field is therefore expected to be below 1.3°, and even in the worst case scenario it is below 2° (see Fig. 4.1). This is of the same order as the angular resolution of the detector, the influence of the magnetic field on hadronic reactions can therefore be neglected.

4.0.2 Influence on Electromagnetic Background

While protons with momenta below $300\,\mathrm{MeV}/c$—i.e. with a kinetic energy below $50\,\mathrm{MeV}$—will not be detected, this is of course not true for electrons and positrons, for which a momentum of $30\,\mathrm{MeV}/c$ can be sufficient to result in an energy deposit above the cluster threshold. For these particles, deflection angles $\gg 10°$ are possible. Being only background particles, their energy and direction do not need to be determined, the impact of the magnetic field on the angular resolution is therefore of no importance here. Nevertheless, the large deflection angle is expected to have a significant impact on the measurements: Without the magnetic field, electrons and positrons from pair production are produced mostly at very forward angles due to the forward-peaking cross section, where they are identified and vetoed on the trigger level by the CO_2 Cherenkov detector. With the magnetic field, these particles get deflected to much larger angles and can be detected in the Forward Plug of the Crystal Barrel or even the Inner Detector, and do not reach the CO_2 Cherenkov detector. This is expected to have a large (negative) impact on the trigger performance. A more detailed investigation is therefore required, which is presented in the following.
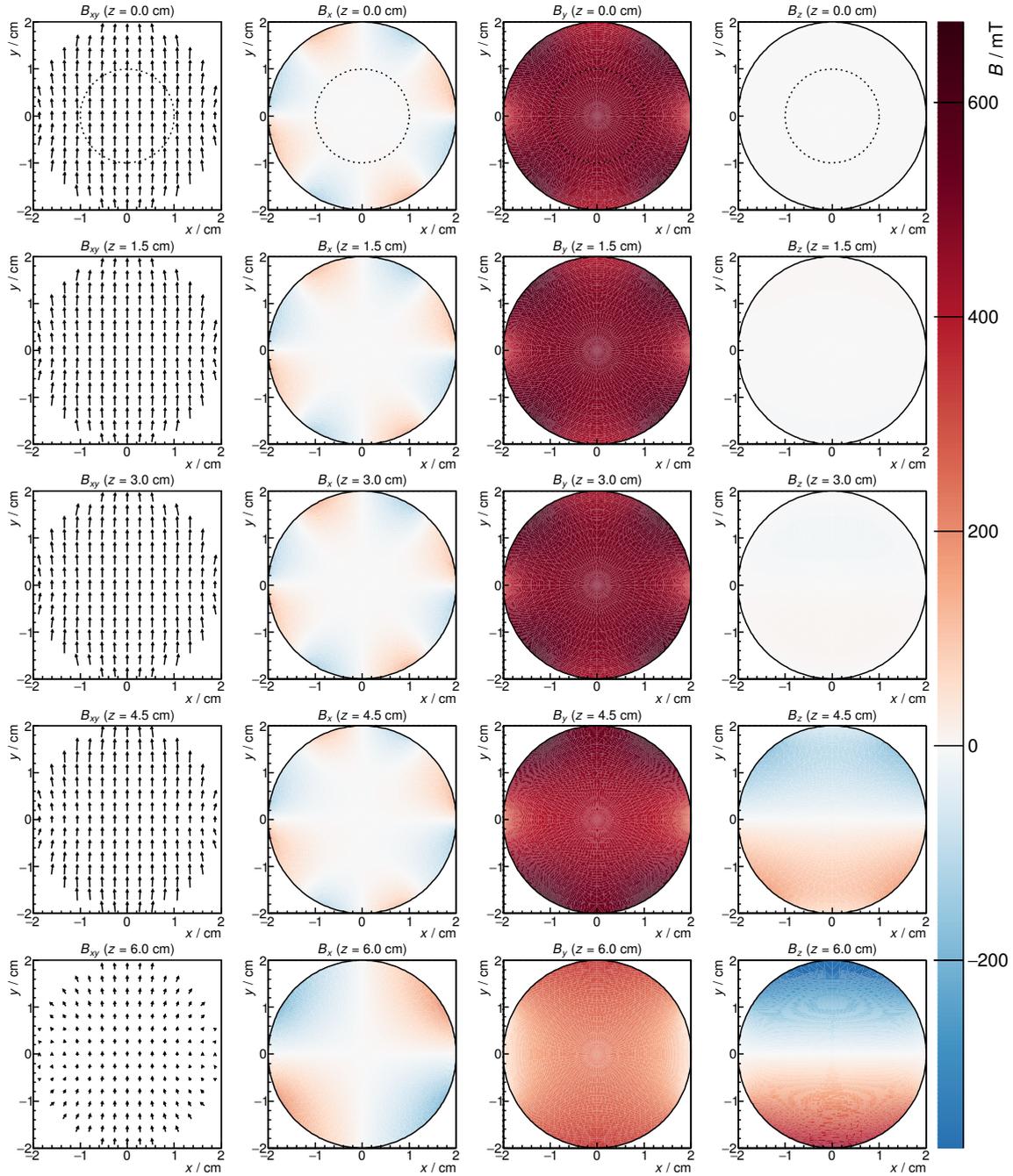
Figure 4.2: The magnetic field of the transversely polarized target [Dut16]. The target cell has a radius of $1\,\mathrm{cm}$ and a length of $2\,\mathrm{cm}$ (from $z = -1\,\mathrm{cm}$ to $z = 1\,\mathrm{cm}$). At the center of the coil, at the target cell (dotted circle), the field is homogeneous along the (vertical) y-axis. Only the field inside the holding coil cylinder with $r = 2\,\mathrm{cm}$ is shown. Outside the coil the stray field falls off quickly.

4.1 Monte Carlo Studies

A detailed study of the influence of the magnetic field on the trigger performance is done using the Monte Carlo simulation of the experiment. For this, the magnetic field inside the holding coil needs to be included in the simulation packages (see Section 3.3), using the calculated field strength inside the radius of the coil at a length of 12 cm, which is ≈ 2 cm longer than the coil itself. The stray field outside of the radius of the coil is sufficiently small to be neglected. Figure 4.2 shows the field map at different distances from the target center.

4.1.1 Deflection of Protons

As a first test of the simulation, the influence of the field on protons is studied in more detail. The largest effect is expected for protons at very forward angles, where the trajectory of the particles in the magnetic field is maximal. Therefore, 500 000 Monte Carlo events with a single proton were generated, both with and without magnetic field around the target. The generated proton polar angle was limited to the very forward direction, i.e. $0° \leq \theta \leq 5°$, and the proton momenta were evenly distributed between 250 MeV/c and 1 GeV/c, which corresponds to a kinetic energy between 33 MeV and 433 MeV. Protons with lower energies are not detected in the calorimeter, and for protons with momenta > 1 GeV/c the deflection by the magnetic field is insignificantly small.

(a) without magnetic field   (b) with transverse magnetic field
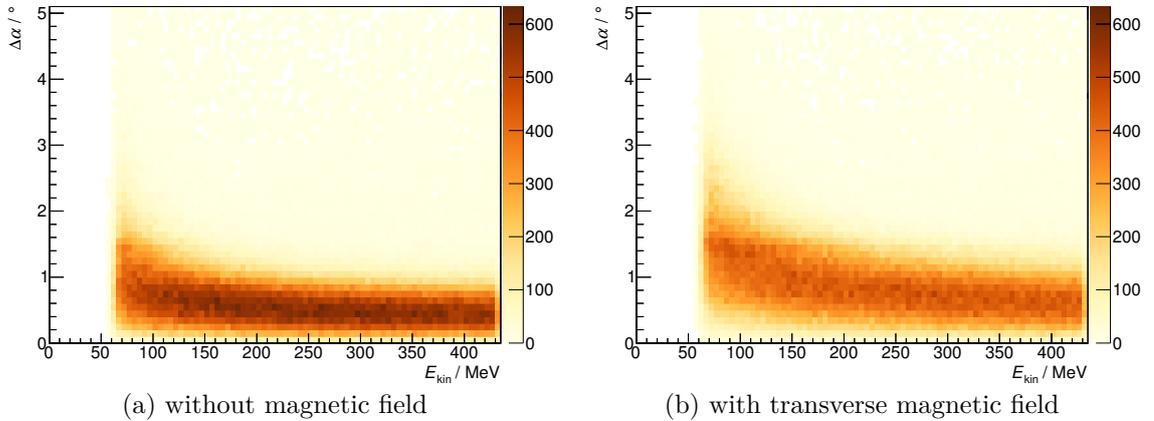
Figure 4.3: The angle $\Delta\alpha$ between the generated and reconstructed proton in TAPS, plotted versus the kinetic energy E_{kin} of the generated proton. The cut-off around $E_{\text{kin}} \approx 60$ MeV is a consequence of the reconstruction threshold.

With these Monte Carlo events, the angular resolution for protons can be investigated, by comparing the direction of the generated proton with the direction that is reconstructed from the detector data. The opening angle $\Delta\alpha$ between these two directions is shown in Fig. 4.3 as a function of the proton kinetic energy. In accordance to the previous section, the angular resolution is worsened by the magnetic field, but even for low momenta, the effect is smaller than 50%, i.e. the resolution is worsened by less than a factor 1.5. This can also be seen in more detail in Fig. 4.4a, where the angular difference distribution is

(a) $E_{\text{kin}} < 100$ MeV

(b) $E_{\text{kin}} > 350$ MeV
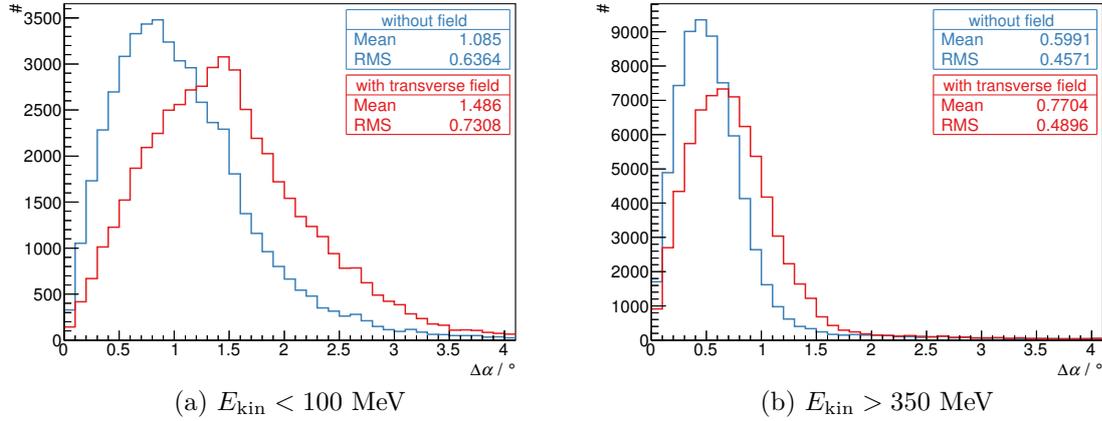
Figure 4.4: The angle $\Delta\alpha$ between the generated and reconstructed proton in TAPS.

shown for low proton momenta. It should be noted that this decrease in angular resolution is of no consequence for the double polarization measurements. Due to the high granularity of TAPS, which is required to cope with the high rates in forward direction, the angular resolution, even with the transverse magnetic field, is much higher than the resolution of the Crystal Barrel calorimeter, which is sufficient to identify and reconstruct the hadronic reactions. Any systematic shift can be eliminated by regularly switching the direction of the magnetic field.

The result of the simulation is consistent with the estimate described in Section 4.0.1.

4.1.2 Deflection of Electrons and Positrons

To verify the large deflection angles of electrons and positrons produced in forward direction, 500 000 Monte Carlo events with a single electron leaving the target at $\theta = 0°$ were generated. The electron momenta were evenly distributed between 10 MeV and 250 MeV. As can be seen in Fig. 4.5, a non-negligible amount of electrons reaches the Forward Plug of the Crystal Barrel calorimeter ($\theta > 13.5°$),[2] and is therefore not detected by the CO_2 Cherenkov veto detector, confirming the estimate described in Section 4.0.2.

4.1.3 Angular Distribution of Electromagnetic Background

In order to get a quantitative estimate of the expected trigger rates due to electromagnetic background, a more detailed study is required. For this, 30 million photons on the target were simulated, both with and without the transverse magnetic field around the target. The energy of the photons follows a $1/E_\gamma$ distribution between 30 MeV and 3.1 GeV. This approximates the bremsstrahlung spectrum of a 3.2 GeV electron beam sufficiently well for the purpose of this investigation. The low-energy cut-off at 30 MeV has no influence on the results, since photons with an energy below 30 MeV can only produce particles with an

---

[2] Even though the Forward Plug covers the polar angles between $11.2° < \theta < 27.5°$ (cf. Section 3.2.6) the smallest angle that can be reconstructed for a hit in the Forward Plug is the center of the first ring at $\theta = 13.5°$.
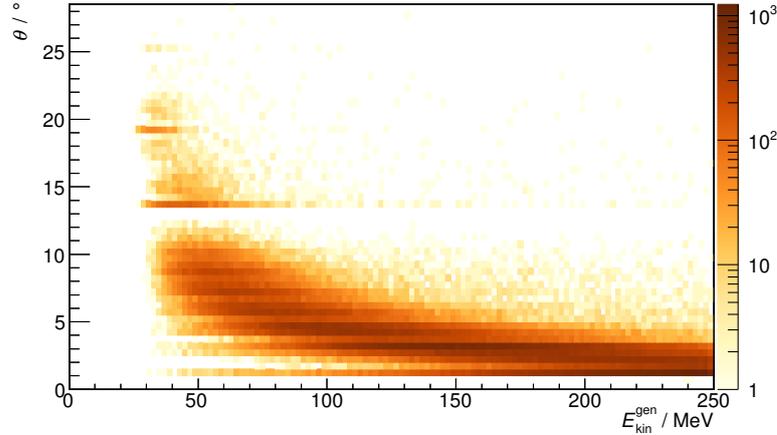
Figure 4.5: Deflection of single electrons produced at the target position in forward direction ($\theta = 0°$). The reconstructed polar angle θ is shown as a function of the generated electron energy for all events with an energy deposit above the reconstruction threshold.

energy below the trigger and reconstruction thresholds of the calorimeters. As can be seen in Fig. 4.6, the 30 million photons correspond to approximately 8 million photons in the energy range of the tagging system, between 480 MeV and 3.1 GeV.

If the transverse magnetic field is switched on, the number of reconstructed particles increases significantly, as is shown in Fig. 4.7. In particular in the Forward Plug of the Crystal Barrel calorimeter ($\theta > 13.5°$), where nearly no background particles (≈ 850) are reconstructed without the magnetic field, a large amount of particles (≈ 12000) with energies just above the threshold are detected if the transverse field is present. Unlike the additional background particles detected in TAPS, which are also identified by the CO_2 Cherenkov detector and can therefore be rejected by the trigger, the only feasible method to remove this additional background in the Crystal Barrel from the trigger is to increase the trigger threshold of the Forward Plug crystals. Following the simulation, an estimated threshold between 35 MeV and 40 MeV seems reasonable, as it would eliminate most of the background (see Fig. 4.7b). The optimal threshold value needs to be determined in an actual test measurement (see Section 4.2). The influence of the increased threshold on the acceptance is small (cf. Section 5.5).

Another detector component that suffers additional background due to the magnetic field is the Inner Detector. Figure 4.8 shows the total number of reconstructed hits, both with and without the magnetic field. There is no way to reduce this additional background without significant changes to the detector system (e.g. additional shielding). As the increase is only a factor of 5 it is possible to tolerate the additional background, resulting in a slightly reduced livetime caused by the readout of additional background events.

The number of generated trigger signals for each detector is, in general, not identical to the number of hits. For example, two simultaneous hits in the Inner Detector (e.g. an e^+e^- pair) result in a single trigger signal. The numbers of simulated trigger signals, and the corresponding rates, are listed in Table 4.1 for all detectors.
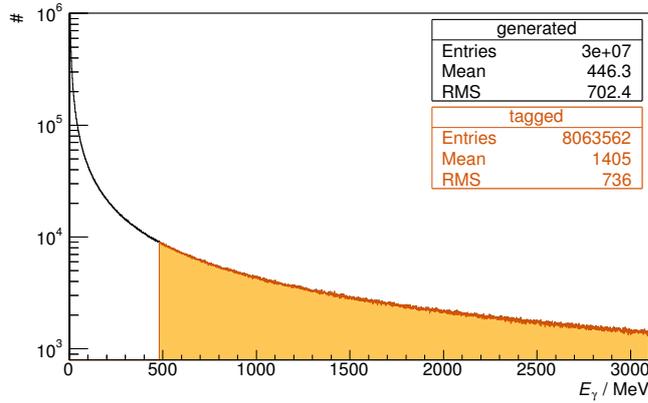
Figure 4.6: The simulated photon spectrum for electromagnetic background studies. The energy range covered by the tagging system is highlighted in orange.

(a) without magnetic field

(b) with transverse magnetic field
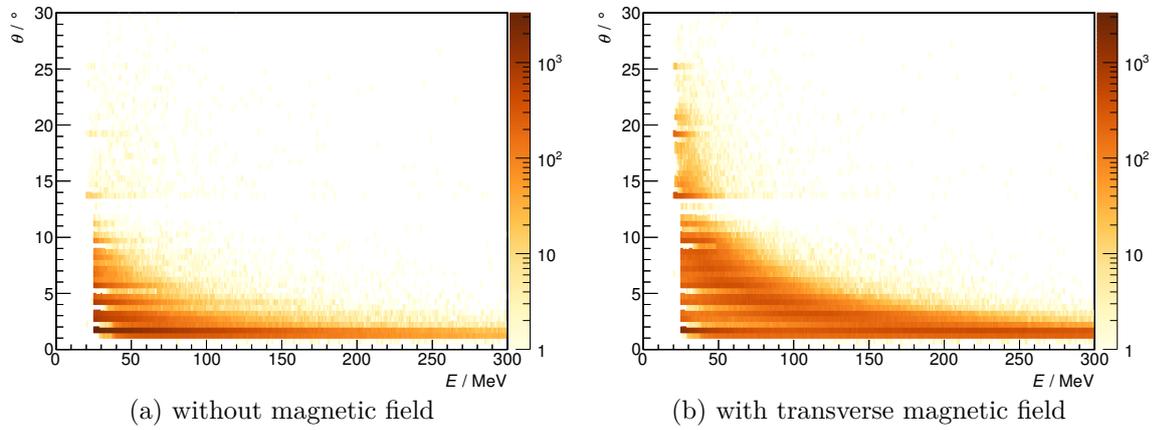
Figure 4.7: Distribution of particles reconstructed from simulated electromagnetic background.
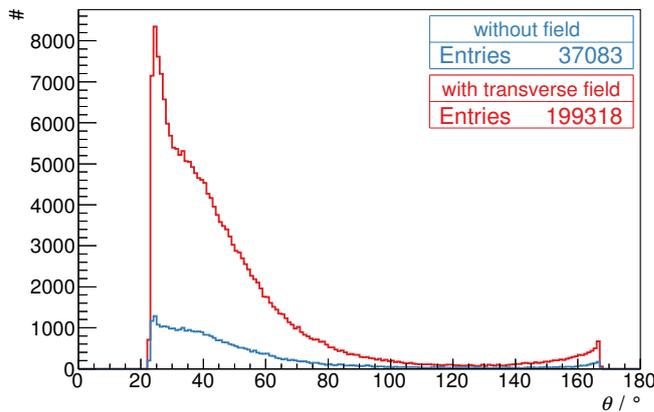
Figure 4.8: Distribution of reconstructed hits in the Inner Detector from simulated electromagnetic background.

Table 4.1: Expected trigger rates (see Table 3.1 for a description of the trigger signals) due to electromagnetic background with and without transverse magnetic field, based on 10 MHz tagger rate.

Trigger Signal	# Events		rate / Hz			
	w/o field	w/ field	w/o field	w/ field	increase	rel. change
tagger_coinc	8063562	8063562	10000000	10000000	1.00	
inner	37083	137020	45988	169925	123937	3.69
cf1	493	4798	611	5950	5339	9.74
cf2	19	61	24	76	52	3.17
taps1	74333	225494	92184	279646	187462	3.03
taps2	91	833	113	1033	920	9.14

4.2 Test Measurement for Background Studies

As a final step, the results obtained from the simulation need to be verified by an actual measurement. For this purpose, a short test measurement with beam from the accelerator was performed in June 2010, prior to the production data-taking. The objective was to directly compare the change of measurement conditions with and without the magnetic field.

The change of trigger rates while the transverse magnetic field is ramped up can be seen in Fig. 4.9. As expected, the Tagger and the Gamma Intensity Monitor are not influenced by the magnetic field.[3] The rate of the CO_2 Cherenkov detector decreases slightly when the field is switched on. Since the detector covers the whole forward region (without a hole at very forward angles $< 1°$ as it is the case for TAPS), nearly all produced electrons and positrons are detected, even without the magnetic field. With the presence of the magnetic field, however, some particles are deflected to larger angles and therefore not detected anymore, thus decreasing the rate. The rate of all other detector trigger signals is increasing, just as expected from the simulation. The exact numbers, however, are significantly different compared to the simulation. There are several reasons for this:

- In the simulation, only electromagnetic background reactions are considered, but the actual rates also contain hadronic reactions. The total hadronic cross section is several orders of magnitude smaller than the total electromagnetic cross section, but the electromagnetic cross section is strongly peaking in forward direction. At larger angles (covered by the Forward Plug and the Inner Detector) the rate of hadronic reactions is therefore not negligible compared to the rate of electromagnetic reactions.

- The electromagnetic background rates resulting from the simulation are extremely sensitive to the thresholds used in the simulation, especially in forward direction: A change of the TAPS trigger thresholds (which are set around 80 MeV) by just a few MeV can result in a change of almost a factor 2 in the trigger rate. The simulation has not been tuned to exactly match the thresholds used in the test measurement.

---

[3] The rate fluctuations are caused by small fluctuations in the beam current.
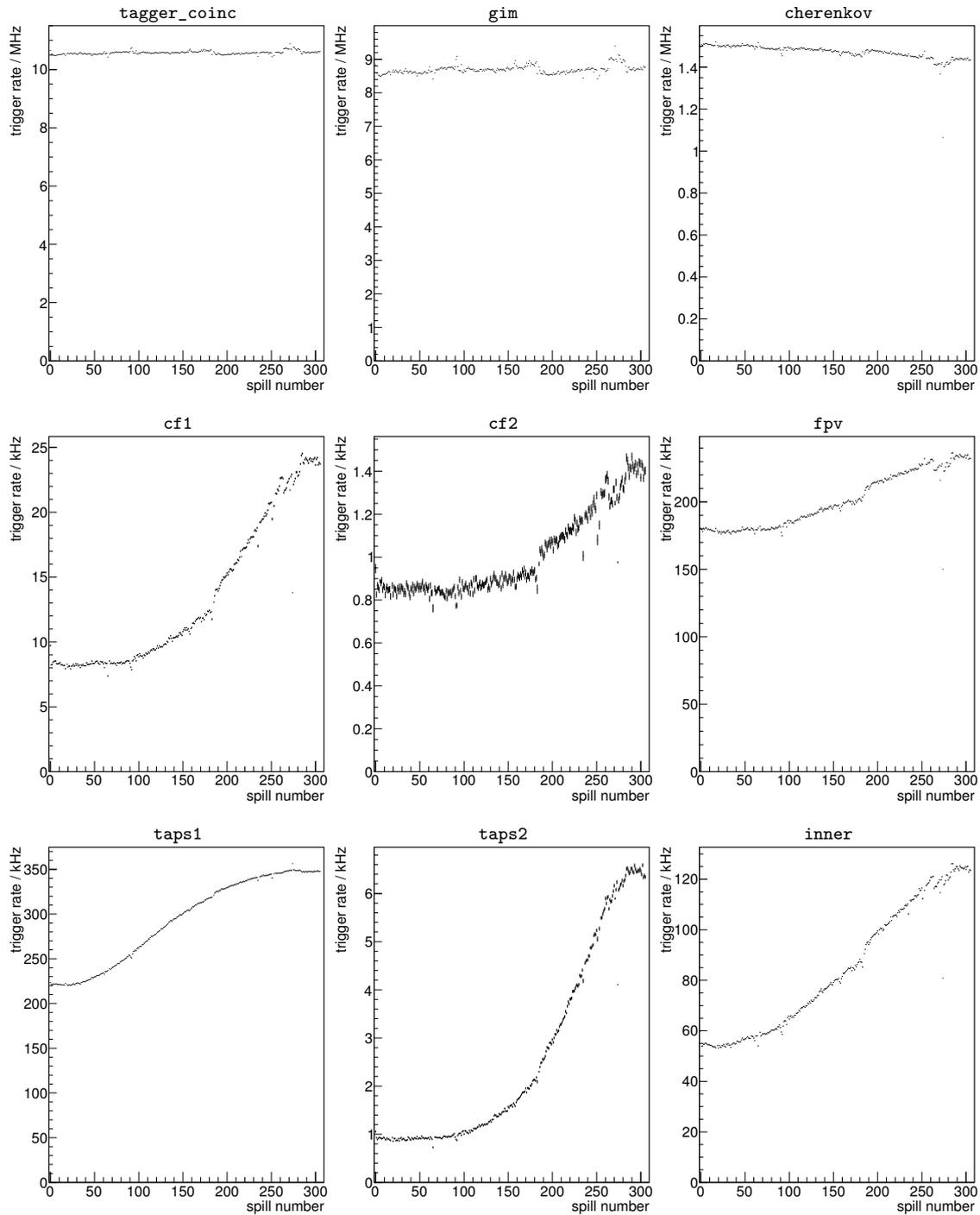
Figure 4.9: Changing trigger rates while the transverse magnetic field is ramped up over a period of 1500 s. One spill from the accelerator corresponds to 5.7 s (with 4 s of beam on target). The ramping started between spills 20 and 25.

The thresholds of the Forward Plug crystals cannot be adjusted for each crystal individually, but only in groups of 4 adjacent crystals [Fun08]. As a consequence, the thresholds of the 90 crystals are not identical, but are distributed over an $\approx 5\,\mathrm{MeV}$ wide energy interval, resulting in significantly larger trigger rates compared to the simulation because of the crystals with the lower thresholds.

A closer look at TAPS shows that the rate increase is concentrated in one plane perpendicular to the magnetic field, as can be seen in Fig. 4.10. This plane is not exactly parallel to the horizontal, apparently the coil has been installed slightly tilted.[4] The increase in the direction of positive x values, corresponding to the direction of deflection for negatively charged particles, is larger than the increase in the opposite direction. For each positron produced in a pair production reaction, there is also a corresponding electron. But there are additional electrons produced in Compton scattering reactions, resulting in more background particles with negative charge than with positive charge.
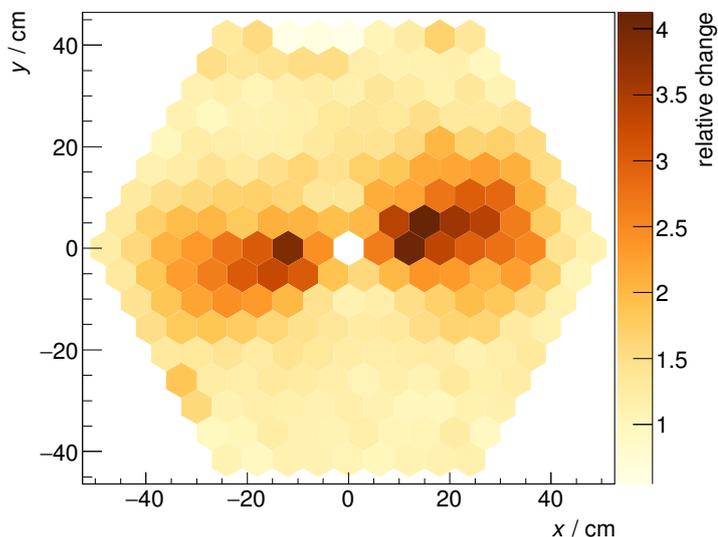
Figure 4.10: Rate increase in the TAPS crystals due to the transverse magnetic field.

The same behavior can also be seen in the plastic scintillators of the Forward Plug detector, as shown in Fig. 4.11. Again, more electrons (peaking around 10°) than positrons (peaking at the opposite direction around 190°) are detected. The rate increase is less pronounced at larger angles.

The position of the electron and positron peaks in each ring can be used to precisely determine the direction of the magnetic field. Using the average of all 6 peaks[5] results in

$$\phi_B = (99.7 \pm 0.3)°. \tag{4.3}$$

---

[4] The direction of the magnetic field is not important, as long as it is transverse to the beam direction. The exact orientation, which of course needs to be known, can be determined from the orientation of the background plane, as will be shown later (cf. Eq. (4.3)).

[5] Only the scintillators of the Forward Plug detector are used, since they provide a much better ϕ resolution compared to the TAPS crystals. Nevertheless, a consistent result of $\phi_B = (99.3 \pm 0.2_{\mathrm{stat}} \pm 0.5_{\mathrm{sys}})°$ is obtained using TAPS.
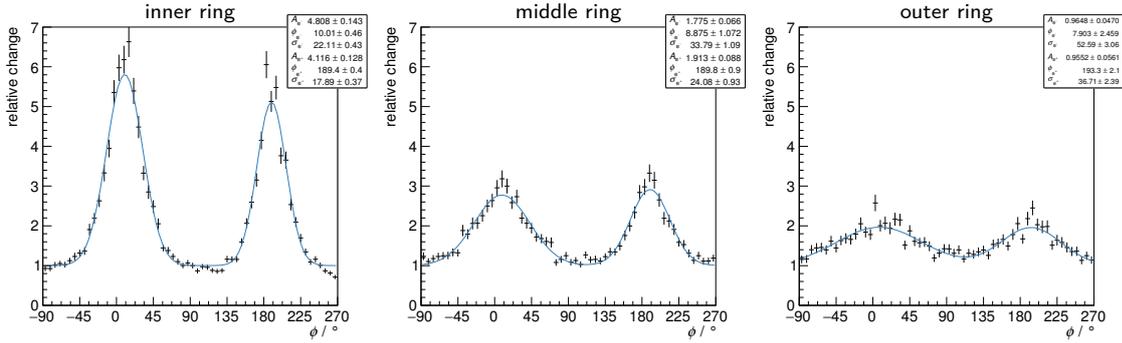
Figure 4.11: Rate increase in the Forward Plug veto scintillators because of the transverse magnetic field, with a fit of two Gaussian peaks to the data, which is used to determine the orientation of the magnetic field.

Another objective of the test measurement was the optimization of the trigger thresholds for the Forward Plug detector. For this purpose, the thresholds were increased from 25 MeV (the thresholds used for previous measurements with a longitudinally polarized target) to various higher values. As can be seen in Fig. 4.12, the additional background, while clearly visible at 25 MeV, is nearly completely eliminated with the 48 MeV thresholds. However, thresholds around 35 MeV already provide sufficient reduction of the background, the total rate is lower compared to the 25 MeV thresholds without the magnetic field. To influence the acceptance for hadronic reactions as little as possible, the 35 MeV thresholds were chosen to be used during the production data-taking period in October 2010. The analysis of this data set will be discussed in detail in the following chapters.
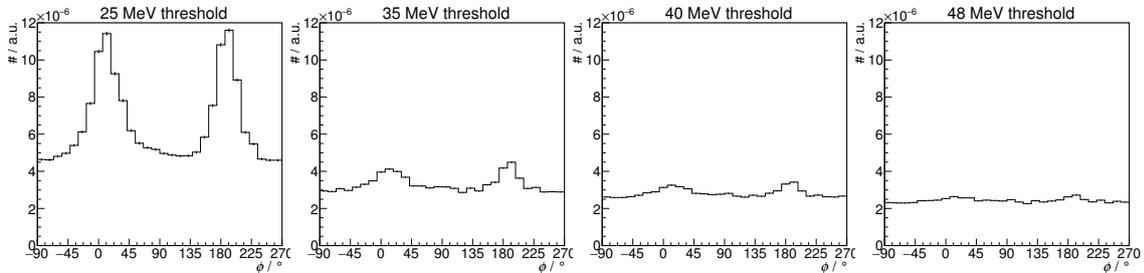
Figure 4.12: Number of hits in the crystals of the Forward Plug (normalized to the number of tagged beam photons) for different energy thresholds.

Chapter 5

Event Reconstruction

In this chapter, all steps are presented which are needed to reconstruct and select the reactions $\gamma p \to p\pi^0$ and $\gamma p \to p\eta$ from the recorded raw-data of the detector systems. This includes the calibration of the detector, the reconstruction of the final state particles and their properties from the detector data, and finally the selection of events belonging to the reactions of interest. But first, the data sets, which are used in this analysis, are presented.

5.1 Datasets

5.1.1 Double Polarization Measurement: Polarized Butanol Target

The analysis presented in this thesis is mostly based on the data taken with the Crystal Barrel/TAPS experiment during October (and November) 2010. In that data-taking period, the transversely polarized target was used in combination with a linearly polarized photon beam, produced from a $3.2\,\mathrm{GeV}$ primary electron beam.

The diamond radiator was oriented such that the coherent edge was at $E_\gamma \approx 950\,\mathrm{MeV}$, resulting in a high degree of linear polarization for $600\,\mathrm{MeV} \lesssim E_\gamma \lesssim 975\,\mathrm{MeV}$. Two orthogonal settings were used for the orientation of the polarization plane: $\phi = +45°$ and $\phi = -45°$.[1] The target was re-polarized every 2–4 days and the target polarization direction was flipped regularly by reversing the direction of the transverse magnetic holding field after re-polarization. Additionally, once, approximately in the middle of the data-taking period, the direction of the target polarization w.r.t. the magnetic field was inverted. Further details on the beam and target polarization degree will be given in Section 6.2. The data-taking periods with the butanol target are listed in Table 5.1.

5.1.2 Background Measurement: Carbon Target

Since the butanol target is not a pure (polarized) proton target, the background from unpolarized nuclei needs to be determined in an additional measurement in which the free (polarized) protons are removed, while everything else is kept unchanged. For this measurement, the butanol target was replaced by a carbon foam target with a density similar[2] to butanol. The target cryostat was filled with liquid helium—although the cooling is not needed for an unpolarized solid state target measurement—to provide conditions

---

[1] The reason for this choice are the significantly different size and divergence of the ELSA beam in the horizontal and vertical direction, which lead to differently shaped coherent enhancements in the $\phi = 0°$ (horizontal) and $\phi = 90°$ (vertical) settings, and thus to significantly different polarization degrees. In the $\phi = +45°$ and $\phi = -45°$ settings, however, the coherent enhancements are nearly identical [Ebe12].

[2] For a detailed comparison of the target densities see Section 6.1.1.

Table 5.1: Details of the October 2010 data-taking periods (butanol target).

start date	end date	energy of coherent edge	direction of magnetic field	direction of target pol.	hours of data trigger	recoreded data events
2010-10-11	2010-10-13	950 MeV	↑	↑	26	47 million
2010-10-13	2010-10-15	950 MeV	↑	↑	31	57 million
2010-10-15	2010-10-18	950 MeV	↑	↑	54	99 million
2010-10-27	2010-10-28	950 MeV	↑	↑	9	17 million
2010-10-28	2010-10-31	950 MeV	↓	↓	49	88 million
2010-10-31	2010-11-03	950 MeV	↓	↓	54	98 million
2010-11-03	2010-11-06	950 MeV	↑	↑	46	81 million
2010-11-06	2010-11-09	950 MeV	↓	↓	50	98 million
2010-11-09	2010-11-12	950 MeV	↑	↓	54	98 million
2010-11-12	2010-11-15	950 MeV	↓	↑	56	100 million
2010-11-15	2010-11-17	950 MeV	↑	↓	31	55 million
2010-11-17	2010-11-19	950 MeV	↓	↑	31	57 million
2010-11-19	2010-11-22	950 MeV	↑	↓	56	100 million

comparable to the polarized target measurement. The detector settings, like thresholds and trigger conditions, were kept identical compared to the butanol measurement, and a similar beam current was used.

The carbon measurement was not an exclusive background measurement for the double polarization measurement with the transversely polarized target and linearly polarized beam, but also for the other double polarization measurements that have been performed with the Crystal Barrel/TAPS experiment using a longitudinally polarized target in combination with a linearly or circularly polarized photon beam. Therefore, only about half of the carbon data were taken with a primary electron energy of 3.2 GeV and a linearly polarized photon beam. The other half—with a primary electron energy of 2.35 GeV, as it was used for the measurements with circularly polarized photon beam—is not included in this analysis because the measurement conditions are too different compared to the 3.2 GeV data.[3] With the 3.2 GeV beam, different settings for the coherent enhancement were used, with the coherent edge at $E_\gamma \approx 950$ MeV, 1150 MeV, and 1350 MeV. Like with the butanol data, the orientation of the photon polarization plane was switched regularly between $\phi = +45°$ and $\phi = -45°$. For part of the data the transverse magnetic field in the target was switched off to provide conditions more similar to the longitudinally polarized target. However, since the influence of the magnetic field on hadronic reactions is small (cf. Chapter 4), these data are included in this analysis for improved statistics. The data-taking periods with the carbon target are listed in Table 5.2.

---

[3] As will be seen in Chapter 6 the statistical uncertainty is dominated by the butanol data. Adding more carbon data at the cost of an additional systematic uncertainty is therefore not useful.

Table 5.2: Details of the November 2011 data-taking periods (carbon target).

start date	end date	energy of coherent edge	direction of magnetic field	hours of data trigger	recorded data events
2011-11-13	2011-11-14	950 MeV	↑	25	46 million
2011-11-14	2011-11-20	1350 MeV	↑	99	203 million
2011-11-21	2011-11-25	1150 MeV	off	71	174 million
2011-11-25	2011-11-28	1350 MeV	off	53	126 million

5.1.3 Monte Carlo Simulation

In addition to the measured data, a large amount of simulated Monte Carlo data were generated using the Virtual Monte Carlo based simulation (see Section 3.3) for the three reactions

$$(1)\ \gamma\,p \to p\,\pi^0_{2\gamma} \qquad (2)\ \gamma\,p \to p\,\eta_{2\gamma} \qquad (3)\ \gamma\,p \to p\,\eta_{3\pi}$$
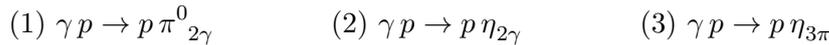
with $\pi^0_{2\gamma}$ and $\eta_{2\gamma}$ decaying exclusively into $2\,\gamma$, and $\eta_{3\pi}$ decaying exclusively into $3\,\pi^0_{2\gamma}$, i.e. $6\,\gamma$.

To simulate the reaction off a free proton, e.g. a pure hydrogen target, the target proton is generated at rest. To simulate the reaction off a proton which is bound in a carbon (or oxygen) nucleus, the target proton is generated with a momentum given by the distribution

(a) 1D momentum p_x, p_y, p_z (b) 3D momentum $|\vec{p}|$ (c) kinetic energy E_{kin}
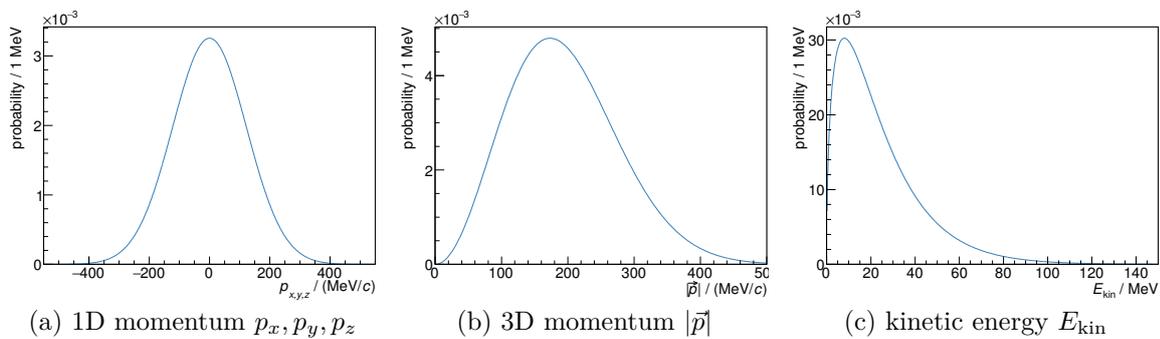
Figure 5.1: The nucleon momentum and kinetic energy distributions of carbon as used for the simulation. The distributions are obtained from the nucleon momentum distribution of carbon in one dimension, which is consistent with a Gaussian distribution with $\sigma = 120\,\text{MeV}/c$ [CHM52]. Since the momentum distributions in each spatial dimension are independent of each other, and the kinetic energy is proportional to the momentum squared, this results in a kinetic energy distribution in the shape of a (scaled) χ^2-distribution (with 3 degrees of freedom). The magnitude of the 3D momentum $|\vec{p}|$ follows a χ-distribution.

Table 5.3: Details of the simulated Monte Carlo datasets.

set	reaction	Fermi motion	final state distribution	events	comments
(1)	$\gamma\,p \to p\,\pi^0{}_{2\gamma}$	no	phase-space	3×10^7	
	$\gamma\,p \to p\,\eta_{2\gamma}$	no	phase-space	3×10^7	
	$\gamma\,p \to p\,\eta_{3\pi}$	no	phase-space	3×10^7	
(2)	$\gamma\,p \to p\,\pi^0{}_{2\gamma}$	yes	phase-space	3×10^7	
	$\gamma\,p \to p\,\eta_{2\gamma}$	yes	phase-space	3×10^7	
	$\gamma\,p \to p\,\eta_{3\pi}$	yes	phase-space	3×10^7	
(3)	$\gamma\,p \to p\,\pi^0{}_{2\gamma}$	no	$\mathrm{d}\sigma/\mathrm{d}\Omega$	3×10^7	
	$\gamma\,p \to p\,\eta_{2\gamma}$	no	$\mathrm{d}\sigma/\mathrm{d}\Omega$	3×10^7	
	$\gamma\,p \to p\,\eta_{3\pi}$	no	$\mathrm{d}\sigma/\mathrm{d}\Omega$	3×10^7	
(4)	$\gamma\,p \to p\,\pi^0{}_{2\gamma}$	yes	$\mathrm{d}\sigma/\mathrm{d}\Omega$	3×10^7	
	$\gamma\,p \to p\,\eta_{2\gamma}$	yes	$\mathrm{d}\sigma/\mathrm{d}\Omega$	3×10^7	
	$\gamma\,p \to p\,\eta_{3\pi}$	yes	$\mathrm{d}\sigma/\mathrm{d}\Omega$	3×10^7	
(5)	$\gamma\,p \to p\,\pi^0{}_{2\gamma}$	no	$\mathrm{d}\sigma/\mathrm{d}\Omega$	3×10^7	shifted target: $\Delta z = -1\,\mathrm{cm}$
(6)	$\gamma\,p \to p\,\pi^0{}_{2\gamma}$	no	$\mathrm{d}\sigma/\mathrm{d}\Omega$	3×10^7	shifted target: $\Delta z = +1\,\mathrm{cm}$
(7)	$\gamma\,p \to p\,\pi^0{}_{2\gamma}$	yes	$\mathrm{d}\sigma/\mathrm{d}\Omega$	3×10^7	shifted target: $\Delta z = -1\,\mathrm{cm}$
(8)	$\gamma\,p \to p\,\pi^0{}_{2\gamma}$	yes	$\mathrm{d}\sigma/\mathrm{d}\Omega$	3×10^7	shifted target: $\Delta z = +1\,\mathrm{cm}$

shown in Fig. 5.1 to account for the Fermi momentum of the bound proton. Data with a butanol target can then be approximated by adding free proton and bound proton events in a ratio as given by the number of free and bound protons in the butanol molecule,[4] i.e. 10 : 32. Since the detection of the recoiling proton is required in the analysis (as will be discussed in Chapter 6), reactions off bound neutrons can be neglected because the detection efficiency for neutrons ($\varepsilon_n < 0.3$ [Jae+11]) is significantly smaller than the proton efficiency.

In the most simple case, the generated final state is phase-space distributed for a photon beam energy distribution according to the Bethe-Heitler bremsstrahlung cross section (Eq. (3.2)). These simulations are used to investigate only the detector properties, e.g. the acceptance, without any bias from the physics that is to be investigated by the actual experiment. For a more realistic simulation, the final state can also be distributed according to the cross section $\mathrm{d}\sigma/\mathrm{d}\Omega$ of the reaction, with the data for $\mathrm{d}\sigma/\mathrm{d}\Omega$ taken from the BnGa 2011-02 partial wave analysis solution[5] [Ani+12].

---

[4] The Fermi momentum distributions of carbon and oxygen are very similar [CHM52] due to the similar size of the two nuclei. Thus, the oxygen contribution can be approximated by additional carbon events.

[5] See `http://pwa.hiskp.uni-bonn.de` for plots and data files of the BnGa solutions.

For the study of systematic uncertainties (cf. Chapter 7), additional data sets were simulated in which the position of the target has been shifted along the beam axis w.r.t. the detector system. All the different sets of Monte Carlo data that were simulated are summarized in Table 5.3.

5.2 Detector Calibration

5.2.1 Time Calibration

For almost all detector channels, the time of a detected signal is measured by a TDC.[6] The raw TDC values need to be converted to a meaningful time information. This is done for each channel with a function of the form

$$t = a + g \cdot T, \tag{5.1}$$

where t is the calibrated time (usually given in ns) and T is the uncalibrated TDC value. The calibration factor g converts the TDC value to a time value, which then needs to be corrected by the calibration offset a to ensure that coincident detector hits are reconstructed at the same time. Both g and a need to be determined for each detector channel. The calibration can be done using the measured data themselves, by iteratively correcting the time difference of coincident hits in the detector that is to be calibrated and one or more (not necessarily fully calibrated) reference detectors. The calibration procedure is described in detail in [Har08]. The time resolution after calibration is summarized in Table 5.4 for the different detector components.

Table 5.4: The time resolution of the detector components after calibration, given by the width of the time coincidence peak using a reference detector. Note that the width is influenced by both the resolution of the detector and the reference. See [Har08] for details.

detector	reference detector	FWHM/ns
Tagger scintillator bars	TAPS, BaF_2 crystals	0.830 ± 0.006
Tagger scintillator bars	Tagger scintillator bars	0.635 ± 0.003
Tagger scintillating fibers	TAPS, BaF_2 crystals	1.45 ± 0.03
Tagger scintillating fibers	Tagger scintillator bars	1.694 ± 0.006
Inner Detector scintillating fibers	Tagger scintillator bars	2.093 ± 0.013
Forward Plug, CsI(Tl) crystals	Tagger scintillator bars	1.861 ± 0.016
Forward Plug, veto scintillators	Tagger scintillator bars	4.434 ± 0.013
TAPS, BaF_2 crystals	Tagger scintillator bars	0.872 ± 0.006
TAPS, veto scintillators	Tagger scintillator bars	3.06 ± 0.05
CO_2 Cherenkov detector	Tagger scintillator bars	1.194 ± 0.014
GIM	Tagger scintillator bars	3.1 ± 0.3

---

[6] Only the CsI crystals of the Crystal Barrel calorimeter, that are read out by PIN photo diodes, do not provide individual time information because of their insufficient time resolution.

5.2.2 Energy Calibration

The energy deposit in the crystals of the calorimeters is measured by ADCs. The raw ADC values need to be converted to a meaningful energy information. Assuming a linear relationship between energy deposit, amount of scintillation light, and charge of the analog signal, this is done for each channel with a function of the form

$$E = g \cdot (A - p), \tag{5.2}$$

where E is the calibrated energy (usually given in MeV) and A is the uncalibrated ADC value. The offset p, called *pedestal*, is the ADC value measured when no energy is deposited in the crystal. It is determined regularly during data-taking. The calibration factor g needs to be determined by the energy calibration.

5.2.2.1 Crystal Barrel Calorimeter

To cover a large dynamic range up to $\approx 1.1\,\mathrm{GeV}$ for the Crystal Barrel and $\approx 2\,\mathrm{GeV}$ for the Forward Plug, but at the same time provide a sufficient energy resolution for low energies, a dual-range ADC is used (see also Section 3.2.5). The input signal is divided approximately $8:1:1$ and directed to a *high* range and a *low* range channel (the third *reference* channel is not used). Using two discriminators, an internal logic determines which of the two channels is digitized [Ehm00]. Alternatively, only the *high* channel can be used for calibration and testing purposes.
Instead of calibrating both channels individually using Eq. (5.2), the ADC values of the high range channel A_{high} are converted to a low range equivalent A_{low} using

$$A_{\text{low}} = f_{\text{range}} \cdot A_{\text{high}} + a_{\text{range}} \qquad \text{with } a_{\text{range}} = p_{\text{low}} - f_{\text{range}} \cdot p_{\text{high}}. \tag{5.3}$$

Consequently, the calibration is done in two steps: First, f_{range} and a_{range} are determined using a light-pulser system, and then g is determined using the measured data themselves, using the decay $\pi^0 \to \gamma\gamma$.

Light-Pulser Calibration

The relative calibration of the low and high range ADC channels is done using a light-pulser system [Bös06]. Light pulses matching the spectrum of the CsI(Tl) scintillation light are injected into the wavelength shifter of each detector module. To simulate the crystal response to different energy deposits, the intensity of the pulses can be varied using a combination of filters with different levels of transmission. To obtain the relative calibration parameters f_{range} and a_{range}, the ADC values for different levels of transmission are measured separately for the high and low channels and plotted versus the transmission T, as is visualized in Fig. 5.2. Two linear functions are fitted to the data points. The factor f_{range} is then given by the ratio of the two slopes, and the offset a_{range} can be calculated from the pedestal values p_{low} and p_{high}, obtainable from the y-intercepts.
During data-taking periods, the relative calibration is monitored at regular intervals by dedicated light-pulser measurements, usually every two or three days during the re-polarization of the target. As can be seen in Fig. 5.3, the factor f_{range} is distributed around the expected value of $f_{\text{range}} = 8$.
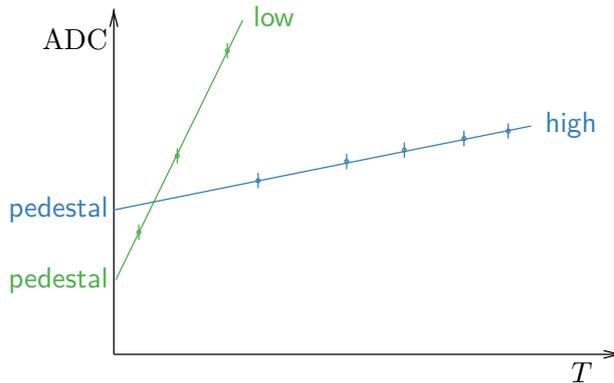
Figure 5.2: Sketch of the relative calibration of the Crystal Barrel dual-range ADCs using the light-pulser system [Bös06]. The average measured ADC values at different transmissions T are determined for both high- and low-range channels.
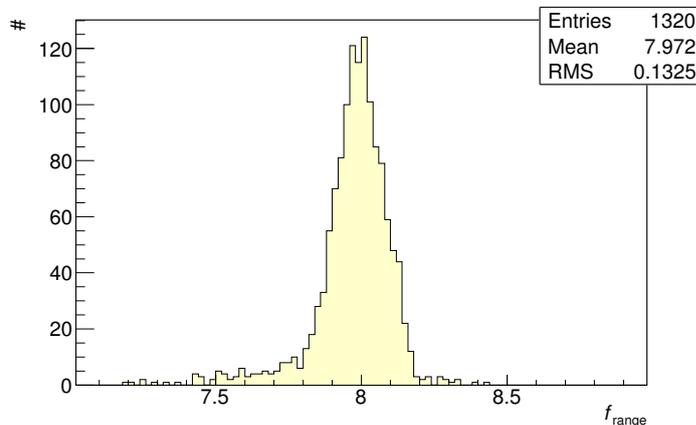
Figure 5.3: Histogram of the dual-range calibration factor f_{range} for all 1320 CsI(Tl) crystals during the October 2010 data-taking period. (Data from [Bös15].)

π^0 calibration

The readout chain of the CsI(Tl) crystals is designed such that a dynamic range of ≈ 1.1 GeV is covered [Wal16]. With the 12 bit dual-range ADCs this corresponds to a calibration factor of $g \approx 0.033$ MeV/channel for the low range channel. For the Forward Plug, where a larger dynamic range is required, the calibration factor should be around $g \approx 0.061$ MeV/channel [Mül07]. The exact determination of this value for each crystal is done for each data-taking period using the measured low range data themselves. This is accomplished using the reaction $\gamma p \to p\pi^0$ with the decay $\pi^0 \to \gamma\gamma$ [Jun00]. It requires the reconstruction of individual photons from the measured energy deposits in a cluster of crystals, which will be described in Section 5.3.1.1. Only the low range data are used in order to keep the π^0 calibration results independent of the light-pulser calibration [Mül17].

For each crystal i, all $\pi^0 \to \gamma\gamma$ candidates with one photon reconstructed from a cluster with this crystal as the highest energy deposit, and the second photon reconstructed anywhere in the Crystal Barrel (including Forward Plug) are selected. The two-photon invariant mass
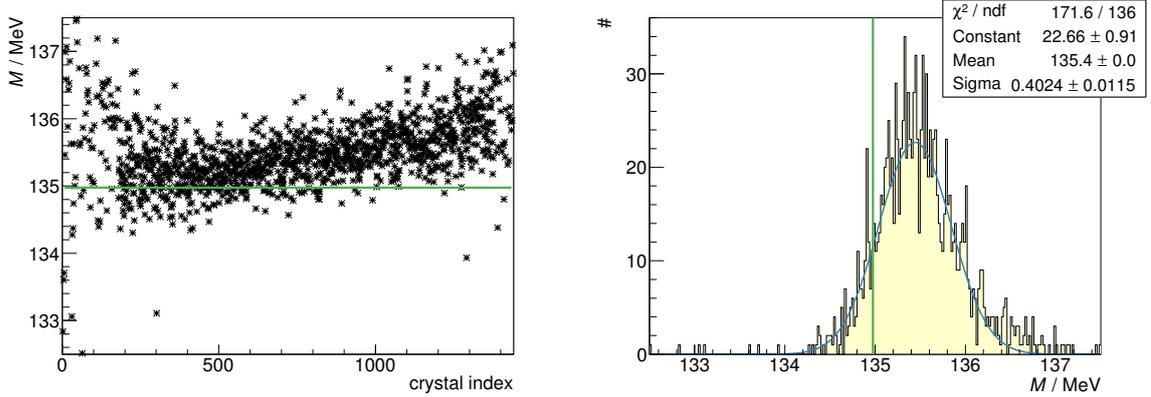
Figure 5.4: The position of the $M_{\gamma\gamma}$ peak for each crystal before the first iteration (left) and a histogram of the positions with a Gaussian fit (right) [Mül15].
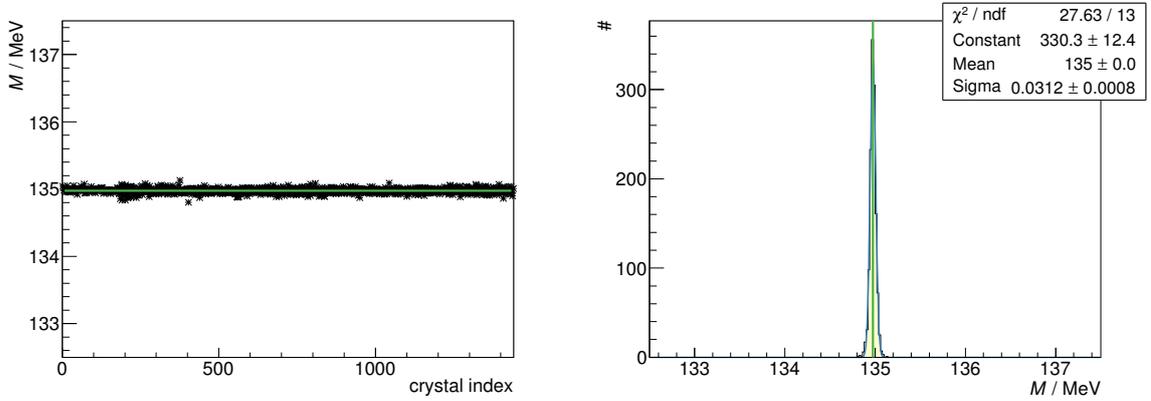
Figure 5.5: The position of the $M_{\gamma\gamma}$ peak for each crystal after the last iteration (left) and a histogram of the positions with a Gaussian fit (right) [Mül15].

$M_{\gamma\gamma}$ is calculated using

$$M_{\gamma\gamma}^2 =: M_i^2 = 2\, E_{\gamma_i} E_{\gamma_j} \left(1 - \cos(\theta_{\gamma_i \gamma_j})\right) \tag{5.4}$$

where E_{γ_i} is the reconstructed energy of the photon with its maximum energy deposit in crystal i (the one to be calibrated), E_{γ_j} is the reconstructed energy of the other photon, and $\theta_{\gamma_i \gamma_j}$ is their opening angle. A histogram of M_i^2 should show a clear peak approximately at $m_{\pi^0}^2 = (135\,\text{MeV})^2$ [Oli+14]. Since the crystals detecting the second photon are (in first approximation) arbitrary, any systematic deviation of the peak position M_i^2 from $m_{\pi^0}^2$ is dominated by the measured energy of the first photon. An improved calibration factor g_i^{n+1} can thus be calculated iteratively from the existing factor g_i^n using

$$g_i^{n+1} = g_i^n \cdot \frac{m_{\pi^0}^2}{M_i^2} \tag{5.5}$$

This process is repeated until a good calibration is obtained. A more detailed description of the calibration procedure can be found in [Mül17].

For the October 2010 data-taking period, 8 iterations were done [Mül15]. The position of the $M_{\gamma_1\gamma_2}$ peak for each crystal is shown in Fig. 5.4 before the first iteration, and in Fig. 5.5 after the final iteration. As can be seen in Fig. 5.6, the calibration factors g are distributed around the expected value of $g = 0.033\,\mathrm{MeV/channel}$ for the Crystal Barrel, while the crystals of the Forward Plug exhibit higher values with a broader distribution due to larger variations in the PMT readout and electronics.
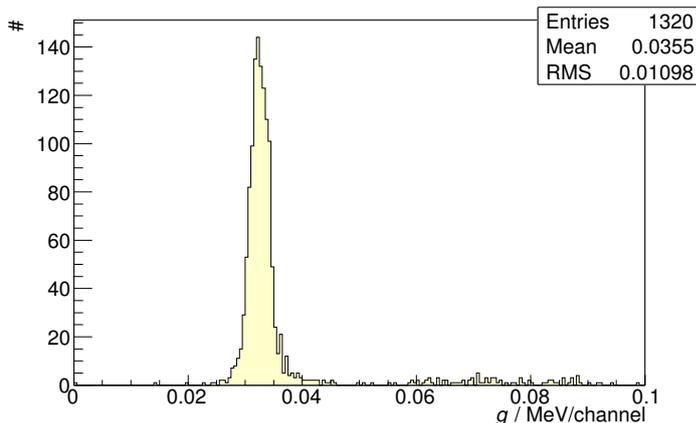
Figure 5.6: Histogram of the energy calibration factor g for all 1320 CsI(Tl) crystals during the October 2010 data-taking period (data from [Mül15]). The values above $g \gtrsim 0.05\,\mathrm{MeV/channel}$ correspond to the Forward Plug crystals.

5.2.2.2 TAPS Calorimeter

As the TAPS detector covers only a small fraction of the solid angle, an independent energy calibration using hadronic reactions, like it is done for the Crystal Barrel calorimeter, is not feasible. Instead, the $\pi^0 \to \gamma\gamma$ decay, with one photon measured in the already calibrated Crystal Barrel and the other one measured in TAPS, is used. Other than that, the calibration procedure is the same as for the Crystal Barrel. A detailed description is given in [Got09].

As can be seen in Fig. 5.7, the calibration factors g are distributed around a value of $g = 0.5\,\mathrm{MeV/channel}$, which corresponds to a dynamic range of $\approx 2\,\mathrm{GeV}$.

5.2.3 Tagging Spectrometer Calibration

In order to calculate the energy E_γ of the tagged beam photons from the primary electron energy E_0 and the energy E' of the secondary electrons using

$$E_\gamma = E_0 - E' \tag{5.6}$$

E' needs to be reconstructed from the measured position in the scintillating fiber detector or the scintillator bar hodoscope. For this purpose, calibration functions need to be determined in order to convert the index i of a scintillator bar or fiber to the corresponding
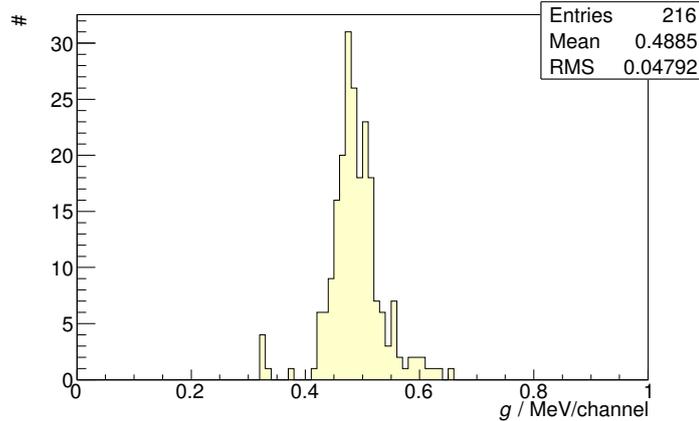
Figure 5.7: Histogram of the energy calibration factor g for all 216 BaF$_2$ crystals during the October 2010 data-taking period (data from [Got14]).

photon energy:

$$E_\gamma = f(E_0, B, i_{\text{fiber}}) \tag{5.7a}$$
$$E_\gamma = g(E_0, B, i_{\text{bar}}) \tag{5.7b}$$

During normal operation, the magnetic field B of the tagging magnet is set, for a given primary electron energy, to a fixed value $B_0(E_0)$. For $E_0 = 3176.1\,\text{MeV}$ a nominal field of $B_0 = 1.594\,\text{T}$ is used. To determine the calibration functions f and g, dedicated calibration measurements have been performed: At various primary electron energies[7] the position of the electron beam on the tagging hodoscope was measured for different magnetic field settings. Using this data, for each E_0 and its corresponding B_0, the calibration functions f and g can be determined by fitting polynomial functions to the calibration data, as is described in [For09]. Since the calibration measurements were not possible below $E_0 = 650\,\text{MeV}$, no reliable calibration could be obtained for the scintillating fibers 1–150, which correspond to $E' \lesssim 700\,\text{MeV}$ (and $E_\gamma \gtrsim 2300\,\text{MeV}$) for $E_0 = 3176.1\,\text{MeV}$. The calibration has been extended to the full range of the detector using a simulation [For09] to create additional calibration data in that energy range.

The calibration has been improved recently in the low E_γ region with additional measurements [Sch13], providing a finer granularity of data points and thus improving the polynomial fit. The final calibration function for the fibers is shown in Fig. 5.8.

The obtained energy resolution consists of a statistical as well as a systematic uncertainty. The statistical part is given by the width and divergence of the electron beam,[8] in addition to the width of the scintillators. The systematic uncertainty is dominated by the precision of the polynomial fit, which is estimated in [For09] to be 1 fiber. With the new calibration, this uncertainty is reduced to 0.5 fibers [Sch13]. For $E_0 = 3176.1\,\text{MeV}$ this corresponds to a systematic uncertainty of approximately $5.7\,\text{MeV}$ at $E_\gamma = 850\,\text{MeV}$ and around $1.9\,\text{MeV}$ at $E_\gamma = 2000\,\text{MeV}$. Above $E_\gamma \gtrsim 2300\,\text{MeV}$, the uncertainty increases up to $25\,\text{MeV}$ due to the extrapolation of the calibration in that region [For09].

---

[7] Measurements have been done for demand energies of 650 MeV, 800 MeV, 1270 MeV, 1800 MeV, 2400 MeV.

[8] Resulting in an uncertainty in the measurement of the position of $\sigma = 1$ fiber, see [For09].
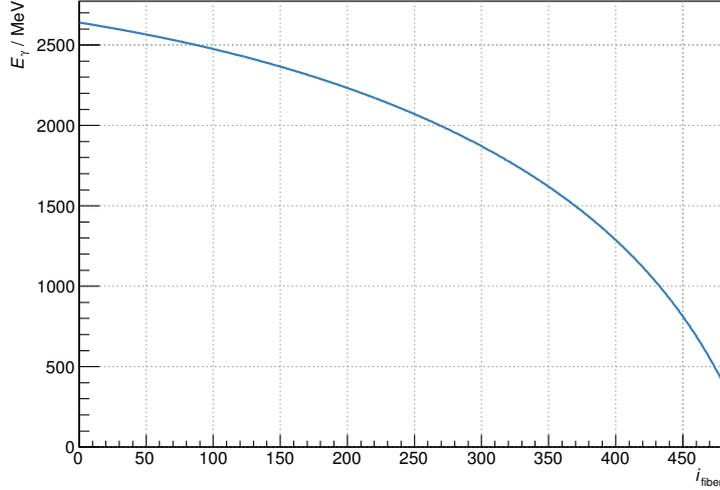
Figure 5.8: The energy calibration function $f(i_{\text{fiber}})$ for the scintillating fiber detector, for a primary electron energy $E_0 = 3176.1\,\text{MeV}$ and a magnetic field $B = 1.594\,\text{T}$ [Sch13].

Additional contributions to the uncertainty are errors in the position and angle of the electron beam at the radiator target, which contribute with 0.25 and 0.5 fibers, respectively [For09]. For short measurements, these are systematic uncertainties. For longer measurement periods, however, where the beam position is regularly corrected toward its nominal position, this systematic uncertainty is randomly distributed, and therefore contributes as a statistical error.

5.3 Sub-Detector Reconstruction

5.3.1 Calorimeters

The aim of the calorimeter reconstruction is to provide the energy and direction of particles. It is optimized for the electromagnetic showers produced by photons, as well as electrons and positrons. Other charged particles can be reconstructed as well, but their reconstructed energy is unreliable since the particle does not necessarily deposit its complete energy in the calorimeter.

5.3.1.1 Crystal Barrel Calorimeter

The energy deposit of a single particle in the calorimeter is, in general, not limited to a single crystal. In particular photons and electrons/positrons create an electromagnetic shower reaching several crystals. Therefore, in the first reconstruction step, a clustering algorithm is used to identify clusters, i.e. contiguous groups of crystals with a measured energy deposit above a given threshold (single crystal threshold). For this analysis, a single crystal threshold of 1 MeV is used, which is well above the noise level. In order to use only clusters that also have been identified by the trigger electronics, only clusters with

at least one crystal energy deposit above a given threshold (maximum crystal threshold) are retained. This threshold needs to be set (slightly) higher than the trigger threshold, this way variations in the trigger thresholds have no further impact on the analysis. In the Forward Plug region, where the trigger threshold was set between 30 MeV and 35 MeV, a maximum crystal threshold of 35 MeV is used, and for the rest of the detector it is set to 20 MeV, which is well above the FACE second level trigger threshold of approximately 15 MeV.

The electromagnetic showers of two incident particles can overlap, resulting in a single cluster. Therefore, all clusters are scanned for local maxima in the deposited energy. If such a maximum is above 20 MeV, it is considered as the central crystal of a particle energy deposit (PED). In case of only one local maximum, the PED is identified with the cluster, and the total energy of the PED is just the sum of the individual crystal energies. In case of more than one local maximum, the cluster energy is distributed among the individual PEDs. The appropriate weighting factor for each PED is calculated from the energy deposit in the PED's central crystal and its direct neighbors, as is described in [Sei09].

The position of the incident particle can be reconstructed by a weighted sum of the θ and ϕ coordinates of the individual crystals of the PED:

$$\theta_{\text{PED}} = \frac{\sum_i w_i \theta_i}{\sum_i w_i}, \qquad \phi_{\text{PED}} = \frac{\sum_i w_i \phi_i}{\sum_i w_i}, \tag{5.8}$$

with

$$w_i = \max\left(0; W_0 + \ln\left(\frac{E_i}{\sum_i E_i}\right)\right) \tag{5.9}$$

The logarithmic weighting takes into account the exponential decline of the transverse shower profile, giving larger relative weight to the outside crystals for improved angular resolution. The cut-off parameter W_0 defines the lowest energy fraction with which a crystal is used for the position reconstruction. Its optimum value of $W_0 = 4.25$ has been determined using Monte Carlo simulations [Jun00]. This results in an average angular resolution of around 1.2° for photons [Mül17] and electrons with energies > 400 MeV, which is much smaller than the size of the crystals ($\Delta\theta = 6°$, $\Delta\phi = 12°$ in the Forward Plug and the last ring of the Crystal Barrel and $\Delta\phi = 6°$ in all other rings). The angular resolution for other particles which do not produce an electromagnetic shower is of course given by the size of the crystals.

The segmentation of the detector, though important for the angular resolution, introduces insensitive material into the calorimeter. Part of the deposited energy is therefore not measured. Further energy is lost if the total deposit in a crystal is below the single crystal threshold of 1 MeV. The average total loss depends on the energy of the incident particle, as well as its direction.[9] To correct these losses, an energy correction function (ECF) is applied, which depends on the reconstructed energy and direction. It was obtained using Monte Carlo simulations of photons in the detector [Mül07] and verified with measured π^0 decays.

---

[9] The shower of a photon impinging on the calorimeter at the edge of a crystal is expected to deposit more energy in insensitive material than the shower of a photon impinging at the center of a crystal.

The achieved energy resolution for photons was measured to be [Ake+92]

$$\frac{\sigma_E}{E} = 2.5\,\% \cdot \left(\frac{E}{1\,\text{GeV}}\right)^{\frac{1}{4}}.\tag{5.10}$$

The reconstructed energy of charged particles is not used in the analysis.

5.3.1.2 TAPS Calorimeter

The reconstruction of the TAPS calorimeter works in nearly the same way as the Crystal Barrel reconstruction, but there are three differences:

1. As the readout modules of the BaF$_2$ crystals contain TDCs and therefore provide time information for all recorded energy deposits, a time difference cut can be applied during clustering: the time difference between crystals in one cluster needs to be $< 5\,$ns, otherwise two distinct clusters are reconstructed.

2. Different energy thresholds are used for clustering: The cluster energy threshold is set to 25 MeV, and the single crystal threshold is set to 17 MeV for the two innermost rings and to 13 MeV for all other crystals, which is just above the readout thresholds used for TAPS. The higher thresholds are required to reduce the high rate in forward direction to a level manageable by the readout electronics (max. 100 kHz per crystal).

3. Unlike the Crystal Barrel, where all crystals are facing the target center,[10] all TAPS crystals are aligned parallel to the beam axis. Therefore, the electromagnetic showers develop toward the outside of the detector, and the center of the energy deposit is not the point of entry of the incident particle, as is illustrated by Fig. 5.9. Thus, all directions need to be corrected by an offset d. This offset depends not only on the angle of the incident particle, but also on the penetration depth of the shower, which in turn depends on the energy of the incident particle. Therefore, an energy and angle dependent correction is applied, which is part of the full ECF for TAPS. The ECF is described in full detail in [Dah08].
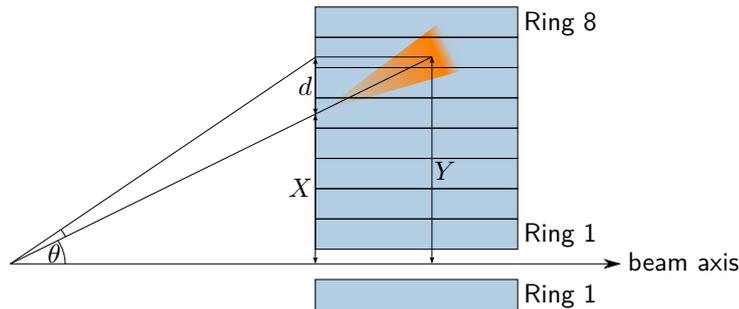
Figure 5.9: TAPS shower penetration depth correction (not drawn to scale): To obtain the incident position X, the center of energy position Y needs to be corrected by the offset d.

---

[10] As the Forward Plug is moved 3 cm downstream, these crystals are, in fact, not facing the target center. But the effect on the direction reconstruction is small and (mostly) corrected by the ECF [Mül07].

5.3.2 Charge Sensitive Detectors

The purpose of the detectors sensitive to charged particles is to measure only the direction of all charged particles. The direction is reconstructed by measuring the incidence point of the particle in the detector, assuming the particle originated from the center of the target.

5.3.2.1 Inner Detector

To reconstruct the incidence point of a particle in the Inner Detector, it must be measured in at least 2 of the 3 layers. The reconstruction is done in four steps:

1. Clustering within each layer ↝ *fiber cluster*
   A charged particle passing through a layer of the Inner Detector does not always deposit energy in exactly one fiber. Due to secondary particles from the interaction with the primary fiber, an energy deposit in the neighboring fiber(s) is also possible. Therefore, in this first reconstruction step, clusters of neighboring fibers within one layer are reconstructed. A cut on the time difference between the individual hits is applied (see Fig. 5.10a). The cut width can be chosen rather wide (14 ns, which is more than $5\,\sigma$) to maximize the reconstruction efficiency. Accidental coincidences are still completely negligible.

2. Combining the hits in different layers ↝ *two-layer hits*
   From each combination of intersecting fiber clusters in different layers, a direction from the target center can be reconstructed. Again, a time difference of less than 14 ns between the two clusters is required (see Fig. 5.10b). The calculation of the intersection point, using the geometry of the detector, is described in [PG08].

3. Matching of two-layer hits if possible ↝ *three-layer hits*
   In the previous reconstruction step, a particle that was measured in all three layers is reconstructed to three individual two-layer hits. In this last step, these need to be combined into a single three-layer hit. First, all three-layer hit candidates are identified by searching all sets of three two-layer hits, which were reconstructed from the

(a) fiber cluster reconstruction   (b) two-layer hit reconstruction
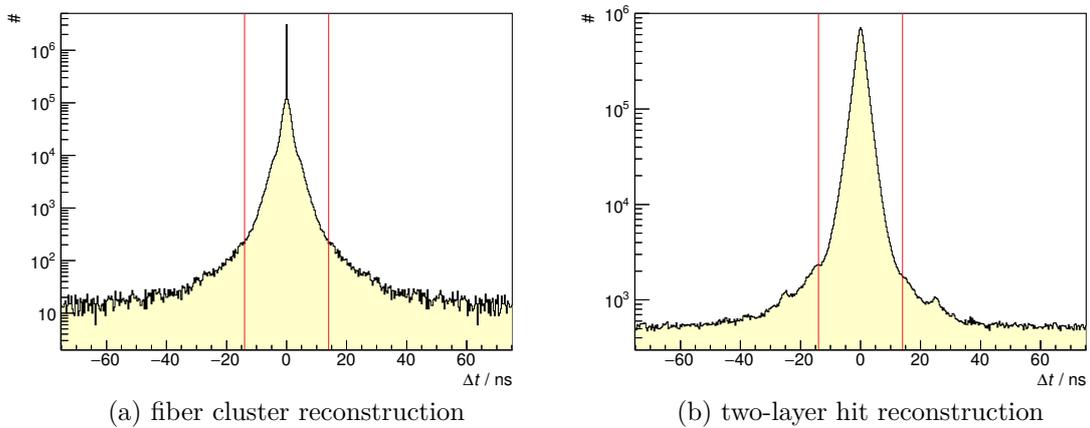
Figure 5.10: Time cuts used for the Inner Detector reconstruction.

(a) reconstructed hits on ϕ-z-plane

(b) cut on area of triangle in ϕ-z-plane
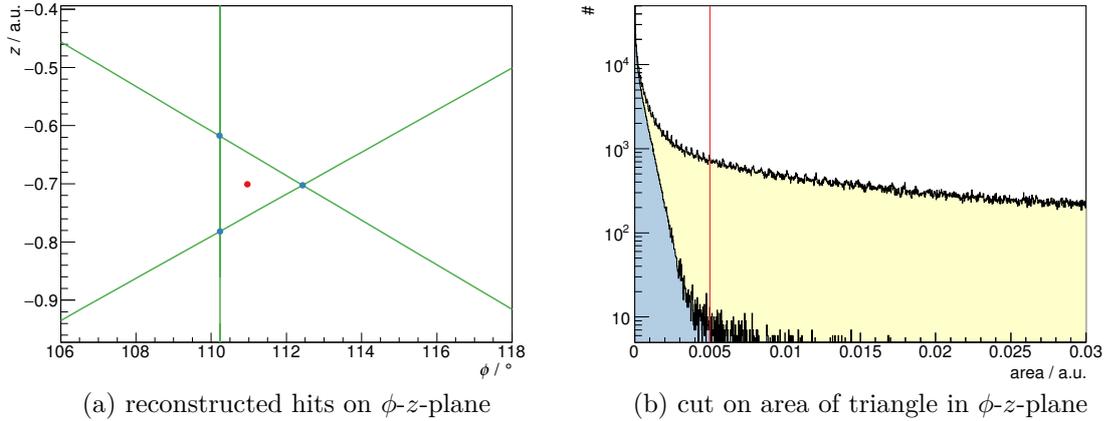
Figure 5.11: Reconstruction of the three-layer hits of the Inner Detector: The three re-
constructed two-layer hits at the intersection points (blue) of the three fibers
(green) form a triangle on the ϕ-z-plane. If the area of that triangle is small
enough they get combined to one three-layer hit (red). A histogram of the area
is shown in (b), in blue for Monte-Carlo data containing only single proton
events, and in yellow for the measured data containing additional background.

same fiber cluster in each of the three layers. But not all these candidates are actual
three-layer hits: a particle that was measured in only two layers and an independent
hit in the third layer (either a noisy channel or a hit from an independent particle)
is also identified as a three-layer hit candidate. Therefore, an additional distance
cut needs to be applied. To evaluate the distance of the three hits, their direction
from the target is projected onto a cylinder with unit diameter along the beam axis,
resulting in a z value and a ϕ angle for each hit (Fig. 5.11a). The three hits form a
triangle on the ϕ-z-plane, and a cut is applied on the area of that triangle (Fig. 5.11b)
to select the three-layer hits. Their reconstructed direction is given by the center of
gravity of the triangle.

4. Removal of two-layer ghost hits ⤳ *combined two- and three-layer hits*
   After the three-layer hits have been identified, not all the remaining two-layer hits
   are necessarily valid hits caused by the passage of a charged particle through the
   detector. In case of more than one simultaneous hit in the detector, additional so-
   called *ghost hits* are reconstructed in addition to the physical hits. For example, in
   the case of two particles being detected in two layers, the corresponding fibers in
   general have four crossing points, resulting in two additional ghost hits. In case of
   more hits and hits in more layers, the amount of reconstructed ghost hits increases
   drastically. Almost all ghost hits are reconstructed as a two-layer hit, the probability
   for a randomly matching fiber in the third layer is negligible for the rates observed
   in the experiment.
   With the reconstructed three-layer hits it is now possible to eliminate a large number
   of ghost hits: The probability for a single fiber to be hit simultaneously by two
   particles is also negligible. Therefore, all two-layer hits that were reconstructed from

at least one fiber cluster that was already used to reconstruct a valid three-layer hit are assumed to be ghost hits and are eliminated. This is illustrated in Fig. 5.12. Ghost hits caused by multiple simultaneous two-layer hits, however, cannot be identified this way.
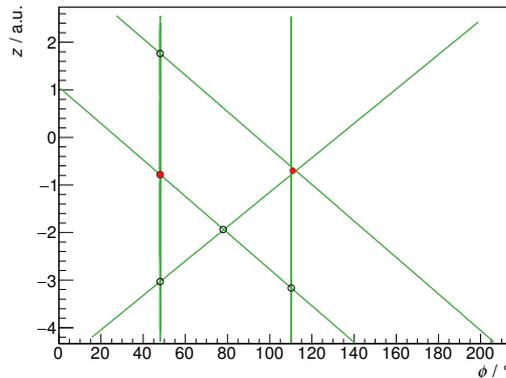
Figure 5.12: Example for ghost hits in the Inner Detector: In an event with one three-layer and one two-layer hit (red), the corresponding fibers have additional intersection points (open circles). These ghost hits can be eliminated (see text).

5.3.2.2 Forward Plug Veto Detector

The reconstructed incidence point of a charged particle that was detected in a single scintillator plate is just given by the center of that plate. However, since the detector consists of two layers, a particle is usually detected in two plates. Therefore, a coincident hit[11] in two overlapping plates is reconstructed at the center of the overlap region, improving the azimuthal resolution from 12° for a single hit to 6° for a two-layer hit.

5.3.2.3 TAPS Veto Detector

Since the scintillator plates in front of the TAPS crystals are not overlapping, a charged particle is in general only detected in one plate. Hence, it is sufficient to treat each measured hit individually. The reconstructed incidence point is just the center of the plate which detected the hit.

5.3.3 Identification of Charged Particles in the Calorimeters

The information from the charge sensitive detectors can be used to identify charged particles in the calorimeters. This is done by matching the particle directions obtained from the calorimeter reconstruction with the directional information from the charge sensitive detectors. The exact procedure differs slightly for each sub-detector, as discussed in the following.

---

[11] A time-cut $\Delta t \leq 20\,\text{ns}$ is used to identify coincident hits. Accidental coincidences are negligible even with a $\gtrsim 5\,\sigma$ cut.

(a) polar angle difference $\Delta\theta$

(b) azimuthal angle difference $\Delta\phi$
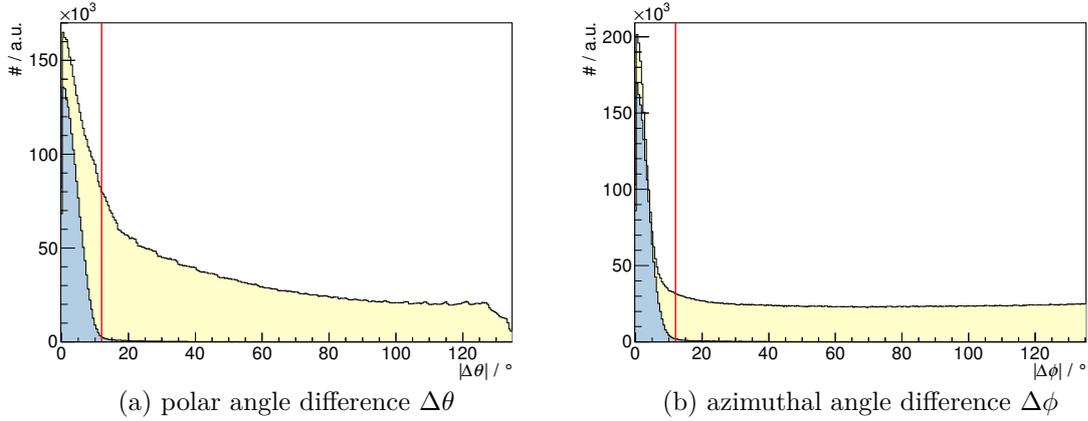
Figure 5.13: Polar and azimuthal angle difference between particles reconstructed in the Crystal Barrel/Forward Plug calorimeter and directions reconstructed using the Inner Detector. Monte-Carlo data containing only single proton events are shown in blue. The measured data, containing additional background due to uncorrelated hits in the Crystal Barrel or the Inner Detector, are shown in yellow.

(a) polar angle difference $\Delta\theta$

(b) azimuthal angle difference $\Delta\phi$
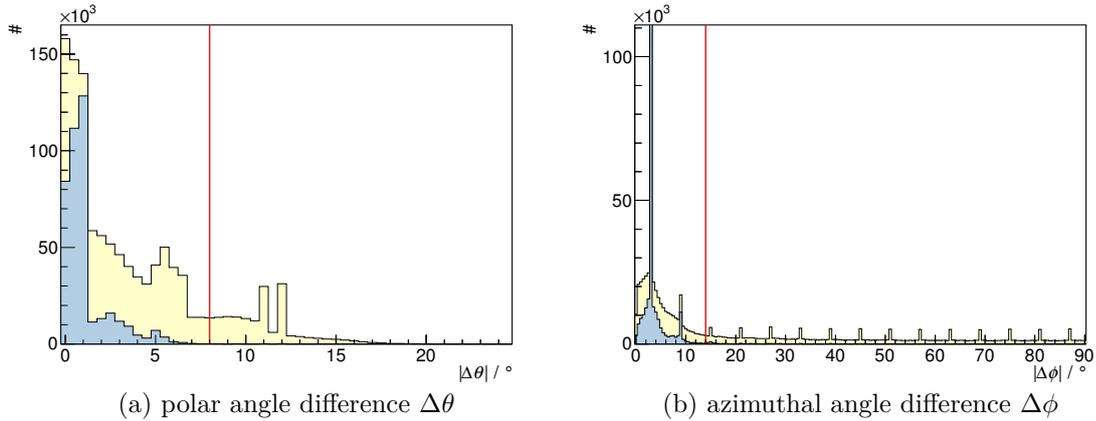
Figure 5.14: Polar and azimuthal angle difference between particles reconstructed in the Crystal Barrel/Forward Plug calorimeter and directions reconstructed using the Forward Plug Veto Detector. Monte-Carlo data containing only single proton events are shown in blue. The measured data, containing additional background due to uncorrelated hits in the Crystal Barrel or the Forward Plug Veto Detector, are shown in yellow. The visible structure of peaks with a distance of 6° is caused by particles which were measured by a single crystal of the calorimeter. The direction of these particles is reconstructed to the center of the crystal, resulting in discrete values. Since the Forward Plug crystals do not point exactly at the target, the reconstructed θ of single crystal hits is not exactly a multiple of 6°, but slightly different for each ring, resulting in multiple close-by peaks around $|\Delta\theta| = 6°$ and $|\Delta\theta| = 12°$.

(a) impact point distance d

(b) time difference Δt
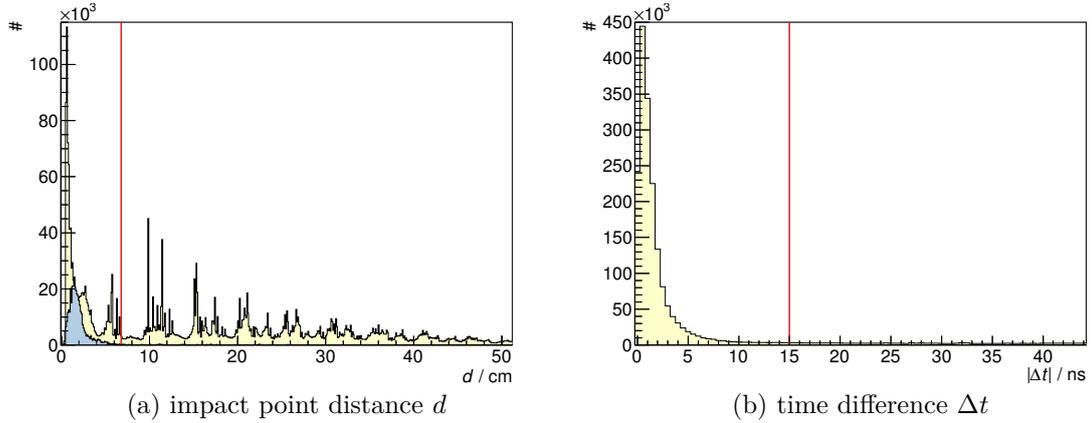
Figure 5.15: Impact point distance d and time difference Δt between particles reconstructed in the TAPS calorimeter and directions reconstructed using the TAPS veto detectors. Monte-Carlo data containing only single proton events are shown in blue (no time information is available in the Monte-Carlo simulation). The measured data, containing additional background due to uncorrelated hits in the calorimeter or the veto detectors, are shown in yellow. The various peaks visible in the measured impact point distance distribution are caused by uncorrelated hits in a single crystal of the calorimeter and a single veto scintillator. These hits are reconstructed with a direction toward the center of the crystal and scintillator, respectively. Due to the hexagonal shape of the crystals, various distances between two crystal centers are possible, resulting in many distinct peaks.

5.3.3.1 Crystal Barrel/Forward Plug Calorimeter and Inner Detector

The direction of a particle reconstructed in the Crystal Barrel calorimeter and the direction reconstructed from the Inner Detector are compared using their polar angle difference $\Delta\theta$ and their azimuthal angle difference $\Delta\phi$. A particle is identified as charged if $|\Delta\theta| < 12°$ and $|\Delta\phi| < 12°$ for any hit in the Inner Detector (see Fig. 5.13).[12] If the reconstructed particle has a time information available,[13] a time difference $|\Delta t| \leq 15\,\mathrm{ns}$ is also required.

5.3.3.2 Crystal Barrel/Forward Plug Calorimeter and Forward Plug Veto Detectors

This is done nearly the same way as described above, only with slightly adjusted cut limits due to different angular and time resolution. A particle is identified as charged if $|\Delta\theta| \leq 8°$, $|\Delta\phi| \leq 14°$, and $|\Delta t| \leq 20\,\mathrm{ns}$ for any hit in the Forward Plug veto detector (see Fig. 5.14).

5.3.3.3 TAPS Calorimeter and Veto Detectors

Due to the different geometry of the TAPS detector as a forward wall, a comparison between directions in spherical coordinates is not useful. Instead, the distance d of the reconstructed

---

[12] 12° equals two times the angle covered by a single crystal, both in ϕ and θ.

[13] This can only be the case if it was detected in the Forward Plug, which has only a small overlap (≈ 1 of 3 rings) with the Inner Detector.

impact points on the surface of the TAPS detector is calculated. All particles with $d \leq$ 6.8 cm (which is equal to the excircle diameter of the TAPS crystals) and $|\Delta t| \leq 15$ ns for any hit in the TAPS veto detector are marked as charged (see Fig. 5.15).

5.3.4 Tagging System

The aim of the tagging system reconstruction is to provide precise energy and time information of all tagged beam photons. First, the reconstruction is done independently for the scintillator bars and the scintillating fiber detector, before the information from both detectors is combined in the last reconstruction step.

5.3.4.1 Plastic Scintillator Bars

The scintillator bar hodoscope is designed such that each electron should be detected in (at least) two adjacent scintillators [For09]. To ensure that only one beam photon is reconstructed for each electron, all detector hits caused by that electron need to be identified. This is achieved by combining all hits in neighboring bars which occurred within a time interval of at most 4 ns (see Fig. 5.16a) into a single beam photon candidate. Only candidates that were reconstructed from at least two bars are retained in order to suppress background due to electrons not originating from the radiator target.

5.3.4.2 Scintillating Fiber Detector

The reconstruction of beam photon candidates from the scintillating fiber detector is done similarly as with the bars. Due to the worse time resolution of the fibers [Har08], a larger time interval of 7 ns (see Fig. 5.16b) is used. Since the geometry of the detector allows for electrons to pass through only a single fiber, all beam photon candidates that were reconstructed from only one hit are retained as well.

(a) scintillator bars   (b) scintillating fibers
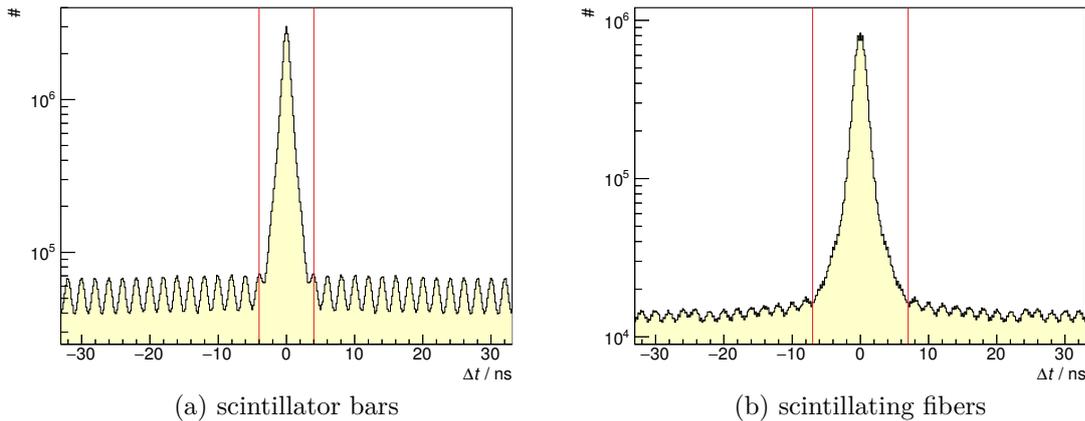
Figure 5.16: Time cuts used for the tagging system reconstruction. The periodic 2 ns structure of the background is a result of the distance of the electron bunches in the accelerator.

5.3.4.3 Combined Reconstruction of Bars and Fibers

The scintillator bar detector provides a good time resolution and allows for a low-background reconstruction of beam photon candidates. However, its energy resolution is insufficient due to the size of the bars. The fiber detector, on the other hand, has good energy resolution, at the expense of time resolution and background suppression capability. For optimal reconstruction quality, the information of both detectors needs to be combined. Only beam photon candidates with geometrically matching hits in the bar and fiber detector are retained. Additionally, the difference between the mean time of the bar hits to the mean time of the fiber hits is required to be less than $4\,\text{ns}$.[14]
The reconstructed beam photon energy is given by the average of the energies associated with the individual fiber hits:

$$E_\gamma = \frac{1}{N_{\text{fiber}}} \sum_{i=1}^{N_{\text{fiber}}} E_i, \tag{5.11}$$

where the energy E_i is given by the calibration function (cf. Eq. (5.7a) and Fig. 5.8). The time of the reconstructed beam photon is given by the average of all bar and fiber hit times, weighted with the corresponding squared time resolution of the detector (cf. Table 5.4):

$$t_\gamma = \frac{w_{\text{fiber}} \sum_{i=1}^{N_{\text{fiber}}} t_i + w_{\text{bar}} \sum_{j=1}^{N_{\text{bar}}} t_j}{w_{\text{fiber}} N_{\text{fiber}} + w_{\text{bar}} N_{\text{bar}}} \qquad \text{with } \frac{w_{\text{fiber}}}{w_{\text{bar}}} = 0.5. \tag{5.12}$$

This procedure limits the reconstruction to the energy range covered by both detectors, i.e. to $E_\gamma \lesssim 2.6\,\text{GeV}$. To extend the reconstruction to higher energies covered only by the bars, a fiber hit in that region is not required and only the information from the bars is used. Further details on the reconstruction of the tagging system can be found in [Har08] and [For09].

5.3.5 Gamma Intensity Monitor and Flux Monitor

The aim of the gamma intensity monitor reconstruction is to provide time information of all detected photons. Since a directional information is not needed, no clustering needs to be done. Instead, all hits measured by any crystal are used. To avoid multiple counting of photons that were measured in more than one crystal, all hits measured within $12\,\text{ns}$ after a hit are rejected. The $12\,\text{ns}$ correspond to the double pulse resolution of a single crystal. The detector is thus effectively treated as if it consisted of a single crystal.
Hits in the Flux Monitor are reconstructed by requiring a coincident hit in the two scintillators behind the pair production target, and no hit in the veto scintillator. A time cut of $\Delta t = 10\,\text{ns}\ (\approx 5\,\sigma)$ is used for the coincidence.

---

[14] Here, a smaller time cut can be used, because the resolution of the mean time is better than the resolution of the individual fiber times.

5.4 Event Selection

Both reactions of interest for this work, namely $\gamma p \rightarrow p\pi^0$ and $\gamma p \rightarrow p\eta$, are described by the four-momenta of the involved particles. Energy and momentum conservation yields

$$\begin{pmatrix} E_\gamma \\ \vec{p}_\gamma \end{pmatrix} + \begin{pmatrix} m_p \\ \vec{0} \end{pmatrix} = \begin{pmatrix} E_{p'} \\ \vec{p}_{p'} \end{pmatrix} + \begin{pmatrix} E_{\pi^0,\eta} \\ \vec{p}_{\pi^0,\eta} \end{pmatrix} \qquad (c = 1). \qquad (5.13)$$

The kinematics of the two-body final state are, if the initial state is known and the masses of the particles are fixed, fully described by two variables. Most commonly used are the center-of-mass energy W and the angle θ in the center-of-mass frame between the incoming photon and the produced meson. Alternatively, the energy E_γ of the beam particle in the laboratory frame can be used instead of W.

Based on the results of the particle reconstruction, i.e. energy and direction of all measured particles, it is now possible to select events of the reactions. The aim is to retain as many events as possible for the reactions of interest, while at the same time reducing the background contamination from other reactions.

The selection is optimized to select the desired reactions with a (polarized) free proton as the target. For the butanol target, there are also reactions occurring on a bound nucleon inside the carbon or oxygen nuclei. Due to Fermi motion, the target particle is not at rest and Eq. (5.13) is not fulfilled for these reactions. This results in a different selection efficiency for these background reactions. The implications this has for the analysis will be discussed in detail Section 6.3.

5.4.1 Reaction $\gamma p \rightarrow p\pi^0$

The dominant decay mode of the π^0 meson is the decay $\pi^0 \rightarrow 2\gamma$ with a branching ratio of $\Gamma_i/\Gamma = (98.823 \pm 0.034)\,\%$ [Oli+14]. It is the only decay mode of the π^0 investigated in this work.

Pre-Selection

In the first selection step, all events with exactly three reconstructed particles in the calorimeters are selected as candidates for the $p\gamma\gamma$ final state. If timing information has been reconstructed for a given particle, a time cut $-20\,\text{ns} \leq t \leq 50\,\text{ns}$[15] is applied to ensure the particle is correlated with the trigger at $t = 0$.

Combinatorics

It is a priori unknown which of the three reconstructed particles in the final state corresponds to the proton, and which to the two decay photons of the meson. Each reconstructed particle could be the proton, it is thus required to consider all three possible combinations. This increases the number of events by a factor of three and introduces combinatorial background, which of course has to be eliminated again by the following steps of the selection.

---

[15] The asymmetric cut is required to account for jitter in the trigger signals.

For each event, the energy and momentum of the pion can be calculated from the reconstructed photons.

$$\begin{pmatrix} E_{\pi^0} \\ \vec{p}_{\pi^0} \end{pmatrix} = \begin{pmatrix} E_{\gamma_1} \\ \vec{p}_{\gamma_1} \end{pmatrix} + \begin{pmatrix} E_{\gamma_2} \\ \vec{p}_{\gamma_2} \end{pmatrix} \tag{5.14}$$

Since the recoiling proton is not necessarily stopped in the calorimeter, only its measured direction $(\theta_{p'}, \phi_{p'})$ can be used.

Beam Photon Candidate Selection

Due to the large rate of electrons detected by the Photon Tagging System ($> 10\,\text{MHz}$), the number of reconstructed beam photon candidates for each event greatly exceeds one, as can be seen in Fig. 5.17. The time difference Δt_reaction between the beam photon candidates and the reconstructed reactions products[16] is used to identify the correct beam photon. This is done by applying the cut $-15\,\text{ns} \le \Delta t_\text{reaction} \le 5\,\text{ns}$, which must be asymmetric to account for the time of flight of low-energetic protons detected in TAPS.[17] However, as can be seen in Fig. 5.18, there is a non-negligible amount of background below the coincidence peak, which needs to be subtracted. This is done by a sideband subtraction. Events selected by a second cut $(-270\,\text{ns} \le \Delta t_\text{reaction} \le -70\,\text{ns}) \vee (70\,\text{ns} \le \Delta t_\text{reaction} \le 270\,\text{ns})$ are retained as well, but get assigned a negative weight w_bg given by the ratio between the cut width around the peak and the sideband cut width:

$$w_\text{bg} = -\frac{20\,\text{ns}}{400\,\text{ns}} = -0.05. \tag{5.15}$$
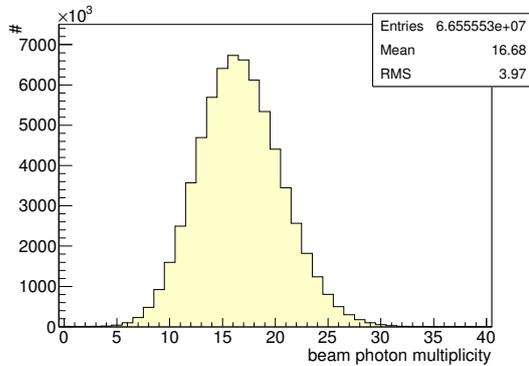
Figure 5.17: Number of reconstructed beam photon candidates per event.
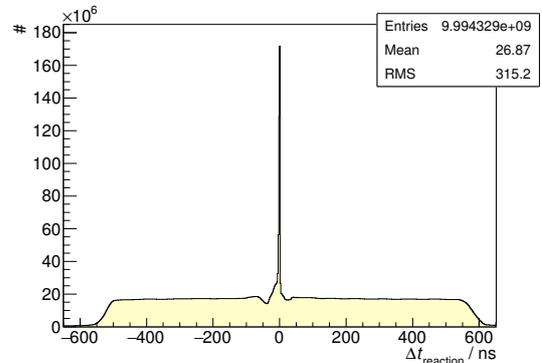
Figure 5.18: Time difference Δt_reaction between the beam photon candidates and the reconstructed reaction products.

---

[16] If more than one particle in the final state has timing information available, the average is used. If no timing information is available for the reconstructed final state particles (which can happen if all particles were detected in the Crystal Barrel Calorimeter and the trigger was issued by the Inner Detector only), the time of the trigger ($t = 0$) is used instead.

[17] All protons that are reconstructed (i.e. deposit an energy of at least $25\,\text{MeV}$ in the TAPS calorimeter, see Section 5.3.1.2) have a time of flight difference to photons of less than $15\,\text{ns}$ [Har08].

By using this weight when filling histograms at any later analysis step, the background of random coincidences between reconstructed beam photon candidates and reconstructed final state are subtracted.

There is one important limitation to the sideband subtraction. As long as the actual beam photon that initiated the reconstructed reaction has been energy tagged and reconstructed, the background in the time difference spectrum is flat and can be subtracted as described. However, if the actual beam photon has not been reconstructed, the background is not flat. The reason for this lies in the trigger conditions used during data-taking: the trigger required a hit in the Photon Tagging System, which obviously can only be fulfilled by a random coincidence if the actual beam photon has not been tagged. As a consequence, the background is peaking around the time of the trigger at $\Delta t_{\text{reaction}} = 0$, but only for events where the actual beam photon has not been energy tagged. Thus, reactions without the correct energy tagged beam photon are not properly subtracted. There are two possible reasons for untagged beam photons.

1. The detection efficiency of the Photon Tagging System is smaller than $100\,\%$, as for any detector. However, the efficiency is very close to $100\,\%$ [For09], and the number of events with untagged beam photons and at least one uncorrelated tagged beam photon at the same time is negligible.

2. The tagger does not cover the photon energy range below $E_\gamma \approx 550\,\text{MeV}$, and the cross section for π^0 photoproduction in that energy range, in particular around the $\Delta(1232)$ resonance, is much larger compared to the cross section at higher energies (see Fig. 2.1). Thus, there is significant background contribution from reactions below the threshold of the Photon Tagging System, which has to be eliminated by other means.

The energy of the beam photon can be calculated from the meson's four-momentum using energy and momentum conservation, if the target proton is assumed to be at rest.

$$E_\gamma^{\text{calc}} = \frac{m_p E_{\pi^0} - \frac{1}{2} M_{\pi^0}^2}{m_p - E_{\pi^0} + p_{\pi^0}^z} \qquad \text{with } M_{\pi^0} = \sqrt{E_{\pi^0}^2 - \vec{p}_{\pi^0}^{\,2}} \tag{5.16}$$

The energy resolution obtained using Eq. (5.16) is of course worse than the energy resolution of the Photon Tagging System. Nevertheless, this can be used to eliminate most of the background from reactions with beam photons outside the tagged energy range by requiring $E_\gamma^{\text{calc}} > 530\,\text{MeV}$.[18] The effect of this cut can be seen in Fig. 5.19 where E_γ^{calc} is plotted versus the tagged E_γ. There is some background remaining, which will be eliminated by the kinematic cuts described in the following and can therefore be neglected.

Kinematic Cuts

With the known kinematic quantities, namely the four-momenta of the initial state, as well as the four-momentum of the π^0 and the direction of the recoiling proton, the reaction

---

[18] Due to the worse energy resolution of Eq. (5.16) the cut needs to be applied 20 MeV below the threshold of the Tagging System, in order to not eliminate any valid reactions just above the threshold of the Tagging System.
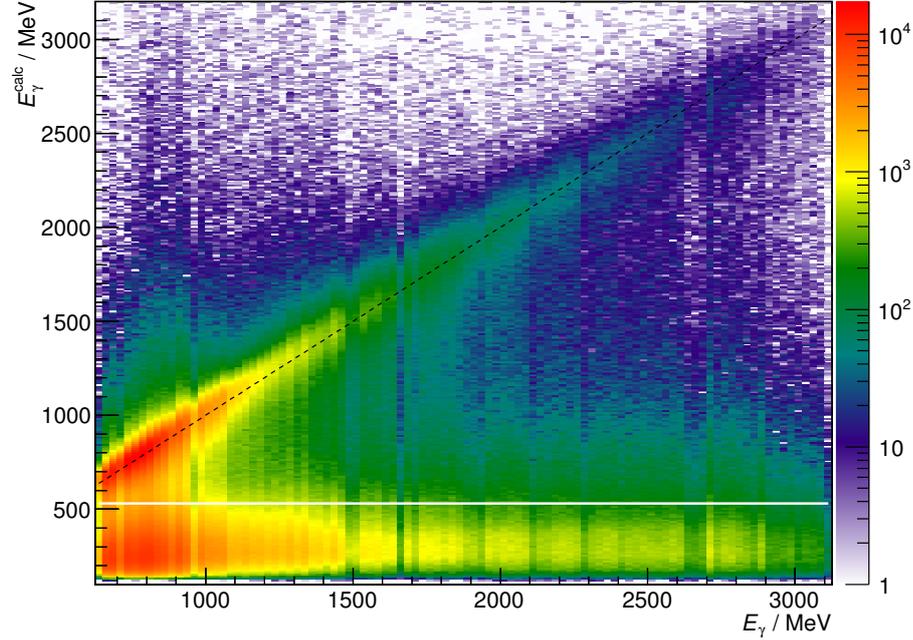
Figure 5.19: The beam photon energy E_γ^{calc} calculated from the reconstructed π^0 candidate, plotted versus the tagged beam photon energy E_γ. Valid events are clustered around the $E_\gamma = E_\gamma^{\mathrm{calc}}$ line (dashed), while the background at low E_γ^{calc} is eliminated by the cut (white line).

is over-determined. As a consequence, energy and momentum conservation can be used to select the desired reaction and eliminate background from other reactions by applying several kinematic cuts.

Azimuthal angle difference Because of momentum conservation, the three momentum vectors of the beam photon, the produced meson and the recoiling proton span a plane, the so-called reaction plane. Consequently, the azimuthal angle difference $\Delta\phi$ between meson and recoiling proton has to be 180° and can be used as a selection criterion.

Polar angle difference Momentum conservation allows another cut: since the reaction is over-determined, the recoiling proton can be treated as a missing particle, and its energy and momentum can be calculated from the energies and momenta of the other particles. The polar angle difference $\Delta\theta$ between the measured and the missing proton can then be used as another selection criterion.

Invariant mass of the missing recoiling proton Treating the recoiling proton as a missing particle allows another selection criterion, by calculating its invariant mass $M_{p'}$:

$$M_{p'}^2 = \begin{pmatrix} E_{p'} \\ \vec{p}_{p'} \end{pmatrix}^2 = \left[\begin{pmatrix} E_\gamma \\ \vec{p}_\gamma \end{pmatrix} + \begin{pmatrix} m_p \\ \vec{0} \end{pmatrix} - \begin{pmatrix} E_{\pi^0} \\ \vec{p}_{\pi^0} \end{pmatrix} \right]^2 \tag{5.17}$$
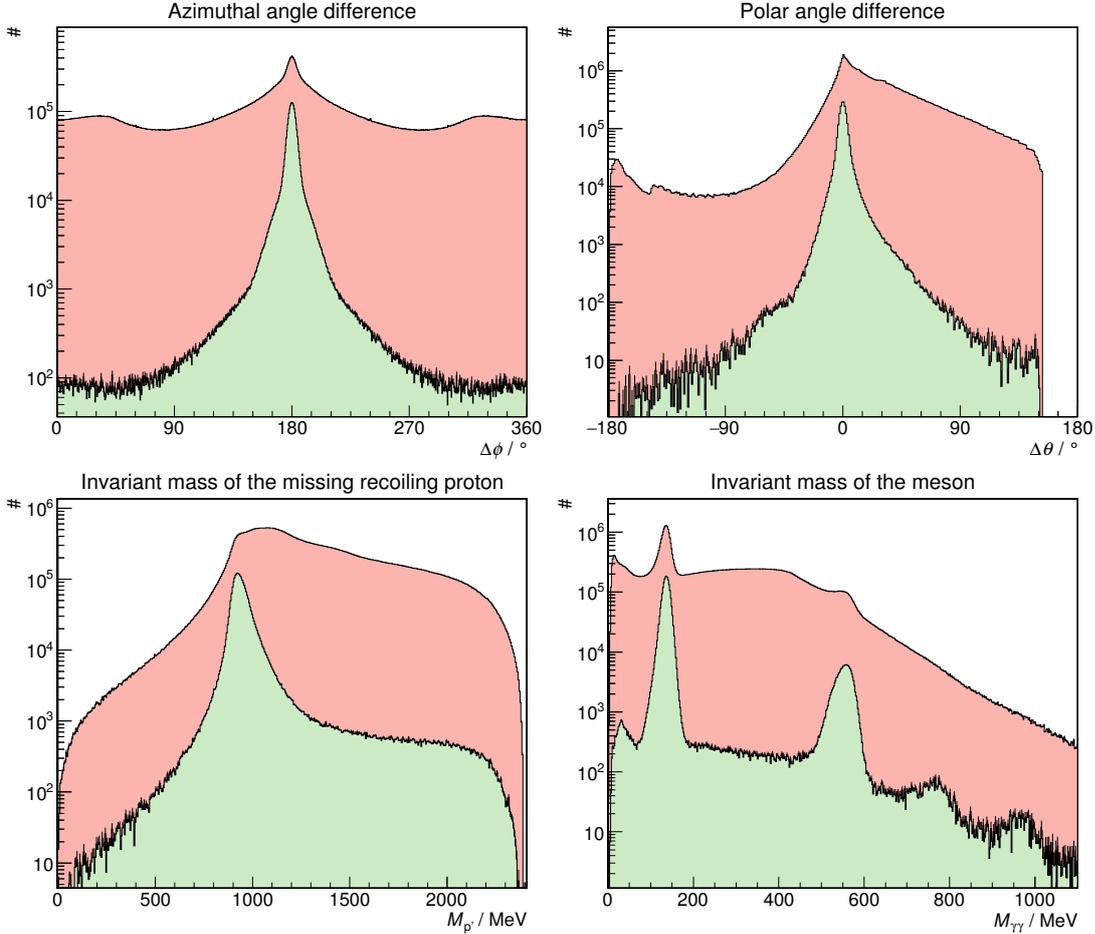
Figure 5.20: The effect of the four kinematic cuts on the butanol data. The corresponding spectra are shown before all cuts (red), and after the other three cuts were applied (green). For all spectra, the previously discussed cut on E_γ^{calc} was applied, and random coincidences were subtracted.

Invariant mass of the meson So far, no constraint on the invariant mass of the meson has been imposed. Therefore, all reactions with a meson decaying into 2γ have been retained so far. By applying a cut on the invariant mass $M_{\gamma\gamma}$ of the two photons, reactions with the π^0 as the meson are selected. By changing the value of this cut, it is also possible to select other mesons decaying into 2γ like the η or $\eta^{'}$.

The width of the kinematic cuts has to be optimized in such a way that the selection efficiency is as high as possible (requiring wide cuts), but also rejecting as much background as possible (requiring narrow cuts). A 2σ wide cut has proven to be a good compromise: around 83% of all valid events should be retained.[19] A more detailed investigation of different cut widths is described in Section 6.3.

---

[19] Assuming a normal distribution, four independent 2σ cuts lead to $\mathrm{erf}\left(\frac{2\sigma}{\sigma\sqrt{2}}\right)^4 = 83\%$ retained events.
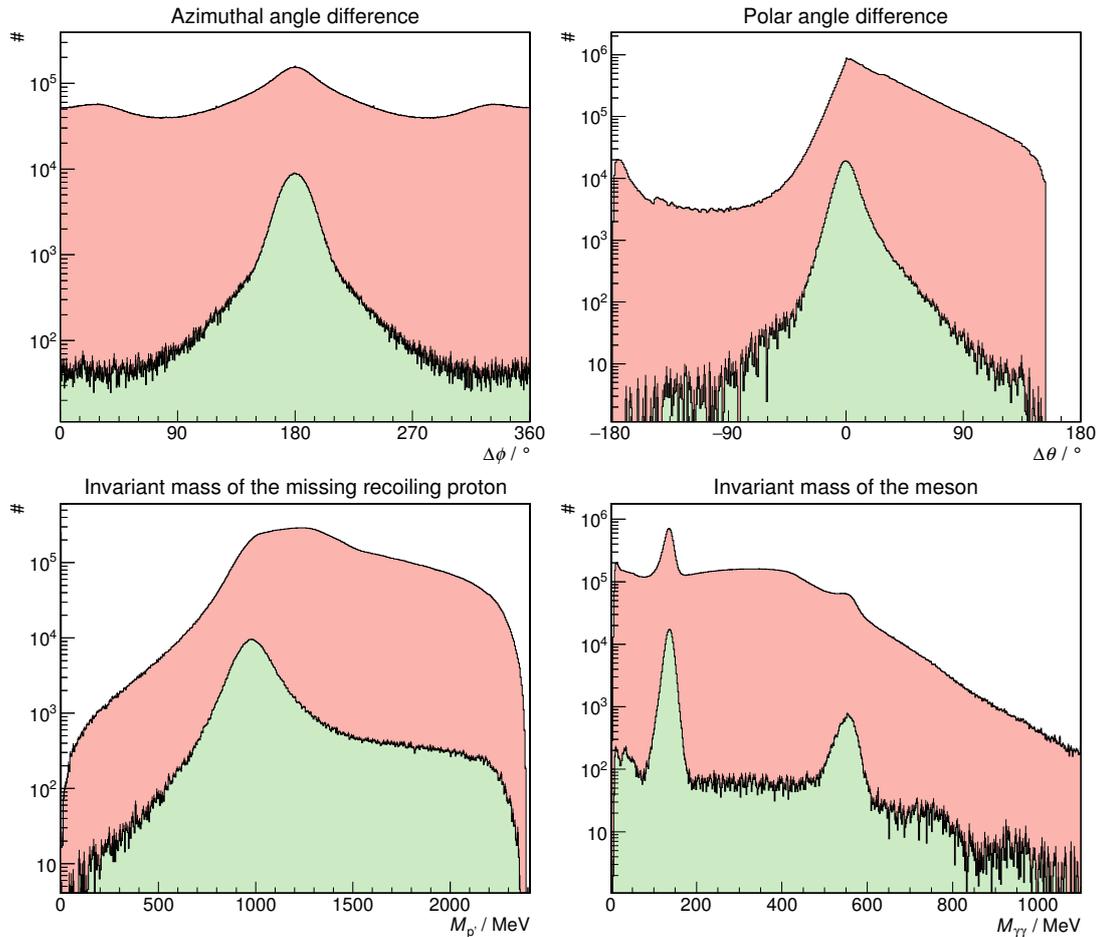
Figure 5.21: The effect of the four kinematic cuts on the carbon data. The corresponding spectra are shown before all cuts (red), and after the other three cuts were applied (green). For all spectra, the previously discussed cut on E_γ^{calc} was applied, and random coincidences were subtracted.

Determining the cut width corresponding to 2σ of the signal is not straight-forward, due to the fact that there is not only signal but also background visible in the corresponding spectra (see Fig. 5.20). The cut limits for each of the four kinematic cuts are therefore determined in an iterative process: By applying the *other* three cuts, in the first iteration with a rough estimate for the cut width, the background is greatly suppressed, as can be seen in Fig. 5.20. However, the shape of the signal of interest—resulting from the free protons in the butanol—cannot yet be clearly identified, since there is still a significant amount of background from reactions off bound nucleons inside the carbon and oxygen nuclei of the butanol target.

The shape of this background can be seen in the corresponding spectra for the carbon target, which are shown in Fig. 5.21. It can be subtracted from the butanol data to obtain the spectra with only contributions from reactions off the free proton. For this to work, both butanol and carbon data need to be (relatively) normalized. The normalization will be
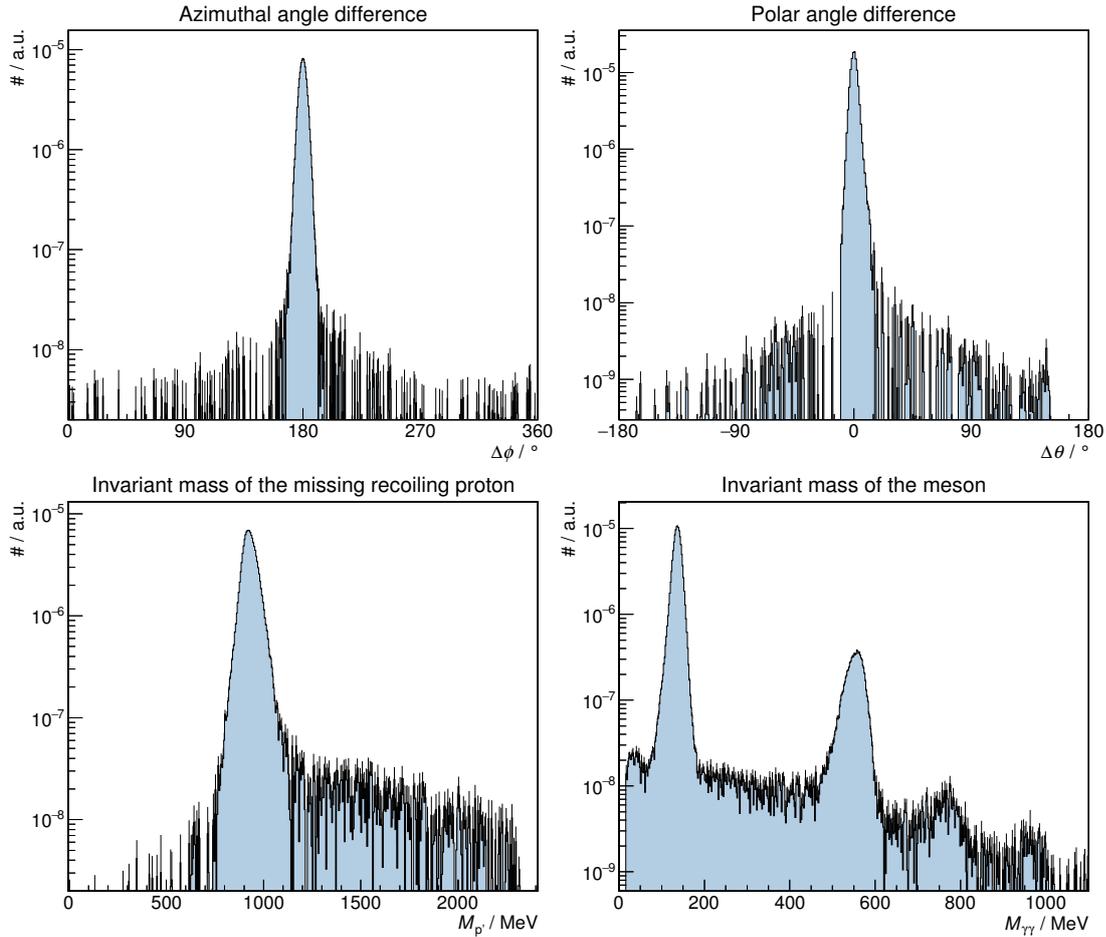
Figure 5.22: The spectra for the four kinematic cuts on the free proton data, obtained by subtracting the normalized carbon data from the normalized butanol data. The corresponding spectra are shown for all E_γ and $\cos\theta$ after the other three cuts were applied. For all spectra, the previously discussed cut on E_γ^{calc} was applied, random coincidences were subtracted, and a normalization to the photon flux was performed prior to the subtraction.

described in detail in the next chapter, in Sections 6.1 and 6.3. The resulting distributions are shown in Fig. 5.22 (note the change of scale on the ordinate axis due to the photon flux normalization). Now the background contribution is small enough in each spectrum so that the cut limits can be determined reliably.

Another complication arises from the fact that the distributions shown in Fig. 5.22 exhibit a strong dependence on the kinematic variables, as can be seen in Figs. 5.23 and 5.24, where they are plotted versus the beam photon energy E_γ and the meson center-of-mass angle θ, respectively. A fixed cut width would thus be either too wide or too narrow, depending on the kinematic region. Therefore, the cut limits are determined in $(E_\gamma, \cos\theta)$ bins with variable bin width such that there are enough entries in each bin to do this reliably. The final cut limits are listed in Appendix C.1.
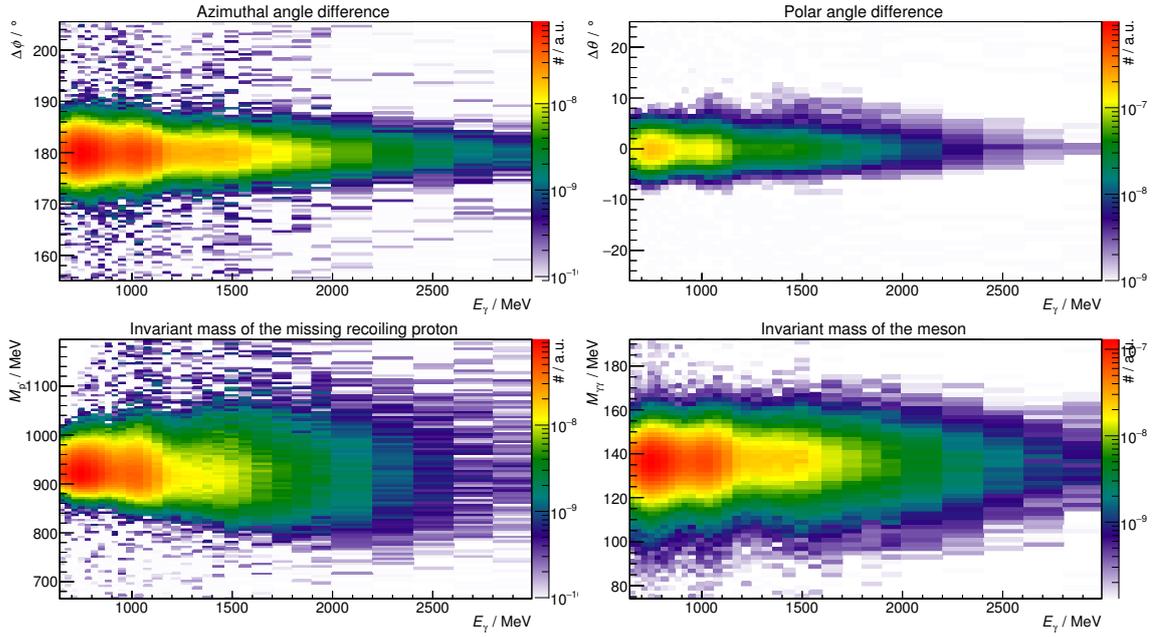
Figure 5.23: The spectra for the four kinematic cuts as a function of the beam photon energy E_γ. For each spectrum, the other three cuts and the cut on E_γ^{calc} were applied, the spectrum was normalized to the photon flux, and the random coincidences and the carbon data were subtracted.
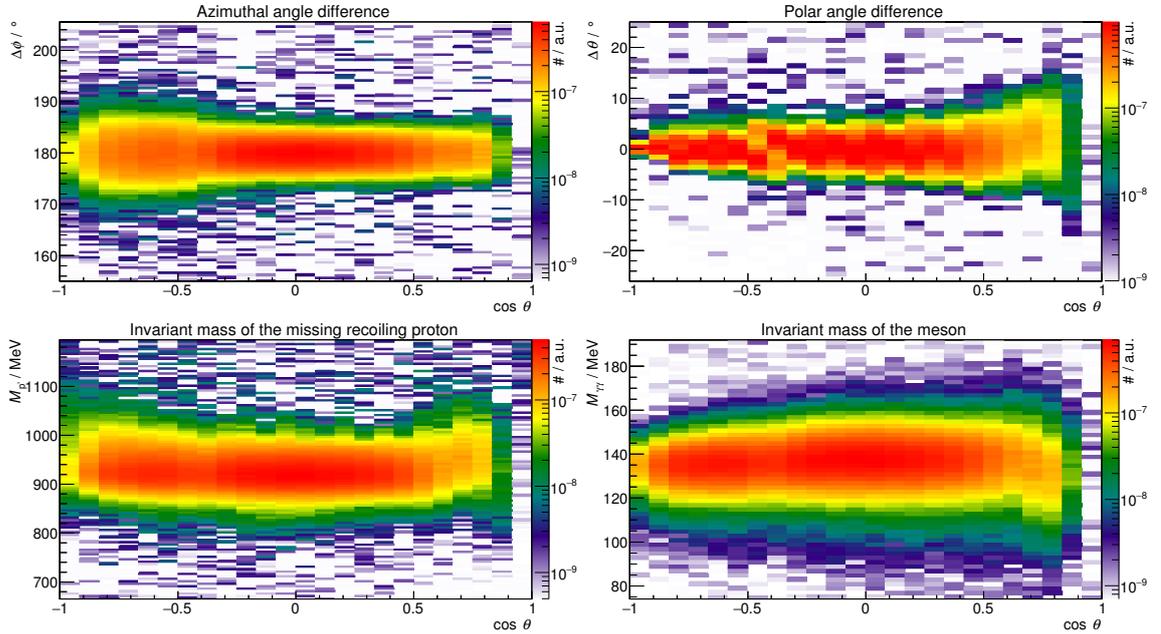
Figure 5.24: The spectra for the four kinematic cuts as a function of the meson center-of-mass angle θ. For each spectrum, the other three cuts and the cut on E_γ^{calc} were applied, the spectrum was normalized to the photon flux, and the random coincidences and the carbon data were subtracted.

Charge Identification

So far, the reconstructed charge information has not been used. As can be seen in Fig. 5.25, any cut on the reconstructed charge information reduces the number of reconstructed events. It does, however, not significantly improve the signal-to-background ratio. Hence, such a cut is not useful. On top of that, the efficiency of the charge identification detectors is not uniform in the kinematic variables of the reaction, as can be seen in Fig. 5.26.
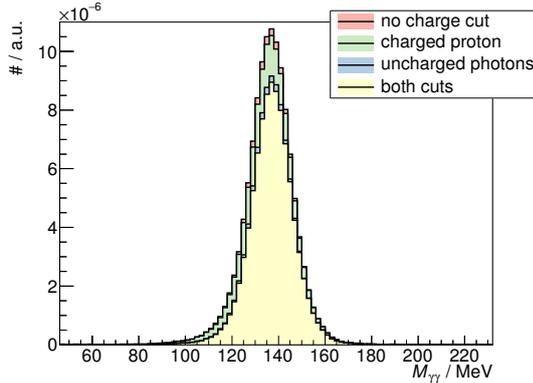
Figure 5.25: The effect of a cut on the reconstructed charge information on the $M_{\gamma\gamma}$ distribution. All other cuts have been applied, and the random coincidences and the carbon data have been subtracted.
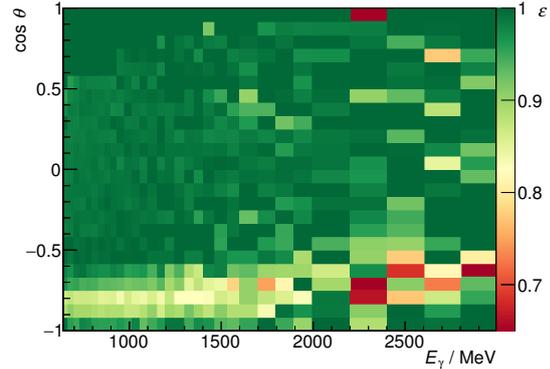
Figure 5.26: Distribution of inefficiencies caused by a cut on the reconstructed proton charge.

One advantage of using the charge information would be the elimination of the combinatorial background, since only one combination of the three reconstructed particles would be possible instead of three. However, the combinatorial background *after* all cuts is completely negligible: only a total of 7 events (out of $\approx$ 1.7 million) with more than one combination are retained. As a consequence, a cut on the charge information is not used in this analysis.

5.4.2 Reaction $\gamma p \to p\eta$

As can be seen in Table 5.5, the η has two main decay modes with only photons in the final state, namely $\eta \to 2\gamma$ and $\eta \to 3\pi^0 \to 6\gamma$, where the latter has a total branching ratio of

$$\Gamma_i/\Gamma(\eta \to 6\gamma) = \Gamma_i/\Gamma(\eta \to 3\pi^0) \cdot \left(\Gamma_i/\Gamma(\pi^0 \to 2\gamma)\right)^3 = (31.54 \pm 0.23)\,\% \qquad (5.18)$$

5.4.2.1 Decay Mode $\eta \to 2\gamma$

Since the final state is the same as for the $\gamma p \to p\pi^0 \to p\gamma\gamma$, the selection can be done as described in Section 5.4.1, with the cut on the invariant mass $M_{\gamma\gamma}$ of the two photons modified to select the η meson instead of the π^0. The cut limits are listed in Appendix C.2.

Table 5.5: The dominant decay modes ($\Gamma_i/\Gamma > 1\,\%$) of the η meson [Oli+14].

decay mode	branching ratio Γ_i/Γ
2γ	$(39.41 \pm 0.20)\,\%$
$3\pi^0$	$(32.68 \pm 0.23)\,\%$
$\pi^+\pi^-\pi^0$	$(22.92 \pm 0.28)\,\%$
$\pi^+\pi^-\gamma$	$(4.22 \pm 0.08)\,\%$

5.4.2.2 Decay Mode $\eta \to 3\pi^0$

In principle, the reaction $\gamma p \to p\eta \to p\,3\pi^0 \to p\,6\gamma$ can be selected in a very similar way as the decay mode $\eta \to \gamma\gamma$. The main difference is that the four-momentum of the η is calculated from six photons instead of two. If all other selection steps are done as described in Section 5.4.1, it is, however, not possible to select the reaction without significant background contamination, as can be seen in Fig. 5.27a. But the background can be reduced by an additional cut on the mass of the three π^0 from the η decay: For all 15 possible combinations of 6γ into $3\pi^0$, the three $\gamma\gamma$ invariant masses are calculated. Only events for which at least one combination has all three invariant masses between the cut limits around m_{π^0} are retained. If this is the case for more than one combination, the best[20] combination is chosen for further analysis. The background level below the η peak in the 6γ invariant mass spectrum is thus reduced by more than a factor 2, as can be seen in Fig. 5.27b.

(a) before cut on π^0 mass (b) after cut on π^0 mass (c) after γ-energy correction
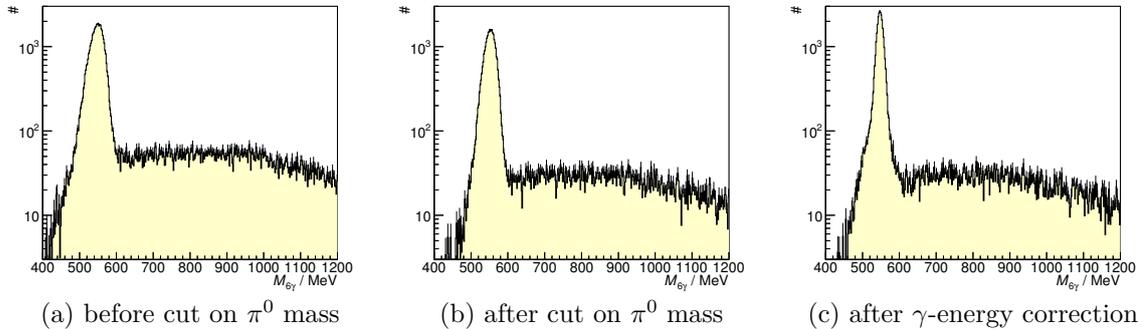
Figure 5.27: The 6γ invariant mass distribution, showing a clear $\eta \to 3\pi^0 \to 6\gamma$ signal.

It is possible to improve the invariant mass resolution using a "poor man's kinematic fit": Since the relative angular resolution of the calorimeter is much better than the relative energy resolution, any deviation of the reconstructed $M_{\gamma\gamma}$ from the actual mass is dominated by a deviation of the reconstructed photon energies. Using m_{π^0} as a constraint for $M_{\gamma\gamma}$ it is possible to correct these energies using

$$E_{\gamma_i}^{\mathrm{corr}} = E_{\gamma_i} \cdot \frac{m_{\pi^0}}{M_{\gamma_1\gamma_2}} \qquad (\text{for } i = 1, 2). \tag{5.19}$$

---

[20] The best combination is defined as the combination with minimal quadratic deviation of the three $\gamma\gamma$ invariant masses from m_{π^0}.

(a) $E_\gamma < 1\,\mathrm{GeV}$ (b) $E_\gamma > 1\,\mathrm{GeV}$
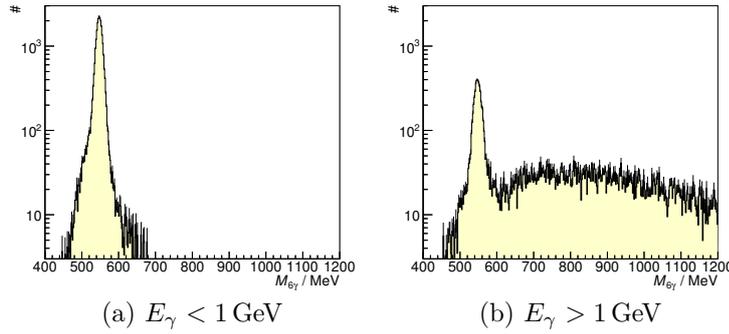
Figure 5.28: The 6γ invariant mass distribution, showing significant background below the η peak for $E_\gamma > 1\,\mathrm{GeV}$.

This results in an exact two-photon invariant mass $M^{\mathrm{corr}}_{\gamma\gamma} = m_\gamma$. The effect of this correction on the $3\pi^0$ invariant mass can be seen in Fig. 5.27c.

It is still not possible to select the reaction $\gamma p \to p\eta \to p6\gamma$ without significant background contamination. In particular for $E_\gamma \gtrsim 1\,\mathrm{GeV}$ the contribution from other events with $3\pi^0$ that do not originate from an η decay is around $10\,\%$ (see Fig. 5.28), and increasing further for higher E_γ. This introduces a large systematic uncertainty, or drastically complicates further analysis. Since the number of reconstructed events for this decay mode is significantly lower than for the $\eta \to \gamma\gamma$ decay mode,[21] and would thus only slightly reduce the statistical errors, this decay mode is not used for further analysis, but only as a systematic cross check (see Section 7.4.2).

5.5 Acceptance

In order to judge the efficiency of the event selection process, the acceptance ε can be investigated. It is defined as the fraction of all events that survive the reconstruction and selection process:

$$\varepsilon(E_\gamma, \theta) = \frac{N_{\mathrm{selected}}}{N_{\mathrm{total}}}. \tag{5.20}$$

The acceptance cannot be determined from the measured data alone, because N_{total} is not known. Instead, ε is determined from the Monte Carlo simulated data (see Section 5.1.3), by using exactly the same reconstruction and selection procedure as for the measured data. The resulting acceptance is shown in Fig. 5.29 for a target proton at rest. The maximum acceptance is around $65\,\%$, which is consistent with a detection efficiency of $90\,\%$ per

---

[21] While the branching ratio for the $3\pi^0$ decay mode is only about $20\,\%$ lower than the 2γ decay mode (see Table 5.5), one also needs to consider the photon detection efficiency of the detector in order to get an estimate for the number of $\eta \to 3\pi^0$ events. The average efficiency is at most $\approx 90\,\%$ per photon (see Section 5.5), it further decreases for events with a larger number of photons in the final state due to increased chance for overlapping energy deposits in the calorimeter. On top of that, additional cuts are performed on the π^0 mass for the $\eta \to 3\pi^0$ decay, thus further reducing the reconstruction efficiency. Therefore, the number of reconstructed $\eta \to 3\pi^0$ events is less than $25\,\%$ of the $\eta \to \gamma\gamma$ events (see also Table 5.6).

(a) $\gamma p \to p\pi^0$ (b) $\gamma p \to p\eta$
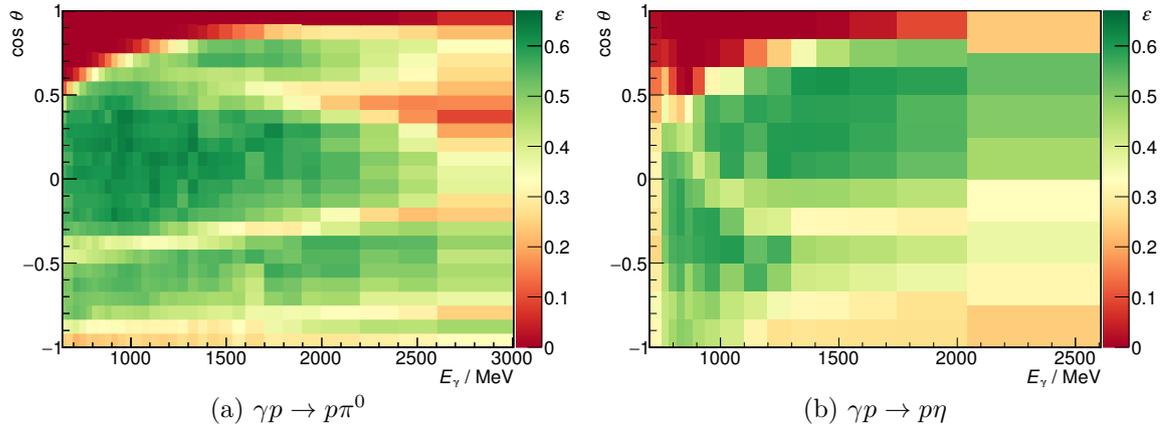
Figure 5.29: The acceptance ε for the reactions $\gamma p \to p\pi^0 \to p\gamma\gamma$ and $\gamma p \to p\eta \to p\gamma\gamma$, for a free proton target (Monte Carlo dataset (3)).

photon, and four 2σ cuts: $0.95^4 \cdot 0.9^2 \approx 0.66$. The acceptance hole at large $\cos\theta$ corresponds to low-energetic protons (going in backward direction in the CM system), which do not deposit enough energy in the calorimeter to be reconstructed, or are absorbed in the target or inactive material in front of the detector. The other prominent structures with lower acceptance correspond to inefficient regions of the detector system. This can be seen in Fig. 5.30, where the distribution of events for which the proton is emitted in the direction of a detector inefficiency is shown. A clear analogy to the acceptance shown in Fig. 5.29 can be seen.

For a target proton with Fermi motion, i.e. for protons bound in nuclei, the acceptance is very different, as can be seen in Fig. 5.31. Most obvious, the acceptance is considerably lower compared to the free proton target, which is a consequence of the broader distributions on which the kinematic cuts are applied. Also, the structures caused by detector inefficiencies are less clearly visible. This is a direct consequence of the Fermi motion: For a given (E_γ, θ), the direction of the recoiling proton is no longer fixed; thus, all detector inefficiencies appear blurred. Since the reactions off bound protons are background for the double polarization measurements with the butanol target, a lower acceptance for these background reactions is of course an advantage.

The total number of reconstructed events is summarized in Table 5.6 for the different targets and reactions. Based on this event sample the polarization observables can be extracted from the data. The analysis is presented in detail in the next chapter.

Table 5.6: Total number of reconstructed events for the different targets and reactions.

	$\gamma p \to p\pi^0$	$\gamma p \to p\eta$	
	$\pi^0 \to \gamma\gamma$	$\eta \to \gamma\gamma$	$\eta \to 3\pi^0$
butanol	1 691 572	170 734	39 451
carbon	194 759	21 737	4 803

(a) $\gamma p \to p\pi^0$

(b) $\gamma p \to p\eta$
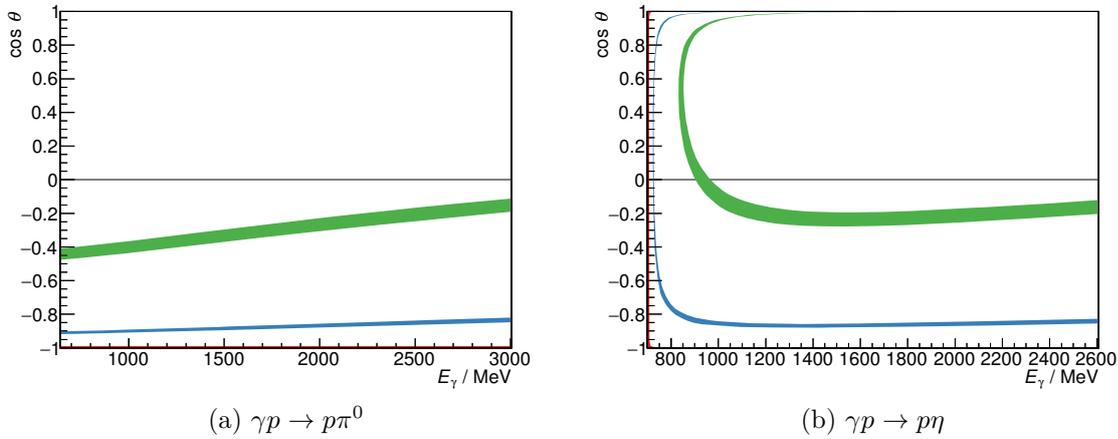
Figure 5.30: Distribution of generated events with no acceptance due to the proton escaping through the central hole in TAPS (red, barely visible, at $\cos\theta = \pm 1$ and for all angles at the η threshold), and events with reduced acceptance due to reduced proton detection efficiency between TAPS and the Forward Plug (blue), and between the Forward Plug and the Crystal Barrel (green). (Note: This is a purely geometrically motivated estimate, assuming a point target and without any interactions of the produced particles. The actual distribution will be slightly blurred due to the size of the target and multiple scattering of the protons.)

(a) $\gamma p \to p\pi^0$ (with $\pi^0 \to \gamma\gamma$)

(b) $\gamma p \to p\eta$ (with $\eta \to \gamma\gamma$)
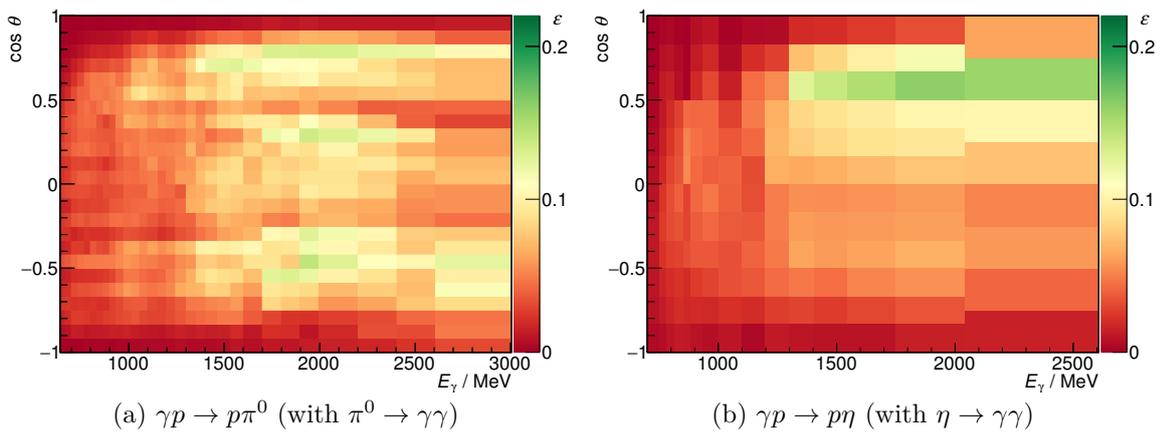
Figure 5.31: The acceptance ε for the reactions $\gamma p \to p\pi^0$ and $\gamma p \to p\eta$, for a bound target proton with Fermi motion (Monte Carlo dataset (4)). Note the different scale compared to Fig. 5.29.

Chapter 6

Determination of the Polarization Observables

In this chapter, two different methods to determine the polarization observables from the data will be presented. But first, the prerequisites are discussed, the most important being the polarization degree of the photon beam and the target protons, but also the normalization of the data.

6.1 Normalization

In order to combine the data from the different data sets, each set must be normalized to the corresponding luminosity integrated over the livetime of the data acquisition, or at least to a number that is proportional to the integrated luminosity for a relative normalization. For a fixed target experiment, the luminosity L is given by the product of target area density n_A and incoming photon rate $\dot{N}_\gamma$, resulting in

$$\int\limits_{\text{livetime}} L \, \mathrm{d}t = n_A \int\limits_{\text{livetime}} \dot{N}_\gamma \, \mathrm{d}t = n_A \cdot N_\gamma. \tag{6.1}$$

Thus, the area density of the different targets and the photon flux, integrated over the livetime, need to be determined for the normalization, which is discussed in the following.

6.1.1 Area Density of the Targets

The area density is constant for a given target. For a relative normalization of different data sets obtained with the same target, it is not needed at all. However, since different targets were used (i.e. the butanol and the carbon foam target), their relative area density needs to be known.
The carbon target was used to approximate the bound nucleons of the butanol target (cf. Section 6.3). Thus, only the bound nucleons inside the C (and O) nuclei of the targets are considered here. The area density n_p^b of the bound protons, which is identical to the area density n_n^b of bound neutrons,[1] can then be calculated using

$$n_p^b = \frac{N_\text{A} \, \rho \, \ell \, N_p^b}{m_\text{mol}}, \tag{6.2}$$

---

[1] Both ^{12}C and ^{16}O contain the same number of protons as neutrons. Contributions from other isotopes can be neglected.

where ρ and ℓ are the density of the target and its length, N_p and m_{mol} are the number of bound protons per target molecule and its molar mass, and N_{A} is the Avogadro constant. The target cell for the butanol target is covered with a thin polytetrafluoroethylene (PTFE) window and filled with butanol beads (diameter $\approx 2\,\mathrm{mm}$ [RD04]). The effective density ρ_{eff} of the butanol target is given by the nominal density of butanol and the filling factor f, which depends on the geometry of the beads and has a large uncertainty, in particular for a narrow (collimated) photon beam, due to local density variations. Measurements of the filling factor for similar butanol targets of various sizes resulted in an average filling factor between $60\,\%$ and $65\,\%$ [Roh03; RD04]. For this analysis, an average filling factor of $62\,\%$ is assumed, with an relative uncertainty of $10\,\%$, which is a conservative estimate also taking the local density fluctuations into account.

Table 6.1: Parameters of the butanol target.

$\rho_{\mathrm{eff}} = 0.94\,\mathrm{g/cm^3} \cdot (0.62 \pm 0.06)$	[RD04]
$\ell = (2.000 \pm 0.005)\,\mathrm{cm}$	[Grü16a]
$m_{\mathrm{mol}} = 74.12\,\mathrm{g/mol}$	[Oli+14]
$N_p = 32$	
$n_b = (0.303 \pm 0.030)\,\mathrm{barn^{-1}}$	

Table 6.2: Parameters of the PTFE window.

$\rho = 2.2\,\mathrm{g/cm^3}$	[Oli+14]
$\ell = (0.050 \pm 0.005)\,\mathrm{cm}$	[Grü16a]
$m_{\mathrm{mol}} = 100\,\mathrm{g/mol}$	[Oli+14]
$N_p = 48$	
$n_b = (0.032 \pm 0.003)\,\mathrm{barn^{-1}}$	

Using the parameters of the butanol target listed in Table 6.1 and the PTFE window listed in Table 6.2, the area density of bound protons in the target material can be calculated as

$$n_b^{\mathrm{butanol}} = (0.33 \pm 0.03)\,\mathrm{barn^{-1}}. \tag{6.3}$$

For the carbon target measurement, the target cell including the PTFE window was replaced by a piece of carbon foam, with the parameters as listed in Table 6.3.

Table 6.3: Parameters of the carbon foam target.

$\rho = (0.5000 \pm 0.0005)\,\mathrm{g/cm^3}$	[Grü16a]
$\ell = (2.040 \pm 0.005)\,\mathrm{cm}$	[Grü16a]
$m_{\mathrm{mol}} = 12\,\mathrm{g/mol}$	
$N_p = 6$	
$n_b = (0.3071 \pm 0.0008)\,\mathrm{barn^{-1}}$	

For a relative normalization, the carbon data thus needs to be scaled by a factor

$$c = \frac{n_b^{\mathrm{butanol}}}{n_b^{\mathrm{carbon}}} = 1.09 \pm 0.10. \tag{6.4}$$

The quoted uncertainty is dominated by the uncertainty of the filling factor of the butanol target, the uncertainties of the target dimensions are significantly smaller. There are, however, additional uncertainties, most importantly the liquid helium surrounding the target material. The carbon target was also operated with liquid helium surrounding the target cell. Therefore, the total amount of helium should be similar for both targets;

however, it is not precisely known. An additional complication arises from the fact that the location of the phase separation between the ^{3}He-enriched and the ^{3}He-diluted phase is unknown, i.e. the photon beam could be passing through either phase. In summary, the precision of the direct determination of the relative target densities is unsatisfactory. Therefore, the value given in Eq. (6.4) will not be used directly for the analysis, but only as a plausibility cross-check. Instead, a carbon scaling factor containing the relative target densities is obtained directly from the data, as will be described in Section 6.3.2.1.

6.1.2 Integrated Photon Flux

While the target area density is an energy-independent normalization factor, the integrated photon flux is energy-dependent. For measurements with coherent bremsstrahlung in different settings, e.g. with the coherent peak at different energies, even the relative photon flux is energy-dependent. Therefore, the determination of the energy-dependent integrated photon flux is indispensable.

The Gamma Intensity Monitor (GIM) as a total absorbing photon detector can be used to count all photons with energies above its threshold.[2] However, it does not measure the energy of the photons. The Photon Tagging System (Tagger), while providing precise information on the energy of the beam photons, also detects electrons that do not correspond to a photon reaching the target. This is mostly due to the photon beam collimator, but also due to background in the tagging hodoscope, e.g. from the electron beam halo. To count the number of beam photons N_γ at the target as a function of their energy E_γ, it is therefore required to count coincident hits in the Tagger and the GIM. This is done using

$$N_\gamma(E_\gamma) = N_{\text{Tagger}\wedge\text{GIM}}(E_\gamma) = N_{\text{Tagger}}(E_\gamma) \cdot \underbrace{\frac{N_{\text{Tagger}\wedge\text{GIM}}(E_\gamma)}{N_{\text{Tagger}}(E_\gamma)}}_{=:P_\gamma(E_\gamma)}, \tag{6.5}$$

where N_{Tagger} is the total number of tagged beam photon candidates that are properly reconstructed (see Section 5.3.4) during the livetime of the experiment, and P_γ is the probability that an electron detected by the Tagger corresponds to a photon on the target. The determination of both N_{Tagger} and P_γ is discussed in the following.

6.1.2.1 Determination of N_{Tagger}

The total number of tagged beam photon candidates cannot be determined directly, because the readout of the detectors has been triggered only for a small fraction of hits in the Tagger. To obtain the number integrated over the livetime of the experiment, livetime-gated scaler modules need to be used. However, the reconstruction of tagged beam photon candidates (cf. Section 5.3.4) involves the combination of data from the bar and fiber detector and cannot easily be implemented in hardware. Instead, the scalers only count coincident hits in neighboring scintillator bars, yielding an N_{scaler} than differs from the desired N_{Tagger}. In addition, the reconstructed beam photon candidates in a time window of $\Delta t = 1.2\,\mu\text{s}$

---

[2] At least if the photon flux is small enough for deadtime effects to be negligible. This is not the case during normal data-taking, but the deadtime effects can be corrected, as will be shown later in this section.

around each recorded event can be counted, with Δt given by the width of the time window of the multi-hit TDC that is read out for each event. The number $N_{\text{Tagger}}^{\text{recon}}$ thus obtained needs to be scaled up to the livetime of the experiment. To achieve this, the number N_{TDC} of coincident TDC hits in neighboring bars during the time window Δt is also determined, and compared to the number N_{scaler} of coincident hits in neighboring bars during the full livetime, which is determined by the scalers. The quotient of the two numbers yields the needed scaling factor, the total number of tagged beam photon candidates integrated over the livetime is therefore given by

$$N_{\text{Tagger}}(E_\gamma) = N_{\text{Tagger}}^{\text{recon}}(E_\gamma) \cdot \frac{N_{\text{scaler}}}{N_{\text{TDC}}}. \tag{6.6}$$

The method is described in more detail in [Har08].
An additional complication arises because the CO_2 Cherenkov detector is used as a trigger veto. It causes additional deadtime, which is not excluded from the livetime gate provided to the scaler modules due to limitations of the trigger system. To manually account for the trigger veto deadtime, both the deadtime Δt_{veto} caused by a single veto and the veto trigger rate $\dot{N}_{\text{veto}}$ need to be determined, resulting in a relative deadtime given by

$$\frac{t_{\text{dead}}}{t_{\text{total}}} = \Delta t_{\text{veto}} \cdot \dot{N}_{\text{veto}}. \tag{6.7}$$

The veto trigger rate is obtained directly from the scalers in the trigger FPGA module. The deadtime Δt_{veto} depends on the length of the veto trigger signals, it can easily be determined from the TDC spectrum of the CO_2 Cherenkov veto detector by measuring the width of the "hole" around the time of the trigger, as can be seen in Fig. 6.1. To account for fluctuations in the beam current and therefore in $\dot{N}_{\text{veto}}$, the relative deadtime is determined on a per datafile[3] basis. A typical rate $\dot{N}_{\text{veto}} \approx 1.3\,\text{MHz}$ results in an additional relative deadtime of $\frac{t_{\text{dead}}}{t_{\text{total}}} \approx 7\,\%$.
The total number of tagged beam photon candidates, also considering the veto deadtime, can then be calculated using

$$N_{\text{Tagger}}(E_\gamma) = N_{\text{Tagger}}^{\text{recon}}(E_\gamma) \cdot \frac{N_{\text{scaler}}}{N_{\text{TDC}}} \cdot \left(1 - \Delta t_{\text{veto}} \dot{N}_{\text{veto}}\right). \tag{6.8}$$

6.1.2.2 Determination of P_γ

The probability P_γ that an electron detected by the Tagger corresponds to a photon at the target is given by

$$P_\gamma(E_\gamma) = \frac{N_{\text{Tagger} \wedge \text{GIM}}(E_\gamma)}{N_{\text{Tagger}}(E_\gamma)} \qquad \text{(see Eq. (6.5)).} \tag{6.9}$$

It is thus required to determine $N_{\text{Tagger} \wedge \text{GIM}}$, the number of coincident hits in the Tagger and the GIM. In principle, this can be done by counting the reconstructed Tagger hits for which a hit in the GIM with a time difference $\Delta t < 8\,\text{ns}$ is also reconstructed. However,

---

[3] The acquisition of one datafile containing 500000 events takes approximately 15 minutes.
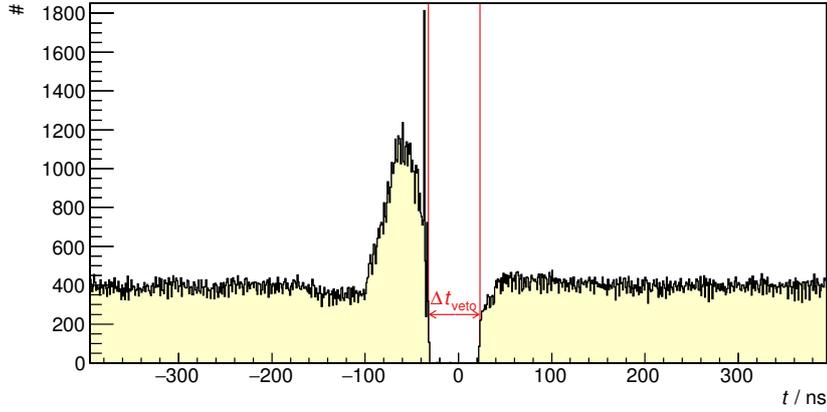
Figure 6.1: The TDC spectrum of the CO_2 Cherenkov detector for a trigger condition that includes this detector as a veto. A hole around the time of the trigger at $t = 0$ is clearly visible, with the width of the hole corresponding to the deadtime $\Delta t_{\text{veto}} = 55$ ns caused by a single veto signal. The peak at the left edge of the veto hole is a consequence of the limited double pulse resolution of the veto: an uncorrelated signal just before the time of the trigger at $t = 0$ causes deadtime on the veto itself, which makes the trigger more sensitive to background during that deadtime, since no veto signal can then be provided. As a consequence, more (background) events are written to disk directly after a Cherenkov veto signal, which is equivalent to an increased probability to observe an uncorrelated signal in the Cherenkov detector just before the trigger, resulting in a peak in the TDC spectrum.
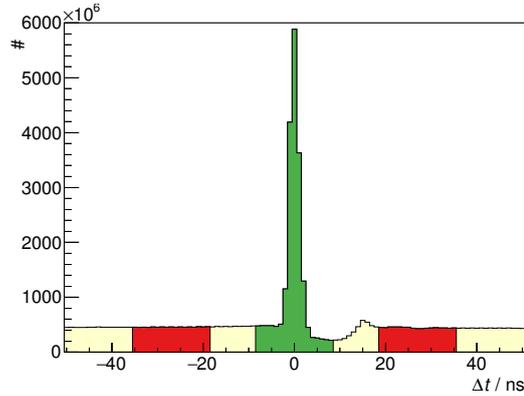
Figure 6.2: Time difference $\Delta t = t_{\text{GIM}} - t_{\text{Tagger}}$ between electrons reconstructed by the Tagger and photons reconstructed by the GIM. The time intervals used to select peak and sideband events are marked in green and red, respectively. The background level in the peak interval is lower (to the right of the peak) because of the reduced livetime. To correctly subtract the background, the livetime needs to be determined (see text).

as can be seen in Fig. 6.2, there is significant background due to random coincidences, distributed over the full time span and especially underneath the coincidence peak. A closer look reveals that the background is *not* flat below the coincidence peak. Instead, there is an approx. 12 ns wide region next to the peak with significantly less background. This is due to the deadtime caused by the limited double pulse resolution $t_{\text{DPR}} = 12$ ns of the GIM[4] which is effectively a single channel detector (cf. Section 5.3.5). Since each hit causes subsequent deadtime, the total deadtime in a given time cut interval depends on the total number of counts in that interval. There is more total deadtime in a time interval around the coincidence peak compared to a time interval of the same size in the sideband, simply because there are more hits in the peak interval. Consequently, less background is counted around the coincidence peak. To correctly eliminate the background using a sideband subtraction, the different deadtimes in the peak and sideband intervals need to be taken into account.

This is done by normalizing the number of peak and sideband events to the corresponding livetimes $t_{\text{live}}^{\text{peak}}$ and $t_{\text{live}}^{\text{side}}$.[5] The total number of peak and sideband hits $N_{\text{Tagger}\wedge\text{GIM}}^{\text{peak,side}}$, and the corresponding accumulated livetimes $t_{\text{live}}^{\text{peak,side}}$, are determined event-by-event. For each hit in the Tagger, the time difference to the hits in the GIM is investigated, and three intervals are defined: one peak interval -8 ns $< \Delta t < 8$ ns and two sideband intervals -35 ns $< \Delta t < -19$ ns and 19 ns $< \Delta t < 35$ ns. For each hit in the Tagger, the width of each interval is added to the corresponding accumulated livetime. Each coincident hit within the intervals is counted, and the corresponding livetime is decreased again by t_{DPR} (or less, if the hit is closer to the end of the interval).

The background-subtracted number of coincident hits in the Tagger and the GIM is then given by

$$N_{\text{Tagger}\wedge\text{GIM}} = N_{\text{Tagger}\wedge\text{GIM}}^{\text{peak}} - \frac{t_{\text{live}}^{\text{peak}}}{t_{\text{live}}^{\text{side}}} \cdot N_{\text{Tagger}\wedge\text{GIM}}^{\text{side}}. \qquad (6.10)$$

Here, the relative livetime of the peak and sideband intervals is only used to correctly subtract the background. But the limited double pulse resolution does not only influence the sideband subtraction of random coincidences, it also reduces the detection efficiency of the GIM. How the reduced efficiency can also be corrected is discussed in the next section.

GIM Efficiency Correction

The P_γ calculated using Eq. (6.9) is only correct if the detection efficiency of the GIM is 100 %. In general, the detection efficiency $\varepsilon_{\text{GIM}} < 1$ decreases the measured P_γ, which needs to be taken into account and corrected.[6]

$$P_\gamma(E_\gamma) = \frac{1}{\varepsilon_{\text{GIM}}(E_\gamma)} \cdot P_\gamma^{\text{meas}}(E_\gamma) = \frac{1}{\varepsilon_{\text{GIM}}(E_\gamma)} \cdot \frac{N_{\text{Tagger}\wedge\text{GIM}}(E_\gamma)}{N_{\text{Tagger}}(E_\gamma)} \qquad (6.11)$$

---

[4] For the Tagger the double pulse resolution of the single channels can be neglected because of the segmentation of the detector.

[5] The livetimes $t_{\text{live}}^{\text{peak}}$ and $t_{\text{live}}^{\text{side}}$ are the livetimes within the time intervals used to select peak and sideband events. They have nothing to do with the data acquisition livetime t_{live} mentioned earlier.

[6] The detection efficiency of the Tagger does *not* need to be taken into account: it affects $N_{\text{Tagger}\wedge\text{GIM}}$ in the numerator and N_{Tagger} in the denominator the same way and cancels in the calculation of P_γ.

The efficiency can be separated into a rate-independent and a rate-dependent part:

$$\varepsilon_{\mathrm{GIM}} = \varepsilon_{\mathrm{GIM}}^0 \cdot \varepsilon_{\mathrm{GIM}}^{\mathrm{rate}}. \tag{6.12}$$

The *rate-independent efficiency* $\varepsilon_{\mathrm{GIM}}^0$ is mostly influenced by the threshold of the detector (discriminator threshold). At high E_γ, it approaches nearly $\varepsilon_{\mathrm{GIM}}^0 \approx 1$, but drops significantly below $E_\gamma \lesssim 1\,\mathrm{GeV}$, as can be seen in Fig. 6.3. The threshold, which is set below $500\,\mathrm{MeV}$ for each crystal, influences the efficiency even at energies twice as large due to the fact that the energy deposited in the detector—in an electromagnetic shower—can spread over more than one crystal.

It should be noted that for a relative normalization of different data sets the rate-independent efficiency can be ignored, since it is identical for each data set used in this analysis. It is only relevant for the absolute measurement of cross sections and not needed for this analysis.
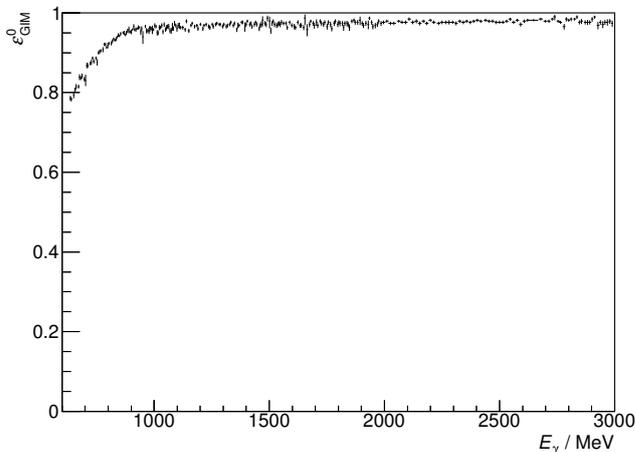
Figure 6.3: The GIM efficiency ε as a function of the beam photon energy E_γ, measured with a low-intensity photon beam such that deadtime effects can be neglected. The method used to determine the efficiency is described in Appendix D.

At higher rates, the deadtime caused by the limited double pulse resolution t_{DPR} reduces the detection efficiency. The *rate-dependent efficiency* $\varepsilon_{\mathrm{GIM}}^{\mathrm{rate}}$ deviates significant from 1 if the rate $\dot{N}$ is high enough that the condition

$$\dot{N} \cdot t_{\mathrm{DPR}} \ll 1 \tag{6.13}$$

is not fulfilled. With $t_{\mathrm{DPR}} \approx 12\,\mathrm{ns}$, this is the case for rates of $\dot{N} \gtrsim 10\,\mathrm{MHz}$ or more, occurring during normal data-taking. There are two options how to take the rate dependent efficiency into account:

1. Calculate deadtime losses:
   The production of bremsstrahlung photons can be approximated as a Poisson process. The distribution of the time difference τ between two photons for a given rate $\dot{N}$ is then given by an exponential probability density function

   $$f(\tau, \dot{N}) = \dot{N} \cdot \exp\left(-\dot{N} \cdot \tau\right). \tag{6.14}$$

A photon can be detected by the GIM if the time difference to the previous photon is larger than the double pulse resolution of the detector. The rate-dependent efficiency ε is thus given by

$$\varepsilon(\dot{N}) = \int\limits_{t_{\mathrm{DPR}}}^{\infty} f(\tau, \dot{N})\,\mathrm{d}\tau = \exp\left(-\dot{N} \cdot t_{\mathrm{DPR}}\right). \tag{6.15}$$

In reality, the actual rate $\dot{N}$ is unknown. Instead, one knows only the measured rate

$$\dot{N}_{\mathrm{meas}} = \dot{N} \cdot \varepsilon(\dot{N}) = \dot{N} \cdot \exp\left(-\dot{N} \cdot t_{\mathrm{DPR}}\right). \tag{6.16}$$

By inverting Eq. (6.16) using the Lambert$W$ function[7] one obtains

$$\varepsilon(\dot{N}_{\mathrm{meas}}) = \frac{\dot{N}_{\mathrm{meas}} \cdot t_{\mathrm{DPR}}}{-W\left(-\dot{N}_{\mathrm{meas}} \cdot t_{\mathrm{DPR}}\right)}. \tag{6.17}$$

Figure 6.4 shows $\varepsilon(\dot{N}_{\mathrm{meas}})$ for $t_{\mathrm{DPR}} = 12\,\mathrm{ns}$. As long as the rate is below the saturation rate,[8] the efficiency for any given rate can be calculated and corrected.

Since the filling of the ELSA ring is not perfectly homogeneous, the distribution of the beam photons in time is not perfectly uniform. The actual distribution is unknown, and the Poisson process is only an approximation. Also, other (unknown) effects could influence the detection efficiency in a rate-dependent way and are not included in the calculation. This introduces additional systematic errors which can be avoided by using option 2.

2. Determine P_γ using a low-intensity beam:
   By measuring P_γ with a low-intensity photon beam, the deadtime effects become negligible and the rate-dependent efficiency approaches $\varepsilon_{\mathrm{GIM}}^{\mathrm{rate}} = 1$. The drawback of this method is that P_γ cannot be determined in parallel to the normal data-taking operation. Instead, a dedicated P_γ measurement has to be performed regularly with low beam current. Any change in P_γ between these dedicated measurements, e.g. caused by a drift in the beam position, cannot be accounted for that way. As an alternative, the rate-dependent efficiency can be measured using the low-intensity measurement and a measurement at nominal intensity performed directly afterwards:[9]

$$\frac{P_\gamma^{\mathrm{meas}}(\dot{N}_{\mathrm{nominal}})}{P_\gamma^{\mathrm{meas}}(\dot{N} \to 0)} = \frac{\cancel{P_\gamma} \cdot \cancel{\varepsilon_{\mathrm{GIM}}^0} \cdot \varepsilon_{\mathrm{GIM}}^{\mathrm{rate}}(\dot{N}_{\mathrm{nominal}})}{\cancel{P_\gamma} \cdot \cancel{\varepsilon_{\mathrm{GIM}}^0} \cdot \underbrace{\varepsilon_{\mathrm{GIM}}^{\mathrm{rate}}(\dot{N} \to 0)}_{\to 1}} = \varepsilon_{\mathrm{GIM}}^{\mathrm{rate}}(\dot{N}_{\mathrm{nominal}}) \tag{6.18}$$

   The P_γ measured in parallel to the normal data-taking can then be corrected using this efficiency.

---

[7] The Lambert$W$ function is defined by $x = W(x)\exp\left(W(x)\right)$. For numerical approximations see [Cor+96].

[8] The saturation rate is defined as the rate at which the highest possible rate is measured. A further rate increase beyond the saturation rate results in lower measured rates, as can be seen in Fig. 6.4.

[9] To exclude any change in the position of the extracted electron beam when the intensity is changed, the intensity is *not* reduced by changing the extraction parameters of the ELSA accelerator to extract fewer electrons, but by reducing the total current in the ELSA ring while keeping all other parameters of the accelerator constant.
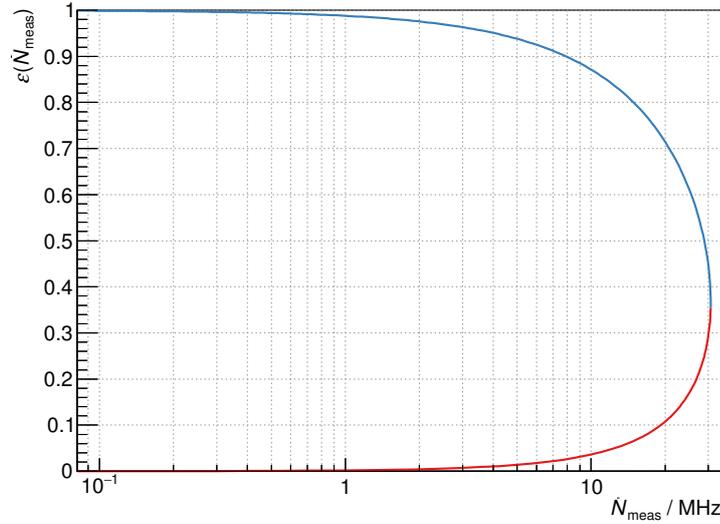
Figure 6.4: The relative detection efficiency ε as a function of the measured rate $\dot{N}_{\mathrm{meas}}$. The curve has been calculated for varying actual rates $\dot{N}$ using Eq. (6.15) for the ordinate and Eq. (6.16) for the abscissa. The blue part of the curve is also given by Eq. (6.17). The red part of the curve shows the decrease in efficiency for even higher beam intensities which result in a decrease of the measured rate due to saturation.

A comparison of the two methods can be seen in Fig. 6.5. Considering that both methods have independent systematic uncertainties, either because of a possible change of the measurement conditions between low and high rate, or because of the approximations of the calculation, the agreement of the two methods within a few percent is excellent. However, at the high rates used during data-taking with the diamond radiator, the rate-dependent efficiency is not independent of E_γ. An explanation for the decrease toward lower energies might be a rate-dependent behavior of the readout electronics,[10] which was operated near the maximum design rate. This decrease is not included in the calculation. Therefore, the measurement and not the calculation is used for the analysis. That way, the rate- and energy-dependent detection efficiency is fully corrected in the determination of P_γ.

The resulting P_γ, corrected for the rate-dependent GIM efficiency, is shown in Fig. 6.6 as a function of E_γ. The drop toward lower energies is a consequence of the rate-independent GIM efficiency, which is not corrected. Since the opening angle of coherent bremsstrahlung is smaller compared to incoherent bremsstrahlung, a larger fraction of the photons produced by coherent bremsstrahlung passes through the collimator. This results in a higher P_γ in the region of the coherent peak, as can be seen in Figs. 6.6b and 6.6c. The time development of the average P_γ over all E_γ is shown in Fig. 6.7. As can be seen, P_γ fluctuates by several percent during a longer measurement period. These fluctuations, which are caused by slow drifts of the beam position, highlight the importance of frequent measurements of P_γ.

---

[10] One possible explanation is a temporary drop of the HV of the PMTs because of the higher PMT current at high rates, which temporarily increases the threshold and reduces the efficiency for lower energies.

(a) Copper, $\dot{N} = 7.0\,\mathrm{MHz}$ (b) Diamond $-45°$, $\dot{N} = 13.7\,\mathrm{MHz}$ (c) Diamond $+45°$, $\dot{N} = 13.9\,\mathrm{MHz}$
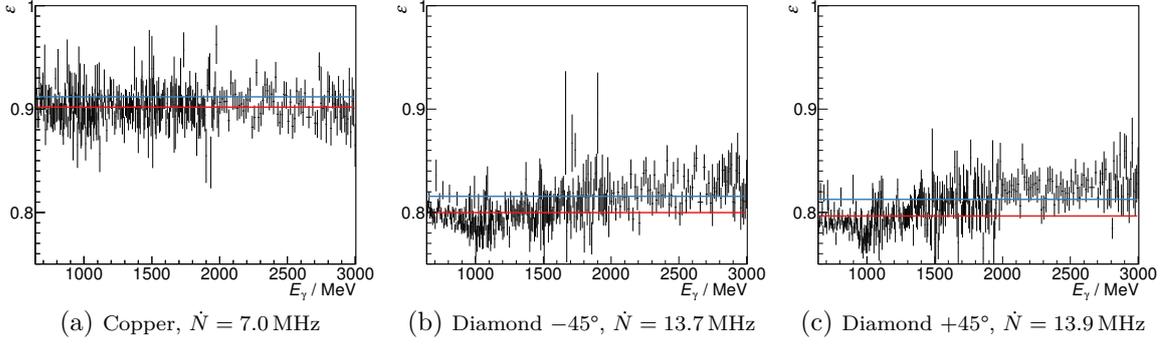
Figure 6.5: The rate-dependent GIM efficiency $\varepsilon_{\mathrm{GIM}}^{\mathrm{rate}}$ as a function of E_γ (determined using Eq. (6.18) [method 2]), for different radiator settings. The red line shows the average over all E_γ, the blue line shows the result of the calculation using Eq. (6.17) [method 1].

(a) Copper (b) Diamond $-45°$ (c) Diamond $+45°$

Figure 6.6: P_γ as a function of E_γ, for different radiator settings.

(a) Butanol data (October 2010) (b) Carbon data (November 2011)
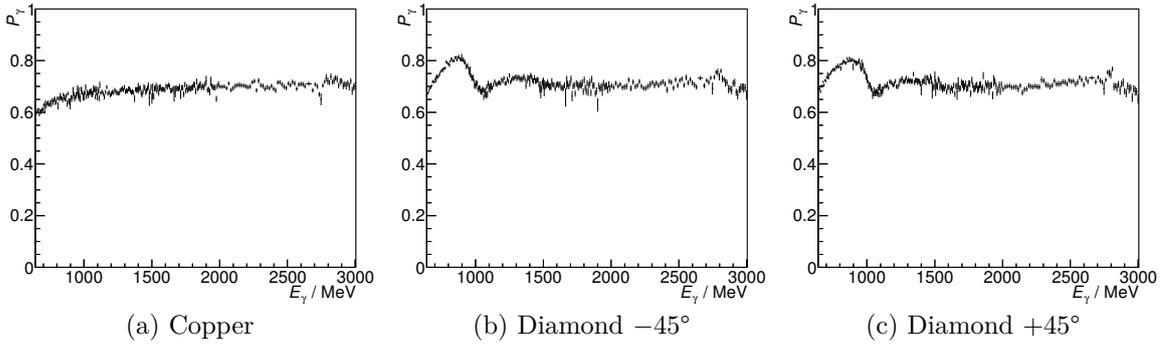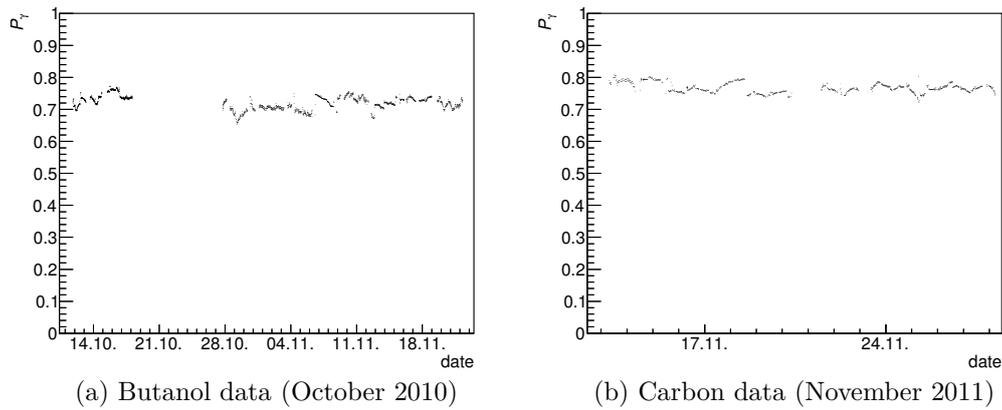
Figure 6.7: P_γ (averaged over all E_γ) over time for the butanol and carbon measurements.

96

6.2 Polarization Degree

In order to extract the polarization observables from the data, the exact degree of beam and target polarization needs to be known (cf. Eq. (2.18)).

6.2.1 Beam Polarization

The beam polarization δ for a given crystal setting can be calculated from the measured bremsstrahlung spectrum. This is done using an analytic calculation of the bremsstrahlung process [Nat+03]. The procedure is described in detail in [Ebe12]. Figure 6.8 shows the measured relative intensity compared to the analytic calculation. The corresponding polarization degree is shown in Fig. 6.9. The relative uncertainty of the polarization degree is less than 5 % [Ebe12], which is a conservative estimate for the full energy range. However, for energies below $E_\gamma < 933\,\text{MeV}$, i.e. well below the coherent edge, the deviations between the analytic calculation and the measured spectrum are smaller (cf. Fig. 6.8). Therefore, a relative uncertainty of 4 % is more realistic in the energy range below the coherent edge. At the coherent edge, however, the polarization degree changes strongly if the position of the coherent edge changes during data-taking. Such a change can, for example, be caused by a small drift of the beam direction during the measurement. The magnitude of such a drift is limited by the size of the collimator;[11] thus, the position of the coherent edge is stable within $\approx 10\,\text{MeV}$. Taking this into account, the estimate of the relative uncertainty of the polarization degree has to be increased to 8 % around the coherent edge, i.e. between 933 MeV and 1050 MeV.

6.2.2 Target Polarization

During the data-taking, while the target is in frozen spin mode, the target polarization cannot be monitored. Only the starting value of the polarization at the beginning of each measurement period, directly after re-polarization, and the end value before re-polarization, are measured using NMR [Rei+95; Rei94]. During data-taking, the conditions inside the target cell (temperature, magnetic field) are very stable, resulting in a constant relaxation time. The polarization for each event can therefore be calculated using exponential interpolation. The NMR measurement is calibrated using the proton polarization Λ_{TE} in thermal equilibrium at $B = 2.5\,\text{T}$ and $T \approx 1\,\text{K}$, which can be calculated from [Ave+99]

$$\Lambda_{\text{TE}} = \tanh\left(\frac{\mu\,B}{k_{\text{B}}T}\right), \tag{6.19}$$

where μ is the magnetic moment of the proton and k_{B} is the Boltzmann constant. Since the relative uncertainty of the magnetic field $\frac{\Delta B}{B}$ is less than 10^{-4} [RD04], the uncertainty of P_{TE} is dominated by the uncertainty of the temperature measurement, which is done with an accuracy of 1 % using a calibrated carbon resistor [RD04]. Including the uncertainties of the NMR measurement [Rei+95; Rei94], the total relative uncertainty of the proton polarization measurement is 2 % [Dut16]. The changing target polarization during data-taking is shown in Fig. 6.10.

---

[11] A larger drift would result in significantly fewer photons reaching the target, which would be detected on-line and corrected.
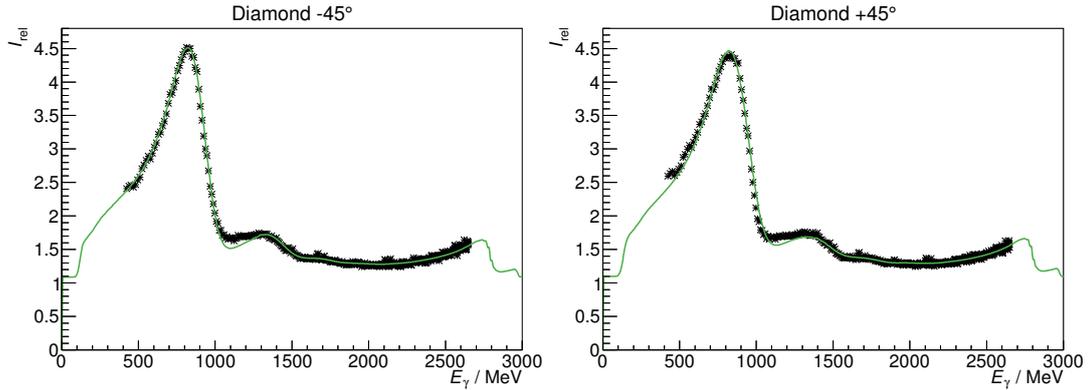
Figure 6.8: Measured relative bremsstrahlung intensity spectra (data points) compared to analytic calculations (solid line), for both crystal orientations [Ebe12]. Around $E_\gamma \approx 1100\,\text{MeV}$ the analytic calculation deviates from the measured spectrum, leading to a large systematic uncertainty of the calculated polarization degree in that region [Ebe12]. However, since the analysis involving linear polarization is only done for $E_\gamma \leq 975\,\text{MeV}$, this is of no consequence.
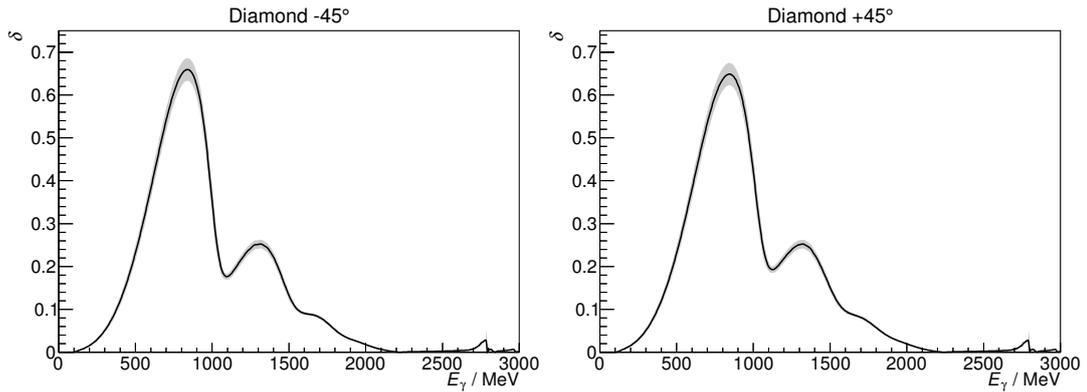
Figure 6.9: Calculated linear polarization degree δ as a function of E_γ for both crystal orientations [Ebe12]. The systematic uncertainty is shown as the gray band.
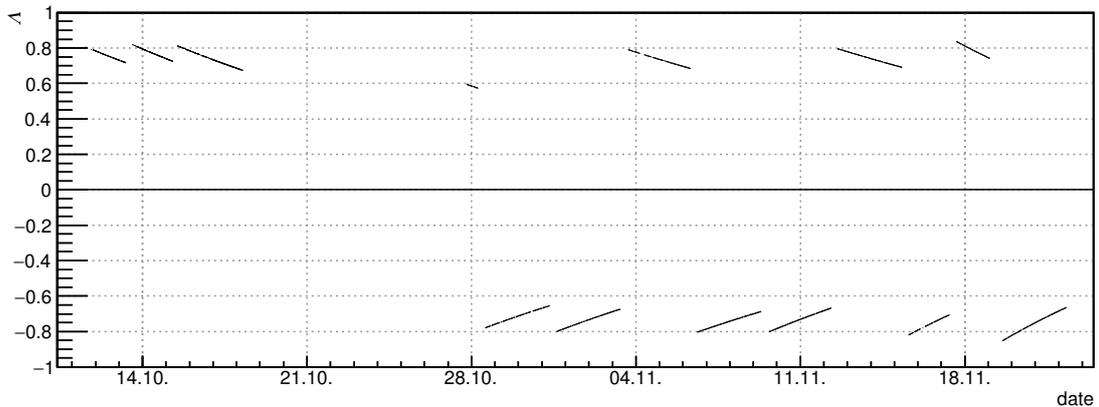
Figure 6.10: The target polarization degree Λ during the 2010 data-taking periods [Dut16].

6.3 Dilution Factor

As the polarized target does not only consist of polarized protons, π^0 and η mesons can not only be produced off the polarized protons in the reactions

$$\vec{\gamma}\,\vec{p} \to p\,\pi^0 \quad \text{and} \quad \vec{\gamma}\,\vec{p} \to p\,\eta \tag{6.20}$$

but also off the unpolarized bound nucleons inside the carbon and oxygen nuclei of the butanol target:

$$\vec{\gamma}\,p_b \to p\,\pi^0 \quad \text{and} \quad \vec{\gamma}\,p_b \to p\,\eta \tag{6.21a}$$
$$\vec{\gamma}\,n_b \to n\,\pi^0 \quad \text{and} \quad \vec{\gamma}\,n_b \to n\,\eta \tag{6.21b}$$

Additionally, coherent meson photoproduction off the nucleons is also possible, but with negligible cross section [Tar07; Mag+13] compared to (6.20), (6.21a), and (6.21b) in the energy range covered in this analysis:

$$\vec{\gamma}\,\mathrm{C} \to \mathrm{C}\,\pi^0 \quad \text{and} \quad \vec{\gamma}\,\mathrm{C} \to \mathrm{C}\,\eta \tag{6.22a}$$
$$\vec{\gamma}\,\mathrm{O} \to \mathrm{O}\,\pi^0 \quad \text{and} \quad \vec{\gamma}\,\mathrm{O} \to \mathrm{O}\,\eta \tag{6.22b}$$

Obviously, the reactions (6.21b) (and of course also (6.22)) do not contribute if the recoiling proton in the final state is measured and identified. Since in this analysis the information of the charge sensitive detectors is not used, reaction (6.21b) does indeed contribute. However, the detection efficiency for neutrons in the calorimeter is significantly smaller than for protons ($\varepsilon_n < 0.3$ [Jae+11]). Therefore, the contribution from bound neutrons is expected to be significantly smaller compared to bound protons.

As the bound nucleons are not polarized, and the measured target polarization is only that of the free protons, these background reactions effectively dilute the target polarization by a factor $d \in [0,1]$, the so called *dilution factor*. The value of the target polarization that enters Eq. (2.18) is therefore an effective polarization, given by the product of the measured target polarization Λ_{NMR} and the dilution factor d.

$$\Lambda \to \Lambda_{\mathrm{eff}} = \Lambda_{\mathrm{NMR}} \cdot d \tag{6.23}$$

One might naively expect that d can easily be determined from the molecular formula of butanol ($\mathrm{C_4H_9OH}$), by calculating the ratio of the number of free (polarized) protons to the number of all nucleons in the butanol molecule.

$$d_{\mathrm{mol}} = \frac{10}{10 + 4\cdot 6 + 8} = \frac{10}{42} \qquad \text{(in case the recoiling proton is identified)}$$

However, the measured target polarization is diluted by an effective dilution factor $d_{\mathrm{eff}} \neq d_{\mathrm{mol}}$. This is due to the fact that the reactions (6.20) and (6.21), although having the same final state, are very different, for two reasons:

- **Fermi motion:** While the free protons in the initial state are at rest, the bound nucleons inside the nuclei have an (unknown) initial momentum in the order of a few $100\,\mathrm{MeV}$.[12] During event reconstruction, the target proton is assumed to be at

---

[12] For the Fermi momentum distribution in carbon, see e.g. Fig. 5.1b or [CHM52].

rest. Thus, the reactions (6.21a) and (6.21b) do not necessarily fulfill energy and momentum conservation and have therefore, compared to reaction (6.20), a higher chance of being outside the applied cut ranges (see Sections 5.4 and 5.5).

- **Final state interaction:** The mesons produced inside the nuclei can interact with the nucleus via final state interaction, thus changing the observed cross section. This can be described by the transparency ratio T, which compares the cross section per nucleon off a nucleus with the cross section off the free proton.

$$T = \frac{\sigma_A}{A \cdot \sigma_N} \tag{6.24}$$

Without any interaction, the transparency ratio would be equal to 1. Measurements in various final states like η' or ω show a decrease of T which is more pronounced for heavy nuclei, but nevertheless also observable for carbon [Nan+13; Die+15].

This results in an effective dilution factor, given by the ratio of the number of reconstructed reactions on a free (polarized) proton to the number of all reconstructed reactions. The effective dilution factor depends on the reaction, the kinematics, and also on the applied cuts. It is therefore necessary to determine this factor independently for each (E_γ, θ) bin and for each reaction. There are two different ways to accomplish this, each requiring an additional measurement.

6.3.1 Normalization Measurement Using a Liquid Hydrogen Target

With an additional measurement using an (unpolarized) liquid hydrogen target, it is possible to measure the cross section for reaction (6.20), and then calculate the dilution factor using

$$d_{\text{eff}} = \frac{\sigma^{\text{hydrogen}}}{\sigma^{\text{butanol}}}, \tag{6.25}$$

where σ^{butanol} is the combined cross section for reactions (6.20) and (6.21a) (and (6.21b) if the recoiling proton is not identified), as it is measured with a butanol target.
While this method seems fairly straightforward, it has a very serious drawback: The available liquid hydrogen target apparatus is different compared to the frozen spin butanol target cryostat. Neither the dimensions of the target cell (5.275 cm length for hydrogen compared to 2 cm for butanol) nor the material budget of the surroundings ($\approx 0.006\, X_0$ at $\theta = 90°$ for hydrogen compared to $\approx 0.09\, X_0$ for butanol) are comparable, which results in a different acceptance for the two targets.[13] This obviously needs to be corrected, but an acceptance correction using Monte Carlo simulation introduces additional systematic uncertainties. On top of that, the cross section for electromagnetic background differs significantly for hydrogen and butanol (cf. Fig. 3.18), resulting in different measurement conditions due to very different rates in the detectors. This severely complicates the relative normalization of the two measurements. This method is therefore not investigated any further.

---

[13] A longer target cell reduces the angular resolution of all measured particles (since all particles are assumed to originate from the target center) and therefore also the invariant mass and missing mass resolution. More material around the target leads to more multiple scattering of charged particles, resulting in broader $\Delta\phi$ and $\Delta\theta$ distributions.

6.3.2 Background Measurement Using a Carbon Target

A different approach is to measure the contribution from the bound nucleons and subtract it from the full butanol cross section:

$$d_{\text{eff}} = \frac{\sigma^{\text{butanol}} - \sigma^{\text{bound}}}{\sigma^{\text{butanol}}} \tag{6.26}$$

The contribution from bound nucleons in butanol can e.g. be approximated experimentally by a pure carbon target.

As will be seen later in this chapter, an absolute determination of cross sections is not necessary for the determination of the polarization observables. It should therefore be avoided, in order to eliminate the systematic uncertainties of an absolute normalization. This requires Eq. (6.26) to be rewritten in terms of event yields (only relatively normalized to the corresponding energy-dependent integrated photon flux), which introduces an additional scaling factor for the carbon measurement:

$$d_{\text{eff}} = \frac{N^{\text{butanol}} - c \cdot N^{\text{carbon}}}{N^{\text{butanol}}} \tag{6.27}$$

Using this method, all systematic effects of the detector system will cancel out, as long as all measurements are done under identical conditions. It is therefore crucial to do the background measurement using the frozen spin target cryostat, including liquid helium around the target cell, with a target of similar dimensions and density. All these requirements were satisfied in the carbon foam target measurement.

The dominant contribution to the scaling factor arises from the (minor) differences in the target density of the butanol and the carbon target measurements (cf. Section 6.1.1). But also all other known or unknown differences between the butanol and carbon measurement, including all energy-independent systematic uncertainties of the relative normalization, can be absorbed in this factor as well.

So, before the dilution factor can be calculated, the carbon scaling factor c needs to be determined experimentally.

6.3.2.1 Determination of the Carbon Scaling Factor

To directly compare the carbon measurement to the reactions off the bound nucleons in the butanol data, the reactions off the free protons in the butanol data need to be excluded by additional cuts. This can easily be done by exploiting the fact that the $\Delta\phi$ or $M_{p'}$ distributions are very different for reactions off free and bound nucleons, as can bee seen in Fig. 6.11. By replacing the narrow $\Delta\phi$ cut by a $180° \pm 20°$ anti-cut, which is more than $3\,\sigma_{\text{free}}$ wide, only reactions off bound nucleons are retained.

The carbon scaling factor is then simply the ratio of normalized events yields on the butanol and the carbon target after the anti-cut.

$$c = \frac{N^{\text{butanol}}_{\text{anticut}}}{N^{\text{carbon}}_{\text{anticut}}} \tag{6.28}$$

The width of the anti-cut was chosen conservatively, as can be seen in Fig. 6.12, where the scaling factor is plotted versus the width of the anti-cut.

(a) Azimuthal angle difference $\Delta\phi$ (b) Invariant mass of the missing proton $M_{p'}$
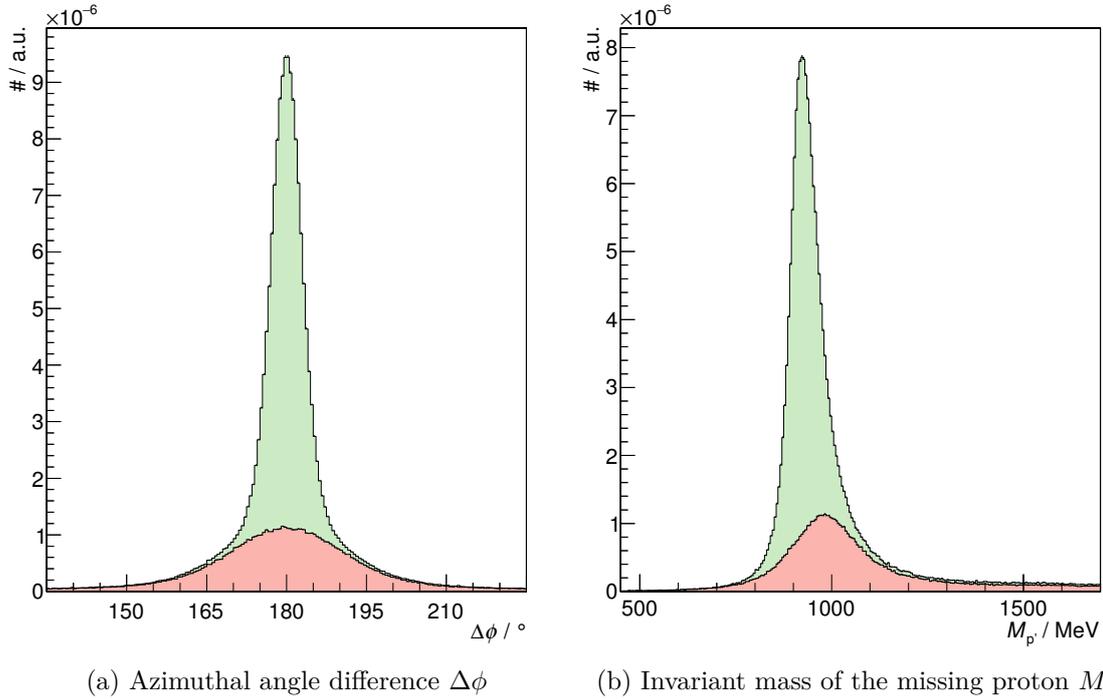
Figure 6.11: $\Delta\phi$ and $M_{p'}$ distributions for butanol (green) and carbon (red) data, integrated over E_γ and $\cos\theta$, for the reaction $\gamma p \rightarrow p\pi^0$. The reactions off free protons can be eliminated by e.g. applying a $180° \pm 20°$ anti-cut on $\Delta\phi$. Note that the carbon spectra shown here are not yet scaled, but nevertheless match the butanol data rather well since the scaling factor is close to 1.
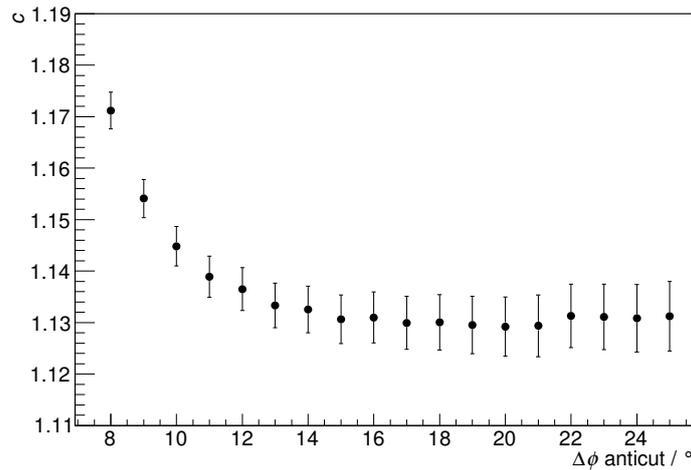
Figure 6.12: Effect of the $\Delta\phi$ anti-cut width on the carbon scaling factor for the reaction $\gamma p \rightarrow p\pi^0$. (Note that the individual data points for different anti-cuts are highly correlated.)

The resulting scaling factor for the reaction $\gamma p \to p\pi^0$ is

$$c_{\pi^0} = 1.129 \pm 0.006, \tag{6.29}$$

which is in perfect agreement with the value that is expected from the target density difference (see Eq. (6.4)). The result should be independent of all kinematic variables, and it should be the same for the π^0 and η reactions. However, the resulting scaling factor for the reaction $\gamma p \to p\eta \to p\gamma\gamma$ is significantly larger:

$$c_\eta = 1.228 \pm 0.012. \tag{6.30}$$

As can be seen in Fig. 6.13, both scaling factors depend slightly on both E_γ and $\cos\theta$. There are two possible reasons for this:

- Differences in the acceptances for the butanol and carbon targets.

- Different backgrounds in the butanol and carbon data.

A detailed investigation has proven to be impossible due to limited statistics, in particular of the carbon data. The changes in the measured scaling factor are only visible after integration over one of the two kinematic variables, as has been done in Fig. 6.13. A two-dimensional determination of the scaling factor as a function of both E_γ and $\cos\theta$ reveals no significant deviation from the average scaling factor, as can be seen in Fig. 6.14 where a histogram of the deviation of the bin-wise scaling factors to the average scaling factor given in Eq. (6.29) is shown.

(a) Beam energy dependence   (b) Angular dependence
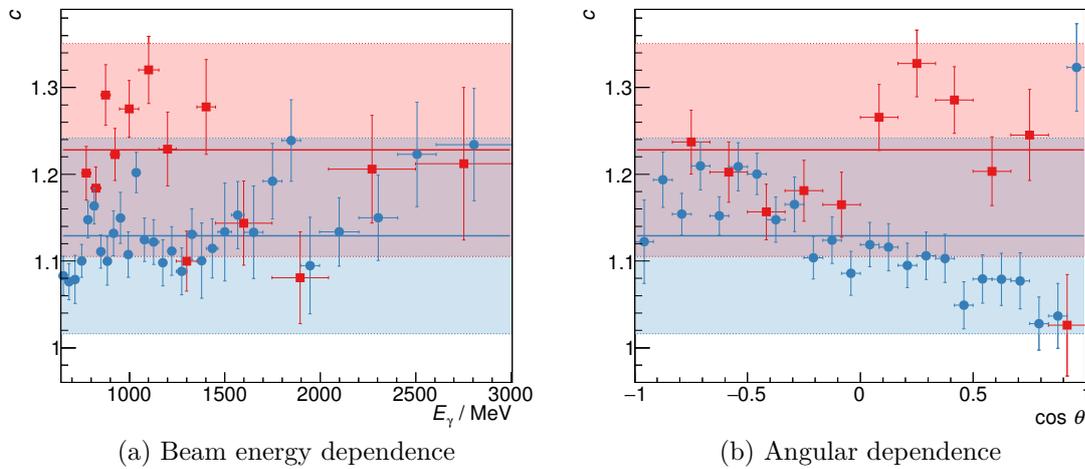
Figure 6.13: Dependence of the carbon scaling factor c on the beam energy E_γ (integrated over all angles) (a) and meson center-of-mass angle θ (integrated over E_γ) (b), for $\gamma p \to p\pi^0$ ($\bullet$) and $\gamma p \to p\eta(\eta \to \gamma\gamma)$ ($\blacksquare$). The average scaling factors c_{π^0} and c_η are shown as horizontal lines, the surrounding shaded areas indicate the estimated systematic uncertainty (see text). Since the acceptance for $\cos\theta \approx 1$ is very small, even for the carbon data (see Section 5.5), the determination of the scaling factor in the last angular bin is more sensitive to background contamination, which explains the large deviation of that data point.
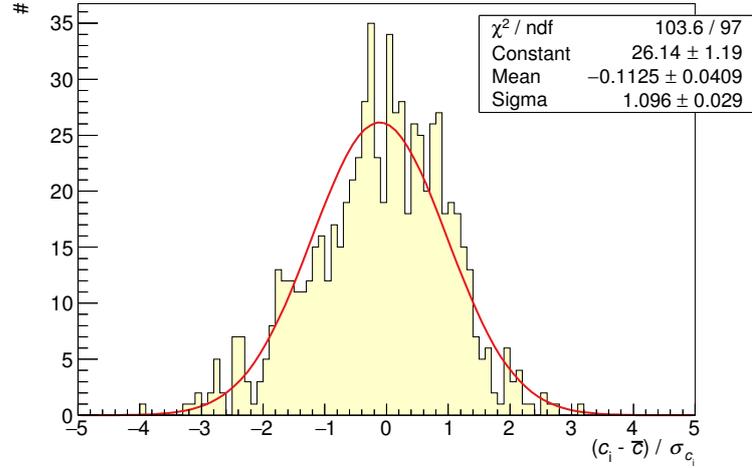
Figure 6.14: Histogram of the deviation of the individual carbon scaling factors for each $(E_\gamma, \cos\theta)$ bin to the average scaling factor (normalized to the individual statistical error), together with a Gaussian curve fitted to the histogram, for the reaction $\gamma p \to p\pi^0$.

In conclusion, a per bin determination of the scaling factor to eliminate possible systematic errors caused by an E_γ and $\cos\theta$ dependence of the scaling factor is of no use since in that case the statistical errors would be even larger than the systematic errors avoided by the per bin method. The better approach is to use one global scaling factor for each reaction and assume a 10 % systematic error caused by neglecting the E_γ and $\cos\theta$ dependence. This value is a conservative estimate. However, as will be seen in Chapter 7, this error does not have a strong influence on the total systematic error of the polarization observables.

6.3.3 Determination of the Dilution Factor for the Reaction $\gamma p \to p\pi^0$

With the carbon scaling factor it is now possible to determine the dilution factor d for each $(E_\gamma, \cos\theta)$ bin using Eq. (6.27). The result is shown in Fig. 6.15.
The statistical error σ_d of the dilution factor can be calculated using Gaussian error propagation as

$$
\begin{aligned}
\sigma_d &= \sqrt{\left(\sigma_{cN^{\text{carbon}}} \cdot \frac{1}{N^{\text{butanol}}}\right)^2 + \left(\sigma_{N^{\text{butanol}}} \cdot \frac{cN^{\text{carbon}}}{(N^{\text{butanol}})^2}\right)^2} \\
&= \frac{1}{N^{\text{butanol}}} \cdot \sqrt{\sigma_{cN^{\text{carbon}}}^2 + \sigma_{N^{\text{butanol}}}^2 \cdot (1-d)^2} \\
&\overset{(*)}{\approx} \frac{\sigma_{cN^{\text{carbon}}}}{N^{\text{butanol}}}.
\end{aligned}
\tag{6.31}
$$

The approximation $(*)$ is valid because for the available data $\sigma_{cN^{\text{carbon}}}^2 \approx 10\,\sigma_{N^{\text{butanol}}}^2$. Thus, the statistical error of the butanol data has only a negligible influence on σ_d. This is of consequence for the further analysis, because it means that no correlation between the dilution factor and the butanol data needs to be considered.
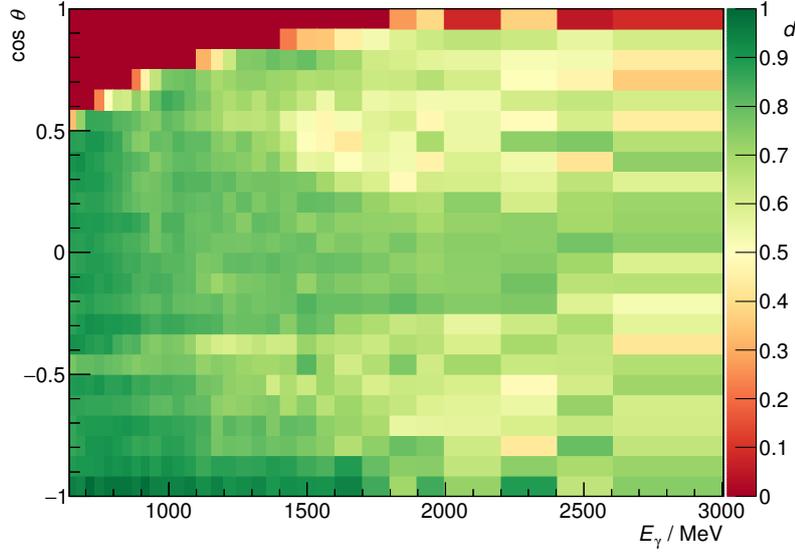
Figure 6.15: The dilution factor d for the reaction $\gamma p \to p\pi^0$ as a function of E_γ and $\cos\theta$.

The systematic error σ_d^{sys} due to the uncertainty of the carbon scaling factor is given by

$$\sigma_d^{\mathrm{sys}} = \sigma_c^{\mathrm{sys}} \cdot \frac{N^{\mathrm{carbon}}}{N^{\mathrm{butanol}}} = \frac{\sigma_c^{\mathrm{sys}}}{c} \cdot (1 - d) \tag{6.32}$$

using Gaussian error propagation. Even with the rather large error $\sigma_c^{\mathrm{sys}}/c \approx 10\,\%$, the error σ_d^{sys} is significantly smaller than 0.1, in particular in the bins where the dilution factor is large, and therefore $1 - d \ll 1$.

To better visualize the structures in the energy and angular dependence of the dilution factor, it is shown in Fig. 6.16 after integration over all angles or over all beam energies, respectively. The decrease of d with increasing E_γ is a consequence of the much wider cut needed on the missing recoiling proton mass for higher energies (cf. Fig. 5.23 and Appendix C.1), which results in more carbon events being reconstructed. The structures visible in Fig. 6.16a are mainly caused by the shape of the cross section for the reaction $\gamma p \to p\pi^0$, while the structures visible in Fig. 6.16b are mostly a consequence of the detector acceptance. This can be understood qualitatively using the Monte Carlo simulated data, as discussed in the following.

6.3.3.1 Comparison to Monte Carlo Simulations

In order to determine a dilution factor using the Monte Carlo simulation, generated data with and without Fermi motion are used.[14] The phasespace-distributed Monte Carlo datasets (1) and (2) (see Table 5.3) can be used to study the influence of the detector

---

[14] This only takes into account the effects of Fermi motion. Final state interaction in the C and O nuclei is neglected. As a consequence, a quantitative comparison of d_{MC} to the dilution factor obtained from data will have a large systematic uncertainty. However, this study is only done to qualitatively understand the shape of the dilution factor.

(a) Beam energy dependence   (b) Angular dependence
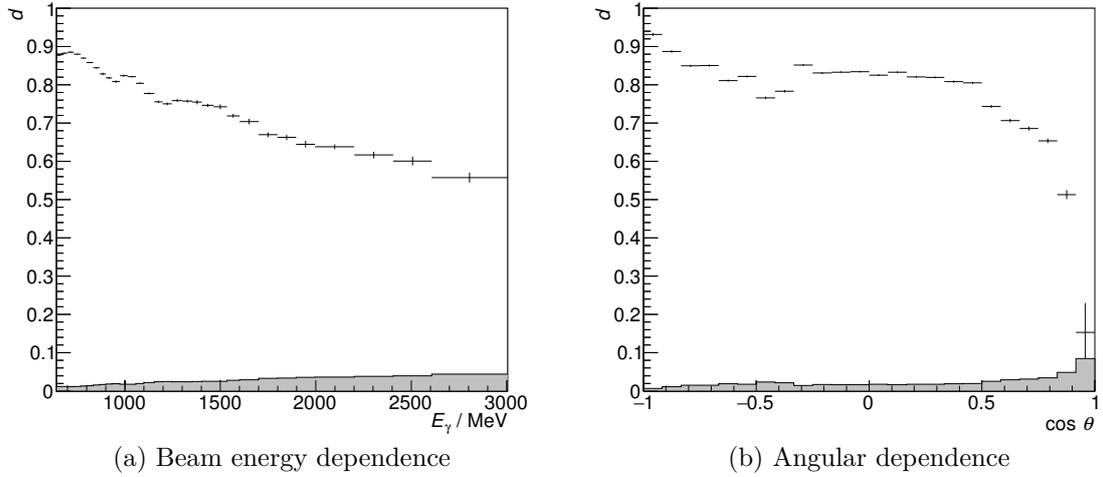
Figure 6.16: The dilution factor d for the reaction $\gamma p \rightarrow p\pi^0$ as a function of E_γ (integrated over all angles) and $\cos\theta$ (integrated over E_γ). The systematic error due to the uncertainty of the carbon scaling factor is shown as gray bars.

acceptance on the dilution factor. To also study the influence of the shape of the cross section on the dilution factor, the Monte Carlo datasets (3) and (4) can be used. It should be noted that the contribution from bound neutrons is neglected in the simulation. This is expected to influence the absolute value of the simulated dilution factor, but is adequate for a qualitative comparison to the data. In general, the Monte Carlo dilution factor is given by

$$d_{\mathrm{MC}} = \frac{N_{\mathrm{MC}}^{\mathrm{free}}}{N_{\mathrm{MC}}^{\mathrm{free}} + c \cdot N_{\mathrm{MC}}^{\mathrm{fermi}}}. \tag{6.33}$$

In case the same number of Monte Carlo events with and without Fermi motion are generated, the scaling factor $c = 3.2$ is given only by the molecular composition of butanol. Otherwise, the ratio of the number of generated events has to be taken into account as well. As a first cross check, a dilution factor can be calculated from the *generated* events of the phasespace-distributed Monte Carlo data. This of course yields the molecular dilution factor $d_{\mathrm{mol}} = 10/42$, as can be seen in Fig. 6.17a. By calculating a dilution factor using the *reconstructed* Monte Carlo events, one can see the influence of the detector acceptance (cf. Fig. 5.29a) on the dilution factor. As can be seen in in Fig. 6.17b, this dilution factor is already significantly larger than d_{mol} and largely resembles the dilution factor obtained from the data.

The influence of the cross section on the dilution factor can be studied using the *generated* events of the Monte Carlo data distributed according to the cross section as given by the BnGa PWA. The resulting dilution factor is shown in Fig. 6.18a. On average, one still obtains the molecular dilution factor. However, local maxima in the cross section lead to a larger dilution factor, whereas local minima in the cross section decrease the dilution factor. This is a consequence of the Fermi motion of the bound nucleons, which leads to a blurring of the structures observed in the cross section. Hence, peaks and dips are less

(a) generated

(b) reconstructed
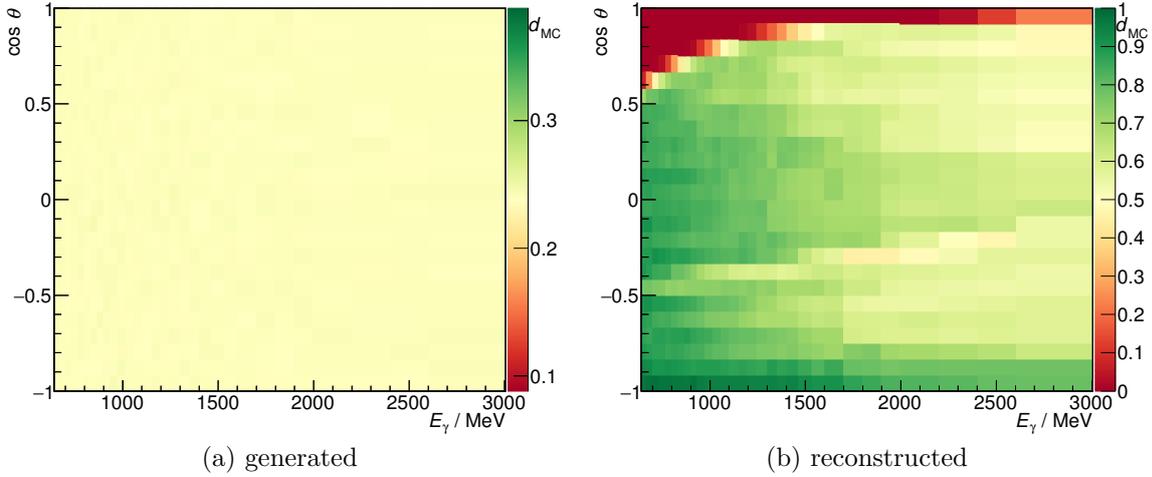
Figure 6.17: The simulated dilution factor d_{MC} for the reaction $\gamma p \rightarrow p\pi^0$ as obtained using the phasespace-distributed Monte Carlo data.

(a) generated

(b) reconstructed
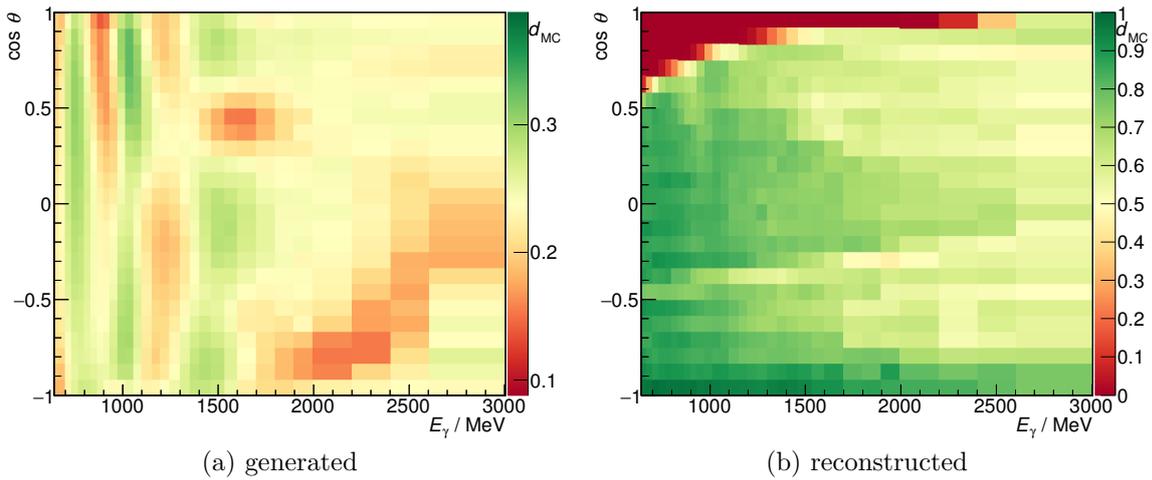
Figure 6.18: The simulated dilution factor d_{MC} for the reaction $\gamma p \rightarrow p\pi^0$ as obtained using the Monte Carlo data distributed according to the cross sections as given by the BnGa PWA. (Note the difference in scale on the color axis.)

pronounced in the cross section for bound nucleons compared to the free proton, and these structures remain visible in the ratio.

The combined effect of the acceptance and the cross section on the dilution factor can be seen in Fig. 6.18b, where the dilution factor calculated from the *reconstructed* events of the $\mathrm{d}\sigma/\mathrm{d}\Omega$-distributed Monte Carlo data is shown. The qualitative agreement with the measured dilution factor is very good. The (minor) quantitative difference can be attributed to uncertainties in the simulation, in particular concerning the Fermi motion which is only approximated. Also, the absence of final state interaction in the simulation is expected to have an influence in the order of a few percent.

In summary, the shape of the dilution factor is mostly determined by the detector acceptance. Prominent structures in the cross section have a smaller, but also clearly visible influence on the dilution factor. In particular the structures in the energy dependence can be attributed to the cross section, as can seen in Fig. 6.19b.

(a) phasespace

(b) $d\sigma/d\Omega$ from BnGa PWA
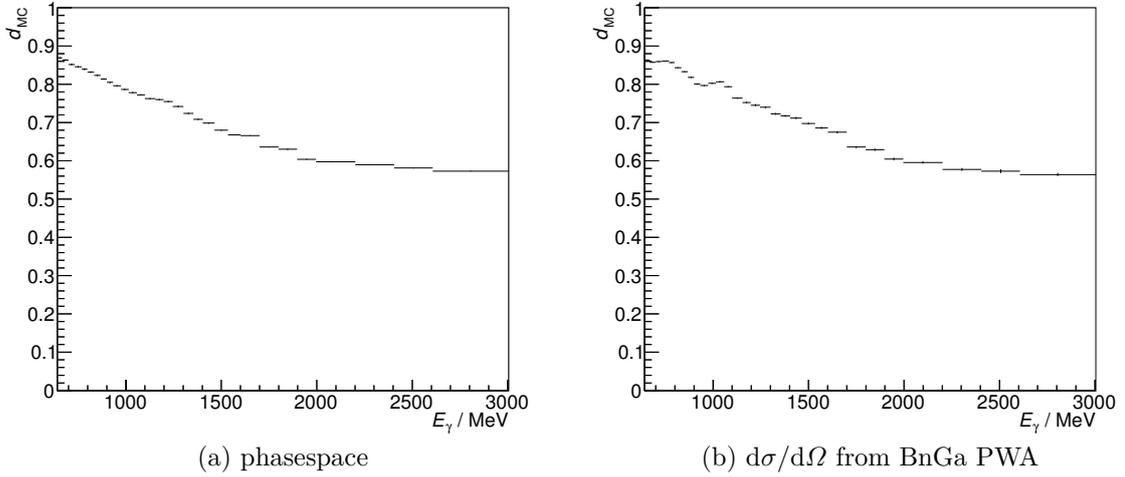
Figure 6.19: The energy dependence of the simulated dilution factor d_{MC} for the reaction $\gamma p \to p\pi^0$, shown for the phasespace- and $d\sigma/d\Omega$-distributed Monte Carlo data. The difference between the two highlights the influence of the resonance structures on the dilution factor. In particular the second and third resonance regions are visible as clear peaks in (b), at $E_\gamma \approx 800\,\mathrm{MeV}$ and $E_\gamma \approx 1050\,\mathrm{MeV}$, respectively.

6.3.3.2 Comparison for Different Cut Widths

As mentioned earlier, the widths of the kinematic cuts used in the event selection (cf. Section 5.4) have an influence on the dilution factor. Wider cuts, leading to a larger event sample, also result in a larger carbon background in the event sample, yielding a smaller dilution factor. This can be seen in Fig. 6.20, where the energy and angular dependence of the dilution factor are shown for different cut widths.

As will be seen later in this chapter, the statistical error of the polarization observables is proportional to the inverse dilution factor. Therefore, a large dilution factor is desirable, incentivizing narrow cuts. But narrower cuts also reduce the size of the reconstructed event sample, resulting in a larger statistical error. To find the optimal cut width, the figure of merit $\mathfrak{F}$, which is proportional to the statistical error of the polarization observables, is defined as

$$\mathfrak{F} = \frac{1}{d} \cdot \frac{1}{\sqrt{\varepsilon}}, \tag{6.34}$$

where ε is the efficiency of the cuts, i.e. $\varepsilon = 1$ for infinitely wide cuts and

$$\varepsilon = \mathrm{erf}\left(\frac{n}{\sqrt{2}}\right)^m \tag{6.35}$$

(a) Beam energy dependence (integrated over $\cos\theta$)   (b) Angular dependence (integrated over E_γ)
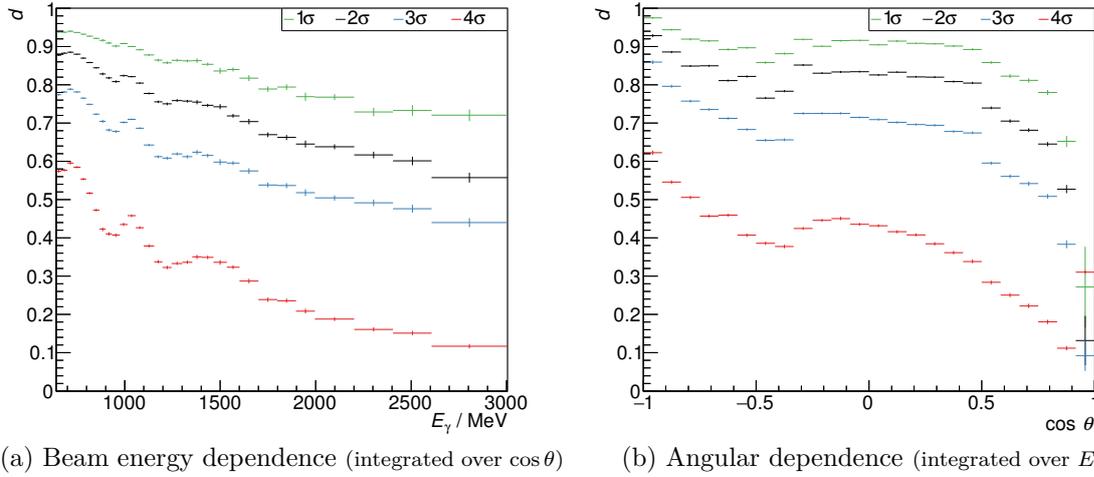
Figure 6.20: The dilution factor d for the reaction $\gamma p \to p\pi^0$, for different cut widths used in the event selection (cf. Section 5.4). The dilution factor decreases for wider cuts, and the influence of structures in the cross section (e.g. the second, third, and fourth resonance region) on the dilution factor becomes much more pronounced for wider cuts.

Table 6.4: The figure of merit for different cut widths. The average dilution factor d is determined from the data, the cut efficiency ε of the four cuts is estimated assuming independent normal distributions (cf. Eq. (6.35)).

cut width	d	ε	$\mathfrak{F}$
$1\,\sigma$	0.89	0.217	2.41
$2\,\sigma$	0.80	0.830	1.37
$3\,\sigma$	0.68	0.989	1.48
$4\,\sigma$	0.36	0.999	2.78

for m independent $n\,\sigma$ wide cuts, assuming normal distributions. The optimal cut width is then given by the minimum of $\mathfrak{F}$. Table 6.4 shows the figure of merit for different cut widths. The minimum lies between $2\,\sigma$ and $3\,\sigma$ wide cuts. Since a narrower cut also reduces a possible background contamination of the event sample and therefore the systematic uncertainty,[15] a $2\,\sigma$ wide cut was chosen for this analysis.

6.3.4 Determination of the Dilution Factor for the Reaction $\gamma p \to p\eta$

The dilution factor for the reaction $\gamma p \to p\eta(\eta \to \gamma\gamma)$ is determined exactly the same way as for the reaction $\gamma p \to p\pi^0$, using Eq. (6.27). The result is shown in Fig. 6.21. Because of the coarser binning the structures caused by the detector acceptance are less pronounced. Again, to better visualize the energy and angular dependence, the dilution factor is shown in Fig. 6.22 after integration over all angles or beam energies, respectively.

---

[15] A detailed investigation of background contamination will be given in Chapter 7.
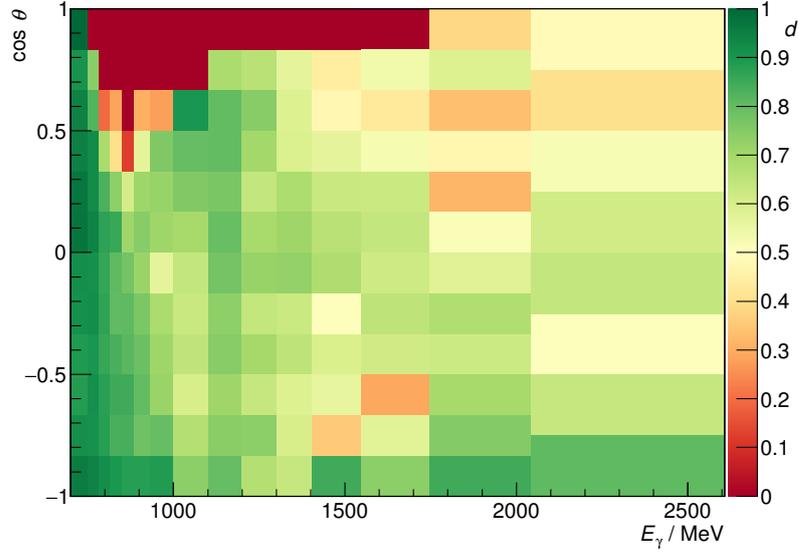
Figure 6.21: The dilution factor d for the reaction $\gamma p \to p\eta$ as a function of E_γ and $\cos\theta$. In the region of vanishing acceptance for the free proton reactions (cf. Fig. 5.29b) d is close to 0, because only reactions off bound protons contribute.

(a) Beam energy dependence

(b) Angular dependence
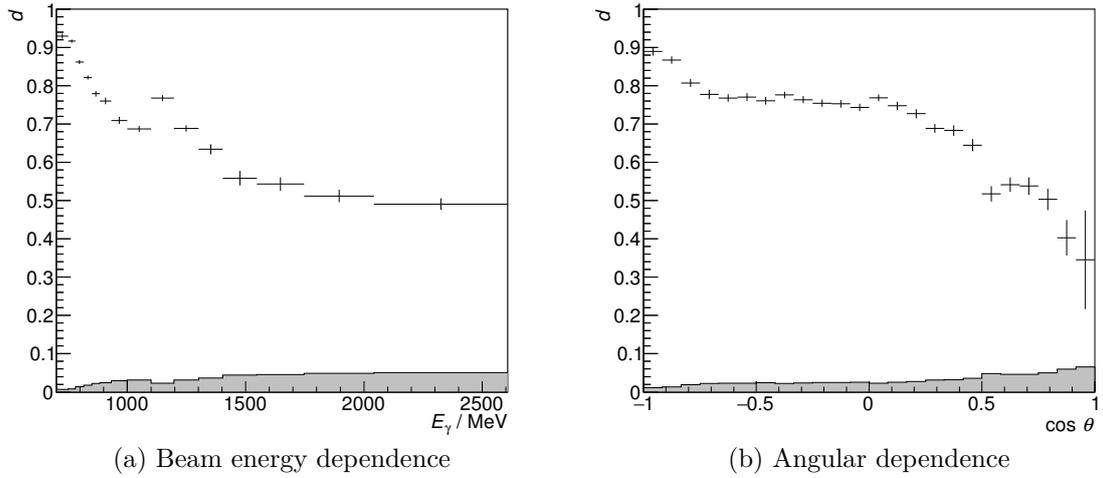
Figure 6.22: The dilution factor d for the reaction $\gamma p \to p\eta$ as a function of E_γ (integrated over all angles) and $\cos\theta$ (integrated over E_γ). The systematic error due to the uncertainty of the carbon scaling factor is shown as gray bars. The peak at $E_\gamma = 1150\,\text{MeV}$ coincides with a local maximum of the η photoproduction cross section (cf. Fig. 2.1).

With the polarization degree and dilution factor determined, all prerequisites for the determination of the polarization observables are now available. Two different methods to extract the polarization observables from the reconstructed event sample are presented in the next section.

6.4 Determination of the Polarization Observables

While the process of single pseudoscalar meson photoproduction using an unpolarized beam and an unpolarized target is rotationally symmetric around the beam axis, this symmetry is broken by a transversely polarized target or a linearly polarized photon beam. In this case, the cross section is given by (cf. Eq. (2.18))

$$\frac{\mathrm{d}\sigma}{\mathrm{d}\Omega} = \left(\frac{\mathrm{d}\sigma}{\mathrm{d}\Omega}\right)_0 \cdot \left(1 - \delta\Sigma\cos(2\varphi) + \Lambda_y(T - \delta P\cos(2\varphi)) - \Lambda_x\delta H\sin(2\varphi)\right), \qquad (6.36)$$

where $\left(\frac{\mathrm{d}\sigma}{\mathrm{d}\Omega}\right)_0$ is the unpolarized cross section, Σ, T, P, and H are the occurring polarization observables, δ is the degree of linear photon polarization, and φ the angle of the photon polarization plane (defined by the momentum and the polarization vector of the photon) with respect to the reaction plane (see Fig. 6.23), which contains all initial and final state particles of the reaction. Λ_x and Λ_y are the degrees of target polarization along the respective axes of the coordinate system, which is defined as follows by the direction of the particles (see also Fig. 2.2):

$$\vec{e}_z = \frac{\vec{p}_\gamma}{|\vec{p}_\gamma|} \qquad\qquad \vec{e}_y = \frac{\vec{e}_z \times \vec{p}_{\text{meson}}}{|\vec{e}_z \times \vec{p}_{\text{meson}}|} \qquad\qquad \vec{e}_x = \vec{e}_y \times \vec{e}_z \qquad (6.37)$$

This coordinate system is related to the detector coordinate system through a rotation around the beam axis. With ϕ being the measured azimuthal angle of the produced meson, Eq. (6.36) can be transformed to the detector coordinate system, resulting in

$$\frac{\mathrm{d}\sigma}{\mathrm{d}\Omega} = \left(\frac{\mathrm{d}\sigma}{\mathrm{d}\Omega}\right)_0 \cdot \Big(1 - \delta\Sigma\cos\big(2(\alpha - \phi)\big) + \Lambda T\sin(\beta - \phi) \qquad\qquad (6.38)$$

$$- \delta\Lambda P\cos\big(2(\alpha - \phi)\big)\sin(\beta - \phi) - \delta\Lambda H\sin\big(2(\alpha - \phi)\big)\cos(\beta - \phi)\Big)$$

where α is the azimuthal angle of the beam photon polarization plane, β the azimuthal angle of the target polarization direction, and Λ the degree of target polarization. The relation of the various angles in the different coordinate systems is also shown in Fig. 6.23.

The polarization observables can now be determined using the ϕ distribution of the reconstructed reactions. However, Eq. (6.38) is not used directly, since the measurement of ϕ-dependent cross sections requires precise control of all intrinsic asymmetries of the detector system. This is not possible without introducing additional systematic uncertainties due to acceptance and efficiency correction. Instead, two different methods are used which do not require the absolute measurement of the polarized cross section, resulting in much smaller systematic uncertainties.

6.4.1 Determination Using the Event Yield Asymmetries

One way of measuring the polarization observables is the measurement of asymmetries instead of cross sections. To achieve this, measurements were performed using two opposite directions of target polarization $\beta_\uparrow = \beta$ and $\beta_\downarrow = \beta + 180°$ as well as two orthogonal
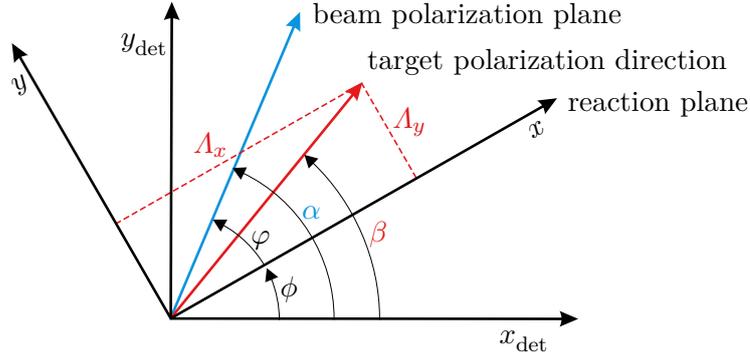
Figure 6.23: Definition of coordinate systems and polarization directions. The z-axis, which is not shown in the figure, points along the beam axis, i.e. toward the reader.

directions of beam polarization $\alpha^{\parallel} = \alpha$ and $\alpha^{\perp} = \alpha + 90°$, resulting in four different combinations of beam and target polarization. This allows the measurement of the following asymmetries:

$$A_{\Sigma}(\phi) := \frac{1}{\delta} \cdot \frac{\sigma_{\uparrow}^{\perp} + \sigma_{\downarrow}^{\perp} - \sigma_{\uparrow}^{\parallel} - \sigma_{\downarrow}^{\parallel}}{\sigma_{\uparrow}^{\perp} + \sigma_{\downarrow}^{\perp} + \sigma_{\uparrow}^{\parallel} + \sigma_{\downarrow}^{\parallel}} = \frac{1}{\delta} \cdot \frac{\sigma^{\perp} - \sigma^{\parallel}}{\sigma^{\perp} + \sigma^{\parallel}} = \Sigma \, \cos(2(\alpha - \phi)) \tag{6.39a}$$

$$A_{T}(\phi) := \frac{1}{\Lambda} \cdot \frac{\sigma_{\uparrow}^{\parallel} + \sigma_{\uparrow}^{\perp} - \sigma_{\downarrow}^{\parallel} - \sigma_{\downarrow}^{\perp}}{\sigma_{\uparrow}^{\parallel} + \sigma_{\uparrow}^{\perp} + \sigma_{\downarrow}^{\parallel} + \sigma_{\downarrow}^{\perp}} = \frac{1}{\Lambda} \cdot \frac{\sigma_{\uparrow} - \sigma_{\downarrow}}{\sigma_{\uparrow} + \sigma_{\downarrow}} = d \cdot T \, \sin(\beta - \phi) \tag{6.39b}$$

$$A_{PH}(\phi) := \frac{1}{\delta\Lambda} \cdot \frac{\sigma_{\uparrow}^{\perp} - \sigma_{\downarrow}^{\perp} - \sigma_{\uparrow}^{\parallel} + \sigma_{\downarrow}^{\parallel}}{\sigma_{\uparrow}^{\perp} + \sigma_{\downarrow}^{\perp} + \sigma_{\uparrow}^{\parallel} + \sigma_{\downarrow}^{\parallel}} = d \cdot P \, \cos(2(\alpha - \phi)) \sin(\beta - \phi) \tag{6.39c}$$

$$+ d \cdot H \, \sin(2(\alpha - \phi)) \cos(\beta - \phi)$$

As the acceptance and other systematic effects of the detector are the same for each setting, the cross sections σ can be replaced by the normalized event yield N.

An additional difficulty arises from the fact that, in general, the degrees of beam and target polarization are different for each of the four combinations. This can be taken into account by normalizing the event yields to the corresponding polarization values, resulting in

$$A_{\Sigma}(\phi) = \frac{1}{2N_0} \cdot \left(\frac{N^{\perp}}{\delta^{\perp}} - \frac{N^{\parallel}}{\delta^{\parallel}} \right) - \frac{1}{2} \cdot \left(\frac{1}{\delta^{\perp}} - \frac{1}{\delta^{\parallel}} \right) \tag{6.40a}$$

$$A_{T}(\phi) = \frac{1}{2N_0} \cdot \left(\frac{N_{\uparrow}}{\Lambda_{\uparrow}} - \frac{N_{\downarrow}}{\Lambda_{\downarrow}} \right) - \frac{1}{2} \cdot \left(\frac{1}{\Lambda_{\uparrow}} - \frac{1}{\Lambda_{\downarrow}} \right) \tag{6.40b}$$

$$A_{PH}(\phi) = \frac{1}{4N_0} \cdot \left(\frac{N_{\uparrow}^{\perp}}{\delta_{\uparrow}^{\perp}\Lambda_{\uparrow}^{\perp}} - \frac{N_{\downarrow}^{\perp}}{\delta_{\downarrow}^{\perp}\Lambda_{\downarrow}^{\perp}} - \frac{N_{\uparrow}^{\parallel}}{\delta_{\uparrow}^{\parallel}\Lambda_{\uparrow}^{\parallel}} + \frac{N_{\downarrow}^{\parallel}}{\delta_{\downarrow}^{\parallel}\Lambda_{\downarrow}^{\parallel}} \right) \tag{6.40c}$$

$$- \frac{A_{\Sigma}}{2} \cdot \left(\frac{1}{\Lambda_{\uparrow}} - \frac{1}{\Lambda_{\downarrow}} \right) - \frac{A_{T}}{2} \cdot \left(\frac{1}{\delta^{\perp}} - \frac{1}{\delta^{\parallel}} \right) + \frac{1}{4} \cdot \left(\frac{1}{\delta^{\perp}} - \frac{1}{\delta^{\parallel}} \right) \cdot \left(\frac{1}{\Lambda_{\uparrow}} - \frac{1}{\Lambda_{\downarrow}} \right)$$

with the polarization weighted average event yields given by

$$N^{\|/\perp} := N_0 \cdot \left(1 - \delta^{\|/\perp} \Sigma \cos(2(\alpha - \phi))\right) = \left(\frac{N_\uparrow^{\|/\perp}}{\Lambda_\uparrow^{\|/\perp}} + \frac{N_\downarrow^{\|/\perp}}{\Lambda_\downarrow^{\|/\perp}}\right) \cdot \left(\frac{1}{\Lambda_\uparrow^{\|/\perp}} + \frac{1}{\Lambda_\downarrow^{\|/\perp}}\right)^{-1}$$

$$N_{\uparrow/\downarrow} := N_0 \cdot \left(1 + \Lambda_{\uparrow/\downarrow} T \sin(\beta - \phi)\right) = \left(\frac{N_{\uparrow/\downarrow}^{\|}}{\delta_{\uparrow/\downarrow}^{\|}} + \frac{N_{\uparrow/\downarrow}^{\perp}}{\delta_{\uparrow/\downarrow}^{\perp}}\right) \cdot \left(\frac{1}{\delta_{\uparrow/\downarrow}^{\|}} + \frac{1}{\delta_{\uparrow/\downarrow}^{\perp}}\right)^{-1}$$

$$N_0 = \left(\frac{N_\uparrow^{\|}}{\delta_\uparrow^{\|}\Lambda_\uparrow^{\|}} + \frac{N_\uparrow^{\perp}}{\delta_\uparrow^{\perp}\Lambda_\uparrow^{\perp}} + \frac{N_\downarrow^{\|}}{\delta_\downarrow^{\|}\Lambda_\downarrow^{\|}} + \frac{N_\downarrow^{\perp}}{\delta_\downarrow^{\perp}\Lambda_\downarrow^{\perp}}\right) \cdot \left(\frac{1}{\delta_\uparrow^{\|}\Lambda_\uparrow^{\|}} + \frac{1}{\delta_\uparrow^{\perp}\Lambda_\uparrow^{\perp}} + \frac{1}{\delta_\downarrow^{\|}\Lambda_\downarrow^{\|}} + \frac{1}{\delta_\downarrow^{\perp}\Lambda_\downarrow^{\perp}}\right)^{-1}$$

The statistical errors σ_{A_i} of the asymmetries A_i are calculated from the statistical errors σ_N of the normalized counts using Gaussian error propagation.

$$\sigma_{A_i} = \sqrt{\left(\sigma_{N_\uparrow^{\|}} \frac{\partial A_i}{\partial N_\uparrow^{\|}}\right)^2 + \left(\sigma_{N_\uparrow^{\perp}} \frac{\partial A_i}{\partial N_\uparrow^{\perp}}\right)^2 + \left(\sigma_{N_\downarrow^{\|}} \frac{\partial A_i}{\partial N_\downarrow^{\|}}\right)^2 + \left(\sigma_{N_\downarrow^{\perp}} \frac{\partial A_i}{\partial N_\downarrow^{\perp}}\right)^2} \tag{6.41}$$

This, however, requires the number of events in each $(E_\gamma, \cos\theta, \phi)$ bin and for each polarization setting to be $\gg 1$. With the available data sample, it is therefore not possible to analyze the η reaction (where several $(E_\gamma, \cos\theta, \phi)$ bins are empty because of statistical fluctuations) using this method. For the π^0 reaction, the data above $E_\gamma > 1900\,\text{MeV}$ also need to be excluded from the analysis due to the limited sample size. An alternative analysis, which is also feasible for these excluded data, will be presented in Section 6.4.2. Only for the reaction $\gamma p \to p\pi^0$ the polarization observables Σ, T, P, and H are determined by a χ^2-fit to the ϕ distributions of A_Σ, A_T, and A_{PH}, respectively.

6.4.1.1 Beam Asymmetry Σ

Using Eq. (6.39a), the beam asymmetry Σ can be determined with a one-parameter χ^2-fit, with fixed $\alpha = 45°$. The fits are shown for one energy bin in Fig. 6.24, all fits are shown in Appendix B. It can be seen that in forward direction there are too few reconstructed events for the fit to work. This is due to vanishing acceptance in that region.

To judge the quality of all fits, the confidence level of all fits is plotted in a histogram in Fig. 6.25. If the statistical errors of all data points are correct, and the data match the fit hypothesis, the confidence level is expected to be uniformly distributed between 0 and 1. For most fits this is the case, but additionally there is a peak at low confidence levels. These are fits of bins with vanishing acceptance (in forward direction), in which a few background events result in a $A_\Sigma(\phi)$ distribution which cannot be described by the fit function. Also, the assumption of Gaussian errors may not hold in these bins. If all bins with an acceptance below $10\,\%$ (cf. Section 5.5) are excluded, the confidence level distribution is indeed flat, as can be seen in Fig. 6.25. Therefore, only bins with an acceptance larger than $10\,\%$ are retained for further analysis.

In addition, it is possible to confirm the angle of the photon polarization plane, which was set up to $\alpha = 45°$. This is done by including α as a free parameter in the fit to $A_\Sigma(\phi)$.
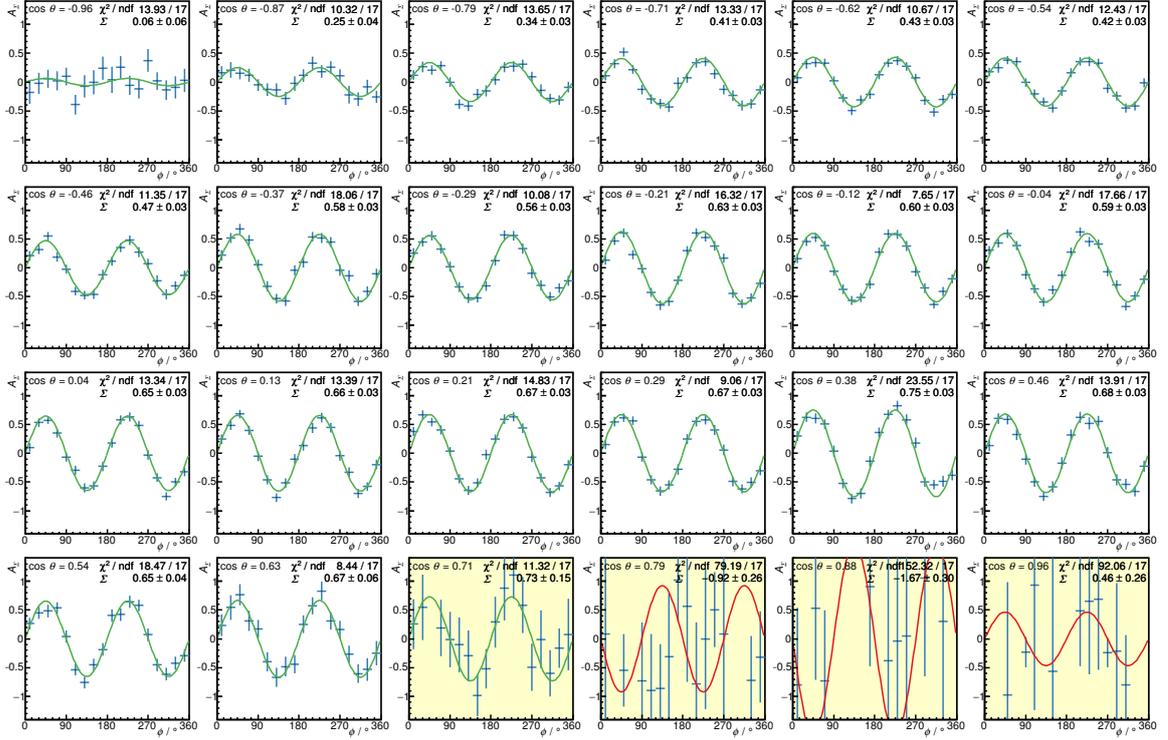
Figure 6.24: The fits to $A_\Sigma(\phi)$ for the energy bin $833\,\text{MeV} < E_\gamma < 868\,\text{MeV}$ for the reaction $\gamma p \to p\pi^0$. Bins with an acceptance $< 10\,\%$ are marked in yellow.
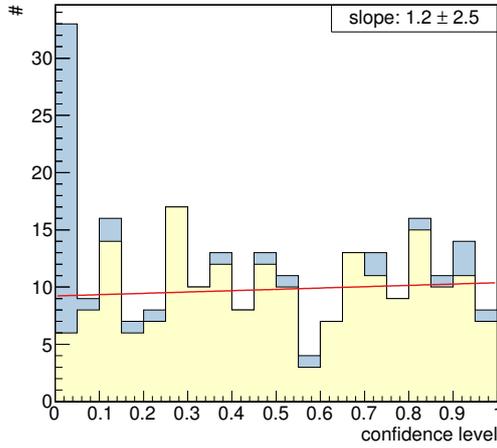
Figure 6.25: The confidence level of all $A_\Sigma(\phi)$ fits (blue) and the fits in bins with an acceptance $> 10\,\%$ (yellow). The slope, determined by a maximum likelihood fit [BC84] (red line), is consistent with 0.
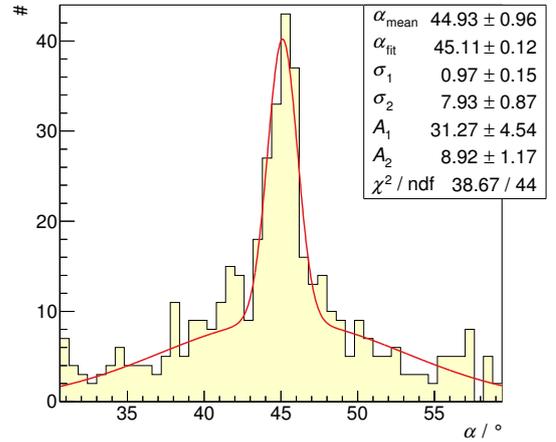
Figure 6.26: Histogram of the fitted angle α of the photon polarization plane. The error weighted average α_{mean} of all values, as well as the value α_{fit} determined by a fit to the histogram, are compatible with $\alpha = 45°$.
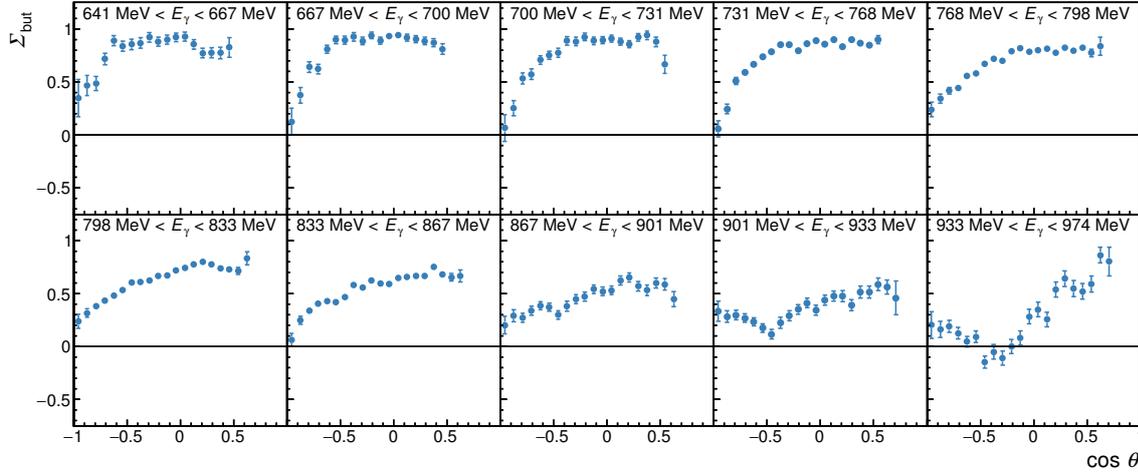
Figure 6.27: The beam asymmetry Σ_{but} as obtained using the fit to the event yield asymmetry A_Σ. The error bars represent the statistical uncertainty only. The missing data points at large $\cos\theta$ are due to the low acceptance in that kinematic region (cf. Section 5.5, Fig. 5.29a).

As can be seen in Fig. 6.26, the average from all fits is compatible with $\alpha = 45°$, as is the mean value determined by a multi-Gaussian[16] fit to the histogram. Since the distribution of the values of the fit parameter α is rather wide, α is fixed to its expected value for the fits used to determine the polarization observables.

The resulting beam asymmetry Σ is shown in Fig. 6.27. The error bars shown include statistical errors only. A detailed discussion of systematic uncertainties will be given in Chapter 7.

It should be noted at this point that the beam asymmetry Σ determined in this experiment is *not* identical to the beam asymmetry of reactions off the free proton, but instead contains also the beam asymmetry of reactions off bound nucleons in the butanol target:

$$\Sigma = d \cdot \Sigma_{\mathrm{free}} + (1 - d) \cdot \Sigma_{\mathrm{bound}} =: \Sigma_{\mathrm{but}} \tag{6.42}$$

The results for Σ are therefore not used any further, except for a qualitative comparison to other high-precision measurements of Σ performed by other experiments using a liquid hydrogen target. This comparison will be presented in Chapter 8.

6.4.1.2 Target Asymmetry *T*

Using Eq. (6.39b) the target asymmetry T can be determined with a one-parameter χ^2-fit, with fixed $\beta = 99.7°$.[17] The fits are shown for one energy bin in Fig. 6.28, all fits are shown

---

[16] For each $(E_\gamma, \cos\theta)$ bin, the determined value of α has a different statistical uncertainty, which is influenced by the number of events and the amplitude of the asymmetry in that bin. The distribution of all n α values is therefore given by the sum of n Gaussian distributions with the same mean and different widths. An adequate description can already be achieved by the sum of two Gaussians $f(\alpha) = A_1 \exp(-(\alpha - \alpha_{\mathrm{fit}})^2/2\sigma_1^2) + A_2 \exp(-(\alpha - \alpha_{\mathrm{fit}})^2/2\sigma_2^2)$, as can be seen in Fig. 6.26.

[17] See Section 4.2, Eq. (4.3).
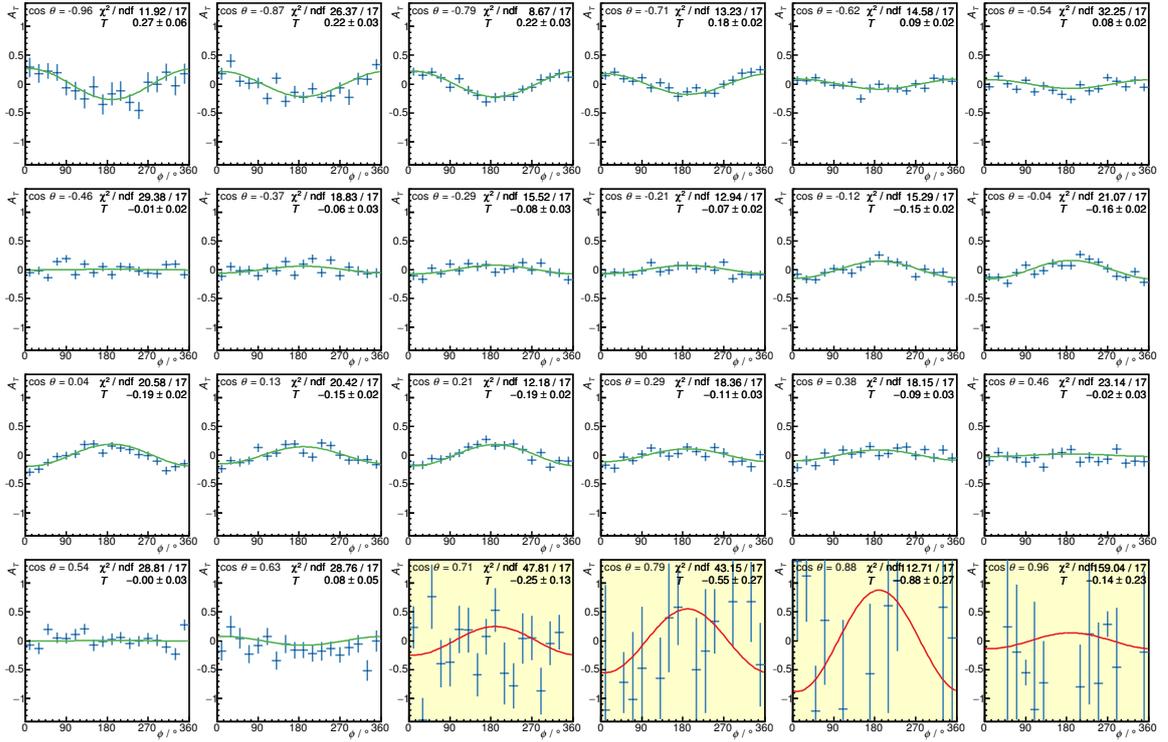
Figure 6.28: The fits to $A_T(\phi)$ for the energy bin $833\,\mathrm{MeV} < E_\gamma < 868\,\mathrm{MeV}$ for the reaction $\gamma p \to p\pi^0$. Bins with an acceptance $< 10\,\%$ are marked in yellow.
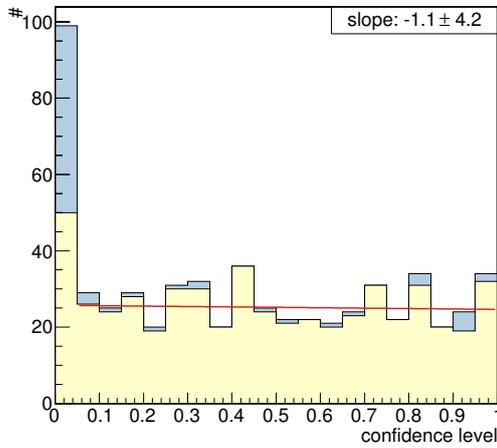
Figure 6.29: The confidence level of all $A_T(\phi)$ fits (blue) and the fits in bins with an acceptance $> 10\,\%$ (yellow). The slope, determined by a maximum likelihood fit [BC84] (red line) to all bins $> 10\,\%$, is consistent with 0.
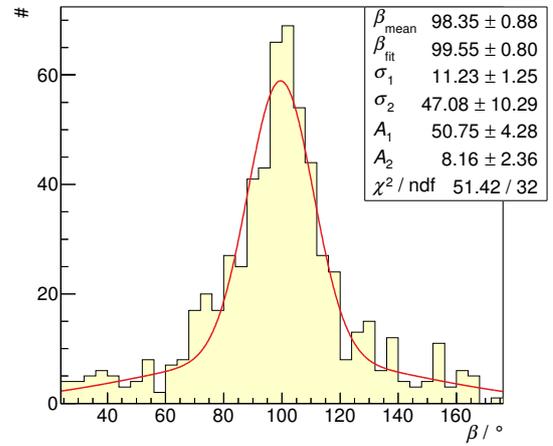
Figure 6.30: Histogram of the fitted angle β of the target polarization direction. The error weighted average β_{mean} of all values, as well as the value β_{fit} determined by a fit to the histogram, are compatible with $\beta = (99.7 \pm 0.3)°$. The fit function is of the form $f(\beta) = A_1 \exp(-(\beta - \beta_{\mathrm{fit}})^2/2\sigma_1^2) + A_2 \exp(-(\beta - \beta_{\mathrm{fit}})^2/2\sigma_2^2)$.

in Appendix B. The confidence level of all fits is plotted in a histogram in Fig. 6.29. Again, the confidence level distribution is flat, except for a peak at low values which is eliminated if only bins with an acceptance $> 10\%$ are used. The results for T are shown in Fig. 6.31. Again, it is possible to confirm the angle of the target polarization direction, which was determined to $\beta = (99.7 \pm 0.3)°$ using the deflection of electromagnetic background particles by the magnetic field surrounding the target (for details, see Eq. (4.3) in Section 4.2). As can be seen in Fig. 6.30, the average from all fits is compatible with this value. Hence, β is fixed to its expected value for the fits used to determine the polarization observables.
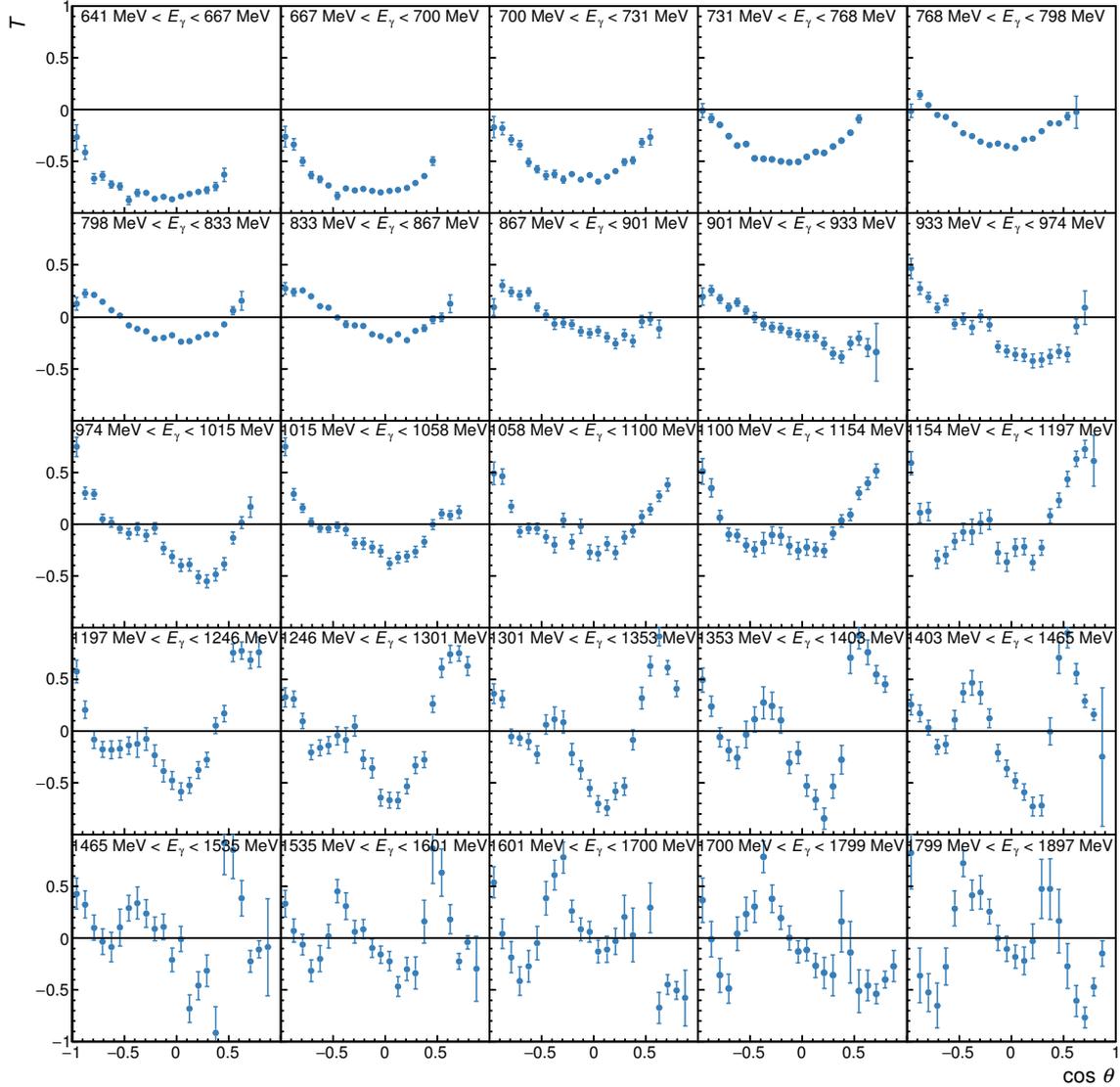
Figure 6.31: The target asymmetry T as obtained using the fit to the event yield asymmetry A_T. The error bars represent the statistical uncertainty only. A detailed discussion of the results will be given in Chapter 8.

6.4.1.3 Recoil Polarization *P* and Double Polarization Observable *H*

Using Eq. (6.39c) the recoil polarization P and the double polarization observable H can be determined simultaneously from

$$A_{PH} = d \cdot P \cos(2(\alpha - \phi)) \sin(\beta - \phi) + d \cdot H \sin(2(\alpha - \phi)) \cos(\beta - \phi) \qquad (6.43)$$

with a two-parameter χ^2-fit, with fixed $\alpha = 45°$ and $\beta = 99.7°$. The fits are shown for one energy bin in Fig. 6.32, all fits are shown in Appendix B. The confidence level of all fits is plotted in a histogram in Fig. 6.33. As with the fits for Σ and T, a peak is visible at low confidence level values, which is eliminated by excluding bins with an acceptance $< 10\%$ from further analysis.

Unlike the fits to A_Σ and A_T, the fit to A_{PH} has more than one parameter. It is therefore necessary to consider a possible correlation between the results for P and H. As can be seen in Fig. 6.34, however, the correlation coefficient is small for all fits. Therefore, P and H can be treated as uncorrelated. The results for P are shown in Fig. 6.35, and the results for H are shown in Fig. 6.36.
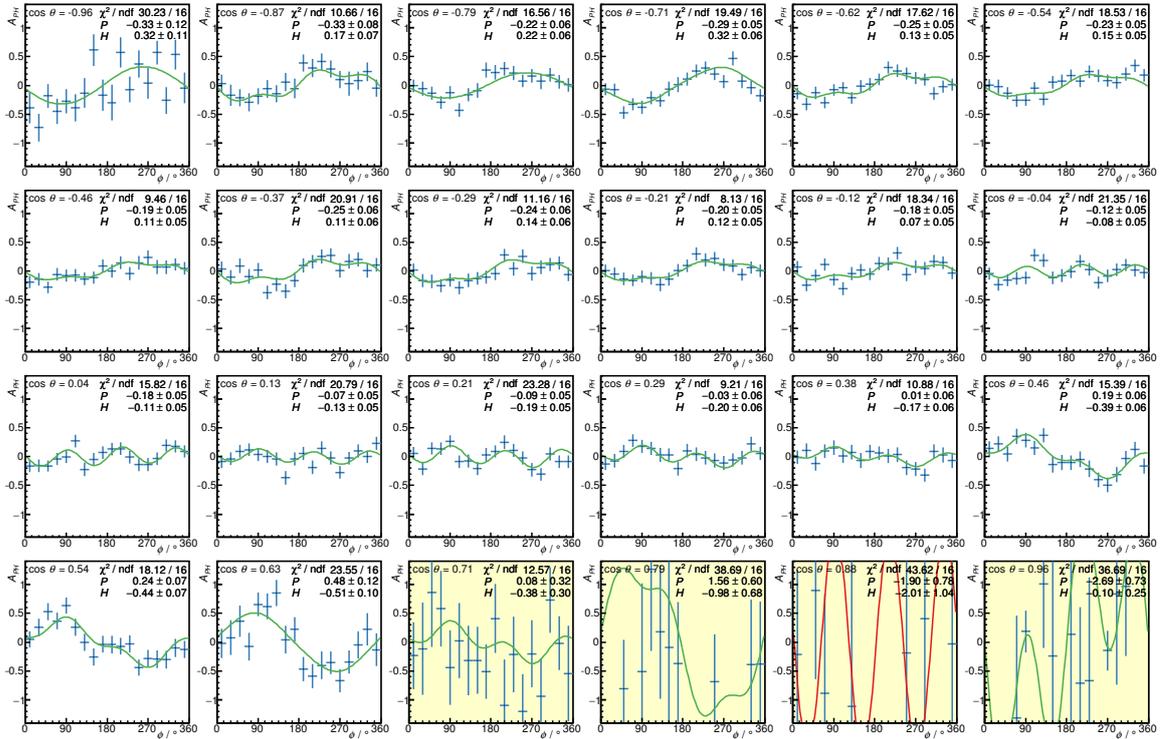
Figure 6.32: The fits to $A_{PH}(\phi)$ for the energy bin $833\,\text{MeV} < E_\gamma < 868\,\text{MeV}$ for the reaction $\gamma p \to p\pi^0$. Bins with an acceptance $< 10\%$ are marked in yellow.
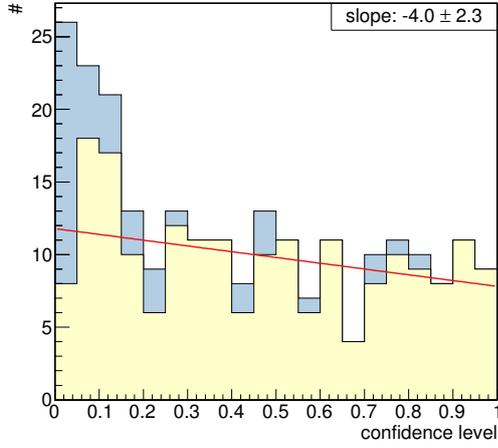
Figure 6.33: The confidence level of all $A_{PH}(\phi)$ fits (blue) and the fits in bins with an acceptance $> 10\%$ (yellow). The slope, determined by a maximum likelihood fit [BC84] (red line), is consistent with 0 on the 2σ level.
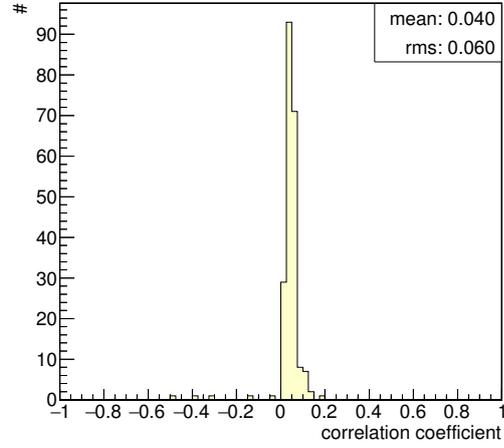
Figure 6.34: The correlation coefficient of P and H for all $A_{PH}(\phi)$ fits, as given by MINUIT [JR75].
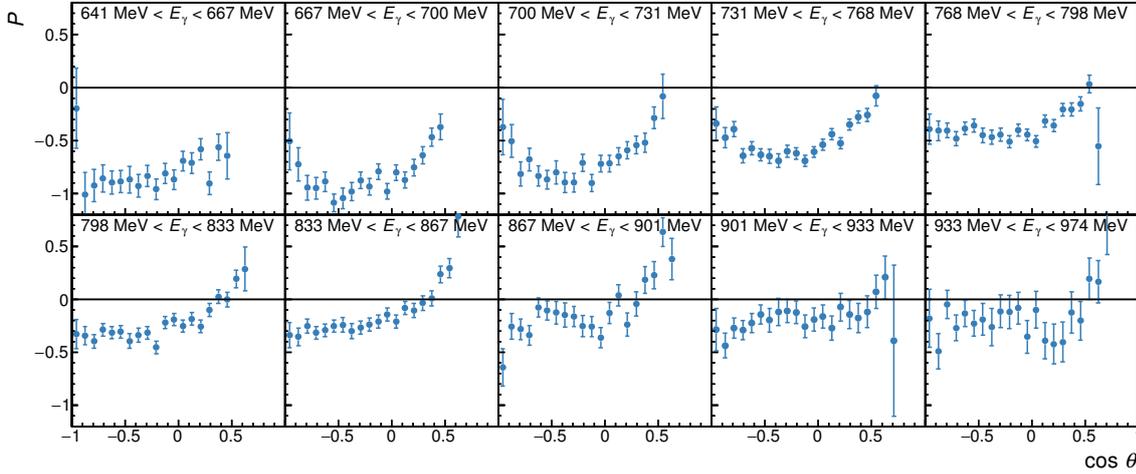
Figure 6.35: The recoil polarization P as obtained using the fit to the event yield asymmetry A_{PH}. The error bars represent the statistical uncertainty only. A detailed discussion of the results will be given in Chapter 8.
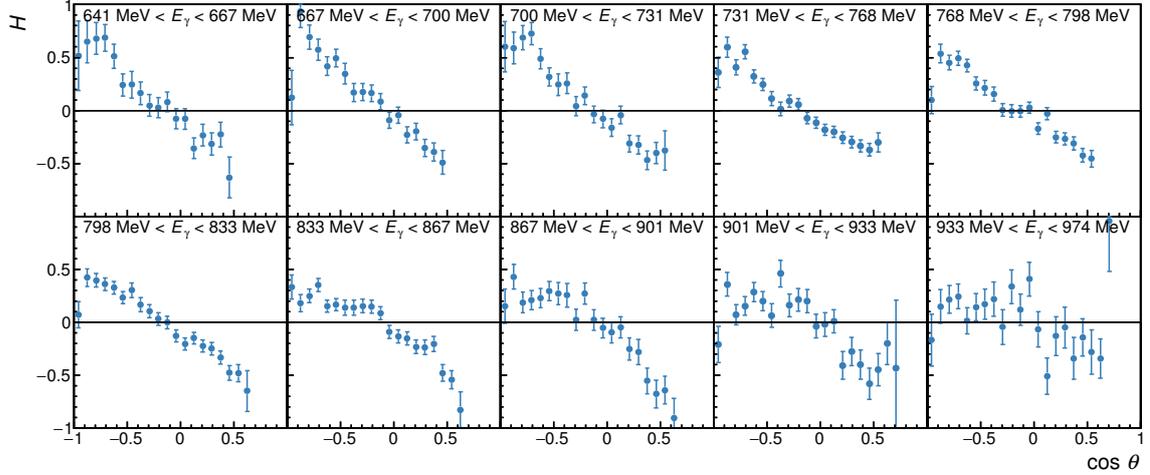
Figure 6.36: The double polarization observable H as obtained using the fit to the event yield asymmetry A_{PH}. The error bars represent the statistical uncertainty only. A detailed discussion of the results will be given in Chapter 8.

6.4.2 Determination Using an Event Based Maximum Likelihood Fit

In case of a very limited number of events, the previous method to determine the polarization observables cannot be used: the event yield asymmetry method requires the number of events in each $(E_\gamma, \cos\theta, \phi)$ bin, for each polarization setting, to be $\gg 1$, in order to correctly calculate the statistical errors using the Gaussian approximation. This, however, is not the case for the highest E_γ bins for the reaction $\gamma p \to p\pi^0$, and the majority of bins for the reaction $\gamma p \to p\eta$. On the other hand, if the total number of events is not too large, an event based maximum likelihood fit is possible without too much computational cost. The data are still binned in E_γ and $\cos\theta$, but the polarization observables are extracted from the ϕ distribution of the events in an unbinned fit.

In case of a flat detector acceptance, the azimuthal distribution of the measured events is given by the cross section as stated in Eq. (6.38). The normalized[18] probability density function (PDF) for one event is thus given by[19]

$$
\begin{aligned}
f_{\text{phy}}(\phi, \delta, \Lambda, \Sigma, T, P, H) = {} & 1 - \delta\Sigma\cos(2(\alpha-\phi)) + \Lambda T \sin(\beta-\phi) \\
& - \delta\Lambda P \cos(2(\alpha-\phi))\sin(\beta-\phi) \\
& - \delta\Lambda H \sin(2(\alpha-\phi))\cos(\beta-\phi).
\end{aligned} \tag{6.44}
$$

---

[18] For improved readability, all probability density functions in this chapter are normalized to 2π. To calculate actual probabilities, a factor of $\frac{1}{2\pi}$ has to be included in each PDF. However, for the likelihood fit the normalization only needs to be constant, i.e. it must not depend on any fit parameter. The factor $\frac{1}{2\pi}$ can thus be omitted, resulting in $f_{\text{phy}} = \frac{d\sigma}{d\Omega} / \left(\frac{d\sigma}{d\Omega}\right)_0$.

[19] Please note that the dilution factor is not included in Eq. (6.44) to avoid the complicated treatment of its uncertainty in the fit. As a result, the values for the observables obtained from the fit are diluted and need to be corrected afterwards by the dilution factor.

This can be rewritten as a Fourier series

$$f_{\text{phy}} = 1 + \sum_{k=1}^{3} a_k \sin(k\phi) + b_k \cos(k\phi) \tag{6.45}$$

with the coefficients

$$
\begin{aligned}
a_1 &= -\Lambda T \cos(\beta) - \tfrac{1}{2}\delta\Lambda \left(P - H\right) \left[\sin(2\alpha)\sin(\beta) + \cos(2\alpha)\cos(\beta)\right] \\
b_1 &= +\Lambda T \sin(\beta) - \tfrac{1}{2}\delta\Lambda \left(P - H\right) \left[\cos(2\alpha)\sin(\beta) - \sin(2\alpha)\cos(\beta)\right] \\
a_2 &= -\delta\Sigma \sin(2\alpha) \\
b_2 &= -\delta\Sigma \cos(2\alpha) \\
a_3 &= -\tfrac{1}{2}\delta\Lambda \left(P + H\right) \left[\sin(2\alpha)\sin(\beta) - \cos(2\alpha)\cos(\beta)\right] \\
b_3 &= -\tfrac{1}{2}\delta\Lambda \left(P + H\right) \left[\cos(2\alpha)\sin(\beta) + \sin(2\alpha)\cos(\beta)\right].
\end{aligned}
$$

The likelihood function $\mathcal{L}$ for a data set consisting of n events is defined as the product of the probabilities given by the PDF for each event [Bar89]:

$$\mathcal{L}(\Sigma, T, P, H) = \prod_{i=1}^{n} f_{\text{phy}}(\phi_i, \delta_i, \Lambda_i, \Sigma, T, P, H) \tag{6.46}$$

In the limit $n \to \infty$, $\mathcal{L}$ approaches a 4-dimensional Gaussian, as a consequence of the central limit theorem. The best estimator for the parameters Σ, T, P, and H is given by the position of the maximum of $\mathcal{L}$ [Bar89], and the uncertainty of the estimators is given by the σ of the Gaussian in the corresponding dimension. An equivalent approach, but much better suited for numerical calculations, is the minimization of $-\ln(\mathcal{L})$ instead of the maximization of $\mathcal{L}$. The smallest 1σ interval for the parameter estimators is then given by the interval in which

$$-\ln(\mathcal{L}) < -\ln(\mathcal{L}_{\text{max}}) + 0.5. \tag{6.47}$$

Before this method can be applied to extract the observables from the selected events, two additional problems need to be considered:

1. For the binned analysis, random coincidences between the tagged beam photons and the reaction products were eliminated by a sideband subtraction in the time difference spectrum (see Section 5.4). In an unbinned fit, the subtraction of sideband events is not possible. Instead, the sideband events, and the values of the observables for the sideband-background, need to be included in the likelihood function. The latter is done by replacing the PDF in the likelihood function by individual PDFs for the signal and the background contribution, resulting in

$$\mathcal{L} = \prod_{i=1}^{n} \xi \cdot f_{\text{phy}} + (1 - \xi) \cdot f_{\text{phy}}^{\text{bg}}, \tag{6.48}$$

   where ξ is the fraction of signal events after the cut around the coincidence peak. The PDF for the background $f_{\text{phy}}^{\text{bg}}$ is given by Eq. (6.45) as well, but with different values

for the polarization observables and therefore the coefficients a_i, b_i. To determine these values, the sideband events are also included in the likelihood function, with only $f_{\text{phy}}^{\text{bg}}$ contributing since no signal events are expected in the sideband.

The combined likelihood function for peak $(i = 1, \ldots, n)$ and sideband $(j = 1, \ldots, m)$ events is thus given by

$$\mathcal{L} = \prod_{i=1}^{n} \xi \cdot f_{\text{phy}}(\phi_i, \delta_i, \Lambda_i, \Sigma, T, P, H) + (1 - \xi) \cdot f_{\text{phy}}(\phi_i, \delta_i, \Lambda_i, \Sigma^{\text{bg}}, T^{\text{bg}}, P^{\text{bg}}, H^{\text{bg}})$$
$$\cdot \prod_{j=1}^{m} f_{\text{phy}}(\phi_j, \delta_j, \Lambda_j, \Sigma^{\text{bg}}, T^{\text{bg}}, P^{\text{bg}}, H^{\text{bg}}). \tag{6.49}$$

The weighting factor ξ can be calculated from the total number of peak events n and sideband events m using

$$\xi = \frac{n - s \cdot m}{n}, \tag{6.50}$$

where $s = 20$ is the ratio between the cut width around the peak and the sideband cut width (cf. Eq. (5.15)).

2. In general, the detector acceptance is not flat in ϕ. While it cancels in the calculation of asymmetries and does not need to be considered for the binned analysis discussed previously, the acceptance needs to be incorporated into the PDF for the unbinned analysis. If the acceptance f_{det} is known, this can be trivially accomplished:

$$\tilde{f}(\phi) = f_{\text{phy}}(\phi) \cdot f_{\text{det}}(\phi) \tag{6.51}$$

Since $\tilde{f}$ is not normalized, the normalized full PDF is given by[20]

$$f(\phi) = \frac{\tilde{f}(\phi)}{\frac{1}{2\pi} \int \tilde{f}(\varphi) \, d\varphi}. \tag{6.52}$$

However, $f_{\text{det}}(\phi)$ is not precisely known. But even an unknown f_{det} can be incorporated into the PDF, using its normalized Fourier series decomposition:

$$\tilde{f}(\phi) = f_{\text{phy}}(\phi) \cdot f_{\text{det}}(\phi) = f_{\text{phy}}(\phi) \cdot \left(\sum_{k=0}^{\infty} c_k \sin(k\phi) + d_k \cos(k\phi) \right), \tag{6.53}$$

where $c_0 = 0$ and $d_0 = 1$ without loss of generality. Using the definition of f_{phy} given in Eq. (6.45) one obtains

$$f(\phi) = \frac{\left(1 + \sum\limits_{k=1}^{3} a_k \sin(k\phi) + b_k \cos(k\phi) \right) \cdot \left(1 + \sum\limits_{k=1}^{\infty} c_k \sin(k\phi) + d_k \cos(k\phi) \right)}{1 + \dfrac{1}{2} \sum\limits_{k=1}^{3} a_k c_k + b_k d_k}. \tag{6.54}$$

---

[20] As a reminder, all the PDFs given in this chapter are normalized to 2π instead of 1 for improved readability.

Because of the orthogonality of the sin and cos functions, only the diagonal terms contribute to the normalization in the denominator of Eq. (6.54).

From Eq. (6.54) one might think that the parameters a_k and c_k, as well as b_k and d_k, are not independent, and therefore cannot be determined unambiguously. This is of course true for a data set with only one direction of beam and target polarization. However, by using all four combinations of the beam and target polarization directions, the coefficients a_k and b_k appear with different signs[21] for each of the four combinations, while the coefficients c_k and d_k remain unchanged. This allows the unambiguous separation of the physics coefficients a_k and b_k from the detector efficiency coefficients c_k and d_k.

Obviously, it is impossible to use an infinite number of parameters in the fit. The question is therefore, up to which order the Fourier expansion of the detector acceptance PDF needs to be done. To study this, it is useful to expand the product of the two Fourier series in the numerator of Eq. (6.54), and regroup the terms with the same coefficients c_k and d_k, resulting in an equation of the form

$$\tilde{f}(\phi) = \sum_{k=0}^{\infty} c_k \cdot \frac{1}{2} \left(\sum_{\ell=-3}^{3} -a_\ell \cos\big((k+\ell)\phi\big) + b_\ell \sin\big((k+\ell)\phi\big) \right) \tag{6.55}$$

$$+ d_k \cdot \frac{1}{2} \left(\sum_{\ell=-3}^{3} +a_\ell \sin\big((k+\ell)\phi\big) + b_\ell \cos\big((k+\ell)\phi\big) \right)$$

with $a_{-\ell} := -a_{+\ell}$, $b_{-\ell} := +b_{+\ell}$, $a_0 = c_0 = 0$, and $b_0 = d_0 = 1$. The coefficients c_k and d_k are occurring only in front of sin and cos terms of at least order $k-3$ in the trigonometric functions. For the determination of the coefficients a_k and b_k, which contain the polarization observables, only terms of total order up to 3 are relevant. Thus, it is sufficient to include only the detector asymmetry coefficients c_k and d_k that are influencing these terms. All coefficients c_k and d_k for $k > 6$ can therefore be ignored without influencing the results for the polarization observables because of the orthogonality of the $\sin(k\phi)$ and $\cos(k\phi)$ functions.

The full likelihood function is hence given by

$$\mathcal{L} = \prod_{i=1}^{n} \Big(\xi \cdot f(\phi_i, \delta_i, \Lambda_i, \Sigma, T, P, H, c_1, \ldots, c_6, d_1, \ldots, d_6) \tag{6.56}$$

$$+ (1-\xi) \cdot f(\phi_i, \delta_i, \Lambda_i, \Sigma^{\mathrm{bg}}, T^{\mathrm{bg}}, P^{\mathrm{bg}}, H^{\mathrm{bg}}, c_1^{\mathrm{bg}}, \ldots, c_6^{\mathrm{bg}}, d_1^{\mathrm{bg}}, \ldots, d_6^{\mathrm{bg}}) \Big)$$

$$\cdot \prod_{j=1}^{m} f(\phi_j, \delta_j, \Lambda_j, \Sigma^{\mathrm{bg}}, T^{\mathrm{bg}}, P^{\mathrm{bg}}, H^{\mathrm{bg}}, c_1^{\mathrm{bg}}, \ldots, c_6^{\mathrm{bg}}, d_1^{\mathrm{bg}}, \ldots, d_6^{\mathrm{bg}}),$$

with f given by Eq. (6.54). This function has 32 free parameters: 4 polarization observables,

---

[21] In Eq. (6.45) the change of the beam polarization direction $\alpha \to \alpha + 90°$ is equivalent to changing the sign of the polarization degree $\delta \to -\delta$. Analogously, $\beta \to \beta + 180°$ is equivalent to $\Lambda \to -\Lambda$.

12 Fourier coefficients of the detector asymmetry, and another $4 + 12$ parameters[22] for the sideband background.

Before the full likelihood function as given in Eq. (6.56) is used to extract the polarization observables, one needs to ascertain that the fit result is unbiased and the statistical errors obtained from the fit are correct. This can be studied using a toy Monte Carlo simulation.

6.4.2.1 Toy Monte Carlo Simulation

A toy Monte Carlo experiment is performed by generating pseudo events using a simple Monte Carlo simulation and applying the likelihood fit to the simulated events. By comparing the result with the simulation input, the likelihood method discussed above can be tested. One such experiment is done in the following steps:

1. Choose parameters:
   Beam and target polarization (δ and Λ) are set to plausible given values. Additionally, values are chosen for the fraction of background events ξ and the ratio s between peak and sideband cut width, as well as for the total number of events $n_{\alpha\beta}$ that are to be generated for each direction of the beam (α) and target (β) polarization.

2. Generate signal events:
   The parameters of the polarization observables in f_{phy} are also set to given values, and an arbitrary function f_{det} is chosen for the detector efficiency.[23] Then, for each beam and target polarization direction, the number of signal events that are to be generated needs to be determined. Since the number of signal events detected in a single experiment is not fixed but follows a Poisson distribution, this is done by choosing a random number $n_{\alpha\beta}^{\text{sig}}$ which is distributed according to $\text{Pois}((1 - \xi) \cdot n_{\alpha\beta})$. The simulated events can then be generated by choosing $n_{\alpha\beta}^{\text{sig}}$ random angles ϕ which are distributed according to $f_{\text{phy}} \cdot f_{\text{det}}$ with the given parameters.

3. Generate background events:
   This is done the same way as the signal events, but with different values for the polarization observables and possibly a different detector efficiency. However, this needs to be done twice: First, $n_{\alpha\beta}^{\text{bg}} \sim \text{Pois}(\xi \cdot n_{\alpha\beta})$ background events are generated and combined with the signal events. Then, additional $n_{\alpha\beta}^{\text{side}} \sim \text{Pois}(s \cdot \xi \cdot n_{\alpha\beta})$ sideband events are generated.

4. Perform the likelihood fit on the generated events:
   Using the likelihood function given in Eq. (6.56), the polarization observables and their statistical uncertainties can be determined from the simulated events using the maximum-likelihood method described previously in this chapter. The fit result can then be compared to the values originally used as input for the simulation.

---

[22] One might naively expect that the 12 Fourier coefficients of the detector asymmetry are identical for the signal and the sideband background. However, since the background events are due to random coincidences between the tagged beam photons and the reaction products, the beam energy and therefore the reaction kinematics are not identical. Because of the kinematic cuts used for the event selection, the differences in kinematics between signal and background events are small, but nevertheless non-negligible because of the finite width of the cuts. As a consequence, the detector asymmetry can be different for the signal and the sideband background.

[23] Here, it is not necessary to use the Fourier series decomposition of f_{det}, but any function can be used.

parameter	value
N	10000
$n_{\parallel\uparrow}$	500
$n_{\perp\uparrow}$	750
$n_{\parallel\downarrow}$	900
$n_{\perp\downarrow}$	660
$\delta_{\parallel\uparrow}, \Lambda_{\parallel\uparrow}$	$+0.65, +0.60$
$\delta_{\perp\uparrow}, \Lambda_{\perp\uparrow}$	$-0.55, +0.70$
$\delta_{\parallel\downarrow}, \Lambda_{\parallel\downarrow}$	$+0.50, -0.65$
$\delta_{\perp\downarrow}, \Lambda_{\perp\downarrow}$	$-0.60, -0.55$
$\Sigma, \Sigma^{\mathrm{bg}}$	$+0.5, -0.5$
T, T^{bg}	$-0.3, +0.3$
P, P^{bg}	$+0.2, -0.2$
H, H^{bg}	$-0.4, +0.4$
ξ	0.05
s	20

Table 6.5: Parameters used for the toy Monte Carlo simulation that is shown here as an example.
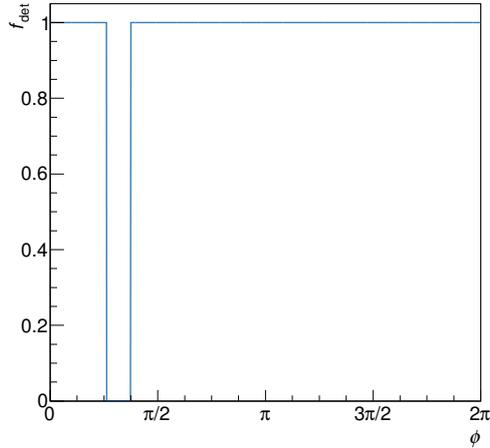
Figure 6.37: Detector efficiency f_{det} which was used as the worst case scenario for the toy Monte Carlo simulation.

In order to obtain statistically significant information on the quality of the fit procedure, a large number N of toy Monte Carlo experiments are performed. The quantities of interest are the normalized residuals of the polarization observables O:

$$\rho_O = \frac{O_{\mathrm{fit}} - O_{\mathrm{input}}}{\sigma_O} \qquad \text{with } O \in \{\Sigma, T, P, H\}, \tag{6.57}$$

where σ_O is the statistical uncertainty of the best estimator O_{fit}, as determined by the fit using Eq. (6.47). Ideally, the distribution of ρ_O should be normal, i.e. a Gaussian with mean $\mu = 0$ and width $\sigma = 1$. A biased fit would result in $\mu \neq 0$, and over- or underestimation of statistical errors would lead to $\sigma < 1$ or $\sigma > 1$, respectively.

Extensive studies were done with the toy Monte Carlo simulation, using various values for the parameters and different simulated detector efficiencies. For each of the simulations, the normalized residuals of the polarization observables have not shown any significant deviation from the normal distribution. It can thus be concluded that the likelihood function given in Eq. (6.56) provides an unbiased method to determine the polarization observables, and the statistical errors are accurately estimated.

The results of one simulation are shown here as an example, with the parameters as given in Table 6.5, and a detector efficiency f_{det} describing an acceptance hole with sharp edges as shown in Fig. 6.37, as a worst case scenario. The distributions of the parameters obtained from the fit are shown in Fig. 6.38 for the polarization observables, and in Fig. 6.39 for the Fourier coefficients of the detector efficiency. The distributions of the normalized residuals of the polarization observables are shown in Fig. 6.40, together with a normal distribution, showing good agreement with the expectations. The detector efficiency reconstructed from the Fourier coefficients is—in this extreme example with a large acceptance hole—only a very poor approximation of the actual efficiency, as can be seen in Fig. 6.41. Clearly, additional higher order coefficients would be needed to achieve an adequate description of the efficiency. It is, in principle, possible to include these higher order coefficients as parameters in the fit, although at the expense of a huge increase in computational effort.
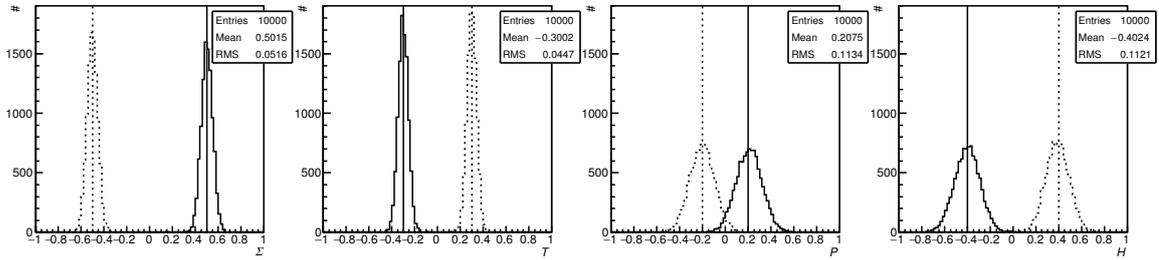
Figure 6.38: The distribution of the polarization observables as obtained from the likelihood fit to the toy Monte Carlo data. The solid histogram shows the signal observables, with the simulated value indicated as a vertical line, and the dotted histogram shows the background observables which are in this simulation expected to have the exact opposite sign.
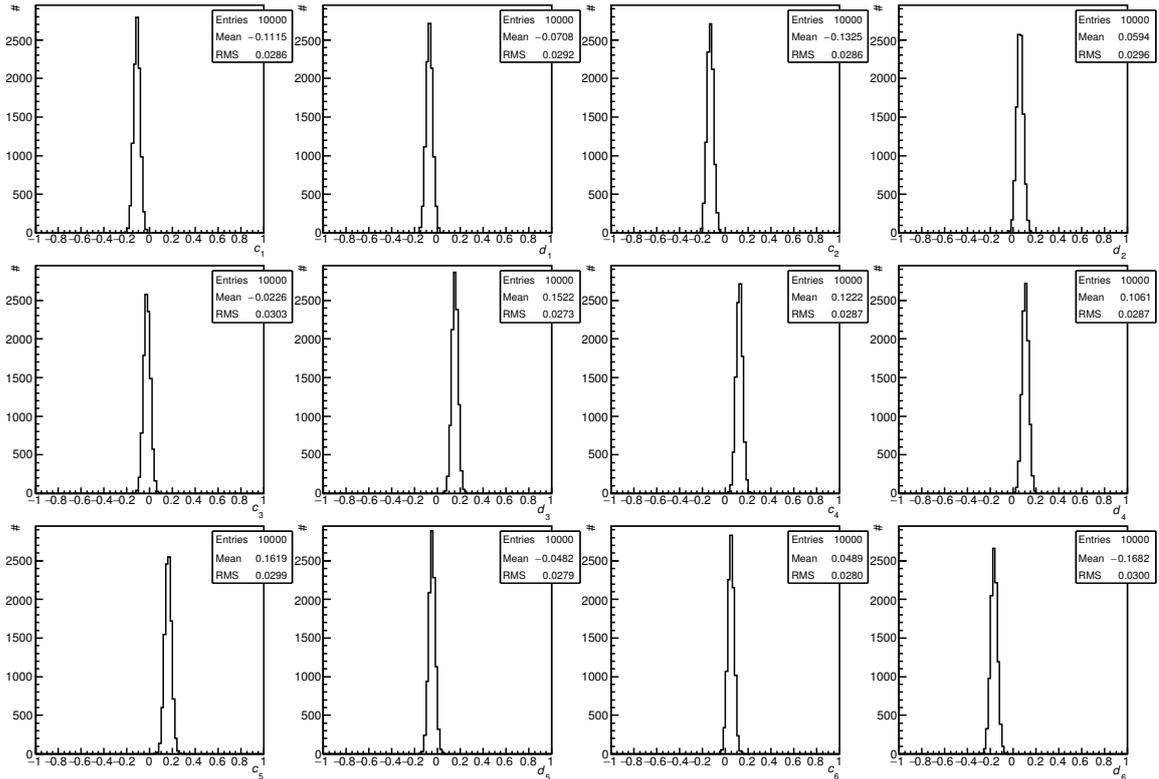
Figure 6.39: The distribution of the Fourier coefficients c_k and d_k of the detector efficiency f_{det}, as obtained from the likelihood fit to the toy Monte Carlo data.
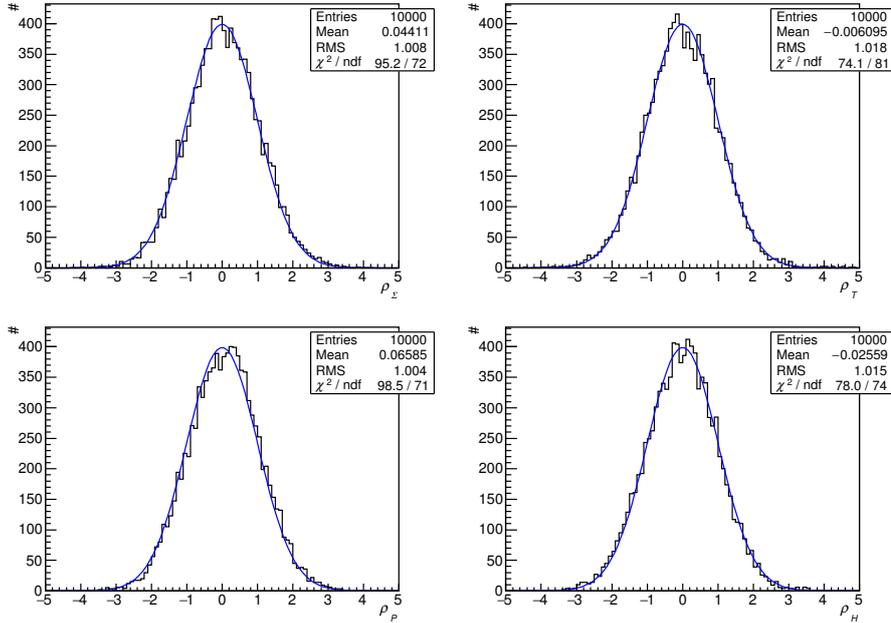
Figure 6.40: The distribution of the normalized residuals of the polarization observables, compared to a normal distribution.

Indeed, this leads to a better reconstruction of the detector efficiency, as can be seen in Fig. 6.41 for $k_{max} = 18$ and $k_{max} = 54$. But since these coefficients do not influence the determination of the polarization observables (because of the aforementioned orthogonality of the $\sin(k\phi)$ and $\cos(k\phi)$ functions), and since precise knowledge of any ϕ-asymmetry of the detector is not needed for this analysis, the higher order coefficients are not included in the fit.
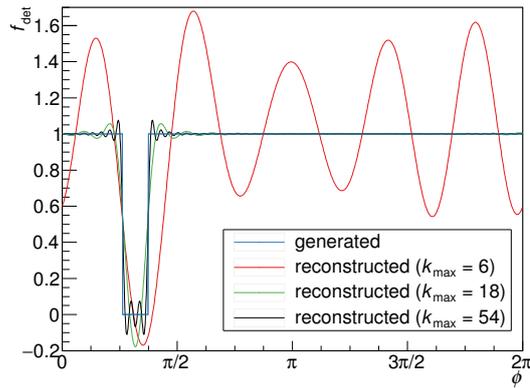
Figure 6.41: Detector efficiency f_{det} which was used as the worst case scenario for the toy Monte Carlo simulation, compared to the efficiency reconstructed from the Fourier coefficients as determined by the fit.

6.4.2.2 Results for the Polarization Observables

The likelihood fit can be used independently for each (E_γ, θ) bin to determine the four polarization observables. The values obtained from the fit are, however, not the polarization observables for a free proton target, but also receive contributions from the bound protons in the carbon and oxygen nuclei of the butanol target. For T, P, and H, where the unpolarized bound protons dilute the measured observables, the values obtained from the fit are divided by the dilution factor (see Section 6.3) to obtain the observables for a free proton target. Since the bound protons also contribute to the beam asymmetry (see Eq. (6.42)), the beam asymmetry for a free proton target cannot be obtained this way, and only Σ_{but} for the butanol is determined.

The results for the polarization observables Σ_{but}, T, P, and H in the bins where the fit did converge,[24] and where the acceptance is larger than $10\,\%$, are shown in Figs. 6.42 to 6.45 for the reaction $\gamma p \to p\pi^0$, and in Figs. 6.46 to 6.48 for the reaction $\gamma p \to p\eta$. A detailed discussion of the results will be given in Chapter 8.
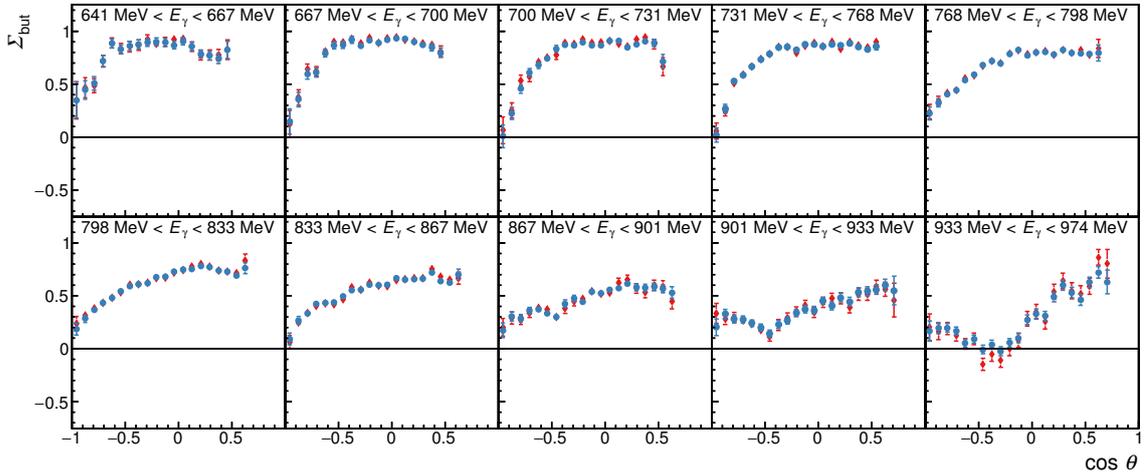
Figure 6.42: The beam asymmetry Σ_{but} for the reaction $\gamma p \to p\pi^0$ as obtained using the event based likelihood fit (blue). The error bars represent the statistical uncertainty only. Additionally, the results as obtained using the event yield asymmetry are shown for comparison (red).

---

[24] In a few bins the fit did not converge. These are mostly the bins where the χ^2 fit to the event yield asymmetry resulted in a low confidence level. In all bins with an acceptance $> 10\,\%$ the fit did converge.
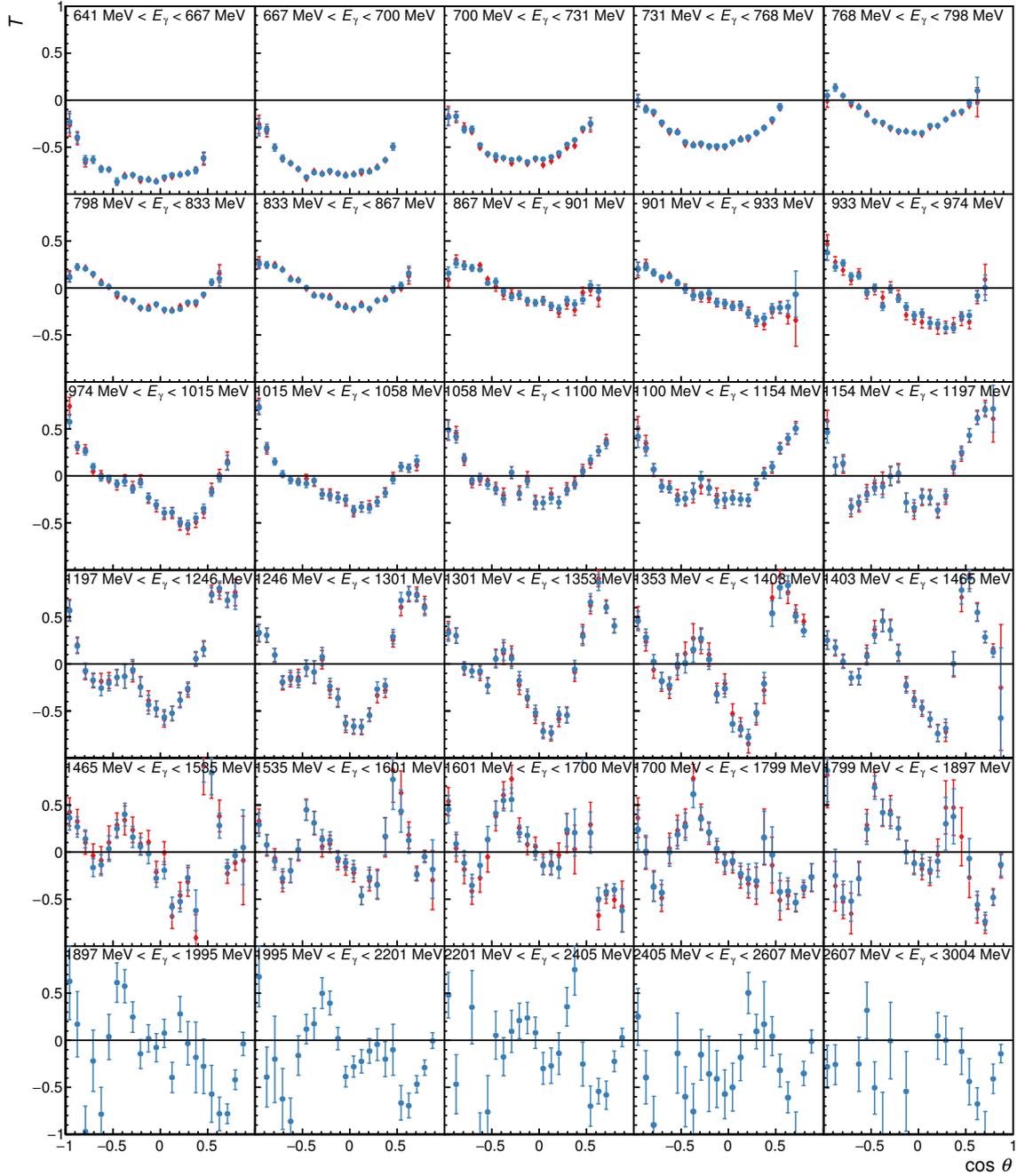
Figure 6.43: The target asymmetry T for the reaction $\gamma p \rightarrow p\pi^0$ as obtained using the event based likelihood fit (blue). The error bars represent the statistical uncertainty only. Additionally, the results as obtained using the event yield asymmetry are shown for comparison (red). With the likelihood fit, results in 5 additional energy bins are obtained.
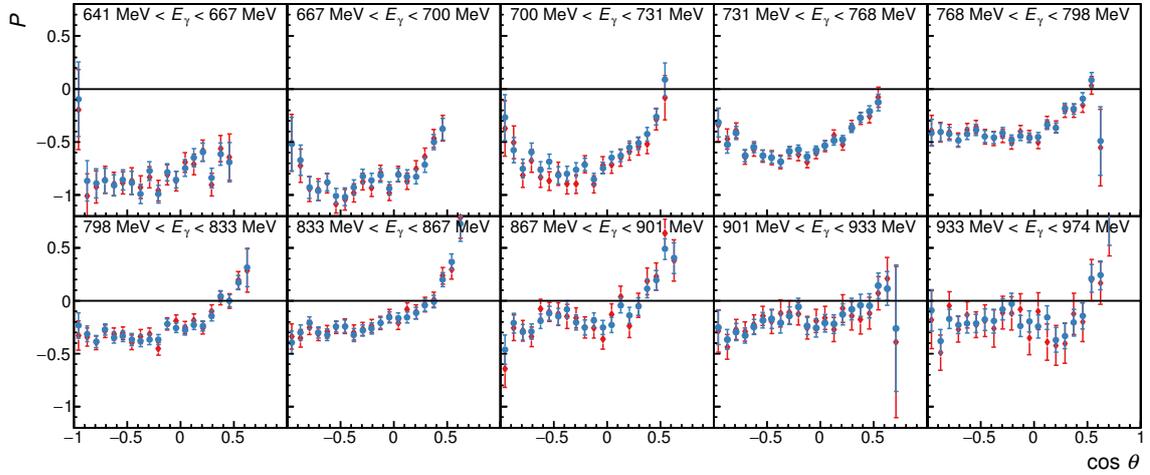
Figure 6.44: The recoil polarized P for the reaction $\gamma p \to p\pi^0$ as obtained using the event based likelihood fit (blue). The error bars represent the statistical uncertainty only. Additionally, the results as obtained using the event yield asymmetry are shown for comparison (red).
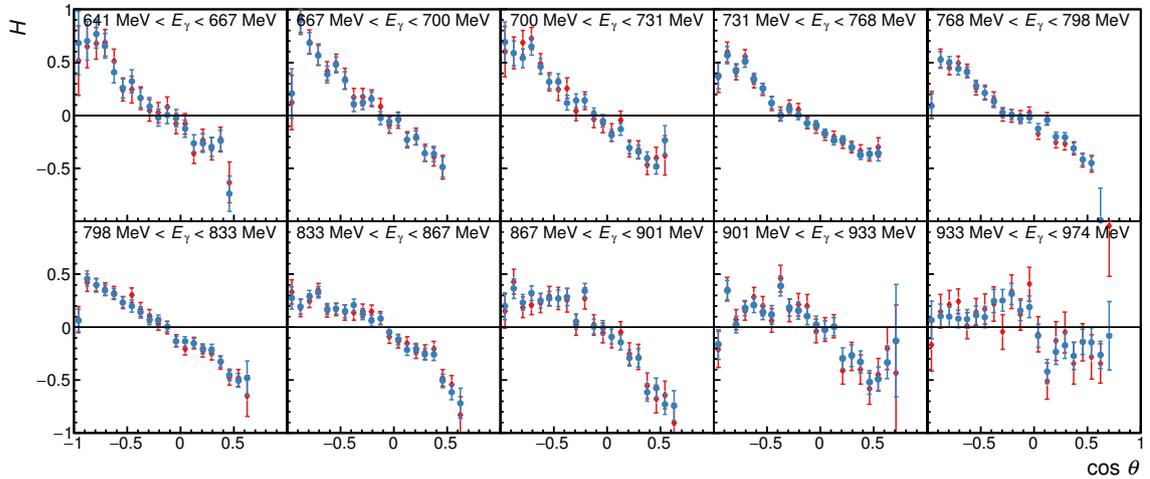
Figure 6.45: The double polarization observable H for the reaction $\gamma p \to p\pi^0$ as obtained using the event based likelihood fit (blue). The error bars represent the statistical uncertainty only. Additionally, the results as obtained using the event yield asymmetry are shown for comparison (red).
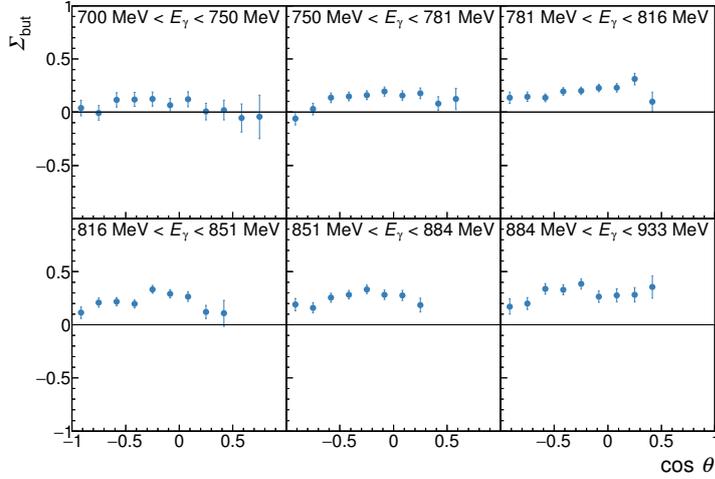
Figure 6.46: The beam asymmetry Σ_{but} for the reaction $\gamma p \to p\eta$ as obtained using the event based likelihood fit. The error bars represent the statistical uncertainty only.
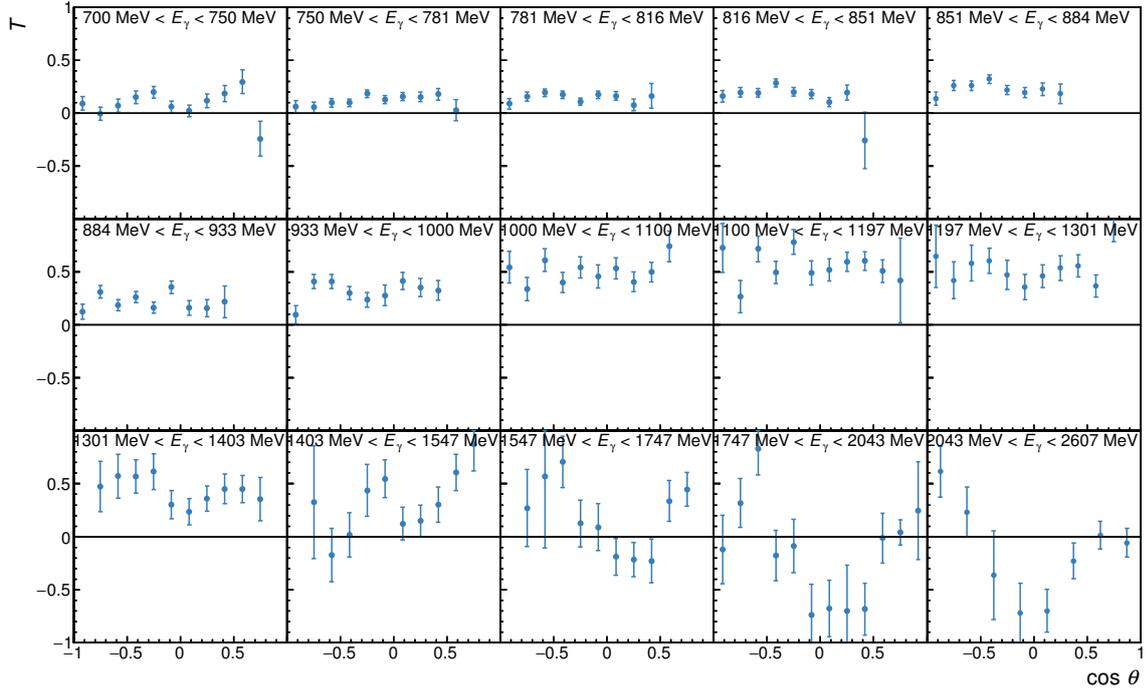
Figure 6.47: The target asymmetry T for the reaction $\gamma p \to p\eta$ as obtained using the event based likelihood fit. The error bars represent the statistical uncertainty only. A detailed discussion of the results will be given in Chapter 8.

(a) *P*   (b) *H*
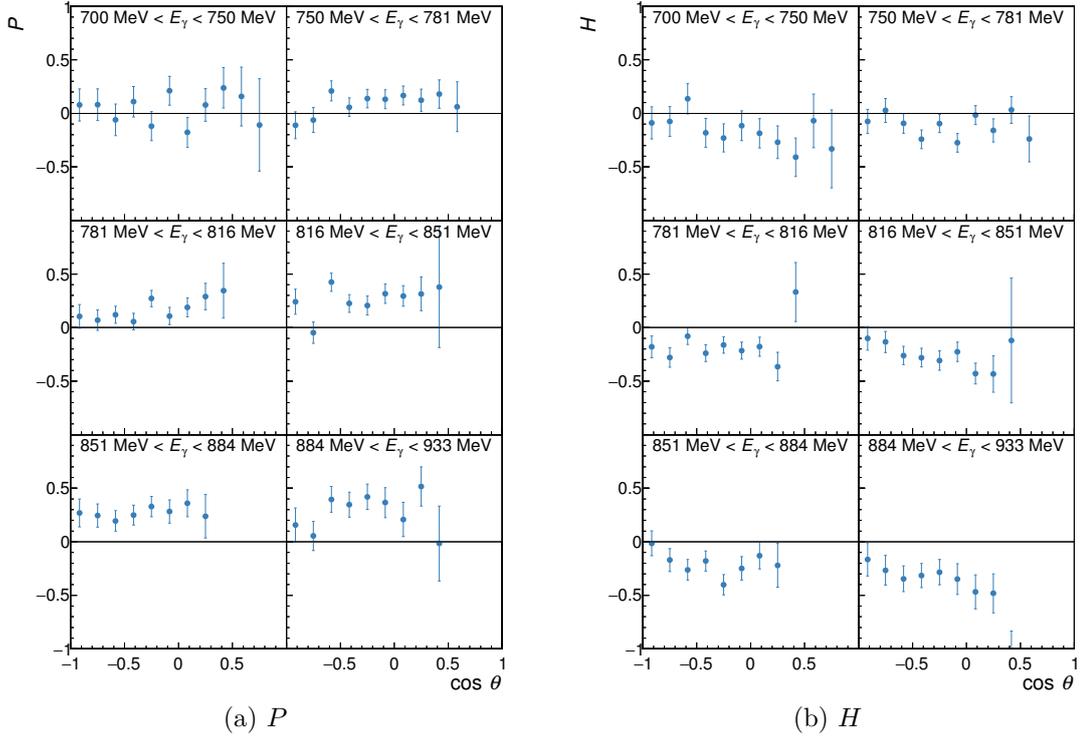
Figure 6.48: The recoil polarization *P* and the double polarization observable *H* for the reaction $\gamma p \to p\eta$ as obtained using the event based likelihood fit. The error bars represent the statistical uncertainty only. A detailed discussion of the results will be given in Chapter 8.

Additionally, the Fourier coefficients of the detector efficiency are shown in Fig. 6.49. Most coefficients are close to 0, corresponding to a flat detector efficiency, as expected. The few outliers are a result of some inefficient detector channels.

A comparison of the π^0 results with the results obtained using the event yield asymmetry method reveals no obvious discrepancy. By plotting the result of the likelihood fit versus the result of the event yield asymmetry method for each bin that has been analyzed using both methods (see Fig. 6.50), it can be easily seen that the two methods produce compatible results. Plotting the statistical uncertainties of the two methods versus each other it becomes obvious that the likelihood method is more precise in most of the bins. Therefore, the event yield asymmetry method is not used any further, except for a more detailed statistical analysis of possible systematic differences between the two methods, which will be discussed in Section 7.4.1. But first, the systematic uncertainties are discussed in detail the next chapter.
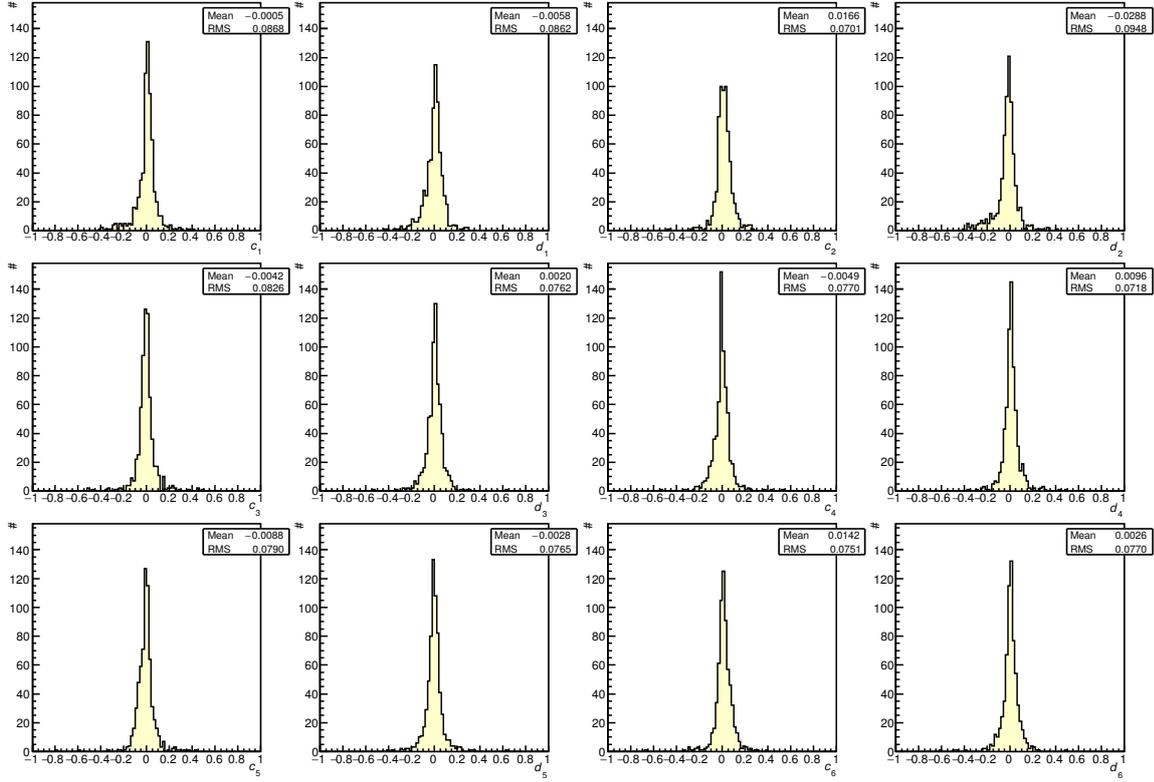
Figure 6.49: Histograms of the Fourier coefficients c_k and d_k of the detector efficiency f_{det}, as obtained from the likelihood fit to the π^0 data. Except for a few outliers, the coefficients are distributed around 0.

(a) Σ_{but} (b) T (c) P (d) H
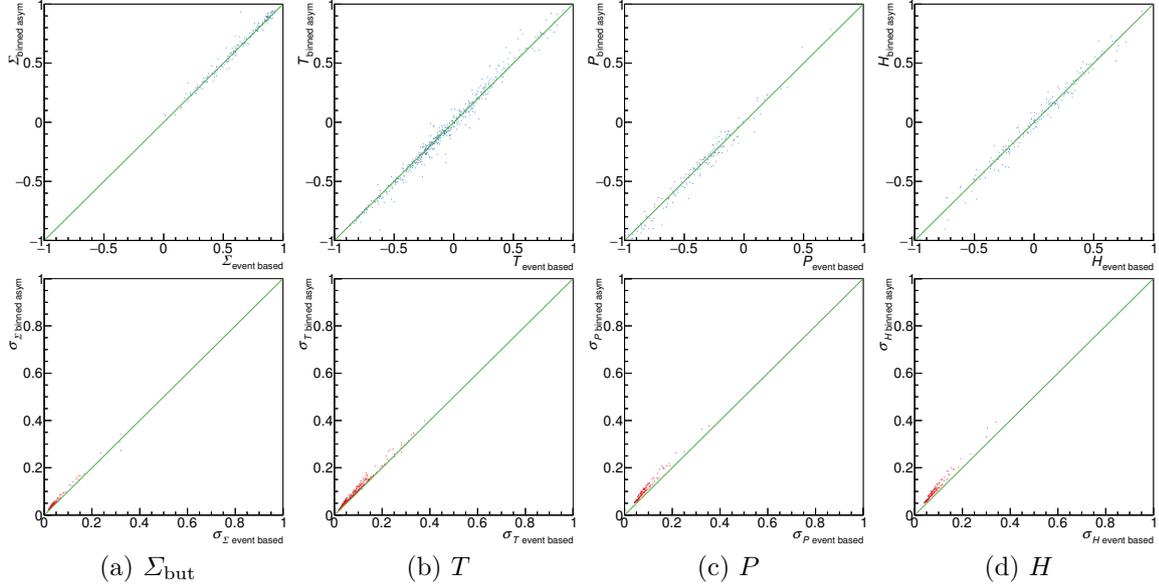
Figure 6.50: The results from the event yield asymmetry method plotted versus the event based likelihood fit. Top row: values, bottom row: statistical uncertainties.

Chapter 7

Discussion of Systematic Uncertainties

Before the results will be discussed in the next chapter, a detailed investigation of possible systematic uncertainties is presented. First, the dominant contributions are given, and then combined into an estimate for the total uncertainty. After that, further checks of consistency will be shown.

7.1 Dominant Contributions to the Systematic Uncertainty

7.1.1 Uncertainty of the Polarization Degree

The relative uncertainty of the polarization degree (cf. Section 6.2) contributes directly to the uncertainty of the determined polarization observables, since the measured asymmetry is the product of the observable and the corresponding polarization degree. For the target asymmetry T only the target polarization degree Λ contributes, resulting in

$$\frac{\Delta T_{\mathrm{pol}}}{T} = \frac{\Delta\Lambda}{\Lambda}, \tag{7.1}$$

whereas for the observables P and H also the beam polarization degree δ contributes. Since the two polarizations are uncorrelated, this results in

$$\frac{\Delta P_{\mathrm{pol}}}{P} = \frac{\Delta H_{\mathrm{pol}}}{H} = \sqrt{\left(\frac{\Delta\Lambda}{\Lambda}\right)^2 + \left(\frac{\Delta\delta}{\delta}\right)^2}. \tag{7.2}$$

The uncertainty of the target polarization degree is identical for each data point, the resulting systematic errors are therefore fully correlated between all bins. For the beam polarization, this is also true for all bins with the same E_γ (and different angles), but the correlation between data points at different E_γ is unknown. It is nevertheless reasonable to assume a large correlation between neighboring bins, which is decreasing with the distance of the bins in E_γ.

7.1.2 Uncertainty of the Dilution Factor

The relative systematic uncertainty of the dilution factor d (cf. Section 6.3) contributes the same way as the uncertainty of the polarization degree:

$$\frac{\Delta T_{\mathrm{dil}}}{T} = \frac{\Delta P_{\mathrm{dil}}}{P} = \frac{\Delta H_{\mathrm{dil}}}{H} = \frac{\Delta d}{d}. \tag{7.3}$$

Since the systematic uncertainty of the dilution factor is a result of energy and angle dependent deviations of the carbon scaling factor from its global average (cf. Section 6.3.2.1) the correlation between the individual data points is unknown.

7.1.3 Background Contamination

The selected data samples still contain some background events from other reactions. Since the background events can, in general, also exhibit an asymmetry, the measured observable O_{meas} also contains a contribution from the background events, resulting in

$$O_{\text{meas}} = (1 - \xi) \, O + \xi \, O_{\text{bg}}, \tag{7.4}$$

where ξ is the relative background contamination of the data sample. If O_{bg} and ξ are known, the actual observable can be calculated. In principle, O_{bg} could be measured using a sideband analysis, e.g. by selecting events which are next to the π^0 or η peaks in the $\gamma\gamma$ invariant mass spectrum. However, the total amount of background is very low, and the observables measured using such an analysis have a statistical uncertainty in the order of $\pm 100\,\%$. It is therefore not possible to constrain O_{bg} in any significant way.

An alternative approach is to neglect the background, using $O \approx O_{\text{meas}}$. This of course introduces an additional systematic uncertainty, which needs to be estimated for each data point, i.e. for each observable in every bin. Given the large number of data points, this allows for a statistical estimate of the uncertainty. The expected absolute error caused by neglecting the background is given by

$$(\Delta O)^2 = \mathbb{E}\left((O - O_{\text{meas}})^2 \right) \overset{(7.4)}{=} \mathbb{E}\left(\left(\frac{\xi}{1 - \xi} (O_{\text{meas}} - O_{\text{bg}}) \right)^2 \right), \tag{7.5}$$

where $\mathbb{E}$ denotes the expected value. With O_{bg} distributed according to the probability density function $f(O_{\text{bg}})$, the expected value can be calculated using

$$(\Delta O)^2 = \int \left(\frac{\xi}{1 - \xi} (O_{\text{meas}} - O_{\text{bg}}) \right)^2 \cdot f(O_{\text{bg}}) \, \mathrm{d}O_{\text{bg}}. \tag{7.6}$$

In order to calculate $(\Delta O)^2$ one needs to make an assumption about f. Without further information, the most reasonable assumption—motivated by the principle of maximum entropy [Jay57]—is that any value for O_{bg} from the physically allowed interval $[-1, 1]$ is equally probable. In that case, performing the integral in Eq. (7.6) yields

$$(\Delta O)^2 = \left(\frac{\xi}{1 - \xi} \right)^2 \left(\frac{1}{3} + O_{\text{meas}}^2 \right) \overset{\xi \ll 1}{\approx} \xi^2 \left(\frac{1}{3} + O_{\text{meas}}^2 \right). \tag{7.7}$$

With $O_{\text{meas}} \in [-1, 1]$ an upper bound for ΔO is given by

$$\Delta O \le \xi \sqrt{\tfrac{4}{3}} \qquad (\text{using } O_{\text{meas}}^2 = 1). \tag{7.8}$$

This upper bound overestimates the error, because for nearly all data points the values of O_{meas}^2 are significantly smaller than 1. A more realistic, and at the same time much simpler estimate is given by

$$\Delta O \lesssim \xi. \tag{7.9}$$

It is still a strict upper bound for all bins with $|O_{\mathrm{meas}}| < \sqrt{2/3} \approx 0.82$ (cf. Eq. (7.7)). For larger values, which occur only in very few bins, it slightly underestimates the error (by at most $\approx 15\%$ for $|O_{\mathrm{meas}}| = 1$). However, for large values of $|O_{\mathrm{meas}}|$ the absolute values of the previously discussed relative uncertainties due to polarization degree and dilution factor are also large, dominating the total systematic uncertainty. Thus, the slight underestimation for large $|O_{\mathrm{meas}}|$ has no significant impact, and the systematic uncertainty of the polarization observables due to background contamination can be approximated by

$$\Delta T_{\mathrm{bg}} = \Delta P_{\mathrm{bg}} = \Delta H_{\mathrm{bg}} = \xi. \tag{7.10}$$

What remains is the determination of the background contamination ξ in each bin. This can be done using the $\gamma\gamma$ invariant mass spectrum where the background is clearly visible, as can be seen in Fig. 7.1. This background is mostly caused by other reactions with multiple particles in the final state, with one or more particles having escaped detection. It is only marginally reduced if the reactions off bound protons are subtracted using the carbon data. Therefore, the background contamination can be determined for the butanol data set alone. This results in a minor overestimation of the background contamination, but keeps it independent of the carbon scaling factor. Assuming a featureless shape of
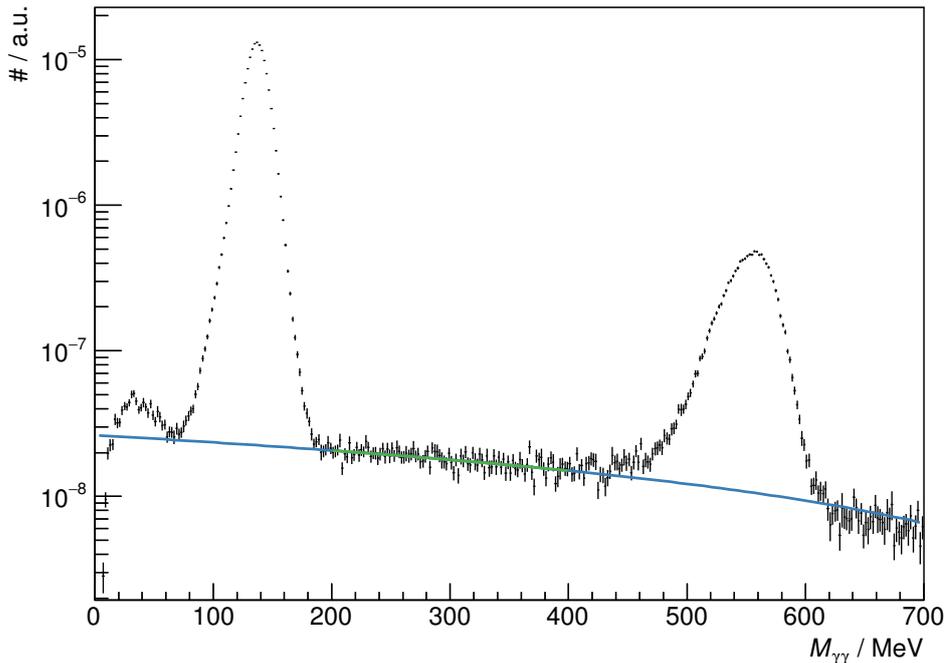
Figure 7.1: Estimation of the background contamination using a linear extrapolation in the $\gamma\gamma$ invariant mass spectrum. A linear function describing the background was fitted to the data in the region $200\,\mathrm{MeV} < M_{\gamma\gamma} < 400\,\mathrm{MeV}$ (green) and extrapolated over the full range (blue). This extrapolation overestimates the background at the η peak slightly. However, since the extrapolation is only used to estimate the systematic uncertainty, this overestimation is of no consequence.

the background underneath the π^0 and η peaks,[1] the background contamination can be estimated using a linear extrapolation from the region between the two peaks. This is done by fitting a linear function

$$f_{\mathrm{bg}}(M_{\gamma\gamma}) = a + b \cdot M_{\gamma\gamma} \tag{7.11}$$

to the background in the region $200\,\mathrm{MeV} < M_{\gamma\gamma} < 400\,\mathrm{MeV}$. For a bin-wise determination of the background contamination, this needs to be done for each bin. However, there are less than $21\,000$ background events between the π^0 and η peaks in the full data set. With 720 $(E_\gamma, \cos\theta)$ bins for the π^0 analysis, this results in an average of less than 30 events per bin, which is not enough to determine the shape of the background. On the other hand, a one-dimensional investigation, i.e. integrating over either E_γ or $\cos\theta$, shows no significant change of the background shape with angle or energy. It is therefore reasonable to assume the same background shape for each bin. The background contamination in each $(E_\gamma, \cos\theta)$ bin can then be estimated by counting the background events in the region $200\,\mathrm{MeV} < M_{\gamma\gamma} < 400\,\mathrm{MeV}$, and extrapolating that number to the π^0 or η peak using the global background shape. The relative background contamination is then given by

$$\xi(E_\gamma, \cos\theta) = \frac{\kappa \cdot \int_{M_{\mathrm{bg}}^{\mathrm{low}}}^{M_{\mathrm{bg}}^{\mathrm{up}}} h(M, E_\gamma, \cos\theta)\,\mathrm{d}M}{\int_{M_{\mathrm{sig}}^{\mathrm{low}}}^{M_{\mathrm{sig}}^{\mathrm{up}}} h(M, E_\gamma, \cos\theta)\,\mathrm{d}M} \quad \text{with } \kappa = \frac{\int_{M_{\mathrm{sig}}^{\mathrm{low}}}^{M_{\mathrm{sig}}^{\mathrm{up}}} f_{\mathrm{bg}}(M)\,\mathrm{d}M}{\int_{M_{\mathrm{bg}}^{\mathrm{low}}}^{M_{\mathrm{bg}}^{\mathrm{up}}} f_{\mathrm{bg}}(M)\,\mathrm{d}M} \tag{7.12}$$

where $h(M, E_\gamma, \cos\theta)$ is the measured $\gamma\gamma$ invariant mass distribution in a given $(E_\gamma, \cos\theta)$ bin, $M_{\mathrm{sig}}^{\mathrm{low}}$ and $M_{\mathrm{sig}}^{\mathrm{up}}$ are the cut limits used to select the π^0 or η events in that bin,[2] and $M_{\mathrm{bg}}^{\mathrm{low}} = 200\,\mathrm{MeV}$ and $M_{\mathrm{bg}}^{\mathrm{up}} = 400\,\mathrm{MeV}$ define the region in which the background is evaluated for extrapolation. The factor κ takes care of the extrapolation based on the global background shape f_{bg}. The resulting background contamination is shown in Fig. 7.2 for both the π^0 and the η data samples. The overall background contamination is very low. In particular for $E_\gamma < 1600\,\mathrm{MeV}$, it is below $1\,\%$ in all bins with non-vanishing acceptance. At higher energies, the overall background contamination is slightly higher. In particular in the bins where the acceptance is small (cf. Section 5.5, in particular Fig. 5.29) it can get as high as $5\,\%$.

---

[1] The shape of the background was investigated using Monte Carlo simulated data for various possible background reactions. Almost all final states that have been considered (e.g. $p\pi^0\pi^0$, $p\pi^+\pi^-$, $p\pi^0\eta$) show no peak-like structures in the $\gamma\gamma$ invariant mass spectrum, with the exception of $n\pi^+\pi^0$ which shows a tiny peak at the π^0 mass. However, the probability to misreconstruct the $n\pi^+\pi^0$ final state as $p\pi^0$ after all cuts have been applied is $\approx 10^{-5}$, as determined from the simulation. Since the cross sections for multi-meson final states are smaller than the $p\pi^0$ cross section below $E_\gamma \lesssim 2\,\mathrm{GeV}$ (cf. Fig. 2.1) and even beyond $E_\gamma = 3\,\mathrm{GeV}$ at most an order of magnitude larger, the contamination with $n\pi^+\pi^0$ events is at most 10^{-4} and can therefore be neglected.

[2] Since the width of the π^0 and η peak depends on both E_γ and $\cos\theta$ and a 2σ cut are used (cf. Section 5.4), $M_{\mathrm{sig}}^{\mathrm{low}}$ and $M_{\mathrm{sig}}^{\mathrm{up}}$ are (slightly) different for each bin (cf. Appendix C).
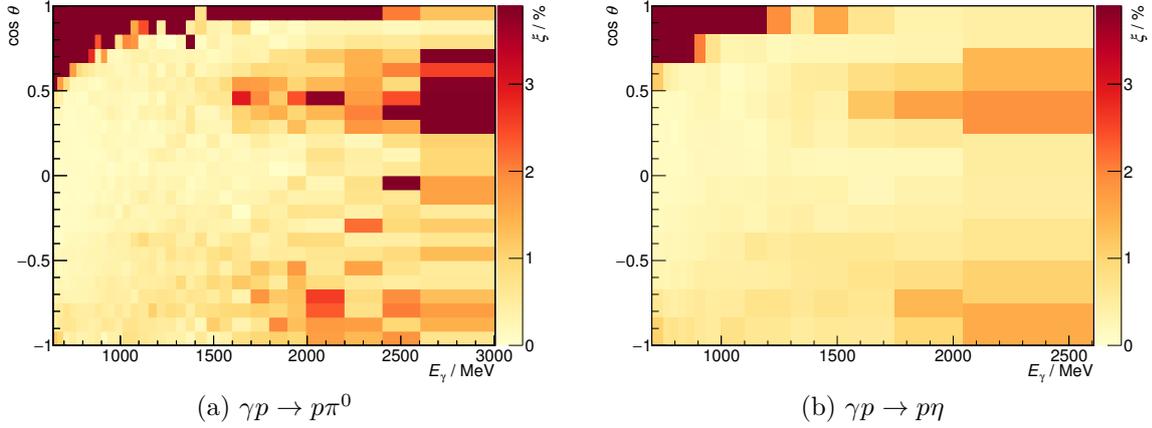
Figure 7.2: The background contamination ξ for the reactions $\gamma p \rightarrow p\pi^0$ and $\gamma p \rightarrow p\eta$. Note that the large relative background contamination in the kinematic region of vanishing acceptance (cf. Fig. 5.29) is of no consequence, since no results were obtained in that region.

7.2 Combined Systematic Uncertainty

Since the uncertainty of the polarization degree, the uncertainty of the dilution factor, and the uncertainty due to background contamination are uncorrelated, the combined systematic uncertainty can be obtained by adding the individual contributions in quadrature. All contributions except for the background contamination are relative contributions, they are multiplied by the value of the observable itself. This value, however, is not exactly known because of its uncertainty. This is particularly problematic in bins where the determined value is smaller than its statistical uncertainty. In that case, the absolute systematic uncertainty can be underestimated. To avoid that, the conversion function

$$\Delta O_{\text{sys}}^{\text{abs}} = \Delta O_{\text{sys}}^{\text{rel}} \cdot |O| \tag{7.13}$$

which converts the relative uncertainty of observable O into an absolute uncertainty needs to be convoluted with the probability density function for the true value of the observable $\hat{O}$, given its measured value O with statistical uncertainty σ_O. This probability density function is given by the normal distribution $\mathcal{N}$:

$$\mathcal{N}(\hat{O} - O, \sigma_O) = \frac{1}{\sqrt{2\pi\sigma_O^2}} \exp\left(-\frac{(\hat{O} - O)^2}{2\sigma_O^2}\right). \tag{7.14}$$

Writing down the convolution integral yields

$$\Delta O_{\text{sys}}^{\text{abs}} = \int\limits_{-\infty}^{\infty} \Delta O_{\text{sys}}^{\text{rel}} \cdot |O - x| \cdot \mathcal{N}(x, \sigma_O)\, \mathrm{d}x. \tag{7.15}$$

The integration is done numerically, the integration range can be restricted to $\pm 5\,\sigma_O$ without a significant influence on the result.

Combining all the contributions, the total systematic uncertainty for the three observables is then given by

$$\Delta T_{\text{sys}} = \sqrt{\left[\int\limits_{-5\sigma_T}^{5\sigma_T} \sqrt{\left(\frac{\Delta\Lambda}{\Lambda}\right)^2 + \left(\frac{\Delta d}{d}\right)^2} \cdot |T - x| \cdot \mathcal{N}(x, \sigma_T)\, \mathrm{d}x \right]^2 + \xi^2} \qquad (7.16a)$$

$$\Delta P_{\text{sys}} = \sqrt{\left[\int\limits_{-5\sigma_P}^{5\sigma_P} \sqrt{\left(\frac{\Delta\Lambda}{\Lambda}\right)^2 + \left(\frac{\Delta\delta}{\delta}\right)^2 + \left(\frac{\Delta d}{d}\right)^2} \cdot |P - x| \cdot \mathcal{N}(x, \sigma_P)\, \mathrm{d}x \right]^2 + \xi^2} \quad (7.16b)$$

$$\Delta H_{\text{sys}} = \sqrt{\left[\int\limits_{-5\sigma_H}^{5\sigma_H} \sqrt{\left(\frac{\Delta\Lambda}{\Lambda}\right)^2 + \left(\frac{\Delta\delta}{\delta}\right)^2 + \left(\frac{\Delta d}{d}\right)^2} \cdot |H - x| \cdot \mathcal{N}(x, \sigma_H)\, \mathrm{d}x \right]^2 + \xi^2} \quad (7.16c)$$

where $\frac{\Delta\Lambda}{\Lambda}$ and $\frac{\Delta\delta}{\delta}$ are the relative uncertainties in the target and beam polarization, $\frac{\Delta d}{d}$ is the relative uncertainty in the dilution factor, and ξ is the relative background contamination of the event sample.

In the low energy region, where the background contamination is small and the dilution factor is large, the total uncertainty is dominated by the polarization degree. In particular for the observables P and H, which require the linear polarization of the beam, all other contributions are negligible. At higher energies, where only the observable T can be measured in this analysis, the systematic uncertainty increases due to a smaller dilution factor and slightly more background. However, the statistical uncertainty is also much larger at higher energies due to the lower cross section and the smaller dilution factor. Therefore, the systematic uncertainty is still significantly smaller than the statistical error, as can be seen in Fig. 7.3.

(a) $\gamma p \to p\pi^0$

(b) $\gamma p \to p\eta$
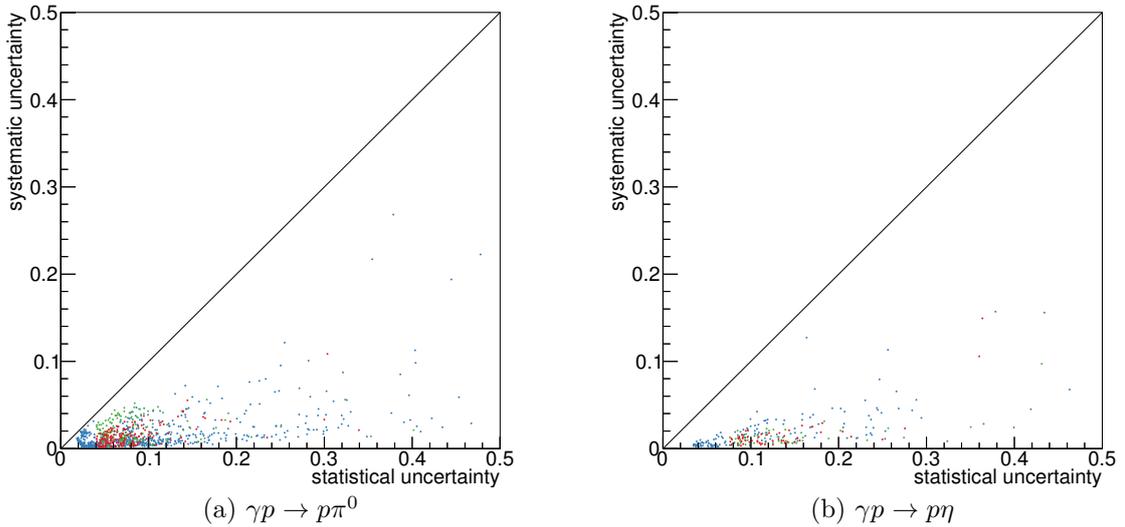
Figure 7.3: The systematic uncertainty of each data point plotted versus the statistical uncertainty. (T: blue, P: green, H: red)

7.3 Systematic Uncertainty of the Bin Position

So far, the uncertainty of the value of the observables in each bin has been discussed. Additionally, there is also an uncertainty of the bin position, i.e. an uncertainty of E_γ and $\cos\theta$. The uncertainty of E_γ is a result of the uncertainty of the tagger calibration (see Section 5.2.3), it is shown in Fig. 7.4 for the bins used in the analysis.

(a) $\gamma p \to p\pi^0$ (b) $\gamma p \to p\eta$
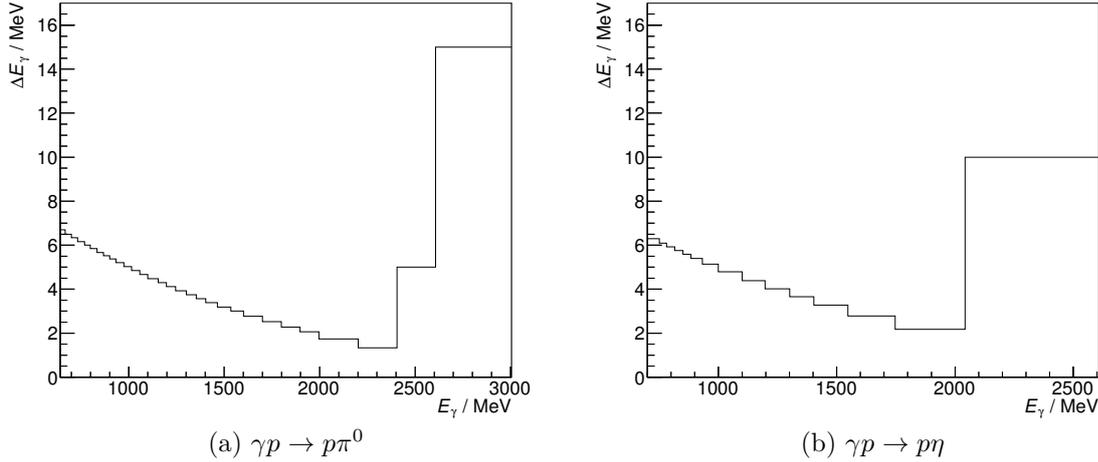
Figure 7.4: The systematic uncertainty of the beam energy, as a function of the beam energy. The increase above $E_\gamma \gtrsim 2500\,\text{MeV}$ is due to fact that there are no calibration measurements available in that energy range and the calibration is extrapolated to higher energies using a simulation (cf. Section 5.2.3).

The uncertainty of $\cos\theta$ is a bit more complicated to estimate. It is discussed here for the reaction $\gamma p \to p\pi^0$. The absolute uncertainty is of similar size for the reaction $\gamma p \to p\eta$. However, due to the larger size of the $\cos\theta$ bins, the uncertainty is only of minor importance for the η analysis.

Since $\cos\theta$ is not measured directly, but is calculated from various measured quantities, its uncertainty also depends on these quantities and their uncertainties. In order to get an estimate, the Monte Carlo simulation (see Section 5.1.3) is used to compare, for each simulated event, the measured value $\cos\theta$ with the generated value $\cos\tilde{\theta}$. From the resulting distribution of $\cos\theta - \cos\tilde{\theta}$, in each $(E_\gamma, \cos\theta)$ bin, the uncertainty of $\cos\theta$ in that bin can be estimated. The statistical uncertainty—caused by the detector resolution—is given by the standard deviation σ, and any systematic uncertainty is indicated by a non-vanishing mean value μ.

Using the Monte Carlo dataset (1), one gets a lower limit for the uncertainty under ideal conditions. The resulting systematic and statistical uncertainties are shown in Fig. 7.5. The statistical uncertainty is at least a factor of 2 smaller than the bin width, which is $\Delta\cos\theta = 1/12$ for 24 bins. It is rather independent of E_γ, and smaller toward negative $\cos\theta$. The systematic uncertainty is negligible in this ideal scenario, since it is significantly smaller than the bin width. Nevertheless, there are some structures visible in Fig. 7.5a, which directly correspond to the structures visible in the acceptance (cf. Fig. 5.29a).

(a) systematic

(b) statistical
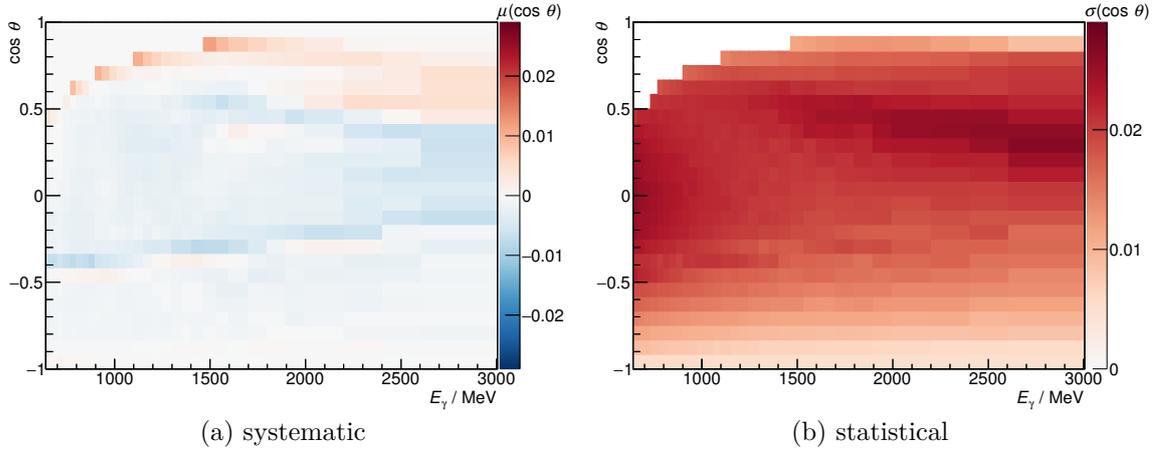
Figure 7.5: The uncertainty of the center-of-mass angle θ for each data point. Using the Monte Carlo simulation, the difference between measured and generated $\cos\theta$ can be studied. The mean value μ of the deviation indicates a systematic uncertainty, and the standard deviation σ corresponds to the statistical uncertainty due to the detector resolution.

(a) $\Delta E_\gamma = -10\,\mathrm{MeV}$

(b) $\Delta E_\gamma = +10\,\mathrm{MeV}$
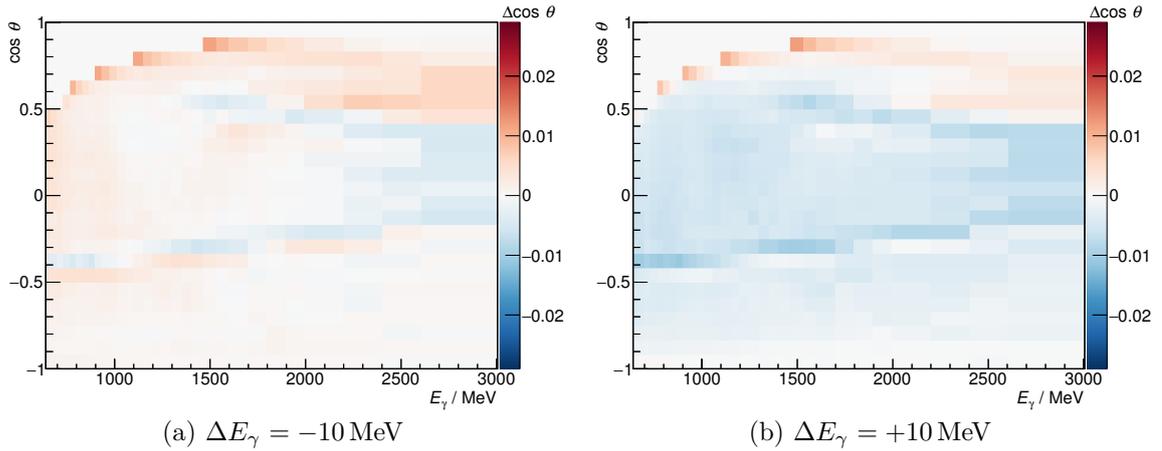
Figure 7.6: The systematic uncertainty of $\cos\theta$ caused by a shift ΔE_γ in the measured beam energy. Using the Monte Carlo simulation, the mean difference between measured and generated $\cos\theta$ can be determined as a function of ΔE_γ, the results are shown for the two worst-case scenarios.

Since the measured $\cos\theta$ also depends on the beam energy E_γ, the systematic uncertainty of E_γ also contributes to the systematic uncertainty of $\cos\theta$. To study the magnitude of this influence, an offset ΔE_γ is added to the beam energy in the analysis of the Monte Carlo data. Even for a shift of $\Delta E_\gamma = \pm 10\,\mathrm{MeV}$, which is larger than the systematic uncertainty, the effect is small, as can be seen in Fig. 7.6. Nevertheless, a small anti-correlation between E_γ and $\cos\theta$ is visible. A shift of $\Delta E_\gamma = \pm 10\,\mathrm{MeV}$ leads to an average change of $\Delta\cos\theta = \mp 0.0022$. This corresponds to $\approx 3\,\%$ of the bin width and is therefore completely negligible.

(a) $\Delta z = -1\,\mathrm{cm}$ (upstream)　　　　(b) $\Delta z = +1\,\mathrm{cm}$ (downstream)
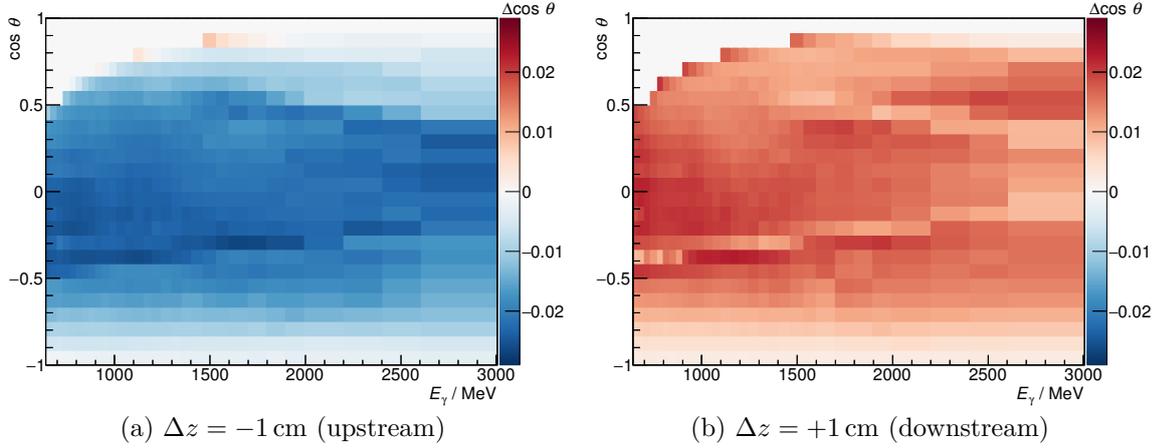
Figure 7.7: The systematic uncertainty of $\cos\theta$ caused by a shift Δz of the target position along the beam axis. Using the Monte Carlo simulation, the mean difference between measured and generated $\cos\theta$ can be determined as a function of Δz, the results are shown for the two worst-case scenarios.

The uncertainty of the target position is also expected to have an influence on $\cos\theta$, since a shift of the target along the beam axis influences all measured angles. To study the magnitude of this influence, the Monte Carlo datasets (5) and (6), where the target position is shifted by $\Delta z = \pm 1\,\mathrm{cm}$ along the beam axis, are used. The magnitude of this shift is larger than the alignment precision of the experimental setup,[3] thus providing a worst-case estimate. The resulting limits for the systematic uncertainty are shown in Fig. 7.7. The uncertainty is as high as $33\,\%$ of the bin width for a wide range of the data points. For simplicity, the dependence on E_γ and $\cos\theta$ can be neglected, and a global upper limit of $\Delta \cos\theta = 0.03_{\mathrm{sys}}$ can be used for all bins, and also for the reaction $\gamma p \to p\eta$.

7.4 Additional Checks of Consistency

7.4.1 Comparison Between the Event Based Maximum Likelihood Fit and the Binned Event Yield Asymmetry

Since, at least for the reaction $\gamma p \to p\pi^0$ below $E_\gamma < 1900\,\mathrm{MeV}$, the polarization observables have been determined using two different methods, the results can be compared for an additional check of consistency. All systematic uncertainties discussed so far influence both methods in exactly the same way. Any statistically significant difference between the two methods would, therefore, indicate an additional systematic error.

A visual comparison of the results yields no obvious discrepancy (cf. Figs. 6.42 to 6.45). Instead, a statistical analysis needs to be performed. For each data point and each observable O, the difference ΔO between the two results, and its error $\sigma_{\Delta O}$, are calculated. If the two methods are indeed compatible, $\frac{\Delta O}{\sigma_{\Delta O}}$ is expected to be normal-distributed with mean

---

[3] The alignment precision of the detectors is in the order of a few mm [Wen08; Wal16; Hän17].

$\mu = 0$ and width $\sigma = 1$. Any deviation would indicate an additional systematic error in at least one of the two methods.

One challenge with this approach is the calculation of $\sigma_{\Delta O}$. Since the results obtained using the two different methods are based on the same data sample, they are expected to be highly correlated. The error of the difference is thus given by

$$\sigma_{\Delta O}^2 = \sigma_1^2 + \sigma_2^2 - 2\,\kappa\,\sigma_1\sigma_2 \tag{7.17}$$

where σ_1 and σ_2 are the errors of the results from the two methods, and $\kappa \in [-1, 1]$ is the correlation coefficient. Its exact value is unknown, but expected to be large; negative values for κ can safely be excluded. To make things more complicated, κ can be different for each data point and each observable. To get a meaningful estimate on $\sigma_{\Delta O}$, it is necessary to constrain κ further. For this purpose, Eq. (7.17) is rewritten by decomposing the individual errors σ_i ($i = 1, 2$) into a common, fully correlated error $\hat{\sigma}$ and individual, uncorrelated errors $\tilde{\sigma}_i$:

$$\sigma_i^2 = \hat{\sigma}^2 + \tilde{\sigma}_i^2 \qquad (i = 1, 2). \tag{7.18}$$

Only the individual errors contribute to the error of the difference.

$$\sigma_{\Delta O}^2 = \tilde{\sigma}_1^2 + \tilde{\sigma}_2^2 \tag{7.19}$$

This error is minimal if one of the $\tilde{\sigma}_i$ vanishes, i.e. if the common error $\hat{\sigma}$ is maximal and identical to the smaller of the two errors.

$$\sigma_{\Delta O_{\min}}^2 = \begin{cases} \tilde{\sigma}_1^2 = \sigma_1^2 - \sigma_2^2 & \text{if } \tilde{\sigma}_2^2 = 0 \\ \tilde{\sigma}_2^2 = \sigma_2^2 - \sigma_1^2 & \text{if } \tilde{\sigma}_1^2 = 0 \end{cases} \tag{7.20}$$

By combining Eqs. (7.17) and (7.20), this lower bound for $\sigma_{\Delta O}$ provides an upper bound for the correlation coefficient κ.

$$-2\,\kappa_{\max}\,\sigma_1\sigma_2 = \begin{cases} -2\,\sigma_2^2 & \text{if } \tilde{\sigma}_2^2 = 0 \\ -2\,\sigma_1^2 & \text{if } \tilde{\sigma}_1^2 = 0 \end{cases} \tag{7.21}$$

$$\implies \kappa_{\max} = \begin{cases} \sigma_2/\sigma_1 & \text{if } \tilde{\sigma}_2^2 = 0 \\ \sigma_1/\sigma_2 & \text{if } \tilde{\sigma}_1^2 = 0 \end{cases} \tag{7.22}$$

The largest possible correlation coefficient is thus given by the ratio of the smaller and the larger error. A histogram of this upper bound in each bin is shown in Fig. 7.8.

Assuming maximum correlation, it is possible to calculate $\frac{\Delta O}{\sigma_{\Delta O}}$ for each data point.[4] Histograms of the resulting values for each observable are shown in Fig. 7.9. The distributions can indeed be described by a Gaussian distribution. There are, however, some deviations from $\mu = 0$ and $\sigma = 1$, the most prominent being the width of the distribution in case of the observable T, which deviates by more than 6 standard deviations from $\sigma = 1$. While this seems highly significant, one needs to take in to account the possibility that the correlation is smaller than the maximum allowed value. And indeed, if the correlation is assumed to be just $4\,\%$ smaller than maximum, the width is consistent with 1, as can be seen in Fig. 7.10.

(a) T (b) P (c) H
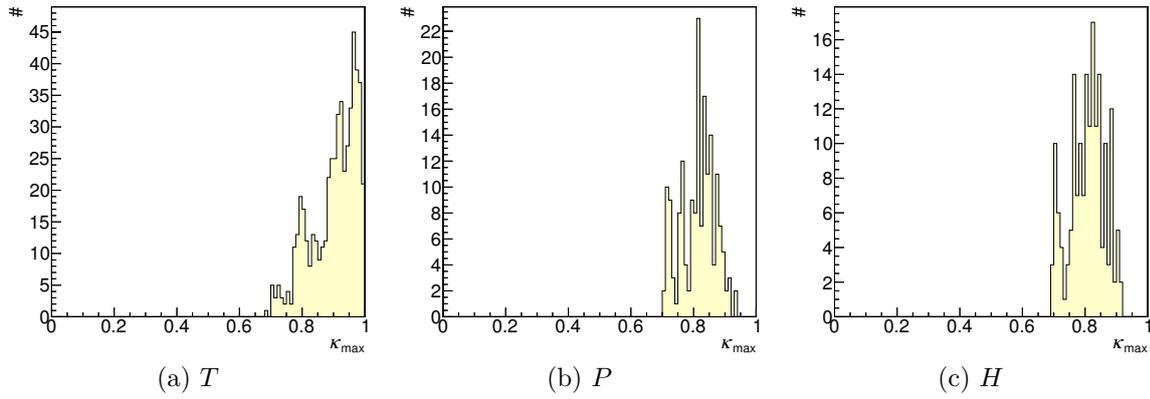
Figure 7.8: Histograms of the upper bound κ_{max} for the correlation coefficient between the two different analysis methods.

(a) T (b) P (c) H
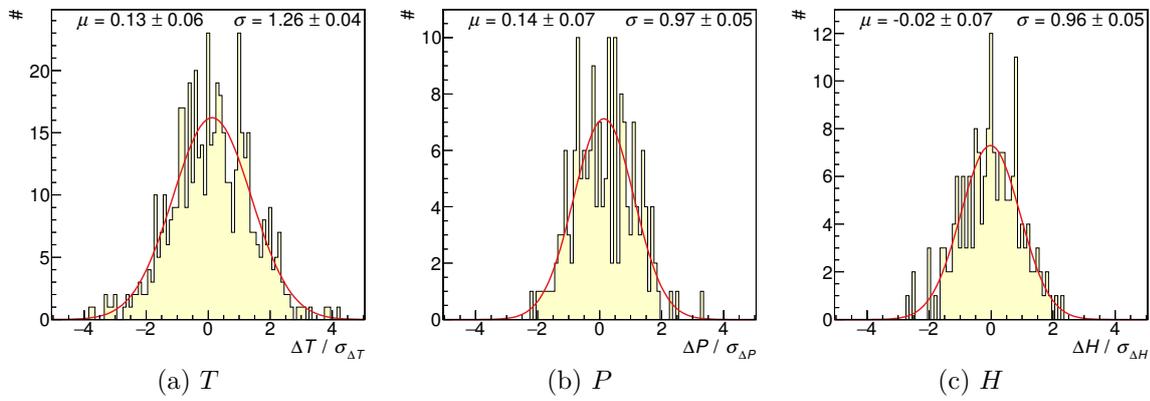
Figure 7.9: Histograms of the difference between the results obtained using the different analysis methods, divided by its statistical uncertainty assuming maximum correlation κ_{max}. A Gaussian with mean μ and width σ was fitted to the histograms using the binned-likelihood method [BC84].
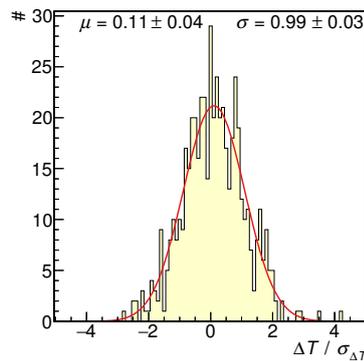
Figure 7.10: Histograms of the difference between the results for T obtained using the different analysis methods, divided by its statistical uncertainty assuming a reduced correlation of $\kappa = 0.96\,\kappa_{max}$.

145

There is, in fact, a strong indication that the correlation is indeed smaller than maximum. Maximum correlation is only possible if, for each data point, only one of the two methods has an individual, uncorrelated error $\tilde{\sigma}$ (cf. Eqs. (7.18) and (7.19)). It is reasonable to assume that this would be the same method in each data point, i.e. for maximum correlation one would expect one method to be *always* at least as precise as the other one. However, while the unbinned likelihood method is indeed more precise than the binned method for *most* of the data points, this is not the case for *all* data points.[5] This indicates that the correlation has to be smaller than the maximum possible value. It is therefore reasonable to assume that the width of the $\frac{\Delta O}{\sigma_{\Delta O}}$ distribution is in agreement with the expected width, and the too large width of the distribution for $\kappa = \kappa_{\mathrm{max}}$ is only caused by overestimating the correlation.

The remaining issue that needs to be addressed is the deviation from $\mu = 0$ by 2 standard deviations in case of the observables T and P. This deviation could still be attributed to random chance; nevertheless, this is worth investigating further. To that end, it is useful to look at the distributions of ΔO directly, without dividing them by their uncertainty. The results are shown, for each observable, in Fig. 7.11. Since the uncertainty for each data point differs, the distributions are not necessarily Gaussian. Nevertheless, the mean of the distribution can be used to judge any systematic discrepancy between the two analysis methods.

In all cases, the difference to 0 is less than 0.01, the average for all observables combined is 0.0041 ± 0.0018. Since this deviates from 0 by more than 2 standard deviations, it is added to the total systematic uncertainty of each data point. However, it should also be mentioned that this additional uncertainty is, for nearly all data points, much smaller compared to the other systematic uncertainties and has thus hardly any influence on the total uncertainty.

(a) T (b) P (c) H
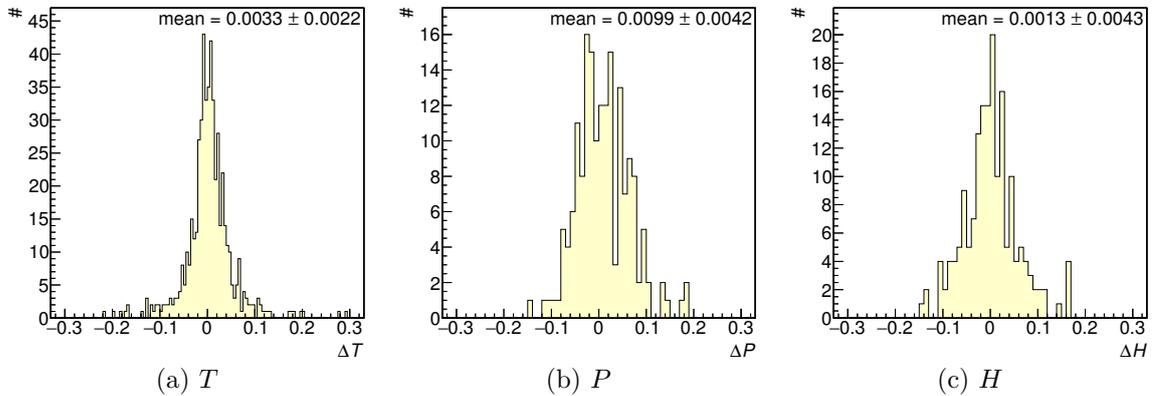
Figure 7.11: Histograms of the difference between the results obtained using the different analysis methods, together with the arithmetic mean and its statistical uncertainty.

---

[4] With an individual value of κ_{max} for each data point.

[5] For the observables P and H the value obtained using the unbinned likelihood fit is more precise in all 176 bins, for the observable T the unbinned likelihood fit is more precise in 512 bins, whereas the binned method is more precise in 12 bins.

7.4.2 Comparison Between the $\eta \to 2\gamma$ and $\eta \to 3\pi^0$ Decay Modes

The reaction $\gamma p \to p\eta$ can also be studied using the decay mode $\eta \to 3\pi^0 \to 6\gamma$. Since the reconstructed event sample for this decay channel contains only about $25\,\%$ as many events as the $\eta \to \gamma\gamma$ event sample, and it also contains more than $10\,\%$ background events at higher E_γ, these events have not been used for the analysis, as was already mentioned in Section 5.4.2. However, below $E_\gamma \lesssim 1\,\mathrm{GeV}$ the background contamination is below $3\,\%$. It is therefore possible to compare the results for the polarization observables in that energy range for the two decay channels. This is discussed in the following.

The analysis of the $\eta \to 3\pi^0$ event sample was done exactly the same way as for the $\eta \to 2\gamma$ event sample, as described in Chapter 6. The dilution factor was determined as described in Section 6.3, and the observables were determined using the event based maximum likelihood fit described in Section 6.4.2, but limited to the energy of the coherent peak below $E_\gamma = 950\,\mathrm{MeV}$. At higher energies, the number of reconstructed $\eta \to 3\pi^0$ events per bin is too small and the statistical uncertainty of each data point is close to 1. The results for the observables T, P, and H for both decay channels are shown in Fig. 7.12. No obvious discrepancies between the two decay modes can be seen.
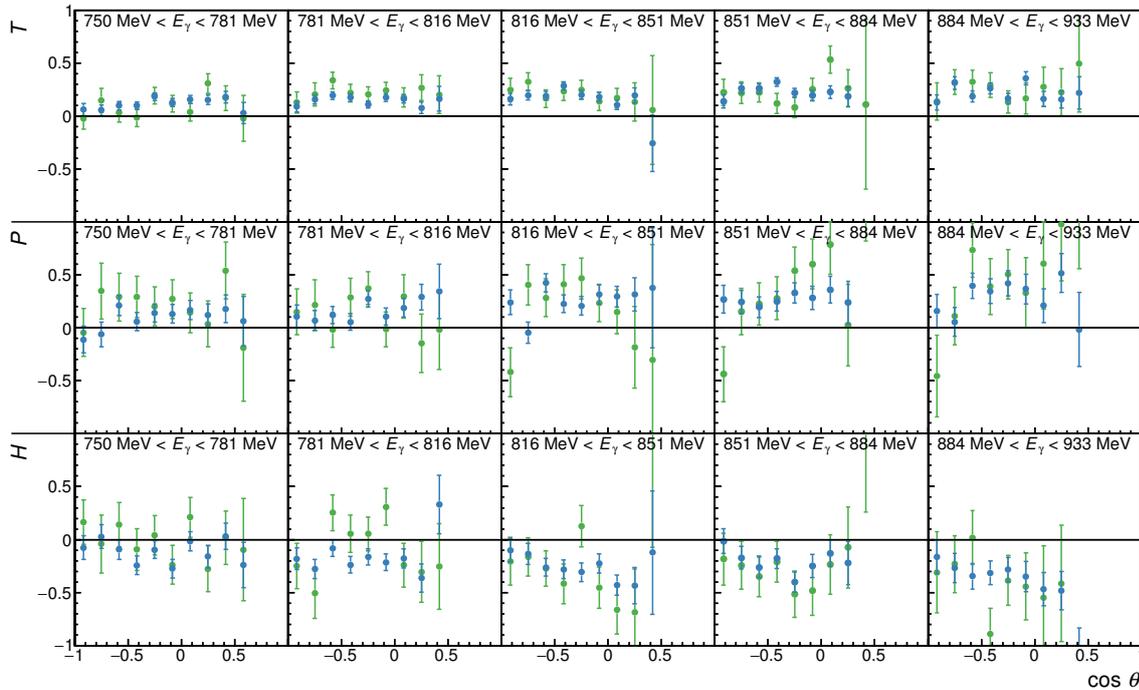
Figure 7.12: The polarization observables T, P, and H for the reaction $\gamma p \to p\eta$, compared between the decay modes $\eta \to 2\gamma$ (blue) and $\eta \to 3\pi^0$ (green).

For a quantitative comparison of the two data sets, a statistical analysis needs to be performed. Similar to the previous section, the difference ΔO between the two decay channels and its uncertainty $\sigma_{\Delta O}$ are calculated for each observable O and each data point. However, this time the results for the two data sets are completely uncorrelated, which drastically simplifies the calculation of $\sigma_{\Delta O}$. A histogram of $\frac{\Delta O}{\sigma_{\Delta O}}$ is shown in Fig. 7.13 for each ob-

servable. The distributions are in good agreement with a Gaussian distribution with mean $\mu = 0$ and width $\sigma = 1$. Thus, the analysis of the two decay modes yields compatible results, showing no evidence for additional systematic errors.

| (a) T | (b) P | (c) H |
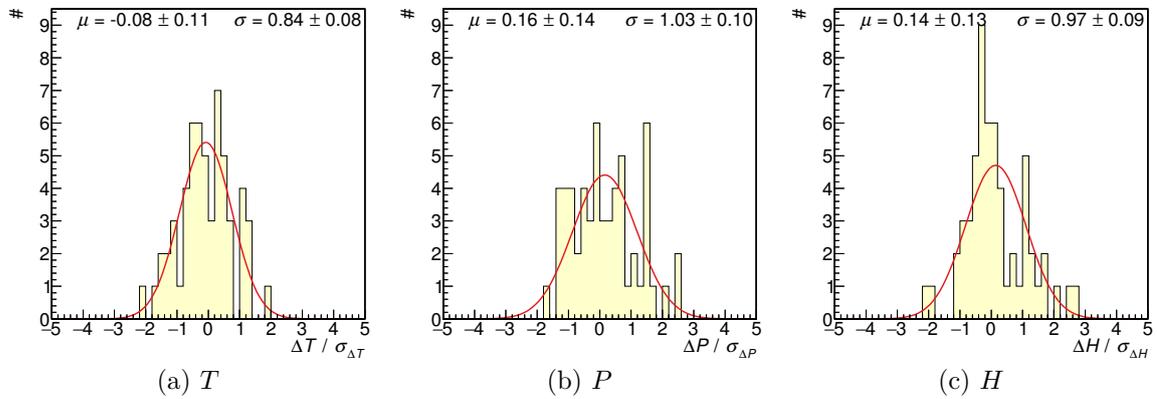
Figure 7.13: Histograms of the difference between the results obtained using the two different decay modes $\gamma \to 2\gamma$ and $\gamma \to 3\pi^0$, divided by its statistical uncertainty. A Gaussian with mean μ and width σ was fitted to the histograms using the binned-likelihood method [BC84].

Chapter 8

Discussion of the Results

8.1 Comparison to Previous Measurements

8.1.1 Beam Asymmetry Σ

The beam asymmetry Σ has already been measured by several experiments (cf. Section 2.2). Since it is also obtained as a by-product in this analysis, a comparison of the results serves as a cross-check. However, as was mentioned in Section 6.4.1.1, the beam asymmetry measured using a butanol target is not identical to the beam asymmetry of reactions off the free proton. Instead, it also contains contributions from reactions off bound nucleons:

$$\Sigma = d \cdot \Sigma_{\text{free}} + (1 - d) \cdot \Sigma_{\text{bound}}, \tag{8.1}$$

where the relative contribution of Σ_{free} and Σ_{bound} is given by the dilution factor d. Nevertheless, bound protons still behave as protons, and the contribution from bound neutrons is suppressed because of the lower detection efficiency for neutrons ($\varepsilon_n < 0.3$ [Jae+11]). Therefore, Σ_{bound} is expected to be similar to Σ_{free}, except for additional blurring in energy and angle due to Fermi motion. The effect of the blurring is expected to be most prominent in kinematic regions where Σ exhibits a large variation with energy or angle. But even then, the rather large dilution factor still ensures $\Sigma \approx \Sigma_{\text{free}}$.

8.1.1.1 Reaction $\gamma p \rightarrow p\pi^0$

The most precise measurement of the beam asymmetry for the reaction $\gamma p \rightarrow p\pi^0$ was performed by the GRAAL collaboration [Bar+05a]. A direct comparison of their results with the results from this analysis is shown in Fig. 8.1. As can be seen, the agreement between the two data sets is quite good.

8.1.1.2 Reaction $\gamma p \rightarrow p\eta$

Also for the reaction $\gamma p \rightarrow p\eta$, the most precise measurement was done by GRAAL [Bar+07]. Again, the two data sets are in excellent agreement, as can be seen in Fig. 8.2. This confirms that the influence of the bound protons on the result of the measurement is indeed small. It also proves that the method used to extract the polarization observables from the data works as expected, and the systematics are well under control.[1]

---

[1] Although it should be noted that the agreement on Σ does not prove that the target polarization degree and the dilution factor are well under control, since Σ is independent of the target polarization.
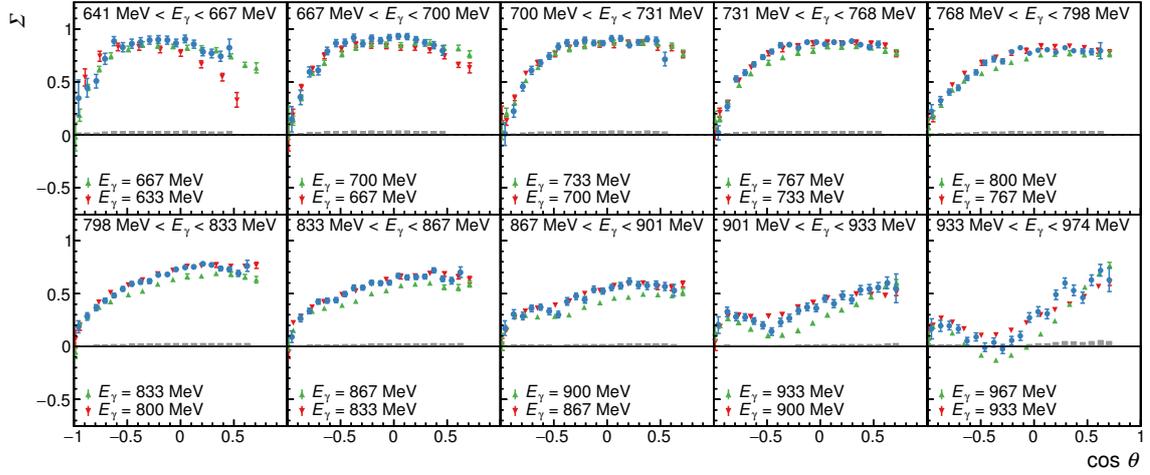
Figure 8.1: The results for the beam asymmetry Σ in the reaction $\gamma p \rightarrow p\pi^0$ (blue points, systematic uncertainty shown as gray bars), compared to the measurement by the GRAAL collaboration [Bar+05a]. Since the GRAAL data were measured E_γ in between our bins, both the nearest data points at smaller (red) and larger (green) E_γ are shown in for each bin.
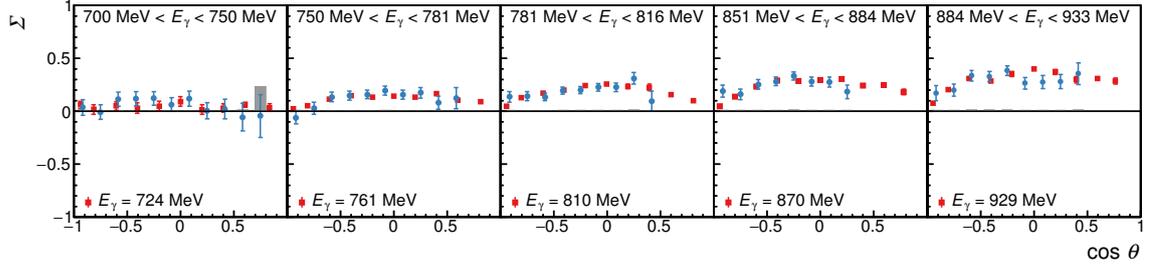
Figure 8.2: The results for the beam asymmetry Σ in the reaction $\gamma p \rightarrow p\eta$ (blue points, systematic uncertainty shown as gray bars), compared to the measurement by the GRAAL collaboration [Bar+07] (red). The GRAAL data were measured at slightly different E_γ.

8.1.2 Target Asymmetry T

8.1.2.1 Reaction $\gamma p \rightarrow p\pi^0$

The target asymmetry T in the reaction $\gamma p \rightarrow p\pi^0$ has previously been measured by various experiments (cf. Section 2.2). Most of these measurements are limited to a narrow kinematic region, both in energy and angle. The notable exception are the measurements performed at the NINA synchrotron at Daresbury Laboratory in the 1970s [Boo+77; Bus+79a], which cover an energy range from $E_\gamma \approx 700\,\text{MeV}$ up to $E_\gamma \approx 2200\,\text{MeV}$, with full polar angle coverage up to $E_\gamma \approx 1500\,\text{MeV}$ and just a few missing data points in backward direction at higher energies. The error bars of the previous measurements are significantly larger. A comparison between the older data and this analysis is shown in Fig. 8.3. As can be seen,
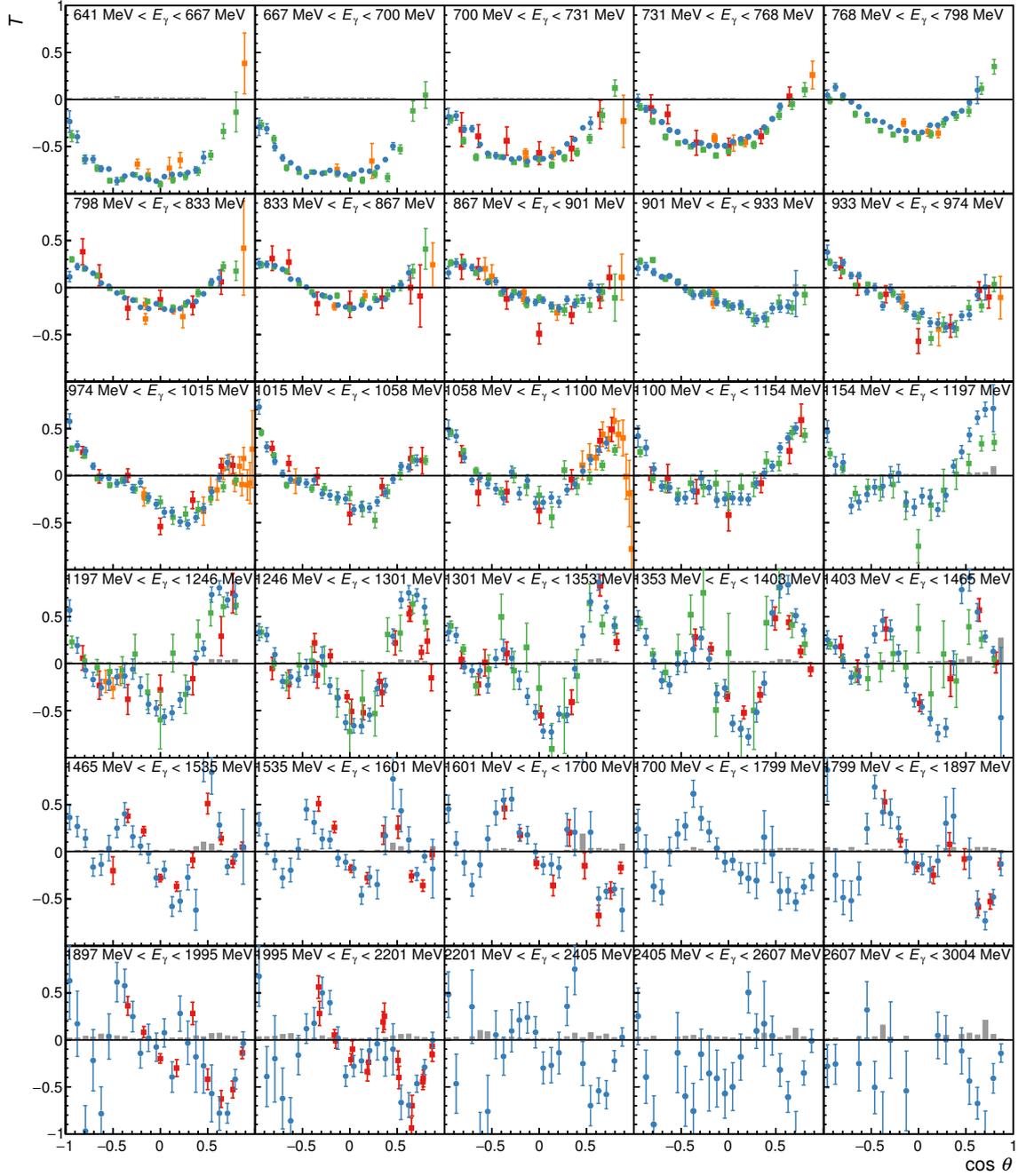
Figure 8.3: The results for the target asymmetry T in the reaction $\gamma p \to p\pi^0$ (blue points, systematic uncertainty shown as gray bars), compared to previous measurements. The data points measured at Daresbury Laboratory [Boo+77; Bus+79a] are shown in red. The recently published results from MAMI [Ann+16], which were measured in parallel to this work, are shown in green. All other measurements [Gor+74; Gor+75; Gor+78; Fel+76; Her+77; Fuk+78; Aga+89; Asa+86], each in a rather limited kinematic region, are shown in orange. Due to different binning, the energies differ by up to half of the bin size.

the present analysis extends the kinematic coverage to higher energies up to $E_\gamma = 3\,\text{GeV}$, and exceeds the older data in precision, in particular for $E_\gamma < 950\,\text{MeV}$.

In parallel to this work, the target asymmetry was also measured by the A2 collaboration at MAMI [Ann+16], for photon energies below 1.45 GeV. The number of angular bins of the MAMI data set is lower compared to this analysis, as is their statistical precision. The MAMI data cover a slightly larger polar angle range in forward direction, where this analysis has vanishing acceptance, in particular in the lower energy bins. However, the very forward angles close to $\cos\theta \approx 1$ are also missing in the MAMI data.

The agreement between this analysis and the other data is excellent, which is a strong indication that no systematic effects have been overlooked in this analysis, in particular regarding the target polarization and the dilution factor.

8.1.2.2 Reaction $\gamma p \to p\eta$

For the reaction $\gamma p \to p\eta$, the target asymmetry T has previously been measured by the PHOENICS collaboration at ELSA [Boc+98], with complete angular coverage up to $E_\gamma \approx 900\,\text{MeV}$ and a few additional data points at energies up to $E_\gamma \approx 1100\,\text{MeV}$ in backward direction. Achieving an adequate description of the PHOENICS data has proven quite challenging for the PWA groups. In particular, a sign-change in the angular distribution of T close to threshold cannot be reproduced by either BnGa [Ani+12], SAID [M+10], or the η-MAID isobar model [Chi+03]. Only a model-independent fit by Tiator et al. [Tia+99] is able to describe the data. However, it requires a strongly energy dependent phase difference between the $N(1535)\,1/2^-$ and $N(1520)\,3/2^-$ resonances, which is entirely unexpected for two close-by resonances of similar width. The nature of this phase change has hitherto not been understood. It should, however, be noted that the PHOENICS measurement of T close to threshold is still perfectly compatible with $T = 0$ at all angles ($\chi^2/\text{ndf} = 5.9/6$), and there might be no sign change after all. And indeed, the results from the present analysis show no evidence of any negative value for T close to threshold.

While the discrepancy between the two data sets close to the threshold could still be attributed to chance, a further comparison of the two data sets, which is shown in Fig. 8.4, reveals little agreement. Over all bins combined, the discrepancy between the two data sets appears significant.[2]

In parallel to this work, the target asymmetry was also measured by the A2 collaboration at MAMI [Ako+14]. As can be seen in Fig. 8.4, their results show a compatible shape, in particular also no zero-crossing close to threshold. However, the absolute values of T seem systematically lower compared to this analysis. This indicates an additional systematic error in one of the two analyses. Since each data point seems to be affected in the same way, the most probable source of this error is the polarization degree of the target. In that case, the systematic error should influence the results for other reactions in the same way. However, the results for the reaction $\gamma p \to p\pi^0$ from this analysis are in excellent agreement with previous measurements. Therefore, an additional systematic error in our measurement of the polarization degree seems unlikely. Other systematic errors limited to the reaction

---

[2] Due to the different binning in energy and angle, the discrepancy is hard to quantify. But just a visual inspection of the data reveals that roughly half of the PHOENICS data points deviate from the results of this analysis by more than 1σ, which is significantly more that expected for two compatible data sets.
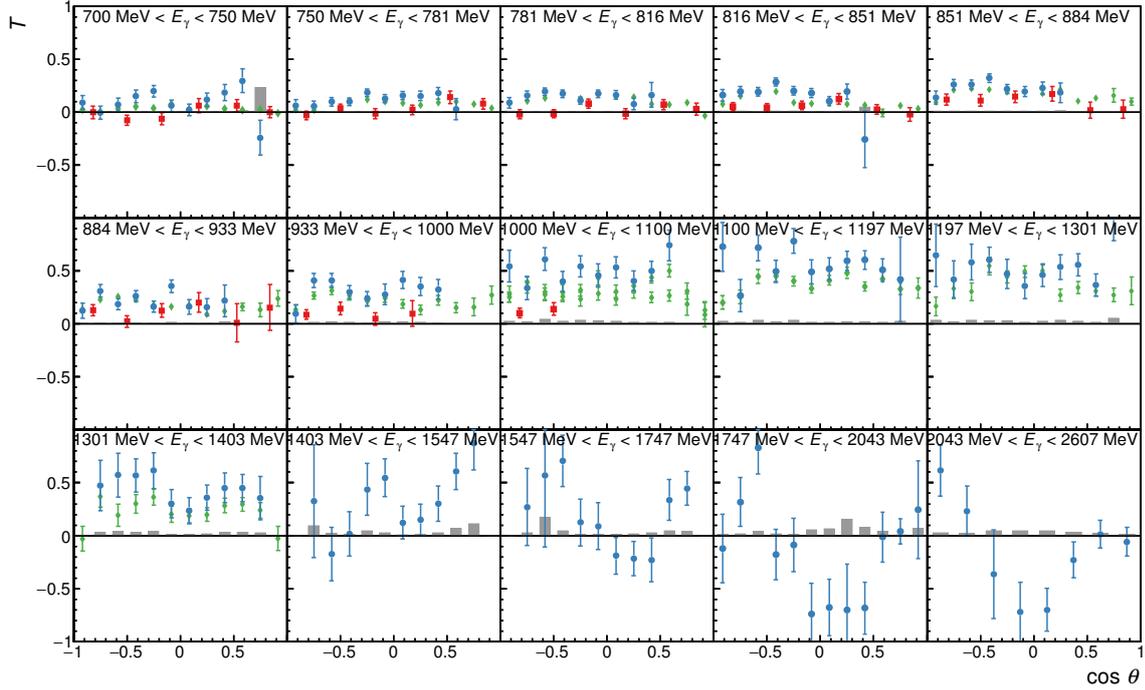
Figure 8.4: The results for the target asymmetry T in the reaction $\gamma p \to p\eta$ (blue points, systematic uncertainty shown as gray bars), compared to previous measurements by the PHOENICS collaboration [Boc+98] (red), and the recently published results from MAMI [Ako+14] (green) which were measured in parallel to this work. Due to different binning, the energies differ by up to half of the bin size.

$\gamma p \to p\eta$, e.g. background contamination of the event sample, should also influence the measurement of the other observables. But again, the measurement of the beam asymmetry Σ is also in excellent agreement with previous measurements (see Section 8.1.1).

In conclusion, there is no indication of any additional systematic error in this analysis. Thus, we expect the source of the discrepancy to be found more likely in the MAMI data. For further details, a quantitative discussion of the discrepancy is given in Appendix E.

8.1.3 Recoil Polarization P

8.1.3.1 Reaction $\gamma p \to p\pi^0$

The recoil polarization P has previously been measured for the reaction $\gamma p \to p\pi^0$ by various experiments (cf. Section 2.2). Some measurements at higher energies ($E_\gamma > 1300\,\text{MeV}$) were done in a double polarization experiment involving linearly polarized photon beams and transversely polarized target protons, similar to this analysis. But most experiments, in particular all experiments in the energy range covered by this analysis, directly measured the transverse polarization of the recoiling proton in a secondary scattering process. These types of measurements have, in general, the disadvantage of low analyzing power and lim-
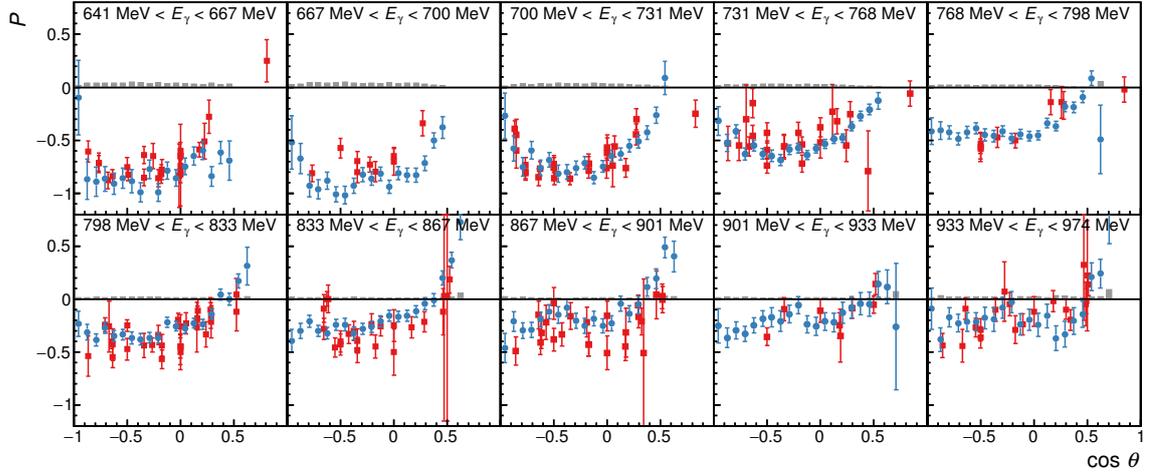
Figure 8.5: The results for the recoil polarizations P in the reaction $\gamma p \to p\pi^0$ (blue points, systematic uncertainty shown as gray bars), compared to previous measurements [Gor+74; Bel+83; Kat+80; Bra+80; Bra+86; Mal61] (red). Due to different binning, the energies differ by up to half of the bin size.

ited acceptance, leading to large uncertainties and limited angular coverage. Nevertheless, these previous results are in rather good agreement with the results from this analysis, as can be seen in Fig. 8.5.

The new results exceed the older data in precision, both statistical and systematic. Instead of several experiments, each with different and rather large, in some cases even uninvestigated, systematic uncertainties, the energy range from $E_\gamma = 640\,\mathrm{MeV}$ to $975\,\mathrm{MeV}$ is now covered by a single experiment with small, and well-under-control systematic uncertainties.

8.1.3.2 Reaction $\gamma p \to p\eta$

For the recoil polarization in the reaction $\gamma p \to p\eta$, only very few data points with very large uncertainty exist. Heusch et al. [Heu+70] measured a positive polarization value at $\theta = 90°$, at five different energies between $E_\gamma = 800\,\mathrm{MeV}$ and $1.1\,\mathrm{GeV}$. However, the large uncertainty of their measurement does not allow any further conclusions. The positive values are consistent with this analysis (cf. Fig. 6.48a).

Hongoh et al. [Hon+71] reported possible evidence for a sign change of P at $E_\gamma = 890\,\mathrm{MeV}$, with $P = 0.27 \pm 0.25$ at $\theta = 108.3°$ and $P = -0.15 \pm 0.30$ at $\theta = 82.3°$. Regarding the huge uncertainty of the negative data point this conclusion seems far-fetched, and indeed it is not confirmed by this analysis.

8.1.4 Double Polarization Observable *H*

For both reactions $\gamma p \to p\pi^0$ and $\gamma p \to p\eta$, there are no previous results available in the energy range covered in this work, so no comparison is possible.

8.2 Comparison to Model Predictions

8.2.1 Reaction $\gamma p \to p\pi^0$

Even though the reaction $\gamma p \to p\pi^0$ is the best-studied photoproduction reaction, the data available prior to this work are insufficient for the complete experiment (see Section 2.3). However, close to threshold, where only few partial waves contribute, the measurement of $\frac{d\sigma}{d\Omega}$ and Σ has proven to be sufficient for a determination of the S- and P-wave amplitudes [Sch+01]. Below the $2\pi^0$ threshold, the Fermi-Watson theorem [Wat54] helps to provide further constraints from the πN scattering data, by relating the complex phases of the photoproduction multipoles to the pion-scattering phase shifts. But even above the 2π threshold, in the second resonance region, where the t-channel contributions to the higher multipoles are still small [Sar16] and can be neglected, the number of observables needed for a determination of the multipoles in a truncated PWA can be expected to be smaller than the 8 observables needed for the complete experiment [WBT14]. One would therefore expect similar predictions[3] from the various analysis groups for the polarization observables in the second resonance region.[4] At even higher energies, beyond the second resonance region, higher partial waves also contribute and the previously available data provide insufficient constraints.

For the observable H, where no other results are available, the shape is accurately predicted by all PWAs in the lower energy bins, as can be seen in Fig. 8.8. And even in the higher energy bins, the data deviate mostly only by a constant offset from the predictions by SAID, MAID, and BnGa. Only the Jülich-Bonn model shows a larger deviation here.

For the observable P, shown in Fig. 8.7, the agreement between PWAs and data is even better, although this is not surprising considering the fact that this observables has already been measured by other experiments. Nevertheless, the new data will be able to constrain the PWAs further due to the significantly smaller uncertainty compared to the older data. The observable T exhibits a more surprising behavior, as can be seen in Fig. 8.6. While the overall agreement between the PWAs and the data is still pretty good, there is an unexpectedly large discrepancy around $W = 1600\,\mathrm{MeV}$ between MAID (and to a smaller extent also SAID) on one hand, and the other PWAs and the data on the other hand. An similar discrepancy has also been observed recently for the observables G [Thi+12] and E [Got+14]. This discrepancy for G, which is even more pronounced over a wider energy range compared to T, has been traced by Thiel et al. [Thi+12] to differences between the PWAs in the multipoles E_{0+} and E_{2-}. These deviations between the PWAs clearly show that a model-independent PWA has not been possible up to now, and highlight the importance of the new double polarization data from this work, combined with the recent results on E and G, to resolve the remaining ambiguities in the PWAs.

---

[3] For the observables T and P, which have previously been measured (albeit with large uncertainty), these are strictly speaking not predictions, but nevertheless completely independent from the results presented here. On the other hand, the observable H has not previously been measured in the energy range covered by this analysis, so here one can truly speak of predictions.

[4] Although it should be noted that recently published results on G [Thi+12] and E [Got+14] already showed unexpectedly large deviations between the PWAs.
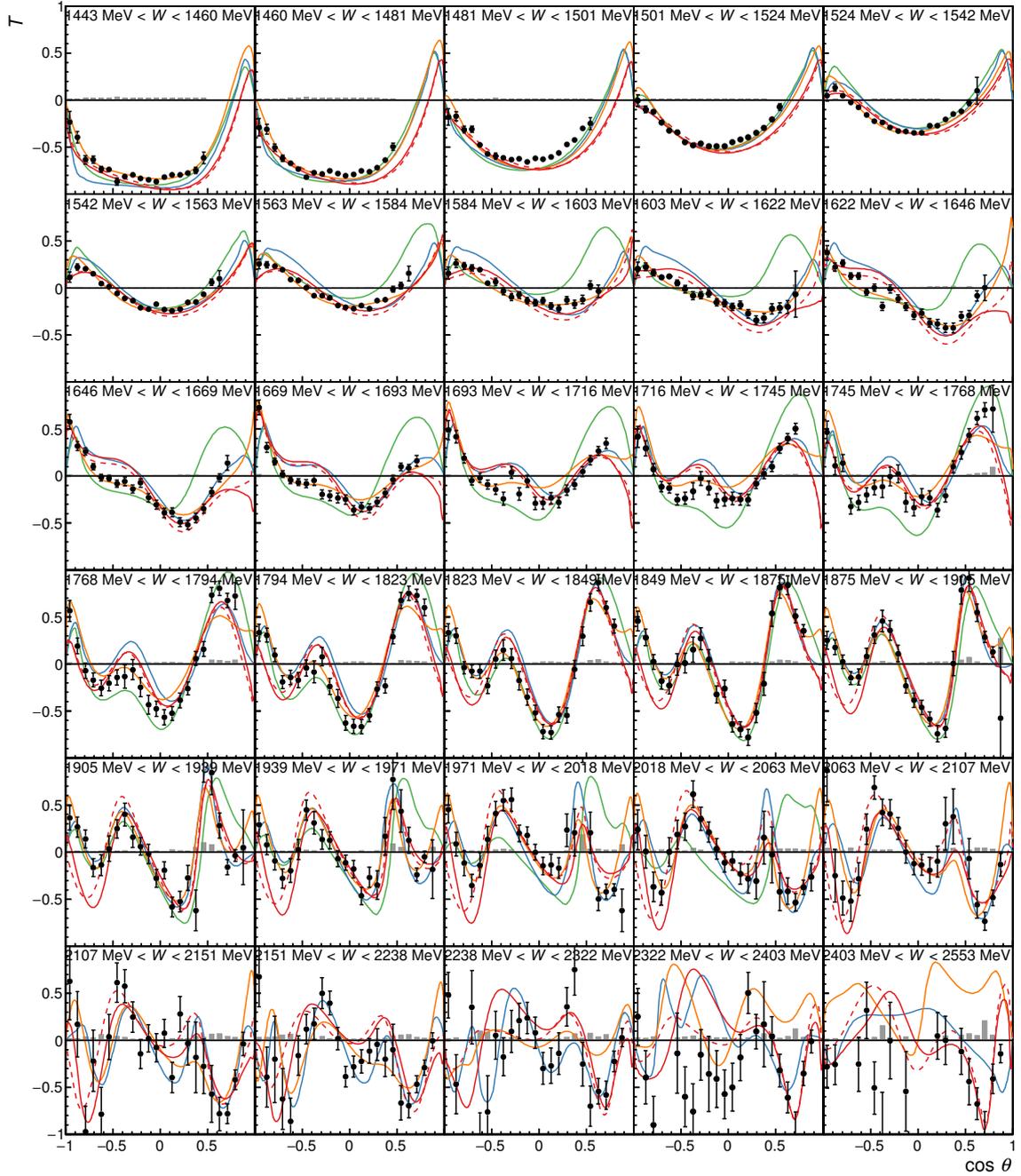
Figure 8.6: The results for the target asymmetry T in the reaction $\gamma p \to p\pi^0$, compared to the predictions by the SAID [Wor+12b] (blue), BnGa [Ani+12] (red) solutions 2011-01 (dashed) and 2011-02 (solid), and MAID [DKT07] (green) partial wave analyses, and the Jülich-Bonn model [Rön+15] (orange).
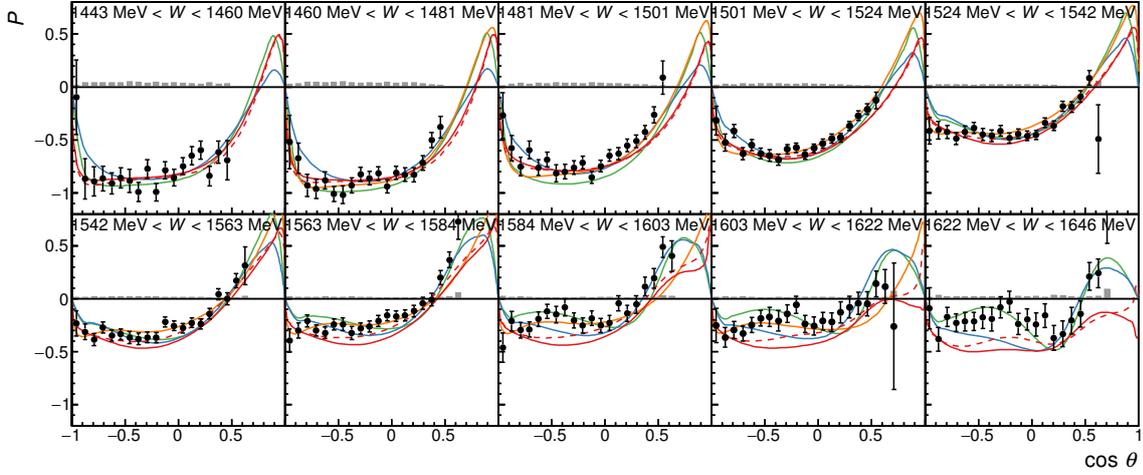
Figure 8.7: The results for the recoil polarization P in the reaction $\gamma p \rightarrow p\pi^0$, compared to the predictions by the SAID [Wor+12b] (blue), BnGa [Ani+12] (red) solutions 2011-01 (dashed) and 2011-02 (solid), and MAID [DKT07] (green) partial wave analyses, and the Jülich-Bonn model [Rön+15] (orange).
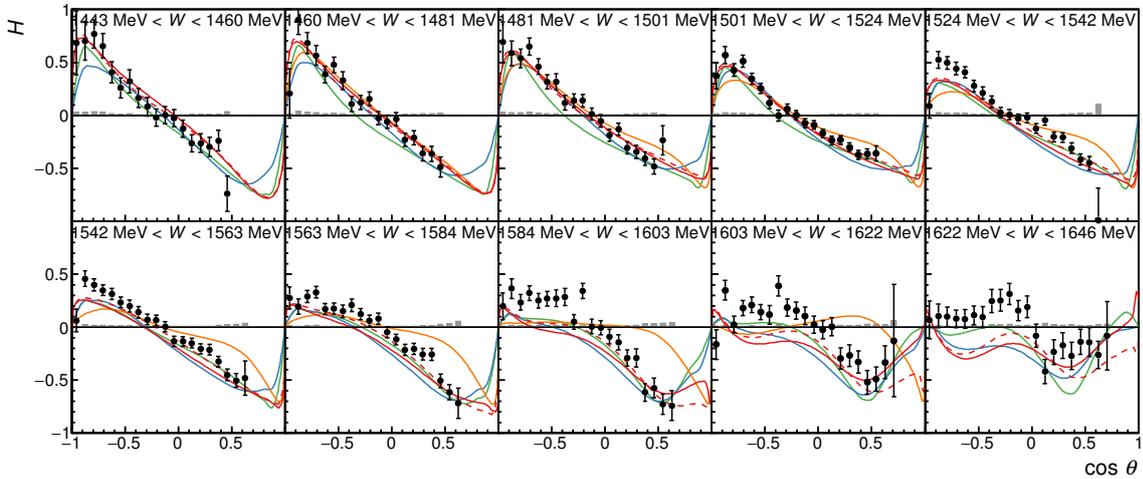
Figure 8.8: The results for the double polarization observable H in the reaction $\gamma p \rightarrow p\pi^0$, compared to the predictions by the SAID [Wor+12b] (blue), BnGa [Ani+12] (red) solutions 2011-01 (dashed) and 2011-02 (solid), and MAID [DKT07] (green) partial wave analyses, and the Jülich-Bonn model [Rön+15] (orange).

8.2.2 Reaction $\gamma p \to p\eta$

A comparison between the PWAs and the measured data for the observables T, P, and H in the reaction $\gamma p \to p\eta$ is shown in Figs. 8.9 and 8.10. Close to threshold, where the $N(1535)\,1/2^-$ resonance dominates the cross section, the observables are rather small and featureless, although T and P are clearly positive around $W = 1535\,\text{MeV}$, while H is negative. But even at higher energies, T exhibits fewer structures compared to the π^0 reaction. Only above $W \gtrsim 1900\,\text{MeV}$, more structures appear in the angular distributions of the data.

Unlike π photoproduction, where πN scattering data provides additional important constraints, there is essentially no agreement among the various PWAs, and no good agreement between any PWA and the data. Already close to threshold, the predictions from the PWAs cannot even agree on the sign of the observables P and H. At higher energies, the predictions are completely diverging, and exhibit very different structures in the angular distributions of T. Only the MAID and Jülich-Bonn model predict the correct sign over a wide energy range up to $W \lesssim 1900\,\text{MeV}$, but are not able to describe all the structures observed in the angular distributions.

Clearly, η photoproduction cannot presently be considered understood at all. The results from this analysis, together with recent measurements of the observables E [Mül17], F [Ako+14], and G [Grü16b] are therefore crucial to further constrain the PWAs.
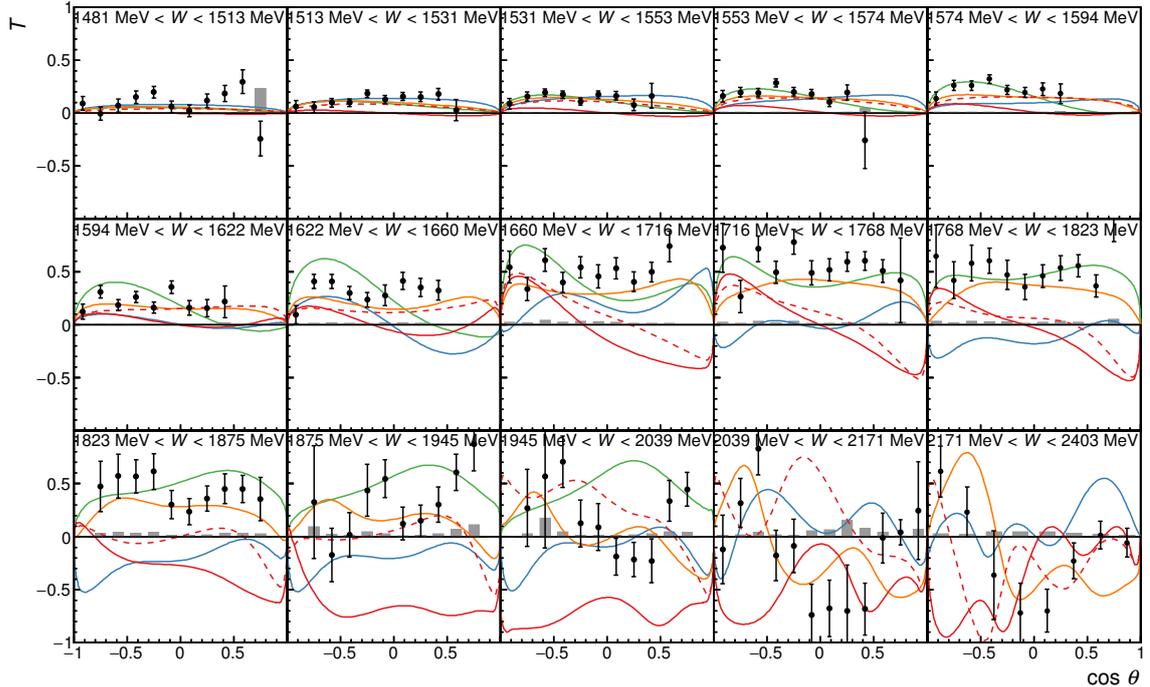
Figure 8.9: The results for the target asymmetry T in the reaction $\gamma p \to p\eta$, compared to the predictions by the SAID [M+10] (blue), BnGa [Ani+12] (red) solutions 2011-01 (dashed) and 2011-02 (solid), and MAID [Chi+03] (green) partial wave analyses, and the Jülich-Bonn model [Rön+15] (orange).

(a) Recoil polarization P

(b) Double polarization observable H
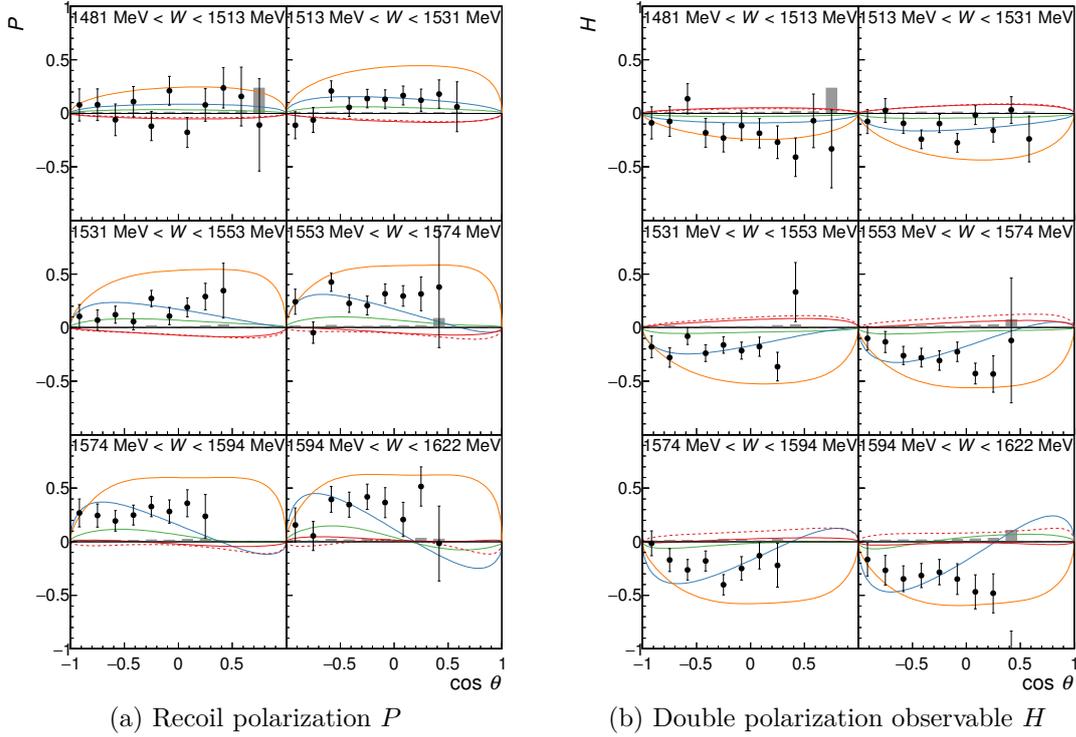
Figure 8.10: The results for the recoil polarization P and the double polarization observable H in the reaction $\gamma p \to p\eta$, compared to the predictions by the SAID [M+10] (blue), BnGa [Ani+12] (red) solutions 2011-01 (dashed) and 2011-02 (solid), and MAID [Chi+03] (green) partial wave analyses, and the Jülich-Bonn model [Rön+15] (orange).

The impact that the new data will have on the PWA will be discussed in more detail in Section 8.4. But first, a more model-independent approach is discussed, which at least seems feasible for the reaction $\gamma p \to p\pi^0$ with the newly available data.

8.3 Energy-Independent Extraction of Multipoles

The first step to obtain information on the contributing resonances from the polarization observables is the determination of the multipole amplitudes. As described in Section 2.1, this can be done by expanding, for each energy, the angular dependence of the corresponding profile function for each observable in powers of $\cos\theta$ (see Eq. (2.20)).

To obtain the corresponding profile functions $\check{O} = O \cdot \frac{d\sigma}{d\Omega}$ for each measured observable O, the unpolarized cross section $\frac{d\sigma}{d\Omega}$ is needed. Here, the fit of the SAID CM12 analysis [Wor+12b] is used. In contrast to using an individual measurement of the cross section this has the advantage that the fit describes the full world database of measurements, leading to negligible uncertainties.[5]

---

[5] Of course, this introduces a possible model-dependence; however, in particular for the differential cross section the SAID fit is in excellent agreement with the measurements, so the model-dependence can be neglected compared to the precision of the measured polarization observables.

159

For the observables T, P, and H, the explicit form of the expansion is given by (cf. Eq. (2.20) with $\alpha = 1$ and $\beta = -1$)

$$\check{O}(\theta) = \frac{q}{k}\,\sin(\theta)\sum_{\kappa=0}^{2\ell_{\max}-1}a_\kappa^O(W)\cos^\kappa(\theta),\tag{8.2}$$

where the phasespace factor q/k is given by the CM momenta of the initial and the final states:

$$\frac{q}{k} = \frac{\sqrt{(W^2-(m_p+m_{\pi^0,\eta})^2)\cdot(W^2-(m_p-m_{\pi^0,\eta})^2)}}{W^2-m_p^2}.\tag{8.3}$$

To simplify the expansion, all data points ca be divided by the factor $\frac{q}{k}\sin(\theta)$ to form the reduced profile functions $\tilde{O}$, which are just polynomials in $\cos\theta$.

$$\tilde{O}(\cos\theta) = \sum_{\kappa=0}^{2\ell_{\max}-1}a_\kappa^O(W)\cos^\kappa(\theta)\tag{8.4}$$

To perform the expansion, functions of this form are fitted to the angular distributions of the reduced profile functions. The expansion is truncated at $\ell_{\max}$ between 1 and 4. The fits are shown in Figs. 8.11 to 8.13 for the reaction $\gamma p \to p\pi^0$. The χ^2 of the fits for various $\ell_{\max}$ are shown in Figs. 8.14 to 8.16.

As can be seen, a truncation at $\ell_{\max} = 1$ is inadequate to describe the data for the observables T and P, resulting in $\chi^2/\text{ndf} \gg 1$ for all measured energies. For $E_\gamma < 950\,\text{MeV}$ it is, however, possible to achieve a satisfactory description of the data with a truncation at $\ell_{\max} = 2$. For the observable H, even $\ell_{\max} = 1$ is sufficient with the available precision. At higher energies, where only the results for T are available, contributions from higher angular momenta are getting more important. Nevertheless, $\ell_{\max} = 3$ is sufficient to describe the data up to $E_\gamma \lesssim 1300\,\text{MeV}$. With $\ell_{\max} = 4$ it is possible to adequately describe the data over the full energy range. However, it should be noted that this does not exclude any contribution from partial waves with higher angular momentum,[6] it merely shows that the available data sample for the individual observables is not sensitive to these contributions. This becomes particularly apparent for the reaction $\gamma p \to p\eta$, where the available data for the observables T, P, and H can be described reasonably well with just $\ell_{\max} = 1$.[7] The statistical quality of the η data is simply insufficient to gain much information from the individual measurements. Therefore, the energy independent analysis of the individual observables is not pursued any further for the reaction $\gamma p \to p\eta$. Instead, the data on all measured observables needs to be analyzed simultaneously in a multi-channel PWA to extract the most possible information from the data. This approach will be discussed in more detail in Section 8.4. On the other hand, in case of π^0 photoproduction, the data quality is sufficient to gain some information on the multipole amplitudes from the performed expansion. This will be discussed in the following.

---

[6] Even if no s-channel resonances above a given ℓ contributes, there can also be t-channel contributions.
[7] Since the expansion of the individual observables is essentially meaningless because of the large statistical uncertainty, the fits are not shown here.
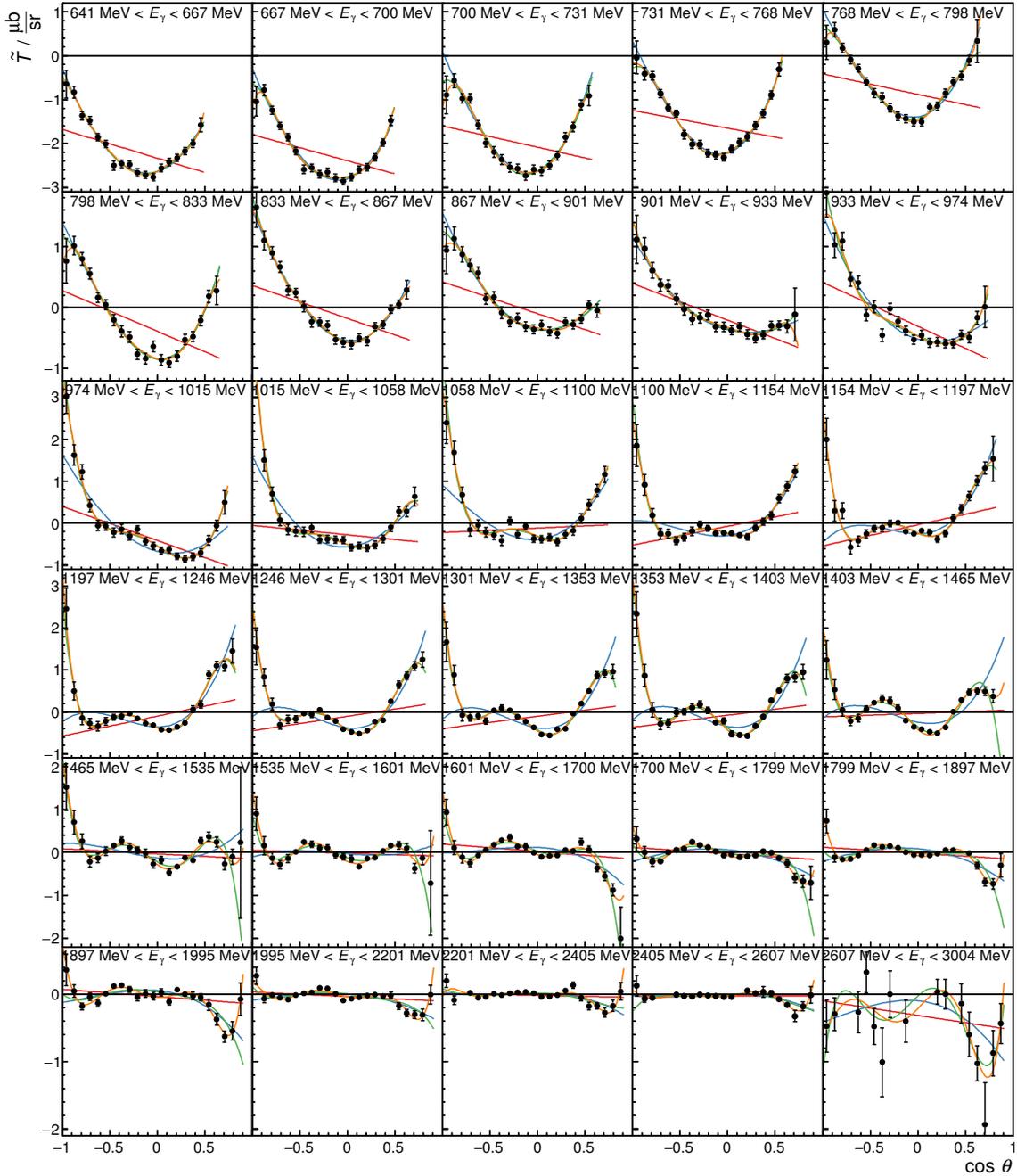
Figure 8.11: The reduced profile function $\tilde{T}$ for the target asymmetry in the reaction $\gamma p \to p\pi^0$, fitted by functions of the form given in Eq. (8.4) with truncation at $\ell_{\max} = 1$ (red), $\ell_{\max} = 2$ (blue), $\ell_{\max} = 3$ (green), and $\ell_{\max} = 4$ (orange). The error bars shown include only the statistical uncertainty of the polarization observable, the dominant systematic uncertainty (the polarization degrees, cf. Chapter 7) is only a global uncertainty and does not affect the shape of the angular distributions.
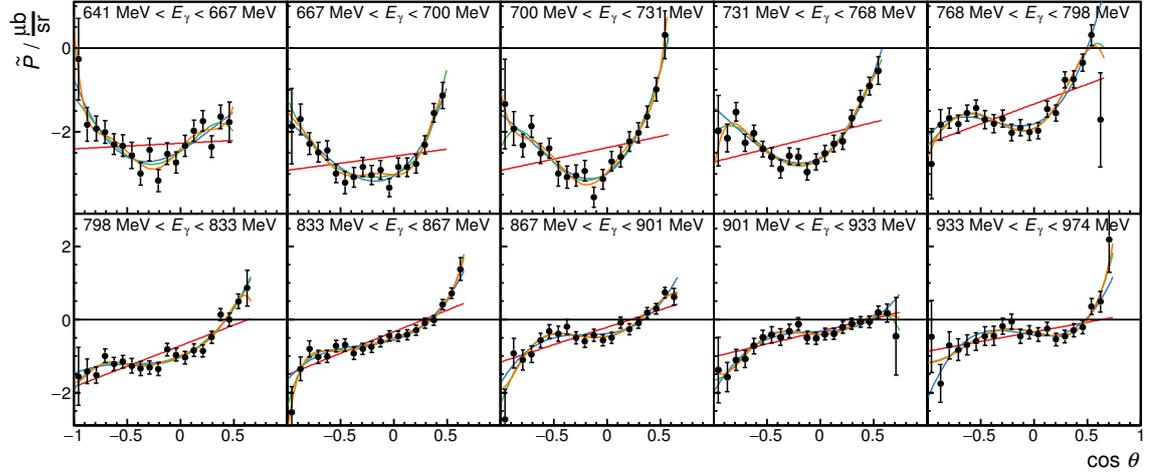
Figure 8.12: The reduced profile function $\tilde{P}$ for the recoil polarization in the reaction $\gamma p \to p\pi^0$, fitted by functions of the form given in Eq. (8.4) with truncation at $\ell_{\max} = 1$ (red), $\ell_{\max} = 2$ (blue), $\ell_{\max} = 3$ (green), and $\ell_{\max} = 4$ (orange). The error bars shown include only the statistical uncertainty of the polarization observable, the dominant systematic uncertainty (the polarization degrees, cf. Chapter 7) is only a global uncertainty and does not affect the shape of the angular distributions.
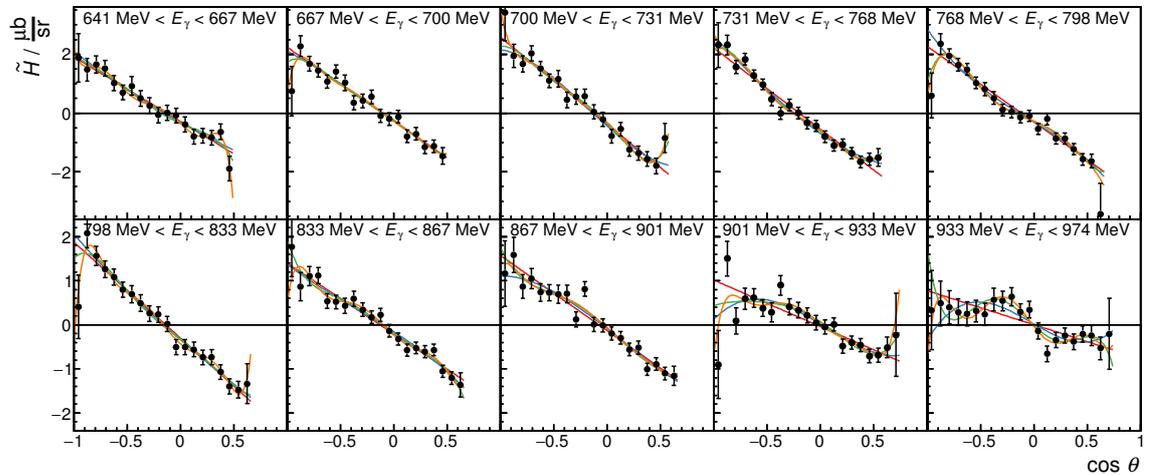
Figure 8.13: The reduced double polarization profile function $\tilde{H}$ in the reaction $\gamma p \to p\pi^0$, fitted by functions of the form given in Eq. (8.4) with truncation at $\ell_{\max} = 1$ (red), $\ell_{\max} = 2$ (blue), $\ell_{\max} = 3$ (green), and $\ell_{\max} = 4$ (orange). The error bars shown include only the statistical uncertainty of the polarization observable, the dominant systematic uncertainty (the polarization degrees, cf. Chapter 7) is only a global uncertainty and does not affect the shape of the angular distributions.
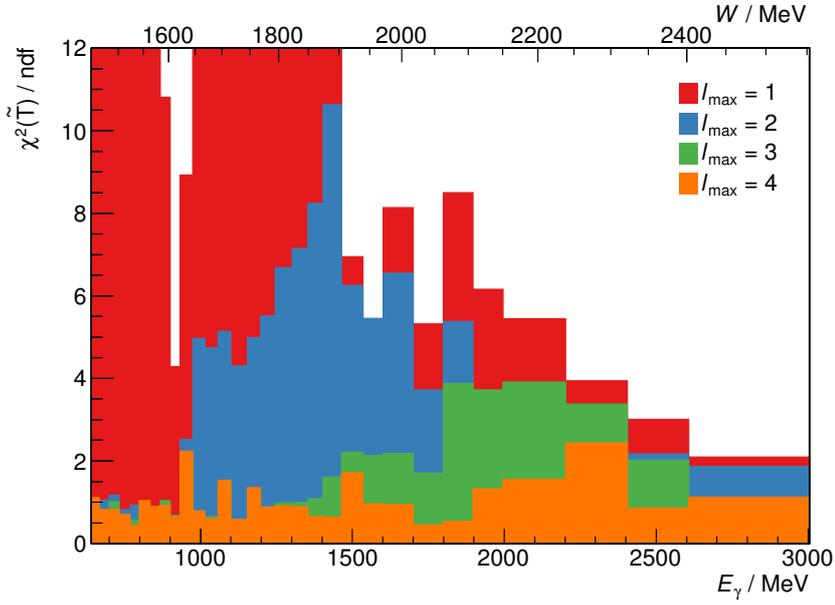
Figure 8.14: The reduced χ^2 of the fits to $\tilde{T}$ shown in Fig. 8.11.
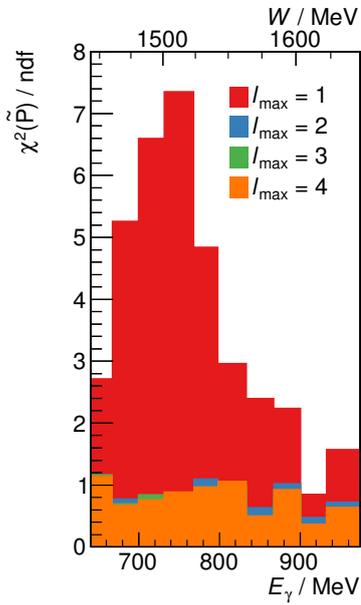
Figure 8.15: The reduced χ^2 of the fits to $\tilde{P}$ shown in Fig. 8.12.
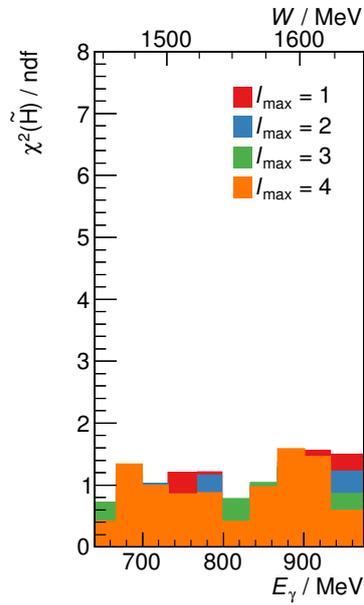
Figure 8.16: The reduced χ^2 of the fits to $\tilde{H}$ shown in Fig. 8.13.

The coefficients a_κ^O of the expansion, which are shown in Figs. 8.17 to 8.19 as a function of the CM energy W, depend on the multipoles $E_{\ell\pm}$ and $M_{\ell\pm}$ (see Eq. (2.21)). In case of truncation at $\ell_{\max} = 2$, which is reasonable below $W < 1.63\,\text{GeV}$, there are 8 complex multipoles contributing: $E_{0+}, E_{1+}, M_{1+}, M_{1-}, E_{2+}, E_{2-}, M_{2+}, M_{2-}$.[8]

Obviously, the 12 real coefficients $a_\kappa^T, a_\kappa^P, a_\kappa^H$ ($\kappa \in \{0, 1, 2, 3\}$) are not sufficient to determine the 8 complex multipoles. However, it is possible to obtain additional coefficients by performing the same expansion on other polarization observables that have been measured with high precision, namely $\frac{d\sigma}{d\Omega}$ [Wor+12b], Σ [Bar+05a], G [Thi12; Thi+12; Thi+17], and E [Got13; Got+14]. From the expansion coefficients for all these observables it should be possible to constrain the multipoles for each W by numerically solving Eq. (2.21). A better approach is to directly express the expansion coefficients a_κ^O in terms of the multipoles and simultaneously fit the multipoles to all observables. A further improvement is not to neglect the $\ell = 3$ and higher multipoles, but use their values from the BnGa PWA [Gut+14] instead. This of course introduces a small model-dependence, but is expected to yield more realistic results since the higher multipoles also contribute to the lower expansion coefficients through interference terms with the lower multipoles.

An energy-independent fit to the data, performed by Anisovich [H+14], reveals only negligible contribution from the multipoles E_{1+}, E_{2+}, and M_{2+} for all $W < 1.63\,\text{GeV}$. The other multipoles are shown in Fig. 8.20 as a function of W. Since one overall phase remains undetermined, all phases are shown relative to M_{2-}. For this fit, the statistical and systematic errors of the individual data points were added quadratically. This overestimates the errors of the determined multipoles because the systematic errors are correlated to some degree (cf. Chapter 7). Nevertheless, it is a better approach than to neglect the systematic errors, which would underestimate the errors of the multipoles significantly.

For some multipoles, in particular E_{0+} and M_{1-}, a strong variation of the magnitude is observed around $W = 1.51\,\text{GeV}$, which is not accompanied by a strong variation of the phase that one would expect in the presence of a resonance. As it turns out, the variation of the magnitude is an artifact of the fit: the χ^2 shows not only one isolated minimum. Instead, other local minima exist that describe the data with similar quality. To choose among these solutions, a penalty function can be applied which adds the squared difference between the fitted multipole and the multipole from the full BnGa PWA [Gut+14], normalized to the corresponding squared statistical uncertainty of the fitted multipole, to the χ^2 of the fit. This introduces an additional model-dependence by favoring the solution closest to the energy-dependent BnGa PWA. However, the penalty has hardly any visible impact on the fit to the observables E, G, T, P, and H, and the resulting multipoles are in most cases compatible with the results without penalty, but show a much smoother variation with W, as can be seen in Fig. 8.20. Thus, the penalty function successfully eliminates the fit artifacts without significantly changing the actual results. To achieve a truly model-independent fit without the penalty function, more data with smaller statistical errors would be required.

In case of a rather isolated resonance it is possible to extract resonance parameters directly from the multipoles. This is e.g. possible for the $N(1520)\,3/2^-$ resonance, which contributes

---

[8] The exact relations between the coefficients and the multipoles are rather lengthy and not given here. Up to $\ell_{\max} = 2$ they can be found e.g. in [Wun12].
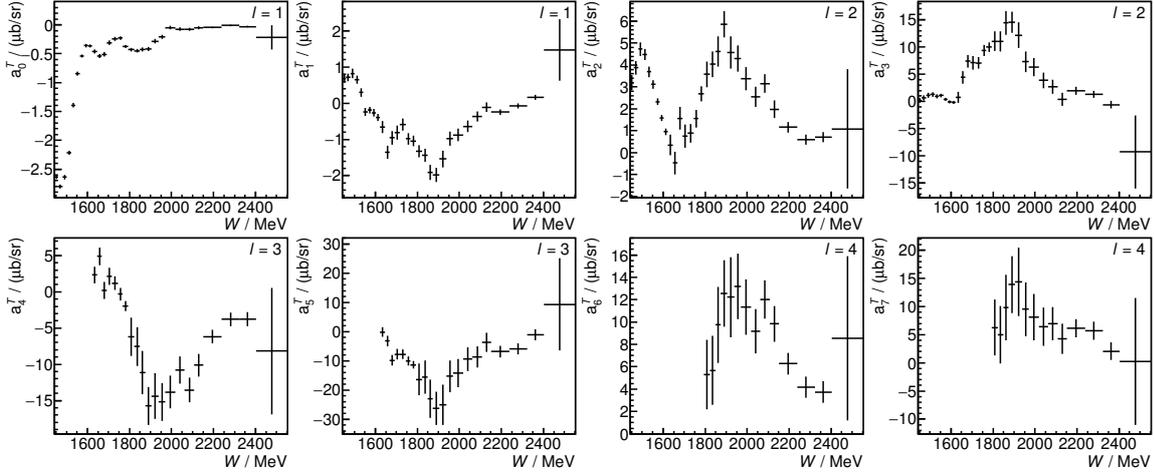
Figure 8.17: The coefficients for the truncated expansion (see Eq. (8.3)) of the profile function for the target asymmetry T in the reaction $\gamma p \to p \pi^0$. The error bars shown include only the statistical uncertainty. Below $W = 1.8\,\mathrm{GeV}$ the expansion is truncated at $\ell_{\max} = 3$ and the coefficients a_6^T and a_7^T vanish. Below $W = 1.63\,\mathrm{GeV}$, where the expansion is truncated at $\ell_{\max} = 2$, also the coefficients a_4^T and a_5^T vanish.
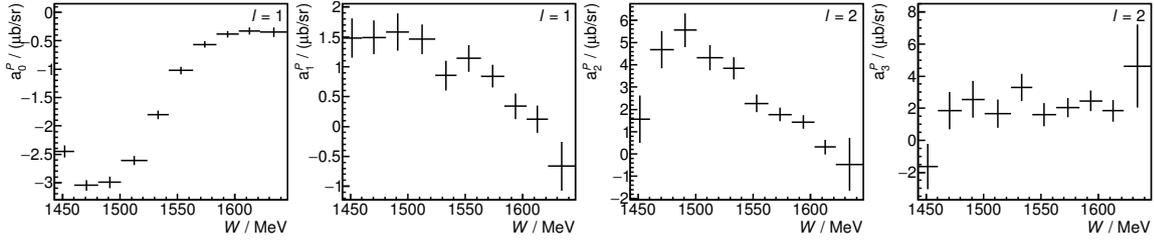
Figure 8.18: The coefficients for the truncated expansion (see Eq. (8.3)) of the profile function for the recoil polarization P in the reaction $\gamma p \to p \pi^0$. The error bars shown include only the statistical uncertainty. In the given energy range the expansion is truncated at $\ell_{\max} = 2$, the coefficients a_4^P and higher vanish.
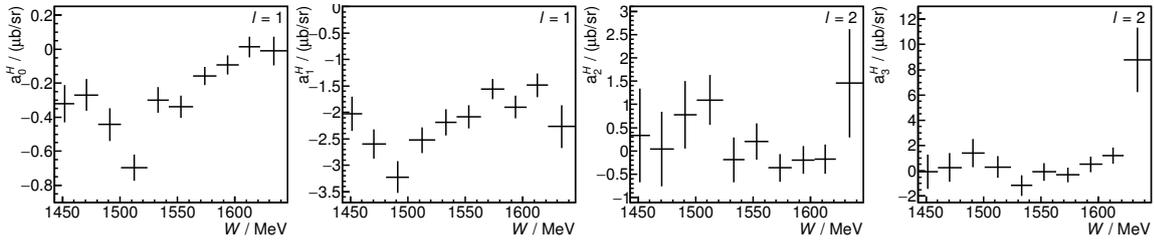
Figure 8.19: The coefficients for the truncated expansion (see Eq. (8.3)) of the profile function for the double polarization observable H in the reaction $\gamma p \to p \pi^0$. The error bars shown include only the statistical uncertainty. In the given energy range the expansion is truncated at $\ell_{\max} = 2$, the coefficients a_4^H and higher vanish.
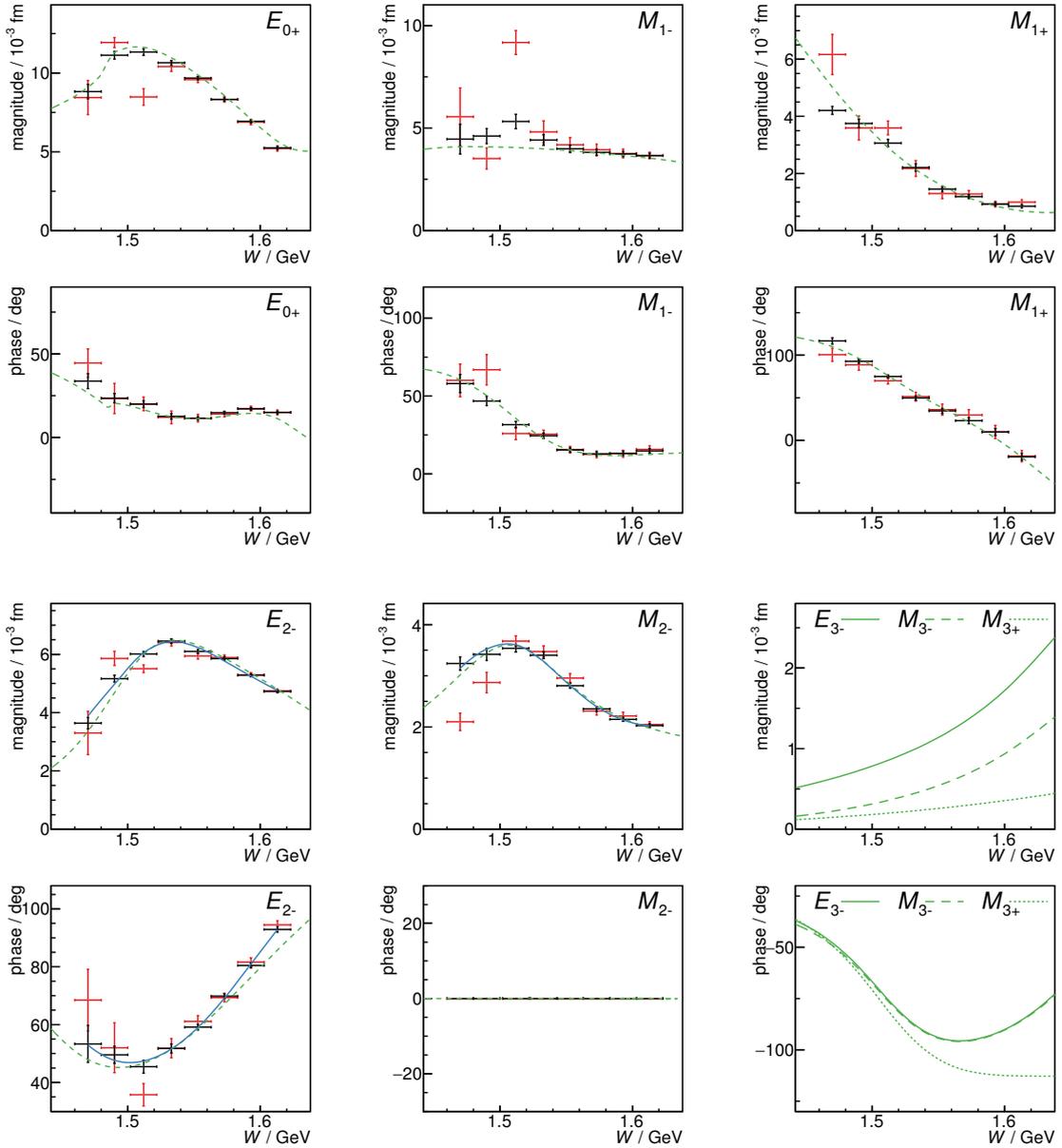
Figure 8.20: Magnitude and phase of the multipoles determined from the energy-independent fit [H+14]. The results of an unbiased fit are shown in red, and results of a fit with a penalty function are shown in black (for details see text). The blue curve represents a Breit-Wigner plus background fit to the black data points for E_{2-} and M_{2-}. The full energy-dependent BnGa2014 PWA solution [Gut+14] is shown for comparison as the green curve. In addition, the largest multipoles for $\ell \geq 3$ (taken from the BnGa PWA) are shown, with E_{2-} and M_{2-} receiving contributions from the $N(1680)\,5/2^+$ resonance.

to the E_{2-} and M_{2-} multipoles. The $\Delta(1700)\,3/2^-$ is far enough away, its phase variation in the $W = 1500\,\mathrm{MeV}$ region has been found to be smooth by the BnGa PWA [Ani+12]. By fitting the E_{2-} and M_{2-} magnitudes and their respective phase difference using a Breit-Wigner plus background amplitude (blue curve in Fig. 8.20) the helicity couplings $A_{1/2}$ and $A_{3/2}$ of the $N(1520)\,3/2^-$ can be determined [WTS13], resulting in [H+14]

$$A_{1/2} = (-0.022 \pm 0.006_{\mathrm{stat}} \pm 0.007_{\mathrm{sys}})\,\mathrm{GeV}^{-1/2} \tag{8.5a}$$

$$A_{3/2} = (0.118 \pm 0.010_{\mathrm{stat}} \pm 0.019_{\mathrm{sys}})\,\mathrm{GeV}^{-1/2}. \tag{8.5b}$$

The systematic error receives contributions from several sources, which are added in quadrature:

1. The uncertainty of the incoming photon energy (see Section 7.3): The data on T, P, and H (this analysis) were combined with the data on the other observables with relative energy shifts of $0\,\mathrm{MeV}$, $\pm 5\,\mathrm{MeV}$ and $\pm 10\,\mathrm{MeV}$. No evidence for any systematic shifts was found, but an additional spread of the results was observed. This spread is taken as an additional systematic uncertainty. It amounts to $\Delta A_{1/2} = 0.005\,\mathrm{GeV}^{-1/2}$ and $\Delta A_{3/2} = 0.015\,\mathrm{GeV}^{-1/2}$.

2. The background amplitude: It is assumed to be a constant, linear, or quadratic function in s, or given by the $\Delta(1700)\,3/2^-$ amplitude of the BnGa PWA. The spread of the different background parameterizations is used to define a systematic error. It amounts to $\Delta A_{1/2} = 0.005\,\mathrm{GeV}^{-1/2}$ and $\Delta A_{3/2} = 0.011\,\mathrm{GeV}^{-1/2}$.

3. The $N(1520)\,3/2^-$ branching ratio: It is needed to calculate the helicity coupling from the Breit-Wigner fit. Here, the value $\frac{\Gamma_{\pi N}}{\Gamma_{\mathrm{total}}} = 0.63 \pm 0.03$, given by the BnGa PWA [Ani+12], is used. Its uncertainty is a further systematic error.

A comparison of the determined helicity couplings to the results from other analyses is shown in Table 8.1. The various results for $A_{1/2}$ are in good agreement, but previous determinations of $A_{3/2}$ are significantly larger compared to result from this analysis. It is still compatible with the BnGa PWA [Ani+12], but strongly disagrees with the extremely precise results given by the SAID group [Wor+12a; Wor+12b]. It should be noted that the result from the energy-independent fit is expected to exhibit the smallest model-dependence, even though it is not completely model independent because of the penalty function used for the fit, and the use of the higher-order multipoles from the BnGa PWA.

Table 8.1: A comparison of the $N(1520)\,3/2^-$ helicity couplings (in $\mathrm{GeV}^{-1/2}$) determined by various analyses.

	this analysis [H+14]	SAID CM12 [Wor+12b]	SAID SN11 [Wor+12a]	BnGa 2011 [Ani+12]	PDG [Nak+10]
$A_{1/2}$	-0.022 ± 0.009	-0.019 ± 0.002	-0.016 ± 0.002	-0.022 ± 0.004	-0.024 ± 0.009
$A_{3/2}$	0.118 ± 0.021	0.141 ± 0.002	0.156 ± 0.002	0.131 ± 0.010	0.166 ± 0.005

A similar analysis is possible to determine the helicity coupling of the $N(1535)\,1/2^-$ resonance from the E_{0+} multipole.[9] However, the result exhibits a much stronger dependence on the background model used, resulting in a coupling in the range $0.070\,\mathrm{GeV}^{-1/2}$ to $0.140\,\mathrm{GeV}^{-1/2}$, including systematic uncertainties [H+14].

Since the energy-independent determination of the multipole amplitudes can, in principal, be done in a model-independent way, it should be the preferred method. It is, however, only possible if high precision data are available for a large enough number of observables, which is currently only the case for the reaction $\gamma p \to p\pi^0$ at low energies. To extract significant information from lower-statistics data samples, it is indispensable to utilize the correlation between neighboring energies and also data from other reaction channels to provide further constraints, instead of analyzing each energy bin individually. This approach is implemented e.g. by the BnGa PWA group, the impact of the new results on the PWA will be discussed in the following.

8.4 Energy-Dependent Partial Wave Analysis

8.4.1 Reaction $\gamma p \to p\pi^0$

The first analysis group that included the new double polarization data in their fit was the BnGa PWA group. Starting from the solutions BnGa2011-01 and BnGa2011-02 [Ani+12] (cf. Section 2.3.2) new data were included for the reaction $\gamma p \to p\pi^0$, namely the results on the observables T, P, and H from this analysis, and recent results on the observables G [Thi12; Thi+12] and E [Got13; Got+14]. In addition, new data were included for other reactions,[10] but these are expected to have only a minor influence on the multipole decomposition for the reaction $\gamma p \to p\pi^0$.

For the new fit, the 12 different solutions from 2011 were taken as starting values, and all parameters were optimized with the addition of the new data. All fits converged, but 6 fits resulted in a significantly worse description of the data compared to the other fits, and could thus be eliminated [H+15]. The best fit achieves a reasonably good description of the results from this work, as can be seen in Fig. 8.21 for the target asymmetry, in Fig. 8.22 for the recoil polarization, and in Fig. 8.23 for the double polarization observable H. There are, however, a few minor deviations visible, e.g. around $W = 1480\,\mathrm{MeV}$ the fit seem to require larger negative values for T than were measured. Also around $W = 1690\,\mathrm{MeV}$ some deviations remain, although the refit achieves a much better description of the data compared to the solutions from 2011. These deviations could indicate an inconsistency in the world data base, but with the available data it is presently impossible to identify a single inconsistent measurement.

From the new fits the multipole amplitudes for the reaction $\gamma p \to p\pi^0$ can be derived. The errors can be estimated from the distribution of the different solutions. Since 6 of the 12 solutions were eliminated by the refit, one would expect a decrease of the errors. And indeed, as can be seen in Fig. 8.24, the error bands of the multipoles are significantly smaller

---

[9] The $N(1535)\,1/2^-$, having $J = 1/2$, cannot be excited from a helicity 3/2 state; hence, there is only one coupling $A_{1/2}$.

[10] Most of these are multi-meson final states like $p\pi^0\pi^0$ [Sok+15b; Sok+15a] and $p\pi^0\eta$ [Gut+14], but also final states with strangeness. For a full list see Ref. [25] in [H+15].
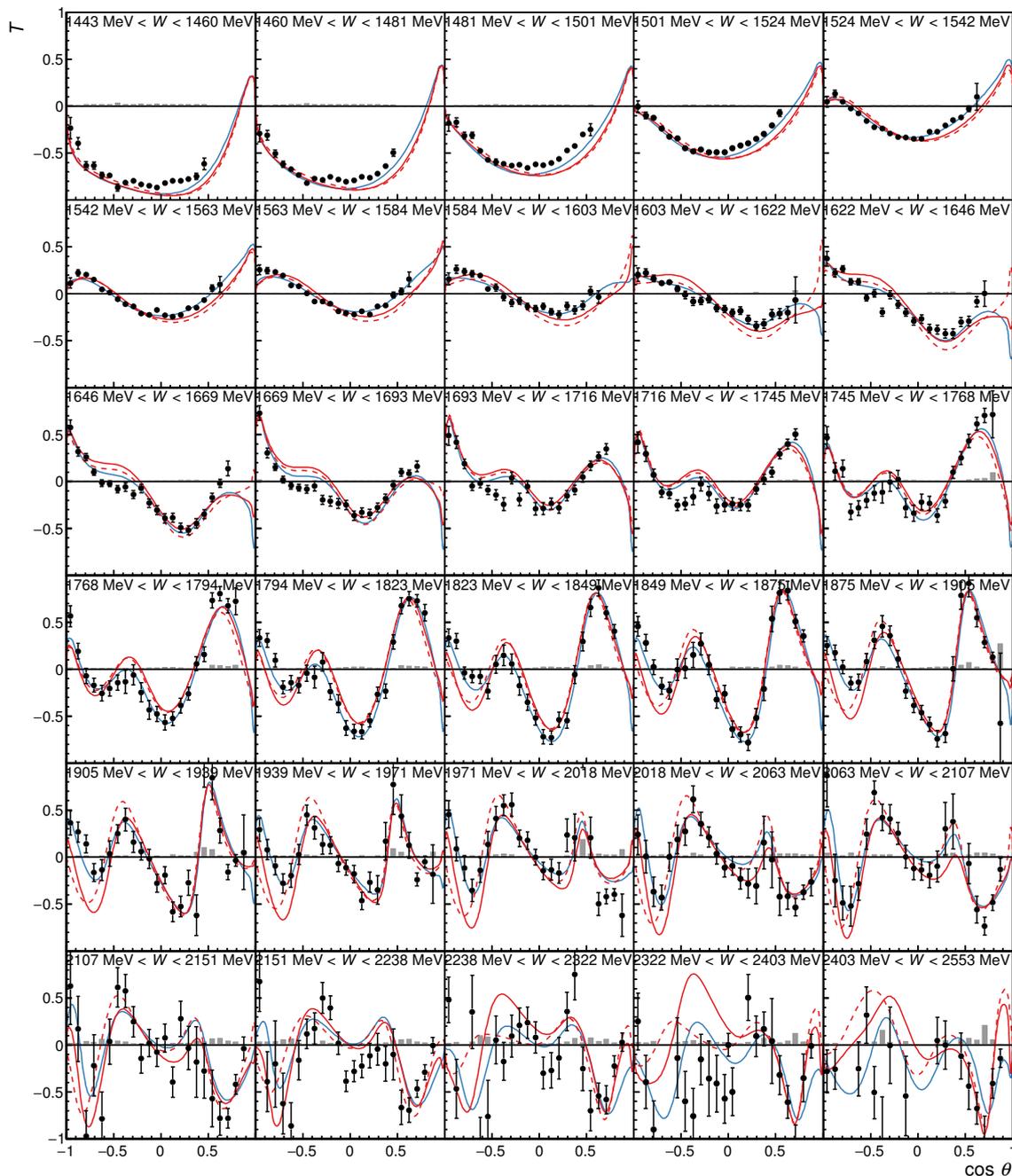
Figure 8.21: The results for the target asymmetry T in the reaction $\gamma p \rightarrow p\pi^0$, together with a BnGa refit [H+15] (blue). The older BnGa solutions [Ani+12] (red) 2011-01 (dashed) and 2011-02 (solid) are also shown for comparison.
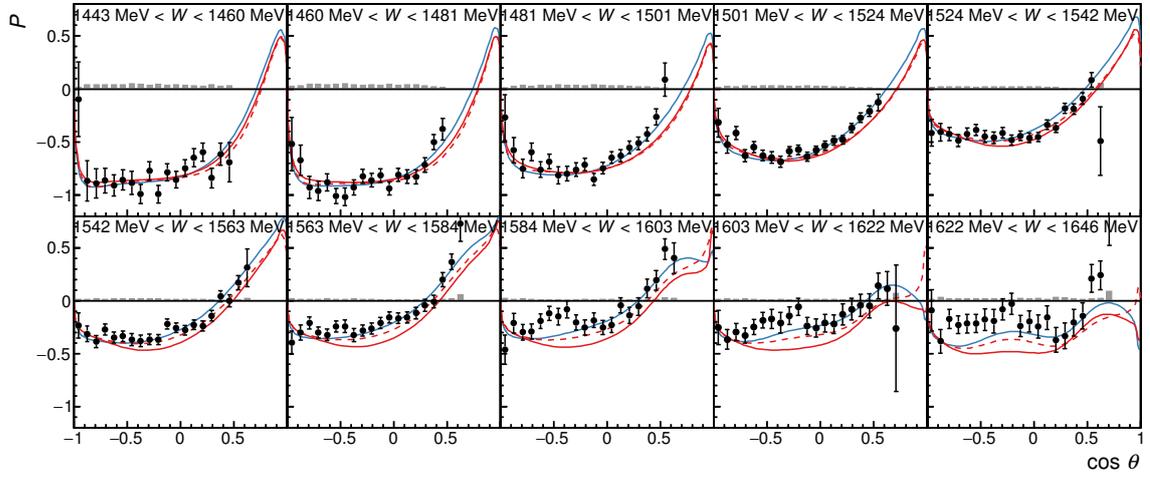
Figure 8.22: The results for the recoil polarization P in the reaction $\gamma p \rightarrow p\pi^0$, together with a BnGa refit [H+15] (blue). The older BnGa solutions [Ani+12] (red) 2011-01 (dashed) and 2011-02 (solid) are also shown for comparison.
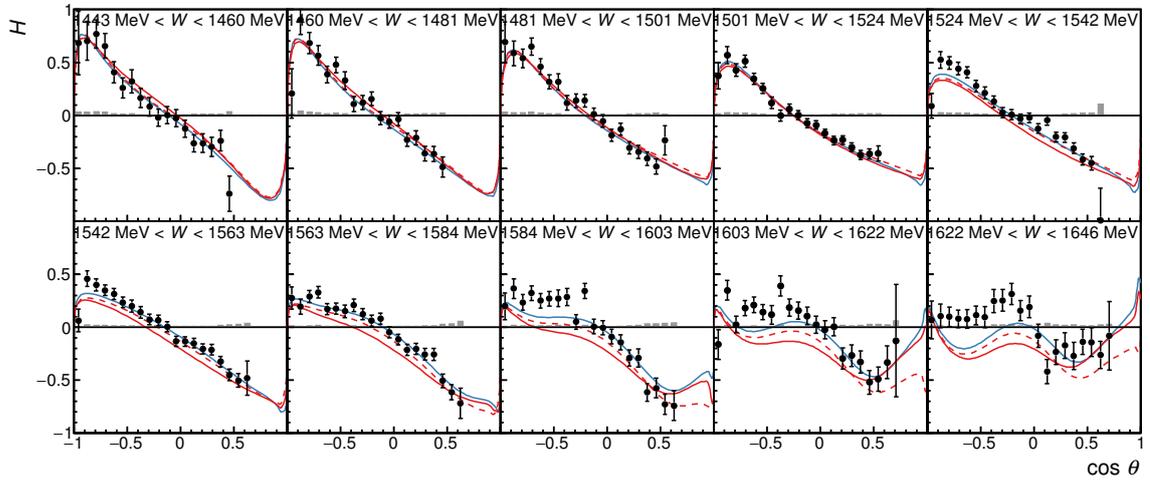
Figure 8.23: The results for the double polarization H in the reaction $\gamma p \rightarrow p\pi^0$, together with a BnGa refit [H+15] (blue). The older BnGa solutions [Ani+12] (red) 2011-01 (dashed) and 2011-02 (solid) are also shown for comparison.
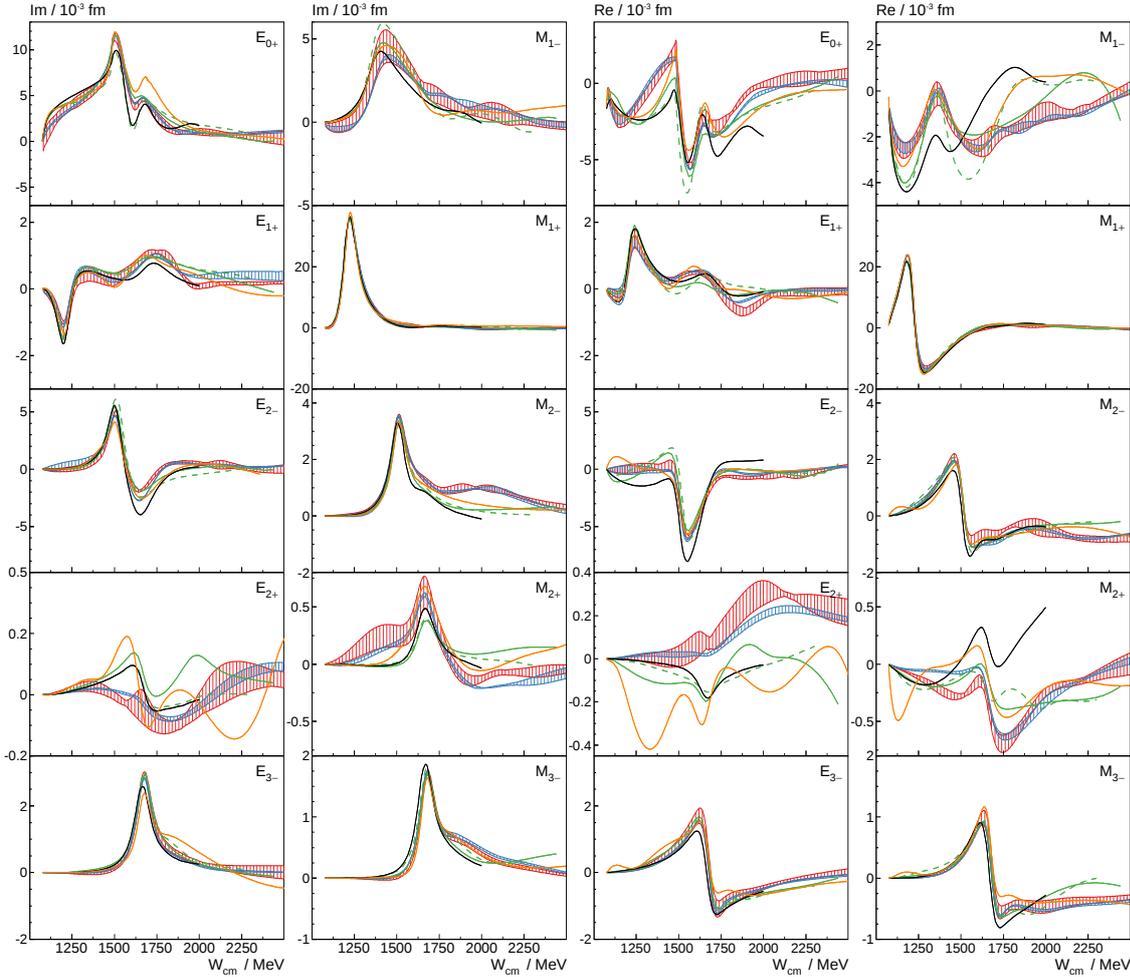
Figure 8.24: Multipole decomposition of the $\gamma p \rightarrow p\pi^0$ transition amplitudes [H+15]. The red shaded areas give the range derived from a variety of different fits from BnGa2011-01 and BnGa2011-02 [Ani+12]. The blue shaded area represents the range of solutions when the new data are included in the fit. The curves representing the MAID fit [DKT07] (black), SAID (green) CM12 [Wor+12b] (solid) and SN11 [Wor+12a] (dashed), and JüBo 2015 [Rön+15] (orange) are shown for comparison. Note that an error band is presently not provided by the other analyses.

for the refit compared to the solution from 2011. In particular, substantial improvement can be seen for the M_{1-} multipole, to which the Roper resonance $N(1440)\,1/2^+$ and the $N(1710)\,1/2^+$ contribute, and for the E_{2+} multipole to which the $J^P = 5/2^-$ resonances contribute. Averaged over all multipoles and energies, the errors are reduced by a factor of 2.25 [H+15]. The values of the multipoles, on the other hand, were not changed very much by the refit. While there are some minor changes visible e.g. in the imaginary part of the E_{1+} multipole, the refit is compatible with the old solutions at the 2σ level over the full mass range.
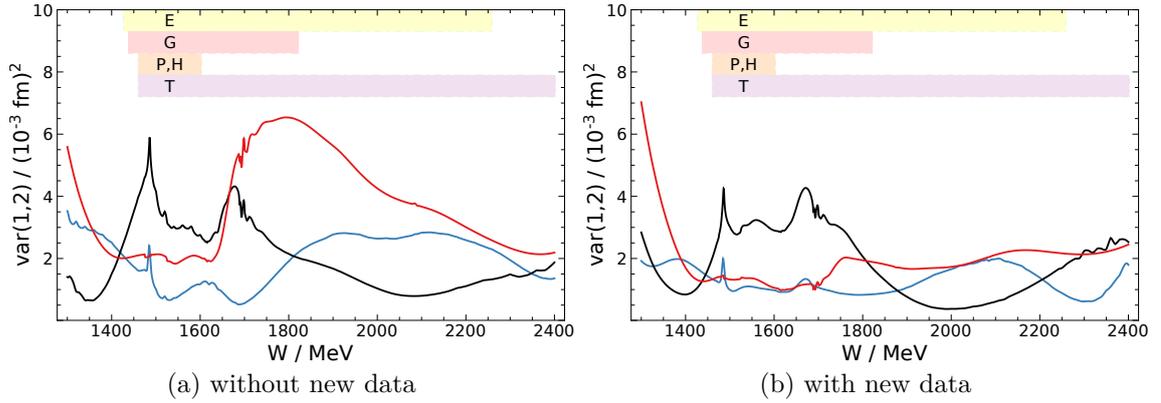
Figure 8.25: The pairwise variances between BnGa, JüBo, and SAID analyses, summed over all $\gamma p \rightarrow p\pi^0$ multipoles up to $\ell = 4$ [Ani+16]. Blue: SAID, BnGa; black: SAID, JüBo; red: BnGa, JüBo. The range covered by the new results on T, P, H (this work), E [Got+14], and G [Thi+12; Thi+17] is indicated by shaded areas.

The other analyses, which did not yet include the new double polarization data, show significant deviations to the BnGa, both the old solution and the refit. This is most obvious for the E_{2+} and M_{2+} multipoles, but also for the M_{1-} multipole. Since for these multipoles the new data resulted in a drastic reduction of the errors in the BnGa PWA, one can hope that with the inclusion of the new data all analyses will converge to a single solution.

This was investigated in a combined effort by the various analysis groups [Ani+16]. To quantify the differences between two partial wave analyses, the variance, defined as the sum over the squared differences of the 16 complex multipole amplitudes $\mathcal{M}$ up to $\ell = 4$, can be used:

$$\mathrm{var}(1,2) = \frac{1}{2} \sum_{i=1}^{16} \left(\mathcal{M}_i(1) - \mathcal{M}_i(2)\right)\left(\mathcal{M}_i^*(1) - \mathcal{M}_i^*(2)\right). \tag{8.6}$$

The pairwise variances between the BnGa, JüBo, and SAID analyses are shown in Fig. 8.25a before and in Fig. 8.25b after the new data on the observables T, P, and H from this work, as well as new data on E [Got+14] and G [Thi+12; Thi+17] were included in the fits. The combined variance of all three analyses is shown in Fig. 8.26. Overall, the variance is reduced considerably due to the impact of the new polarization observables. A significant fraction of the improvements stems from the E_{0+} multipole [Ani+16]. The multipole amplitudes from the different analyses indeed converge to similar values in the energy range covered by the new data.

8.4.1.1 Evidence for resonance $\Delta(2200)\,7/2^-$

As already mentioned in Section 1.3, many experimentally observed excited baryon states appear as nearly mass-degenerate doublets with the same total angular momentum J and opposite parity P, an observation that is in contrast to the constituent quark models [CI86;
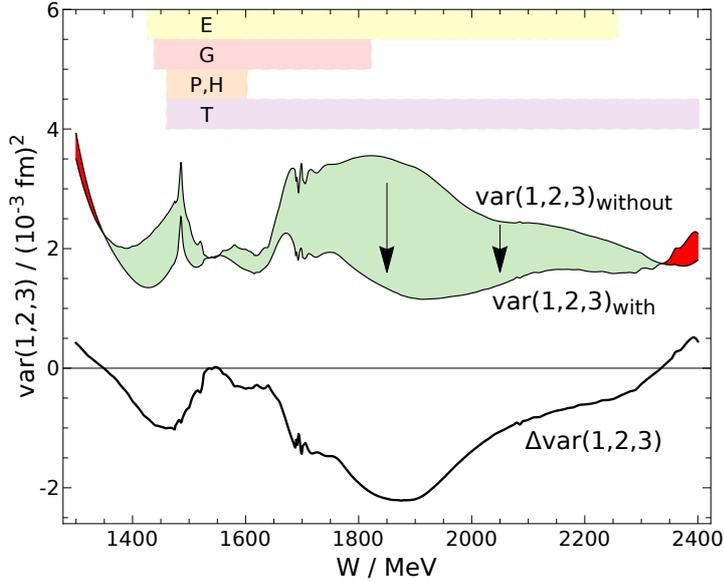
Figure 8.26: The variance between BnGa, JüBo, and SAID analyses, summed over all $\gamma p \rightarrow$
$p\pi^0$ multipoles up to $\ell = 4$ [Ani+16]. The range covered by the new results
on T, P, H (this work), E [Got+14], and G [Thi+12; Thi+17] is indicated
by shaded areas. Over the largest part of the energy range the new data
have enforced an improvement of the overall consistency. The improvement is
displayed as light green area. Ranges with an overall deterioration are marked
in red.

LMP01] and lattice QCD calculations [Edw+11]. A similar observation also holds for the
meson sector [Oli+14]. Since the observed mass gap of the lower-mass chiral partners like
the $\rho(770)$ ($J^P = 1^-$) and the $a_1(1260)$ ($J^P = 1^+$) or the $N(938)\,1/2^+$ and the $N(1535)\,1/2^-$
is a consequence of the spontaneous chiral symmetry breaking, this has lead to the conjec-
ture that chiral symmetry might be effectively restored in highly excited hadrons [Glo00;
Glo04] and has stimulated a vivid discussion in the literature [JPS06; Glo07; Afo07; SV08].
Consider the Δ^* resonances around $M \approx 1900\,\text{MeV}$. The Particle Data Group [Oli+14]
lists seven states with a rating of at least $\star\star$, i.e. with at least fair evidence of existence:

$\Delta(1910)\,1/2^+$	$\Delta(1920)\,3/2^+$	$\Delta(1905)\,5/2^+$	$\Delta(1950)\,7/2^+$
$\Delta(1900)\,1/2^-$	$\Delta(1940)\,3/2^-$	$\Delta(1930)\,5/2^-$.	

Restoration of chiral symmetry would imply that there should also be a parity partner
of the $\Delta(1950)\,7/2^+$ at a similar mass. However, the only $J^P = 7/2^-$ state listed by
the Particle Data Group is the $\Delta(2200)\,7/2^-$ [Oli+14]. The mass splitting of $250\,\text{MeV}$
is unexpectedly large if chiral symmetry were restored in highly excited hadrons, but in
good agreement with the prediction of the quark model [LMP01]. However, the Particle
Data Group assigned only a rating of $\star$ to the $\Delta(2200)\,7/2^-$, i.e. its evidence is only poor
[Oli+14]. To decide on this issue, it is essential to refute or confirm the existence of this
state.

Based on the new double polarization data on $\gamma p \to p\pi^0$ from this work (observables T, P, H) and [Spa+10; Thi+12; Got13] (observables Σ, G, E), and on $\gamma p \to n\pi^+$ from CLAS [Dug+13; Ani+17] (observables Σ, E), the BnGa group performed a new partial wave analysis [Ani+17] to determine the properties of the $\Delta(1950)\,7/2^+$ and $\Delta(2200)\,7/2^-$ (among many other resonances). The new data were fitted jointly with data on $N\pi$, $N\eta$, ΛK, ΣK, $N\pi^0\pi^0$, and $N\pi^0\eta$ from both photo- and pion-induced reactions, for a full list see [Ani+12; Ani+13; Sok+15b; Gut+14].

The fit to the data confirms both the $\Delta(1950)\,7/2^+$ and $\Delta(2200)\,7/2^-$ resonances [Ani+17], their resulting properties are listed in Table 8.2. Again, the values and uncertainties are derived from the mean values and the spread of the results of various fits. Within their uncertainties, most properties of the well-established $\star\star\star\star$ resonance $\Delta(1950)\,7/2^+$ are in good agreement with those reported by the Particle Data Group [Oli+14].

To explicitly search for a mass-degenerate parity partner of the $\Delta(1950)\,7/2^+$, the BnGa group did additional fits to the data, trying to impose a $\Delta(1950)\,7/2^-$ (with its mass restricted to the range $1920\,\mathrm{MeV}$ to $1980\,\mathrm{MeV}$) in addition to the $\Delta(2200)\,7/2^-$. However, in all fits, its helicity couplings converged to zero: there is no mass-degenerate parity partner of the $\Delta(1950)\,7/2^+$ in the data [Ani+17]. In conclusion, the observed mass of the $\Delta(2200)\,7/2^-$ is in conflict with the effective restoration of chiral symmetry and favors the quark model.

A comparison of the $N\pi$ branching ratios of the $\Delta(1950)\,7/2^+$ and $\Delta(2200)\,7/2^-$ resonances (see Table 8.2) explains why the $\Delta(1950)\,7/2^+$ is a well-established resonance and the $\Delta(2200)\,7/2^-$ is not: in elastic πN scattering, the $N\pi$ branching ratio contributes twice, both from the coupling to the initial and to the final state, resulting in a more than 100 times weaker contribution from the $\Delta(2200)\,7/2^-$. Nevertheless, with the new analysis including the new photoproduction data, the greatest evidence for the $\Delta(2200)\,7/2^-$ comes from single pion photoproduction, in spite of the small $N\pi$ branching ratio [Ani+17]. This underlines the importance of the new double polarization data, and highlights their power in constraining the partial wave analysis.

Table 8.2: Properties of the $\Delta(1950)\,7/2^+$ and $\Delta(2200)\,7/2^-$ resonances, obtained from the BnGa fit [Ani+17]. Previous estimates by the Particle Data Group (only available for the $\Delta(1950)\,7/2^+$) are shown in parentheses. The helicity couplings $A_{1/2}$ and $A_{3/2}$ are given in units of $10^{-3}\,\mathrm{GeV}^{-1/2}$.

$\Delta(1950)\,7/2^+$ $\star\star\star\star$		$\Delta(2200)\,7/2^-$ $\star$	
$M\ =\ 1917 \pm 4\,\mathrm{MeV}$	(1915 to 1950 MeV)	$M\ =\ 2176 \pm 40\,\mathrm{MeV}$	
$\Gamma\ =\ 251 \pm 8\,\mathrm{MeV}$	(235 to 335 MeV)	$\Gamma\ =\ 210 \pm 70\,\mathrm{MeV}$	
$A_{1/2} = -67 \pm 5$	(-76 ± 12)	$A_{1/2} = 60 \pm 20$	
$A_{3/2} = -94 \pm 4$	(-97 ± 10)	$A_{3/2} = 20 \pm 8$	
BR:		BR:	
$N\pi$: $\quad 46 \pm 2\,\%$	(35 to 45 %)	$N\pi$: $\quad 3.5 \pm 1.5\,\%$	
ΣK: $\quad 0.6 \pm 0.2\,\%$	(seen)	ΣK: $\quad 4 \pm 3\,\%$	
$\Delta\pi$: $\quad 4 \pm 3\,\%$	(20 to 30 %)	$\Delta\pi$: $\quad 85 \pm 33\,\%$	
$\Delta\eta$: $\quad 0.3 \pm 0.3\,\%$		$\Delta\pi$: $\quad \sim 1\,\%$	

8.4.2 Reaction $\gamma p \to p\eta$

In a next step, new data on the reaction $\gamma p \to p\eta$ were included in the BnGa PWA. In addition to the results on the observables T, P, and H from this work, recent results on the observables E [Mül17] and G [Grü16b], as well as recent MAMI results on T and F [Ako+14] were added to the data base. For the BnGa refit, all couplings to multi-meson final states like $\pi^0\pi^0 p$ and $\pi^0\eta p$ were frozen to simplify the fitting procedure. After the refit, the BnGa PWA is able to describe the data for all observables, as can be seen in Figs. 8.27 and 8.28. Only at higher energies, above $W \geq 2\,\text{GeV}$, there are some deviations remaining, which will be discussed in Section 8.4.2.2 in more detail. But first, the results of the refit are presented.

8.4.2.1 Branching ratios for for $N^* \to N\eta$ decays

The N^* resonances used in the BnGa refit are listed in Table 8.3. From the best fit, the branching ratios for the decays of the N^* resonances into the ηp final state can be calculated [Gut+14]. The uncertainty of the branching ratios is estimated from the distribution of different PWA solutions after a variation of the fit hypothesis [M+17].[11]
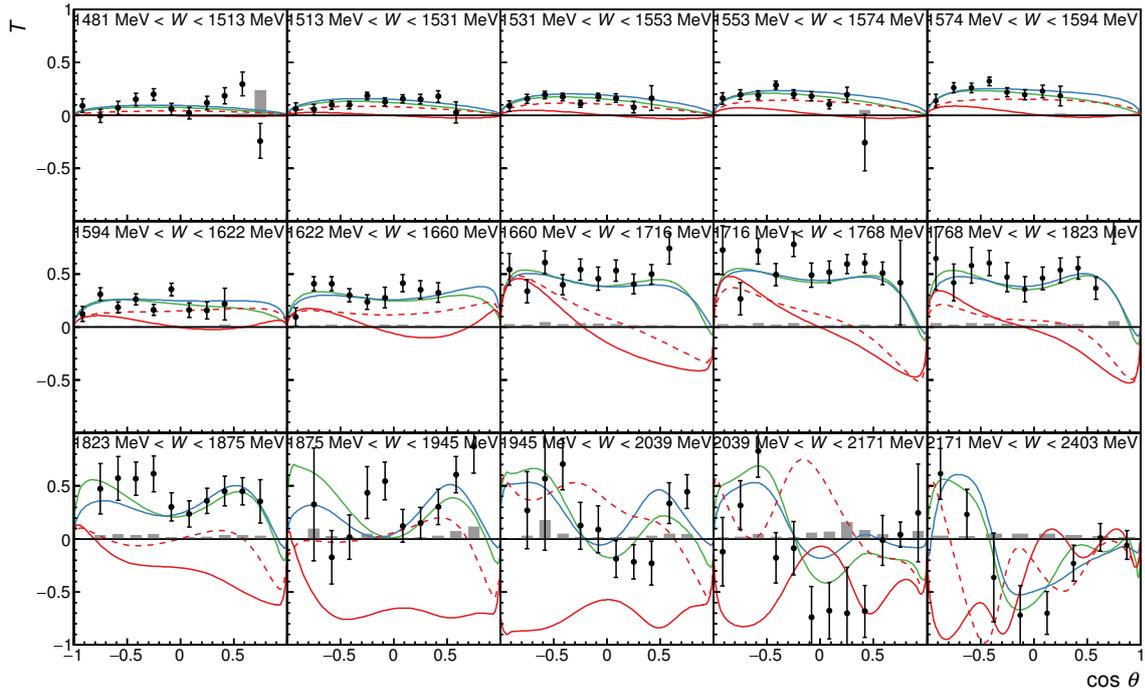
Figure 8.27: The results for the target asymmetry T in the reaction $\gamma p \to p\eta$, together with the BnGa refit [M+17] without any new resonances (blue), and with a new $N\,5/2^-$ resonance added (green). The older BnGa solutions [Ani+12] (red) 2011-01 (dashed) and 2011-02 (solid) are also shown for comparison.

---

[11] This is the same method used to estimate the uncertainty of the π^0 photoproduction multipoles, see Section 8.4.1.

(a) Recoil polarization P (b) Double polarization observable H
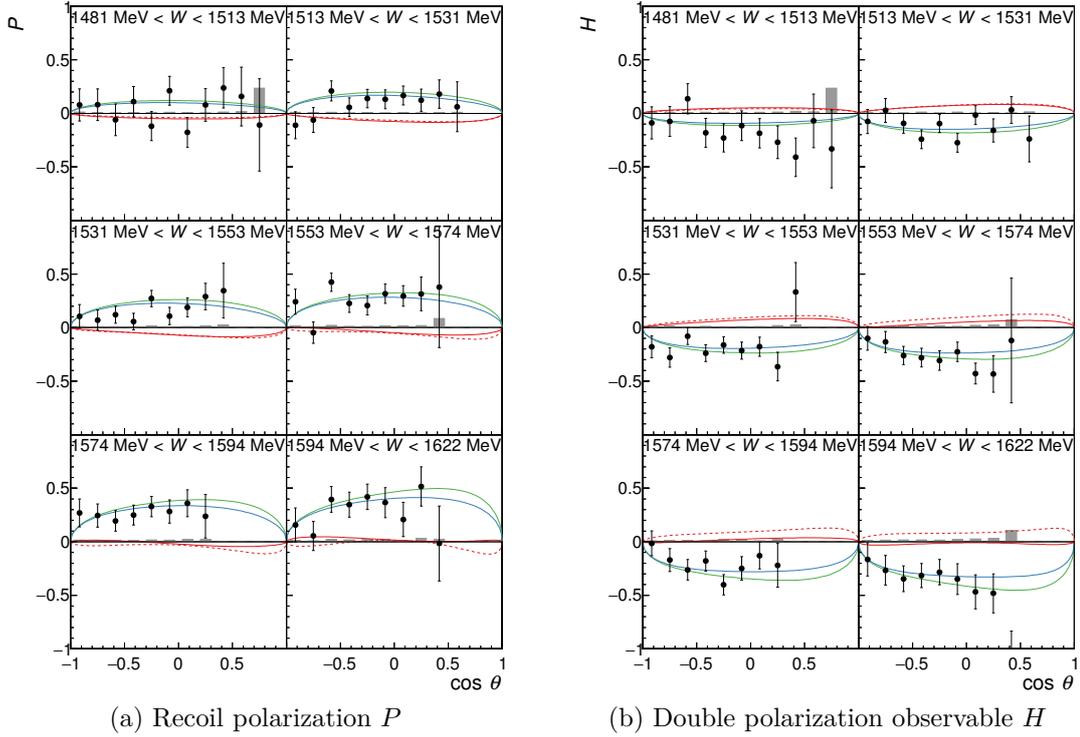
Figure 8.28: The results for the recoil polarization P and the double polarization observable H in the reaction $\gamma p \to p\eta$, together with the BnGa refit [M+17] without any new resonances (blue), and with a new $N\,5/2^-$ resonance added (green). The older BnGa solutions [Ani+12] (red) 2011-01 (dashed) and 2011-02 (solid) are also shown for comparison.

A comparison of the newly obtained branching ratios with the results from the BnGa2011 PWA solution [Ani+12] or the values listed by the Particle Data Group [Oli+14], which are also shown in Table 8.3, reveals first of all significantly smaller uncertainties due to the inclusion of the new data in the fit. Apart from this, there are further interesting observations. While most new values agree with earlier results within their error bars, two branching ratios changed significantly:

1. The $N(1650)\,1/2^- \to N\eta$ branching ratio of $(32 \pm 4)\,\%$ is substantially larger than the estimate by the Particle Data Group (between $5\,\%$ and $15\,\%$). In 2010, before the earlier BnGa results were included, the estimate by the PDG was even smaller at $(2.3 \pm 2.2)\,\%$ [Nak+10]. The new value is much closer to the $N(1535)\,1/2^- \to N\eta$ branching ratio of $(42 \pm 4)\,\%$. This is remarkable, because the supposedly large difference between the resonances $N(1535)\,1/2^-$ and $N(1650)\,1/2^-$ has always been a challenge for models. Various interpretations within quark models are found in the literature [IK77; GR96], but also explanations by pentaquarks [Zou08] or quasi-bound $K\Sigma$ or $K\Lambda$ states [MBM12; KSW95].[12] With the significantly increased branching ratio, these interpretations have to be revised based on the new result.

---

[12] A more detailed summary on the discussion in the literature can be found in [KS03].

2. The $N(1900)\,3/2^+ \to N\eta$ branching ratio changes from $\approx 12\,\%$ to $(3 \pm 1)\,\%$.

In addition, with the new data it is possible to obtain some previously undetermined branching ratios, even though they are small. This clearly shows the power of polarization observables to constrain PWAs.

Table 8.3: Branching ratios for $N^* \to N\eta$ decays obtained from the BnGa2014 fit to the new double polarization data [M+17], compared to the values (where available) from the previous BnGa2011 solution [Ani+12] and the Particle Data Group [Oli+14]. Additionally, the values given by the Particle Data Group in 2010 [Nak+10], before the earlier BnGa PWA results were included, are shown.

Resonance	BnGa2014	BnGa2011	PDG2014	PDG2010
$N(1535)\,1/2^-$	0.42 ± 0.04	0.33 ± 0.05	0.42 ± 0.10	0.45 to 0.60
$N(1650)\,1/2^-$	0.32 ± 0.04	0.18 ± 0.04	0.05 to 0.15	0.023 ± 0.022
$N(1895)\,1/2^-$	0.10 ± 0.05	0.21 ± 0.06	-	-
$N(1710)\,1/2^+$	0.27 ± 0.09	0.17 ± 0.10	0.10 to 0.30	0.062 ± 0.010
$N(1880)\,1/2^+$	0.19 ± 0.07	$0.25\,^{+\,0.30}_{-\,0.20}$	-	-
$N(2100)\,1/2^+$	0.25 ± 0.10	-	0.61 ± 0.61	0.61 ± 0.61
$N(1520)\,3/2^-$	< 0.001	-	0.0023 ± 0.0004	0.0023 ± 0.0004
$N(1700)\,3/2^-$	0.01 ± 0.01	-	0.00 ± 0.01	0.00 ± 0.01
$N(1875)\,3/2^-$	0.02 ± 0.01	0.05 ± 0.02	0.012 ± 0.018	0.035 ± 0.035[13]
$N(2120)\,3/2^-$	≤ 0.01	-	-	
$N(1720)\,3/2^+$	0.03 ± 0.02	0.03 ± 0.02	0.021 ± 0.014	0.04 ± 0.01
$N(1900)\,3/2^+$	0.03 ± 0.01	0.10 ± 0.04	≈ 0.12	014 ± 0.05
$N(\ ?\ )\,3/2^{+}$[14]	0.04 ± 0.02	-	-	-
$N(1675)\,5/2^-$	0.005 ± 0.005	-	0.000 ± 0.007	0.00 ± 0.01
$N(2060)\,5/2^-$	0.04 ± 0.01	0.04 ± 0.02	-	-
$N(1680)\,5/2^+$	0.002 ± 0.001	-	0.000 ± 0.007	0.00 ± 0.01
$N(1860)\,5/2^+$	0.02 ± 0.02	-	-	-
$N(2000)\,5/2^+$	0.02 ± 0.01	-	0.02 ± 0.02	-
$N(2190)\,7/2^-$	0.025 ± 0.005	-	0.00 ± 0.01	0.00 ± 0.01
$N(1990)\,7/2^+$	≤ 0.01	-	-	-

---

[13] Before 2012, the Particle Data Group listed only one state $N(2080)\,3/2^-$ instead of the two states $N(1875)\,3/2^-$ and $N(2120)\,3/2^-$.

[14] Note: The $N(?)\,3/2^+$ resonance with a pole-position below $M < 2\,\mathrm{GeV}$ is needed to achieve good convergence of the fit, but its properties remain badly defined, so its existence is uncertain [M+17].

8.4.2.2 Indication for a new resonance $N(2200)\,5/2^-$

As was mentioned before, the BnGa refit did not reproduce well the high-mass range above $W \geq 2\,\text{GeV}$ (see Fig. 8.27). This can be quantified, the χ^2 of the best fit to the T data is 223 for 147 data points [Sar16].[15] This discrepancy is not limited to the observable T: the new data on the observable E [Mül17], which is the only other observable presently available in the high-mass range, is described even worse by the fit, with a χ^2 of 193 for 93 data points. Therefore, the BnGa group tried to improve the fit by adding one additional resonance with $J^P = 1/2^\pm, \ldots, 9/2^\pm$. The best result was achieved by introducing a $J^P = 5/2^-$ resonance with $M = (2200.0 \pm 5.0)\,\text{MeV}$ and $\Gamma = (260.0 \pm 5.0)\,\text{MeV}$ [M+17]. Figure 8.29 shows the performed mass scan where, starting from the best fit solution, a Breit-Wigner amplitude was added. Its mass was fixed to various values, while all other parameters were fitted freely. While the total improvement of the χ^2 is not overwhelming, the fact that the χ^2 scan for both observables shows a clear minimum at approximately the same mass is at least an indication for the presence of an additional $N(2200)\,5/2^-$ resonance. Of course, this state still needs independent confirmation. It should, however, be noted that in the 2010 edition of the Review of Particle Physics [Nak+10] a $N(2200)\,5/2^-$ state is listed, observed in $\pi N \to \pi N$ [Cut+79]. In 2012, the Particle Data Group removed this state in favor of the newly added $N(2060)\,5/2^-$ which was found by the earlier BnGa analysis [Ani+12]. The new data indicate that these are in fact two separate states.

(a) T (b) E
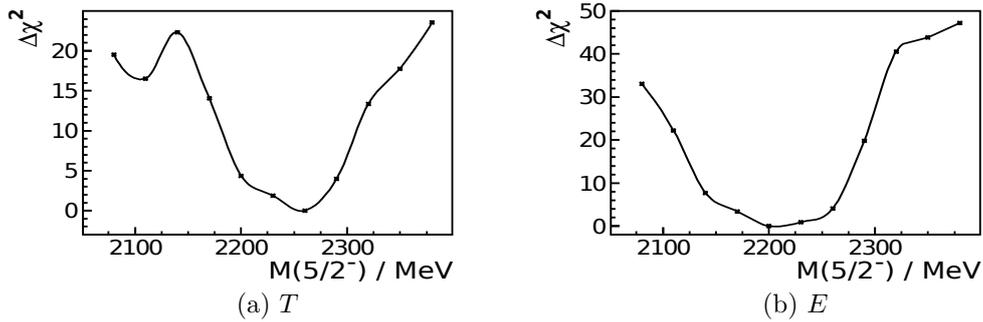
Figure 8.29: Mass scan for a resonance with $J^P = 5/2^-$. Shown is the χ^2-change for the observables E and T as a function of the imposed mass [M+17]. $\Delta\chi^2 = 0$ corresponds to the best fit in the respective mass scan, which is not equal to the global best fit solution.

---

[15] The total χ^2 value of the fit is meaningless, because some of the data (multi-meson final states) are fitted using an event-based likelihood fit, where the likelihood value $\mathcal{L}$ is converted into a pseudo-χ^2 using $\chi^2_{\text{pseudo}} = -2\ln\mathcal{L}$. Also, various data sets are included in the fit with different weights, for details see e.g. [Ani+12]. Therefore, instead of the total χ^2, an individual χ^2 for each data set is calculated (with the weight factor set to unity) for the best fit solution.

Chapter 9

Summary and Outlook

In this work, the analysis and the results of a double polarization measurement performed with the Crystal Barrel/TAPS experiment at the accelerator facility ELSA in Bonn have been presented. The photoproduction of single π^0 and η mesons using a linearly polarized photon beam impinging on a transversely polarized proton target was investigated. A nearly background-free data sample of approximately 1.7 million $\gamma p \to p\pi^0$ and 170 thousand $\gamma p \to p\eta$ events has been selected by fully reconstructing the $p\gamma\gamma$ final state in an incoming photon energy range from 640 MeV to 3000 MeV.

To extract the polarization observables from the data, a new method was developed using an event-based maximum-likelihood fit. Compared to previously used methods, e.g. using event yield asymmetries or a Fourier moments analysis, the event-based method yields, on average, smaller statistical uncertainties. Systematic errors were investigated in detail and found to be significantly smaller compared to the statistical uncertainty of the data. The new event-based method has been adopted for other analyses of Crystal Barrel/TAPS data (e.g. [Sei17]) and is also being used by the A2 collaboration at MAMI for their analyses of double polarization data (e.g. [Spi17]).

The target asymmetry T was measured for both reactions $\gamma p \to p\pi^0$ and $\gamma p \to p\eta$ as a function of the beam energy and the scattering angle, for the full energy range of the available event sample and with nearly complete angular coverage (except for a few data points missing at forward angles due to acceptance). The results are more precise compared to earlier data from other experiments, and extend the covered range in energy and angle substantially. In the incoming photon energy range below 975 MeV, where a high degree of linear polarization of the photon has been achieved, also the recoil polarization P and the double polarization observable H were measured simultaneously. In η photoproduction, it is the first measurement of H and the first measurement of P not restricted to a very limited angular coverage. In π^0 photoproduction, it is the first measurement of H in the energy range $E_\gamma < 1300$ MeV.

Within the Bonn-Gatchina partial wave analysis, the new results, together with the results obtained on E [Got+14] and G [Thi+12; Thi+17], lead to a significant narrowing of the error band for the π^0 photoproduction multipoles, a more precise determination of resonance parameters, in particular $N^* \to N\eta$ branching ratios, and indications for a new resonance $N(2200)\,5/2^-$. Another analysis within the BnGa formalism, based—among others—on the results of this work, reveals further evidence for the baryon resonance $\Delta(2200)\,7/2^-$ [Ani+17], the lowest-mass $J^P = 7/2^-$ Δ-resonance, whose evidence of existence has been hitherto only poor.

If the published results on $\gamma p \to p\pi^0$ are included not only in the BnGa analysis, but also

in the JüBo and SAID analyses, their differences are significantly reduced. Their multipole amplitudes now converge toward similar values in the energy range covered by the new data [Ani+16]. A similar improvement can also be expected for the reaction $\gamma p \rightarrow p\eta$. This will be investigated as soon as these results are also published and thus made available to the other analysis groups.

In the near future, additional measurements with the Crystal Barrel/TAPS experiment are planned to further reduce the statistical uncertainty of the results and, more importantly, to extend the covered energy range of the P and H measurements up to $E_\gamma \approx 1600\,\text{MeV}$. These data, analyzed with the technique developed in this work, will provide important constraints for the PWA in the third resonance region and beyond, allowing for a precise determination of resonance parameters and hopefully leading to a better understanding of the bound states of QCD in the baryon sector.

Appendix A

Data Points

The results for the polarization observables T, P, and H are listed here for all $(E_\gamma, \cos\theta)$ bins. The individual systematic uncertainties are shown, as well as the total systematic uncertainty obtained by quadratically adding the individual contributions. The individual systematic uncertainties allow for a correct treatment of their correlations (see Chapter 7) in a fit to these results.

In addition, the experimentally determined effective dilution factor d is shown, including its systematic uncertainty because of the carbon scaling factor.

A.1 Reaction $\gamma p \rightarrow p\pi^0$

Table A.1: Energy bin $641\,\text{MeV} < E_\gamma < 667\,\text{MeV}$. Systematic uncertainty $\Delta E_\gamma = 10\,\text{MeV}$.

$\cos\theta$	d	σ_d	Δd_sys	T	σ_T	ΔT_sys	$\Delta T_\text{sys}^\Lambda$	ΔT_sys^d	ΔT_sys^{bg}
-0.958	0.947	0.022	0.005	-0.2347	0.1162	0.0130	0.0047	0.0013	0.0120
-0.875	0.894	0.016	0.011	-0.3951	0.0626	0.0100	0.0079	0.0047	0.0041
-0.792	0.864	0.013	0.014	-0.6364	0.0447	0.0170	0.0127	0.0100	0.0052
-0.708	0.866	0.011	0.013	-0.6353	0.0384	0.0163	0.0127	0.0099	0.0028
-0.625	0.875	0.009	0.013	-0.7356	0.0321	0.0182	0.0147	0.0105	0.0018
-0.542	0.891	0.008	0.011	-0.7394	0.0303	0.0174	0.0148	0.0090	0.0020
-0.458	0.770	0.012	0.023	-0.8678	0.0373	0.0313	0.0174	0.0260	0.0023
-0.375	0.914	0.007	0.009	-0.8138	0.0290	0.0180	0.0163	0.0076	0.0007
-0.292	0.877	0.007	0.012	-0.7941	0.0285	0.0194	0.0159	0.0111	0.0010
-0.208	0.861	0.007	0.014	-0.8363	0.0281	0.0215	0.0167	0.0135	0.0013
-0.125	0.904	0.006	0.010	-0.8483	0.0263	0.0192	0.0170	0.0090	0.0009
-0.042	0.866	0.007	0.013	-0.8696	0.0263	0.0220	0.0174	0.0134	0.0015
0.042	0.884	0.007	0.012	-0.8191	0.0267	0.0196	0.0164	0.0107	0.0008
0.125	0.900	0.006	0.010	-0.7985	0.0276	0.0183	0.0160	0.0089	0.0008
0.208	0.882	0.007	0.012	-0.7950	0.0282	0.0192	0.0159	0.0107	0.0013
0.292	0.893	0.007	0.011	-0.7761	0.0300	0.0181	0.0155	0.0093	0.0015
0.375	0.909	0.008	0.009	-0.7501	0.0342	0.0169	0.0150	0.0075	0.0019
0.458	0.883	0.016	0.012	-0.6165	0.0628	0.0158	0.0123	0.0081	0.0055

$\cos\theta$	P	σ_P	ΔP_sys	$\Delta P_\text{sys}^\delta$	$\Delta P_\text{sys}^\Lambda$	ΔP_sys^d	ΔP_sys^{bg}	H	σ_H	ΔH_sys	$\Delta H_\text{sys}^\delta$	$\Delta H_\text{sys}^\Lambda$	ΔH_sys^d	ΔH_sys^{bg}
-0.958	-0.0966	0.3531	0.0178	0.0117	0.0058	0.0016	0.0120	0.6849	0.3000	0.0332	0.0275	0.0137	0.0038	0.0120
-0.875	-0.8668	0.1908	0.0403	0.0347	0.0173	0.0103	0.0041	0.7038	0.1831	0.0328	0.0282	0.0141	0.0083	0.0041
-0.792	-0.8925	0.1375	0.0426	0.0357	0.0178	0.0141	0.0052	0.7696	0.1335	0.0369	0.0308	0.0154	0.0121	0.0052
-0.708	-0.8655	0.1162	0.0411	0.0346	0.0173	0.0134	0.0028	0.6570	0.1158	0.0312	0.0263	0.0131	0.0102	0.0028
-0.625	-0.9108	0.0994	0.0428	0.0364	0.0182	0.0130	0.0018	0.4071	0.1005	0.0192	0.0163	0.0081	0.0058	0.0018
-0.542	-0.8595	0.0945	0.0399	0.0344	0.0172	0.0105	0.0020	0.2596	0.0939	0.0122	0.0104	0.0052	0.0032	0.0020
-0.458	-0.8886	0.1104	0.0479	0.0355	0.0178	0.0266	0.0023	0.3205	0.1093	0.0174	0.0128	0.0064	0.0096	0.0023
-0.375	-0.9916	0.0890	0.0453	0.0397	0.0198	0.0093	0.0007	0.1650	0.0905	0.0077	0.0067	0.0033	0.0016	0.0007
-0.292	-0.7755	0.0866	0.0363	0.0310	0.0155	0.0108	0.0010	0.0823	0.0871	0.0047	0.0039	0.0020	0.0014	0.0010
-0.208	-0.9943	0.0836	0.0473	0.0398	0.0199	0.0161	0.0013	-0.0208	0.0825	0.0035	0.0027	0.0014	0.0011	0.0013
-0.125	-0.7867	0.0803	0.0362	0.0315	0.0157	0.0084	0.0009	0.0030	0.0791	0.0030	0.0025	0.0013	0.0007	0.0009
-0.042	-0.8572	0.0791	0.0406	0.0343	0.0171	0.0132	0.0015	-0.0263	0.0803	0.0035	0.0027	0.0014	0.0010	0.0015
0.042	-0.7480	0.0799	0.0349	0.0299	0.0150	0.0098	0.0008	-0.1242	0.0809	0.0060	0.0051	0.0026	0.0017	0.0008
0.125	-0.6504	0.0844	0.0300	0.0260	0.0130	0.0072	0.0008	-0.2648	0.0822	0.0122	0.0106	0.0053	0.0029	0.0008
0.208	-0.5954	0.0852	0.0278	0.0238	0.0119	0.0080	0.0013	-0.2624	0.0865	0.0123	0.0105	0.0052	0.0035	0.0013
0.292	-0.8415	0.0914	0.0390	0.0337	0.0168	0.0100	0.0015	-0.2975	0.0888	0.0139	0.0119	0.0059	0.0035	0.0015
0.375	-0.6139	0.1047	0.0282	0.0246	0.0123	0.0061	0.0019	-0.2383	0.0983	0.0111	0.0096	0.0048	0.0024	0.0019
0.458	-0.6919	0.1871	0.0327	0.0277	0.0138	0.0091	0.0055	-0.7399	0.1644	0.0349	0.0296	0.0148	0.0098	0.0055

Appendix A Data Points

Table A.2: Energy bin 667 MeV < E_γ < 700 MeV. Systematic uncertainty $\Delta E_\gamma = 10$ MeV.

$\cos\theta$	d	σ_d	$\Delta d_{\rm sys}$	T	σ_T	$\Delta T_{\rm sys}$	$\Delta T_{\rm sys}^{\Lambda}$	$\Delta T_{\rm sys}^{d}$	$\Delta T_{\rm sys}^{bg}$
−0.958	0.935	0.018	0.006	−0.2910	0.0935	0.0118	0.0058	0.0020	0.0101
−0.875	0.900	0.014	0.010	−0.3098	0.0513	0.0093	0.0062	0.0035	0.0060
−0.792	0.877	0.011	0.012	−0.5048	0.0385	0.0135	0.0101	0.0071	0.0055
−0.708	0.885	0.009	0.012	−0.6201	0.0326	0.0152	0.0124	0.0081	0.0037
−0.625	0.871	0.009	0.013	−0.6715	0.0294	0.0169	0.0134	0.0099	0.0027
−0.542	0.895	0.007	0.011	−0.7326	0.0262	0.0171	0.0147	0.0086	0.0016
−0.458	0.802	0.010	0.020	−0.8218	0.0308	0.0262	0.0164	0.0202	0.0021
−0.375	0.907	0.006	0.009	−0.7712	0.0270	0.0173	0.0154	0.0079	0.0007
−0.292	0.896	0.006	0.010	−0.7853	0.0245	0.0182	0.0157	0.0091	0.0010
−0.208	0.871	0.006	0.013	−0.7530	0.0244	0.0188	0.0151	0.0112	0.0010
−0.125	0.899	0.006	0.010	−0.7824	0.0232	0.0180	0.0156	0.0088	0.0009
−0.042	0.878	0.006	0.012	−0.8046	0.0227	0.0196	0.0161	0.0112	0.0008
0.042	0.879	0.006	0.012	−0.7894	0.0231	0.0192	0.0158	0.0108	0.0010
0.125	0.894	0.006	0.011	−0.7542	0.0239	0.0176	0.0151	0.0089	0.0008
0.208	0.870	0.006	0.013	−0.7628	0.0247	0.0191	0.0153	0.0114	0.0014
0.292	0.900	0.006	0.010	−0.7192	0.0256	0.0165	0.0144	0.0080	0.0012
0.375	0.921	0.006	0.008	−0.6392	0.0263	0.0140	0.0128	0.0055	0.0019
0.458	0.876	0.010	0.012	−0.4949	0.0380	0.0128	0.0099	0.0070	0.0039

$\cos\theta$	P	σ_P	$\Delta P_{\rm sys}$	$\Delta P_{\rm sys}^{\delta}$	$\Delta P_{\rm sys}^{\Lambda}$	$\Delta P_{\rm sys}^{d}$	$\Delta P_{\rm sys}^{bg}$	H	σ_H	$\Delta H_{\rm sys}$	$\Delta H_{\rm sys}^{\delta}$	$\Delta H_{\rm sys}^{\Lambda}$	$\Delta H_{\rm sys}^{d}$	$\Delta H_{\rm sys}^{bg}$
−0.958	−0.5206	0.2506	0.0258	0.0210	0.0105	0.0036	0.0101	0.2073	0.2348	0.0153	0.0102	0.0051	0.0018	0.0101
−0.875	−0.6742	0.1443	0.0317	0.0270	0.0135	0.0075	0.0060	0.9018	0.1393	0.0420	0.0361	0.0180	0.0101	0.0060
−0.792	−0.9304	0.1053	0.0440	0.0372	0.0186	0.0131	0.0055	0.6832	0.1021	0.0325	0.0273	0.0137	0.0096	0.0055
−0.708	−0.9645	0.0903	0.0451	0.0386	0.0193	0.0125	0.0037	0.5652	0.0922	0.0266	0.0226	0.0113	0.0073	0.0037
−0.625	−0.8838	0.0818	0.0417	0.0354	0.0177	0.0130	0.0027	0.3866	0.0791	0.0184	0.0155	0.0077	0.0057	0.0027
−0.542	−1.0109	0.0722	0.0468	0.0404	0.0202	0.0119	0.0016	0.4778	0.0742	0.0222	0.0191	0.0096	0.0056	0.0016
−0.458	−1.0186	0.0841	0.0520	0.0407	0.0204	0.0251	0.0021	0.3289	0.0846	0.0169	0.0132	0.0066	0.0081	0.0021
−0.375	−0.9313	0.0723	0.0427	0.0373	0.0186	0.0095	0.0007	0.1069	0.0715	0.0052	0.0044	0.0022	0.0011	0.0007
−0.292	−0.8264	0.0668	0.0382	0.0331	0.0165	0.0096	0.0010	0.1218	0.0678	0.0058	0.0049	0.0025	0.0014	0.0010
−0.208	−0.8621	0.0652	0.0406	0.0345	0.0172	0.0128	0.0010	0.1563	0.0653	0.0075	0.0063	0.0031	0.0023	0.0010
−0.125	−0.8182	0.0629	0.0377	0.0327	0.0164	0.0092	0.0009	−0.0266	0.0629	0.0027	0.0022	0.0011	0.0006	0.0009
−0.042	−0.9389	0.0614	0.0440	0.0376	0.0188	0.0131	0.0008	−0.0573	0.0615	0.0033	0.0028	0.0014	0.0010	0.0008
0.042	−0.8107	0.0621	0.0379	0.0324	0.0162	0.0111	0.0010	−0.0344	0.0624	0.0029	0.0023	0.0011	0.0008	0.0010
0.125	−0.8287	0.0641	0.0383	0.0331	0.0166	0.0093	0.0008	−0.2296	0.0625	0.0107	0.0092	0.0046	0.0027	0.0008
0.208	−0.8298	0.0664	0.0392	0.0332	0.0166	0.0124	0.0014	−0.2113	0.0660	0.0101	0.0085	0.0042	0.0032	0.0014
0.292	−0.7176	0.0682	0.0331	0.0287	0.0144	0.0080	0.0012	−0.3612	0.0670	0.0167	0.0144	0.0072	0.0040	0.0012
0.375	−0.5002	0.0716	0.0229	0.0200	0.0100	0.0043	0.0019	−0.3648	0.0700	0.0167	0.0146	0.0073	0.0031	0.0019
0.458	−0.3791	0.1030	0.0182	0.0152	0.0076	0.0054	0.0039	−0.4883	0.0939	0.0233	0.0195	0.0098	0.0069	0.0039

Table A.3: Energy bin 700 MeV < E_γ < 731 MeV. Systematic uncertainty $\Delta E_\gamma = 10$ MeV.

$\cos\theta$	d	σ_d	$\Delta d_{\rm sys}$	T	σ_T	$\Delta T_{\rm sys}$	$\Delta T_{\rm sys}^{\Lambda}$	$\Delta T_{\rm sys}^{d}$	$\Delta T_{\rm sys}^{bg}$
−0.958	0.991	0.009	0.001	−0.1807	0.0873	0.0049	0.0036	0.0002	0.0033
−0.875	0.899	0.016	0.010	−0.1715	0.0483	0.0078	0.0034	0.0019	0.0067
−0.792	0.904	0.012	0.010	−0.3143	0.0355	0.0101	0.0063	0.0033	0.0072
−0.708	0.893	0.011	0.011	−0.3088	0.0337	0.0077	0.0062	0.0037	0.0028
−0.625	0.863	0.011	0.014	−0.4782	0.0299	0.0124	0.0096	0.0076	0.0021
−0.542	0.890	0.010	0.011	−0.5701	0.0273	0.0135	0.0114	0.0070	0.0020
−0.458	0.803	0.013	0.020	−0.5966	0.0329	0.0190	0.0119	0.0147	0.0021
−0.375	0.889	0.008	0.011	−0.6151	0.0285	0.0146	0.0123	0.0077	0.0018
−0.292	0.917	0.007	0.008	−0.6366	0.0271	0.0140	0.0127	0.0058	0.0012
−0.208	0.883	0.008	0.012	−0.6260	0.0251	0.0151	0.0125	0.0083	0.0015
−0.125	0.895	0.007	0.011	−0.6562	0.0243	0.0153	0.0131	0.0077	0.0010
−0.042	0.887	0.007	0.011	−0.6182	0.0237	0.0147	0.0124	0.0079	0.0013
0.042	0.888	0.007	0.011	−0.6294	0.0236	0.0149	0.0126	0.0079	0.0008
0.125	0.889	0.007	0.011	−0.6058	0.0244	0.0143	0.0121	0.0076	0.0012
0.208	0.881	0.007	0.012	−0.5626	0.0249	0.0137	0.0113	0.0076	0.0013
0.292	0.892	0.008	0.011	−0.4708	0.0259	0.0110	0.0094	0.0057	0.0010
0.375	0.893	0.008	0.011	−0.4243	0.0274	0.0099	0.0085	0.0051	0.0007
0.458	0.901	0.010	0.010	−0.3004	0.0314	0.0069	0.0060	0.0033	0.0011
0.542	0.861	0.022	0.014	−0.2506	0.0635	0.0109	0.0050	0.0040	0.0088

$\cos\theta$	P	σ_P	$\Delta P_{\rm sys}$	$\Delta P_{\rm sys}^{\delta}$	$\Delta P_{\rm sys}^{\Lambda}$	$\Delta P_{\rm sys}^{d}$	$\Delta P_{\rm sys}^{bg}$	H	σ_H	$\Delta H_{\rm sys}$	$\Delta H_{\rm sys}^{\delta}$	$\Delta H_{\rm sys}^{\Lambda}$	$\Delta H_{\rm sys}^{d}$	$\Delta H_{\rm sys}^{bg}$
−0.958	−0.2704	0.2169	0.0135	0.0117	0.0058	0.0003	0.0033	0.6911	0.1931	0.0311	0.0276	0.0138	0.0006	0.0033
−0.875	−0.5782	0.1210	0.0275	0.0231	0.0116	0.0065	0.0067	0.5863	0.1171	0.0278	0.0235	0.0117	0.0066	0.0067
−0.792	−0.7529	0.0877	0.0353	0.0301	0.0151	0.0080	0.0072	0.5403	0.0881	0.0258	0.0216	0.0108	0.0057	0.0072
−0.708	−0.5958	0.0829	0.0277	0.0238	0.0119	0.0072	0.0028	0.6486	0.0814	0.0302	0.0259	0.0130	0.0078	0.0028
−0.625	−0.7623	0.0739	0.0362	0.0305	0.0152	0.0121	0.0021	0.4614	0.0724	0.0220	0.0185	0.0092	0.0073	0.0021
−0.542	−0.6857	0.0682	0.0319	0.0274	0.0137	0.0085	0.0020	0.3164	0.0670	0.0148	0.0127	0.0063	0.0039	0.0020
−0.458	−0.8160	0.0803	0.0417	0.0326	0.0163	0.0201	0.0021	0.3175	0.0767	0.0163	0.0127	0.0063	0.0078	0.0021
−0.375	−0.7997	0.0685	0.0372	0.0320	0.0160	0.0100	0.0018	0.1174	0.0690	0.0059	0.0048	0.0024	0.0015	0.0018
−0.292	−0.7618	0.0641	0.0348	0.0305	0.0152	0.0069	0.0012	0.1389	0.0637	0.0065	0.0056	0.0028	0.0013	0.0012
−0.208	−0.7138	0.0594	0.0333	0.0286	0.0143	0.0095	0.0015	0.1395	0.0590	0.0067	0.0056	0.0028	0.0019	0.0015
−0.125	−0.8536	0.0579	0.0395	0.0341	0.0171	0.0101	0.0010	0.0116	0.0573	0.0024	0.0019	0.0009	0.0005	0.0010
−0.042	−0.7473	0.0556	0.0348	0.0299	0.0149	0.0095	0.0013	−0.0522	0.0575	0.0032	0.0025	0.0013	0.0008	0.0013
0.042	−0.6480	0.0560	0.0301	0.0259	0.0130	0.0082	0.0008	−0.1878	0.0562	0.0088	0.0075	0.0038	0.0024	0.0008
0.125	−0.6314	0.0579	0.0293	0.0253	0.0126	0.0079	0.0012	−0.1317	0.0568	0.0063	0.0053	0.0026	0.0017	0.0012
0.208	−0.5525	0.0595	0.0258	0.0221	0.0110	0.0075	0.0013	−0.3074	0.0575	0.0144	0.0123	0.0061	0.0042	0.0013
0.292	−0.5135	0.0608	0.0238	0.0205	0.0103	0.0062	0.0010	−0.3451	0.0605	0.0160	0.0138	0.0069	0.0042	0.0010
0.375	−0.4276	0.0646	0.0198	0.0171	0.0086	0.0051	0.0007	−0.4088	0.0642	0.0189	0.0164	0.0082	0.0049	0.0007
0.458	−0.2640	0.0744	0.0122	0.0106	0.0053	0.0029	0.0011	−0.4830	0.0711	0.0223	0.0193	0.0097	0.0053	0.0011
0.542	0.0870	0.1567	0.0111	0.0058	0.0029	0.0023	0.0088	−0.2357	0.1371	0.0144	0.0096	0.0048	0.0039	0.0088

Table A.4: Energy bin $731\,\mathrm{MeV} < E_\gamma < 768\,\mathrm{MeV}$. Systematic uncertainty $\Delta E_\gamma = 9\,\mathrm{MeV}$.

$\cos\theta$	d	σ_d	Δd_{sys}	T	σ_T	ΔT_{sys}	$\Delta T^\Lambda_{\mathrm{sys}}$	$\Delta T^d_{\mathrm{sys}}$	$\Delta T^{bg}_{\mathrm{sys}}$
−0.958	0.956	0.011	0.004	−0.0065	0.0601	0.0050	0.0010	0.0002	0.0049
−0.875	0.905	0.010	0.010	−0.1003	0.0354	0.0067	0.0020	0.0011	0.0063
−0.792	0.904	0.007	0.010	−0.1251	0.0265	0.0059	0.0025	0.0013	0.0052
−0.708	0.893	0.007	0.011	−0.2403	0.0252	0.0062	0.0048	0.0029	0.0027
−0.625	0.863	0.007	0.014	−0.3231	0.0226	0.0087	0.0065	0.0051	0.0027
−0.542	0.904	0.006	0.010	−0.3433	0.0210	0.0081	0.0069	0.0037	0.0023
−0.458	0.812	0.008	0.019	−0.4476	0.0238	0.0139	0.0090	0.0104	0.0025
−0.375	0.879	0.006	0.012	−0.4805	0.0231	0.0118	0.0096	0.0066	0.0018
−0.292	0.908	0.005	0.009	−0.4618	0.0207	0.0104	0.0092	0.0047	0.0012
−0.208	0.865	0.005	0.014	−0.4914	0.0200	0.0125	0.0098	0.0077	0.0013
−0.125	0.881	0.005	0.012	−0.4895	0.0195	0.0119	0.0098	0.0066	0.0011
−0.042	0.885	0.005	0.011	−0.4932	0.0187	0.0118	0.0099	0.0064	0.0008
0.042	0.876	0.005	0.012	−0.4511	0.0185	0.0111	0.0090	0.0064	0.0012
0.125	0.892	0.005	0.011	−0.4204	0.0191	0.0099	0.0084	0.0051	0.0009
0.208	0.876	0.005	0.012	−0.3980	0.0190	0.0098	0.0080	0.0057	0.0010
0.292	0.893	0.005	0.011	−0.3505	0.0195	0.0082	0.0070	0.0042	0.0008
0.375	0.883	0.005	0.012	−0.2969	0.0207	0.0072	0.0059	0.0039	0.0008
0.458	0.901	0.006	0.010	−0.2068	0.0221	0.0049	0.0041	0.0023	0.0015
0.542	0.859	0.010	0.014	−0.0746	0.0349	0.0031	0.0015	0.0012	0.0024

$\cos\theta$	P	σ_P	ΔP_{sys}	$\Delta P^\delta_{\mathrm{sys}}$	$\Delta P^\Lambda_{\mathrm{sys}}$	$\Delta P^d_{\mathrm{sys}}$	$\Delta P^{bg}_{\mathrm{sys}}$	H	σ_H	ΔH_{sys}	$\Delta H^\delta_{\mathrm{sys}}$	$\Delta H^\Lambda_{\mathrm{sys}}$	$\Delta H^d_{\mathrm{sys}}$	$\Delta H^{bg}_{\mathrm{sys}}$
−0.958	−0.3182	0.1365	0.0151	0.0128	0.0064	0.0015	0.0049	0.3743	0.1224	0.0175	0.0150	0.0075	0.0017	0.0049
−0.875	−0.5269	0.0817	0.0250	0.0211	0.0105	0.0055	0.0063	0.5686	0.0823	0.0269	0.0227	0.0114	0.0060	0.0063
−0.792	−0.4169	0.0610	0.0199	0.0167	0.0083	0.0044	0.0052	0.4278	0.0610	0.0203	0.0171	0.0086	0.0045	0.0052
−0.708	−0.6288	0.0577	0.0292	0.0252	0.0126	0.0075	0.0027	0.5102	0.0570	0.0238	0.0204	0.0102	0.0061	0.0027
−0.625	−0.5510	0.0520	0.0263	0.0220	0.0110	0.0087	0.0027	0.3454	0.0514	0.0166	0.0138	0.0069	0.0055	0.0027
−0.542	−0.6285	0.0480	0.0290	0.0251	0.0126	0.0067	0.0023	0.2539	0.0472	0.0119	0.0102	0.0051	0.0027	0.0023
−0.458	−0.6485	0.0541	0.0328	0.0259	0.0130	0.0151	0.0025	0.1183	0.0542	0.0065	0.0048	0.0024	0.0028	0.0025
−0.375	−0.6871	0.0511	0.0322	0.0275	0.0137	0.0094	0.0018	−0.0024	0.0504	0.0026	0.0016	0.0008	0.0006	0.0018
−0.292	−0.5899	0.0457	0.0271	0.0236	0.0118	0.0059	0.0012	0.0613	0.0454	0.0032	0.0026	0.0013	0.0007	0.0012
−0.208	−0.5754	0.0436	0.0273	0.0230	0.0115	0.0090	0.0013	0.0011	0.0435	0.0021	0.0014	0.0007	0.0005	0.0013
−0.125	−0.6391	0.0427	0.0299	0.0256	0.0128	0.0086	0.0011	−0.0729	0.0426	0.0037	0.0030	0.0015	0.0010	0.0011
−0.042	−0.5792	0.0409	0.0270	0.0232	0.0116	0.0075	0.0008	−0.0920	0.0407	0.0044	0.0037	0.0018	0.0012	0.0008
0.042	−0.5349	0.0409	0.0251	0.0214	0.0107	0.0076	0.0012	−0.1701	0.0411	0.0081	0.0068	0.0034	0.0024	0.0012
0.125	−0.4867	0.0418	0.0226	0.0195	0.0097	0.0059	0.0009	−0.2367	0.0405	0.0110	0.0095	0.0047	0.0029	0.0009
0.208	−0.4805	0.0416	0.0226	0.0192	0.0096	0.0068	0.0010	−0.2323	0.0412	0.0109	0.0093	0.0046	0.0033	0.0010
0.292	−0.3692	0.0427	0.0171	0.0148	0.0074	0.0044	0.0008	−0.3003	0.0415	0.0139	0.0120	0.0060	0.0036	0.0008
0.375	−0.2731	0.0455	0.0128	0.0109	0.0055	0.0036	0.0008	−0.3733	0.0444	0.0174	0.0149	0.0075	0.0049	0.0008
0.458	−0.2096	0.0491	0.0098	0.0084	0.0042	0.0023	0.0015	−0.3631	0.0472	0.0168	0.0145	0.0073	0.0040	0.0015
0.542	−0.1277	0.0780	0.0067	0.0052	0.0026	0.0021	0.0024	−0.3601	0.0707	0.0173	0.0144	0.0072	0.0059	0.0024

Table A.5: Energy bin $768\,\mathrm{MeV} < E_\gamma < 798\,\mathrm{MeV}$. Systematic uncertainty $\Delta E_\gamma = 9\,\mathrm{MeV}$.

$\cos\theta$	d	σ_d	Δd_{sys}	T	σ_T	ΔT_{sys}	$\Delta T^\Lambda_{\mathrm{sys}}$	$\Delta T^d_{\mathrm{sys}}$	$\Delta T^{bg}_{\mathrm{sys}}$
−0.958	0.975	0.008	0.003	0.0463	0.0585	0.0035	0.0012	0.0002	0.0033
−0.875	0.920	0.009	0.008	0.1323	0.0366	0.0060	0.0026	0.0011	0.0053
−0.792	0.907	0.007	0.009	0.0445	0.0276	0.0051	0.0009	0.0005	0.0050
−0.708	0.891	0.007	0.011	−0.0232	0.0263	0.0028	0.0006	0.0004	0.0027
−0.625	0.865	0.007	0.014	−0.0779	0.0242	0.0036	0.0016	0.0012	0.0030
−0.542	0.878	0.007	0.012	−0.1595	0.0243	0.0044	0.0032	0.0022	0.0021
−0.458	0.798	0.009	0.020	−0.2233	0.0265	0.0075	0.0045	0.0056	0.0021
−0.375	0.894	0.006	0.011	−0.2416	0.0263	0.0059	0.0048	0.0029	0.0018
−0.292	0.895	0.005	0.011	−0.2927	0.0238	0.0069	0.0059	0.0034	0.0012
−0.208	0.861	0.006	0.014	−0.3299	0.0232	0.0086	0.0066	0.0053	0.0014
−0.125	0.889	0.005	0.011	−0.3355	0.0218	0.0079	0.0067	0.0042	0.0008
−0.042	0.880	0.005	0.012	−0.3474	0.0213	0.0085	0.0069	0.0047	0.0011
0.042	0.861	0.006	0.014	−0.3470	0.0215	0.0090	0.0069	0.0056	0.0013
0.125	0.882	0.005	0.012	−0.2714	0.0218	0.0066	0.0054	0.0036	0.0010
0.208	0.860	0.006	0.014	−0.2711	0.0219	0.0071	0.0054	0.0044	0.0010
0.292	0.869	0.006	0.013	−0.2062	0.0226	0.0053	0.0041	0.0031	0.0011
0.375	0.858	0.006	0.014	−0.1492	0.0245	0.0041	0.0030	0.0025	0.0014
0.458	0.876	0.007	0.012	−0.1210	0.0256	0.0030	0.0024	0.0017	0.0006
0.542	0.855	0.009	0.015	−0.0288	0.0317	0.0022	0.0007	0.0006	0.0020
0.625	0.502	0.044	0.050	0.0972	0.1432	0.0169	0.0028	0.0138	0.0093

$\cos\theta$	P	σ_P	ΔP_{sys}	$\Delta P^\delta_{\mathrm{sys}}$	$\Delta P^\Lambda_{\mathrm{sys}}$	$\Delta P^d_{\mathrm{sys}}$	$\Delta P^{bg}_{\mathrm{sys}}$	H	σ_H	ΔH_{sys}	$\Delta H^\delta_{\mathrm{sys}}$	$\Delta H^\Lambda_{\mathrm{sys}}$	$\Delta H^d_{\mathrm{sys}}$	$\Delta H^{bg}_{\mathrm{sys}}$
−0.958	−0.4154	0.1261	0.0189	0.0166	0.0083	0.0011	0.0033	0.0902	0.1147	0.0062	0.0047	0.0024	0.0003	0.0033
−0.875	−0.4090	0.0814	0.0194	0.0164	0.0082	0.0035	0.0053	0.5257	0.0786	0.0245	0.0210	0.0105	0.0046	0.0053
−0.792	−0.4264	0.0612	0.0202	0.0171	0.0085	0.0044	0.0050	0.4968	0.0591	0.0233	0.0199	0.0099	0.0051	0.0050
−0.708	−0.4886	0.0580	0.0228	0.0195	0.0098	0.0060	0.0027	0.4427	0.0573	0.0207	0.0177	0.0089	0.0054	0.0027
−0.625	−0.4239	0.0530	0.0203	0.0170	0.0085	0.0066	0.0030	0.4071	0.0527	0.0195	0.0163	0.0081	0.0064	0.0030
−0.542	−0.3875	0.0531	0.0183	0.0155	0.0077	0.0054	0.0021	0.2764	0.0532	0.0131	0.0111	0.0055	0.0038	0.0021
−0.458	−0.4504	0.0574	0.0232	0.0180	0.0090	0.0114	0.0021	0.2139	0.0573	0.0112	0.0086	0.0043	0.0054	0.0021
−0.375	−0.4596	0.0545	0.0213	0.0184	0.0092	0.0054	0.0018	0.1299	0.0546	0.0063	0.0052	0.0026	0.0015	0.0018
−0.292	−0.4150	0.0494	0.0192	0.0166	0.0083	0.0049	0.0012	0.0276	0.0486	0.0024	0.0018	0.0009	0.0005	0.0012
−0.208	−0.4826	0.0481	0.0230	0.0193	0.0097	0.0078	0.0014	0.0093	0.0475	0.0023	0.0015	0.0008	0.0006	0.0014
−0.125	−0.4447	0.0451	0.0207	0.0178	0.0089	0.0056	0.0008	−0.0329	0.0446	0.0022	0.0018	0.0009	0.0006	0.0008
−0.042	−0.4627	0.0440	0.0217	0.0185	0.0093	0.0063	0.0011	−0.0230	0.0439	0.0021	0.0016	0.0008	0.0005	0.0011
0.042	−0.4541	0.0448	0.0216	0.0182	0.0091	0.0073	0.0013	−0.1237	0.0445	0.0060	0.0050	0.0025	0.0020	0.0013
0.125	−0.3379	0.0454	0.0158	0.0135	0.0068	0.0045	0.0010	−0.0469	0.0451	0.0027	0.0022	0.0011	0.0007	0.0010
0.208	−0.3664	0.0454	0.0175	0.0147	0.0073	0.0060	0.0010	−0.2039	0.0446	0.0098	0.0082	0.0041	0.0033	0.0010
0.292	−0.1835	0.0468	0.0087	0.0073	0.0037	0.0028	0.0011	−0.2088	0.0464	0.0099	0.0084	0.0042	0.0031	0.0011
0.375	−0.1890	0.0508	0.0091	0.0076	0.0038	0.0031	0.0014	−0.3096	0.0493	0.0148	0.0124	0.0062	0.0051	0.0014
0.458	−0.0912	0.0542	0.0044	0.0037	0.0019	0.0013	0.0006	−0.4154	0.0511	0.0195	0.0166	0.0083	0.0059	0.0006
0.542	0.0852	0.0675	0.0048	0.0037	0.0018	0.0016	0.0020	−0.4500	0.0643	0.0216	0.0180	0.0090	0.0077	0.0020
0.625	−0.4940	0.3235	0.0564	0.0205	0.0102	0.0507	0.0093	−0.9909	0.3035	0.1082	0.0396	0.0198	0.0982	0.0093

Table A.6: Energy bin $798\,\mathrm{MeV} < E_\gamma < 833\,\mathrm{MeV}$. Systematic uncertainty $\Delta E_\gamma = 9\,\mathrm{MeV}$.

$\cos\theta$	d	σ_d	Δd_sys	T	σ_T	ΔT_sys	$\Delta T_\mathrm{sys}^\Lambda$	ΔT_sys^d	$\Delta T_\mathrm{sys}^{bg}$
−0.958	0.974	0.009	0.003	0.1152	0.0553	0.0040	0.0023	0.0003	0.0033
−0.875	0.909	0.009	0.009	0.2244	0.0336	0.0069	0.0045	0.0023	0.0048
−0.792	0.896	0.008	0.010	0.2045	0.0264	0.0064	0.0041	0.0024	0.0044
−0.708	0.900	0.007	0.010	0.1537	0.0246	0.0047	0.0031	0.0017	0.0032
−0.625	0.858	0.008	0.014	0.0475	0.0242	0.0031	0.0010	0.0008	0.0029
−0.542	0.878	0.007	0.012	0.0142	0.0237	0.0028	0.0004	0.0003	0.0027
−0.458	0.790	0.009	0.021	−0.0596	0.0270	0.0033	0.0012	0.0016	0.0026
−0.375	0.845	0.008	0.016	−0.1109	0.0264	0.0036	0.0022	0.0020	0.0019
−0.292	0.899	0.006	0.010	−0.1347	0.0244	0.0035	0.0027	0.0015	0.0016
−0.208	0.854	0.006	0.015	−0.2089	0.0239	0.0057	0.0042	0.0036	0.0014
−0.125	0.873	0.006	0.013	−0.2251	0.0233	0.0057	0.0045	0.0033	0.0011
−0.042	0.869	0.006	0.013	−0.1707	0.0234	0.0044	0.0034	0.0026	0.0011
0.042	0.855	0.006	0.015	−0.2301	0.0230	0.0061	0.0046	0.0039	0.0011
0.125	0.873	0.006	0.013	−0.2453	0.0232	0.0061	0.0049	0.0036	0.0010
0.208	0.847	0.006	0.015	−0.2233	0.0235	0.0061	0.0045	0.0040	0.0011
0.292	0.851	0.007	0.015	−0.1532	0.0245	0.0042	0.0031	0.0027	0.0012
0.375	0.854	0.007	0.015	−0.1464	0.0252	0.0041	0.0029	0.0025	0.0013
0.458	0.858	0.008	0.014	−0.0688	0.0275	0.0020	0.0014	0.0011	0.0009
0.542	0.821	0.010	0.018	0.0627	0.0330	0.0030	0.0013	0.0014	0.0023
0.625	0.626	0.028	0.037	0.1004	0.0835	0.0096	0.0022	0.0066	0.0067

$\cos\theta$	P	σ_P	ΔP_sys	$\Delta P_\mathrm{sys}^\delta$	$\Delta P_\mathrm{sys}^\Lambda$	ΔP_sys^d	$\Delta P_\mathrm{sys}^{bg}$	H	σ_H	ΔH_sys	$\Delta H_\mathrm{sys}^\delta$	$\Delta H_\mathrm{sys}^\Lambda$	ΔH_sys^d	$\Delta H_\mathrm{sys}^{bg}$
−0.958	−0.2353	0.1201	0.0111	0.0095	0.0048	0.0006	0.0033	0.0621	0.1084	0.0056	0.0040	0.0020	0.0003	0.0033
−0.875	−0.3138	0.0737	0.0152	0.0126	0.0063	0.0032	0.0048	0.4575	0.0730	0.0215	0.0183	0.0091	0.0046	0.0048
−0.792	−0.3878	0.0567	0.0184	0.0155	0.0078	0.0045	0.0044	0.3987	0.0561	0.0189	0.0159	0.0080	0.0046	0.0044
−0.708	−0.2743	0.0525	0.0130	0.0110	0.0055	0.0030	0.0032	0.3481	0.0514	0.0164	0.0139	0.0070	0.0039	0.0032
−0.625	−0.3491	0.0517	0.0169	0.0140	0.0070	0.0058	0.0029	0.3112	0.0516	0.0151	0.0124	0.0062	0.0051	0.0029
−0.542	−0.3363	0.0507	0.0160	0.0135	0.0067	0.0047	0.0027	0.2324	0.0504	0.0112	0.0093	0.0046	0.0032	0.0027
−0.458	−0.3672	0.0577	0.0193	0.0147	0.0073	0.0097	0.0026	0.2004	0.0573	0.0107	0.0080	0.0040	0.0053	0.0026
−0.375	−0.3810	0.0541	0.0185	0.0152	0.0076	0.0070	0.0019	0.1391	0.0538	0.0070	0.0056	0.0028	0.0026	0.0019
−0.292	−0.3667	0.0493	0.0170	0.0147	0.0073	0.0041	0.0016	0.0714	0.0486	0.0038	0.0030	0.0015	0.0008	0.0016
−0.208	−0.3687	0.0485	0.0177	0.0147	0.0074	0.0063	0.0014	0.0630	0.0481	0.0035	0.0027	0.0013	0.0012	0.0014
−0.125	−0.2211	0.0472	0.0105	0.0088	0.0044	0.0032	0.0011	0.0049	0.0469	0.0021	0.0015	0.0008	0.0005	0.0011
−0.042	−0.2568	0.0468	0.0122	0.0103	0.0051	0.0039	0.0011	−0.1348	0.0454	0.0065	0.0054	0.0027	0.0020	0.0011
0.042	−0.2795	0.0463	0.0134	0.0112	0.0056	0.0048	0.0011	−0.1354	0.0451	0.0066	0.0054	0.0027	0.0023	0.0011
0.125	−0.2283	0.0469	0.0108	0.0091	0.0046	0.0033	0.0010	−0.1520	0.0446	0.0072	0.0061	0.0030	0.0022	0.0010
0.208	−0.2405	0.0475	0.0116	0.0096	0.0048	0.0043	0.0011	−0.2065	0.0462	0.0100	0.0083	0.0041	0.0037	0.0011
0.292	−0.1428	0.0490	0.0070	0.0057	0.0029	0.0025	0.0012	−0.2136	0.0487	0.0103	0.0085	0.0043	0.0037	0.0012
0.375	0.0411	0.0515	0.0029	0.0021	0.0011	0.0009	0.0013	−0.3272	0.0502	0.0157	0.0131	0.0065	0.0056	0.0013
0.458	−0.0011	0.0566	0.0023	0.0018	0.0009	0.0007	0.0009	−0.4517	0.0549	0.0216	0.0181	0.0090	0.0075	0.0009
0.542	0.1700	0.0681	0.0088	0.0068	0.0034	0.0037	0.0023	−0.5037	0.0656	0.0252	0.0201	0.0101	0.0110	0.0023
0.625	0.3108	0.1768	0.0245	0.0127	0.0063	0.0189	0.0067	−0.4811	0.1622	0.0365	0.0193	0.0096	0.0288	0.0067

Table A.7: Energy bin $833\,\mathrm{MeV} < E_\gamma < 867\,\mathrm{MeV}$. Systematic uncertainty $\Delta E_\gamma = 9\,\mathrm{MeV}$.

$\cos\theta$	d	σ_d	Δd_sys	T	σ_T	ΔT_sys	$\Delta T_\mathrm{sys}^\Lambda$	ΔT_sys^d	$\Delta T_\mathrm{sys}^{bg}$
−0.958	0.972	0.008	0.003	0.2578	0.0525	0.0066	0.0052	0.0007	0.0040
−0.875	0.919	0.009	0.008	0.2456	0.0342	0.0067	0.0049	0.0022	0.0041
−0.792	0.882	0.008	0.012	0.2348	0.0272	0.0074	0.0047	0.0031	0.0048
−0.708	0.906	0.007	0.009	0.1962	0.0253	0.0055	0.0039	0.0020	0.0033
−0.625	0.856	0.008	0.014	0.0898	0.0248	0.0039	0.0018	0.0015	0.0031
−0.542	0.890	0.007	0.011	0.0817	0.0243	0.0032	0.0016	0.0010	0.0025
−0.458	0.770	0.010	0.023	0.0049	0.0283	0.0030	0.0005	0.0007	0.0029
−0.375	0.821	0.008	0.018	−0.0830	0.0299	0.0036	0.0017	0.0018	0.0026
−0.292	0.891	0.006	0.011	−0.0816	0.0261	0.0025	0.0016	0.0010	0.0017
−0.208	0.844	0.007	0.016	−0.1037	0.0263	0.0034	0.0021	0.0019	0.0019
−0.125	0.867	0.006	0.013	−0.1858	0.0259	0.0048	0.0037	0.0029	0.0012
−0.042	0.849	0.007	0.015	−0.2035	0.0255	0.0057	0.0041	0.0036	0.0016
0.042	0.840	0.007	0.016	−0.2197	0.0258	0.0062	0.0044	0.0042	0.0010
0.125	0.879	0.006	0.012	−0.1871	0.0257	0.0046	0.0037	0.0026	0.0009
0.208	0.817	0.008	0.018	−0.2183	0.0271	0.0067	0.0044	0.0049	0.0013
0.292	0.828	0.008	0.017	−0.1321	0.0285	0.0041	0.0026	0.0027	0.0016
0.375	0.833	0.008	0.017	−0.1264	0.0293	0.0037	0.0025	0.0025	0.0010
0.458	0.805	0.010	0.020	−0.0129	0.0327	0.0026	0.0006	0.0007	0.0025
0.542	0.814	0.011	0.019	0.0263	0.0357	0.0019	0.0007	0.0008	0.0016
0.625	0.617	0.026	0.038	0.1544	0.0793	0.0115	0.0031	0.0097	0.0053

$\cos\theta$	P	σ_P	ΔP_sys	$\Delta P_\mathrm{sys}^\delta$	$\Delta P_\mathrm{sys}^\Lambda$	ΔP_sys^d	$\Delta P_\mathrm{sys}^{bg}$	H	σ_H	ΔH_sys	$\Delta H_\mathrm{sys}^\delta$	$\Delta H_\mathrm{sys}^\Lambda$	ΔH_sys^d	$\Delta H_\mathrm{sys}^{bg}$
−0.958	−0.3965	0.1088	0.0182	0.0159	0.0079	0.0011	0.0040	0.2751	0.1044	0.0130	0.0110	0.0055	0.0008	0.0040
−0.875	−0.3017	0.0730	0.0143	0.0121	0.0060	0.0026	0.0041	0.1925	0.0720	0.0097	0.0077	0.0039	0.0017	0.0041
−0.792	−0.2102	0.0576	0.0109	0.0084	0.0042	0.0028	0.0048	0.2911	0.0571	0.0144	0.0116	0.0058	0.0039	0.0048
−0.708	−0.3021	0.0538	0.0142	0.0121	0.0060	0.0031	0.0033	0.3291	0.0538	0.0155	0.0132	0.0066	0.0034	0.0033
−0.625	−0.3235	0.0533	0.0158	0.0129	0.0065	0.0054	0.0031	0.1714	0.0520	0.0087	0.0069	0.0034	0.0029	0.0031
−0.542	−0.2447	0.0517	0.0116	0.0098	0.0049	0.0026	0.0025	0.1743	0.0508	0.0085	0.0070	0.0035	0.0022	0.0025
−0.458	−0.2419	0.0598	0.0133	0.0097	0.0048	0.0072	0.0029	0.1488	0.0606	0.0085	0.0060	0.0030	0.0045	0.0029
−0.375	−0.3250	0.0611	0.0164	0.0130	0.0065	0.0071	0.0026	0.2067	0.0605	0.0106	0.0083	0.0041	0.0045	0.0026
−0.292	−0.2818	0.0523	0.0132	0.0113	0.0056	0.0035	0.0017	0.1211	0.0527	0.0059	0.0049	0.0024	0.0015	0.0017
−0.208	−0.2619	0.0527	0.0128	0.0105	0.0052	0.0048	0.0019	0.0602	0.0510	0.0037	0.0026	0.0013	0.0012	0.0019
−0.125	−0.2121	0.0517	0.0101	0.0085	0.0042	0.0033	0.0012	0.0797	0.0510	0.0041	0.0033	0.0016	0.0013	0.0012
−0.042	−0.1580	0.0509	0.0078	0.0063	0.0032	0.0028	0.0016	−0.0494	0.0511	0.0032	0.0023	0.0012	0.0010	0.0016
0.042	−0.1669	0.0511	0.0082	0.0067	0.0033	0.0032	0.0010	−0.1176	0.0513	0.0058	0.0047	0.0024	0.0023	0.0010
0.125	−0.1588	0.0517	0.0075	0.0064	0.0032	0.0022	0.0009	−0.2159	0.0505	0.0101	0.0086	0.0043	0.0030	0.0009
0.208	−0.1166	0.0547	0.0060	0.0047	0.0023	0.0023	0.0013	−0.2067	0.0532	0.0104	0.0083	0.0041	0.0046	0.0013
0.292	−0.0439	0.0570	0.0033	0.0023	0.0012	0.0012	0.0016	−0.2562	0.0560	0.0127	0.0102	0.0051	0.0053	0.0016
0.375	−0.0101	0.0595	0.0026	0.0019	0.0010	0.0010	0.0010	−0.2584	0.0588	0.0127	0.0103	0.0052	0.0052	0.0010
0.458	0.1991	0.0667	0.0104	0.0080	0.0040	0.0048	0.0025	−0.5079	0.0637	0.0260	0.0203	0.0102	0.0123	0.0025
0.542	0.3667	0.0741	0.0185	0.0147	0.0073	0.0084	0.0016	−0.6147	0.0724	0.0309	0.0246	0.0123	0.0140	0.0016
0.625	0.7275	0.1662	0.0560	0.0291	0.0146	0.0452	0.0053	−0.7194	0.1443	0.0553	0.0288	0.0144	0.0447	0.0053

Table A.8: Energy bin 867 MeV $< E_\gamma <$ 901 MeV. Systematic uncertainty $\Delta E_\gamma = 8$ MeV.

$\cos\theta$	d	σ_d	Δd_{sys}	T	σ_T	ΔT_{sys}	$\Delta T^\Lambda_{\text{sys}}$	ΔT^d_{sys}	$\Delta T^{bg}_{\text{sys}}$
−0.958	0.956	0.015	0.004	0.1587	0.0650	0.0061	0.0032	0.0007	0.0051
−0.875	0.896	0.015	0.010	0.2594	0.0428	0.0075	0.0052	0.0030	0.0044
−0.792	0.861	0.012	0.014	0.2351	0.0341	0.0085	0.0047	0.0038	0.0060
−0.708	0.893	0.010	0.011	0.2136	0.0320	0.0062	0.0043	0.0026	0.0038
−0.625	0.837	0.012	0.016	0.1950	0.0312	0.0069	0.0039	0.0038	0.0042
−0.542	0.855	0.012	0.014	0.0517	0.0310	0.0031	0.0011	0.0009	0.0028
−0.458	0.753	0.016	0.025	0.0660	0.0370	0.0040	0.0013	0.0022	0.0031
−0.375	0.831	0.013	0.017	−0.0341	0.0394	0.0032	0.0009	0.0009	0.0029
−0.292	0.885	0.010	0.011	−0.0973	0.0343	0.0029	0.0019	0.0013	0.0018
−0.208	0.829	0.012	0.017	−0.0740	0.0351	0.0035	0.0015	0.0015	0.0028
−0.125	0.836	0.011	0.016	−0.1341	0.0345	0.0042	0.0027	0.0026	0.0019
−0.042	0.851	0.010	0.015	−0.1594	0.0328	0.0044	0.0032	0.0028	0.0011
0.042	0.837	0.011	0.016	−0.1330	0.0349	0.0040	0.0027	0.0026	0.0014
0.125	0.864	0.010	0.014	−0.1914	0.0350	0.0049	0.0038	0.0030	0.0008
0.208	0.800	0.013	0.020	−0.2212	0.0377	0.0072	0.0044	0.0055	0.0012
0.292	0.783	0.015	0.022	−0.1307	0.0398	0.0048	0.0026	0.0036	0.0016
0.375	0.817	0.013	0.018	−0.1711	0.0424	0.0054	0.0034	0.0038	0.0015
0.458	0.753	0.017	0.025	−0.1218	0.0450	0.0053	0.0024	0.0040	0.0025
0.542	0.797	0.017	0.020	0.0295	0.0466	0.0017	0.0009	0.0011	0.0010
0.625	0.731	0.028	0.027	−0.0338	0.0689	0.0043	0.0012	0.0023	0.0034

$\cos\theta$	P	σ_P	ΔP_{sys}	$\Delta P^\delta_{\text{sys}}$	$\Delta P^\Lambda_{\text{sys}}$	ΔP^d_{sys}	$\Delta P^{bg}_{\text{sys}}$	H	σ_H	ΔH_{sys}	$\Delta H^\delta_{\text{sys}}$	$\Delta H^\Lambda_{\text{sys}}$	ΔH^d_{sys}	$\Delta H^{bg}_{\text{sys}}$
−0.958	−0.4631	0.1396	0.0214	0.0185	0.0093	0.0021	0.0051	0.1968	0.1251	0.0105	0.0081	0.0041	0.0009	0.0051
−0.875	−0.2121	0.0929	0.0108	0.0085	0.0043	0.0025	0.0044	0.3630	0.0915	0.0174	0.0145	0.0073	0.0042	0.0044
−0.792	−0.2977	0.0740	0.0154	0.0119	0.0060	0.0048	0.0060	0.2334	0.0727	0.0126	0.0093	0.0047	0.0038	0.0060
−0.708	−0.2917	0.0697	0.0140	0.0117	0.0058	0.0035	0.0038	0.3203	0.0686	0.0153	0.0128	0.0064	0.0039	0.0038
−0.625	−0.1937	0.0673	0.0103	0.0078	0.0039	0.0038	0.0042	0.2500	0.0689	0.0129	0.0100	0.0050	0.0049	0.0042
−0.542	−0.1199	0.0682	0.0065	0.0049	0.0024	0.0021	0.0028	0.2678	0.0681	0.0131	0.0107	0.0054	0.0045	0.0028
−0.458	−0.1512	0.0800	0.0090	0.0061	0.0031	0.0050	0.0031	0.2720	0.0799	0.0154	0.0109	0.0054	0.0089	0.0031
−0.375	−0.0808	0.0813	0.0055	0.0038	0.0019	0.0019	0.0029	0.2842	0.0796	0.0143	0.0114	0.0057	0.0058	0.0029
−0.292	−0.2068	0.0697	0.0098	0.0083	0.0041	0.0027	0.0018	0.0486	0.0711	0.0037	0.0028	0.0014	0.0009	0.0018
−0.208	−0.2526	0.0718	0.0128	0.0101	0.0051	0.0052	0.0028	0.3425	0.0707	0.0171	0.0137	0.0069	0.0071	0.0028
−0.125	−0.1860	0.0696	0.0093	0.0074	0.0037	0.0037	0.0019	0.0047	0.0698	0.0033	0.0022	0.0011	0.0011	0.0019
−0.042	−0.2554	0.0673	0.0123	0.0102	0.0051	0.0045	0.0011	−0.0060	0.0669	0.0028	0.0021	0.0011	0.0009	0.0011
0.042	−0.2313	0.0710	0.0114	0.0093	0.0046	0.0045	0.0014	−0.0898	0.0690	0.0049	0.0038	0.0019	0.0019	0.0014
0.125	−0.0435	0.0720	0.0033	0.0027	0.0014	0.0011	0.0008	−0.1443	0.0711	0.0069	0.0058	0.0029	0.0023	0.0008
0.208	−0.1392	0.0774	0.0074	0.0057	0.0028	0.0035	0.0012	−0.2919	0.0754	0.0150	0.0117	0.0058	0.0073	0.0012
0.292	−0.0560	0.0822	0.0045	0.0032	0.0016	0.0022	0.0016	−0.2914	0.0840	0.0154	0.0117	0.0058	0.0081	0.0016
0.375	0.1148	0.0882	0.0063	0.0049	0.0025	0.0027	0.0015	−0.6170	0.0845	0.0309	0.0247	0.0123	0.0138	0.0015
0.458	0.1916	0.0934	0.0110	0.0077	0.0039	0.0063	0.0025	−0.5752	0.0923	0.0320	0.0230	0.0115	0.0189	0.0025
0.542	0.4868	0.0986	0.0251	0.0195	0.0097	0.0124	0.0010	−0.7282	0.0945	0.0375	0.0291	0.0146	0.0186	0.0010
0.625	0.4007	0.1475	0.0235	0.0160	0.0080	0.0148	0.0034	−0.7425	0.1393	0.0432	0.0297	0.0149	0.0273	0.0034

Table A.9: Energy bin 901 MeV $< E_\gamma <$ 933 MeV. Systematic uncertainty $\Delta E_\gamma = 8$ MeV.

$\cos\theta$	d	σ_d	Δd_{sys}	T	σ_T	ΔT_{sys}	$\Delta T^\Lambda_{\text{sys}}$	ΔT^d_{sys}	$\Delta T^{bg}_{\text{sys}}$
−0.958	0.987	0.007	0.001	0.2048	0.0719	0.0044	0.0041	0.0003	0.0016
−0.875	0.915	0.011	0.009	0.2242	0.0408	0.0081	0.0045	0.0021	0.0065
−0.792	0.869	0.011	0.013	0.1627	0.0344	0.0065	0.0033	0.0025	0.0050
−0.708	0.891	0.009	0.011	0.1126	0.0312	0.0054	0.0023	0.0014	0.0047
−0.625	0.833	0.011	0.017	0.1236	0.0313	0.0053	0.0025	0.0025	0.0040
−0.542	0.862	0.010	0.014	0.0538	0.0320	0.0039	0.0011	0.0009	0.0037
−0.458	0.765	0.014	0.024	−0.0115	0.0390	0.0030	0.0006	0.0010	0.0028
−0.375	0.770	0.014	0.023	−0.0810	0.0434	0.0039	0.0016	0.0024	0.0026
−0.292	0.856	0.010	0.014	−0.0770	0.0389	0.0027	0.0016	0.0013	0.0017
−0.208	0.812	0.011	0.019	−0.0570	0.0383	0.0033	0.0012	0.0014	0.0027
−0.125	0.829	0.011	0.017	−0.1535	0.0386	0.0047	0.0031	0.0032	0.0015
−0.042	0.830	0.010	0.017	−0.1621	0.0394	0.0052	0.0032	0.0033	0.0024
0.042	0.819	0.011	0.018	−0.1992	0.0389	0.0061	0.0040	0.0044	0.0016
0.125	0.842	0.011	0.016	−0.1802	0.0401	0.0051	0.0036	0.0034	0.0011
0.208	0.780	0.014	0.022	−0.2733	0.0453	0.0097	0.0055	0.0077	0.0024
0.292	0.771	0.014	0.023	−0.3418	0.0463	0.0123	0.0068	0.0101	0.0009
0.375	0.802	0.014	0.020	−0.3188	0.0476	0.0104	0.0064	0.0079	0.0023
0.458	0.744	0.016	0.026	−0.2214	0.0531	0.0090	0.0044	0.0076	0.0019
0.542	0.759	0.018	0.024	−0.2098	0.0538	0.0081	0.0042	0.0067	0.0019
0.625	0.673	0.027	0.033	−0.2021	0.0700	0.0113	0.0040	0.0098	0.0037
0.708	0.455	0.081	0.054	−0.0657	0.2452	0.0306	0.0041	0.0242	0.0181

$\cos\theta$	P	σ_P	ΔP_{sys}	$\Delta P^\delta_{\text{sys}}$	$\Delta P^\Lambda_{\text{sys}}$	ΔP^d_{sys}	$\Delta P^{bg}_{\text{sys}}$	H	σ_H	ΔH_{sys}	$\Delta H^\delta_{\text{sys}}$	$\Delta H^\Lambda_{\text{sys}}$	ΔH^d_{sys}	$\Delta H^{bg}_{\text{sys}}$
−0.958	−0.2540	0.1638	0.0119	0.0105	0.0053	0.0003	0.0016	−0.1649	0.1417	0.0083	0.0073	0.0036	0.0002	0.0016
−0.875	−0.3661	0.0931	0.0179	0.0146	0.0073	0.0034	0.0065	0.3476	0.0918	0.0171	0.0139	0.0070	0.0032	0.0065
−0.792	−0.2968	0.0788	0.0149	0.0119	0.0059	0.0045	0.0050	0.0238	0.0785	0.0059	0.0026	0.0013	0.0010	0.0050
−0.708	−0.3300	0.0719	0.0160	0.0132	0.0066	0.0041	0.0047	0.1807	0.0718	0.0096	0.0072	0.0036	0.0022	0.0047
−0.625	−0.2498	0.0726	0.0129	0.0100	0.0050	0.0050	0.0040	0.2101	0.0727	0.0110	0.0084	0.0042	0.0042	0.0040
−0.542	−0.1859	0.0740	0.0096	0.0074	0.0037	0.0030	0.0037	0.1427	0.0723	0.0078	0.0058	0.0029	0.0023	0.0037
−0.458	−0.1718	0.0900	0.0098	0.0069	0.0035	0.0054	0.0028	0.1163	0.0881	0.0073	0.0050	0.0025	0.0038	0.0028
−0.375	−0.2090	0.0974	0.0116	0.0084	0.0042	0.0063	0.0026	0.3891	0.0959	0.0211	0.0156	0.0078	0.0116	0.0026
−0.292	−0.1427	0.0833	0.0072	0.0058	0.0029	0.0025	0.0017	0.1828	0.0818	0.0089	0.0073	0.0037	0.0031	0.0017
−0.208	−0.0589	0.0816	0.0049	0.0033	0.0016	0.0019	0.0027	0.1546	0.0816	0.0083	0.0063	0.0031	0.0036	0.0027
−0.125	−0.2392	0.0820	0.0119	0.0096	0.0048	0.0049	0.0015	0.1042	0.0827	0.0057	0.0045	0.0022	0.0023	0.0015
−0.042	−0.2597	0.0847	0.0130	0.0104	0.0052	0.0053	0.0024	0.0223	0.0830	0.0041	0.0027	0.0014	0.0014	0.0024
0.042	−0.2132	0.0845	0.0108	0.0085	0.0043	0.0047	0.0016	−0.0260	0.0849	0.0039	0.0028	0.0014	0.0016	0.0016
0.125	−0.2222	0.0872	0.0108	0.0089	0.0045	0.0042	0.0011	0.0037	0.0849	0.0035	0.0027	0.0014	0.0013	0.0011
0.208	−0.1310	0.0994	0.0078	0.0056	0.0028	0.0039	0.0024	−0.2969	0.0997	0.0159	0.0119	0.0059	0.0084	0.0024
0.292	−0.0804	0.1017	0.0057	0.0042	0.0021	0.0031	0.0009	−0.2702	0.1018	0.0145	0.0108	0.0054	0.0080	0.0009
0.375	−0.0449	0.1046	0.0052	0.0036	0.0018	0.0022	0.0023	−0.3302	0.1036	0.0170	0.0132	0.0066	0.0081	0.0023
0.458	−0.0482	0.1148	0.0059	0.0040	0.0020	0.0034	0.0019	−0.5214	0.1124	0.0295	0.0209	0.0104	0.0179	0.0019
0.542	0.1396	0.1202	0.0087	0.0062	0.0031	0.0049	0.0019	−0.4908	0.1129	0.0270	0.0196	0.0098	0.0156	0.0019
0.625	0.1140	0.1597	0.0111	0.0063	0.0032	0.0077	0.0037	−0.3336	0.1543	0.0225	0.0134	0.0067	0.0163	0.0037
0.708	−0.2611	0.5985	0.0691	0.0209	0.0104	0.0625	0.0181	−0.1277	0.5308	0.0585	0.0174	0.0087	0.0521	0.0181

Table A.10: Energy bin $933\,\text{MeV} < E_\gamma < 974\,\text{MeV}$. Systematic uncertainty $\Delta E_\gamma = 8\,\text{MeV}$.

$\cos\theta$	d	σ_d	Δd_{sys}	T	σ_T	ΔT_{sys}	$\Delta T^\Lambda_{\text{sys}}$	ΔT^d_{sys}	$\Delta T^{bg}_{\text{sys}}$
−0.958	0.944	0.014	0.006	0.3742	0.0787	0.0087	0.0075	0.0022	0.0038
−0.875	0.888	0.012	0.011	0.2243	0.0441	0.0079	0.0045	0.0028	0.0059
−0.792	0.858	0.012	0.014	0.2656	0.0349	0.0083	0.0053	0.0044	0.0047
−0.708	0.871	0.010	0.013	0.1284	0.0324	0.0062	0.0026	0.0019	0.0053
−0.625	0.810	0.012	0.019	0.1296	0.0333	0.0063	0.0026	0.0030	0.0049
−0.542	0.841	0.011	0.016	−0.0445	0.0329	0.0039	0.0009	0.0009	0.0036
−0.458	0.768	0.014	0.023	0.0047	0.0390	0.0034	0.0006	0.0009	0.0032
−0.375	0.752	0.016	0.025	−0.1955	0.0451	0.0086	0.0039	0.0064	0.0042
−0.292	0.842	0.012	0.016	−0.0094	0.0414	0.0024	0.0007	0.0006	0.0023
−0.208	0.808	0.012	0.019	−0.1130	0.0412	0.0045	0.0023	0.0027	0.0027
−0.125	0.844	0.011	0.016	−0.1988	0.0397	0.0058	0.0040	0.0037	0.0021
−0.042	0.833	0.012	0.017	−0.2916	0.0411	0.0084	0.0058	0.0058	0.0013
0.042	0.785	0.014	0.022	−0.2686	0.0456	0.0091	0.0054	0.0074	0.0007
0.125	0.782	0.015	0.022	−0.3696	0.0467	0.0128	0.0074	0.0103	0.0020
0.208	0.782	0.015	0.022	−0.3825	0.0484	0.0133	0.0076	0.0107	0.0021
0.292	0.780	0.015	0.022	−0.4253	0.0487	0.0148	0.0085	0.0120	0.0019
0.375	0.752	0.017	0.025	−0.4241	0.0510	0.0167	0.0085	0.0140	0.0035
0.458	0.798	0.015	0.020	−0.3004	0.0494	0.0100	0.0060	0.0076	0.0022
0.542	0.754	0.018	0.025	−0.2908	0.0532	0.0115	0.0058	0.0095	0.0029
0.625	0.797	0.018	0.020	−0.0837	0.0525	0.0039	0.0017	0.0022	0.0027
0.708	0.647	0.046	0.035	0.0031	0.1365	0.0066	0.0022	0.0059	0.0020

$\cos\theta$	P	σ_P	ΔP_{sys}	$\Delta P^\delta_{\text{sys}}$	$\Delta P^\Lambda_{\text{sys}}$	ΔP^d_{sys}	$\Delta P^{bg}_{\text{sys}}$	H	σ_H	ΔH_{sys}	$\Delta H^\delta_{\text{sys}}$	$\Delta H^\Lambda_{\text{sys}}$	ΔH^d_{sys}	$\Delta H^{bg}_{\text{sys}}$
−0.958	−0.0930	0.1959	0.0148	0.0139	0.0035	0.0010	0.0038	0.0656	0.1785	0.0131	0.0122	0.0030	0.0009	0.0038
−0.875	−0.3834	0.1128	0.0325	0.0307	0.0077	0.0048	0.0059	0.1055	0.1111	0.0120	0.0101	0.0025	0.0016	0.0059
−0.792	−0.1721	0.0904	0.0154	0.0139	0.0035	0.0029	0.0047	0.0962	0.0909	0.0104	0.0088	0.0022	0.0018	0.0047
−0.708	−0.2288	0.0824	0.0199	0.0183	0.0046	0.0034	0.0053	0.0793	0.0833	0.0095	0.0076	0.0019	0.0014	0.0053
−0.625	−0.2176	0.0863	0.0193	0.0174	0.0044	0.0051	0.0049	0.0771	0.0866	0.0095	0.0076	0.0019	0.0022	0.0049
−0.542	−0.2150	0.0852	0.0186	0.0172	0.0043	0.0041	0.0036	0.1108	0.0864	0.0107	0.0095	0.0024	0.0022	0.0036
−0.458	−0.1798	0.1017	0.0164	0.0146	0.0037	0.0055	0.0032	0.0921	0.0998	0.0103	0.0089	0.0022	0.0034	0.0032
−0.375	−0.1924	0.1119	0.0179	0.0157	0.0039	0.0065	0.0042	0.2461	0.1117	0.0223	0.0198	0.0049	0.0081	0.0042
−0.292	−0.0833	0.1007	0.0093	0.0085	0.0021	0.0020	0.0023	0.2515	0.1028	0.0214	0.0202	0.0050	0.0047	0.0023
−0.208	−0.0305	0.1002	0.0077	0.0067	0.0017	0.0020	0.0027	0.3115	0.1006	0.0269	0.0249	0.0062	0.0074	0.0027
−0.125	−0.2391	0.0983	0.0204	0.0192	0.0048	0.0044	0.0021	0.1545	0.0961	0.0136	0.0127	0.0032	0.0029	0.0021
−0.042	−0.1965	0.1002	0.0169	0.0159	0.0040	0.0040	0.0013	0.1909	0.1032	0.0165	0.0155	0.0039	0.0039	0.0013
0.042	−0.2423	0.1099	0.0212	0.0195	0.0049	0.0067	0.0007	−0.0823	0.1100	0.0097	0.0089	0.0022	0.0031	0.0007
0.125	−0.1602	0.1129	0.0148	0.0134	0.0034	0.0047	0.0020	−0.4198	0.1133	0.0366	0.0336	0.0084	0.0117	0.0020
0.208	−0.3709	0.1158	0.0324	0.0297	0.0074	0.0103	0.0021	−0.2360	0.1171	0.0208	0.0190	0.0048	0.0066	0.0021
0.292	−0.3326	0.1195	0.0291	0.0266	0.0067	0.0094	0.0019	−0.1740	0.1210	0.0160	0.0146	0.0036	0.0051	0.0019
0.375	−0.2084	0.1272	0.0193	0.0171	0.0043	0.0070	0.0035	−0.2744	0.1284	0.0247	0.0221	0.0055	0.0091	0.0035
0.458	−0.1427	0.1241	0.0138	0.0126	0.0032	0.0040	0.0022	−0.1396	0.1209	0.0135	0.0124	0.0031	0.0039	0.0022
0.542	0.2088	0.1315	0.0193	0.0172	0.0043	0.0070	0.0029	−0.1427	0.1366	0.0148	0.0131	0.0033	0.0053	0.0029
0.625	0.2392	0.1362	0.0212	0.0195	0.0049	0.0062	0.0027	−0.2626	0.1277	0.0230	0.0212	0.0053	0.0067	0.0027
0.708	0.8785	0.3578	0.0871	0.0704	0.0176	0.0480	0.0020	−0.0823	0.3242	0.0265	0.0214	0.0053	0.0146	0.0020

Table A.11: Energy bin $974\,\text{MeV} < E_\gamma < 1015\,\text{MeV}$. Systematic uncertainty $\Delta E_\gamma = 8\,\text{MeV}$.

$\cos\theta$	d	σ_d	Δd_{sys}	T	σ_T	ΔT_{sys}	$\Delta T^\Lambda_{\text{sys}}$	ΔT^d_{sys}	$\Delta T^{bg}_{\text{sys}}$
−0.958	0.942	0.014	0.006	0.5776	0.0775	0.0123	0.0116	0.0035	0.0023
−0.875	0.917	0.010	0.008	0.3187	0.0468	0.0072	0.0064	0.0029	0.0015
−0.792	0.883	0.008	0.012	0.2626	0.0366	0.0065	0.0053	0.0035	0.0015
−0.708	0.874	0.008	0.013	0.1015	0.0344	0.0025	0.0020	0.0015	0.0004
−0.625	0.809	0.009	0.019	−0.0154	0.0344	0.0009	0.0006	0.0007	0.0001
−0.542	0.847	0.008	0.015	−0.0213	0.0327	0.0008	0.0006	0.0006	0.0001
−0.458	0.782	0.011	0.022	−0.0811	0.0397	0.0028	0.0016	0.0023	0.0003
−0.375	0.771	0.011	0.023	−0.0580	0.0464	0.0023	0.0013	0.0019	0.0002
−0.292	0.859	0.009	0.014	−0.1366	0.0436	0.0036	0.0027	0.0022	0.0005
−0.208	0.831	0.010	0.017	−0.0720	0.0448	0.0021	0.0015	0.0015	0.0001
−0.125	0.836	0.010	0.016	−0.2295	0.0450	0.0065	0.0046	0.0045	0.0006
−0.042	0.818	0.011	0.018	−0.3024	0.0472	0.0091	0.0060	0.0067	0.0007
0.042	0.807	0.011	0.019	−0.3905	0.0494	0.0122	0.0078	0.0093	0.0006
0.125	0.835	0.011	0.017	−0.3860	0.0472	0.0109	0.0077	0.0076	0.0009
0.208	0.799	0.011	0.020	−0.4884	0.0483	0.0157	0.0098	0.0123	0.0009
0.292	0.803	0.011	0.020	−0.5171	0.0487	0.0164	0.0103	0.0127	0.0010
0.375	0.785	0.011	0.022	−0.4446	0.0480	0.0151	0.0089	0.0122	0.0011
0.458	0.793	0.012	0.021	−0.3446	0.0476	0.0114	0.0069	0.0090	0.0008
0.542	0.808	0.011	0.019	−0.1690	0.0450	0.0053	0.0034	0.0040	0.0006
0.625	0.850	0.011	0.015	−0.0189	0.0442	0.0010	0.0008	0.0007	0.0000
0.708	0.770	0.021	0.023	0.1404	0.0772	0.0051	0.0028	0.0042	0.0002

Table A.12: Energy bin $1015\,\mathrm{MeV} < E_\gamma < 1058\,\mathrm{MeV}$. Systematic uncertainty $\Delta E_\gamma = 7\,\mathrm{MeV}$.

$\cos\theta$	d	σ_d	Δd_{sys}	T	σ_T	ΔT_{sys}	$\Delta T_{\mathrm{sys}}^{\Lambda}$	$\Delta T_{\mathrm{sys}}^{d}$	$\Delta T_{\mathrm{sys}}^{bg}$
-0.958	0.943	0.010	0.006	0.7299	0.0794	0.0163	0.0146	0.0044	0.0057
-0.875	0.900	0.008	0.010	0.3039	0.0511	0.0073	0.0061	0.0034	0.0021
-0.792	0.880	0.006	0.012	0.1550	0.0374	0.0038	0.0031	0.0021	0.0007
-0.708	0.866	0.006	0.013	0.0207	0.0362	0.0009	0.0007	0.0005	0.0001
-0.625	0.829	0.006	0.017	-0.0441	0.0356	0.0014	0.0010	0.0010	0.0002
-0.542	0.834	0.006	0.017	-0.0648	0.0361	0.0019	0.0013	0.0013	0.0002
-0.458	0.777	0.008	0.022	-0.0788	0.0426	0.0028	0.0016	0.0023	0.0003
-0.375	0.762	0.009	0.024	-0.0477	0.0523	0.0022	0.0012	0.0018	0.0002
-0.292	0.854	0.007	0.015	-0.1956	0.0469	0.0052	0.0039	0.0033	0.0006
-0.208	0.804	0.008	0.020	-0.2094	0.0516	0.0067	0.0042	0.0051	0.0009
-0.125	0.810	0.008	0.019	-0.2342	0.0517	0.0072	0.0047	0.0055	0.0004
-0.042	0.818	0.008	0.018	-0.2493	0.0517	0.0075	0.0050	0.0056	0.0006
0.042	0.828	0.008	0.017	-0.3623	0.0495	0.0105	0.0072	0.0075	0.0006
0.125	0.833	0.008	0.017	-0.3296	0.0490	0.0093	0.0066	0.0066	0.0004
0.208	0.816	0.008	0.018	-0.3425	0.0477	0.0103	0.0069	0.0077	0.0006
0.292	0.832	0.007	0.017	-0.2749	0.0479	0.0078	0.0055	0.0055	0.0003
0.375	0.806	0.007	0.019	-0.1784	0.0458	0.0056	0.0036	0.0043	0.0003
0.458	0.824	0.007	0.018	-0.0357	0.0442	0.0014	0.0009	0.0010	0.0001
0.542	0.791	0.007	0.021	0.0984	0.0406	0.0033	0.0020	0.0026	0.0002
0.625	0.832	0.007	0.017	0.0845	0.0396	0.0024	0.0017	0.0017	0.0002
0.708	0.782	0.010	0.022	0.1616	0.0559	0.0056	0.0032	0.0045	0.0004

Table A.13: Energy bin $1058\,\mathrm{MeV} < E_\gamma < 1100\,\mathrm{MeV}$. Systematic uncertainty $\Delta E_\gamma = 7\,\mathrm{MeV}$.

$\cos\theta$	d	σ_d	Δd_{sys}	T	σ_T	ΔT_{sys}	$\Delta T_{\mathrm{sys}}^{\Lambda}$	$\Delta T_{\mathrm{sys}}^{d}$	$\Delta T_{\mathrm{sys}}^{bg}$
-0.958	0.959	0.010	0.004	0.4894	0.1017	0.0106	0.0098	0.0021	0.0036
-0.875	0.887	0.011	0.011	0.4192	0.0682	0.0104	0.0084	0.0053	0.0030
-0.792	0.857	0.009	0.014	0.1895	0.0513	0.0051	0.0038	0.0031	0.0013
-0.708	0.859	0.008	0.014	-0.0490	0.0463	0.0015	0.0011	0.0009	0.0002
-0.625	0.807	0.009	0.019	-0.0195	0.0477	0.0013	0.0008	0.0010	0.0001
-0.542	0.831	0.008	0.017	-0.0904	0.0475	0.0026	0.0018	0.0019	0.0004
-0.458	0.774	0.010	0.023	-0.1419	0.0548	0.0051	0.0028	0.0042	0.0007
-0.375	0.723	0.012	0.028	-0.2401	0.0688	0.0105	0.0048	0.0092	0.0016
-0.292	0.840	0.009	0.016	0.0381	0.0614	0.0016	0.0012	0.0011	0.0001
-0.208	0.801	0.010	0.020	-0.1907	0.0653	0.0061	0.0038	0.0048	0.0005
-0.125	0.807	0.010	0.019	-0.0543	0.0663	0.0022	0.0014	0.0017	0.0002
-0.042	0.804	0.010	0.020	-0.2911	0.0658	0.0092	0.0058	0.0071	0.0007
0.042	0.803	0.010	0.020	-0.2863	0.0636	0.0091	0.0057	0.0070	0.0007
0.125	0.799	0.009	0.020	-0.2345	0.0595	0.0075	0.0047	0.0059	0.0003
0.208	0.807	0.009	0.019	-0.2789	0.0579	0.0087	0.0056	0.0067	0.0005
0.292	0.820	0.008	0.018	-0.1497	0.0554	0.0045	0.0030	0.0033	0.0003
0.375	0.808	0.008	0.019	-0.0893	0.0502	0.0028	0.0018	0.0022	0.0001
0.458	0.807	0.008	0.019	0.0503	0.0523	0.0019	0.0012	0.0014	0.0001
0.542	0.752	0.009	0.025	0.1695	0.0487	0.0065	0.0034	0.0056	0.0004
0.625	0.792	0.008	0.021	0.2652	0.0474	0.0088	0.0053	0.0069	0.0009
0.708	0.793	0.010	0.021	0.3465	0.0574	0.0114	0.0069	0.0090	0.0013

Table A.14: Energy bin $1100\,\mathrm{MeV} < E_\gamma < 1154\,\mathrm{MeV}$. Systematic uncertainty $\Delta E_\gamma = 7\,\mathrm{MeV}$.

$\cos\theta$	d	σ_d	Δd_{sys}	T	σ_T	ΔT_{sys}	$\Delta T_{\mathrm{sys}}^{\Lambda}$	$\Delta T_{\mathrm{sys}}^{d}$	$\Delta T_{\mathrm{sys}}^{bg}$
-0.958	0.918	0.016	0.008	0.4172	0.1130	0.0095	0.0083	0.0037	0.0026
-0.875	0.855	0.014	0.014	0.2969	0.0801	0.0080	0.0059	0.0050	0.0018
-0.792	0.834	0.012	0.017	0.0702	0.0618	0.0022	0.0016	0.0016	0.0004
-0.708	0.842	0.011	0.016	-0.1116	0.0563	0.0032	0.0023	0.0021	0.0007
-0.625	0.801	0.011	0.020	-0.1281	0.0544	0.0041	0.0026	0.0032	0.0006
-0.542	0.780	0.012	0.022	-0.2518	0.0569	0.0088	0.0050	0.0071	0.0013
-0.458	0.726	0.013	0.027	-0.2375	0.0642	0.0102	0.0047	0.0089	0.0011
-0.375	0.645	0.018	0.035	-0.1599	0.0870	0.0096	0.0032	0.0089	0.0015
-0.292	0.834	0.012	0.017	-0.0247	0.0734	0.0017	0.0012	0.0012	0.0001
-0.208	0.793	0.013	0.021	-0.1260	0.0756	0.0043	0.0026	0.0034	0.0003
-0.125	0.757	0.014	0.024	-0.2607	0.0763	0.0099	0.0052	0.0084	0.0011
-0.042	0.766	0.012	0.023	-0.2466	0.0729	0.0090	0.0049	0.0075	0.0006
0.042	0.793	0.011	0.021	-0.2361	0.0674	0.0078	0.0047	0.0062	0.0002
0.125	0.789	0.011	0.021	-0.2473	0.0613	0.0083	0.0049	0.0066	0.0004
0.208	0.799	0.010	0.020	-0.2540	0.0581	0.0082	0.0051	0.0064	0.0004
0.292	0.820	0.009	0.018	-0.0784	0.0545	0.0024	0.0016	0.0018	0.0001
0.375	0.790	0.009	0.021	0.0253	0.0526	0.0016	0.0009	0.0012	0.0001
0.458	0.805	0.009	0.019	0.1019	0.0517	0.0032	0.0021	0.0025	0.0002
0.542	0.730	0.011	0.027	0.2974	0.0523	0.0125	0.0059	0.0110	0.0008
0.625	0.759	0.011	0.024	0.4005	0.0519	0.0150	0.0080	0.0127	0.0007
0.708	0.739	0.012	0.026	0.5059	0.0585	0.0206	0.0101	0.0179	0.0021

Appendix A Data Points

Table A.15: Energy bin $1154\,\mathrm{MeV} < E_\gamma < 1197\,\mathrm{MeV}$. Systematic uncertainty $\Delta E_\gamma = 6\,\mathrm{MeV}$.

$\cos\theta$	d	σ_d	Δd_{sys}	T	σ_T	ΔT_{sys}	$\Delta T^\Lambda_{\mathrm{sys}}$	$\Delta T^d_{\mathrm{sys}}$	$\Delta T^{bg}_{\mathrm{sys}}$
−0.958	0.947	0.013	0.005	0.4682	0.1166	0.0101	0.0094	0.0026	0.0025
−0.875	0.881	0.015	0.012	0.1089	0.0925	0.0030	0.0024	0.0016	0.0007
−0.792	0.773	0.016	0.023	0.1398	0.0896	0.0054	0.0029	0.0042	0.0015
−0.708	0.771	0.015	0.023	−0.3212	0.0838	0.0117	0.0064	0.0095	0.0021
−0.625	0.740	0.015	0.026	−0.2826	0.0783	0.0115	0.0057	0.0099	0.0014
−0.542	0.772	0.014	0.023	−0.2007	0.0753	0.0072	0.0040	0.0059	0.0012
−0.458	0.745	0.015	0.026	−0.1216	0.0800	0.0050	0.0025	0.0043	0.0007
−0.375	0.608	0.020	0.039	−0.1134	0.1154	0.0090	0.0027	0.0086	0.0007
−0.292	0.826	0.014	0.017	−0.0032	0.0991	0.0023	0.0016	0.0017	0.0000
−0.208	0.804	0.014	0.020	0.0240	0.0955	0.0025	0.0016	0.0019	0.0001
−0.125	0.716	0.016	0.028	−0.2814	0.1010	0.0125	0.0056	0.0111	0.0009
−0.042	0.772	0.014	0.023	−0.3391	0.0856	0.0121	0.0068	0.0100	0.0011
0.042	0.777	0.013	0.022	−0.2164	0.0826	0.0076	0.0043	0.0062	0.0005
0.125	0.804	0.011	0.020	−0.2339	0.0771	0.0074	0.0047	0.0057	0.0008
0.208	0.805	0.011	0.019	−0.3610	0.0700	0.0113	0.0072	0.0087	0.0005
0.292	0.800	0.010	0.020	−0.2074	0.0680	0.0066	0.0041	0.0052	0.0002
0.375	0.764	0.011	0.024	0.0988	0.0657	0.0038	0.0021	0.0032	0.0003
0.458	0.754	0.012	0.025	0.2513	0.0691	0.0097	0.0050	0.0082	0.0008
0.542	0.705	0.013	0.029	0.4350	0.0710	0.0202	0.0087	0.0182	0.0018
0.625	0.705	0.013	0.030	0.6164	0.0707	0.0287	0.0123	0.0258	0.0025
0.708	0.692	0.015	0.031	0.7050	0.0780	0.0344	0.0141	0.0313	0.0018
0.792	0.432	0.038	0.057	0.7164	0.2503	0.0952	0.0143	0.0941	0.0025

Table A.16: Energy bin $1197\,\mathrm{MeV} < E_\gamma < 1246\,\mathrm{MeV}$. Systematic uncertainty $\Delta E_\gamma = 6\,\mathrm{MeV}$.

$\cos\theta$	d	σ_d	Δd_{sys}	T	σ_T	ΔT_{sys}	$\Delta T^\Lambda_{\mathrm{sys}}$	$\Delta T^d_{\mathrm{sys}}$	$\Delta T^{bg}_{\mathrm{sys}}$
−0.958	0.908	0.016	0.009	0.5658	0.1124	0.0130	0.0113	0.0057	0.0028
−0.875	0.879	0.014	0.012	0.1935	0.0831	0.0048	0.0039	0.0027	0.0010
−0.792	0.789	0.016	0.021	−0.0703	0.0809	0.0018	0.0018	0.0023	0.0005
−0.708	0.814	0.014	0.019	−0.1696	0.0741	0.0053	0.0034	0.0039	0.0012
−0.625	0.724	0.017	0.028	−0.2545	0.0834	0.0111	0.0051	0.0097	0.0013
−0.542	0.734	0.016	0.027	−0.2034	0.0803	0.0085	0.0041	0.0074	0.0008
−0.458	0.736	0.016	0.026	−0.1403	0.0805	0.0059	0.0029	0.0051	0.0006
−0.375	0.595	0.023	0.040	−0.1308	0.1226	0.0106	0.0030	0.0101	0.0009
−0.292	0.784	0.018	0.022	−0.0585	0.1069	0.0033	0.0020	0.0027	0.0002
−0.208	0.764	0.017	0.024	−0.2442	0.1031	0.0091	0.0049	0.0076	0.0008
−0.125	0.743	0.017	0.026	−0.4329	0.1008	0.0173	0.0087	0.0150	0.0011
−0.042	0.801	0.013	0.020	−0.4735	0.0820	0.0151	0.0095	0.0117	0.0011
0.042	0.778	0.013	0.022	−0.5653	0.0817	0.0197	0.0113	0.0161	0.0010
0.125	0.782	0.012	0.022	−0.5233	0.0737	0.0181	0.0105	0.0146	0.0022
0.208	0.769	0.013	0.023	−0.3864	0.0764	0.0140	0.0077	0.0116	0.0006
0.292	0.809	0.011	0.019	−0.2584	0.0707	0.0080	0.0052	0.0061	0.0005
0.375	0.763	0.012	0.024	0.0607	0.0733	0.0029	0.0015	0.0024	0.0002
0.458	0.729	0.014	0.027	0.1599	0.0772	0.0068	0.0032	0.0060	0.0002
0.542	0.651	0.016	0.035	0.7361	0.0814	0.0422	0.0147	0.0394	0.0030
0.625	0.682	0.016	0.032	0.8055	0.0782	0.0409	0.0161	0.0376	0.0012
0.708	0.715	0.015	0.029	0.6776	0.0759	0.0304	0.0136	0.0271	0.0023
0.792	0.628	0.029	0.037	0.7250	0.1427	0.0453	0.0145	0.0429	0.0004

Table A.17: Energy bin $1246\,\mathrm{MeV} < E_\gamma < 1301\,\mathrm{MeV}$. Systematic uncertainty $\Delta E_\gamma = 6\,\mathrm{MeV}$.

$\cos\theta$	d	σ_d	Δd_{sys}	T	σ_T	ΔT_{sys}	$\Delta T^\Lambda_{\mathrm{sys}}$	$\Delta T^d_{\mathrm{sys}}$	$\Delta T^{bg}_{\mathrm{sys}}$
−0.958	0.924	0.012	0.008	0.3338	0.0899	0.0073	0.0067	0.0028	0.0014
−0.875	0.867	0.012	0.013	0.3082	0.0753	0.0079	0.0062	0.0047	0.0017
−0.792	0.788	0.014	0.021	0.0947	0.0714	0.0035	0.0020	0.0027	0.0008
−0.708	0.800	0.014	0.020	−0.1905	0.0701	0.0062	0.0038	0.0048	0.0013
−0.625	0.735	0.016	0.027	−0.1416	0.0744	0.0060	0.0029	0.0052	0.0008
−0.542	0.725	0.016	0.027	−0.1688	0.0808	0.0073	0.0034	0.0064	0.0009
−0.458	0.715	0.017	0.028	−0.0421	0.0843	0.0034	0.0015	0.0030	0.0003
−0.375	0.621	0.022	0.038	−0.0824	0.1155	0.0074	0.0023	0.0070	0.0006
−0.292	0.793	0.016	0.021	0.0792	0.0978	0.0034	0.0020	0.0027	0.0004
−0.208	0.790	0.015	0.021	−0.2359	0.0873	0.0079	0.0047	0.0063	0.0007
−0.125	0.764	0.015	0.024	−0.3659	0.0952	0.0136	0.0073	0.0113	0.0016
−0.042	0.805	0.013	0.020	−0.6249	0.0782	0.0197	0.0125	0.0152	0.0019
0.042	0.775	0.013	0.023	−0.6611	0.0764	0.0234	0.0132	0.0192	0.0013
0.125	0.750	0.013	0.025	−0.6655	0.0749	0.0260	0.0133	0.0222	0.0025
0.208	0.802	0.011	0.020	−0.5436	0.0687	0.0174	0.0109	0.0134	0.0021
0.292	0.772	0.013	0.023	−0.2649	0.0779	0.0095	0.0053	0.0078	0.0007
0.375	0.746	0.013	0.025	−0.2309	0.0749	0.0092	0.0046	0.0079	0.0012
0.458	0.769	0.013	0.023	0.2912	0.0746	0.0106	0.0058	0.0088	0.0013
0.542	0.658	0.017	0.034	0.6755	0.0853	0.0377	0.0135	0.0351	0.0022
0.625	0.705	0.016	0.029	0.7550	0.0765	0.0351	0.0151	0.0315	0.0032
0.708	0.734	0.014	0.027	0.7300	0.0676	0.0303	0.0146	0.0264	0.0020
0.792	0.751	0.018	0.025	0.6018	0.0887	0.0233	0.0120	0.0199	0.0002

Table A.18: Energy bin $1301\,\mathrm{MeV} < E_\gamma < 1353\,\mathrm{MeV}$. Systematic uncertainty $\Delta E_\gamma = 6\,\mathrm{MeV}$.

$\cos\theta$	d	σ_d	Δd_{sys}	T	σ_T	ΔT_{sys}	$\Delta T_{\mathrm{sys}}^{\Lambda}$	$\Delta T_{\mathrm{sys}}^{d}$	$\Delta T_{\mathrm{sys}}^{bg}$
-0.958	0.937	0.012	0.006	0.3369	0.0939	0.0072	0.0067	0.0023	0.0013
-0.875	0.874	0.014	0.013	0.3011	0.0788	0.0075	0.0060	0.0043	0.0010
-0.792	0.805	0.013	0.020	-0.0390	0.0661	0.0020	0.0012	0.0015	0.0003
-0.708	0.814	0.014	0.019	-0.0738	0.0665	0.0025	0.0017	0.0019	0.0004
-0.625	0.748	0.016	0.025	-0.0765	0.0744	0.0035	0.0018	0.0030	0.0007
-0.542	0.728	0.017	0.027	-0.2321	0.0821	0.0099	0.0046	0.0087	0.0010
-0.458	0.703	0.020	0.030	0.0543	0.0934	0.0041	0.0017	0.0037	0.0003
-0.375	0.648	0.023	0.035	0.1484	0.1108	0.0092	0.0032	0.0086	0.0006
-0.292	0.793	0.018	0.021	0.0580	0.1051	0.0032	0.0019	0.0025	0.0003
-0.208	0.776	0.017	0.022	-0.1762	0.0975	0.0063	0.0036	0.0052	0.0007
-0.125	0.770	0.015	0.023	-0.3515	0.0859	0.0127	0.0070	0.0105	0.0008
-0.042	0.798	0.013	0.020	-0.5151	0.0784	0.0167	0.0103	0.0131	0.0016
0.042	0.787	0.014	0.021	-0.7178	0.0770	0.0242	0.0144	0.0194	0.0014
0.125	0.804	0.013	0.020	-0.7255	0.0716	0.0229	0.0145	0.0177	0.0013
0.208	0.761	0.014	0.024	-0.5376	0.0805	0.0202	0.0108	0.0169	0.0025
0.292	0.780	0.014	0.022	-0.5482	0.0808	0.0190	0.0110	0.0154	0.0019
0.375	0.718	0.017	0.028	-0.0564	0.0952	0.0039	0.0018	0.0035	0.0002
0.458	0.715	0.019	0.028	0.2948	0.0996	0.0132	0.0059	0.0117	0.0011
0.542	0.651	0.019	0.035	0.6569	0.0915	0.0376	0.0131	0.0351	0.0029
0.625	0.666	0.018	0.033	0.8678	0.0861	0.0469	0.0174	0.0435	0.0021
0.708	0.737	0.013	0.026	0.6026	0.0646	0.0247	0.0121	0.0215	0.0015
0.792	0.757	0.015	0.024	0.4047	0.0737	0.0153	0.0081	0.0130	0.0010

Table A.19: Energy bin $1353\,\mathrm{MeV} < E_\gamma < 1403\,\mathrm{MeV}$. Systematic uncertainty $\Delta E_\gamma = 5\,\mathrm{MeV}$.

$\cos\theta$	d	σ_d	Δd_{sys}	T	σ_T	ΔT_{sys}	$\Delta T_{\mathrm{sys}}^{\Lambda}$	$\Delta T_{\mathrm{sys}}^{d}$	$\Delta T_{\mathrm{sys}}^{bg}$
-0.958	0.900	0.025	0.010	0.4575	0.1041	0.0105	0.0092	0.0051	0.0009
-0.875	0.889	0.016	0.011	0.2834	0.0871	0.0069	0.0057	0.0035	0.0017
-0.792	0.785	0.021	0.021	0.0235	0.0790	0.0022	0.0013	0.0018	0.0001
-0.708	0.759	0.025	0.024	-0.1776	0.0863	0.0068	0.0036	0.0057	0.0012
-0.625	0.759	0.026	0.024	-0.2281	0.0894	0.0086	0.0046	0.0072	0.0010
-0.542	0.614	0.037	0.039	-0.0039	0.1125	0.0059	0.0018	0.0056	0.0000
-0.458	0.701	0.028	0.030	0.0102	0.1061	0.0040	0.0017	0.0036	0.0001
-0.375	0.618	0.038	0.038	0.1538	0.1348	0.0111	0.0034	0.0105	0.0006
-0.292	0.804	0.025	0.020	0.2707	0.1157	0.0086	0.0054	0.0066	0.0009
-0.208	0.783	0.025	0.022	0.0500	0.1051	0.0032	0.0019	0.0026	0.0002
-0.125	0.785	0.023	0.022	-0.3222	0.0909	0.0109	0.0064	0.0088	0.0005
-0.042	0.812	0.018	0.019	-0.2620	0.0906	0.0080	0.0052	0.0061	0.0003
0.042	0.770	0.020	0.023	-0.6367	0.0864	0.0229	0.0127	0.0190	0.0012
0.125	0.798	0.021	0.020	-0.6928	0.0824	0.0224	0.0139	0.0175	0.0019
0.208	0.782	0.020	0.022	-0.7787	0.0874	0.0268	0.0156	0.0217	0.0014
0.292	0.780	0.022	0.022	-0.5187	0.1026	0.0182	0.0104	0.0146	0.0033
0.375	0.754	0.026	0.025	-0.2088	0.1212	0.0083	0.0043	0.0070	0.0013
0.458	0.700	0.033	0.030	0.5379	0.1364	0.0255	0.0108	0.0230	0.0019
0.542	0.673	0.030	0.033	0.8162	0.1130	0.0430	0.0163	0.0397	0.0031
0.625	0.710	0.025	0.029	0.8392	0.0994	0.0385	0.0168	0.0342	0.0049
0.708	0.716	0.020	0.028	0.5113	0.0714	0.0227	0.0102	0.0203	0.0016
0.792	0.794	0.018	0.021	0.3559	0.0661	0.0117	0.0071	0.0092	0.0000

Table A.20: Energy bin $1403\,\mathrm{MeV} < E_\gamma < 1465\,\mathrm{MeV}$. Systematic uncertainty $\Delta E_\gamma = 5\,\mathrm{MeV}$.

$\cos\theta$	d	σ_d	Δd_{sys}	T	σ_T	ΔT_{sys}	$\Delta T_{\mathrm{sys}}^{\Lambda}$	$\Delta T_{\mathrm{sys}}^{d}$	$\Delta T_{\mathrm{sys}}^{bg}$
-0.958	0.921	0.015	0.008	0.2549	0.0948	0.0081	0.0051	0.0022	0.0059
-0.875	0.884	0.015	0.012	0.1786	0.0782	0.0048	0.0036	0.0023	0.0021
-0.792	0.792	0.017	0.021	0.0261	0.0711	0.0082	0.0012	0.0016	0.0080
-0.708	0.805	0.016	0.020	-0.1477	0.0691	0.0081	0.0030	0.0036	0.0066
-0.625	0.688	0.021	0.031	-0.1364	0.0838	0.0094	0.0028	0.0063	0.0063
-0.542	0.680	0.022	0.032	0.0804	0.0896	0.0065	0.0020	0.0046	0.0041
-0.458	0.715	0.021	0.028	0.3101	0.0891	0.0148	0.0062	0.0124	0.0053
-0.375	0.622	0.026	0.038	0.4600	0.1141	0.0305	0.0092	0.0280	0.0078
-0.292	0.745	0.022	0.026	0.3580	0.1057	0.0148	0.0072	0.0123	0.0043
-0.208	0.790	0.017	0.021	0.1124	0.0878	0.0053	0.0024	0.0032	0.0035
-0.125	0.794	0.015	0.021	-0.2300	0.0802	0.0081	0.0046	0.0060	0.0029
-0.042	0.795	0.015	0.020	-0.3833	0.0774	0.0126	0.0077	0.0099	0.0018
0.042	0.785	0.015	0.021	-0.4611	0.0754	0.0157	0.0092	0.0126	0.0014
0.125	0.767	0.015	0.023	-0.5825	0.0763	0.0214	0.0117	0.0177	0.0025
0.208	0.764	0.018	0.024	-0.7389	0.0875	0.0272	0.0148	0.0228	0.0016
0.292	0.772	0.021	0.023	-0.6832	0.0971	0.0245	0.0137	0.0201	0.0029
0.375	0.684	0.026	0.032	0.0070	0.1293	0.0056	0.0021	0.0048	0.0021
0.458	0.644	0.033	0.036	0.7862	0.1455	0.0464	0.0157	0.0434	0.0049
0.542	0.568	0.032	0.043	0.9141	0.1417	0.0721	0.0183	0.0694	0.0067
0.625	0.685	0.023	0.031	0.5465	0.0943	0.0275	0.0109	0.0251	0.0021
0.708	0.713	0.014	0.029	0.2893	0.0596	0.0133	0.0058	0.0117	0.0026
0.792	0.770	0.012	0.023	0.1277	0.0534	0.0047	0.0026	0.0038	0.0010
0.875	0.221	0.079	0.078	-0.5765	0.7507	0.2707	0.0153	0.2701	0.0088

Appendix A Data Points

Table A.21: Energy bin $1465\,\mathrm{MeV} < E_\gamma < 1535\,\mathrm{MeV}$. Systematic uncertainty $\Delta E_\gamma = 5\,\mathrm{MeV}$.

$\cos\theta$	d	σ_d	Δd_{sys}	T	σ_T	ΔT_{sys}	$\Delta T^{\Lambda}_{\mathrm{sys}}$	$\Delta T^{d}_{\mathrm{sys}}$	$\Delta T^{bg}_{\mathrm{sys}}$
−0.958	0.911	0.031	0.009	0.3642	0.1305	0.0085	0.0073	0.0035	0.0026
−0.875	0.853	0.032	0.015	0.2667	0.1065	0.0134	0.0053	0.0046	0.0114
−0.792	0.764	0.027	0.024	0.1407	0.0935	0.0100	0.0029	0.0045	0.0085
−0.708	0.798	0.028	0.020	−0.1652	0.0965	0.0076	0.0034	0.0043	0.0053
−0.625	0.740	0.031	0.026	−0.1368	0.1112	0.0113	0.0030	0.0052	0.0096
−0.542	0.627	0.041	0.037	0.0372	0.1343	0.0101	0.0022	0.0066	0.0073
−0.458	0.817	0.025	0.018	0.2480	0.0989	0.0106	0.0050	0.0056	0.0075
−0.375	0.718	0.030	0.028	0.4017	0.1217	0.0180	0.0080	0.0158	0.0034
−0.292	0.807	0.029	0.019	0.1615	0.1132	0.0065	0.0034	0.0040	0.0038
−0.208	0.826	0.021	0.017	0.0618	0.0932	0.0047	0.0018	0.0019	0.0039
−0.125	0.728	0.029	0.027	−0.0172	0.1025	0.0045	0.0017	0.0031	0.0029
−0.042	0.784	0.024	0.022	−0.2792	0.0944	0.0099	0.0056	0.0077	0.0027
0.042	0.796	0.022	0.020	−0.1936	0.0918	0.0069	0.0039	0.0050	0.0027
0.125	0.731	0.029	0.027	−0.5840	0.1047	0.0246	0.0117	0.0215	0.0017
0.208	0.803	0.027	0.020	−0.5249	0.1105	0.0172	0.0105	0.0129	0.0043
0.292	0.762	0.042	0.024	−0.2736	0.1341	0.0105	0.0055	0.0086	0.0025
0.375	0.559	0.068	0.044	−0.6194	0.2160	0.0505	0.0124	0.0490	0.0019
0.458	0.511	0.069	0.049	1.0260	0.2817	0.1006	0.0205	0.0983	0.0068
0.542	0.521	0.070	0.048	0.8450	0.2331	0.0797	0.0169	0.0777	0.0058
0.625	0.636	0.039	0.036	0.2825	0.1327	0.0176	0.0057	0.0163	0.0034
0.708	0.677	0.027	0.032	−0.1600	0.0815	0.0085	0.0032	0.0077	0.0016
0.792	0.797	0.017	0.020	−0.0338	0.0623	0.0043	0.0011	0.0015	0.0039
0.875	0.345	0.082	0.066	0.0518	0.3965	0.0611	0.0064	0.0607	0.0033

Table A.22: Energy bin $1535\,\mathrm{MeV} < E_\gamma < 1601\,\mathrm{MeV}$. Systematic uncertainty $\Delta E_\gamma = 4\,\mathrm{MeV}$.

$\cos\theta$	d	σ_d	Δd_{sys}	T	σ_T	ΔT_{sys}	$\Delta T^{\Lambda}_{\mathrm{sys}}$	$\Delta T^{d}_{\mathrm{sys}}$	$\Delta T^{bg}_{\mathrm{sys}}$
−0.958	0.909	0.020	0.009	0.2921	0.1247	0.0076	0.0059	0.0029	0.0039
−0.875	0.834	0.022	0.017	0.0802	0.1087	0.0089	0.0022	0.0022	0.0084
−0.792	0.742	0.023	0.026	−0.0915	0.0962	0.0105	0.0022	0.0038	0.0095
−0.708	0.737	0.023	0.026	−0.2802	0.1026	0.0139	0.0056	0.0100	0.0079
−0.625	0.663	0.029	0.034	−0.1961	0.1249	0.0137	0.0040	0.0103	0.0081
−0.542	0.712	0.025	0.029	0.0280	0.1088	0.0056	0.0018	0.0036	0.0039
−0.458	0.709	0.025	0.029	0.4480	0.1075	0.0223	0.0090	0.0184	0.0089
−0.375	0.670	0.027	0.033	0.3128	0.1203	0.0175	0.0063	0.0154	0.0054
−0.292	0.785	0.021	0.021	0.1368	0.1048	0.0060	0.0029	0.0040	0.0034
−0.208	0.795	0.017	0.020	0.1263	0.0898	0.0066	0.0027	0.0034	0.0050
−0.125	0.777	0.016	0.022	−0.0690	0.0855	0.0034	0.0018	0.0026	0.0013
−0.042	0.800	0.015	0.020	−0.1134	0.0811	0.0050	0.0024	0.0030	0.0032
0.042	0.740	0.017	0.026	−0.1796	0.0930	0.0077	0.0036	0.0064	0.0022
0.125	0.761	0.018	0.024	−0.4653	0.0919	0.0175	0.0093	0.0146	0.0027
0.208	0.799	0.020	0.020	−0.2668	0.1057	0.0087	0.0053	0.0067	0.0015
0.292	0.704	0.030	0.030	−0.3506	0.1507	0.0166	0.0070	0.0148	0.0027
0.375	0.572	0.041	0.043	0.1697	0.1990	0.0172	0.0043	0.0160	0.0049
0.458	0.475	0.058	0.052	0.7734	0.3210	0.0873	0.0155	0.0856	0.0068
0.542	0.469	0.044	0.053	0.4375	0.2261	0.0516	0.0088	0.0500	0.0090
0.625	0.543	0.029	0.046	0.1264	0.1364	0.0139	0.0030	0.0129	0.0044
0.708	0.688	0.016	0.031	−0.2382	0.0708	0.0120	0.0048	0.0108	0.0024
0.792	0.729	0.014	0.027	−0.0506	0.0601	0.0034	0.0013	0.0024	0.0021
0.875	0.350	0.049	0.065	−0.1820	0.3105	0.0541	0.0058	0.0537	0.0028

Table A.23: Energy bin $1601\,\mathrm{MeV} < E_\gamma < 1700\,\mathrm{MeV}$. Systematic uncertainty $\Delta E_\gamma = 4\,\mathrm{MeV}$.

$\cos\theta$	d	σ_d	Δd_{sys}	T	σ_T	ΔT_{sys}	$\Delta T^{\Lambda}_{\mathrm{sys}}$	$\Delta T^{d}_{\mathrm{sys}}$	$\Delta T^{bg}_{\mathrm{sys}}$
−0.958	0.944	0.019	0.006	0.4553	0.1446	0.0125	0.0091	0.0027	0.0082
−0.875	0.888	0.026	0.011	0.0872	0.1257	0.0045	0.0025	0.0016	0.0034
−0.792	0.674	0.049	0.033	−0.1173	0.1339	0.0125	0.0029	0.0070	0.0099
−0.708	0.719	0.040	0.028	−0.3561	0.1192	0.0160	0.0071	0.0139	0.0034
−0.625	0.713	0.030	0.029	−0.1381	0.1301	0.0139	0.0031	0.0063	0.0119
−0.542	0.669	0.043	0.033	0.1342	0.1383	0.0110	0.0032	0.0078	0.0071
−0.458	0.615	0.039	0.038	0.4134	0.1287	0.0280	0.0083	0.0259	0.0070
−0.375	0.653	0.034	0.035	0.5518	0.1117	0.0320	0.0110	0.0293	0.0067
−0.292	0.711	0.039	0.029	0.5584	0.1238	0.0255	0.0112	0.0227	0.0030
−0.208	0.795	0.020	0.021	0.2012	0.0883	0.0066	0.0040	0.0052	0.0003
−0.125	0.756	0.024	0.024	0.1762	0.0916	0.0074	0.0036	0.0057	0.0030
−0.042	0.791	0.019	0.021	−0.0018	0.0828	0.0028	0.0013	0.0017	0.0017
0.042	0.759	0.022	0.024	−0.1461	0.0928	0.0061	0.0030	0.0048	0.0022
0.125	0.732	0.030	0.027	−0.1333	0.1112	0.0063	0.0029	0.0053	0.0018
0.208	0.776	0.019	0.022	−0.1681	0.1085	0.0065	0.0035	0.0050	0.0023
0.292	0.631	0.058	0.037	0.2338	0.1721	0.0183	0.0050	0.0145	0.0100
0.375	0.510	0.066	0.049	0.2082	0.2509	0.0280	0.0053	0.0255	0.0103
0.458	0.431	0.098	0.057	1.3990	0.4446	0.1893	0.0280	0.1848	0.0304
0.542	0.527	0.063	0.047	0.2079	0.2200	0.0292	0.0050	0.0223	0.0182
0.625	0.655	0.035	0.035	−0.4995	0.1226	0.0289	0.0100	0.0264	0.0063
0.708	0.670	0.024	0.033	−0.4191	0.0764	0.0226	0.0084	0.0206	0.0040
0.792	0.702	0.020	0.030	−0.3997	0.0641	0.0190	0.0080	0.0169	0.0034
0.875	0.448	0.057	0.055	−0.6189	0.2260	0.0777	0.0124	0.0762	0.0087

Table A.24: Energy bin $1700\,\mathrm{MeV} < E_\gamma < 1799\,\mathrm{MeV}$. Systematic uncertainty $\Delta E_\gamma = 4\,\mathrm{MeV}$.

$\cos\theta$	d	σ_d	Δd_{sys}	T	σ_T	ΔT_{sys}	$\Delta T_{\mathrm{sys}}^{\Lambda}$	$\Delta T_{\mathrm{sys}}^{d}$	$\Delta T_{\mathrm{sys}}^{bg}$
-0.958	0.848	0.042	0.015	0.2385	0.2116	0.0123	0.0053	0.0048	0.0100
-0.875	0.800	0.038	0.020	0.0059	0.1729	0.0080	0.0028	0.0035	0.0067
-0.792	0.737	0.035	0.026	-0.3686	0.1591	0.0186	0.0074	0.0132	0.0109
-0.708	0.690	0.031	0.031	-0.4320	0.1342	0.0283	0.0086	0.0194	0.0186
-0.625	0.665	0.035	0.033	0.0015	0.1527	0.0120	0.0024	0.0061	0.0100
-0.542	0.600	0.033	0.040	0.1876	0.1533	0.0188	0.0041	0.0136	0.0124
-0.458	0.673	0.032	0.033	0.2715	0.1466	0.0151	0.0055	0.0133	0.0044
-0.375	0.628	0.031	0.037	0.6162	0.1416	0.0388	0.0123	0.0366	0.0035
-0.292	0.679	0.026	0.032	0.3560	0.1234	0.0196	0.0071	0.0168	0.0072
-0.208	0.783	0.019	0.022	0.2135	0.1073	0.0089	0.0043	0.0060	0.0050
-0.125	0.739	0.020	0.026	0.0356	0.1084	0.0049	0.0018	0.0032	0.0033
-0.042	0.764	0.018	0.024	-0.1110	0.1010	0.0053	0.0025	0.0039	0.0027
0.042	0.739	0.019	0.026	-0.0908	0.0997	0.0051	0.0022	0.0039	0.0023
0.125	0.732	0.022	0.027	-0.2289	0.1135	0.0100	0.0046	0.0085	0.0027
0.208	0.721	0.028	0.028	-0.2810	0.1542	0.0134	0.0057	0.0111	0.0050
0.292	0.596	0.036	0.040	-0.3069	0.1907	0.0238	0.0063	0.0214	0.0083
0.375	0.551	0.055	0.045	0.1545	0.2810	0.0254	0.0051	0.0210	0.0135
0.458	0.571	0.060	0.043	-0.0283	0.2991	0.0273	0.0048	0.0180	0.0199
0.542	0.580	0.044	0.042	-0.4225	0.2005	0.0364	0.0085	0.0307	0.0176
0.625	0.547	0.030	0.045	-0.4142	0.1420	0.0366	0.0083	0.0344	0.0095
0.708	0.628	0.020	0.037	-0.5332	0.0921	0.0335	0.0107	0.0316	0.0034
0.792	0.617	0.018	0.038	-0.3717	0.0764	0.0244	0.0074	0.0230	0.0034
0.875	0.533	0.030	0.047	-0.2659	0.1464	0.0243	0.0054	0.0237	0.0006

Table A.25: Energy bin $1799\,\mathrm{MeV} < E_\gamma < 1897\,\mathrm{MeV}$. Systematic uncertainty $\Delta E_\gamma = 3\,\mathrm{MeV}$.

$\cos\theta$	d	σ_d	Δd_{sys}	T	σ_T	ΔT_{sys}	$\Delta T_{\mathrm{sys}}^{\Lambda}$	$\Delta T_{\mathrm{sys}}^{d}$	$\Delta T_{\mathrm{sys}}^{bg}$
-0.958	0.706	0.071	0.029	0.8673	0.3300	0.0415	0.0174	0.0361	0.0109
-0.875	0.744	0.058	0.026	-0.2479	0.2804	0.0235	0.0061	0.0105	0.0201
-0.792	0.794	0.040	0.021	-0.4872	0.1796	0.0188	0.0098	0.0126	0.0099
-0.708	0.561	0.046	0.044	-0.5230	0.2109	0.0440	0.0105	0.0411	0.0119
-0.625	0.638	0.041	0.036	-0.2851	0.1745	0.0184	0.0059	0.0166	0.0054
-0.542	0.627	0.038	0.037	0.2457	0.1619	0.0186	0.0051	0.0152	0.0095
-0.458	0.763	0.029	0.024	0.6863	0.1231	0.0260	0.0137	0.0213	0.0056
-0.375	0.679	0.032	0.032	0.4229	0.1392	0.0223	0.0085	0.0200	0.0051
-0.292	0.638	0.033	0.036	0.4046	0.1560	0.0248	0.0081	0.0229	0.0050
-0.208	0.809	0.021	0.019	0.2534	0.1160	0.0089	0.0051	0.0060	0.0042
-0.125	0.761	0.022	0.024	0.0041	0.1217	0.0064	0.0019	0.0030	0.0053
-0.042	0.737	0.022	0.026	-0.1196	0.1201	0.0063	0.0028	0.0050	0.0026
0.042	0.771	0.020	0.023	-0.1341	0.1124	0.0053	0.0029	0.0044	0.0005
0.125	0.727	0.025	0.027	-0.1924	0.1360	0.0088	0.0040	0.0076	0.0020
0.208	0.687	0.031	0.031	-0.0989	0.1638	0.0082	0.0031	0.0070	0.0030
0.292	0.484	0.049	0.052	0.3010	0.2797	0.0375	0.0068	0.0364	0.0058
0.375	0.534	0.058	0.047	0.3790	0.2929	0.0394	0.0081	0.0355	0.0151
0.542	0.602	0.046	0.040	-0.0694	0.2138	0.0198	0.0036	0.0118	0.0155
0.625	0.563	0.031	0.044	-0.5578	0.1436	0.0456	0.0112	0.0432	0.0091
0.708	0.630	0.021	0.037	-0.7337	0.0949	0.0462	0.0147	0.0431	0.0076
0.792	0.604	0.018	0.040	-0.4844	0.0820	0.0332	0.0097	0.0317	0.0011
0.875	0.589	0.027	0.041	-0.1312	0.1216	0.0111	0.0030	0.0104	0.0026

Table A.26: Energy bin $1897\,\mathrm{MeV} < E_\gamma < 1995\,\mathrm{MeV}$. Systematic uncertainty $\Delta E_\gamma = 3\,\mathrm{MeV}$.

$\cos\theta$	d	σ_d	Δd_{sys}	T	σ_T	ΔT_{sys}	$\Delta T_{\mathrm{sys}}^{\Lambda}$	$\Delta T_{\mathrm{sys}}^{d}$	$\Delta T_{\mathrm{sys}}^{bg}$
-0.958	0.850	0.093	0.015	0.6245	0.4090	0.0198	0.0129	0.0114	0.0097
-0.875	0.747	0.084	0.025	0.1704	0.3484	0.0179	0.0062	0.0105	0.0131
-0.792	0.764	0.076	0.024	-0.9743	0.2712	0.0379	0.0195	0.0300	0.0124
-0.708	0.566	0.081	0.043	-0.2190	0.3273	0.0282	0.0064	0.0244	0.0127
-0.625	0.587	0.071	0.041	-0.7875	0.2841	0.0592	0.0158	0.0554	0.0137
-0.542	0.623	0.057	0.038	0.0346	0.2402	0.0220	0.0039	0.0117	0.0182
-0.458	0.619	0.052	0.038	0.6131	0.2093	0.0400	0.0123	0.0377	0.0053
-0.375	0.662	0.042	0.034	0.5766	0.1760	0.0330	0.0115	0.0295	0.0093
-0.292	0.651	0.040	0.035	0.2453	0.1628	0.0150	0.0051	0.0137	0.0037
-0.208	0.773	0.033	0.023	-0.1466	0.1546	0.0094	0.0035	0.0052	0.0071
-0.125	0.731	0.033	0.027	0.0195	0.1451	0.0061	0.0023	0.0043	0.0036
-0.042	0.719	0.030	0.028	-0.0798	0.1479	0.0097	0.0027	0.0053	0.0077
0.042	0.727	0.030	0.027	0.0724	0.1505	0.0059	0.0027	0.0050	0.0014
0.125	0.693	0.036	0.031	-0.3967	0.1600	0.0195	0.0079	0.0176	0.0027
0.208	0.674	0.043	0.033	0.2782	0.1886	0.0153	0.0058	0.0140	0.0019
0.292	0.611	0.051	0.039	-0.0329	0.2309	0.0182	0.0037	0.0118	0.0133
0.375	0.458	0.073	0.054	-0.1838	0.3764	0.0415	0.0067	0.0397	0.0102
0.458	0.690	0.062	0.031	-0.2775	0.2915	0.0297	0.0066	0.0149	0.0248
0.542	0.475	0.064	0.053	-0.5717	0.3024	0.0659	0.0116	0.0641	0.0103
0.625	0.532	0.041	0.047	-0.7830	0.1789	0.0711	0.0157	0.0688	0.0083
0.708	0.668	0.028	0.033	-0.7820	0.1052	0.0426	0.0156	0.0389	0.0079
0.792	0.574	0.026	0.043	-0.4191	0.1046	0.0324	0.0084	0.0312	0.0025
0.875	0.624	0.030	0.038	-0.0390	0.1225	0.0066	0.0021	0.0062	0.0013

Appendix A Data Points

Table A.27: Energy bin $1995\,\mathrm{MeV} < E_\gamma < 2201\,\mathrm{MeV}$. Systematic uncertainty $\Delta E_\gamma = 3\,\mathrm{MeV}$.

$\cos\theta$	d	σ_d	Δd_{sys}	T	σ_T	ΔT_{sys}	$\Delta T^{\Lambda}_{\mathrm{sys}}$	$\Delta T^{d}_{\mathrm{sys}}$	$\Delta T^{bg}_{\mathrm{sys}}$
−0.958	0.725	0.072	0.027	0.6753	0.3220	0.0339	0.0136	0.0257	0.0174
−0.875	0.645	0.078	0.035	−0.3929	0.3197	0.0308	0.0085	0.0234	0.0181
−0.792	0.622	0.095	0.038	−0.2034	0.4589	0.0352	0.0080	0.0244	0.0241
−0.708	0.568	0.082	0.043	−0.6247	0.3254	0.0565	0.0126	0.0481	0.0268
−0.625	0.579	0.057	0.042	−0.8643	0.2483	0.0659	0.0173	0.0629	0.0090
−0.542	0.598	0.048	0.040	−0.1649	0.2088	0.0164	0.0043	0.0145	0.0063
−0.458	0.702	0.035	0.030	0.1188	0.1565	0.0102	0.0032	0.0068	0.0069
−0.375	0.598	0.038	0.040	0.1735	0.1696	0.0166	0.0040	0.0135	0.0089
−0.292	0.563	0.036	0.044	0.4996	0.1632	0.0402	0.0100	0.0388	0.0027
−0.208	0.749	0.026	0.025	0.3947	0.1253	0.0169	0.0079	0.0132	0.0070
−0.125	0.738	0.023	0.026	0.0174	0.1194	0.0056	0.0019	0.0034	0.0040
−0.042	0.740	0.022	0.026	−0.3867	0.1089	0.0158	0.0077	0.0136	0.0025
0.042	0.744	0.022	0.026	−0.2806	0.1119	0.0126	0.0056	0.0097	0.0059
0.125	0.723	0.024	0.028	−0.2252	0.1237	0.0123	0.0046	0.0087	0.0074
0.208	0.739	0.027	0.026	−0.1148	0.1314	0.0074	0.0029	0.0050	0.0046
0.292	0.605	0.034	0.040	−0.0465	0.1688	0.0122	0.0028	0.0091	0.0075
0.375	0.593	0.042	0.041	−0.2033	0.1860	0.0217	0.0046	0.0158	0.0142
0.458	0.554	0.056	0.045	−0.1006	0.2700	0.0436	0.0046	0.0185	0.0392
0.542	0.550	0.040	0.045	−0.6663	0.1837	0.0577	0.0133	0.0544	0.0139
0.625	0.534	0.029	0.047	−0.6951	0.1301	0.0627	0.0139	0.0606	0.0085
0.708	0.608	0.021	0.039	−0.4695	0.0900	0.0338	0.0094	0.0302	0.0119
0.792	0.562	0.019	0.044	−0.2919	0.0823	0.0239	0.0058	0.0227	0.0044
0.875	0.652	0.019	0.035	−0.0052	0.0836	0.0048	0.0013	0.0036	0.0028

Table A.28: Energy bin $2201\,\mathrm{MeV} < E_\gamma < 2405\,\mathrm{MeV}$. Systematic uncertainty $\Delta E_\gamma = 2\,\mathrm{MeV}$.

$\cos\theta$	d	σ_d	Δd_{sys}	T	σ_T	ΔT_{sys}	$\Delta T^{\Lambda}_{\mathrm{sys}}$	$\Delta T^{d}_{\mathrm{sys}}$	$\Delta T^{bg}_{\mathrm{sys}}$
−0.958	0.888	0.048	0.011	0.4795	0.2442	0.0180	0.0097	0.0061	0.0139
−0.875	0.738	0.069	0.026	−0.4685	0.3157	0.0264	0.0098	0.0173	0.0175
−0.708	0.601	0.109	0.040	0.3508	0.3905	0.0311	0.0086	0.0285	0.0089
−0.625	0.553	0.093	0.045	−1.1763	0.4040	0.0980	0.0235	0.0950	0.0060
−0.542	0.485	0.078	0.051	−0.7641	0.3865	0.0849	0.0154	0.0818	0.0168
−0.458	0.634	0.062	0.037	0.0526	0.2558	0.0147	0.0042	0.0120	0.0072
−0.375	0.695	0.046	0.030	−0.1758	0.2007	0.0114	0.0044	0.0095	0.0045
−0.292	0.625	0.052	0.037	0.0932	0.2238	0.0256	0.0039	0.0116	0.0224
−0.208	0.759	0.039	0.024	0.2057	0.1881	0.0097	0.0046	0.0074	0.0043
−0.125	0.780	0.030	0.022	0.2367	0.1683	0.0113	0.0050	0.0070	0.0073
−0.042	0.749	0.032	0.025	0.0787	0.1669	0.0098	0.0030	0.0049	0.0079
0.042	0.735	0.033	0.026	−0.3001	0.1680	0.0133	0.0061	0.0110	0.0042
0.125	0.738	0.034	0.026	−0.2710	0.1876	0.0123	0.0057	0.0101	0.0044
0.208	0.609	0.045	0.039	−0.1411	0.2229	0.0144	0.0042	0.0136	0.0022
0.292	0.574	0.041	0.043	0.3553	0.2042	0.0334	0.0072	0.0268	0.0184
0.375	0.541	0.059	0.046	0.7514	0.2715	0.0688	0.0150	0.0638	0.0208
0.458	0.736	0.049	0.026	−0.2544	0.2315	0.0214	0.0057	0.0103	0.0178
0.542	0.490	0.045	0.051	−0.7026	0.2146	0.0763	0.0141	0.0731	0.0166
0.625	0.614	0.033	0.039	−0.5423	0.1374	0.0389	0.0108	0.0342	0.0152
0.708	0.509	0.033	0.049	−0.5832	0.1497	0.0595	0.0117	0.0563	0.0150
0.792	0.522	0.024	0.048	−0.2245	0.1094	0.0221	0.0045	0.0207	0.0062
0.875	0.628	0.022	0.037	0.0290	0.0985	0.0060	0.0016	0.0049	0.0031

Table A.29: Energy bin $2405\,\mathrm{MeV} < E_\gamma < 2607\,\mathrm{MeV}$. Systematic uncertainty $\Delta E_\gamma = 5\,\mathrm{MeV}$.

$\cos\theta$	d	σ_d	Δd_{sys}	T	σ_T	ΔT_{sys}	$\Delta T^{\Lambda}_{\mathrm{sys}}$	$\Delta T^{d}_{\mathrm{sys}}$	$\Delta T^{bg}_{\mathrm{sys}}$
−0.958	0.651	0.074	0.035	0.2496	0.3029	0.0263	0.0064	0.0171	0.0189
−0.875	0.692	0.064	0.031	−0.3954	0.2825	0.0226	0.0083	0.0186	0.0099
−0.792	0.796	0.086	0.020	−0.8999	0.3018	0.0361	0.0180	0.0231	0.0212
−0.542	0.613	0.100	0.039	−0.1380	0.4262	0.0248	0.0072	0.0226	0.0074
−0.458	0.636	0.072	0.036	−0.6015	0.3197	0.0381	0.0122	0.0349	0.0091
−0.375	0.641	0.072	0.036	−0.7570	0.2932	0.0453	0.0152	0.0424	0.0047
−0.292	0.684	0.065	0.032	−0.1552	0.2702	0.0158	0.0050	0.0116	0.0096
−0.208	0.585	0.084	0.041	−0.3579	0.3989	0.0334	0.0088	0.0311	0.0084
−0.125	0.659	0.066	0.034	−0.4116	0.3022	0.0250	0.0087	0.0225	0.0065
−0.042	0.706	0.054	0.029	−0.5745	0.2607	0.0267	0.0115	0.0241	0.0000
0.042	0.779	0.051	0.022	−0.5004	0.2549	0.0186	0.0101	0.0144	0.0060
0.125	0.699	0.052	0.030	−0.1839	0.2449	0.0121	0.0050	0.0107	0.0026
0.208	0.697	0.050	0.030	0.5047	0.2188	0.0256	0.0101	0.0220	0.0081
0.292	0.653	0.044	0.035	0.0914	0.1822	0.0191	0.0033	0.0087	0.0167
0.375	0.416	0.095	0.058	0.1695	0.4531	0.0719	0.0077	0.0542	0.0466
0.458	0.763	0.045	0.024	0.0426	0.2069	0.0259	0.0034	0.0052	0.0251
0.542	0.606	0.040	0.039	−0.3213	0.1740	0.0240	0.0065	0.0212	0.0094
0.625	0.639	0.038	0.036	−0.6103	0.1640	0.0420	0.0122	0.0344	0.0207
0.708	0.461	0.048	0.054	−1.0163	0.2547	0.1210	0.0203	0.1188	0.0116
0.792	0.531	0.029	0.047	−0.3533	0.1274	0.0325	0.0071	0.0312	0.0057
0.875	0.562	0.027	0.044	−0.0125	0.1217	0.0081	0.0020	0.0076	0.0019

Table A.30: Energy bin $2607\,\mathrm{MeV} < E_\gamma < 3004\,\mathrm{MeV}$. Systematic uncertainty $\Delta E_\gamma = 15\,\mathrm{MeV}$.

$\cos\theta$	d	σ_d	Δd_{sys}	T	σ_T	ΔT_{sys}	$\Delta T_{\mathrm{sys}}^{\Lambda}$	$\Delta T_{\mathrm{sys}}^{d}$	$\Delta T_{\mathrm{sys}}^{bg}$
−0.958	0.747	0.055	0.025	−0.2805	0.2288	0.0138	0.0061	0.0103	0.0069
−0.875	0.719	0.052	0.028	−0.2602	0.2120	0.0196	0.0057	0.0110	0.0152
−0.625	0.608	0.080	0.039	−0.2543	0.2879	0.0220	0.0063	0.0202	0.0058
−0.542	0.710	0.065	0.029	0.3174	0.2983	0.0173	0.0072	0.0147	0.0053
−0.458	0.673	0.072	0.033	−0.5075	0.2788	0.0302	0.0103	0.0250	0.0136
−0.375	0.423	0.126	0.058	−1.1203	0.5669	0.1559	0.0226	0.1541	0.0069
−0.292	0.571	0.098	0.043	−0.0043	0.4052	0.0277	0.0065	0.0243	0.0115
−0.125	0.666	0.090	0.033	−0.5437	0.4230	0.0358	0.0117	0.0292	0.0170
0.208	0.715	0.054	0.028	0.0461	0.2493	0.0139	0.0040	0.0081	0.0106
0.292	0.584	0.069	0.042	−0.0019	0.2581	0.0465	0.0041	0.0147	0.0439
0.458	0.668	0.067	0.033	−0.1200	0.2450	0.0568	0.0044	0.0109	0.0556
0.542	0.440	0.055	0.056	−0.4416	0.2436	0.0703	0.0090	0.0571	0.0399
0.625	0.610	0.039	0.039	−0.6750	0.1700	0.0523	0.0135	0.0431	0.0263
0.708	0.358	0.061	0.064	−1.1152	0.3546	0.2091	0.0223	0.1997	0.0580
0.792	0.438	0.035	0.056	−0.4112	0.1574	0.0541	0.0082	0.0529	0.0077
0.875	0.612	0.024	0.039	−0.1425	0.0958	0.0103	0.0030	0.0094	0.0030

A.2 Reaction $\gamma p \rightarrow p\eta$

Table A.31: Energy bin $700\,\mathrm{MeV} < E_\gamma < 750\,\mathrm{MeV}$. Systematic uncertainty $\Delta E_\gamma = 9\,\mathrm{MeV}$.

$\cos\theta$	d	σ_d	Δd_{sys}	T	σ_T	ΔT_{sys}	$\Delta T_{\mathrm{sys}}^{\Lambda}$	$\Delta T_{\mathrm{sys}}^{d}$	$\Delta T_{\mathrm{sys}}^{bg}$
−0.917	0.956	0.016	0.004	0.0909	0.0645	0.0108	0.0019	0.0004	0.0106
−0.750	0.917	0.020	0.008	−0.0052	0.0619	0.0063	0.0010	0.0004	0.0062
−0.583	0.887	0.022	0.011	0.0691	0.0621	0.0036	0.0015	0.0010	0.0030
−0.417	0.894	0.018	0.011	0.1509	0.0588	0.0041	0.0030	0.0018	0.0022
−0.250	0.913	0.018	0.009	0.1988	0.0545	0.0047	0.0040	0.0019	0.0017
−0.083	0.921	0.018	0.008	0.0590	0.0568	0.0022	0.0014	0.0006	0.0016
0.083	0.972	0.014	0.003	0.0218	0.0545	0.0017	0.0009	0.0001	0.0014
0.250	0.969	0.016	0.003	0.1172	0.0630	0.0027	0.0024	0.0004	0.0013
0.417	0.947	0.030	0.005	0.1871	0.0761	0.0042	0.0037	0.0010	0.0015
0.583	0.944	0.051	0.006	0.2960	0.1124	0.0132	0.0059	0.0018	0.0116
0.750	0.908	0.073	0.009	−0.2418	0.1636	0.2346	0.0050	0.0026	0.2346

$\cos\theta$	P	σ_P	ΔP_{sys}	$\Delta P_{\mathrm{sys}}^{\delta}$	$\Delta P_{\mathrm{sys}}^{\Lambda}$	$\Delta P_{\mathrm{sys}}^{d}$	$\Delta P_{\mathrm{sys}}^{bg}$	H	σ_H	ΔH_{sys}	$\Delta H_{\mathrm{sys}}^{\delta}$	$\Delta H_{\mathrm{sys}}^{\Lambda}$	$\Delta H_{\mathrm{sys}}^{d}$	$\Delta H_{\mathrm{sys}}^{bg}$
−0.917	0.0791	0.1498	0.0123	0.0054	0.0027	0.0006	0.0106	−0.0898	0.1499	0.0124	0.0056	0.0028	0.0006	0.0106
−0.750	0.0814	0.1475	0.0087	0.0054	0.0027	0.0012	0.0062	−0.0765	0.1388	0.0085	0.0051	0.0025	0.0012	0.0062
−0.583	−0.0604	0.1476	0.0067	0.0051	0.0025	0.0016	0.0030	0.1356	0.1420	0.0081	0.0065	0.0032	0.0020	0.0030
−0.417	0.1087	0.1428	0.0071	0.0058	0.0029	0.0017	0.0022	−0.1820	0.1352	0.0092	0.0077	0.0039	0.0023	0.0022
−0.250	−0.1193	0.1349	0.0070	0.0059	0.0029	0.0014	0.0017	−0.2297	0.1315	0.0108	0.0094	0.0047	0.0022	0.0017
−0.083	0.2107	0.1350	0.0100	0.0087	0.0044	0.0019	0.0016	−0.1167	0.1390	0.0069	0.0059	0.0030	0.0013	0.0016
0.083	−0.1783	0.1401	0.0087	0.0077	0.0038	0.0005	0.0014	−0.1864	0.1372	0.0090	0.0079	0.0039	0.0006	0.0014
0.250	0.0777	0.1520	0.0063	0.0055	0.0027	0.0004	0.0013	−0.2704	0.1529	0.0124	0.0110	0.0055	0.0009	0.0013
0.417	0.2383	0.1887	0.0117	0.0103	0.0051	0.0014	0.0015	−0.4093	0.1797	0.0186	0.0164	0.0082	0.0023	0.0015
0.583	0.1568	0.2742	0.0163	0.0101	0.0051	0.0015	0.0116	−0.0702	0.2497	0.0149	0.0083	0.0041	0.0012	0.0116
0.750	−0.1082	0.4310	0.2351	0.0142	0.0071	0.0036	0.2346	−0.3315	0.3635	0.2353	0.0161	0.0081	0.0041	0.2346

Table A.32: Energy bin $750\,\mathrm{MeV} < E_\gamma < 781\,\mathrm{MeV}$. Systematic uncertainty $\Delta E_\gamma = 9\,\mathrm{MeV}$.

$\cos\theta$	d	σ_d	Δd_{sys}	T	σ_T	ΔT_{sys}	$\Delta T_{\mathrm{sys}}^{\Lambda}$	$\Delta T_{\mathrm{sys}}^{d}$	$\Delta T_{\mathrm{sys}}^{bg}$
−0.917	0.941	0.013	0.006	0.0610	0.0560	0.0071	0.0014	0.0004	0.0070
−0.750	0.912	0.013	0.009	0.0542	0.0515	0.0049	0.0012	0.0006	0.0047
−0.583	0.916	0.011	0.008	0.0975	0.0408	0.0035	0.0020	0.0009	0.0027
−0.417	0.901	0.011	0.010	0.0972	0.0374	0.0034	0.0019	0.0011	0.0026
−0.250	0.920	0.010	0.008	0.1827	0.0372	0.0045	0.0037	0.0016	0.0020
−0.083	0.914	0.011	0.009	0.1301	0.0380	0.0032	0.0026	0.0012	0.0015
0.083	0.941	0.009	0.006	0.1573	0.0384	0.0035	0.0031	0.0010	0.0013
0.250	0.925	0.013	0.007	0.1522	0.0454	0.0036	0.0030	0.0012	0.0015
0.417	0.925	0.018	0.007	0.1781	0.0565	0.0040	0.0036	0.0014	0.0013
0.583	0.824	0.045	0.018	0.0272	0.0991	0.0056	0.0016	0.0017	0.0051

$\cos\theta$	P	σ_P	ΔP_{sys}	$\Delta P_{\mathrm{sys}}^{\delta}$	$\Delta P_{\mathrm{sys}}^{\Lambda}$	$\Delta P_{\mathrm{sys}}^{d}$	$\Delta P_{\mathrm{sys}}^{bg}$	H	σ_H	ΔH_{sys}	$\Delta H_{\mathrm{sys}}^{\delta}$	$\Delta H_{\mathrm{sys}}^{\Lambda}$	$\Delta H_{\mathrm{sys}}^{d}$	$\Delta H_{\mathrm{sys}}^{bg}$
−0.917	−0.1111	0.1252	0.0093	0.0055	0.0027	0.0009	0.0070	−0.0763	0.1128	0.0086	0.0044	0.0022	0.0007	0.0070
−0.750	−0.0620	0.1160	0.0068	0.0042	0.0021	0.0010	0.0047	0.0274	0.1113	0.0063	0.0037	0.0018	0.0009	0.0047
−0.583	0.2096	0.0936	0.0100	0.0084	0.0042	0.0019	0.0027	−0.0941	0.0912	0.0056	0.0043	0.0022	0.0010	0.0027
−0.417	0.0573	0.0866	0.0047	0.0033	0.0017	0.0009	0.0026	−0.2425	0.0861	0.0115	0.0097	0.0049	0.0027	0.0026
−0.250	0.1381	0.0852	0.0068	0.0057	0.0028	0.0012	0.0020	−0.0951	0.0852	0.0052	0.0043	0.0021	0.0009	0.0020
−0.083	0.1308	0.0883	0.0064	0.0054	0.0027	0.0013	0.0015	−0.2750	0.0869	0.0127	0.0110	0.0055	0.0026	0.0015
0.083	0.1669	0.0890	0.0077	0.0068	0.0034	0.0011	0.0013	−0.0167	0.0888	0.0035	0.0029	0.0014	0.0004	0.0013
0.250	0.1218	0.1037	0.0063	0.0054	0.0027	0.0011	0.0015	−0.1599	0.1076	0.0077	0.0067	0.0033	0.0013	0.0015
0.417	0.1794	0.1319	0.0087	0.0076	0.0038	0.0015	0.0013	0.0313	0.1251	0.0048	0.0041	0.0021	0.0008	0.0013
0.583	0.0616	0.2323	0.0108	0.0077	0.0038	0.0041	0.0051	−0.2397	0.2142	0.0142	0.0107	0.0054	0.0057	0.0051

Appendix A Data Points

Table A.33: Energy bin $781\,\mathrm{MeV} < E_\gamma < 816\,\mathrm{MeV}$. Systematic uncertainty $\Delta E_\gamma = 9\,\mathrm{MeV}$.

$\cos\theta$	d	σ_d	Δd_{sys}	T	σ_T	ΔT_{sys}	$\Delta T_{\mathrm{sys}}^{\Lambda}$	$\Delta T_{\mathrm{sys}}^{d}$	$\Delta T_{\mathrm{sys}}^{bg}$
−0.917	0.919	0.013	0.008	0.0875	0.0512	0.0078	0.0018	0.0008	0.0075
−0.750	0.882	0.013	0.012	0.1570	0.0429	0.0056	0.0031	0.0021	0.0041
−0.583	0.880	0.012	0.012	0.1924	0.0356	0.0058	0.0038	0.0026	0.0034
−0.417	0.862	0.012	0.014	0.1744	0.0348	0.0050	0.0035	0.0028	0.0023
−0.250	0.871	0.012	0.013	0.1086	0.0349	0.0034	0.0022	0.0016	0.0020
−0.083	0.865	0.012	0.014	0.1743	0.0366	0.0047	0.0035	0.0027	0.0016
0.083	0.873	0.014	0.013	0.1632	0.0398	0.0042	0.0033	0.0024	0.0013
0.250	0.834	0.022	0.017	0.0778	0.0553	0.0025	0.0016	0.0016	0.0011
0.417	0.689	0.050	0.031	0.1620	0.1169	0.0085	0.0034	0.0077	0.0015

$\cos\theta$	P	σ_P	ΔP_{sys}	$\Delta P_{\mathrm{sys}}^{\delta}$	$\Delta P_{\mathrm{sys}}^{\Lambda}$	$\Delta P_{\mathrm{sys}}^{d}$	$\Delta P_{\mathrm{sys}}^{bg}$	H	σ_H	ΔH_{sys}	$\Delta H_{\mathrm{sys}}^{\delta}$	$\Delta H_{\mathrm{sys}}^{\Lambda}$	$\Delta H_{\mathrm{sys}}^{d}$	$\Delta H_{\mathrm{sys}}^{bg}$
−0.917	0.1042	0.1096	0.0094	0.0050	0.0025	0.0011	0.0075	−0.1809	0.1013	0.0112	0.0074	0.0037	0.0016	0.0075
−0.750	0.0691	0.0941	0.0061	0.0038	0.0019	0.0013	0.0041	−0.2796	0.0910	0.0137	0.0112	0.0056	0.0037	0.0041
−0.583	0.1199	0.0795	0.0068	0.0050	0.0025	0.0017	0.0034	−0.0807	0.0779	0.0055	0.0037	0.0019	0.0013	0.0034
−0.417	0.0554	0.0773	0.0043	0.0031	0.0015	0.0012	0.0023	−0.2389	0.0777	0.0116	0.0096	0.0048	0.0038	0.0023
−0.250	0.2707	0.0760	0.0129	0.0108	0.0054	0.0040	0.0020	−0.1627	0.0768	0.0080	0.0065	0.0033	0.0024	0.0020
−0.083	0.1069	0.0806	0.0056	0.0046	0.0023	0.0018	0.0016	−0.2153	0.0787	0.0103	0.0086	0.0043	0.0034	0.0016
0.083	0.1880	0.0876	0.0090	0.0076	0.0038	0.0027	0.0013	−0.1790	0.0894	0.0086	0.0072	0.0036	0.0026	0.0013
0.250	0.2896	0.1229	0.0142	0.0116	0.0058	0.0058	0.0011	−0.3646	0.1327	0.0179	0.0146	0.0073	0.0072	0.0011
0.417	0.3445	0.2564	0.0233	0.0146	0.0073	0.0165	0.0015	0.3306	0.2754	0.0230	0.0145	0.0072	0.0163	0.0015

Table A.34: Energy bin $816\,\mathrm{MeV} < E_\gamma < 851\,\mathrm{MeV}$. Systematic uncertainty $\Delta E_\gamma = 9\,\mathrm{MeV}$.

$\cos\theta$	d	σ_d	Δd_{sys}	T	σ_T	ΔT_{sys}	$\Delta T_{\mathrm{sys}}^{\Lambda}$	$\Delta T_{\mathrm{sys}}^{d}$	$\Delta T_{\mathrm{sys}}^{bg}$
−0.917	0.900	0.015	0.010	0.1596	0.0548	0.0074	0.0032	0.0018	0.0064
−0.750	0.837	0.015	0.016	0.1961	0.0460	0.0074	0.0039	0.0038	0.0050
−0.583	0.851	0.013	0.015	0.1920	0.0396	0.0060	0.0038	0.0034	0.0031
−0.417	0.837	0.013	0.016	0.2867	0.0384	0.0084	0.0057	0.0056	0.0025
−0.250	0.806	0.014	0.019	0.1998	0.0405	0.0067	0.0040	0.0048	0.0023
−0.083	0.809	0.015	0.019	0.1807	0.0420	0.0058	0.0036	0.0043	0.0017
0.083	0.860	0.014	0.014	0.1029	0.0434	0.0030	0.0021	0.0017	0.0013
0.250	0.736	0.028	0.026	0.1966	0.0713	0.0082	0.0039	0.0071	0.0014
0.417	0.402	0.079	0.060	−0.2574	0.2682	0.0458	0.0061	0.0454	0.0012

$\cos\theta$	P	σ_P	ΔP_{sys}	$\Delta P_{\mathrm{sys}}^{\delta}$	$\Delta P_{\mathrm{sys}}^{\Lambda}$	$\Delta P_{\mathrm{sys}}^{d}$	$\Delta P_{\mathrm{sys}}^{bg}$	H	σ_H	ΔH_{sys}	$\Delta H_{\mathrm{sys}}^{\delta}$	$\Delta H_{\mathrm{sys}}^{\Lambda}$	$\Delta H_{\mathrm{sys}}^{d}$	$\Delta H_{\mathrm{sys}}^{bg}$
−0.917	0.2412	0.1162	0.0129	0.0097	0.0049	0.0027	0.0064	−0.1001	0.1103	0.0085	0.0049	0.0024	0.0014	0.0064
−0.750	−0.0477	0.0988	0.0066	0.0035	0.0018	0.0017	0.0050	−0.1350	0.0985	0.0086	0.0057	0.0029	0.0028	0.0050
−0.583	0.4232	0.0849	0.0206	0.0169	0.0085	0.0074	0.0031	−0.2614	0.0854	0.0129	0.0105	0.0052	0.0046	0.0031
−0.417	0.2253	0.0827	0.0113	0.0090	0.0045	0.0044	0.0025	−0.2810	0.0870	0.0139	0.0112	0.0056	0.0055	0.0025
−0.250	0.2064	0.0881	0.0108	0.0083	0.0041	0.0050	0.0023	−0.3085	0.0900	0.0158	0.0123	0.0062	0.0074	0.0023
−0.083	0.3163	0.0900	0.0161	0.0127	0.0063	0.0075	0.0017	−0.2269	0.0907	0.0116	0.0091	0.0045	0.0054	0.0017
0.083	0.2948	0.0967	0.0141	0.0118	0.0059	0.0048	0.0013	−0.4294	0.0967	0.0205	0.0172	0.0086	0.0070	0.0013
0.250	0.3143	0.1575	0.0182	0.0127	0.0063	0.0114	0.0014	−0.4346	0.1701	0.0250	0.0174	0.0087	0.0156	0.0014
0.417	0.3786	0.5659	0.0852	0.0220	0.0110	0.0816	0.0012	−0.1214	0.5826	0.0737	0.0190	0.0095	0.0705	0.0012

Table A.35: Energy bin $851\,\mathrm{MeV} < E_\gamma < 884\,\mathrm{MeV}$. Systematic uncertainty $\Delta E_\gamma = 8\,\mathrm{MeV}$.

$\cos\theta$	d	σ_d	Δd_{sys}	T	σ_T	ΔT_{sys}	$\Delta T_{\mathrm{sys}}^{\Lambda}$	$\Delta T_{\mathrm{sys}}^{d}$	$\Delta T_{\mathrm{sys}}^{bg}$
−0.917	0.884	0.018	0.012	0.1383	0.0609	0.0080	0.0028	0.0018	0.0073
−0.750	0.838	0.018	0.016	0.2611	0.0494	0.0090	0.0052	0.0050	0.0054
−0.583	0.848	0.015	0.015	0.2589	0.0450	0.0078	0.0052	0.0046	0.0036
−0.417	0.814	0.015	0.019	0.3207	0.0426	0.0102	0.0064	0.0073	0.0030
−0.250	0.808	0.016	0.019	0.2174	0.0442	0.0072	0.0043	0.0052	0.0025
−0.083	0.778	0.019	0.022	0.1943	0.0490	0.0070	0.0039	0.0056	0.0017
0.083	0.710	0.023	0.029	0.2259	0.0580	0.0104	0.0045	0.0092	0.0018
0.250	0.609	0.036	0.039	0.1839	0.0936	0.0127	0.0037	0.0119	0.0020

$\cos\theta$	P	σ_P	ΔP_{sys}	$\Delta P_{\mathrm{sys}}^{\delta}$	$\Delta P_{\mathrm{sys}}^{\Lambda}$	$\Delta P_{\mathrm{sys}}^{d}$	$\Delta P_{\mathrm{sys}}^{bg}$	H	σ_H	ΔH_{sys}	$\Delta H_{\mathrm{sys}}^{\delta}$	$\Delta H_{\mathrm{sys}}^{\Lambda}$	$\Delta H_{\mathrm{sys}}^{d}$	$\Delta H_{\mathrm{sys}}^{bg}$
−0.917	0.2690	0.1304	0.0146	0.0108	0.0054	0.0036	0.0073	−0.0148	0.1161	0.0085	0.0037	0.0019	0.0012	0.0073
−0.750	0.2443	0.1082	0.0131	0.0098	0.0049	0.0047	0.0054	−0.1712	0.1076	0.0101	0.0071	0.0035	0.0034	0.0054
−0.583	0.1946	0.0964	0.0101	0.0078	0.0039	0.0035	0.0036	−0.2623	0.0964	0.0131	0.0105	0.0052	0.0047	0.0036
−0.417	0.2499	0.0928	0.0129	0.0100	0.0050	0.0057	0.0030	−0.1799	0.0939	0.0096	0.0073	0.0036	0.0042	0.0030
−0.250	0.3279	0.0946	0.0168	0.0131	0.0066	0.0078	0.0025	−0.4019	0.0943	0.0205	0.0161	0.0080	0.0095	0.0025
−0.083	0.2819	0.1076	0.0151	0.0113	0.0056	0.0081	0.0017	−0.2490	0.1090	0.0134	0.0100	0.0050	0.0071	0.0017
0.083	0.3584	0.1257	0.0218	0.0143	0.0072	0.0147	0.0018	−0.1301	0.1248	0.0092	0.0060	0.0030	0.0061	0.0018
0.250	0.2382	0.2021	0.0206	0.0105	0.0052	0.0168	0.0020	−0.2203	0.2044	0.0196	0.0100	0.0050	0.0160	0.0020

Table A.36: Energy bin $884\,\text{MeV} < E_\gamma < 933\,\text{MeV}$. Systematic uncertainty $\Delta E_\gamma = 8\,\text{MeV}$.

$\cos\theta$	d	σ_d	Δd_{sys}	T	σ_T	ΔT_{sys}	$\Delta T^\Lambda_{\text{sys}}$	ΔT^d_{sys}	$\Delta T^{bg}_{\text{sys}}$
-0.917	0.882	0.023	0.012	0.1262	0.0719	0.0068	0.0026	0.0017	0.0061
-0.750	0.784	0.023	0.022	0.3113	0.0601	0.0121	0.0062	0.0086	0.0059
-0.583	0.802	0.020	0.020	0.1867	0.0521	0.0075	0.0037	0.0046	0.0045
-0.417	0.789	0.020	0.021	0.2615	0.0514	0.0092	0.0052	0.0070	0.0029
-0.250	0.765	0.019	0.024	0.1636	0.0518	0.0067	0.0033	0.0050	0.0030
-0.083	0.719	0.024	0.028	0.3560	0.0613	0.0158	0.0071	0.0139	0.0020
0.083	0.745	0.026	0.026	0.1607	0.0703	0.0068	0.0032	0.0055	0.0022
0.250	0.712	0.032	0.029	0.1566	0.0814	0.0074	0.0032	0.0064	0.0021
0.417	0.567	0.063	0.043	0.2186	0.1503	0.0182	0.0046	0.0174	0.0027

$\cos\theta$	P	σ_P	ΔP_{sys}	$\Delta P^\delta_{\text{sys}}$	$\Delta P^\Lambda_{\text{sys}}$	ΔP^d_{sys}	$\Delta P^{bg}_{\text{sys}}$	H	σ_H	ΔH_{sys}	$\Delta H^\delta_{\text{sys}}$	$\Delta H^\Lambda_{\text{sys}}$	ΔH^d_{sys}	$\Delta H^{bg}_{\text{sys}}$
-0.917	0.1560	0.1590	0.0105	0.0073	0.0037	0.0025	0.0061	-0.1648	0.1558	0.0107	0.0075	0.0038	0.0025	0.0061
-0.750	0.0541	0.1352	0.0085	0.0047	0.0023	0.0032	0.0059	-0.2667	0.1381	0.0153	0.0108	0.0054	0.0074	0.0059
-0.583	0.3955	0.1207	0.0207	0.0158	0.0079	0.0098	0.0045	-0.3457	0.1208	0.0182	0.0138	0.0069	0.0085	0.0045
-0.417	0.3458	0.1169	0.0183	0.0138	0.0069	0.0093	0.0029	-0.3158	0.1119	0.0167	0.0126	0.0063	0.0084	0.0029
-0.250	0.4191	0.1180	0.0229	0.0168	0.0084	0.0129	0.0030	-0.2838	0.1174	0.0157	0.0114	0.0057	0.0087	0.0030
-0.083	0.3651	0.1394	0.0218	0.0146	0.0073	0.0143	0.0020	-0.3489	0.1437	0.0209	0.0140	0.0070	0.0137	0.0020
0.083	0.2081	0.1595	0.0127	0.0089	0.0044	0.0076	0.0022	-0.4682	0.1581	0.0265	0.0187	0.0094	0.0160	0.0022
0.250	0.5160	0.1835	0.0312	0.0207	0.0103	0.0209	0.0021	-0.4820	0.1813	0.0292	0.0193	0.0096	0.0195	0.0021
0.417	-0.0167	0.3504	0.0249	0.0112	0.0056	0.0213	0.0027	-1.1947	0.3599	0.1056	0.0478	0.0239	0.0911	0.0027

Table A.37: Energy bin $933\,\text{MeV} < E_\gamma < 1000\,\text{MeV}$. Systematic uncertainty $\Delta E_\gamma = 8\,\text{MeV}$.

$\cos\theta$	d	σ_d	Δd_{sys}	T	σ_T	ΔT_{sys}	$\Delta T^\Lambda_{\text{sys}}$	ΔT^d_{sys}	$\Delta T^{bg}_{\text{sys}}$
-0.917	0.889	0.020	0.011	0.0970	0.0855	0.0062	0.0022	0.0013	0.0056
-0.750	0.800	0.021	0.020	0.4118	0.0671	0.0142	0.0082	0.0103	0.0051
-0.583	0.718	0.025	0.028	0.4098	0.0655	0.0186	0.0082	0.0161	0.0046
-0.417	0.713	0.022	0.029	0.3013	0.0633	0.0141	0.0060	0.0121	0.0039
-0.250	0.687	0.025	0.031	0.2378	0.0681	0.0122	0.0048	0.0108	0.0030
-0.083	0.568	0.032	0.043	0.2790	0.0964	0.0221	0.0056	0.0212	0.0029
0.083	0.711	0.028	0.029	0.4157	0.0822	0.0189	0.0083	0.0169	0.0021
0.250	0.722	0.027	0.028	0.3540	0.0853	0.0155	0.0071	0.0136	0.0022
0.417	0.759	0.030	0.024	0.3252	0.0933	0.0125	0.0065	0.0103	0.0026

Table A.38: Energy bin $1000\,\text{MeV} < E_\gamma < 1100\,\text{MeV}$. Systematic uncertainty $\Delta E_\gamma = 7\,\text{MeV}$.

$\cos\theta$	d	σ_d	Δd_{sys}	T	σ_T	ΔT_{sys}	$\Delta T^\Lambda_{\text{sys}}$	ΔT^d_{sys}	$\Delta T^{bg}_{\text{sys}}$
-0.917	0.740	0.034	0.026	0.5453	0.1500	0.0234	0.0109	0.0192	0.0078
-0.750	0.671	0.025	0.033	0.3411	0.1093	0.0189	0.0068	0.0167	0.0056
-0.583	0.603	0.024	0.040	0.6110	0.1069	0.0423	0.0122	0.0403	0.0045
-0.417	0.648	0.022	0.035	0.3988	0.0956	0.0234	0.0080	0.0217	0.0041
-0.250	0.630	0.022	0.037	0.5449	0.0994	0.0339	0.0109	0.0319	0.0034
-0.083	0.641	0.023	0.036	0.4592	0.1087	0.0274	0.0092	0.0257	0.0026
0.083	0.697	0.020	0.030	0.5353	0.0998	0.0256	0.0107	0.0232	0.0020
0.250	0.757	0.018	0.024	0.4073	0.0915	0.0155	0.0081	0.0131	0.0019
0.417	0.800	0.018	0.020	0.4982	0.0927	0.0160	0.0100	0.0125	0.0015
0.583	0.901	0.023	0.010	0.7411	0.1451	0.0170	0.0148	0.0081	0.0012

Table A.39: Energy bin $1100\,\text{MeV} < E_\gamma < 1197\,\text{MeV}$. Systematic uncertainty $\Delta E_\gamma = 7\,\text{MeV}$.

$\cos\theta$	d	σ_d	Δd_{sys}	T	σ_T	ΔT_{sys}	$\Delta T^\Lambda_{\text{sys}}$	ΔT^d_{sys}	$\Delta T^{bg}_{\text{sys}}$
-0.917	0.799	0.054	0.020	0.7273	0.2314	0.0243	0.0145	0.0183	0.0065
-0.750	0.742	0.036	0.026	0.2666	0.1533	0.0131	0.0054	0.0095	0.0073
-0.583	0.708	0.028	0.029	0.7172	0.1191	0.0332	0.0143	0.0296	0.0046
-0.417	0.745	0.023	0.026	0.4940	0.1044	0.0206	0.0099	0.0169	0.0064
-0.250	0.737	0.025	0.026	0.7819	0.1168	0.0321	0.0156	0.0279	0.0027
-0.083	0.776	0.021	0.022	0.4919	0.1131	0.0175	0.0098	0.0142	0.0028
0.083	0.795	0.020	0.021	0.5174	0.1047	0.0170	0.0103	0.0133	0.0018
0.250	0.768	0.019	0.023	0.5958	0.0915	0.0217	0.0119	0.0180	0.0016
0.417	0.803	0.017	0.020	0.6044	0.0884	0.0193	0.0121	0.0148	0.0027
0.583	0.803	0.020	0.020	0.5082	0.1081	0.0162	0.0102	0.0124	0.0021
0.750	0.686	0.092	0.031	0.4212	0.3992	0.0243	0.0096	0.0220	0.0036

Table A.40: Energy bin $1197\,\text{MeV} < E_\gamma < 1301\,\text{MeV}$. Systematic uncertainty $\Delta E_\gamma = 6\,\text{MeV}$.

$\cos\theta$	d	σ_d	Δd_{sys}	T	σ_T	ΔT_{sys}	$\Delta T^\Lambda_{\text{sys}}$	ΔT^d_{sys}	$\Delta T^{bg}_{\text{sys}}$
-0.917	0.671	0.067	0.033	0.6492	0.2943	0.0351	0.0130	0.0320	0.0064
-0.750	0.741	0.039	0.026	0.4216	0.1752	0.0185	0.0085	0.0148	0.0073
-0.583	0.636	0.035	0.036	0.5835	0.1677	0.0357	0.0117	0.0334	0.0049
-0.417	0.699	0.025	0.030	0.6065	0.1187	0.0293	0.0121	0.0261	0.0056
-0.250	0.643	0.028	0.036	0.4735	0.1372	0.0283	0.0095	0.0263	0.0040
-0.083	0.721	0.022	0.028	0.3577	0.1186	0.0160	0.0072	0.0138	0.0035
0.083	0.692	0.020	0.031	0.4622	0.1071	0.0227	0.0092	0.0205	0.0029
0.250	0.641	0.022	0.036	0.5369	0.1152	0.0320	0.0107	0.0300	0.0031
0.417	0.702	0.021	0.030	0.5567	0.1047	0.0264	0.0111	0.0236	0.0039
0.583	0.747	0.021	0.025	0.3667	0.1043	0.0148	0.0073	0.0124	0.0034
0.750	0.663	0.048	0.034	1.0149	0.2301	0.0554	0.0203	0.0515	0.0020

Table A.41: Energy bin $1301\,\mathrm{MeV} < E_\gamma < 1403\,\mathrm{MeV}$. Systematic uncertainty $\Delta E_\gamma = 5\,\mathrm{MeV}$.

$\cos\theta$	d	σ_d	Δd_{sys}	T	σ_T	ΔT_{sys}	$\Delta T_{\mathrm{sys}}^{\Lambda}$	$\Delta T_{\mathrm{sys}}^{d}$	$\Delta T_{\mathrm{sys}}^{bg}$
-0.750	0.603	0.079	0.040	0.4741	0.2367	0.0335	0.0096	0.0315	0.0062
-0.583	0.586	0.054	0.041	0.5729	0.2068	0.0425	0.0115	0.0405	0.0058
-0.417	0.651	0.046	0.035	0.5684	0.1584	0.0331	0.0114	0.0304	0.0062
-0.250	0.627	0.043	0.037	0.6143	0.1710	0.0389	0.0123	0.0366	0.0047
-0.083	0.728	0.032	0.027	0.3028	0.1317	0.0133	0.0061	0.0114	0.0034
0.083	0.710	0.027	0.029	0.2367	0.1222	0.0111	0.0048	0.0098	0.0024
0.250	0.685	0.028	0.031	0.3589	0.1179	0.0185	0.0072	0.0165	0.0043
0.417	0.593	0.038	0.041	0.4522	0.1382	0.0327	0.0090	0.0310	0.0050
0.583	0.587	0.032	0.041	0.4516	0.1289	0.0334	0.0090	0.0318	0.0053
0.750	0.568	0.060	0.043	0.3553	0.2062	0.0286	0.0072	0.0276	0.0025

Table A.42: Energy bin $1403\,\mathrm{MeV} < E_\gamma < 1547\,\mathrm{MeV}$. Systematic uncertainty $\Delta E_\gamma = 5\,\mathrm{MeV}$.

$\cos\theta$	d	σ_d	Δd_{sys}	T	σ_T	ΔT_{sys}	$\Delta T_{\mathrm{sys}}^{\Lambda}$	$\Delta T_{\mathrm{sys}}^{d}$	$\Delta T_{\mathrm{sys}}^{bg}$
-0.750	0.358	0.192	0.064	0.3279	0.5326	0.0912	0.0101	0.0903	0.0073
-0.583	0.564	0.085	0.044	-0.1742	0.2531	0.0208	0.0050	0.0192	0.0062
-0.417	0.597	0.076	0.040	0.0170	0.2095	0.0134	0.0034	0.0113	0.0064
-0.250	0.506	0.070	0.049	0.4368	0.2446	0.0444	0.0089	0.0434	0.0032
-0.083	0.681	0.051	0.032	0.5466	0.1770	0.0280	0.0109	0.0256	0.0037
0.083	0.662	0.046	0.034	0.1233	0.1534	0.0090	0.0032	0.0082	0.0020
0.250	0.631	0.045	0.037	0.1486	0.1513	0.0113	0.0035	0.0102	0.0033
0.417	0.570	0.047	0.043	0.3024	0.1676	0.0243	0.0061	0.0232	0.0039
0.583	0.476	0.045	0.052	0.6069	0.1730	0.0682	0.0121	0.0669	0.0053
0.750	0.439	0.067	0.056	0.8751	0.2561	0.1130	0.0175	0.1117	0.0026

Table A.43: Energy bin $1547\,\mathrm{MeV} < E_\gamma < 1747\,\mathrm{MeV}$. Systematic uncertainty $\Delta E_\gamma = 4\,\mathrm{MeV}$.

$\cos\theta$	d	σ_d	Δd_{sys}	T	σ_T	ΔT_{sys}	$\Delta T_{\mathrm{sys}}^{\Lambda}$	$\Delta T_{\mathrm{sys}}^{d}$	$\Delta T_{\mathrm{sys}}^{bg}$
-0.750	0.578	0.091	0.042	0.2710	0.3651	0.0287	0.0074	0.0269	0.0068
-0.583	0.291	0.139	0.071	0.5669	0.6721	0.1751	0.0143	0.1744	0.0072
-0.417	0.617	0.053	0.038	0.7055	0.2435	0.0465	0.0141	0.0438	0.0064
-0.250	0.653	0.060	0.035	0.1244	0.2202	0.0122	0.0041	0.0108	0.0040
-0.083	0.621	0.046	0.038	0.0903	0.2213	0.0125	0.0038	0.0117	0.0021
0.083	0.642	0.041	0.036	-0.1893	0.1726	0.0129	0.0043	0.0119	0.0024
0.250	0.627	0.035	0.037	-0.2150	0.1621	0.0152	0.0046	0.0136	0.0051
0.417	0.530	0.051	0.047	-0.2284	0.2050	0.0263	0.0051	0.0227	0.0123
0.583	0.431	0.044	0.057	0.3367	0.1928	0.0466	0.0069	0.0453	0.0083
0.750	0.537	0.052	0.046	0.4471	0.1589	0.0398	0.0089	0.0386	0.0029

Table A.44: Energy bin $1747\,\mathrm{MeV} < E_\gamma < 2043\,\mathrm{MeV}$. Systematic uncertainty $\Delta E_\gamma = 3\,\mathrm{MeV}$.

$\cos\theta$	d	σ_d	Δd_{sys}	T	σ_T	ΔT_{sys}	$\Delta T_{\mathrm{sys}}^{\Lambda}$	$\Delta T_{\mathrm{sys}}^{d}$	$\Delta T_{\mathrm{sys}}^{bg}$
-0.917	0.850	0.070	0.015	-0.1205	0.3236	0.0123	0.0055	0.0049	0.0099
-0.750	0.752	0.056	0.025	0.3188	0.2315	0.0192	0.0067	0.0111	0.0142
-0.583	0.696	0.059	0.030	0.8299	0.2486	0.0408	0.0166	0.0363	0.0083
-0.417	0.623	0.066	0.038	-0.1788	0.2375	0.0163	0.0048	0.0145	0.0056
-0.250	0.677	0.057	0.032	-0.0884	0.2528	0.0119	0.0043	0.0102	0.0044
-0.083	0.580	0.071	0.042	-0.7400	0.2893	0.0557	0.0148	0.0536	0.0036
0.083	0.515	0.059	0.048	-0.6786	0.2658	0.0654	0.0136	0.0639	0.0024
0.250	0.317	0.066	0.068	-0.7013	0.4340	0.1560	0.0144	0.1552	0.0058
0.417	0.473	0.049	0.053	-0.6839	0.2465	0.0793	0.0137	0.0763	0.0168
0.583	0.333	0.042	0.067	-0.0132	0.2344	0.0390	0.0037	0.0374	0.0101
0.750	0.589	0.028	0.041	0.0407	0.1168	0.0079	0.0020	0.0069	0.0033
0.917	0.385	0.088	0.062	0.2445	0.4629	0.0677	0.0084	0.0671	0.0038

Table A.45: Energy bin $2043\,\mathrm{MeV} < E_\gamma < 2607\,\mathrm{MeV}$. Systematic uncertainty $\Delta E_\gamma = 10\,\mathrm{MeV}$.

$\cos\theta$	d	σ_d	Δd_{sys}	T	σ_T	ΔT_{sys}	$\Delta T_{\mathrm{sys}}^{\Lambda}$	$\Delta T_{\mathrm{sys}}^{d}$	$\Delta T_{\mathrm{sys}}^{bg}$
-0.875	0.808	0.056	0.019	0.6141	0.2394	0.0247	0.0123	0.0146	0.0157
-0.625	0.638	0.062	0.036	0.2333	0.2358	0.0197	0.0055	0.0155	0.0109
-0.375	0.507	0.087	0.049	-0.3621	0.4188	0.0453	0.0090	0.0439	0.0068
-0.125	0.639	0.062	0.036	-0.7217	0.2837	0.0436	0.0145	0.0409	0.0049
0.125	0.616	0.046	0.038	-0.6992	0.2024	0.0460	0.0140	0.0435	0.0051
0.375	0.522	0.038	0.048	-0.2295	0.1692	0.0297	0.0049	0.0222	0.0191
0.625	0.404	0.026	0.060	0.0144	0.1296	0.0210	0.0021	0.0153	0.0142
0.875	0.485	0.029	0.051	-0.0573	0.1369	0.0136	0.0024	0.0126	0.0046

Appendix B

Fits to the Event Yield Asymmetries

B.1 Fits to $A_\Sigma(\phi)$

The fits to $A_\Sigma(\phi)$ (see Section 6.4.1.1) are shown here for all bins. Fits with a confidence level below $0.1\,\%$ are shown in red. Bins which have been excluded from further analysis due to low acceptance are highlighted in yellow.
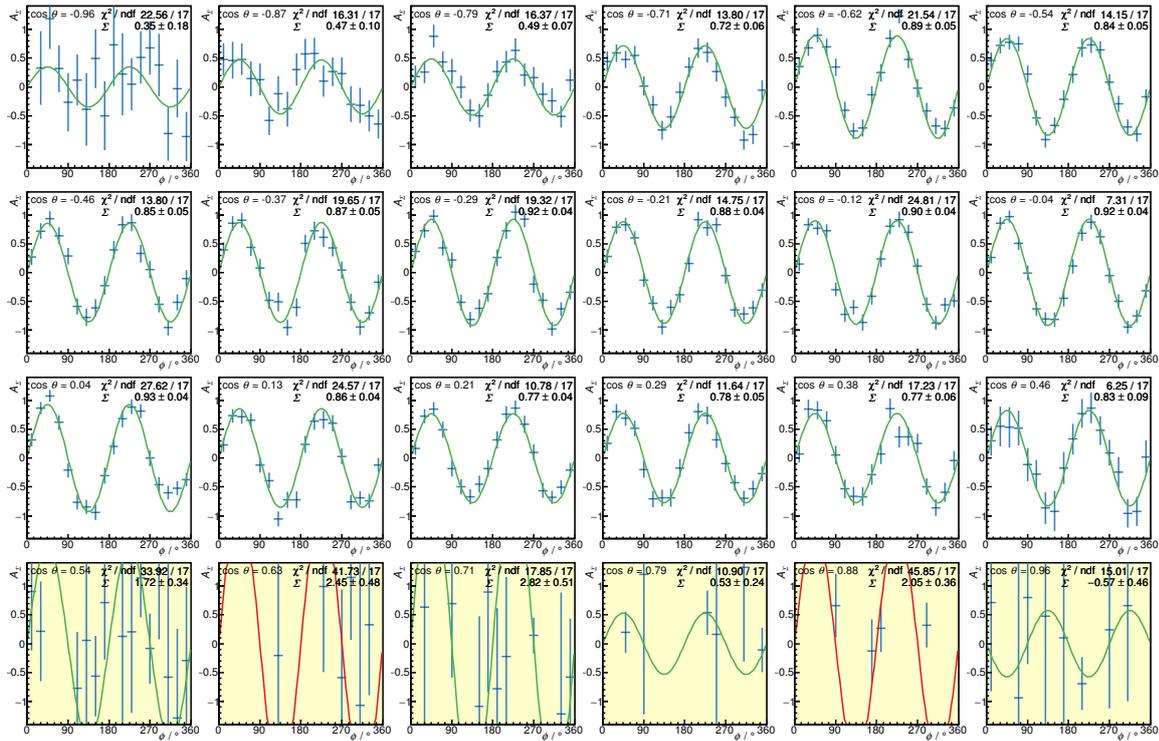
Figure B.1: Energy bin $641\,\text{MeV} < E_\gamma < 667\,\text{MeV}$.
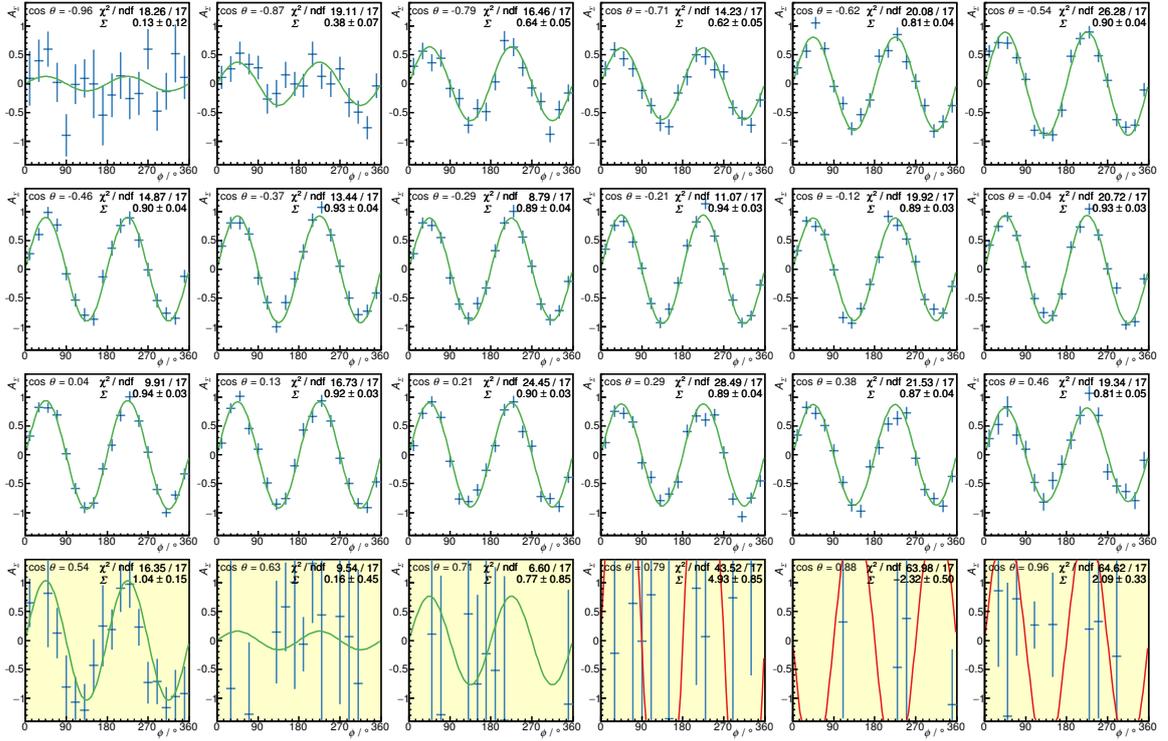
Figure B.2: Energy bin $667\,\mathrm{MeV} < E_\gamma < 700\,\mathrm{MeV}$.
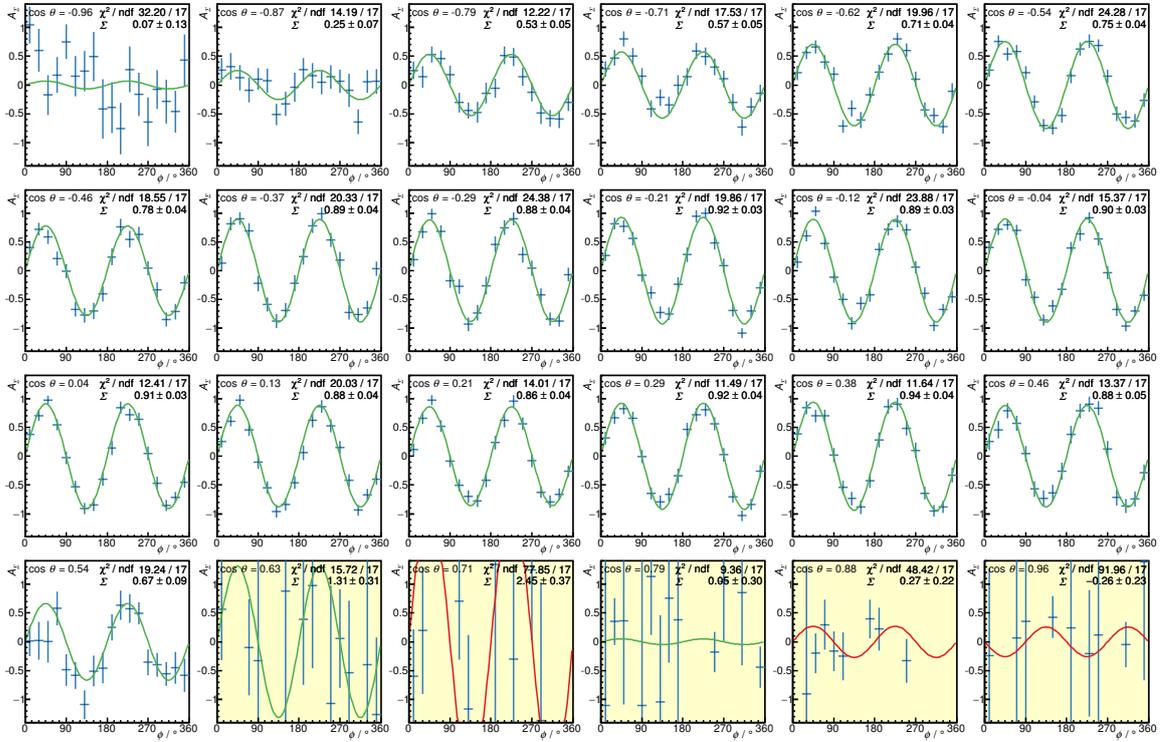
Figure B.3: Energy bin $700\,\mathrm{MeV} < E_\gamma < 732\,\mathrm{MeV}$.
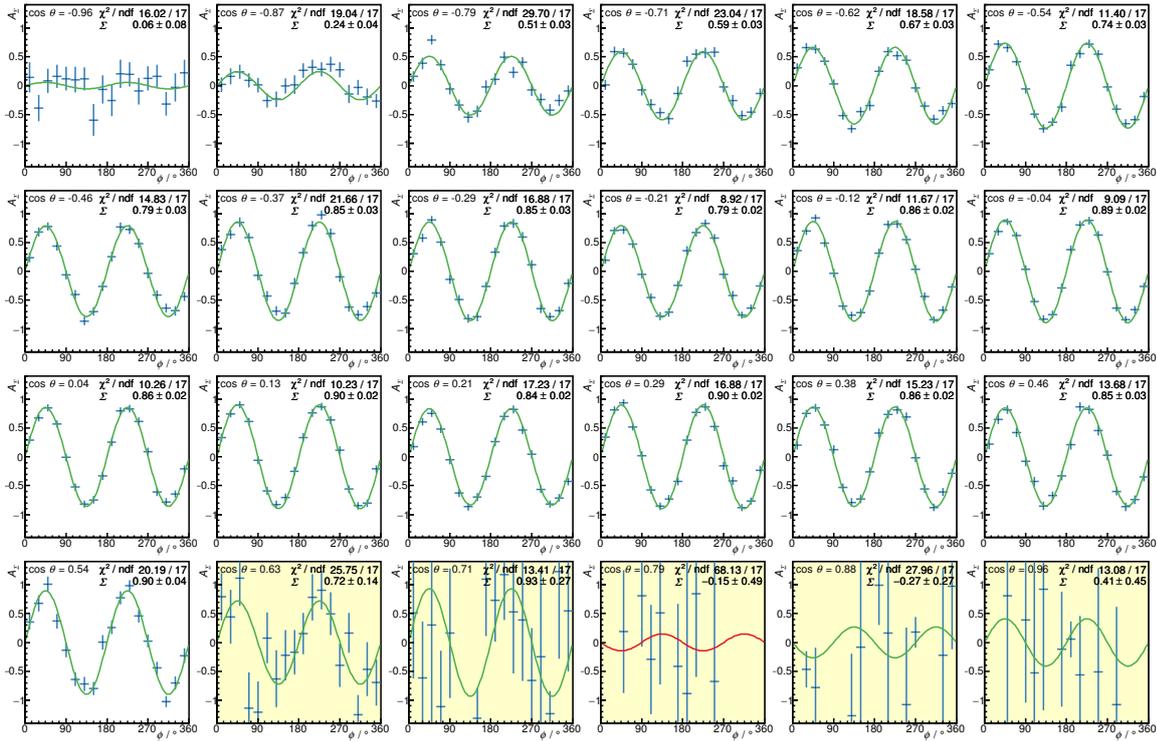
Figure B.4: Energy bin $732\,\text{MeV} < E_\gamma < 768\,\text{MeV}$.
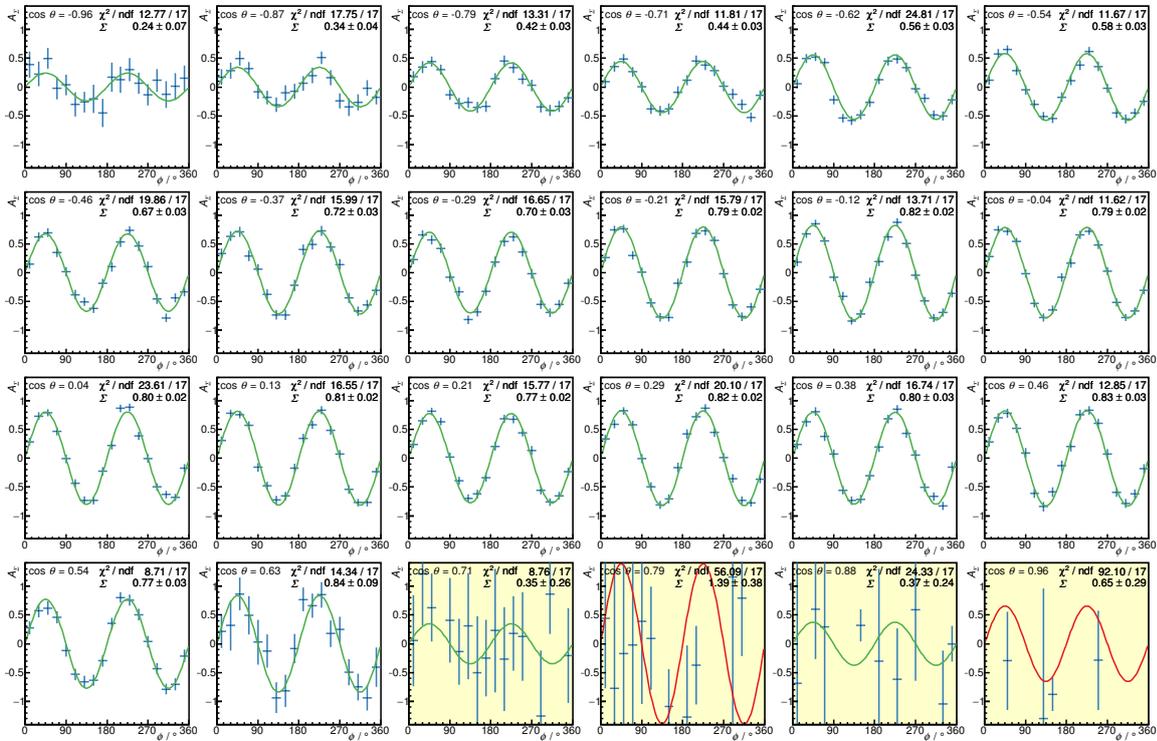
Figure B.5: Energy bin $768\,\text{MeV} < E_\gamma < 798\,\text{MeV}$.

Figure B.6: Energy bin $798\,\mathrm{MeV} < E_\gamma < 833\,\mathrm{MeV}$.
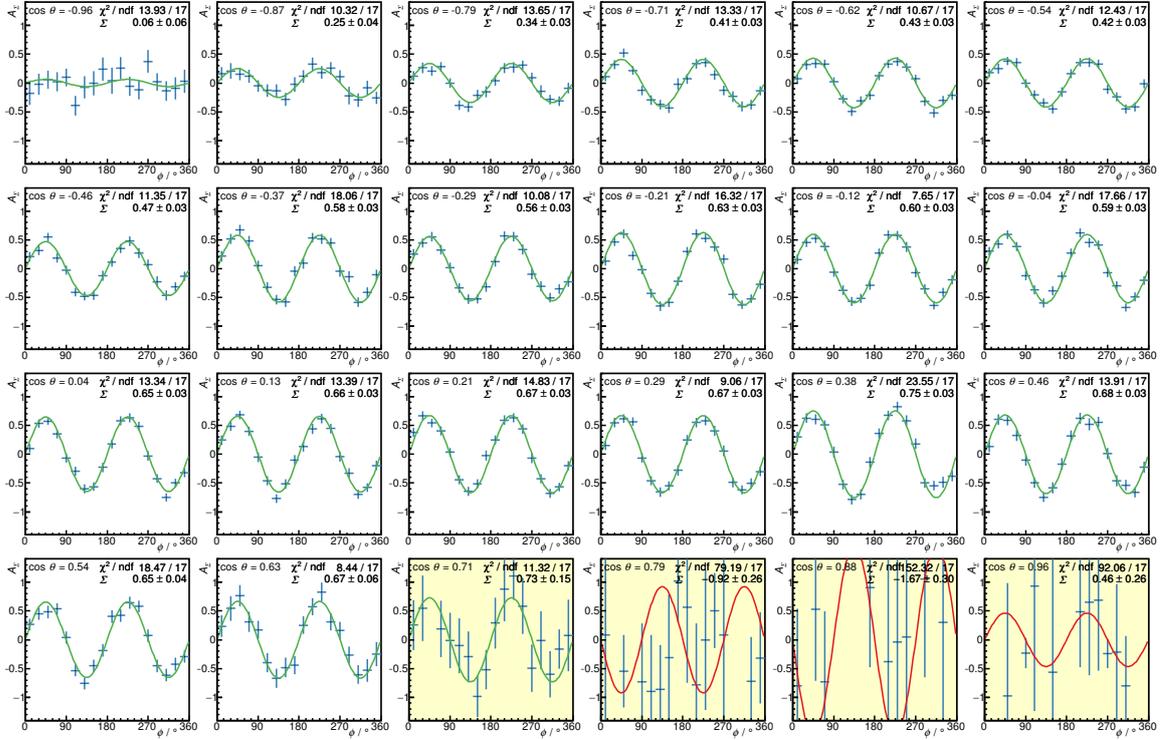
Figure B.7: Energy bin $833\,\mathrm{MeV} < E_\gamma < 868\,\mathrm{MeV}$.
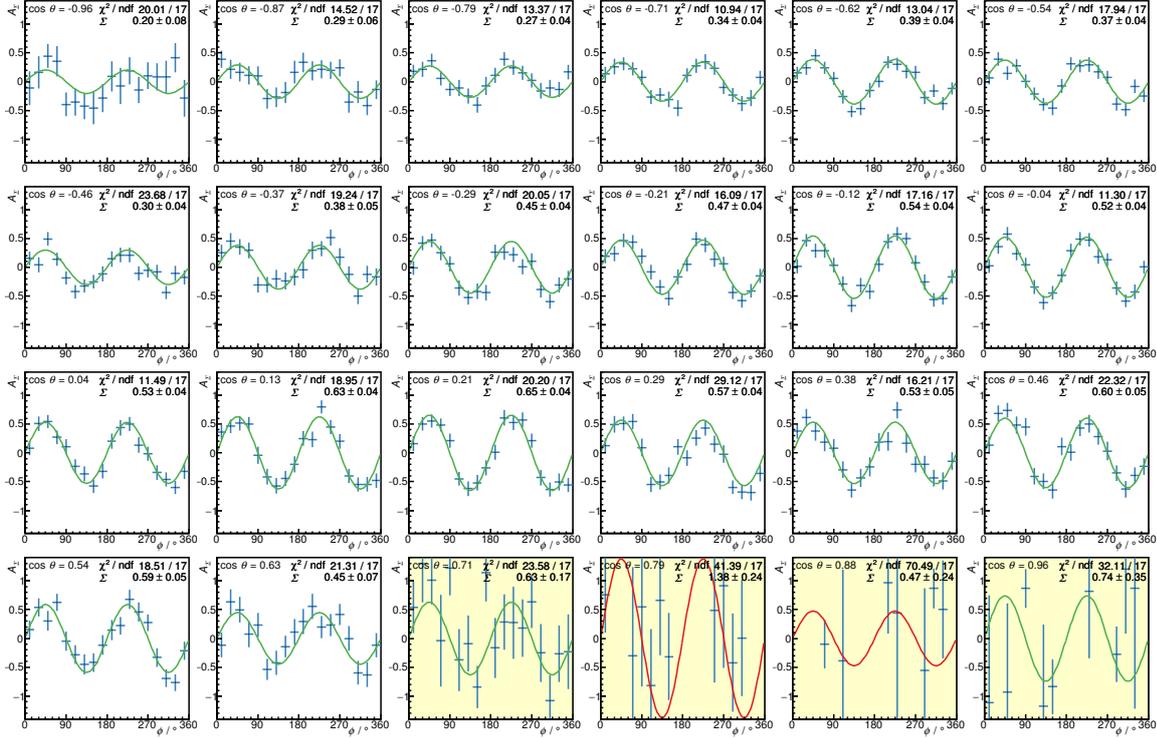
Figure B.8: Energy bin $868\,\mathrm{MeV} < E_{\gamma} < 901\,\mathrm{MeV}$.
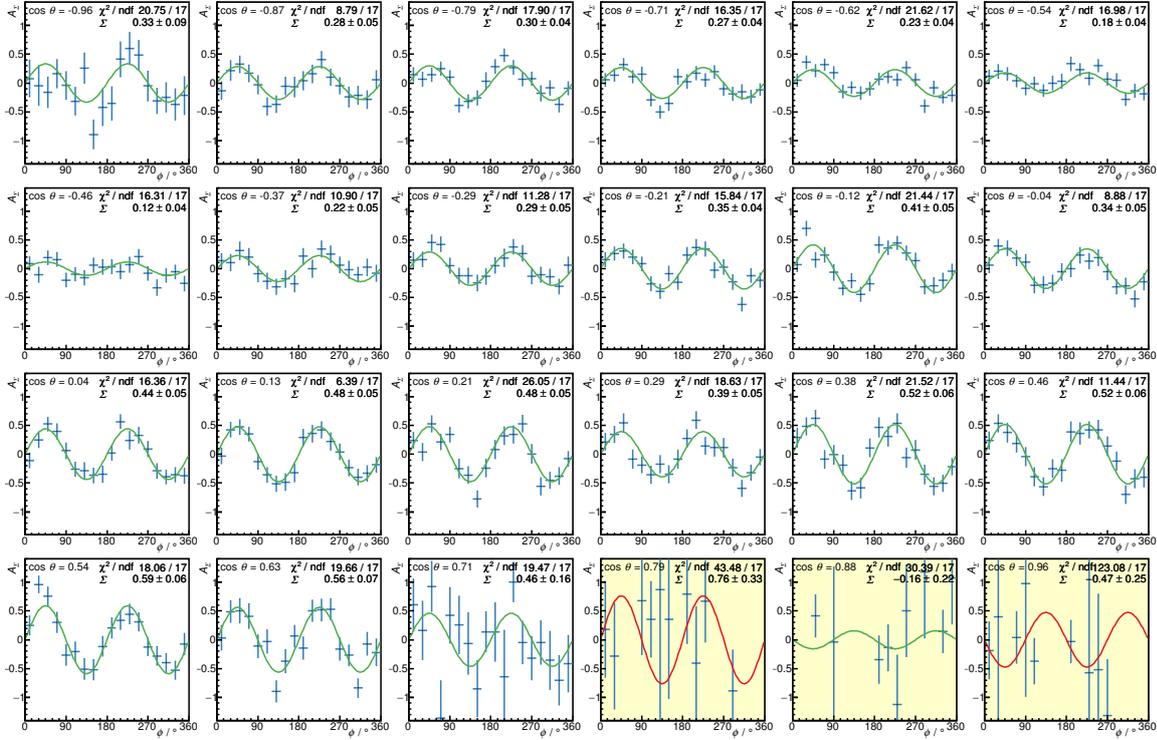
Figure B.9: Energy bin $901\,\mathrm{MeV} < E_{\gamma} < 933\,\mathrm{MeV}$.

Figure B.10: Energy bin $933\,\text{MeV} < E_\gamma < 974\,\text{MeV}$.

B.2 Fits to $A_T(\phi)$

The fits to $A_T(\phi)$ (see Section 6.4.1.2) are shown here for all bins. Fits with a confidence level below $0.1\,\%$ are shown in red. Bins which have been excluded from further analysis due to low acceptance are highlighted in yellow. Note: the fit parameters T are not the final results for the observables, because they are not divided by the dilution factor d.
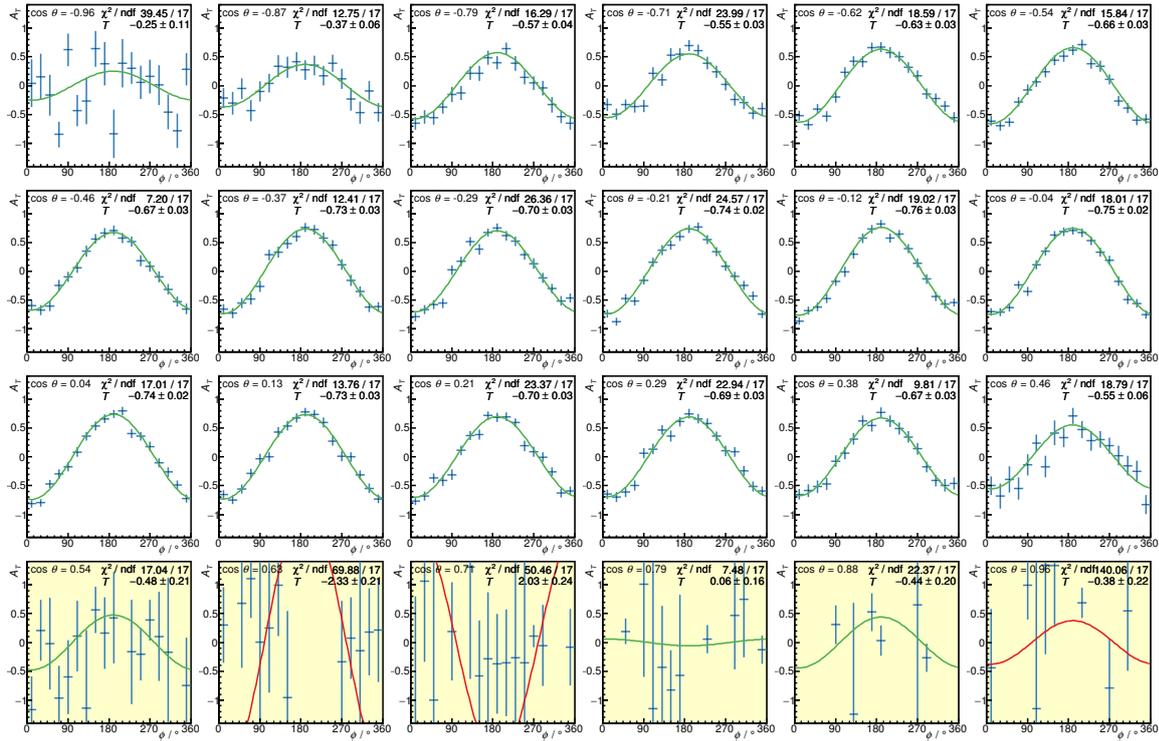
Figure B.11: Energy bin $641\,\mathrm{MeV} < E_\gamma < 667\,\mathrm{MeV}$.
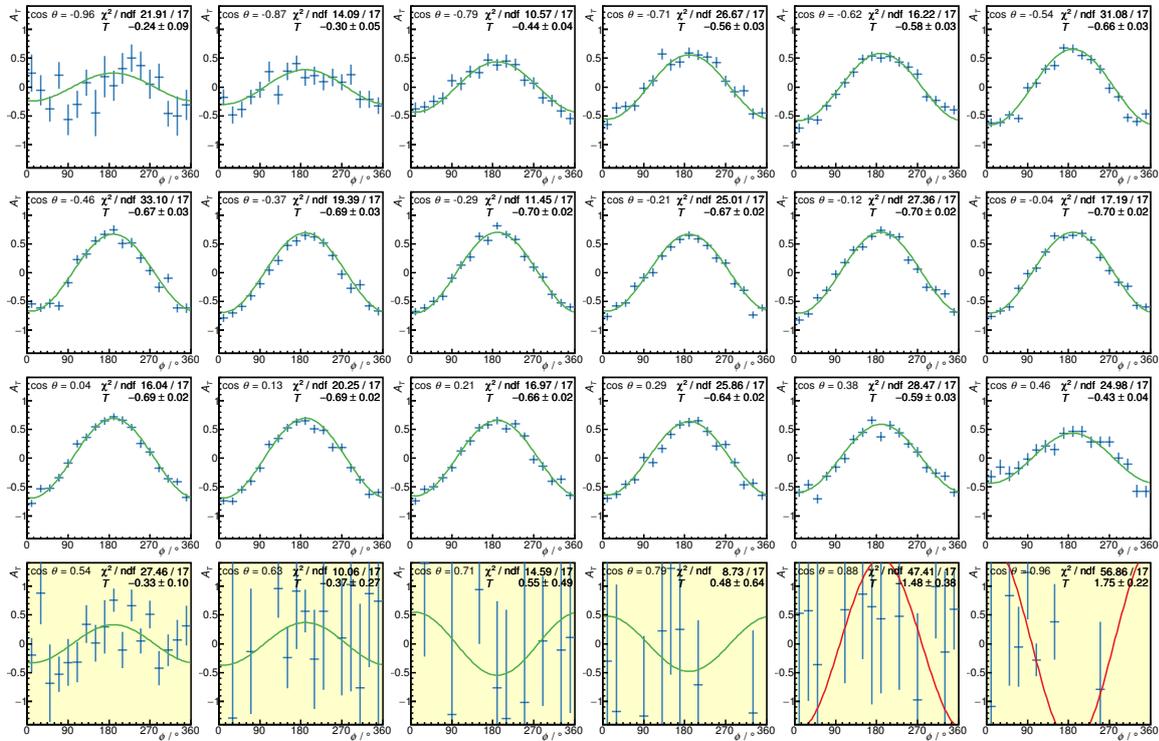
Figure B.12: Energy bin $667\,\mathrm{MeV} < E_\gamma < 700\,\mathrm{MeV}$.

Figure B.13: Energy bin $700\,\text{MeV} < E_\gamma < 732\,\text{MeV}$.
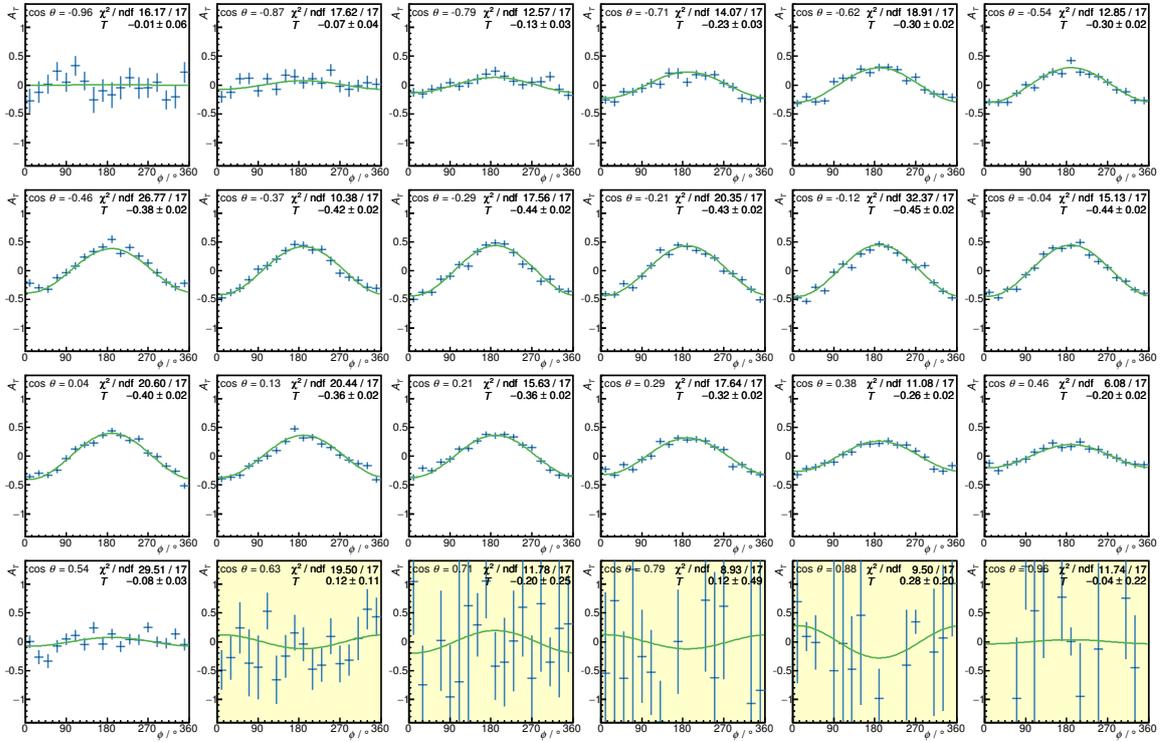
Figure B.14: Energy bin $732\,\text{MeV} < E_\gamma < 768\,\text{MeV}$.
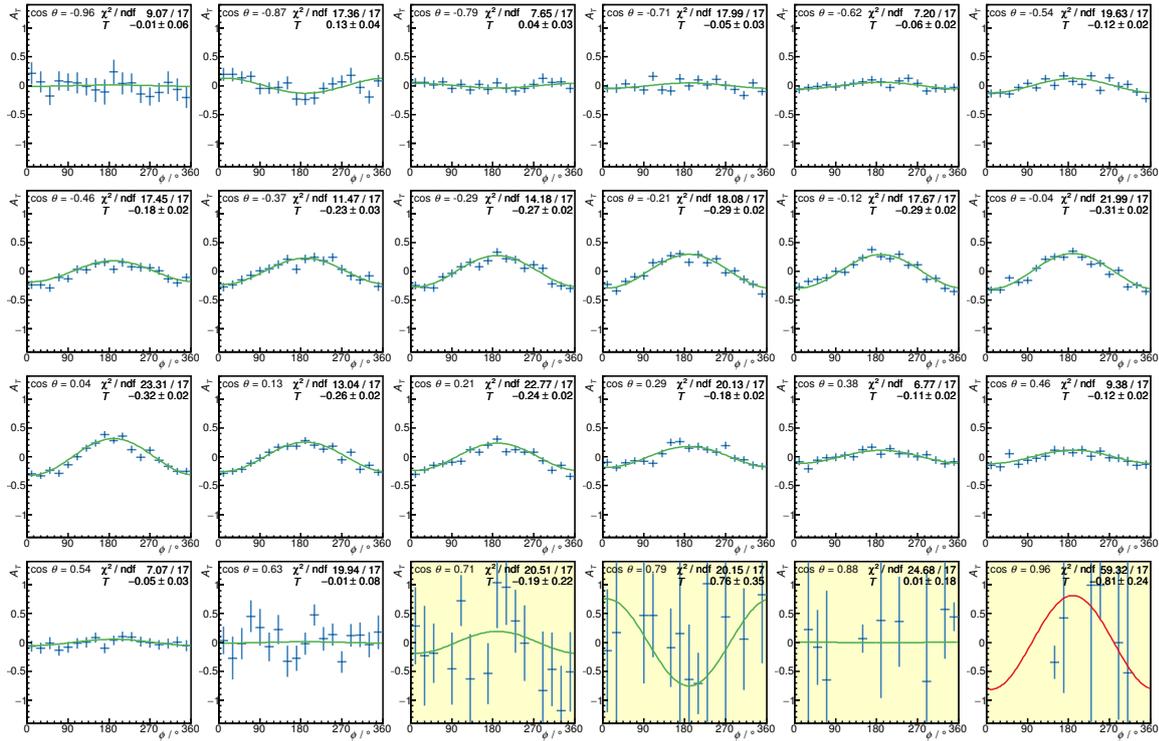
Figure B.15: Energy bin $768\,\text{MeV} < E_\gamma < 798\,\text{MeV}$.
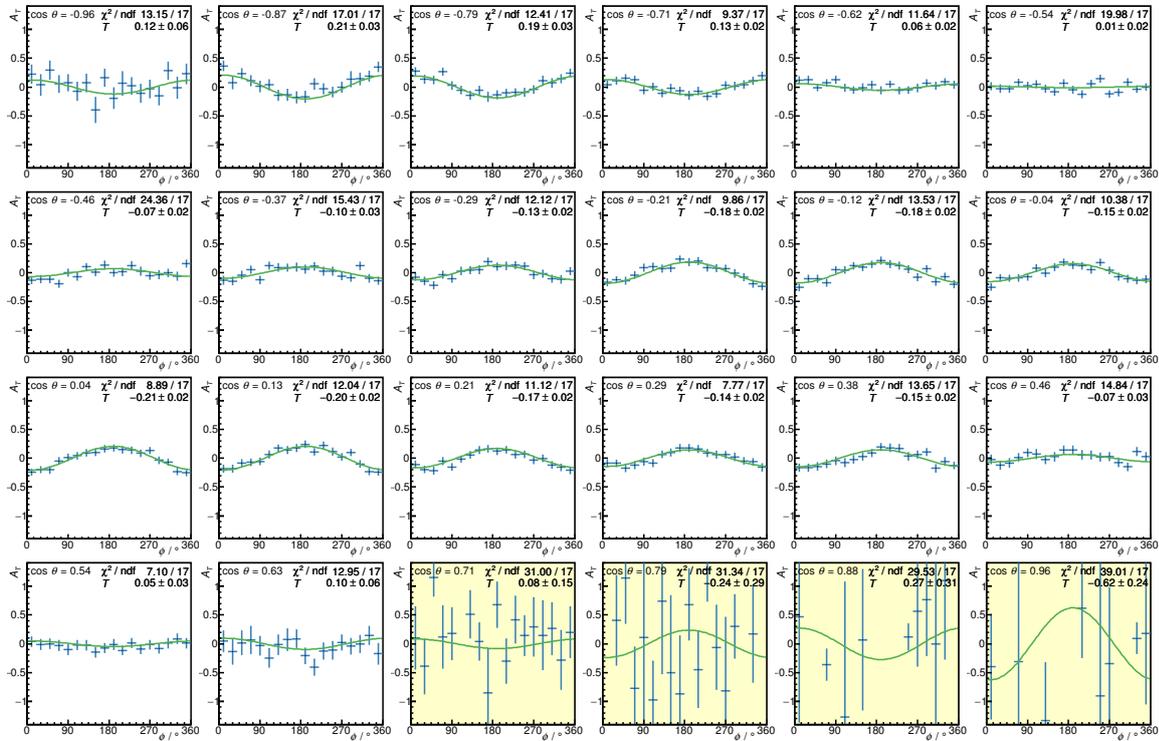
Figure B.16: Energy bin $798\,\text{MeV} < E_\gamma < 833\,\text{MeV}$.

Figure B.17: Energy bin 833 MeV $< E_\gamma <$ 868 MeV.
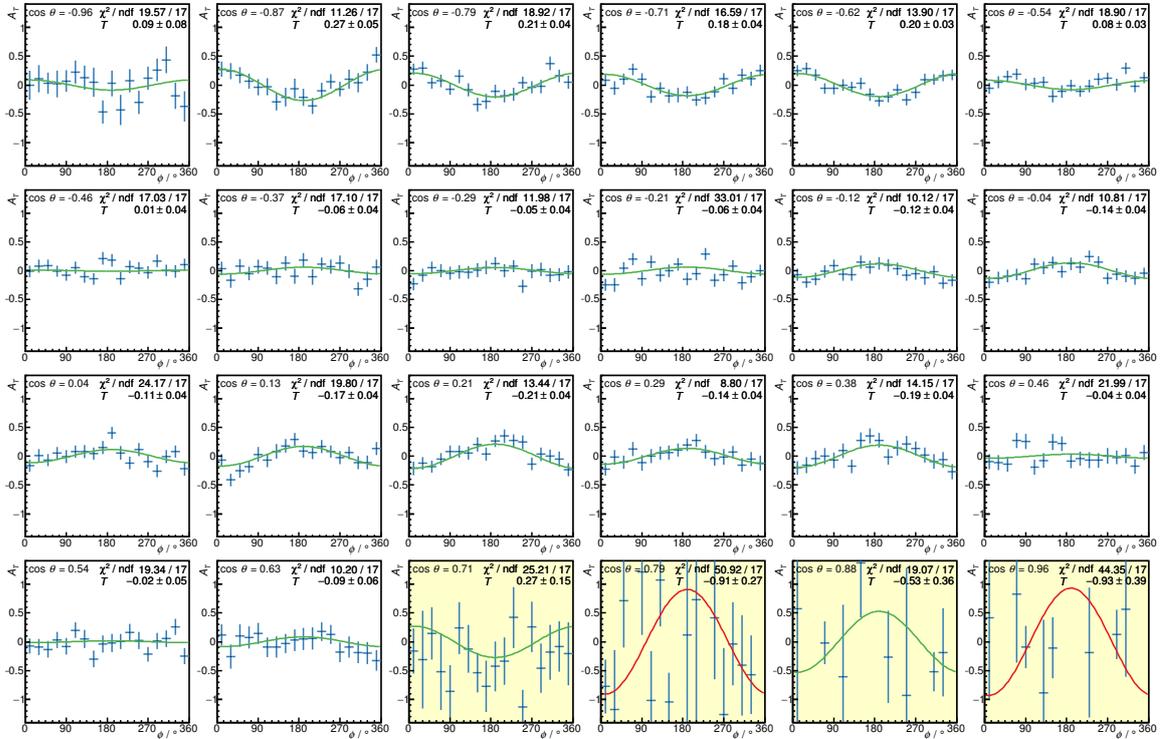
Figure B.18: Energy bin 868 MeV $< E_\gamma <$ 901 MeV.
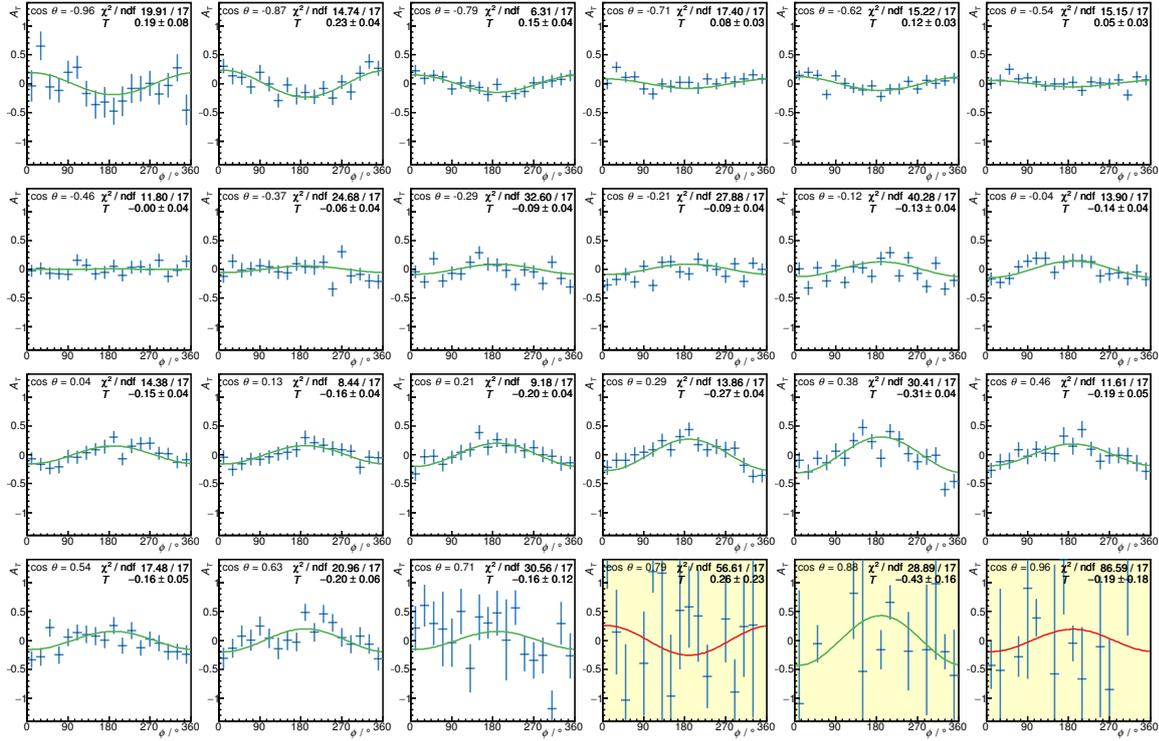
Figure B.19: Energy bin $901\,\mathrm{MeV} < E_\gamma < 933\,\mathrm{MeV}$.
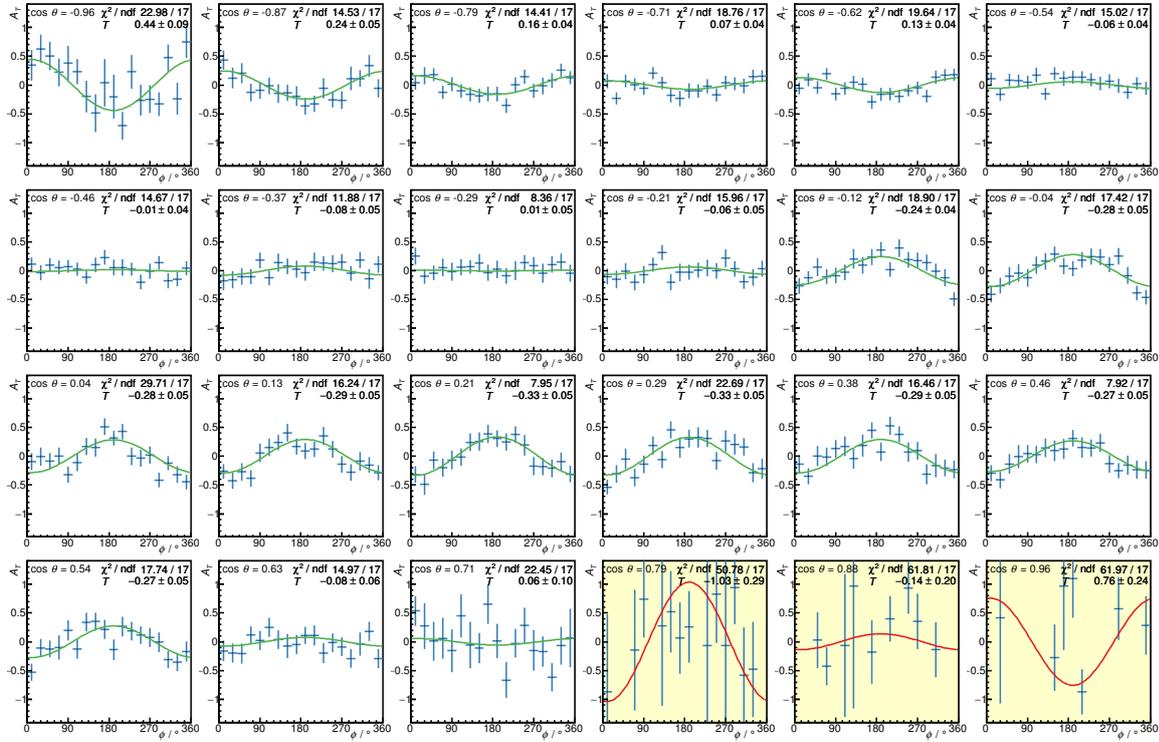
Figure B.20: Energy bin $933\,\mathrm{MeV} < E_\gamma < 974\,\mathrm{MeV}$.

Figure B.21: Energy bin $974\,\text{MeV} < E_\gamma < 1015\,\text{MeV}$.
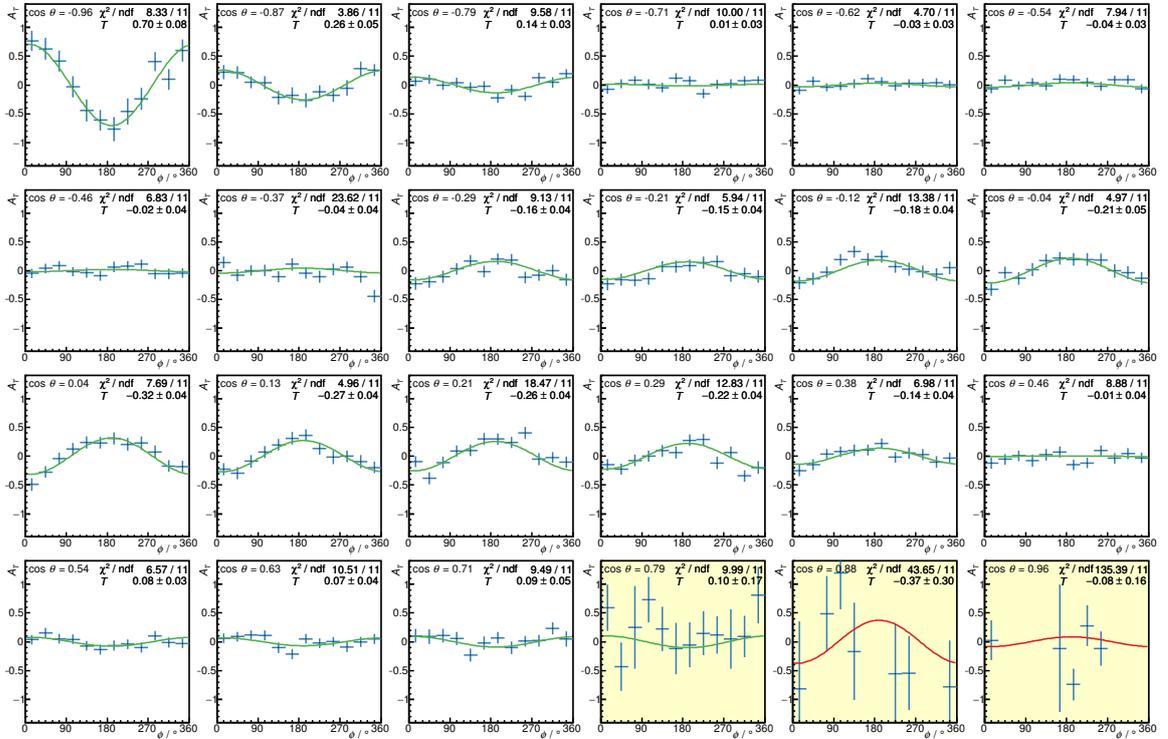
Figure B.22: Energy bin $1015\,\text{MeV} < E_\gamma < 1058\,\text{MeV}$.
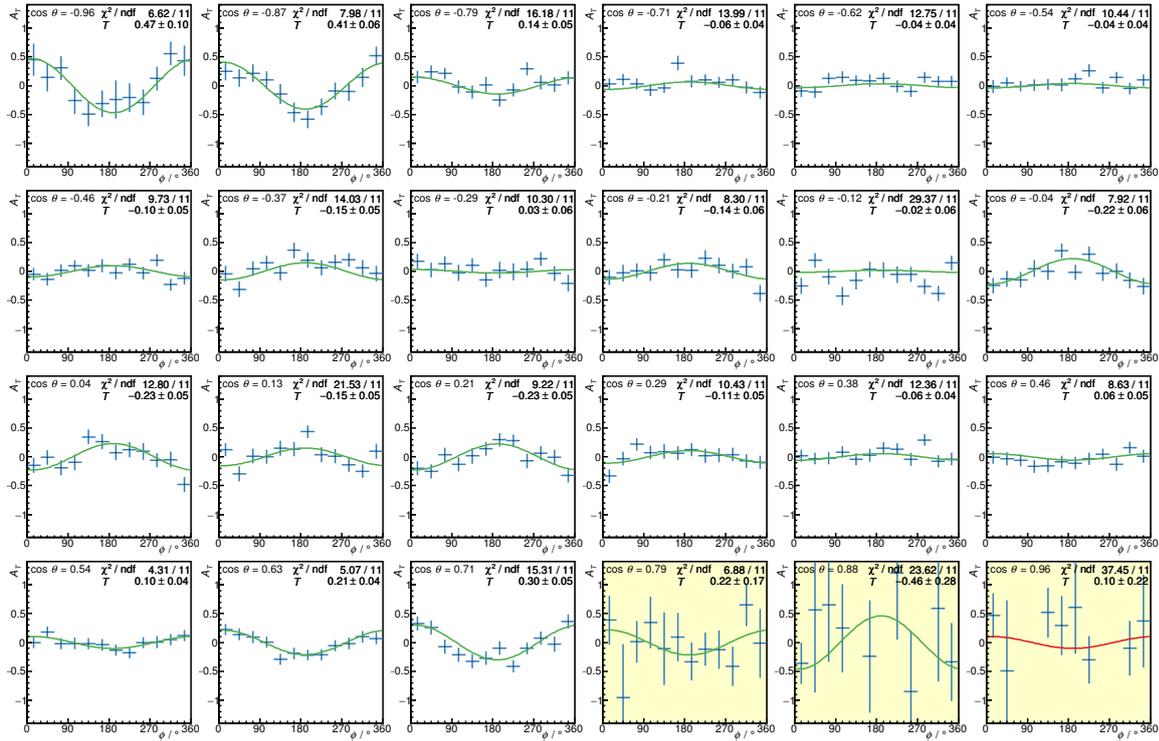
Figure B.23: Energy bin $1058\,\mathrm{MeV} < E_\gamma < 1100\,\mathrm{MeV}$.
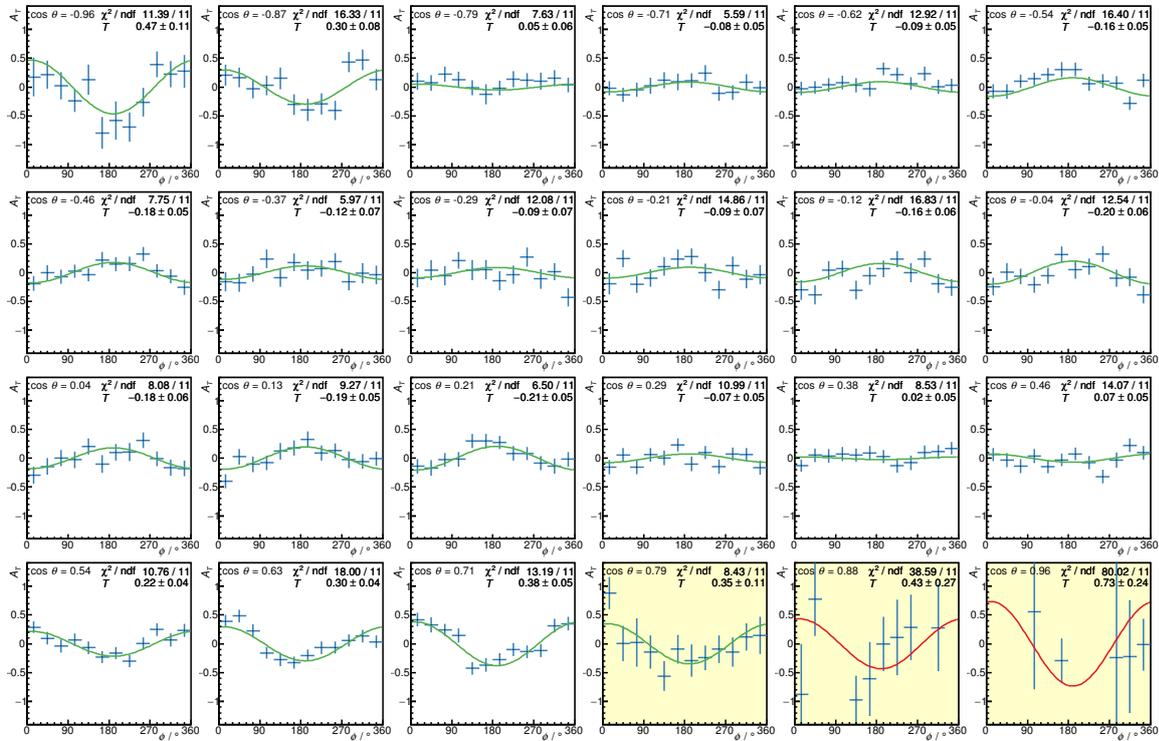
Figure B.24: Energy bin $1100\,\mathrm{MeV} < E_\gamma < 1154\,\mathrm{MeV}$.

Figure B.25: Energy bin $1154\,\mathrm{MeV} < E_\gamma < 1197\,\mathrm{MeV}$.
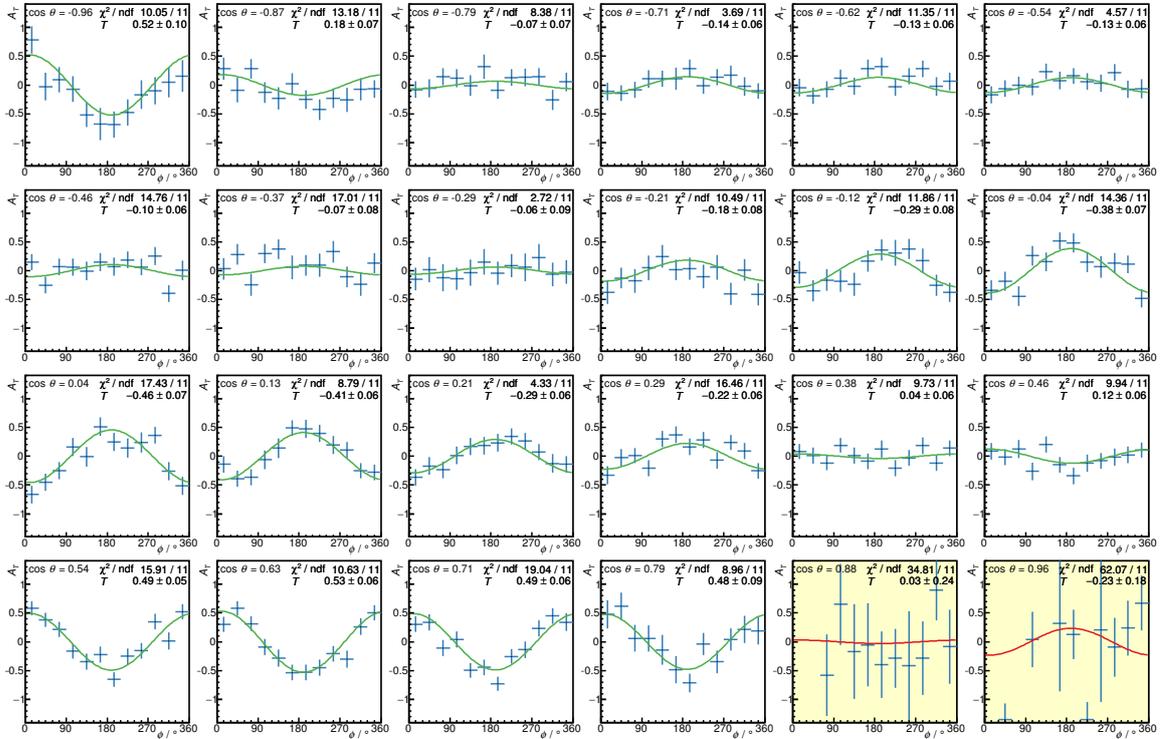
Figure B.26: Energy bin $1197\,\mathrm{MeV} < E_\gamma < 1246\,\mathrm{MeV}$.
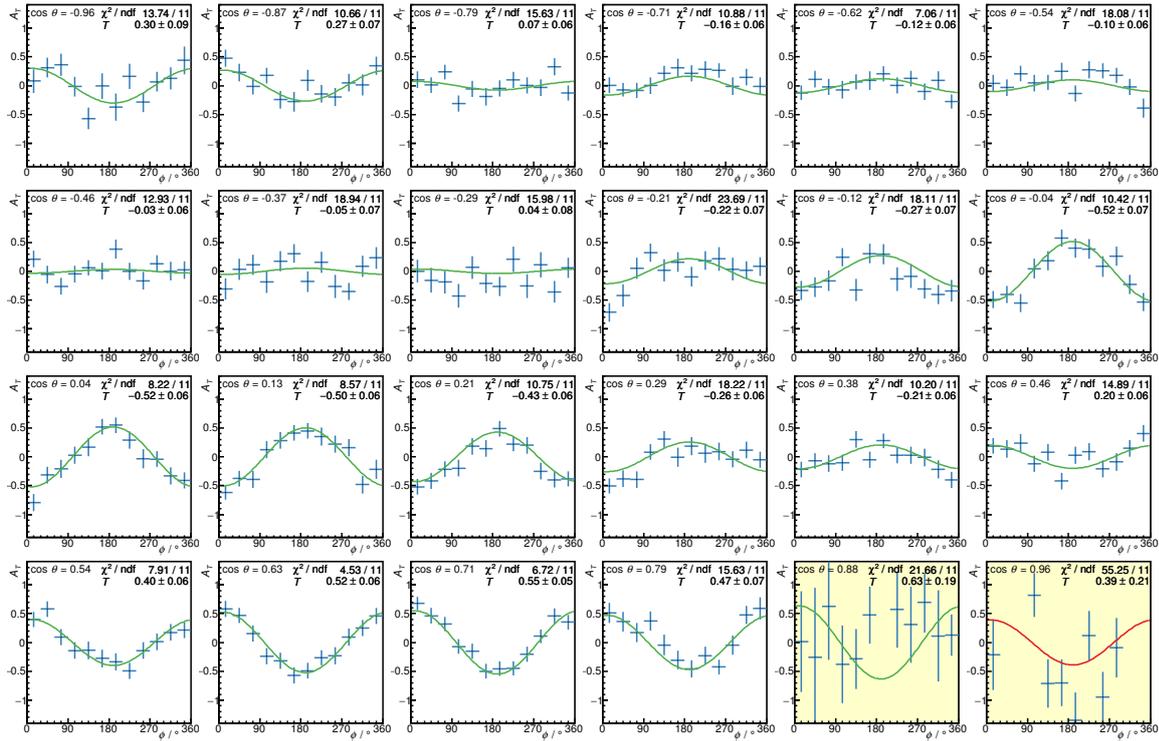
Figure B.27: Energy bin $1246\,\mathrm{MeV} < E_\gamma < 1301\,\mathrm{MeV}$.
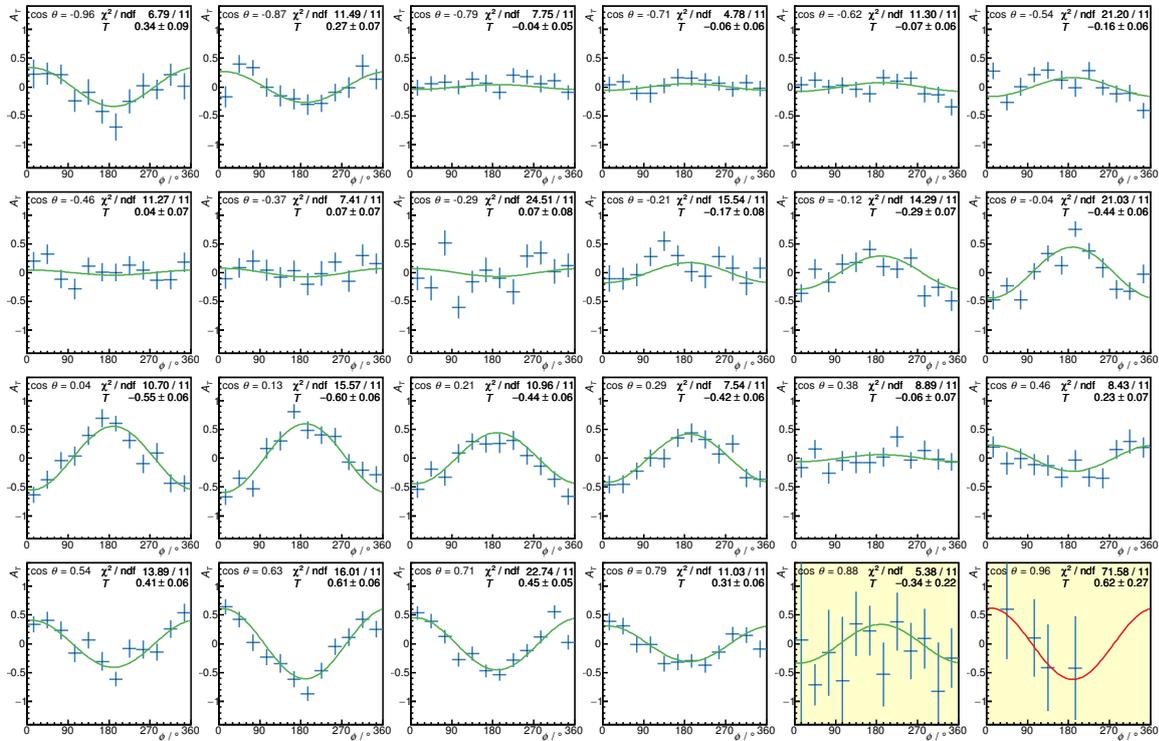
Figure B.28: Energy bin $1301\,\mathrm{MeV} < E_\gamma < 1354\,\mathrm{MeV}$.

Figure B.29: Energy bin $1354\,\text{MeV} < E_\gamma < 1404\,\text{MeV}$.
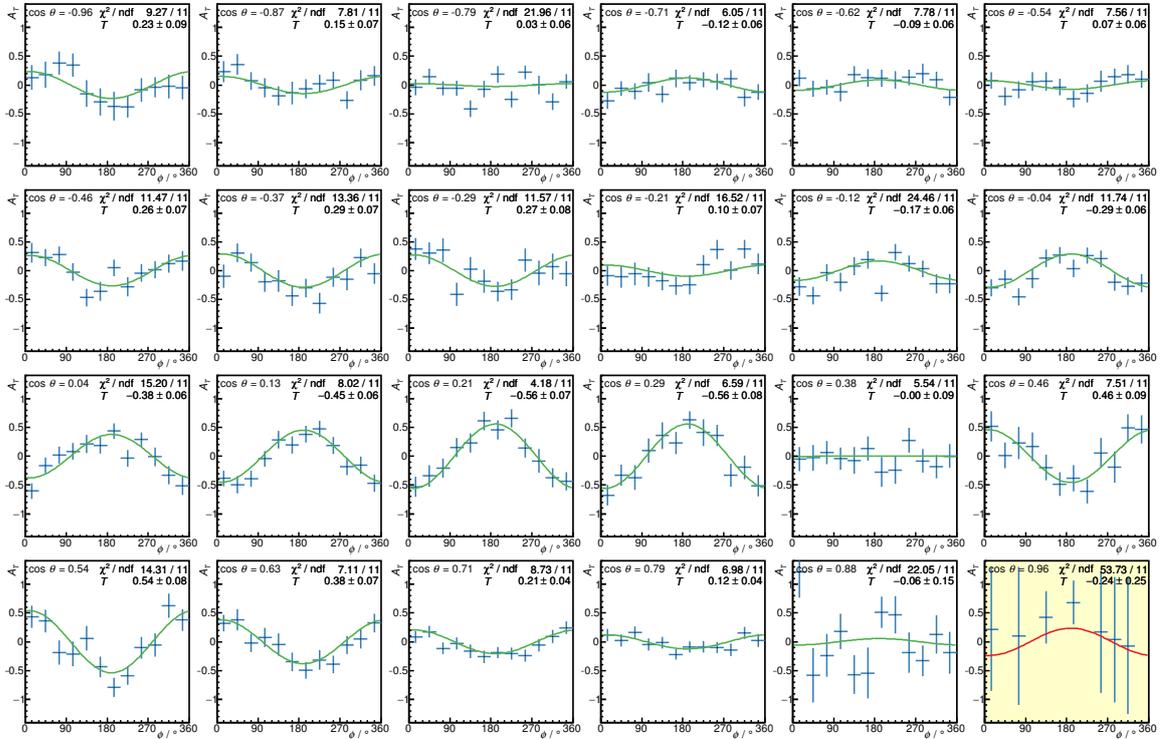
Figure B.30: Energy bin $1404\,\text{MeV} < E_\gamma < 1465\,\text{MeV}$.
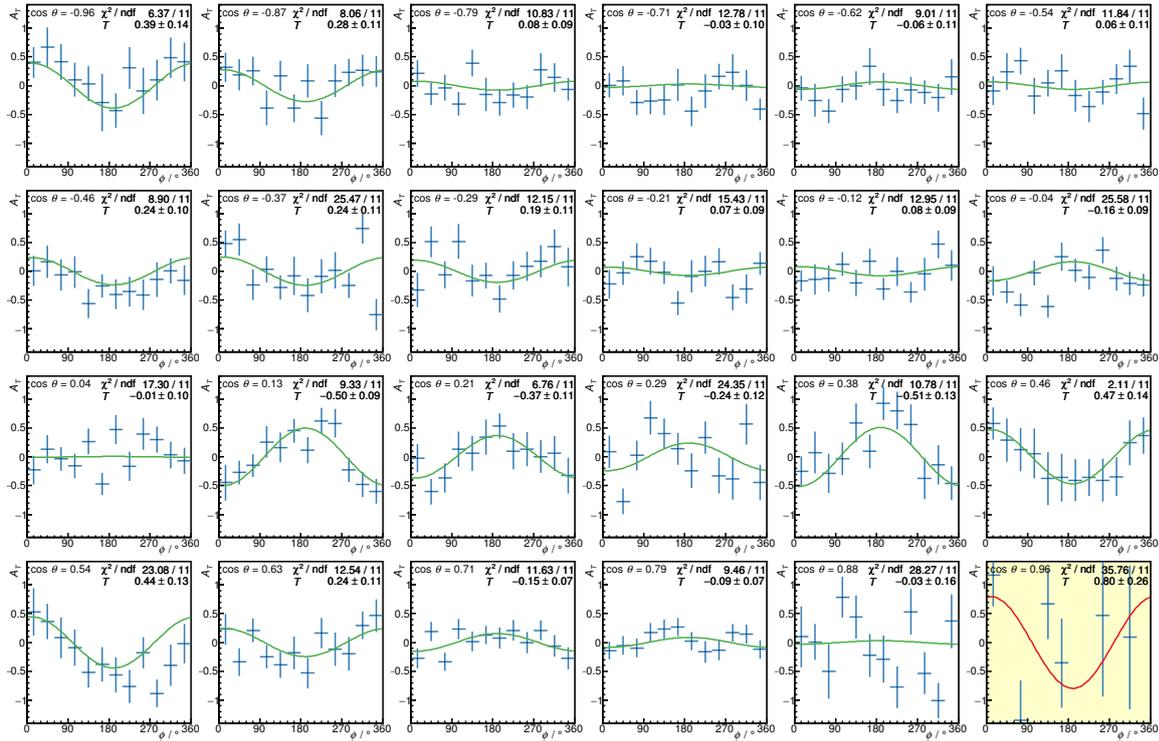
Figure B.31: Energy bin $1465\,\text{MeV} < E_\gamma < 1535\,\text{MeV}$.
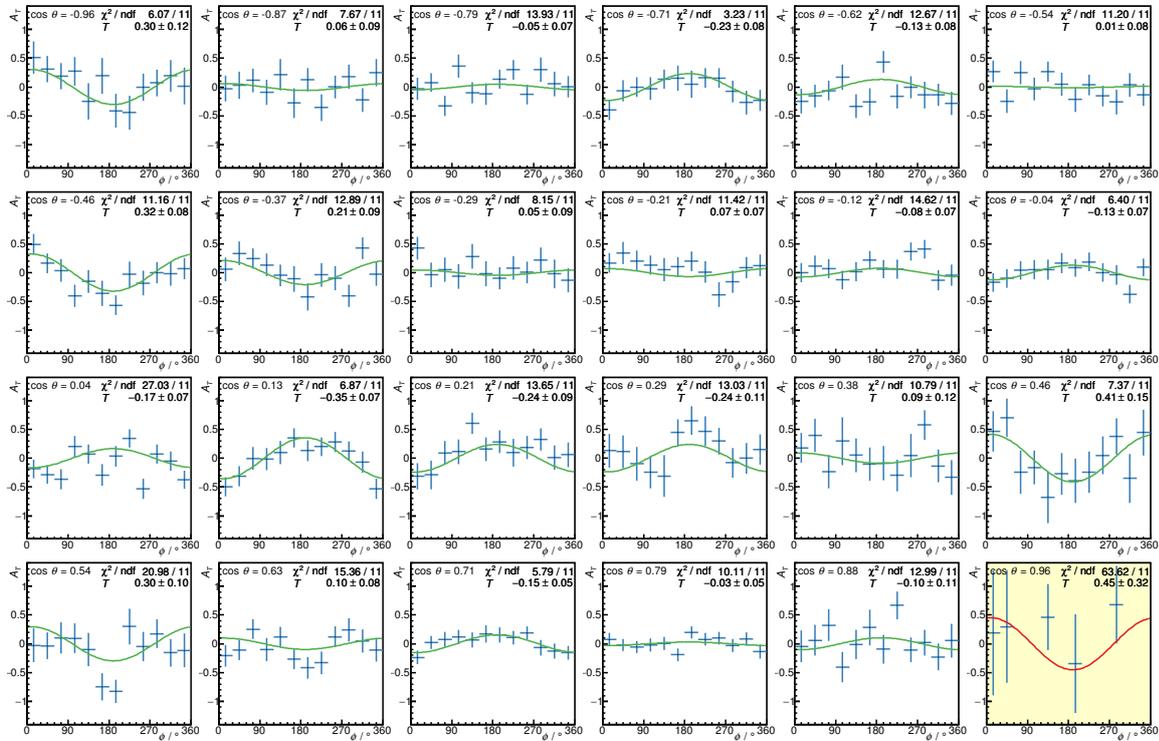
Figure B.32: Energy bin $1535\,\text{MeV} < E_\gamma < 1601\,\text{MeV}$.
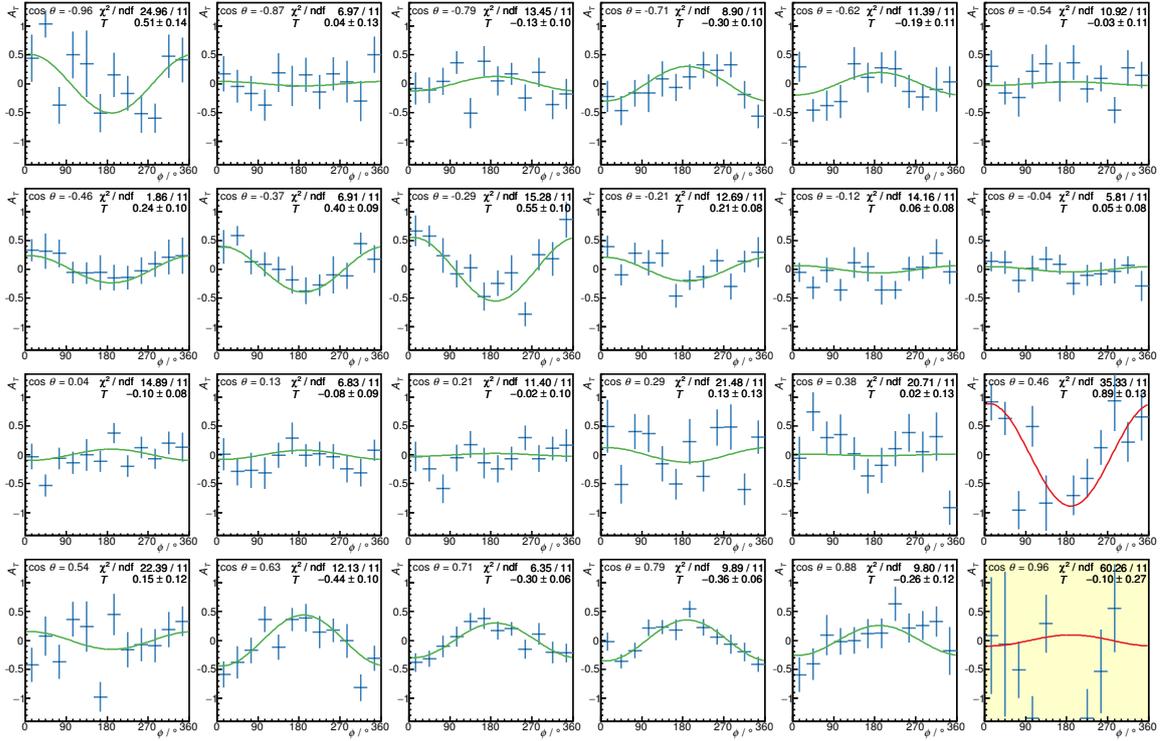
Figure B.33: Energy bin 1601 MeV $< E_\gamma <$ 1701 MeV.
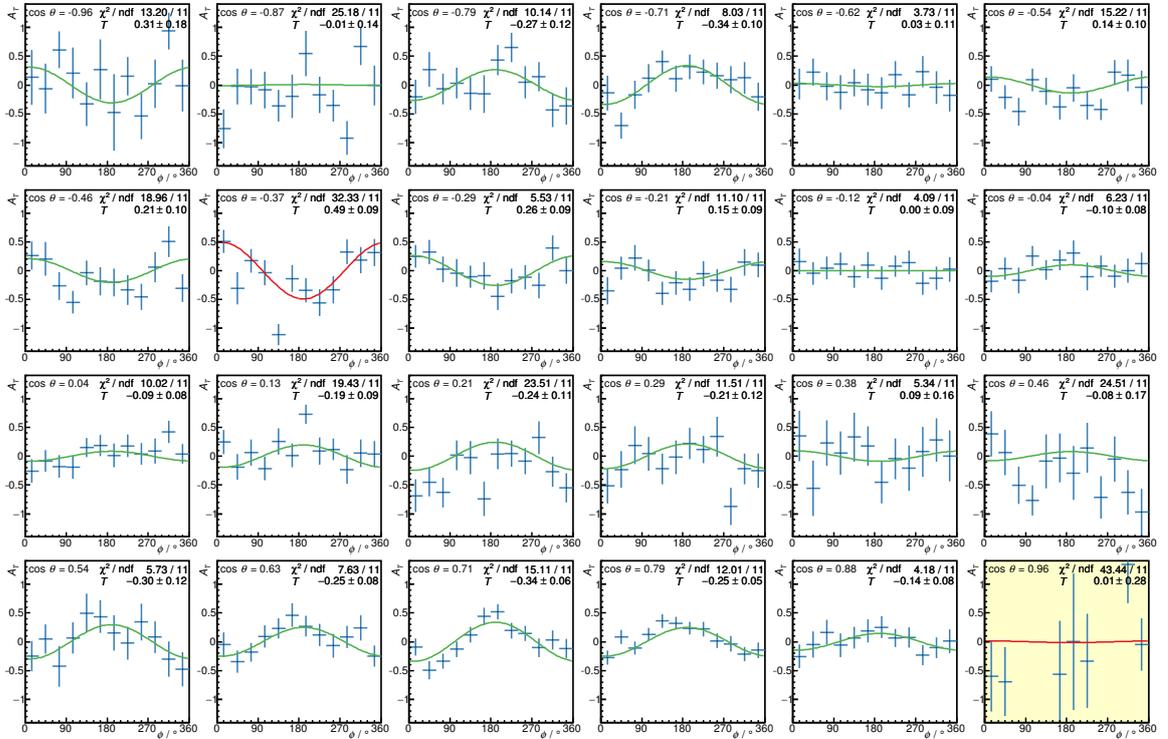
Figure B.34: Energy bin 1701 MeV $< E_\gamma <$ 1799 MeV.
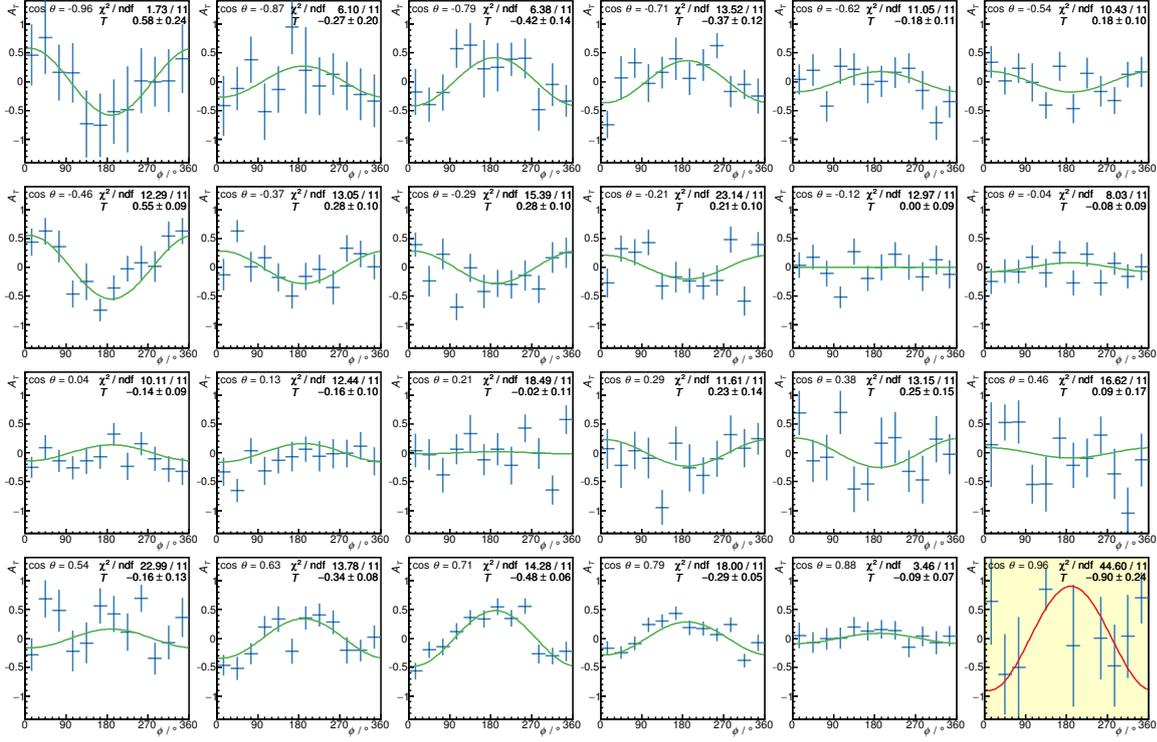
Figure B.35: Energy bin $1799\,\text{MeV} < E_\gamma < 1897\,\text{MeV}$.

B.3 Fits to $A_{PH}(\phi)$

The fits to $A_{PH}(\phi)$ (see Section 6.4.1.3) are shown here for all bins. Fits with a confidence level below $0.1\,\%$ are shown in red. Bins which have been excluded from further analysis due to low acceptance are highlighted in yellow. Note: the fit parameters P and H are not the final results for the observables, because they are not divided by the dilution factor d.
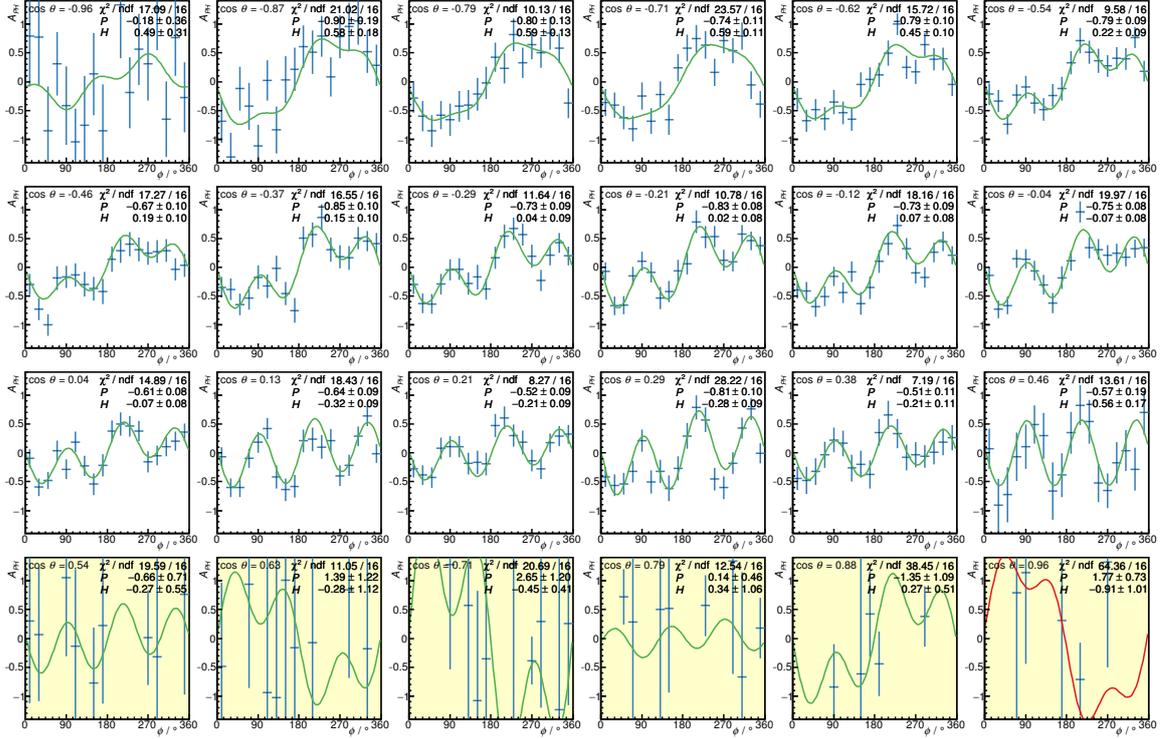
Figure B.36: Energy bin $641\,\mathrm{MeV} < E_\gamma < 667\,\mathrm{MeV}$.
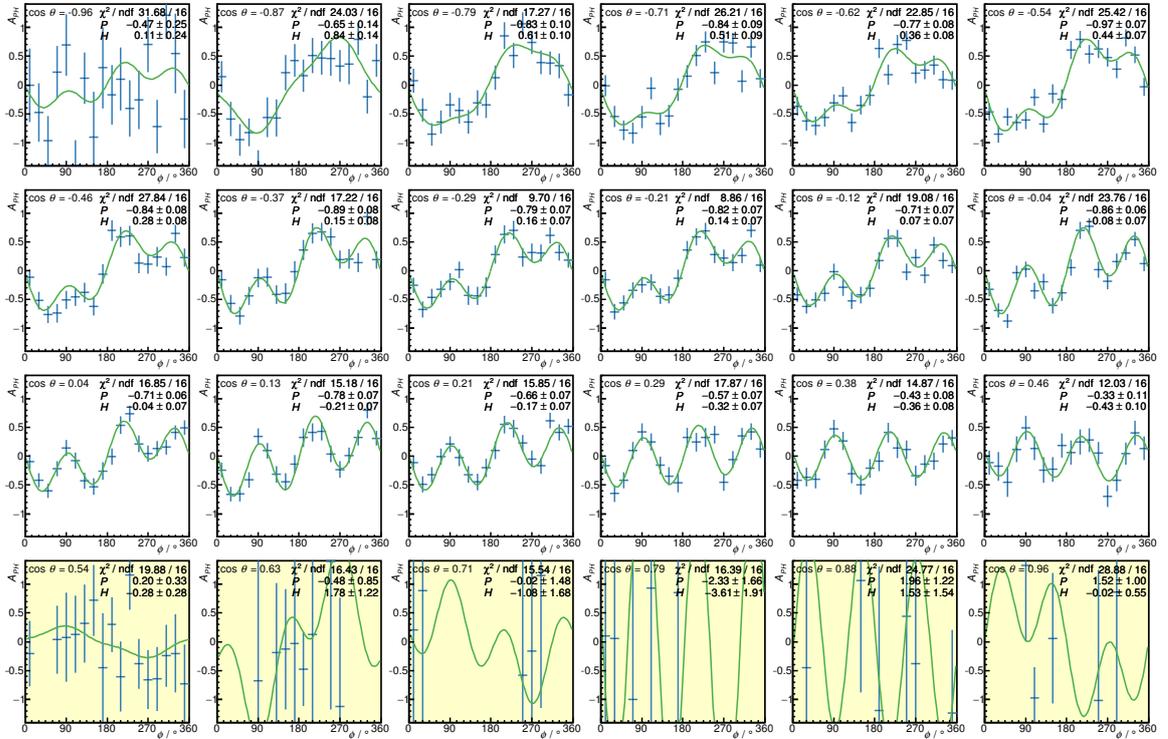
Figure B.37: Energy bin $667\,\mathrm{MeV} < E_\gamma < 700\,\mathrm{MeV}$.
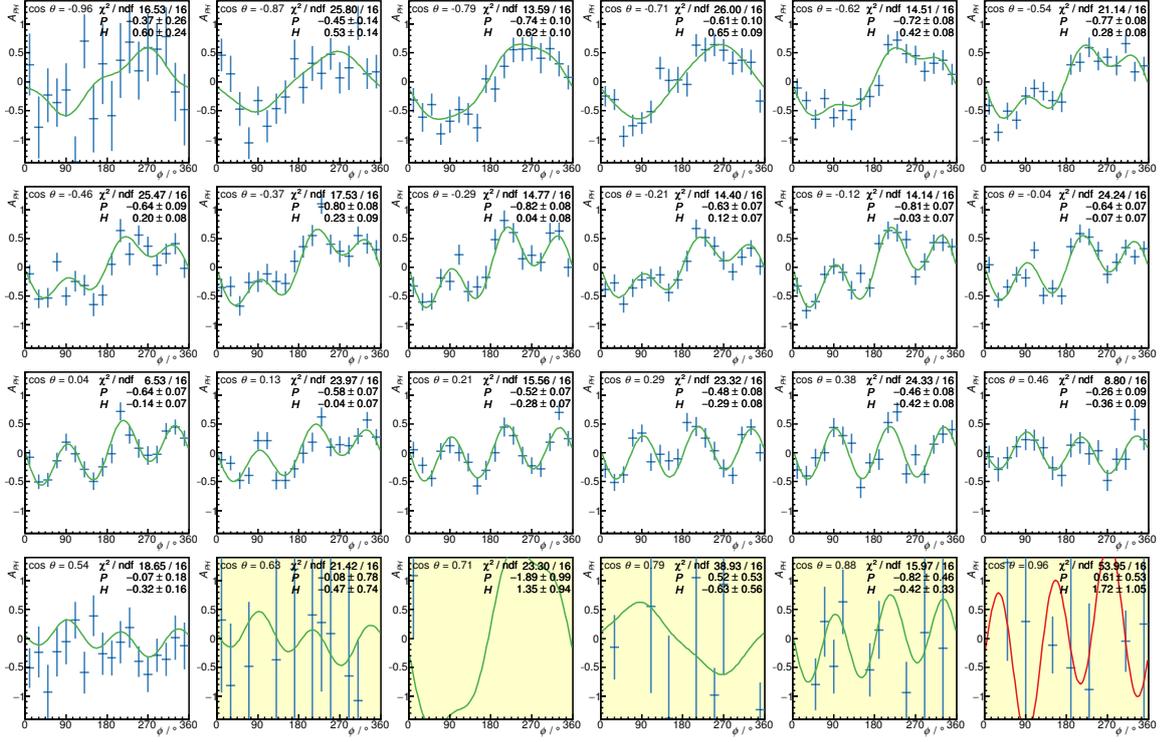
Figure B.38: Energy bin $700\,\mathrm{MeV} < E_\gamma < 732\,\mathrm{MeV}$.
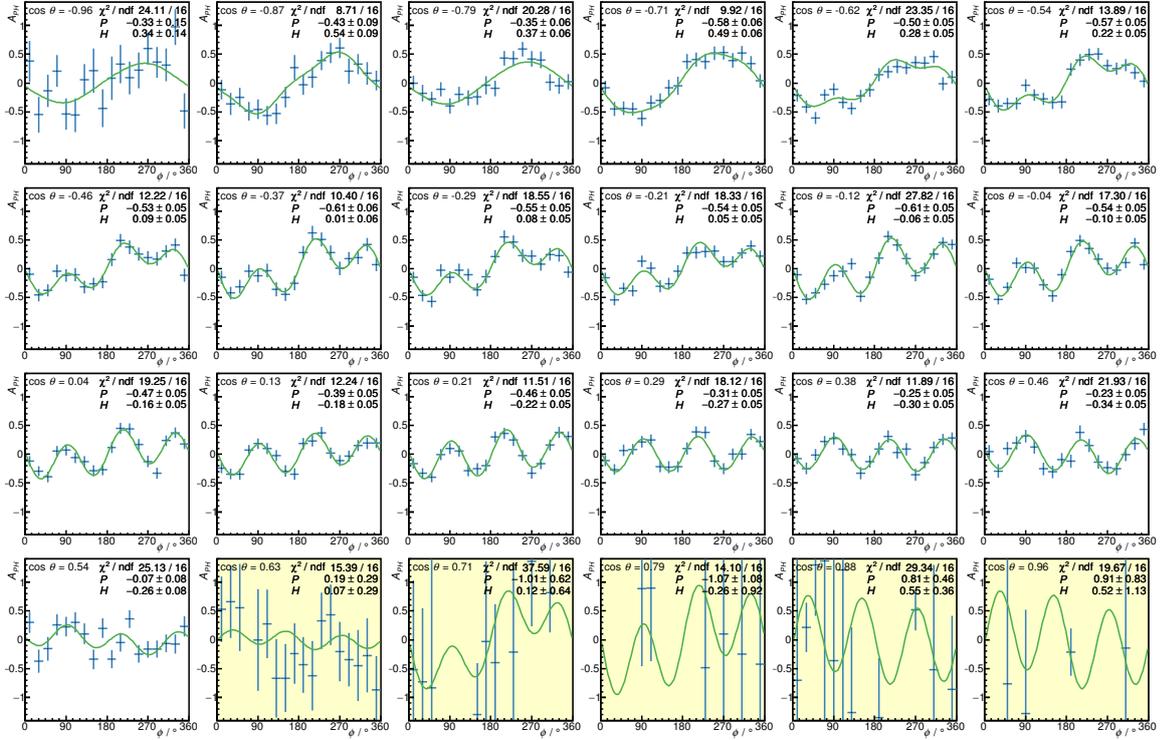
Figure B.39: Energy bin $732\,\mathrm{MeV} < E_\gamma < 768\,\mathrm{MeV}$.
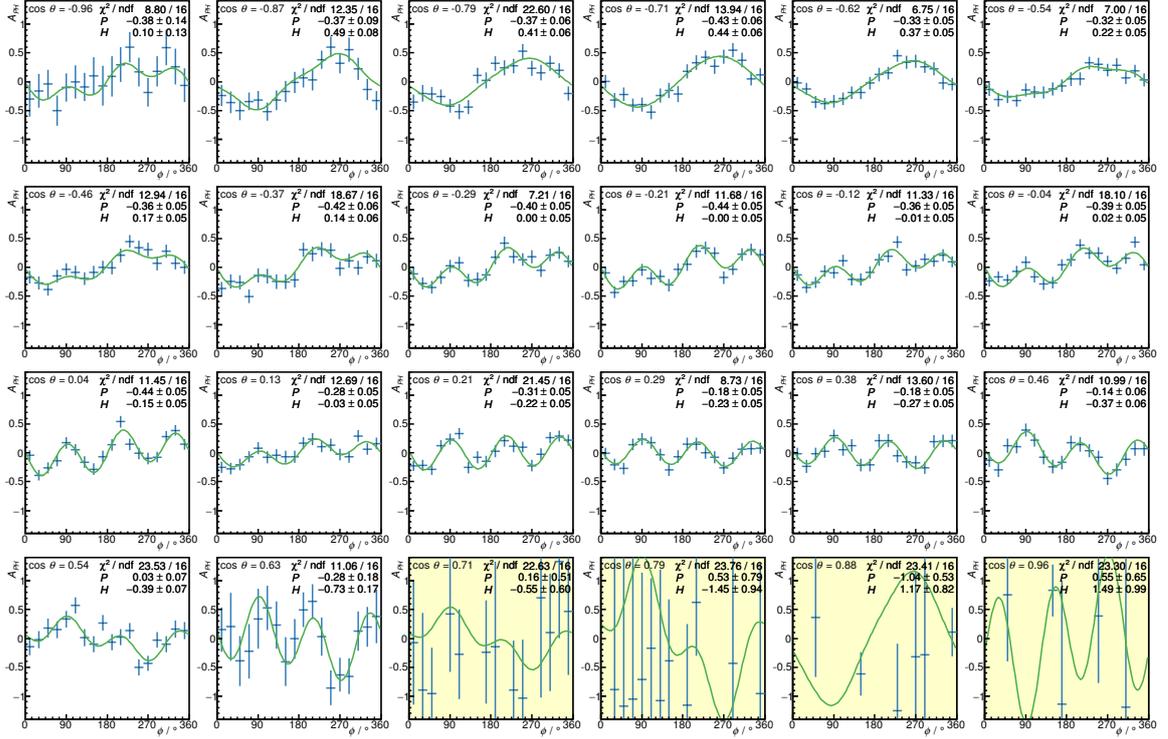
Figure B.40: Energy bin $768\,\text{MeV} < E_\gamma < 798\,\text{MeV}$.
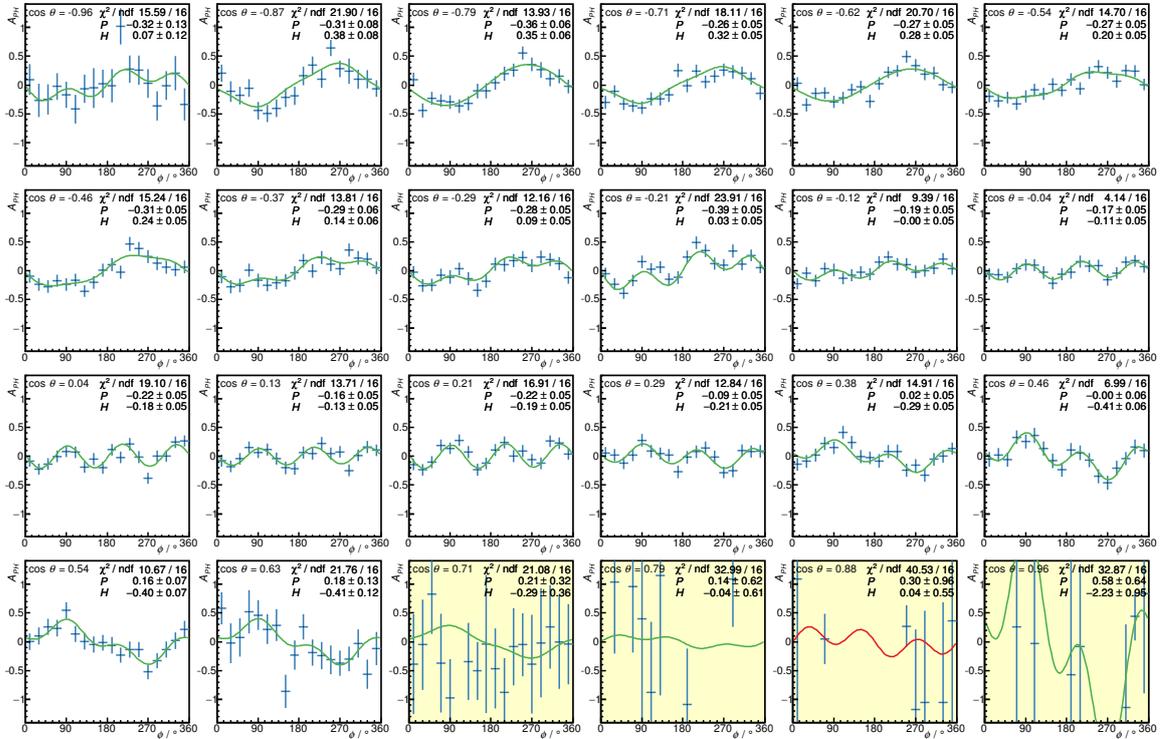
Figure B.41: Energy bin $798\,\text{MeV} < E_\gamma < 833\,\text{MeV}$.
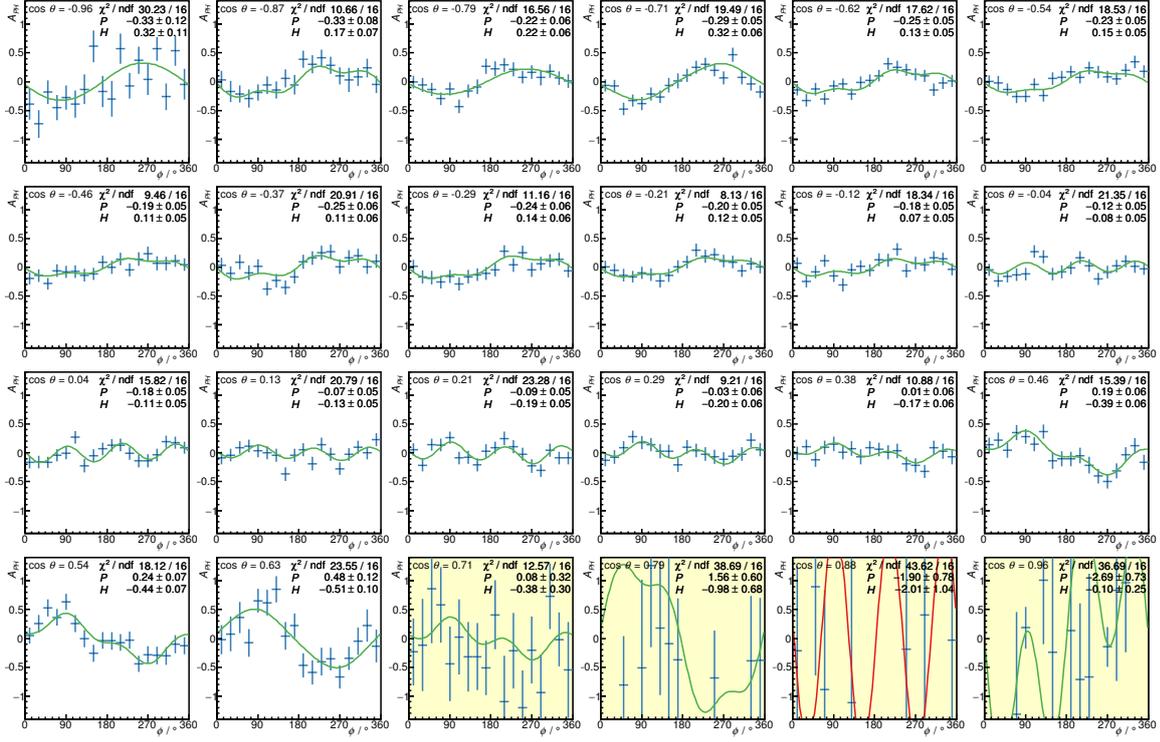
Figure B.42: Energy bin $833\,\mathrm{MeV} < E_\gamma < 868\,\mathrm{MeV}$.
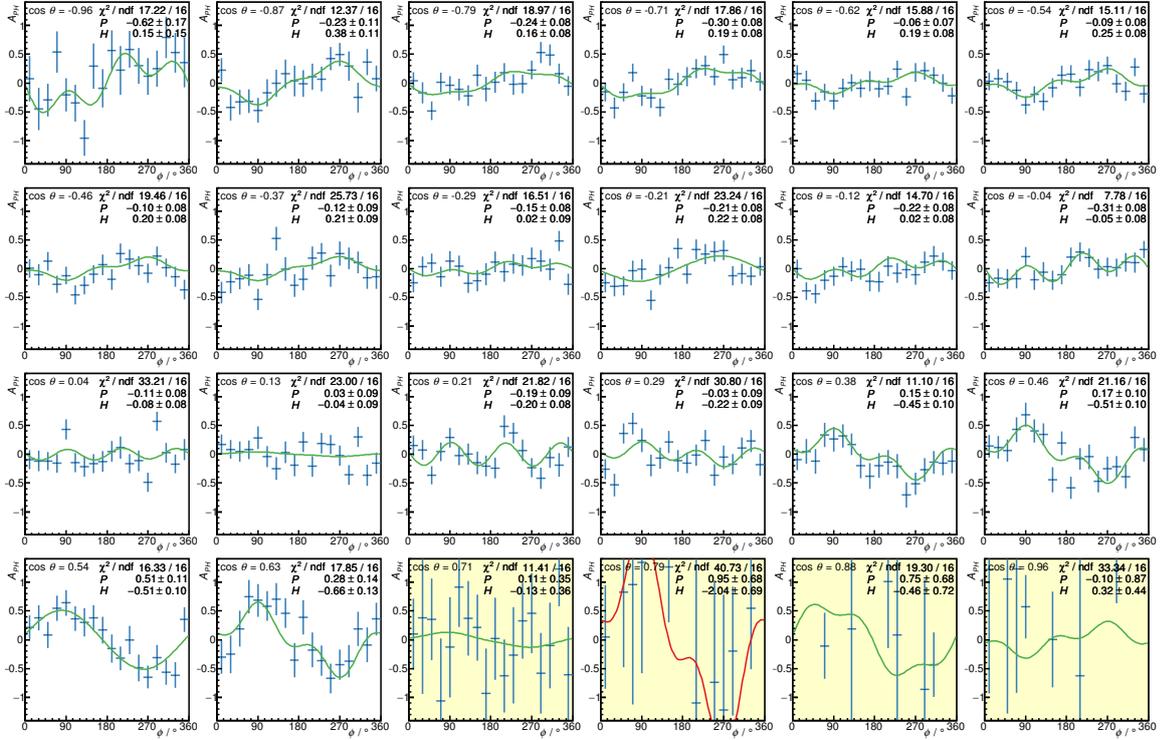
Figure B.43: Energy bin $868\,\mathrm{MeV} < E_\gamma < 901\,\mathrm{MeV}$.
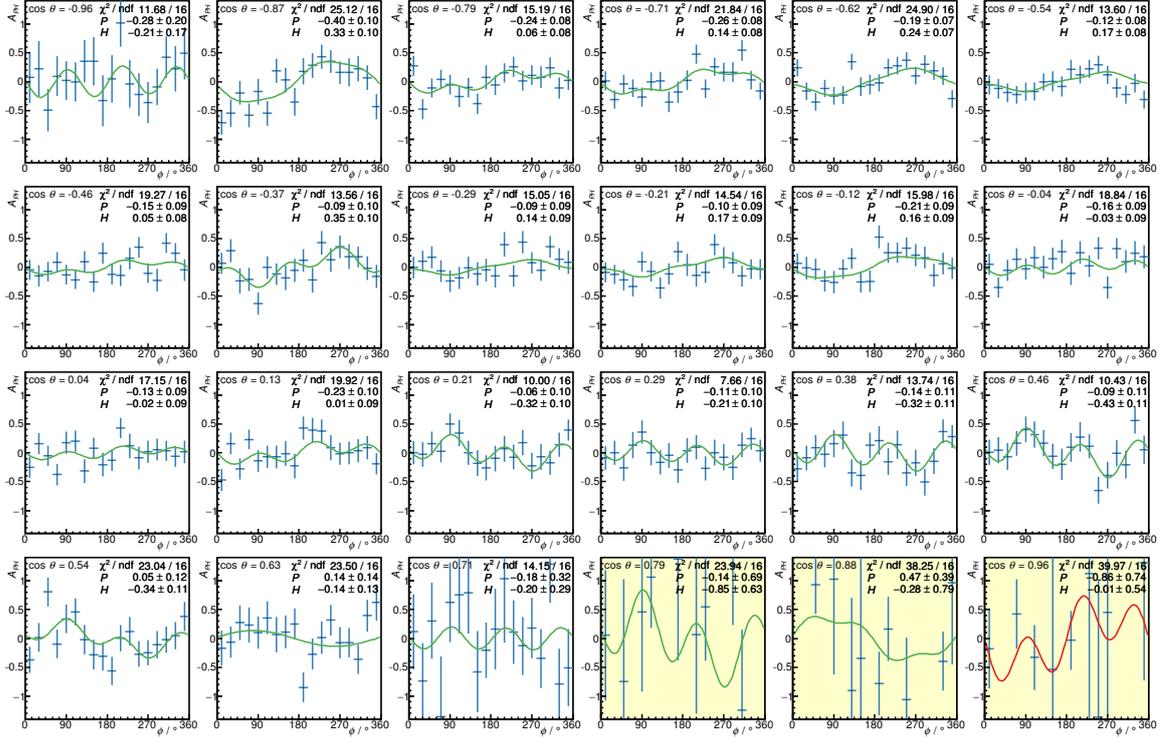
Figure B.44: Energy bin 901 MeV < E_γ < 933 MeV.
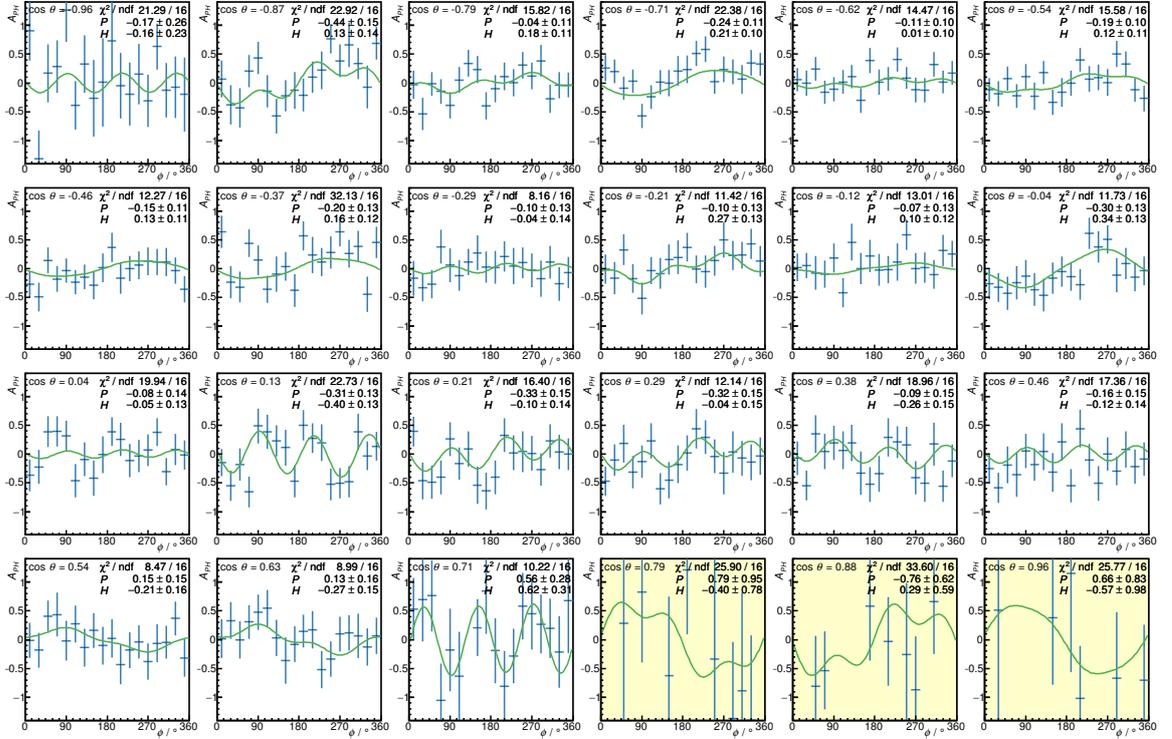
Figure B.45: Energy bin 933 MeV < E_γ < 974 MeV.

Appendix C

Cut Limits

The limits of the kinematic cuts used during the event selection (see Section 5.4) are shown here. The cut limits depend on the kinematic variables E_γ and $\cos\theta$. Their width corresponds to 2σ, i.e. they are set such that $\approx 95\,\%$ of the signal events are retained for each cut.

C.1 Reaction $\gamma p \rightarrow p \pi^0$
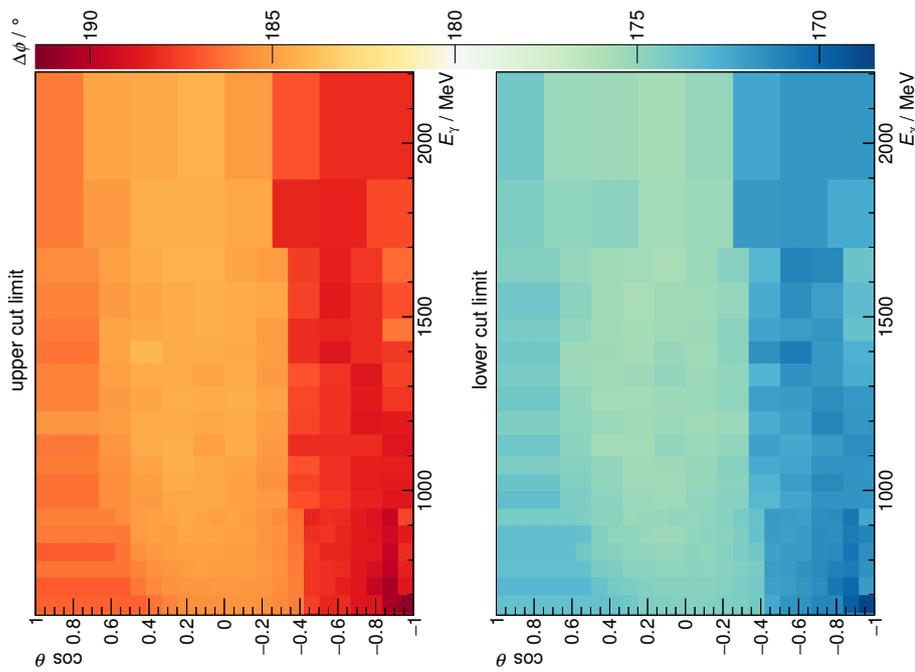
Figure C.1: Cut limits for the azimuthal angle difference $\Delta\phi$.
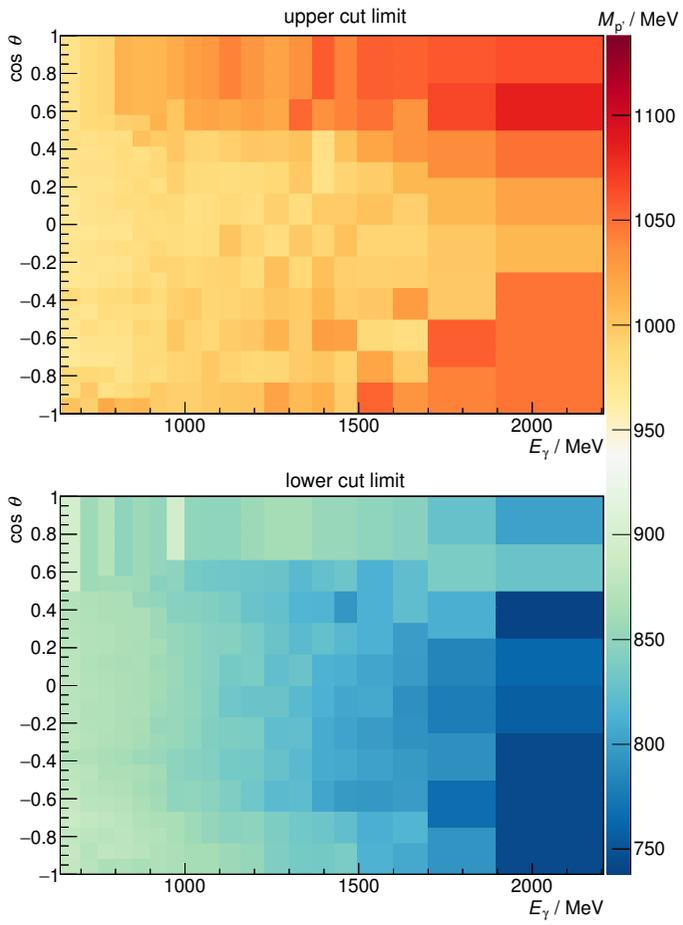
Figure C.3: Cut limits for the invariant mass $M_{p'}$ of the missing recoiling proton.
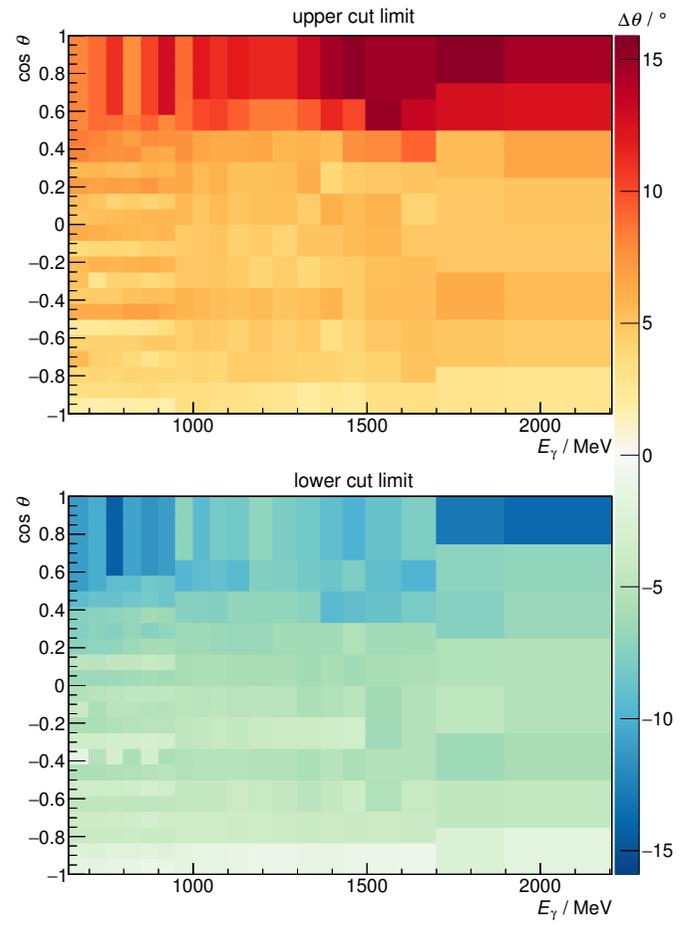
Figure C.2: Cut limits for the polar angle difference $\Delta\theta$.

Figure C.5: Cut limits for the azimuthal angle difference $\Delta\phi$.
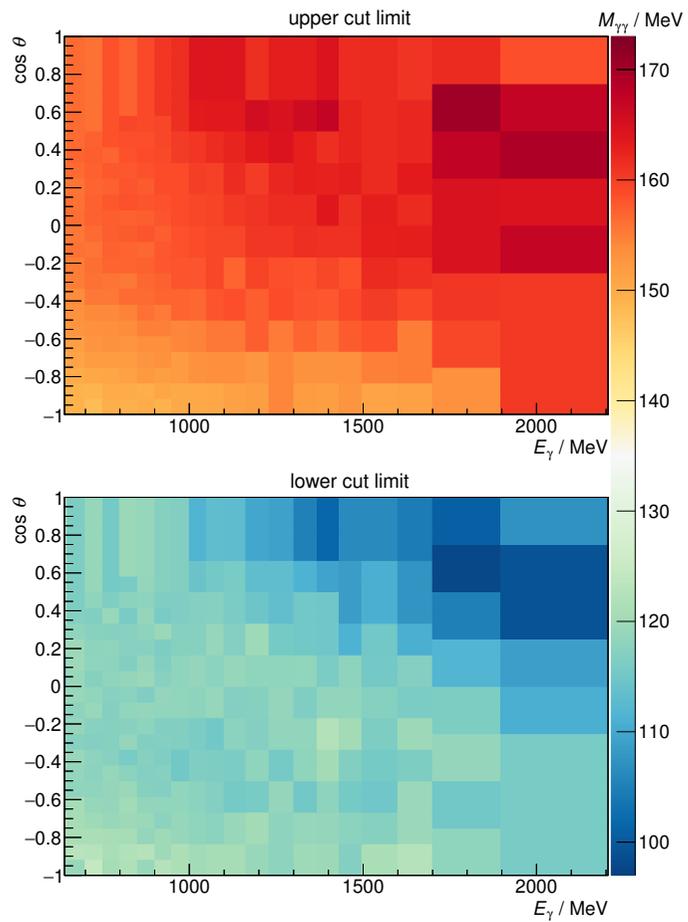
Figure C.4: Cut limits for the invariant mass $M_{\gamma\gamma}$ of the π^0.
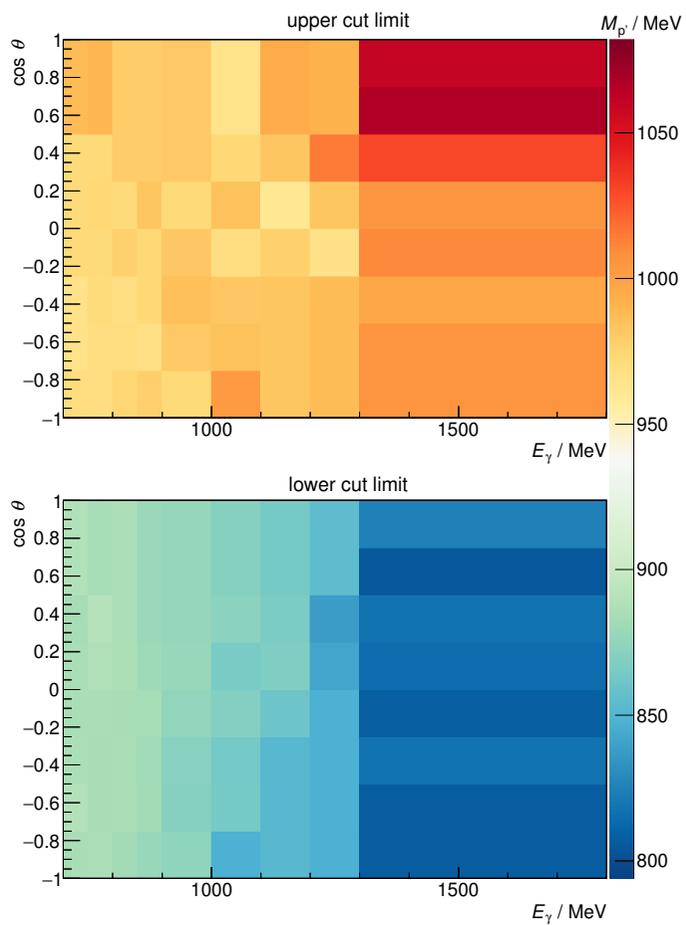
Figure C.7: Cut limits for the invariant mass $M_{p'}$ of the missing recoiling proton.
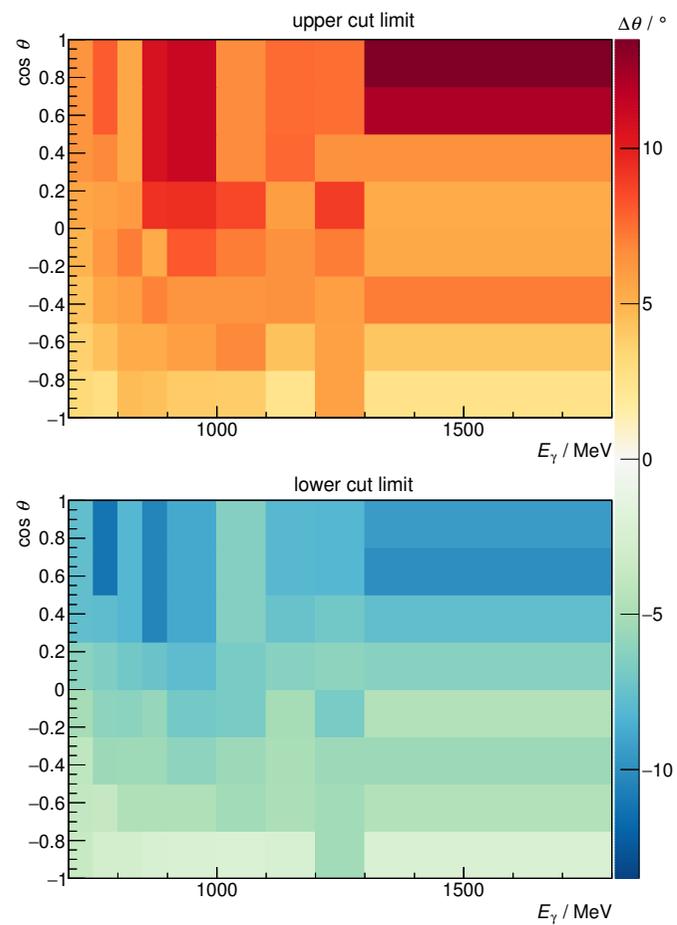
Figure C.6: Cut limits for the polar angle difference $\Delta\theta$.

Figure C.9: Cut limits for the azimuthal angle difference $\Delta\phi$.

Figure C.8: Cut limits for the invariant mass $M_{\gamma\gamma}$ of the η.
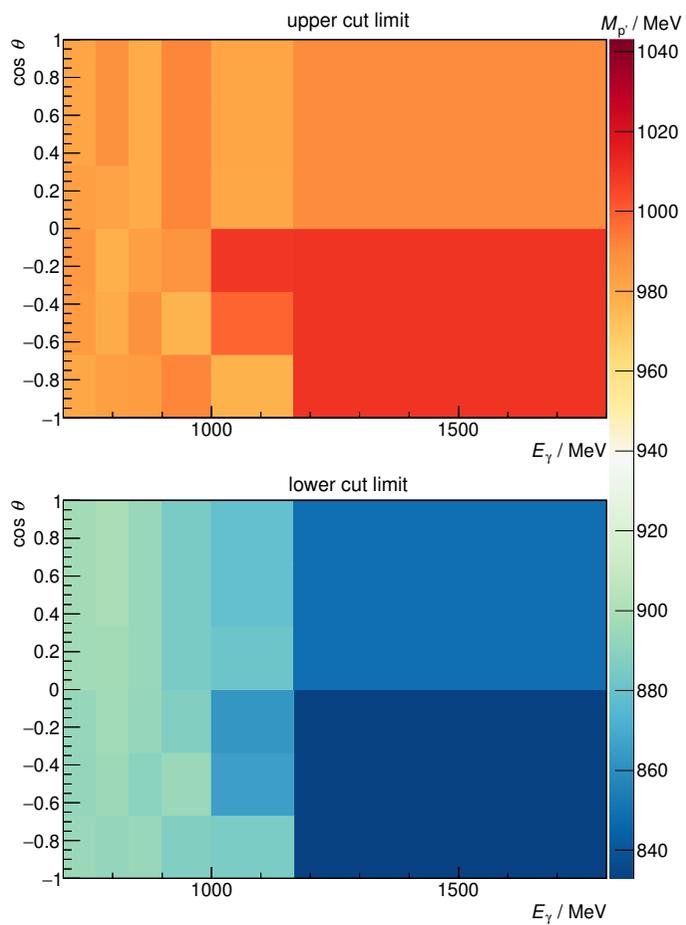
Figure C.11: Cut limits for the invariant mass $M_{p'}$ of the missing recoiling proton.
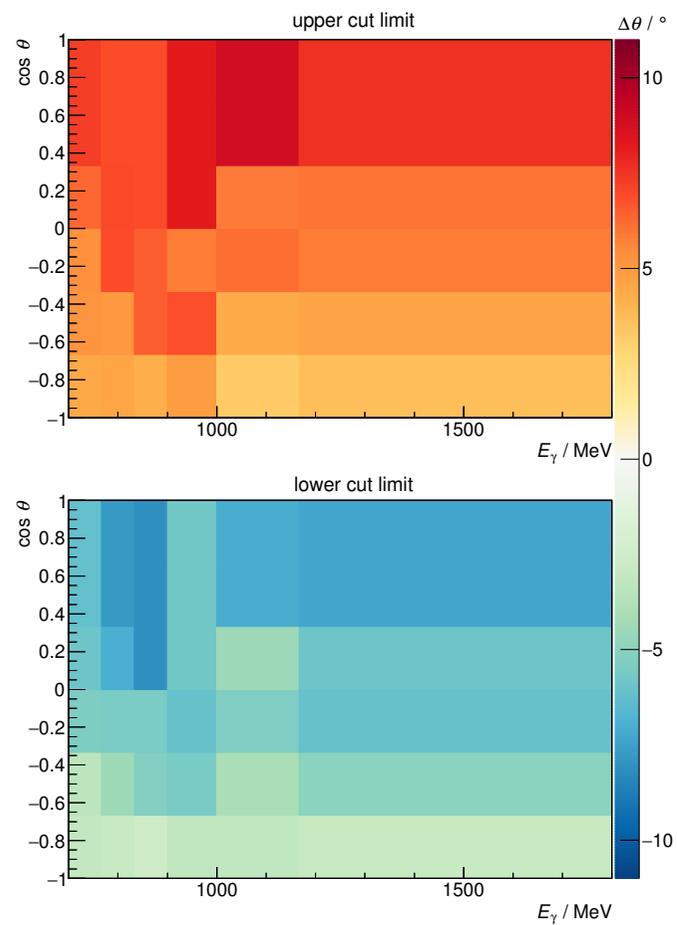
Figure C.10: Cut limits for the polar angle difference $\Delta\theta$.
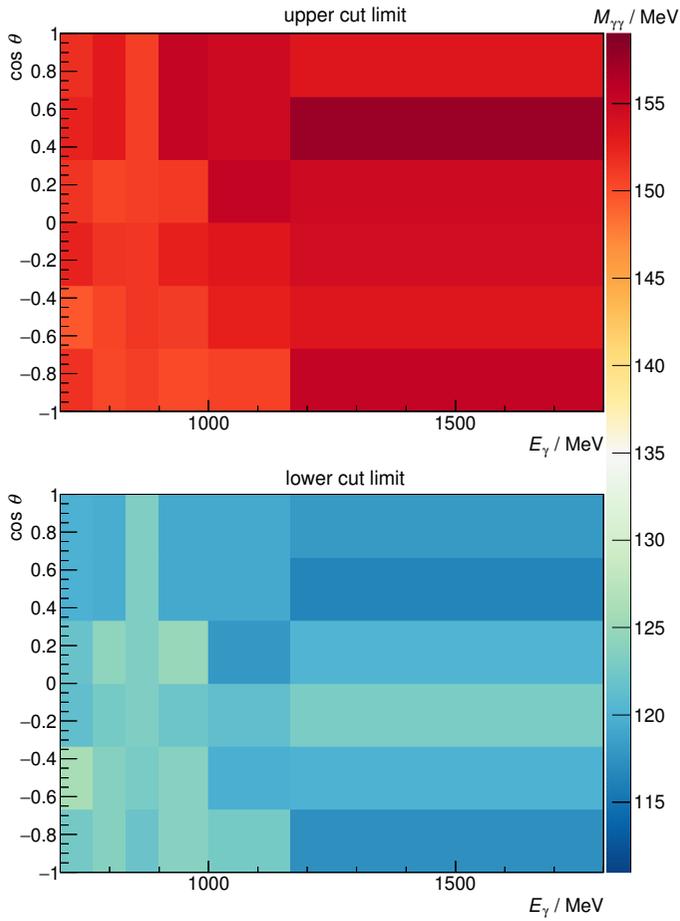
Figure C.13: Cut limits for the invariant mass $M_{\gamma\gamma}$ of the π^0 mesons from $\eta \rightarrow 3\pi^0$.
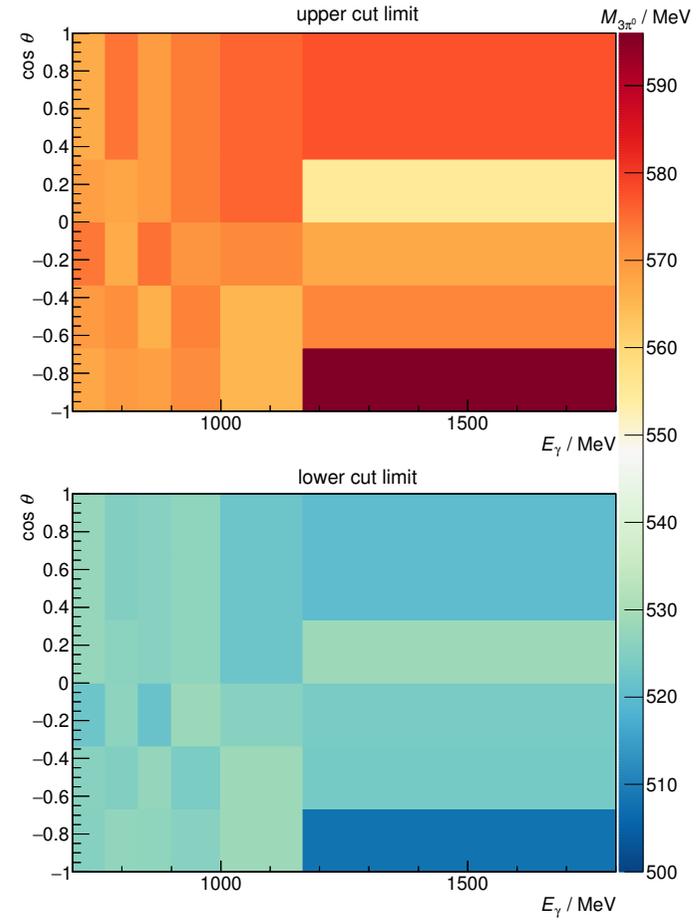
Figure C.12: Cut limits for the invariant mass $M_{3\pi^0}$ of the η.

Appendix D

Measurement of the GIM Efficiency

Initially, the idea of the FluMo detector was to allow for a measurement of the photon flux at rates higher than the saturation rate of the GIM, by measuring only a known—i.e. to be calibrated—fraction of the photons [Die08]. But as it turned out, the FluMo is also ideally suited to measure the detection efficiency of the GIM, as will be presented in this section. The GIM is designed to measure all impinging photons by detecting the Cherenkov light that is emitted in the PbF_2 crystals by the charged particles of the electromagnetic cascade that is produced by the high-energy photons. The FluMo only detects charged particles, i.e. electrons and positrons, that are produced in the conversion foil of the FluMo[1]. But these electrons and positrons also produce an electromagnetic cascade in the PbF_2 crystals, the GIM cannot distinguish them from photons. This allows a measurement of the detection efficiency of the GIM: all e^+e^- pairs measured by the FluMo also have to be detected by the GIM. The efficiency is therefore just given by the number of coincident hits in GIM and FluMo, normalized to all hits in the FluMo.

$$\varepsilon_{\text{GIM}} = \frac{N_{\text{FluMo}\wedge\text{GIM}}}{N_{\text{FluMo}}} \qquad \text{(D.1)}$$

To get the efficiency as a function of the photon energy E_γ, an additional coincidence with a hit in the Tagging System is required.

$$\varepsilon_{\text{GIM}}(E_\gamma) = \frac{N_{\text{Tagger}\wedge\text{FluMo}\wedge\text{GIM}}}{N_{\text{Tagger}\wedge\text{FluMo}}} \qquad \text{(D.2)}$$

The number of coincident hits can be determined by requiring the time difference between the hits in the different detectors to be smaller than $10\,\text{ns}$[2] and performing a sideband-subtraction to eliminate background due to random coincidences. For coincidences involving only two detectors this is a simple subtraction. However, for the triple coincidence Tagger $\wedge$ FluMo $\wedge$ GIM there are several classes of random coincidences:

$N^{\text{fully random}}$ Completely uncorrelated individual hits in all three detectors at the same time.

$N^{\text{FluMo random}}$ A coincident hit in the Tagger and the GIM, and an additional uncorrelated hit in the FluMo at the same time.

$N^{\text{GIM random}}$ A coincident hit in the Tagger and the FluMo, and an additional uncorrelated hit in the GIM at the same time.

---

[1] Or further upstream in case the veto scintillator did not detect them due to its efficiency being < 1.

[2] Corresponding $\approx 5\sigma$ of the combined time resolution.

$N^{\text{Tagger random}}$ A coincident hit in the GIM and the FluMo, and an additional uncorrelated hit in the Tagger at the same time.

$N^{\text{fully random}}$ can be determined by adding a different time offset to the measured times of the three detectors before applying the time cut. The other three are determined by adding only a time offset to the measured times of the corresponding uncorrelated detector. The resulting $N^{\text{FluMo random}}$, $N^{\text{GIM random}}$, and $N^{\text{Tagger random}}$ each also contain $N^{\text{fully random}}$. The full sideband subtraction is therefore done using

$$N_{\text{Tagger}\wedge\text{FluMo}\wedge\text{GIM}} - N^{\text{FluMo random}} - N^{\text{GIM random}} - N^{\text{Tagger random}}$$
$$+ 2\, N^{\text{fully random}}. \quad \text{(D.3)}$$

To determine the efficiency of the GIM without any deadtime effects due to high rates (which is discussed in Section 6.1.2.2), the efficiency measurement needs to be performed at a low beam current such that the condition

$$\dot{N} \cdot t_{\text{DPR}} \ll 1 \qquad (\text{with } t_{\text{DPR}} \approx 12\,\text{ns}) \qquad\qquad \text{(D.4)}$$

is fulfilled, i.e. for $\dot{N} \lesssim 100\,\text{kHz}$. The resulting GIM efficiency is shown in Fig. D.1. It approaches $98\,\%$ at high E_γ and drops significantly below $E_\gamma \lesssim 1\,\text{GeV}$ because of the threshold of the readout electronics.
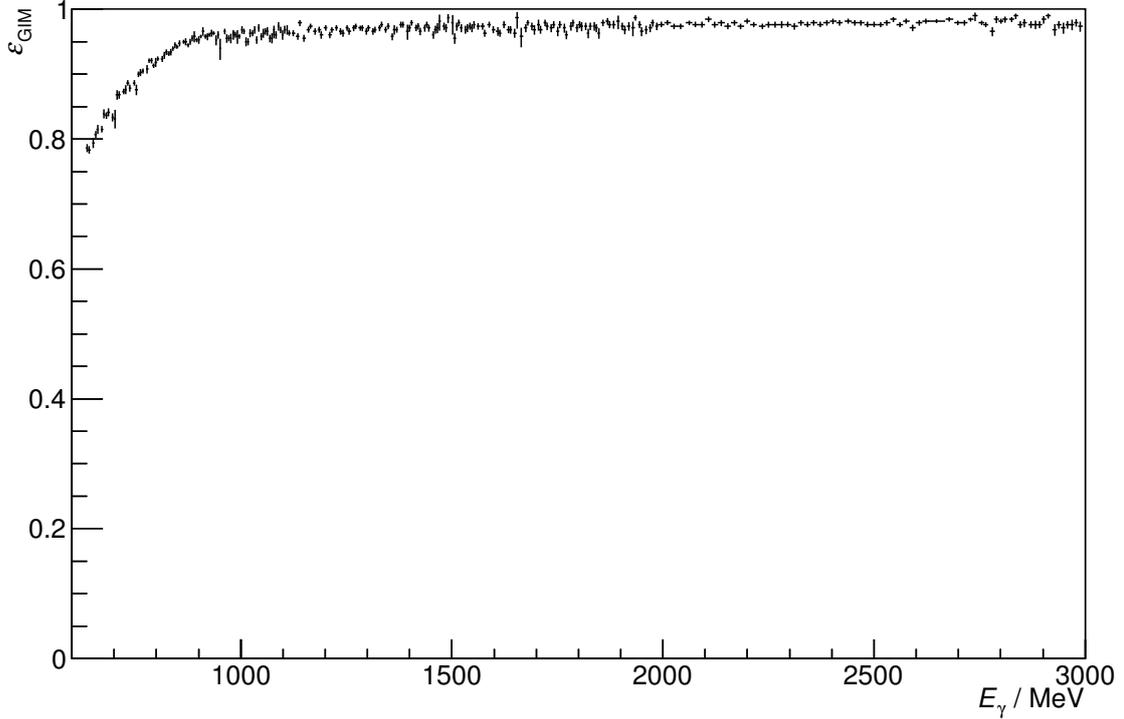
Figure D.1: The GIM efficiency ε as a function of the beam photon energy E_γ.

Appendix E

Discussion of Systematic Deviations from MAMI results for T in $\gamma p \to p\eta$

As was discussed in Section 8.1.2 there is, for the observable T in the reaction $\gamma p \to p\eta$, a systematic discrepancy between the results from this work and the results from the A2 collaboration at MAMI [Ako+14]. Even though the source of the discrepancy is more likely to be found in the MAMI data (cf. Section 8.1.2), a quantitative discussion of the deviations is indispensable. A direct comparison is severely complicated by the different binning used for the two analyses. Therefore, our analysis was repeated in the same $(E_\gamma, \cos\theta)$ bins that were used for the analysis of the MAMI data. The results are shown in Fig. E.1, together with the MAMI data. Again, it is clearly visible that the MAMI values are systematically smaller. As can be seen in Fig. E.2, where a histogram of the ratio of results from the two analyses is shown, the deviation is, on average, 40 %.

For a statistical comparison of the two results, the difference ΔT between the two results is calculated for each data point. Since the two experiments are completely independent, the statistical uncertainty of the difference is just given by the squared sum of the individual statistical uncertainties. All given point-to-point systematic uncertainties are significantly smaller than the statistical uncertainties and can be neglected. A histogram of the $\frac{\Delta T}{\sigma_{\Delta T}}$ for each bin is shown in Fig. E.3a. If the two data sets were compatible, the histogram would follow a normal distribution with mean $\mu = 0$ and width $\sigma = 1$. But since the MAMI results are at systematically smaller values, the distribution is of course shifted. If, however, the MAMI data are multiplied by a factor of 1.4, the two data sets are in perfect agreement, as can be seen in Fig. E.3b. It can therefore be concluded that the two data sets are fully compatible except for a global normalization factor. The most probable systematic error that can explain such a behavior is the target polarization degree. All other sources of systematic errors, e.g. the effective dilution factor or background contamination, should depend on E_γ and θ. If one assumes that only one of the two experiments made an error in the determination of the target polarization degree Λ, the two possible scenarios are:

1. Our measured target polarization is too small
   $\rightsquigarrow \Lambda_{\mathrm{ELSA}}^{\mathrm{real}} = \Lambda_{\mathrm{ELSA}}^{\mathrm{measured}} \cdot 1.4$

2. The target polarization measured by the A2 collaboration is too large
   $\rightsquigarrow \Lambda_{\mathrm{MAMI}}^{\mathrm{real}} = \Lambda_{\mathrm{MAMI}}^{\mathrm{measured}}/1.4$

However, scenario 1 can immediately be excluded: Our average measured polarization is $(74.2 \pm 1.5)\,\%$. Multiplying it by a factor 1.4 would result in a polarization degree > 1, which is impossible.

As an additional cross check, to exclude the (unlikely) case that both measurements are wrong, our results for the observable T in the reaction $\gamma p \to p\pi^0$, which are based on the same data set as the η analysis, can also be compared to previous measurements. The only existing measurement with large coverage in energy and angle was performed at the NINA synchrotron at Daresbury [Boo+77]. For a better comparison, our analysis was repeated at the same $(E_\gamma, \cos\theta)$ points as the NINA data. As can be seen in Fig. E.4, the average ratio of the two results is compatible with 1. A histogram of the difference for each data point, normalized to the statistical uncertainty, is compatible with a normal distribution with mean $\mu = 0$ and width $\sigma = 1$, as can be seen in Fig. E.5. This means that the two measurements are in good agreement, with no significant systematic deviation.

Very recently, the A2 collaboration at MAMI also published results on the target asymmetry T in the reaction $\gamma p \to p\pi^0$ [Ann+16]. Again, our analysis was repeated in the same $(E_\gamma, \cos\theta)$ bins that were used for the analysis of the MAMI data. The results are shown in Fig. E.6, the two data sets seem to be compatible. And indeed, the average ratio of the
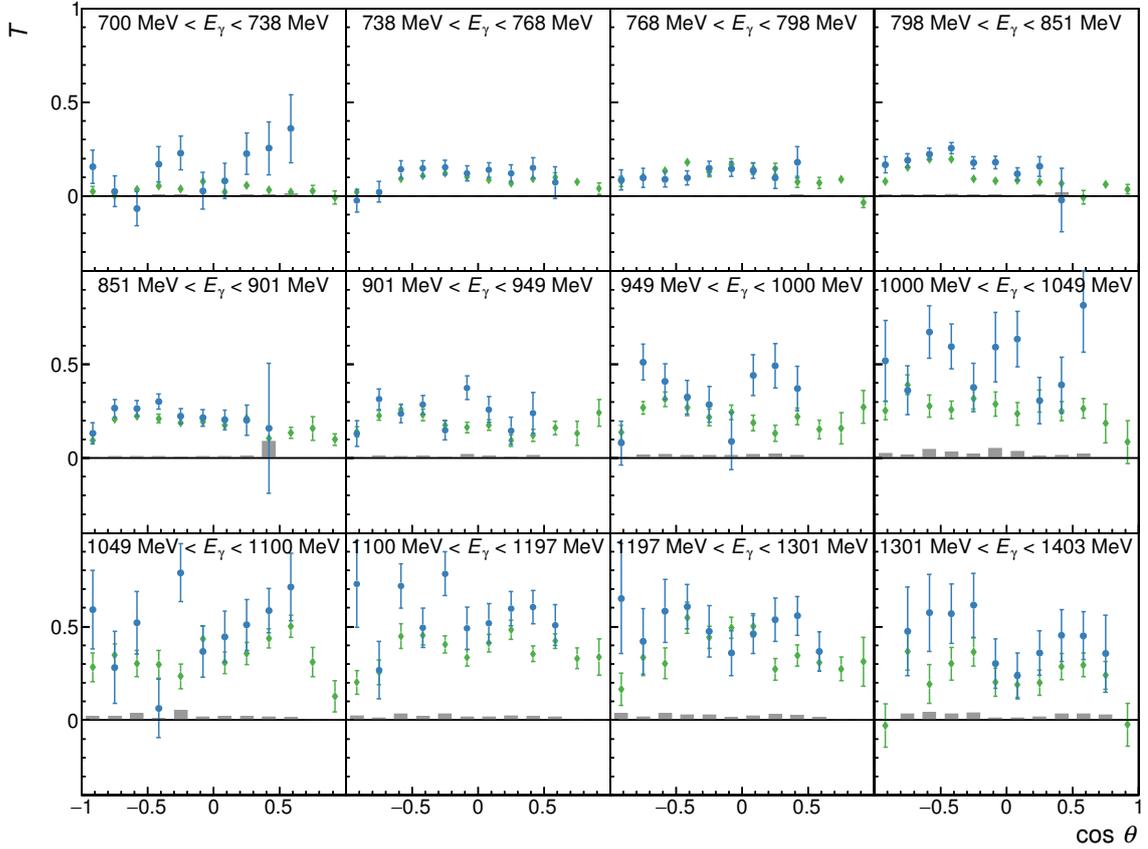
Figure E.1: The results for the target asymmetry T in the reaction $\gamma p \to p\eta$ (blue points, systematic uncertainty shown as gray bars), compared to the recently published results from MAMI [Ako+14] (green) which were measured in parallel to this work. For a better comparison, our analysis was repeated in the same $(E_\gamma, \cos\theta)$ bins that were used for the analysis of the MAMI data.
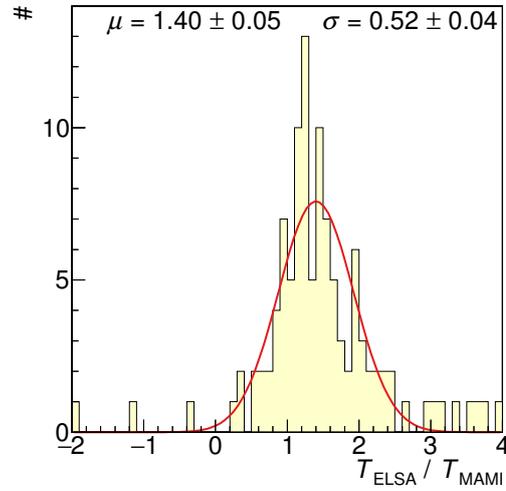
Figure E.2: The ratio between the values of T from this analysis and the recently published results from MAMI [Ako+14]. A Gaussian with mean μ and width σ was fitted to the histograms using the binned-likelihood method [BC84]. To exclude the outliers, which correspond do data points with large uncertainty, the fit range was limited to $0 \leq T_{\text{ELSA}}/T_{\text{MAMI}} \leq 3$.
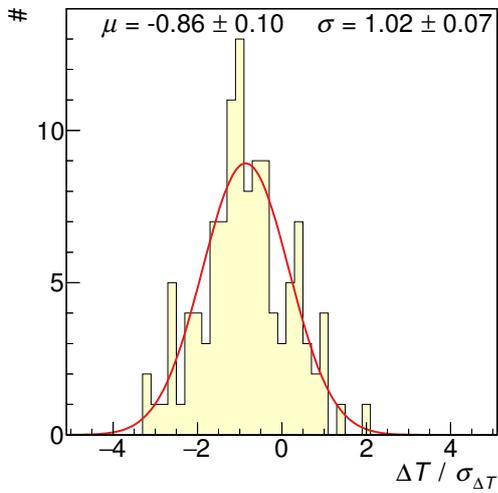
(a) MAMI data as published
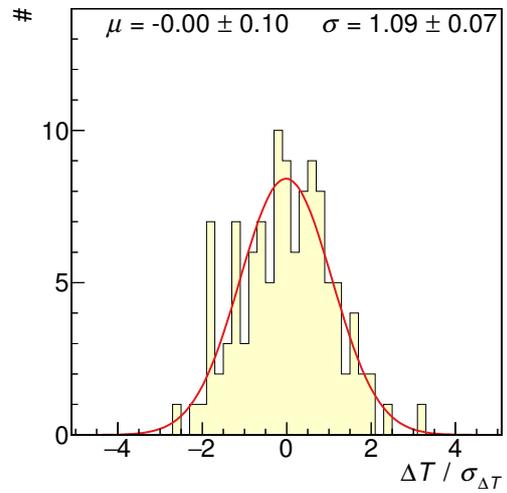
(b) MAMI data multiplied by factor 1.4

Figure E.3: Histograms of the difference $\Delta T = T_{\text{MAMI}} - T_{\text{ELSA}}$, normalized to the statistical uncertainty $\sigma_{\Delta T} = \sqrt{\sigma_{T_{\text{MAMI}}}^2 + \sigma_{T_{\text{ELSA}}}^2}$, between the results from this analysis and the recently published results from MAMI [Ako+14]. A Gaussian with mean μ and width σ was fitted to the histograms using the binned-likelihood method [BC84]. Only if the MAMI results are multiplied by a factor 1.4 are the two data sets in good agreement.
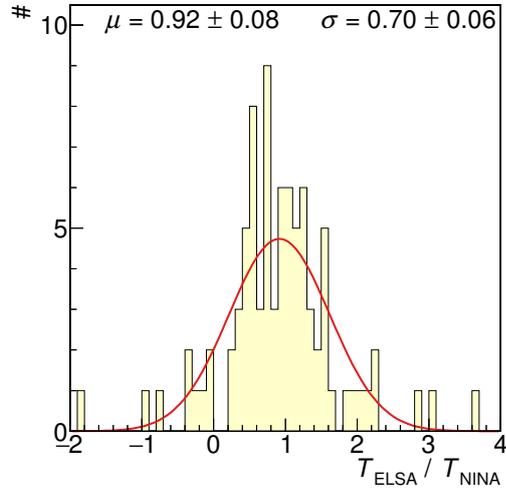
Figure E.4: The ratio between the values of T from this analysis and the older results from NINA [Boo+77]. A Gaussian with mean μ and width σ was fitted to the histograms using the binned-likelihood method [BC84]. To exclude the outliers, which correspond do data points with large uncertainty, the fit range was limited to $-1. \leq T_{\mathrm{ELSA}}/T_{\mathrm{NINA}} \leq 3.5$.
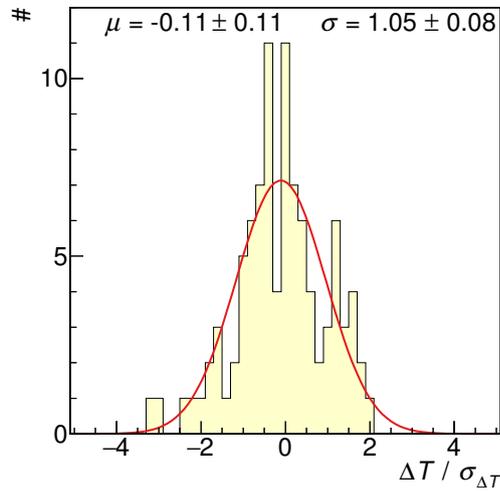
Figure E.5: Histogram of the difference $\Delta T = T_{\mathrm{NINA}} - T_{\mathrm{ELSA}}$, normalized to the statistical uncertainty $\sigma_{\Delta T} = \sqrt{\sigma_{T_{\mathrm{NINA}}}^2 + \sigma_{T_{\mathrm{ELSA}}}^2}$, between the results from this analysis and the older results from NINA [Boo+77]. A Gaussian with mean μ and width σ was fitted to the histograms using the binned-likelihood method [BC84].
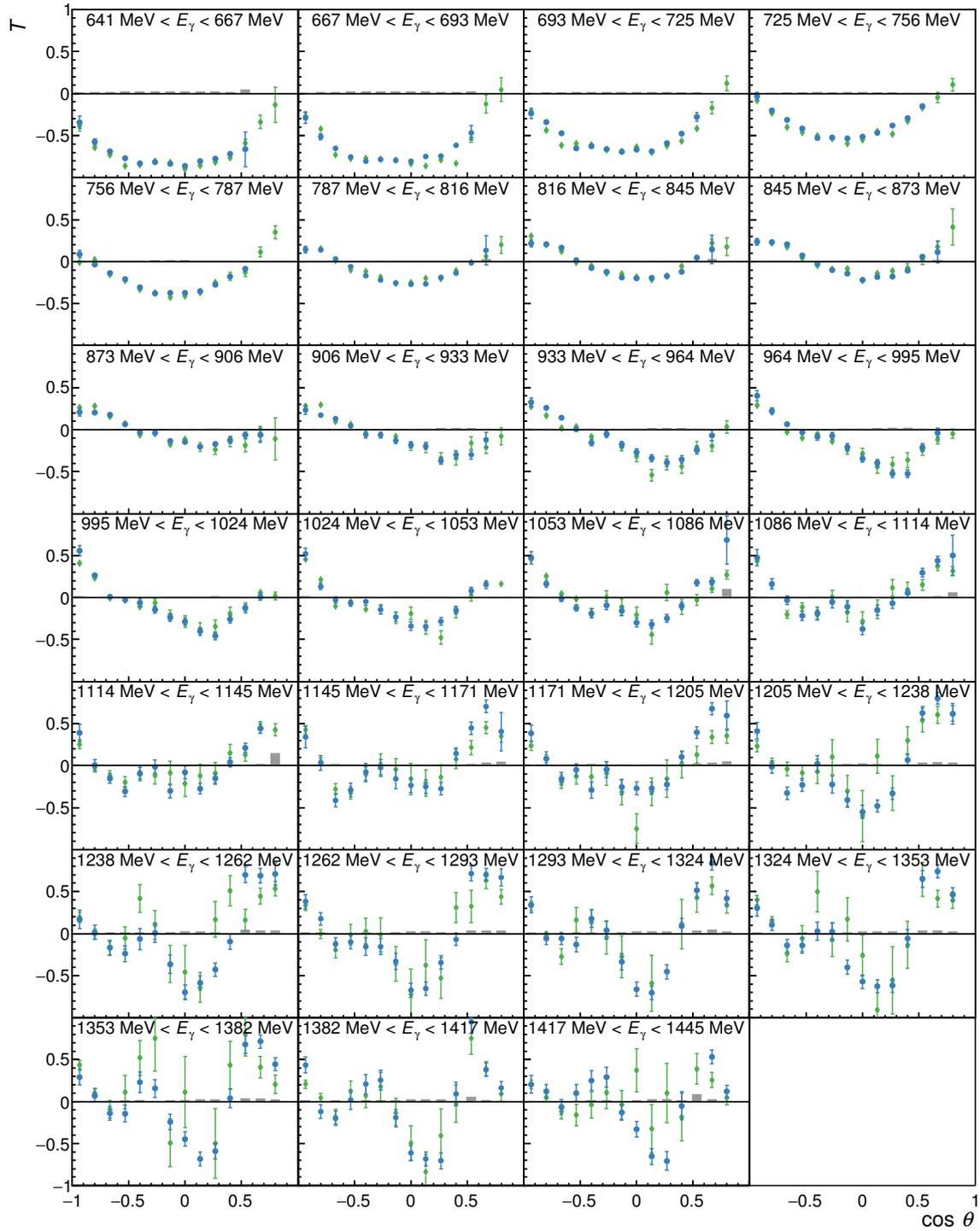
Figure E.6: The results for the target asymmetry T in the reaction $\gamma p \rightarrow p\pi^0$ (blue points, systematic uncertainty shown as gray bars), compared to the very recently published results from MAMI [Ann+16] (green) which were measured in parallel to this work. For a better comparison, our analysis was repeated in the same $(E_\gamma, \cos\theta)$ bins that were used for the analysis of the MAMI data.
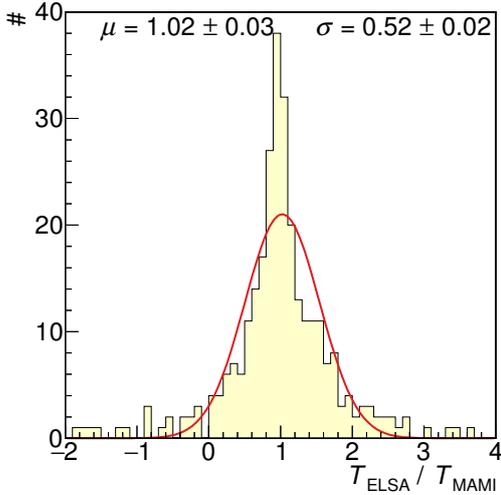
Figure E.7: The ratio between the values of T from this analysis and the very recent results from MAMI [Ann+16]. A Gaussian with mean μ and width σ was fitted to the histograms using the binned-likelihood method [BC84]. To exclude the outliers, which correspond do data points with large uncertainty, the fit range was limited to $-0.5 \leq T_{\text{ELSA}}/T_{\text{MAMI}} \leq 2.5$.
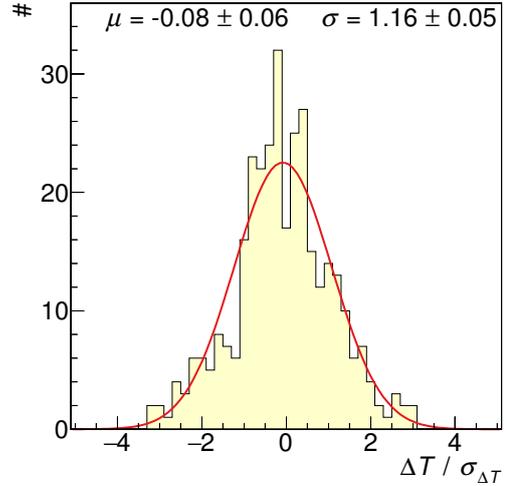
Figure E.8: A Histogram of the difference $\Delta T = T_{\text{MAMI}} - T_{\text{ELSA}}$, normalized to the statistical uncertainty $\sigma_{\Delta T} = \sqrt{\sigma_{T_{\text{MAMI}}}^2 + \sigma_{T_{\text{ELSA}}}^2}$, between the results from this analysis and the very recent results from MAMI [Ann+16]. A Gaussian with mean μ and width σ was fitted to the histograms using the binned-likelihood method [BC84].

two results is compatible with 1, as can be seen in Fig. E.7. A histogram of the difference for each data point, normalized to the statistical uncertainty, is compatible with a normal distribution with mean $\mu = 0$, as can be seen in Fig. E.8. The width σ is $\approx 15\,\%$ larger than 1 ($3\sigma_\sigma$ deviation), because all given systematic uncertainties of both data sets have been neglected. Since the statistical errors are smaller compared to the η reaction, the systematic errors have a significant, but nevertheless still small, contribution to the π^0 reaction. Thus, the two data sets for the reaction $\gamma p \rightarrow p\pi^0$ are in excellent agreement.

In summary, the systematic deviations from the MAMI results for T in the reaction $\gamma p \rightarrow p\eta$ are rather mysterious. The deviations can be explained by a global factor of ≈ 1.4. However, this deviation is not observed in the reaction $\gamma p \rightarrow p\pi^0$, where both our results and the MAMI results are based on exactly the same measurements as for the η reaction. That should exclude any errors in the determination of the target polarization degree, since these would influence both reactions in the same way.

Our results for both the π^0 and the η reactions are obtained using exactly the same analysis method (using exactly the same software to analyze the data, and only changing the cuts in the event selection (cf. Section 5.4) to select either π^0 or η events), the source of the deviation can therefore be expected to be found in the MAMI data. As a final a remark, it might be noteworthy that the factor of ≈ 1.4 is numerically close to $\sqrt{2}$.

List of Figures

List of Tables

Bibliography

[Aad+12]   G. Aad et al. (ATLAS Collaboration),
            *Observation of a new particle in the search for the Standard Model Higgs
            boson with the ATLAS detector at the LHC*, Phys. Lett. B **716** (2012) 1,
            arXiv: `1207.7214 [hep-ex]`.

[ADK13]   C. Amsler, T. DeGrand, and B. Krusche, *Quark Model*,
            in: The Review of Particle Physics [Oli+14] (2013) 259.

[Afo07]   S. S. Afonin, *Parity Doubling in Particle Physics*, in: 41st Annual Winter
            School on Nuclear and Particle Physics (PNPI 2007) Repino, St. Petersburg,
            Russia, February 19-March 2, 2007. Int. J. Mod. Phys. A **22** (2007) 4537,
            arXiv: `0704.1639 [hep-ph]`.

[Aga+89]   K. S. Agababian, A. A. Belyaev, G. A. Vartapetian, et al.,
            *Measurement of Polarization Parameters Σ, T, and P in π^0
            Photoproduction at $E(\gamma) = 0.9$ GeV – 1.35 GeV . (In Russian)*,
            Yad. Fiz. **50** (1989) 1341.

[Ago+03]   S. Agostinelli et al. (GEANT4 Collaboration),
            GEANT4: A Simulation toolkit, Nucl. Instrum. Meth. A **506** (2003) 250.

[AHK13]   D. Asner, C. Hanhart, and E. Klempt, *Resonances*,
            in: The Review of Particle Physics [Oli+14] (2013) 513.

[Ake+92]   E. Aker et al. (Crystal Barrel Collaboration),
            The Crystal Barrel spectrometer at LEAR,
            Nucl. Instrum. Meth. A **321** (1992) 69.

[Ako+14]   C. S. Akondi et al. (A2 Collaboration at MAMI),
            *Measurement of the Transverse Target and Beam-Target Asymmetries in η
            Meson Photoproduction at MAMI*, Phys. Rev. Lett. **113** (2014) 102001,
            arXiv: `1408.3274 [nucl-ex]`.

[Ani+05a]   A. V. Anisovich, A. Sarantsev, O. Bartholomy, et al.,
            Photoproduction of baryons decaying into $N\pi$ and $N\eta$,
            Eur. Phys. J. A **25** (2005) 427, arXiv: `hep-ex/0506010`.

[Ani+05b]   A. Anisovich, E. Klempt, A. Sarantsev, and U. Thoma,
            Partial wave decomposition of pion and photoproduction amplitudes,
            Eur. Phys. J. A **24** (2005) 111, arXiv: `hep-ph/0407211`.

[Ani+10]   A. V. Anisovich, E. Klempt, V. A. Nikonov, et al.,
            *Photoproduction of pions and properties of baryon resonances from a
            Bonn-Gatchina partial wave analysis*, Eur. Phys. J. A **44** (2010) 203,
            arXiv: `0911.5277 [hep-ph]`.

Bibliography

[Ani+11]   A. V. Anisovich, E. Klempt, V. A. Nikonov, et al.,
           Nucleon resonances in the fourth resonance region,
           Eur. Phys. J. A **47** (2011) 153, arXiv: `1109.0970` `[hep-ph]`.

[Ani+12]   A. V. Anisovich, R. Beck, E. Klempt, et al.,
           Properties of baryon resonances from a multichannel partial wave analysis,
           Eur. Phys. J. A **48** (2012) 15, arXiv: `1112.4937` `[hep-ph]`.

[Ani+13]   A. V. Anisovich, E. Klempt, V. A. Nikonov, et al.,
           Sign ambiguity in the $K\Sigma$ channel, Eur. Phys. J. A **49** (2013) 158,
           arXiv: `1310.3610` `[nucl-ex]`.

[Ani+15]   A. V. Anisovich, E. Klempt, V. A. Nikonov, et al.,
           Bonn-Gatchina Partial Wave Analysis, 2015,
           URL: `http://pwa.hiskp.uni-bonn.de/`.

[Ani+16]   A. V. Anisovich, R. Beck, M. Döring, et al., *The Impact of new polarization
           data from Bonn, Mainz, and Jefferson Laboratory on $\gamma p \to \pi N$ multipoles*,
           Eur. Phys. J. A **52** (2016) 284, arXiv: `1604.05704` `[nucl-th]`.

[Ani+17]   A. V. Anisovich, V. Burkert, J. Hartmann, et al.,
           *Evidence for $\Delta(2200)7/2^-$ from photoproduction and consequence for
           chiral-symmetry restoration at high mass*, Phys. Lett. B **766** (2017) 357,
           arXiv: `1503.05774` `[nucl-ex]`.

[Ann+16]   J. R. M. Annand et al. (A2 Collaboration at MAMI),
           T and F asymmetries in π^0 photoproduction on the proton,
           Phys. Rev. C **93** (2016) 055209.

[Ans+93]   M. Anselmino, E. Predazzi, S. Ekelin, et al., *Diquarks*,
           Rev. Mod. Phys. **65** (1993) 1199.

[Arn+02]   R. A. Arndt, W. J. Briscoe, I. I. Strakovsky, and R. L. Workman,
           Analysis of pion photoproduction data, Phys. Rev. C **66** (2002) 055213,
           arXiv: `nucl-th/0205067`.

[Arn+95]   R. A. Arndt, I. I. Strakovsky, R. L. Workman, and M. M. Pavan, *Updated
           analysis of πN elastic scattering data to 2.1 GeV: The Baryon spectrum*,
           Phys. Rev. C **52** (1995) 2120, arXiv: `nucl-th/9505040`.

[Asa+86]   M. M. Asaturian, A. A. Belyaev, G. A. Vartapetian, et al.,
           *Polarization Parameters Σ, T, and P for the Reaction $\gamma p \to p\pi^0$ in the
           Energy Interval 0.9 GeV – 1.5 GeV at $\theta(\pi^0)$ center-of-mass = 120 degrees*,
           JETP Lett. **44** (1986) 341.

[Ave+99]   T. D. Averett et al., *A Solid polarized target for high luminosity experiments*,
           Nucl. Instrum. Meth. A **427** (1999) 440.

[Bar+05a] O. Bartalini et al. (GRAAL Collaboration), *Measurement of π^0
           photoproduction on the proton from 550 MeV to 1500 MeV at GRAAL*,
           Eur. Phys. J. A **26** (2005) 399.

[Bar+05b]   O. Bartholomy et al. (CB-ELSA Collaboration), *Neutral-Pion Photoproduction off Protons in the Energy Range 0.3 GeV < E_γ < 3 GeV*, Phys. Rev. Lett. **94** (2005) 012003, arXiv: `hep-ex/0407022`.

[Bar+07]   O. Bartalini et al. (GRAAL Collaboration), *Measurement of η photoproduction on the proton from threshold to 1500 MeV*, Eur. Phys. J. A **33** (2007) 169, arXiv: `0707.1385 [nucl-ex]`.

[Bar00]   O. Bartholomy, *Test und Modifikation des Lichtpulsersystems für de CB-ELSA-Detektor*, Diploma thesis: Rheinische Friedrich-Wilhelms-Universität Bonn, 2000.

[Bar89]   R. J. Barlow, *Statistics: A Guide to the Use of Statistical Methods in the Physical Science*, Wiley, 1989.

[BC84]   S. Baker and R. D. Cousins, *Clarification of the Use of Chi Square and Likelihood Functions in Fits to Histograms*, Nucl. Instrum. Meth. **221** (1984) 437.

[BDS13]   S. Bethke, G. Dissertori, and G. Salam, *Quantum Chromodynamics*, in: The Review of Particle Physics [Oli+14] (2013) 122.

[BDS75]   I. S. Barker, A. Donnachie, and J. K. Storrow, *Complete Experiments in Pseudoscalar Photoproduction*, Nucl. Phys. B **95** (1975) 347.

[Bel+83]   A. Belyaev, V. Getman, V. Gorbenko, et al., *Experimental Studies of the Σ, T, P Polarization Parameters and the $\gamma p \to p\pi^0$ Reaction Multipole Analysis in the First Resonance Region*, Nucl. Phys. B **213** (1983) 201.

[Ber+12]   J. Beringer et al. (Particle Data Group), *The Review of Particle Physics*, Physical Review D **86** (2012) 010001.

[Ber+14]   M. J. Berger, J. H. Hubbell, S. M. Seltzer, et al., *XCOM: Photon Cross Sections Database - NIST Standard Reference Database 8 (XGAM)*, 2014, URL: `http://www.nist.gov/pml/data/xcom/`.

[Ber+91]   V. Bernard, N. Kaiser, J. Gasser, and U.-G. Meißner, *Neutral pion photoproduction at threshold*, Phys. Lett. B **268** (1991) 291.

[BH34]   H. Bethe and W. Heitler, *On the Stopping of fast particles and on the creation of positive electrons*, Proc. Roy. Soc. Lond. A **146** (1934) 83.

[BKM91]   V. Bernard, N. Kaiser, and U.-G. Meißner, *Chiral perturbation theory in the presence of resonances: Application to $\pi\pi$ and πK scattering*, Nucl. Phys. B **364** (1991) 283.

[BKM95]   V. Bernard, N. Kaiser, and U.-G. Meißner, *Chiral prediction for the πN S-wave scattering length a^- to order $O(M_\pi^4)$*, Phys. Rev. C **52** (1995) 2185, arXiv: `hep-ph/9506204`.

Bibliography

[BKM96]   V. Bernard, N. Kaiser, and U.-G. Meißner,
           Neutral pion photoproduction off nucleons revisited,
           Z. Phys. C **70** (1996) 483, arXiv: hep-ph/9411287.

[Blu+86]   E. Blucher, B. Gittelman, B. K. Heltsley, et al.,
           Tests of Cesium Iodide Crystals for an Electromagnetic Calorimeter,
           Nucl. Instrum. Meth. A **249** (1986) 201.

[BMM11]   P. C. Bruns, M. Mai, and U.-G. Meißner,
           Chiral dynamics of the $S_{11}(1535)$ and $S_{11}(1650)$ resonances revisited,
           Phys. Lett. B **697** (2011) 254, arXiv: 1012.2233 [nucl-th].

[Boc+98]   A. Bock, G. Anton, W. Beulertz, et al., *Measurement of the target
           asymmetry of η and π^0 photoproduction on the proton,*
           Phys. Rev. Lett. **81** (1998) 534.

[Boo+77]   P. S. L. Booth, L. J. Carroll, G. R. Court, et al.,
           *The Polarized Target Asymmetry for Neutral Pion Photoproduction from
           Protons in the Photon Energy Range 0.7 GeV–1.45 GeV,*
           Nucl. Phys. B **121** (1977) 45.

[Bös06]   S. Böse, *Modifikation und Test des Lichtpulsersystems für den Crystal Barrel
           Aufbau an ELSA,*
           Diploma thesis: Rheinische Friedrich-Wilhelms-Universität Bonn, 2006.

[Bös15]   S. Böse, Private communication, 2015.

[BR97]   R. Brun and F. Rademakers,
           ROOT: An object oriented data analysis framework,
           in: New computing techniques in physics research V. Proceedings, 5th
           International Workshop, AIHENP '96, Lausanne, Switzerland, September
           2-6, 1996. Nucl. Instrum. Meth. A **389** (1997) 81.

[Bra+80]   A. S. Bratashevsky, V. G. Gorbenko, A. I. Derebchinsky, et al.,
           *Polarization of Recoil Protons from the Reaction $\gamma p \to \pi^0 p$ in the Photon
           Energy Range 450 MeV – 800 MeV,* Nucl. Phys. B **166** (1980) 525.

[Bra+86]   A. S. Bratashevsky, A. A. Zybalov, S. P. Karasev, et al., *Measurements of
           Polarization of Secondary Protons in the $\gamma p \to p\pi^0$ Reaction at $\theta(\pi) = 150$
           degrees CMS within the Range of $E(\gamma) = 0.45$ GeV – 0.7 GeV. (in russian),*
           Ukr. Fiz. Zh. (Russ. Ed.) **31** (1986) 1306.

[Bra+95]   A. Braghieri et al., *Total cross-section measurement for the three double pion
           production channels on the proton,* Phys. Lett. B **363** (1995) 46.

[Bra+99]   C. Bradtke, H. Dutz, H. Peschel, et al.,
           A new frozen-spin target for 4π particle detection,
           Nucl. Instrum. Meth. A **436** (1999) 430.

[Bri+15]   W. J. Briscoe, D. Schott, I. I. Strakovsky, and R. L. Workman,
           George Washington University Partial Wave Analysis, 2015,
           URL: http://gwdac.phys.gwu.edu/.

[Bru+87]   R. Brun, F. Bruyant, M. Maire, et al., *GEANT3*, (1987),
            eprint: `CERN-DD-EE-84-1`.

[Bus+79a]   P. J. Bussey, C. Raine, J. G. Rutherglen, et al.,
            Polarization Parameters in Neutral Pion Photoproduction,
            Nucl. Phys. B **154** (1979) 492.

[Bus+79b]   P. J. Bussey, J. G. Rutherglen, P. S. L. Booth, et al., *Measurements of the
            Double Polarization Parameters G and H in Neutral Pion Photoproduction*,
            Nucl. Phys. B **159** (1979) 383.

[Cas+98]   C. Caso et al., *The Review of Particle Physics*,
            European Physical Journal C **3** (1998).

[Cha+12]   S. Chatrchyan et al. (CMS Collaboration), *Observation of a new boson at a
            mass of 125 GeV with the CMS experiment at the LHC*,
            Phys. Lett. B **716** (2012) 30, arXiv: `1207.7235 [hep-ex]`.

[Che+57]   G. F. Chew, M. L. Goldberger, F. E. Low, and Y. Nambu,
            Relativistic dispersion relation approach to photomeson production,
            Phys. Rev. **106** (1957) 1345.

[Chi+03]   W.-T. Chiang, S. N. Yang, L. Tiator, et al.,
            A Reggeized model for eta and eta-prime photoproduction,
            Phys. Rev. C **68** (2003) 045202, arXiv: `nucl-th/0212106`.

[CHM52]   J. B. Cladis, W. N. Hess, and B. J. Moyer, *Nucleon Momentum
            Distributions in Deuterium and Carbon Inferred from Proton Scattering*,
            Phys. Rev. **87** (1952) 425.

[Chu+95]   S. U. Chung, J. Brose, R. Hackmann, et al.,
            Partial wave analysis in K matrix formalism, Annalen Phys. **4** (1995) 404.

[CI86]   S. Capstick and N. Isgur,
            Baryons in a Relativized Quark Model with Chromodynamics,
            Phys. Rev. D **34** (1986) 2809.

[CM97]   D. G. Crabb and W. Meyer,
            Solid polarized targets for nuclear and particle physics experiments,
            Ann. Rev. Nucl. Part. Sci. **47** (1997) 67.

[Cor+96]   R. M. Corless, G. H. Gonnet, D. E. G. Hare, et al.,
            On the LambertW function, Adv. Comput. Math. **5** (1996) 329.

[Cre+05]   V. Crede et al. (CB-ELSA Collaboration),
            Photoproduction of eta mesons off protons for 0.75 GeV < E_γ < 3 GeV,
            Phys. Rev. Lett. **94** (2005) 012004, arXiv: `hep-ex/0311045`.

[Cre+09]   V. Crede et al. (CBELSA/TAPS Collaboration),
            Photoproduction of η and η' mesons off protons,
            Phys. Rev. C **80** (2009) 055202, arXiv: `0909.1248 [nucl-ex]`.

[Cre01]   V. Credé, *CBGeant 1.08/01*, CB-Note, 2001.

[CSS08]   J. G. Cham, M. A. Slackenerny, and B. S. Smith, *I should be done in…: A context-changing model of characterizing bio-related buzz-concepts*, Intl. Journal of Temporal Deflective Behavior Vol. 4, No. 1071, 2008.

[CT97]   W.-T. Chiang and F. Tabakin, *Completeness rules for spin observables in pseudoscalar meson photoproduction*, Phys. Rev. C **55** (1997) 2054, arXiv: `nucl-th/9611053`.

[Cut+79]   R. E. Cutkosky, C. P. Forsyth, R. E. Hendrick, and R. L. Kelly, *Pion-Nucleon partial-wave amplitudes*, Phys. Rev. D **20** (1979) 2839.

[Dah08]   T. Dahlke, *Bestimmung einer winkelabhängigen Energiekorrekturfunktion für das TAPS-Kalorimeter des Crystal-Barrel/TAPS-Experimentes an ELSA*, Diploma thesis: Rheinische Friedrich-Wilhelms-Universität Bonn, 2008.

[Die+15]   F. Dietz et al. (CBELSA/TAPS Collaboration), *Photoproduction of ω mesons off protons and neutrons*, Eur. Phys. J. A **51** (2015) 6.

[Die08]   J. Dielmann, *Entwicklung, Aufbau und Test eines Detektors zur Bestimmung des Photonenflusses an der Bonner Photonenmarkierungsanlage*, Diploma thesis: Rheinische Friedrich-Wilhelms-Universität Bonn, 2008.

[DKT07]   D. Drechsel, S. S. Kamalov, and L. Tiator, *Unitary Isobar Model - MAID2007*, Eur. Phys. J. A **34** (2007) 69, arXiv: `0710.0306 [nucl-th]`.

[DM70]   R. H. Dalitz and R. G. Moorhouse, *What is resonance?* Proc. Roy. Soc. Lond. A **318** (1970) 279.

[Dre+99]   D. Drechsel, O. Hanstein, S. S. Kamalov, and L. Tiator, *A Unitary isobar model for pion photoproduction and electroproduction on the proton up to 1 GeV*, Nucl. Phys. A **645** (1999) 145, arXiv: `nucl-th/9807001`.

[Dre04]   P. Drexler, *Entwicklung und Aufbau der neuen TAPS-Elektronik*, Ph.D. thesis: Justus-Liebig-Universität Giessen, 2004.

[Dug+13]   M. Dugger et al. (CLAS Collaboration), *Beam asymmetry Σ for π^+ and π^0 photoproduction on the proton for photon energies from 1.102 to 1.862 GeV*, Phys. Rev. C **88**.6 (2013) 065203, arXiv: `1308.4028 [nucl-ex]`; M. Dugger et al. (CLAS Collaboration), *Addendum: Beam asymmetry Σ for π^+ and π^0 photoproduction on the proton for photon energies from 1.102 to 1.862 GeV*, Phys. Rev. C **89**.2 (2014) 029901.

[Dur+08]   S. Durr et al., *Ab-Initio Determination of Light Hadron Masses*, Science **322** (2008) 1224, arXiv: `0906.3599 [hep-lat]`.

[Dut16]   H. Dutz, Private communication, 2016.

[EB64]   F. Englert and R. Brout, *Broken Symmetry and the Mass of Gauge Vector Mesons*, Phys. Rev. Lett. **13** (1964) 321.

[Ebe12]   H. Eberhardt, *Bestimmung von Polarisationsobservablen in der π^0 und ω Photoproduktion am Proton mit dem CBELSA/TAPS-Experiment*, Ph.D. thesis: Rheinische Friedrich-Wilhelms-Universität Bonn, 2012.

[Edw+11]   R. G. Edwards, J. J. Dudek, D. G. Richards, and S. J. Wallace, *Excited state baryon spectroscopy from lattice QCD*, Phys. Rev. D **84** (2011) 074508, arXiv: `1104.5152 [hep-ph]`.

[Ehm00]   A. Ehmanns, *Entwicklung, Aufbau und Test eines neuen Auslesesystems für den Crystal-Barrel-Detektor zur Messung photoinduzierter Reaktionen an ELSA*, Ph.D. thesis: Rheinische Friedrich-Wilhelms-Universität Bonn, 2000.

[Els+07]   D. Elsner et al. (CBELSA/TAPS Collaboration), *Measurement of the beam asymmetry in η-photoproduction off the proton*, Eur. Phys. J. A **33** (2007) 147, arXiv: `nucl-ex/0702032`.

[Els+09]   D. Elsner et al. (CBELSA/TAPS Collaboration), *Linearly polarised photon beams at ELSA and measurement of the beam asymmetry in π^0-photoproduction off the proton*, Eur. Phys. J. A **39** (2009) 373, arXiv: `0810.1849 [nucl-ex]`.

[Els07]   D. Elsner, *Untersuchung kleiner Partialwellenbeiträge in der Nähe dominierender Resonanzzustände des Protons mit linear polarisierten Photonen*, Ph.D. thesis: Rheinische Friedrich-Wilhelms-Universität Bonn, 2007.

[Fel+76]   P. Feller, M. Fukushima, N. Horikawa, et al., *The Measurement of Polarized Target Asymmetry in $\gamma p \to \pi^0 p$ Between 0.4 GeV–1.0 GeV Around 100 Degrees*, Nucl. Phys. B **110** (1976) 397.

[FKL13]   W. Friedrich, P. Knipping, and M. Laue, *Interferenzerscheinungen bei Röntgenstrahlen*, Ann. Phys. **346** (1913) 971.

[Fle01]   H. Flemming, *Entwurf und Aufbau eines Zellularlogik-Triggers für das Crystal-Barrel-Experiment an der Elektronenbeschleunigeranlage ELSA*, Ph.D. thesis: Ruhr-Universität Bochum, 2001.

[For09]   K. Fornet-Ponse, *Die Photonenmarkierungsanlage für das Crystal-Barrel/TAPS-Experiment an ELSA*, Ph.D. thesis: Rheinische Friedrich-Wilhelms-Universität Bonn, 2009.

[Fro16]   F. Frommberger, Private communication, 2016.

[FTS92]   C. G. Fasano, F. Tabakin, and B. Saghai, *Spin observables at threshold for meson photoproduction*, Phys. Rev. C **46** (1992) 2430.

[Fuk+78]   M. Fukushima, N. Horikawa, R. Kajikawa, et al., *The Measurement of Polarized Target Asymmetry on $\gamma p \to \pi^0 p$ Below 1 GeV*, Nucl. Phys. B **136** (1978) 189.

Bibliography

[Fun08]   C. Funke, *Analyse der Triggerfähigkeiten zur Selektion hadronischer Ereignisse und Entwicklung eines Hochgeschwindigkeits-Triggers für den Vorwärtskonus des Crystal-Barrel-Detektors*, Ph.D. thesis: Rheinische Friedrich-Wilhelms-Universität Bonn, 2008.

[Gel62]   M. Gell-Mann, *Symmetries of baryons and mesons*, Phys. Rev. **125** (1962) 1067.

[GHK64]   G. S. Guralnik, C. R. Hagen, and T. W. B. Kibble, *Global Conservation Laws and Massless Particles*, Phys. Rev. Lett. **13** (1964) 585.

[GL84]   J. Gasser and H. Leutwyler, *Chiral Perturbation Theory to One Loop*, Annals Phys. **158** (1984) 142.

[GL85]   J. Gasser and H. Leutwyler, *Chiral Perturbation Theory: Expansions in the Mass of the Strange Quark*, Nucl. Phys. B **250** (1985) 465.

[Gla61]   S. L. Glashow, *Partial Symmetries of Weak Interactions*, Nucl. Phys. **22** (1961) 579.

[Glo00]   L. Y. Glozman, *Parity doublets and chiral symmetry restoration in baryon spectrum*, Phys. Lett. B **475** (2000) 329, arXiv: `hep-ph/9908207 [hep-ph]`.

[Glo04]   L. Y. Glozman, *Chiral multiplets of excited mesons*, Phys. Lett. B **587** (2004) 69, arXiv: `hep-ph/0312354 [hep-ph]`.

[Glo07]   L. Y. Glozman, *Restoration of chiral and U(1)A symmetries in excited hadrons*, Phys. Rept. **444** (2007) 1, arXiv: `hep-ph/0701081 [hep-ph]`.

[Gol61]   J. Goldstone, *Field Theories with Superconductor Solutions*, Nuovo Cim. **19** (1961) 154.

[Gor+74]   V. G. Gorbenko, A. I. Derebchinskii, Y. V. Zhebrovskii, et al., *Proton polarization in $\gamma + p \to \pi^0 + p$ reaction on a linearly polarized photon beam*, Pisma Zh. Eksp. Teor. Fiz. **19** (1974) 659.

[Gor+75]   V. G. Gorbenko, A. I. Derebchinsky, Y. V. Zhebrovsky, et al., *Measurement of the Longitudinal Component of Proton Polarization in $\gamma p \to \pi^0 p$ Reaction on Linearly Polarized Photons*, Pisma Zh. Eksp. Teor. Fiz. **22** (1975) 393.

[Gor+78]   V. G. Gorbenko, A. I. Derebchinsky, Y. V. Zhebrovsky, et al., *Measurement of Polarization of Secondary Proton from $\gamma p \to \pi^0 p$ Reaction with Polarized Photons at Energies of 360 MeV, 400 MeV, 450 MeV, 500 MeV*, Yad. Fiz. **27** (1978) 1204.

[GOR68]   M. Gell-Mann, R. J. Oakes, and B. Renner, *Behavior of current divergences under $SU_3 \times SU_3$*, Phys. Rev. **175** (1968) 2195.

[Got+14]   M. Gottschall et al. (CBELSA/TAPS Collaboration), *First measurement of the helicity asymmetry for* $\gamma p \to p\pi^0$ *in the resonance region*, Phys. Rev. Lett. **112** (2014) 012003, arXiv: `1312.2187 [nucl-ex]`.

[Got09]   M. Gottschall, *Documentation of the TAPS Energy Calibration*, CB-Note, 2009.

[Got13]   M. Gottschall, *Bestimmung der Doppelpolarisationsobservablen E für die Reaktion* $\gamma p \to p\pi^0$ *am CBELSA/TAPS-Experiment*, Ph.D. thesis: Rheinische Friedrich-Wilhelms-Universität Bonn, 2013.

[Got14]   M. Gottschall, Private communication, 2014.

[GR96]   L. Y. Glozman and D. O. Riska, *Quark model explanation of the* $N^* \to N\eta$ *branching ratios*, Phys. Lett. B **366** (1996) 305, arXiv: `hep-ph/9508327`.

[Gro99]   D. J. Gross, *Twenty five years of asymptotic freedom*, in: QCD'98. Proceedings, 3rd Euroconference, 6th Conference, Montpellier, France, July 2-8, 1998. Nucl. Phys. Proc. Suppl. **74** (1999) 426, arXiv: `hep-th/9809060`.

[Grü06]   M. Grüner, *Modifikation und Test des Innendetektors für das Crystal Barrel Experiment*, Diploma thesis: Rheinische Friedrich-Wilhelms-Universität Bonn, 2006.

[Grü16a]   M. Grüner, Private communication, 2016.

[Grü16b]   M. Grüner, *Bestimmung der Doppelpolarisationsobservablen G in der Reaktion* $\gamma p \to p\eta$ *am CBELSA/TAPS-Experiment*, Ph.D. thesis: Rheinische Friedrich-Wilhelms-Universität Bonn, 2016.

[Gut+14]   E. Gutz et al. (CBELSA/TAPS Collaboration), *High statistics study of the reaction* $\gamma p \to p\pi^0\eta$, Eur. Phys. J. A **50** (2014) 74, arXiv: `1402.4125 [nucl-ex]`.

[GW73]   D. J. Gross and F. Wilczek, *Asymptotically Free Gauge Theories. 1*, Phys. Rev. D **8** (1973) 3633; D. J. Gross and F. Wilczek, *Asymptotically Free Gauge Theories. 2*, Phys. Rev. D **9** (1974) 980.

[H+14]   J. Hartmann, H. Dutz, A. V. Anisovich, et al. (CBELSA/TAPS Collaboration), *The* $N(1520)3/2^-$ *helicity amplitudes from an energy-independent multipole analysis based on new polarization data on photoproduction of neutral pions*, Phys. Rev. Lett. **113** (2014) 062001, arXiv: `1407.2163 [nucl-ex]`.

[H+15]   J. Hartmann, H. Dutz, et al. (CBELSA/TAPS Collaboration), *The polarization observables T, P, and H and their impact on* $\gamma p \to p\pi^0$ *multipoles*, Phys. Lett. B **748** (2015) 212, arXiv: `1506.06226 [nucl-ex]`.

[Hän17]   P. Hänisch, Private communication, 2017.

[Har08]   J. Hartmann, *Zeitkalibrierung und Photonenflussbestimmung für das Crystal-Barrel-Experiment an ELSA*, Diploma thesis: Rheinische Friedrich-Wilhelms-Universität Bonn, 2008.

[Her+77]   H. Herr, D. Husmann, W. Jansen, et al., *Forward Photoproduction of Neutral Pions on Polarized Protons in the Third Resonance Region*, Nucl. Phys. B **125** (1977) 157.

[Heu+70]   C. A. Heusch, C. Y. Prescott, L. S. Rochester, and B. D. Winstein, *Recoil Proton Polarization in Eta Photoproduction*, Phys. Rev. Lett. **25** (1970) 1381.

[Hig64]   P. W. Higgs, *Broken Symmetries and the Masses of Gauge Bosons*, Phys. Rev. Lett. **13** (1964) 508.

[Hil00]   W. Hillert, *Erzeugung eines Nutzstrahls spinpolarisierter Elektronen an der Beschleunigeranlage ELSA*, Habilitationschrift: Rheinische Friedrich-Wilhelms-Universität Bonn, 2000.

[Hil06]   W. Hillert, *The Bonn electron stretcher accelerator ELSA: Past and future*, Eur. Phys. J. A **28S1** (2006) 139.

[Hof04]   P. Hoffmeister, *Konzipierung der Analogsignalverarbeitung für den Crystal Barrel Vorwärtsdetektor*, Diploma thesis: Rheinische Friedrich-Wilhelms-Universität Bonn, 2004.

[Hof16]   P. Hoffmeister, Private communication, 2016.

[Höh97]   G. Höhler, *Against Breit-Wigner parameters—a pole-emic*, in: The Review of Particle Physics [Cas+98] (1997) 624.

[Hon+71]   M. Hongoh, K. Kikuchi, H. Kobayakawa, et al., *Differential cross-section and recoil proton polarization of η-meson photoproduction at 890 MeV*, Lett. Nuovo Cim. **2S2** (1971) 317.

[IK77]   N. Isgur and G. Karl, *Hyperfine Interactions in Negative Parity Baryons*, Phys. Lett. B **72** (1977) 109.

[IK79]   N. Isgur and G. Karl, *Positive Parity Excited Baryons in a Quark Model with Hyperfine Interactions*, Phys. Rev. D **19** (1979) 2653.

[Jae+11]   I. Jaegle et al. (CBELSA/TAPS Collaboration), *Quasi-free photoproduction of η-mesons off the deuteron*, Eur. Phys. J. A **47** (2011) 89, arXiv: `1107.2046 [nucl-ex]`.

[Jan+00]   S. Janssen, W. Doring, V. Metag, and R. Novotny, *The new charged-particle veto detector for the photon spectrometer TAPS*, IEEE Trans. Nucl. Sci. **47** (2000) 798.

[Jay57]   E. T. Jaynes, *Information Theory and Statistical Mechanics*, Phys. Rev. **106** (1957) 620.

[JPS06]   R. L. Jaffe, D. Pirjol, and A. Scardicchio, *Parity doubling among the baryons*, Phys. Rept. **435** (2006) 157, arXiv: `hep-ph/0602010 [hep-ph]`.

[JR75]   F. James and M. Roos, *MINUIT: A System for Function Minimization and Analysis of the Parameter Errors and Correlations*, Comput. Phys. Commun. **10** (1975) 343.

[Jul+08]   B. Julia-Diaz, T.-S. H. Lee, A. Matsuyama, et al.,
            Dynamical coupled-channels effects on pion photoproduction,
            Phys. Rev. C **77** (2008) 045205, arXiv: `0712.2283 [nucl-th]`.

[Jun00]   J. Junkersfeld, *Kalibration des Crystal-Barrel-ELSA Detektors mit Hilfe der*
            Reaktion $\gamma p \to p\pi^0$,
            Diploma thesis: Rheinische Friedrich-Wilhelms-Universität Bonn, 2000.

[Kai07]   D. Kaiser, *Aufbau und Test des Gas-Cerenkov-Detektors für den*
            Crystal-Barrel-Aufbau an ELSA,
            Diploma thesis: Rheinische Friedrich-Wilhelms-Universität Bonn, 2007.

[Kal11]   F. Kalischewski, *Development of a new simulation for the CBELSA/TAPS*
            experiment using Virtual Monte Carlo,
            Diploma thesis: Rheinische Friedrich-Wilhelms-Universität Bonn, 2011.

[Kam+09]   H. Kamano, B. Julia-Diaz, T.-S. H. Lee, et al., *Double and single pion*
            photoproduction within a dynamical coupled-channels model,
            Phys. Rev. C **80** (2009) 065203, arXiv: `0909.1129 [nucl-th]`.

[Kas+09]   V. L. Kashevarov et al. (Crystal Ball at MAMI, TAPS, and A2
            Collaborations),
            Photoproduction of $\pi^0\eta$ on protons and the $\Delta(1700)D_{33}$-resonance,
            Eur. Phys. J. A **42** (2009) 141, arXiv: `0901.3888 [hep-ex]`.

[Kat+80]   S. Kato, T. Miyachi, K. Sugano, et al.,
            Recoil Proton Polarization of Neutral Pion Photoproduction From Proton in
            the Energy Range Between 400 MeV and 1142 MeV,
            Nucl. Phys. B **168** (1980) 1.

[Kla11]   F. Klarner, *Konzeption, Aufbau und Inbetriebnahme eines neuen*
            Vorbeschleunigersystems an ELSA,
            Ph.D. thesis: Rheinische Friedrich-Wilhelms-Universität Bonn, 2011.

[Kre+00]   O. Krehl, C. Hanhart, S. Krewald, and J. Speth,
            What is the structure of the Roper resonance?
            Phys. Rev. C **62** (2000) 025207, arXiv: `nucl-th/9911080`.

[KS03]   B. Krusche and S. Schadmand,
            Study of nonstrange baryon resonances with meson photoproduction,
            Prog. Part. Nucl. Phys. **51** (2003) 399, arXiv: `nucl-ex/0306023`.

[KSW95]   N. Kaiser, P. B. Siegel, and W. Weise,
            Chiral dynamics and the $S_{11}(1535)$ nucleon resonance,
            Phys. Lett. B **362** (1995) 23, arXiv: `nucl-th/9507036`.

[KW12]   E. Klempt and R. L. Workman, *N and Δ Resonances*,
            in: The Review of Particle Physics [Ber+12] (2012) 1268.

[Lan55]   L. Landau, in: Niels Bohr and the Development of Physics ed. by W. Pauli,
            McGraw-Hill, (1955).

[Liv09]   K. Livingston, *The Stonehenge Technique. A new method for aligning coherent bremsstrahlung radiators*, Nucl. Instrum. Meth. A **603** (2009) 205, arXiv: 0809.1739 [nucl-ex].

[LMP01]   U. Löring, B. C. Metsch, and H. R. Petry, *The Light baryon spectrum in a relativistic quark model with instanton induced quark forces: The Nonstrange baryon spectrum and ground states*, Eur. Phys. J. A **10** (2001) 395, arXiv: hep-ph/0103289.

[Lör+01]   U. Löring, K. Kretzschmar, B. C. Metsch, and H. R. Petry, *Relativistic quark models of baryons with instantaneous forces: Theoretical background*, Eur. Phys. J. A **10** (2001) 309, arXiv: hep-ph/0103287.

[M+10]   E. F. McNicoll, S. Prakhov, I. I. Strakovsky, et al. (Crystal Ball Collaboration at MAMI), *Experimental study of the $\gamma p \to \eta p$ reaction with the Crystal Ball detector at the Mainz Microtron (MAMI-C)*, Phys. Rev. C **82** (2010) 035208, arXiv: 1007.0777 [nucl-ex]; E. F. McNicoll, S. Prakhov, I. I. Strakovsky, et al. (Crystal Ball Collaboration at MAMI), *Erratum: Experimental study of the $\gamma p \to \eta p$ reaction with the Crystal Ball detector at the Mainz Microtron (MAMI-C)*, Phys. Rev. C **84** (2011) 029901.

[M+17]   J. Müller, J. Hartmann, M. Grüner, et al. (CBELSA/TAPS Collaboration), *New data on $\vec{\gamma}\vec{p} \to \eta p$ with polarized photons and protons and their implications for $N^* \to N\eta$ decays*, submitted to Phys. Lett. B, 2017.

[Mag+13]   Y. Maghrbi et al. (Crystal Ball at MAMI, TAPS, and A2 Collaborations), *Coherent photoproduction of π^0- and η-mesons off ^7Li*, Eur. Phys. J. A **49** (2013) 38, arXiv: 1303.2254 [nucl-ex].

[Mal61]   J. O. Maloy, *Polarization of Recoil Protons from the Photoproduction of Neutral Pions in Hydrogen at 585 and 660 MeV*, Ph.D. thesis: California Institute of Technology, 1961.

[Man58]   S. Mandelstam, *Determination of the pion - nucleon scattering amplitude from dispersion relations and unitarity. General theory*, Phys. Rev. **112** (1958) 1344.

[Mar+02]   P. Marciniewski, K. Fransson, L. Gustafsson, and H. Calen, *A fast programmable trigger system for the WASA experiment*, IEEE Trans. Nucl. Sci. **49** (2002) 312.

[MBM12]   M. Mai, P. C. Bruns, and U.-G. Meißner, *Pion photoproduction off the proton in a gauge-invariant chiral unitary framework*, Phys. Rev. D **86** (2012) 094033, arXiv: 1207.4923 [nucl-th].

[Met08]   B. Metsch, *Quark models*, in: Proceedings, 6th International Workshop on the Physics of Excited Nucleons (NSTAR 2007). Eur. Phys. J. A **35** (2008) 275.

[MSL07]   A. Matsuyama, T. Sato, and T. .-.-S. H. Lee, *Dynamical coupled-channel model of meson production reactions in the nucleon resonance region*, Phys. Rept. **439** (2007) 193, arXiv: nucl-th/0608051 [nucl-th].

[MU49]   N. Metropolis and S. Ulam, *The Monte Carlo Method*,
J. Amer. Stat. Assoc. **44** (1949) 335.

[Mül07] J. Müller, *Bestimmung einer Energiekorrekturfunktion für das Kalorimeter des Crystal-Barrel-Experiments an ELSA*,
Diploma thesis: Rheinische Friedrich-Wilhelms-Universität Bonn, 2007.

[Mül15] J. Müller, Private communication, 2015.

[Mül17] J. Müller, *Bestimmung der Doppelpolarisationsobservablen E in der Reaktion $\gamma p \to p\eta$ am CBELSA/TAPS-Experiment*, Ph.D. thesis in preparation:
Rheinische Friedrich-Wilhelms-Universität Bonn, 2017.

[Nak+10] K. Nakamura et al. (Particle Data Group), *The Review of Particle Physics*,
J. Phys. G **37** (2010) 075021.

[Nam60] Y. Nambu,
Quasiparticles and Gauge Invariance in the Theory of Superconductivity,
Phys. Rev. **117** (1960) 648.

[Nan+13] M. Nanova et al. (CBELSA/TAPS Collaboration),
Determination of the η'-nucleus optical potential,
Phys. Lett. B **727** (2013) 417, arXiv: `1311.0122` `[nucl-ex]`.

[Nat+03] F. A. Natter, P. Grabmayr, T. Hehl, et al., *Monte Carlo simulation and analytical calculation of coherent bremsstrahlung and its polarisation*,
Nucl. Instrum. Meth. B **211** (2003) 465.

[Nec93] M. Neckenig,
Theoretische und experimentelle Untersuchungen zur Verbesserung der Zeitstruktur des extrahierten Strahles aus dem Stretcherring ELSA,
Ph.D. thesis: Rheinische Friedrich-Wilhelms-Universität Bonn, 1993.

[Nee61] Y. Ne'eman, *Derivation of strong interactions from a gauge invariance*,
Nucl. Phys. **26** (1961) 222.

[Nik+08] V. A. Nikonov, A. V. Anisovich, E. Klempt, et al.,
Further evidence for $N(1900)P_{13}$ from photoproduction of hyperons,
Phys. Lett. B **662** (2008) 245, arXiv: `0707.3600` `[hep-ph]`.

[Nov91] R. Novotny (TAPS Collaboration), *The BaF_2 photon spectrometer TAPS*,
IEEE Trans. Nucl. Sci. **38** (1991) 379.

[Oli+14] K. Olive et al. (Particle Data Group), *The Review of Particle Physics*,
Chin. Phys. C **38** (2014) 090001.

[OM59]   H. Olsen and L. C. Maximon, *Photon and Electron Polarization in High-Energy Bremsstrahlung and Pair Production with Screening*,
Phys. Rev. **114** (1959) 887.

[PG08]   D.-M. Piontek and M. Grüner, *Hit-Reconstruction in ChaPI*, CB-Note, 2008.

[Pus12] T. Pusch, *Bestimmung von Intensität und Position des extrahierten Elektronenstrahls an ELSA mittels Hochfrequenzresonatoren*,
Ph.D. thesis: Rheinische Friedrich-Wilhelms-Universität Bonn, 2012.

[RD04]   C. C. Rohlof and H. Dutz, *Effective densities and polarizations of the targets for the GDH-experiments at MAMI and ELSA*, Nucl. Instrum. Meth. A **526** (2004) 126.

[Rei+95]   G. Reicherz, C. Bradtke, H. Dutz, et al., *The Bonn polarized target NMR system*, Nucl. Instrum. Meth. A **356** (1995) 74.

[Rei94]   G. Reicherz, *Kontroll- und NMR-System eines polarisierten Festkörpertargets*, Ph.D. thesis: Rheinische Friedrich-Wilhelms-Universität Bonn, 1994.

[Roh03]   C. Rohlof, *Entwicklung polarisierter Targets zur Messung der Gerasimov-Drell-Hearn-Summenregel an ELSA*, Ph.D. thesis: Rheinische Friedrich-Wilhelms-Universität Bonn, 2003.

[Rön+13]   D. Rönchen, M. Döring, F. Huang, et al., *Coupled-channel dynamics in the reactions $\pi N \to \pi N$, ηN, $K\Lambda$, $K\Sigma$*, Eur. Phys. J. A **49** (2013) 44, arXiv: 1211.6998 [nucl-th].

[Rön+14]   D. Rönchen, M. Döring, F. Huang, et al., *Photocouplings at the Pole from Pion Photoproduction*, Eur. Phys. J. A **50** (2014) 101, arXiv: 1401.0634 [nucl-th]; D. Rönchen, M. Döring, F. Huang, et al., *Erratum to: Photocouplings at the Pole from Pion Photoproduction*, Eur. Phys. J. A **51** (2015) 63.

[Rön+15]   D. Rönchen, M. Döring, H. Haberzettl, et al., *Eta photoproduction in a combined analysis of pion- and photon-induced reactions*, Eur. Phys. J. A **51** (2015) 70, arXiv: 1504.01643 [nucl-th].

[Sal68]   A. Salam, *Weak and Electromagnetic Interactions*, in: 8th Nobel Symposium Lerum, Sweden, May 19-25, 1968. Conf. Proc. **C680519** (1968) 367.

[San+11]   A. M. Sandorfi, S. Hoblit, H. Kamano, and T.-S. H. Lee, *Determining pseudoscalar meson photo-production amplitudes from complete experiments*, J. Phys. G **38** (2011) 053001, arXiv: 1010.4555 [nucl-th].

[San+12]   A. M. Sandorfi, B. Dey, A. Sarantsev, et al., *A Rosetta Stone Relating Conventions In Photo-Meson Partial Wave Analyses*, AIP Conf. Proc. **1432** (2012) 219, arXiv: 1108.5411 [nucl-th].

[Sar16]   A. Sarantsev, Private communication, 2016.

[Sch+01]   A. Schmidt et al., *Test of Low-Energy Theorems for $p(\vec{\gamma}, \pi^0)p$ in the Threshold Region*, Phys. Rev. Lett. **87** (2001) 232501, arXiv: nucl-ex/0105010; A. Schmidt et al., *Erratum: Test of Low-Energy Theorems for $p(\vec{\gamma}, \pi^0)p$ in the Threshold Region*, Phys. Rev. Lett. **110** (2013) 039903.

[Sch+10]   S. Schumann et al. (Crystal Ball at MAMI, TAPS, and A2 Collaborations), *Radiative π^0 photoproduction on protons in the $\Delta^+(1232)$ region*, Eur. Phys. J. A **43** (2010) 269, arXiv: 1001.3626 [hep-ex].

[Sch13]   C. Schmidt, Private communication, 2013.

[Sei09]   T. Seifen, *Verbesserung der Rekonstruktion und Entwicklung eines First-Level-Triggerschemas für das Crystal-Barrel-Kalorimeter*, Diploma thesis: Rheinische Friedrich-Wilhelms-Universität Bonn, 2009.

[Sei17]   T. Seifen, Ph.D. thesis in preparation: Rheinische Friedrich-Wilhelms-Universität Bonn, 2017.

[SLM12]   V. Shklyar, H. Lenske, and U. Mosel, *Giessen coupled-channel model for pion- and photon-induced reactions*, AIP Conf. Proc. **1432** (2012) 349.

[SLM13]   V. Shklyar, H. Lenske, and U. Mosel, *η-meson production in the resonance-energy region*, Phys. Rev. C **87** (2013) 015201, arXiv: `1206.5414 [nucl-th]`.

[Sok+15a] V. Sokhoyan et al. (CBELSA/TAPS Collaboration), *Data on I^s and I^c in $\overrightarrow{\gamma}p \to p\pi^0\pi^0$ reveal cascade decays of $N(1900)$ via $N(1520)\pi$*, Phys. Lett. B **746** (2015) 127.

[Sok+15b] V. Sokhoyan et al. (CBELSA/TAPS Collaboration), *High statistics study of the reaction $\gamma p \to p\,2\pi^0$*, Eur. Phys. J. A **51** (2015) 95, arXiv: `1507.02488 [nucl-ex]`; V. Sokhoyan et al. (CBELSA/TAPS Collaboration), *Erratum: High statistics study of the reaction $\gamma p \to p\,2\pi^0$*, Eur. Phys. J. A **51** (2015) 187.

[Spa+10]   N. Sparks et al. (CBELSA/TAPS Collaboration), *Measurement of the Beam Asymmetry Σ in the Forward Direction for $\vec{\gamma}p \to p\pi^0$ Photoproduction*, Phys. Rev. C **81** (2010) 065210, arXiv: `1003.1346 [nucl-ex]`.

[Spi17]   K. Spieker, Ph.D. thesis in preparation: Rheinische Friedrich-Wilhelms-Universität Bonn, 2017.

[Str+76]   W. Struczinski et al. (Aachen-Hamburg-Heidelberg-München Collaboration), *Study of photoproduction on hydrogen in a streamer chamber with tagged photons for 1.6 GeV < E_γ < 6.3 GeV*, Nucl. Phys. B **108** (1976) 45.

[Suf+05]   G. Suft, G. Anton, R. Bogendorfer, et al., *A scintillating fibre detector for the Crystal Barrel experiment at ELSA*, Nucl. Instrum. Meth. A **538** (2005) 416.

[SV08]   M. Shifman and A. Vainshtein, *Highly Excited Mesons, Linear Regge Trajectories and the Pattern of the Chiral Symmetry Realization*, Phys. Rev. D **77** (2008) 034002, arXiv: `0710.0863 [hep-ph]`.

[Swi13]   M. Switka, *Optical Beam Diagnosis at ELSA Based on a Streak Camera System with Picosecond Temporal Resolution*, Master thesis: Rheinische Friedrich-Wilhelms-Universität Bonn, 2013.

[T+08]   U. Thoma, M. Fuchs, et al. (CB-ELSA Collaboration), *N^* and Δ^* decays into $N\pi^0\pi^0$*, Phys. Lett. B **659** (2008) 87, arXiv: `0707.3592 [hep-ph]`.

[Tar07]   C. M. Tarbert, *Coherent π^0 photoproduction on nuclei*,
          Ph.D. thesis: University of Edinburgh, School of Physics, 2007.

[Thi+12] A. Thiel et al. (CBELSA/TAPS Collaboration), *Well-established nucleon
          resonances revisited by double-polarization measurements*,
          Phys. Rev. Lett. **109** (2012) 102001, arXiv: `1207.2686 [nucl-ex]`.

[Thi+15] A. Thiel et al. (CBELSA/TAPS Collaboration),
          Three-body nature of N^* and Δ^* resonances from sequential decay chains,
          Phys. Rev. Lett. **114** (2015) 091803, arXiv: `1501.02094 [nucl-ex]`.

[Thi+17] A. Thiel et al. (CBELSA/TAPS Collaboration), *Double-polarization
          observable G in neutral-pion photoproduction off the proton*,
          Eur. Phys. J. A **53** (2017) 8, arXiv: `1604.02922 [nucl-ex]`.

[Thi12]   A. Thiel,
          Bestimmung der Doppelpolarisationsobservablen G in π^0-Photoproduktion,
          Ph.D. thesis: Rheinische Friedrich-Wilhelms-Universität Bonn, 2012.

[Tia+99] L. Tiator, D. Drechsel, G. Knochlein, and C. Bennhold, *Analysis of
          resonance multipoles from polarization observables in eta photoproduction*,
          Phys. Rev. C **60** (1999) 035210, arXiv: `nucl-th/9902028`.

[Tia12]   L. Tiator, *Towards a model-independent partial wave analysis for
          pseudoscalar meson photoproduction*, AIP Conf. Proc. **1432** (2012) 162,
          arXiv: `1109.0608 [nucl-th]`.

[Tim69]   U. Timm, *Coherent bremsstrahlung of electrons in crystals*,
          Fortsch. Phys. **17** (1969) 765.

[Upp74]   D. Upper, *The unsuccessful self-treatment of a case of writer's block*,
          J. Appl. Behav. Anal. **7.3** (1974) 497.

[Wal16]   D. Walther, Private communication, 2016.

[Wat54]   K. M. Watson, *Some General Relations between the Photoproduction and
          Scattering of π Mesons*, Phys. Rev. **95** (1954) 228.

[WBT14]   Y. Wunderlich, R. Beck, and L. Tiator, *The complete-experiment problem of
          photoproduction of pseudoscalar mesons in a truncated partial-wave analysis*,
          Phys. Rev. C **89** (2014) 055203.

[Wei67]   S. Weinberg, *A Model of Leptons*, Phys. Rev. Lett. **19** (1967) 1264.

[Wen08]   C. Wendel, *Design und Aufbau eines Szintillationsdetektors zur
          Identifizierung geladener Teilchen im Crystal-Barrel-Vorwärtsdetektor*,
          Ph.D. thesis: Rheinische Friedrich-Wilhelms-Universität Bonn, 2008.

[Wil05]   F. Wilczek, *Asymptotic freedom: From paradox to paradigm*,
          Rev. Mod. Phys. **77** (2005) 857, arXiv: `hep-ph/0502113`.

[Wil74]   K. G. Wilson, *Confinement of Quarks*, Phys. Rev. D **10** (1974) 2445.

[Win06]   A. Winnebeck, *Entwicklung und Implementierung eines universellen, FPGA
          basierten Triggermoduls für das Crystal-Barrel-Experiment an ELSA*,
          Diploma thesis: Rheinische Friedrich-Wilhelms-Universität Bonn, 2006.

[Wor+12a]   R. L. Workman, W. J. Briscoe, M. W. Paris, and I. I. Strakovsky,
Updated SAID analysis of pion photoproduction data,
Phys. Rev. C **85** (2012) 025201, arXiv: `1109.0722` `[hep-ph]`.

[Wor+12b]   R. L. Workman, M. W. Paris, W. J. Briscoe, and I. I. Strakovsky,
Unified Chew-Mandelstam SAID analysis of pion photoproduction data,
Phys. Rev. C **86** (2012) 015202, arXiv: `1202.0845` `[hep-ph]`.

[WTS13]   R. L. Workman, L. Tiator, and A. Sarantsev,
Baryon photo-decay amplitudes at the pole, Phys. Rev. C **87** (2013) 068201,
arXiv: `1304.4029` `[nucl-th]`.

[Wu+05]   C. Wu et al., *Photoproduction of ρ^0-mesons and Δ-baryons in the reaction
$\gamma p \to p\pi^+\pi^-$ at energies up to $\sqrt{s} = 2.6$ GeV*,
Eur. Phys. J. A **23** (2005) 317.

[Wun12]   Y. Wunderlich,
Studies on a complete experiment for pseudoscalar meson photoproduction,
Diploma thesis: Rheinische Friedrich-Wilhelms-Universität Bonn, 2012.

[Wun17]   Y. Wunderlich, Ph.D. thesis in preparation: Rheinische
Friedrich-Wilhelms-Universität Bonn, 2017.

[Zou08]   B. S. Zou, *On the nature of the lowest $1/2^-$ baryon nonet and decuplet*,
in: Proceedings, 6th International Workshop on the Physics of Excited
Nucleons (NSTAR 2007). Eur. Phys. J. A **35** (2008) 325,
arXiv: `0711.4860` `[nucl-th]`.

[Zwe64]   G. Zweig, *An SU(3) model for strong interaction symmetry and its breaking*,
in: Developments in the Quark Theory of Hadrons, Vol. 1. 1964 – 1978
ed. by D. Lichtenberg and S. P. Rosen, (1964) 22,
URL: `http://inspirehep.net/record/4674/files/cern-th-412.pdf`.

Acknowledgment